In Loving Memory of My Mother

THE EFFECT OF SHAPE, SIZE AND FLEXIBILITY ON THE IMPACT DAMAGE OF COMPOSITE MATERIALS

by

Michael Wing Fat Yau

A thesis submitted for the degree of Doctor of Philosophy of the University of London

September 2003

Strength of Materials Section,
Department of Mechanical Engineering,
Imperial College London,
Exhibition Road
London
SW7 2AZ

Abstract

Polymer composites of many different structures employing different matrix and fibre materials continue to find an increasing number of applications. This is particularly so when materials of low mass, high strength and low maintenance cost are important. A key factor for many applications, where, for example, the composite panels could be subject to vibrations, flexure, impact and other conditions that could cause well hidden partial damage, are methods for assessing the propensity to this type of damage. This is to include a measure of the extent and effect of the partial damage produced on the strength and subsequent durability of the composite material.

Composite panels of varying length, width, and thickness and of different constituent materials have been studied. This includes panels that are flat and curved. For the impact studies, it is shown how the different degrees of flexibility of the panel can affect the extent of partial impact damage that is inflicted. This is for a variety of different impact conditions that include the use of low mass, high velocity impacts and high mass, low velocity impacts. The dynamic behaviour of panels of different size and shape is captured using high-speed photography and sensors are used to produce force-time and related data. A model, based on an established two degrees of freedom spring-mass model, has been developed in order to model and predict impact response of tested composite laminates. This model also tries to incorporate the effect of damage on the impact response by reducing the stiffness of the laminate when damage occurs.

The way and extent a panel can flex is dependent on a number of factors. This includes the shape, size and mass of the panel, the static deformation to which it is subjected and the physical constraints acting at the boundary of the panel. The degrees of freedom the panel has to deflect or vibrate depend on the point it is struck. In some cases, it can be that the form, shape and static stresses on a panel can provide regions that are more prone to partial damage than others. The partial damage that occurs has a significant affect on the impact response and it has been shown that these effects can be adequately modeled.

Acknowledgements

Firstly I would like to thank my supervisor, Dr. John P. Dear, for allowing me this opportunity to pursue a field of research that I was interested in, providing me with support and advice, and allowing me the freedom to explore areas according to my instincts.

My appreciation goes out to my fellow research students, Mr. Hoon Lee and Mr. Seung Tek Oh, for keeping me entertained during my studies and providing some very helpful support in my practical work when times got hectic.

There have been many members of staff that have been available to provide training on the use of all the various machines and equipment necessary for the research reported here to be completed. From the Centre for Composite Materials, Mr. Gary Senior and Mr. Russell Stracey, provided great advice and help with respect to the preparation and machining of the composite samples. Mr. Ian James provided superb instruction on the use of the Drop Weight Facility in the Department of Aeronautics. Mr. Bill Godwin from The Centre of Composite Materials and Dr. Jonathon Allin of The Non-Destructive Testing Group provided great advice on the use of the C-Scan Facilities in their respective research groups.

Thanks go out to members of the Composites Research Group at Qinetiq (formerly known as DERA) for providing me with the curved composite laminates used in part of this study, and for the X-radiography performed there and the advice in the interpretation of the X-radiographs.

Materials were also provided by BAE, for the other studies that were performed so my thanks go to Dr. Dave Townsend and Dr. Martin Gaitonde for sending me useful materials.

On a personal level I need to thank my family for never giving up on me and believing that I would complete this part of my studies. My friends and the Wardening Staff at Clayponds (Mark, Sue, Paul, Stu, Siew Ling and Monah) for bearing with me for the last 4 years.

Finally my thanks and love go to my girlfriend, Wai May, for being there for me through all the good and bad times during the two and half years of our relationship. Thanks for the continued financial support for the last 12 months and being on hand to keep me on track. Thanks for always believing in me.

Table of Contents

Title Page 1
Abstract 2
Acknowledgements 3
Table of Contents 4
List of Figure 7
List of Tables 14

1. Introduction 15
2. Literature Review 18
2.1 Impact 18
2.1.1 Impact Definitions 18
2.1.2 The Impact Event 19
2.1.2.1 Contact Mechanics 19
2.1.2.2 Contact Dynamics 28
2.1.3 Dynamic Response of Composites to an Impact Event 36
2.1.3.1 Dynamic Properties of Composites 36
2.1.3.2 Wave Motions in Composites 37
2.1.3.3 Wave Motions in Composites Under Impact 40
2.2 Impact Damage 43
2.2.1 Low Velocity Impact Damage Development 46
2.3 The Factors that Effect The Impact Response and Impact Damage Development in Composite Materials 57
2.3.1 Effects of Impact Conditions 57
2.3.2 Effects of Material Constituents 59
2.3.2.1 Fibres 59
2.3.2.2 Matrix 60
2.3.2.3 The Interphase Region 62
2.3.3 Effects of Stacking Sequence 62
2.3.4 Effects of Target Geometry 65
3. Materials and Experimental Procedures 69
3.1 Materials 70
3.1.1 Curved Laminates 70
3.1.2 Flexible Thin Laminates 71
3.1.3 Laminates for Thickness and Size Effects 73
3.1.4 Materials Sectioning 74
3.2 Experimental Procedures 74
3.2.1 Clamping Unit and Arrangements 74
3.2.2 Instrumentation 77
3.2.3 Impact Tests 81
3.2.3.1 Gas Gun Impact Experiments 81
3.2.3.2 Drop Weight Impact Experiments 84
3.2.4 Post Impact Analysis 86
3.2.4.1 X-Radiography 86
3.2.4.2 Ultra-Sonic C-Scan 87
3.2.4.3 Scanning Electron Microscopy 87

4. Impact of Curved Carbon Fibre Laminates **90**
4.1 Aims and Objectives 90
4.2 Procedure 91
4.2.1 Experimental details 91
4.3 Results 95
4.3.1 High Speed Photography 95
4.3.2 Post Impact Photographs 109
4.3.3 X-Radiography 117
4.3.4 Scanning Electron Microscopy 127
4.4 Discussion 141
5. Impact of Thin Flexible Laminates **147**
5.1 Aims and Objectives 147
5.2 Procedure 147
5.2.1 Experimental Details 148
5.3 Results 154
5.3.1 High Speed Photography 154
5.3.2 Ultrasonic C-Scan 179
5.3.3 Drop Weight Data 184
5.4 Discussion 191
6. The Effect of Length, Width and Thickness on the Impact Damage of Composite Laminates **192**
6.1 Aims and Objectives 192
6.2 Procedure 192
6.3 Results 194
6.3.1 Drop Weight Data 194
6.3.1.1 Changes in Behaviour due to a Change in Dimension 196
6.3.1.1.1 Low Drop Height Impacts 196
6.3.1.1.2 Higher Drop Impacts 204
6.3.1.1.3 Discussion 209
6.3.1.2 High Energy Drops: Variations in Induced Damage due to Specimen Dimension Changes 210
6.3.1.2.1 The Effects of a change in Thickness 211
6.3.1.2.2 The Effects of a Change in Length and Width 216
6.3.1.2.3 Discussion 227
7. Modelling the Change in Impact Response due to Damage using Closed Form Solutions **229**
7.1 Closed Form Solutions for the Prediction of Impact Response 229
7.2 The Inclusion of Damage and its Effects on Impact Response 231
7.3 Modelling Method 232
7.3.1 Input Data 235
7.4 Results 235
7.5 Discussion 248
8. Discussion **249**
9. Conclusions **258**
9.1 Impact of Curved Composite Laminates 258
9.2 Impact of Thin Laminates 259
9.3 The Effects of Dimension Changes 259
9.4 Analytical Modelling 260
10. Recommendations for Future Work **261**
10.1 Experimental Work 261

10.2 Analytical Modelling 262

References **263**
Appendices **275**
Appendix 1 276
Appendix 2 288
Appendix 3 313
Appendix 4 341

List of Figures

2.1	Two bodies of revolution for Hertzian analysis of contact	21
2.2	Spring mass models	34
2.3	Interactive Dynamic Effects	36
2.4	The two types of matrix cracking	48
2.5	Typical Matrix crack and delamination pattern from line load impact on a 0/90/0 composite	51
2.6	Pine Tree (a) and Reverse Pine Tree (b) damage patterns	54
3.1	Standard convention for fibre direction notation in a composite laminate	71
3.2	Schematics of the two different sample orientations for the curved specimens	72
3.3	Schematic Drawing of the main Clamping Unit	75
3.4	Schematic with dimension for one of the two grooved supports used for holding the curved laminates for impact testing	76
3.5	Schematic of one of the two end clamping supports for impact testing of both flexible and thick laminates	77
3.6	The Hadland 468 High Speed Camera System as borrowed from the EPSRC Instrument Loan Pool	79
3.7	Schematic of the entire test set up.	80
3.8	Example of a calibration picture taken using the gas gun set-up, from which base measurements of distance were provided to the Hadlands Software for the distance and velocity measurement to be calculated	81
3.9	Schematic of camera and lighting set up when used during Drop Weight Tests	82
3.10	A typical image from drop weight testing with the distance and points used for calibration of the system	82
3.11	Schematic of the main Gas-Gun components	83
3.12	Schematic, with dimensions, of an injection-moulded sabot	84
3.13	Schematic of the role the sabot stripper plays in gas gun impact involving ball bearing projectiles	84
3.14	Schematic of Drop Weight Tower set up for Impact Testing	85
3.15	Diagram showing how each sample was sectioned for microscopy	88
4.1	A frame from a typical High Speed Photography sequence showing the specimen at rest, a section of the clamp and the incoming ball bearing projectile	96
4.2	A frame selection showing the response of the specimen to the impact event and delaninations that have reached the edge of the specimen	96
4.3	Two frames taken from the same sequence showing the ability of the specimen to flex during the impact event	97
4.4	High Speed Photography Sequence for Specimen LC6, Longitudinal Curvature, Convex Front Face at 5 Bar Pressure	99
4.5	High Speed Photography Sequence for Specimen LC11, Longitudinal Curvature, Convex Front Face at 8 Bar Pressure	100
4.6	High Speed Photography Sequence for Specimen LC15, Longitudinal Curvature, Concave Front Face at 5 Bar Pressure	101
4.7	High Speed Photography Sequence for Specimen LC18 Longitudinal Curvature concave Front Face at 8 Bar Pressure	102

4.8	High Speed Photography Sequence for Specimen TC6 Transverse Curvature Convex Front Face at 5 Bar Pressure	103
4.9	High Speed Photography Sequence for Specimen TC11 Transverse Curvature Convex Front Face at 8 Bar Pressure	104
4.10	High Speed Photography Sequence for Specimen TC7 Transverse Curvature Concave Front Face at 5 Bar Pressure	105
4.11	High Speed Photography Sequence for Specimen TC15 Transverse Curvature Concave Front Face at 8 Bar Pressure	106
4.12	Typical types of damage that can be seen by the naked eye from the post impact photographs of specimens in the three views that image were taken in	110
4.13	Post-impact Photograph of Specimen LC6: Longitudinal Curvature Convex Front Face at 5 Bar Pressure	112
4.14	Post-impact Photograph of Specimen LC11: Longitudinal Curvature Convex Front Face at 8 Bar Pressure	112
4.15	Post-impact Photograph of Specimen LC15: Longitudinal Curvature Concave Front Face at 5 Bar Pressure	113
4.16	Post-impact Photograph of Specimen LC18: Longitudinal Curvature Concave Front Face at 8 Bar Pressure	113
4.17	Post-impact Photograph of Specimen TC6: Transverse Curvature Convex Front Face at 5 Bar Pressure	114
4.18	Post-impact Photograph of Specimen TC11: Transverse Curvature Convex Front Face at 8 Bar Pressure	114
4.19	Post-impact Photograph of Specimen TC7: Transverse Curvature Concave Front Face at 5 Bar Pressure	115
4.20	Post-impact Photograph of Specimen TC16: Transverse Curvature Concave Front Face at 8 Bar Pressure	115
4.21	An example of an X-Radiograph with the types of Damage that can be Identified	117
4.22	X-Radiographs for Specimen LC6 (Longitudinal Curvature Convex Front Face at 5 Bar Pressure)	120
4.23	X-Radiographs for Specimen LC11 (Longitudinal Curvature Convex Front Face at 8 Bar Pressure)	121
4.24	X-Radiographs for Specimen LC15 (Longitudinal Curvature Concave Front Face at 5 Bar Pressure)	121
4.25	X-Radiographs For Specimen LC18 (Longitudinal Curvature Concave Front Face at 8 Bar Pressure)	122
4.26	X-Radiographs for Specimen TC6 (Transverse Curvature Convex Front Face at 5 Bar Pressure)	122
4.27	X-Radiographs for Specimen TC11 (Transverse Curvature Convex Front Face at 8 Bar Pressure)	123
4.28	X-Radiograph for Specimen TC7 (Transverse Curvature Concave Front Face at 5 Bar Pressure)	123
4.39	X-Radiographs for Specimen TC16 (Transverse Curvature Concave Front Face at 8 Bar Pressure)	124
4.30	Chart Showing Damage Area of Impacted Curved Composite Panels	125
4.31	Typical micrograph with details of damage that can be viewed using electron microscopy	127
4.32	Amalgam of Micrographs for Specimen LC6 (Longitudinal Curvature with Convex Impact Face at 5 bar)	128

4.33	Amalgam of micrographs for Specimen LC11 (Longitudinal Curvature with Convex Impact Face at 8 bar)	129
4.34	Amalgam of Micrographs for Specimen LC15 (Longitudinal Curvature with Concave Impact Face at 5 bar)	130
4.35	Amalgam of Micrographs for Specimen LC18 (Longitudinal Curvature with Concave Impact Face at 8 bar)	131
4.36	Amalgam of Micrographs for Specimen TC6 (Transverse Curvature with Convex Impact Face at 5 bar)	132
4.37	Amalgam of Micrographs for Specimen TC11 (Transverse Curvature with Convex Impact Face at 8 bar)	133
4.38	Amalgam of Micrographs for Specimen TC7 (Transverse Curvature with Concave Impact Face at 5 bar)	134
4.39	Amalgam of Micrographs for Specimen TC16 (Transverse Curvature with Convex Impact Face at 8 bar)	135
4.40	Impact site of Specimen TC6 showing damage at the impact site and it's immediate surroundings	136
4.41	A comparison of the difference in depth of initial indent caused by a 5 and 8 bar impact	137
4.42	Impact areas for Specimens TC7 (a) and TC16 (b) showing the increase in depth of the crushed area directly under the impact site	138
4.43	The central impact zone from Specimen TC6, Transverse curvature impacted on the convex face at 8 bar pressure	139
4.44	Sections of micrographs taken from 8 Bar Impacts of Specimens TC11 and LC18 showing the two different types of back face spalling	140
5.1	A typical pre-impact frame from a High Speed Sequence for the impact of a thin flexible laminate	155
5.2	A typical post impact frame from the High Speed sequence showing the deforming thin flexible panel	155
5.3	High Speed Photography Sequence for Specimen CPPS1, 0.1m Drop on a 120mm x 40mm Carbon Fibre Flexible Specimen	157
5.4	High Speed Photography Sequence for Specimen CPPS7, 0.2m Drop on a 120mm x 40mm Carbon Fibre Flexible Specimen	158
5.5	High Speed Photography Sequence for Specimen CPPS9, 0.3m Drop on a 120mm x 40mm Carbon Fibre Flexible Specimen	159
5.6	High Speed Photography Sequence for Specimen CPPS13, 0.4m Drop on a 120mm x 40mm Carbon Fibre Flexible Specimen	160
5.7	High Speed Photography Sequence for Specimen CPPS16, 0.5m Drop on a 120mm x 40mm Carbon Fibre Flexible Specimen	161
5.8	High Speed Photography Sequence for Specimen GPPS3, 0.1m Drop on a 120mm x 40mm Glass Fibre Flexible Specimen	162
5.9	High Speed Photography Sequence for Specimen GPPS7, 0.2m Drop on a 120mm x 40mm Glass Fibre Flexible Specimen	163
5.10	High Speed Photography Sequence for Specimen GPPS9, 0.3m Drop on a 120mm x 40mm Glass Fibre Flexible Specimen	164
5.11	High Speed Photography Sequence for Specimen GPPS12, 0.4m Drop on a 120mm x 40mm Glass Fibre Flexible Specimen	165
5.12	High Speed Photography Sequence for Specimen GPPS16, 0.5m Drop on a 120mm x 40mm Glass Fibre Flexible Specimen	166
5.13	High Speed Photography Sequence for Specimen 1CPPS1, 0.1m Drop on a 160mm x 40mm Carbon Fibre Flexible Laminate	167

5.14	High Speed Photography Sequence for Specimen 1CPPS3, 0.2m Drop on a 160mm x 40mm Carbon Fibre Flexible Laminate	169
5.15	High Speed Photography Sequence for Specimen 1CPPS6, 0.3m Drop on a 160mm x 40mm Carbon Fibre Flexible Laminate	170
5.16	High Speed Photography Sequence for Specimen 1CPPS11, 0.4m Drop on a 160mm x 40mm Carbon Fibre Flexible Laminate	171
5.17	High Speed Photography Sequence for Specimen 1CPPS14, 0.5m Drop on a 160mm x 40mm Carbon Fibre Flexible Laminate	172
5.18	High Speed Photography Sequence for Specimen 1GPPS3, 0.1m Drop on a 160mm x 40mm R-Glass Fibre Flexible Laminate	173
5.19	High Speed Photography Sequence for Specimen 1GPPS6, 0.2m Drop on a 160mm x 40mm R-Glass Fibre Flexible Laminate	174
5.20	High Speed Photography Sequence for Specimen 1GPPS9, 0.3m Drop on a 160mm x 40mm R-Glass Fibre Flexible Laminate	175
5.21	High Speed Photography Sequence for Specimen 1CPPS13, 0.4m Drop on a 160mm x 40mm R-Glass Fibre Flexible Laminate	176
5.22	High Speed Photography Sequence for Specimen 1CPPS14, 0.5m Drop on a 160mm x 40mm R-Glass Fibre Flexible Laminate	177
5.23	Typical C-Scan Image of a damage Thin Flexible Panel	179
5.24	C-Scan Images for a selection of the short 120mm x 40mm Carbon Fibre Thin Flexible Laminates	180
5.25	C-Scan Images for a selection of the short 120mm x 40mm R-Glass Fibre Thin Flexible Laminates	180
5.26	C-Scan Images for a selection of the short 160mm x 40mm Carbon Fibre Thin Flexible Laminates	182
5.27	C-Scan Images for a selection of the short 160mm x 40mm R-Glass Fibre Thin Flexible Laminates	183
5.28	A comparison of the damaged area of a carbon fibre specimen which broke at the clamped end and one which did not from a 0.5m drop height	184
5.29	Plot showing Force-Time Trace for Specimen Small Specimen CPPS4, 0.1m Drop Height, using 40 and 150 Average Data Points	185
5.30	Corrected Force-Time Plot using 40 Average Points for Small Specimen CPPS4, 0.1m Drop Height	186
5.31	Velocity-Time profile for 0.1m Drop on Small Specimen CPPS4	187
5.32	Displacement-Time Plot for 0.1m Drop on Small Specimen CPPS4	187
5.33	Force-Displacement Plot for 0.1m Drop on Specimen CPPS4	188
5.34	Plot showing the variation of Peak Contact Force with Drop height for all 4 types of specimen tested	189
5.35	Plot showing the variation of Displacement with Drop height for all 4 types of specimen tested	190
6.1	Typical Force versus Time Plot for Dimension Change Investigation.	195
6.2	Force vs Time plots for all B specimens impacted from a drop height of 0.6m showing the reproducibility of the results obtained from the drop weight testing.	195
6.3	Force versus Time Plot showing the Difference in Behaviour due to a change in the Thickness (A: 4mm and B: 10mm) of the Laminate	197
6.4	Velocity versus Time Plot showing the Difference in Behaviour due to a change in the Thickness (A: 4mm and B: 10mm) of the Laminate	198
6.5	Displacement versus Time Plot showing the Difference in Behaviour due to a change in the Thickness (A: 4mm and B: 10mm) of the Laminates	198

6.6	Force versus Displacement Plot showing the Difference in Behaviour due to a change in the Thickness (A: 4mm and B: 10mm) of the Laminate	199
6.7	Plot of Force versus Time for Specimen Types B, C, and D all of 150mm Length but having widths of 80mm, 60mm and 40mm respectively	200
6.8	Plot of Force versus Time for Specimens Types E, F and G all of 120mm Length but having widths of 80mm, 60mm and 40mm respectively	201
6.9	Plot showing the changes in the Velocity Profile of the Impactor due to a change in Length (B, C & D: 150mm and E, F & G: 120mm) and Width (B & E: 80mm, C & F: 60mm and D & G: 40mm) of a Laminate	202
6.10	Plot showing the change in the Displacement of the Laminate due to a change in Length (B, C & D: 150mm and E, F & G: 120mm) and Width (B & E: 80mm, C & F: 60mm and D & G: 40mm) of a Laminate	203
6.11	Plot Showing the Variation in Force versus Displacement Relationship as an effect of a change in Length (B, C & D: 150mm and E, F & G: 120mm) and Width (B & E: 80mm, C & F: 60mm and D & G: 40mm) of a Laminate	204
6.12	Plots of Force versus Time for all specimen types impacted from a drop height of 1.5 m and an Impactor Mass of 1.55kg showing the change in the Thickness (A: 4mm & B: 10mm), Length (B, C & D: 150mm and E, F & G: 120mm) and Width (B & E: 80mm, C & F: 60mm and D & G: 40mm) of the Laminate	205
6.13	Plots of Velocity versus Time showing the Variation of the impactor velocity profile due to a change in the Thickness (A: 4mm & B: 10mm), Length (B, C & D: 150mm and E, F & G: 120mm) and Width (B & E: 80mm, C & F: 60mm and D & G: 40mm) of the Laminate	207
6.14	Plot of Displacement versus Time Showing the Variation due to a Change in Thickness (A: 4mm & B: 10mm), Length (B, C & D: 150mm and E, F & G: 120mm) and Width (B & E: 80mm, C & F: 60mm and D & G: 40mm) of the Laminate	208
6.15	Plot of Force versus Displacement Showing the Variation in Behaviour due to a change in Thickness (A: 4mm & B: 10mm), Length (B, C & D: 150mm and E, F & G: 120mm) and Width (B & E: 80mm, C & F: 60mm and D & G: 40mm) of the Laminate	209
6.16	Time of Flight C-Scan Image of damage caused by a High Energy Impact on Specimen Type A (4mm thickness). The specimen's dimensions are 80 by 150 mm	212
6.17	Time of Flight C-Scan Image of damage induced by a High Energy Impact on Specimen Type B (10mm thickness). The specimen's dimensions are 80 by 150 mm.	212
6.18	A Comparison of the Force-Time Behaviour between Specimen Type A (4mm Thickness) and Specimen Type B (10mm Thickness)	214
6.19	A Comparison of the Velocity Profile between Specimen Type A (4mm Thickness) and Specimen Type B (10mm Thickness)	215
6.20	A Comparison of the Change in Displacement between Specimen Types A (4mm Thickness) and Specimen Type B (10mm Thickness)	215
6.21	A Comparison of the Force-Displacement Behaviour between Specimen Type A (4mm Thickness) and Specimen Type B (10mm Thickness)	216
6.22	Time of Flight C-Scan images for Specimen Types with a length of 150mm: (a) Specimen Type B (80mm width); (b) Specimen Type C (60mm Width); (c) Specimen Type D (40mm Width)	218

6.23	Time of Flight C-Scan image for Specimen Types with a length of 120mm: (a) Specimen Type E (80mm Width); (b) Specimen Type F (60mm Width); (c) Specimen Type G (40mm)	219
6.24	Chart showing a comparison of Force-Time Behaviour for Specimen Types B, C and D (Thickness: 10mm, Length: 150mm, Width: 80, 60 & 40mm respectively)	220
6.25	Chart Showing a Comparison of the Force-Time Behaviour for Specimen Types E, F and G (Thickness: 10mm, Length: 120mm, Width: 80, 60 & 40mm respectively)	220
6.26	Chart Showing a Comparison of the Velocity Profile for Specimen Types B, C and D (Thickness: 10mm, Length: 150mm, Width: 80, 60 & 40mm respectively)	222
6.27	Chart Showing a Comparison of the Velocity Profiles for Specimen Types E, F and G (Thickness: 10mm, Length: 120mm, Width: 80, 60 & 40mm respectively)	223
6.28	Chart Showing a Comparison of the Displacement-Time Behaviour for Specimen Types B, C and D (Thickness: 10mm, Length: 150mm, Width: 80, 60 & 40mm respectively)	224
6.29	Chart Showing a Comparison of the Displacement-Time Behaviour for Specimen Types E, F and G (Thickness: 10mm, Length: 120mm, Width: 80, 60 & 40mm respectively)	225
6.30	Chart Showing a Comparison of the Force-Displacement Behaviour for Specimen Types B, C and D (Thickness: 10mm, Length: 150mm, Width: 80, 60 & 40mm respectively)	226
6.31	Chart Showing a Comparison of the Force-Displacement Behaviour for Specimen Types E, F and G (Thickness: 10mm, Length: 120mm, Width: 80, 60 & 40mm respectively)	227
7.1	Two degree of freedom model for contact proposed by Lal (1983)	230
7.2	Schematic of loading set-up for Contact Stiffness Measurements in the Instron Rig.	233
7.3	Schematic of loading set-up for Bending Stiffness Measurements in the Instron Rig	234
7.4	Comparison of Modelled and Experimental Force-Time Response for Specimen Type A (80mm x 150mm x 4mm) being impacted by a mass of 1.55kg from a drop height of 0.5m	236
7.5	Comparison of Modelled and Experimental Impactor Displacement Behaviour for Specimen Type A (80mm x 150mm x 4mm) being impacted by a mass of 1.55kg from a drop height of 0.5m	236
7.6	Comparison of Modelled and Experimental Force-Time Response for Specimen Type A (80mm x 150mm x 4mm) being impacted by a mass of 1.55kg from a drop height of 1.0m	237
7.7	Comparison of Modelled and Experimental Impactor Displacement Behaviour for Specimen Type A (80mm x 150mm x 4mm) being impacted by a mass of 1.55kg from a drop height of 1.0m	237
7.8	Comparison of Modelled and Experimental Force-Time Response for Specimen Type A (80mm x 150mm x 4mm) being impacted by a mass of 1.55kg from a drop height of 1.5m	238
7.9	Comparison of Modelled and Experimental Impactor Displacement Behaviour for Specimen Type A (80mm x 150mm x 4mm) being impacted by a mass of 1.55kg from a drop height of 1.5m	238

7.10	Comparison of Modelled and Experimental Force-Time Response for Specimen Type B (80mm x 150mm x 10mm) being impacted by a mass of 1.55kg from a drop height of 0.5 m	240
7.11	Comparison of Modelled and Experimental Impactor Displacement Behaviour for Specimen Type B (80mm x 150mm x 10mm) being impacted by a mass of 1.55kg from a drop height of 0.5m	240
7.12	Comparison of Modelled and Experimental Force-Time Response for Specimen Type B (80mm x 150mm x 10mm) being impacted by a mass of 1.55kg from a drop height of 1.0m	241
7.13	Comparison of Modelled and Experimental Impactor Displacement Behaviour for Specimen Type B (80mm x 150mm x 10mm) being impacted by a mass of 1.55kg from a drop height of 1.0m	241
7.14	Comparison of Modelled and Experimental Force-Time Response for Specimen Type B (80mm x 150mm x 10mm) being impacted by a mass of 1.55kg from a drop height of 1.5m	242
7.15	Comparison of Modelled and Experimental Impactor Displacement Behaviour for Specimen Type B (80mm x 150mm x 10mm) being impacted by a mass of 1.55kg from a drop height of 1.5m	242
7.16	Comparison of Modelled and Experimental Force-Time Response for Specimen Type A (80mm x 150mm x 4mm) being impacted by a mass of 5.4kg from a drop height of 1.0m	244
7.17	Comparison of Modelled and Experimental Impactor Displacement Behaviour for Specimen Type A (80mm x 150mm x 4mm) being impacted by a mass of 5.4kg from a drop height of 1.0m	245
7.18	Comparison of Modelled and Experimental Force-Time Response for Specimen Type B (80mm x 150mm x 10mm) being impacted by a mass of 5.4kg from a drop height of 1.0m	246
7.19	Comparison of Modelled and Experimental Impactor Displacement Behaviour for Specimen Type B (80mm x 150mm x 10mm) being impacted by a mass of 5.4kg from a drop height of 1.0m	247

List of Tables

3.1	Dimensions for Panels used in Thickness and Size Effect Investigation	73
3.2	Table showing the grinding and polishing regime for sectioned samples for SEM analysis	89
4.1	Table showing samples and their impact conditions for samples containing a longitudinal curvature	93
4.2	Table showing samples and their impact conditions for samples with a transverse curvature	94
4.3	Damage Observations made from high-speed photographic sequences	107
4.4	Estimated deflections calculated elastic strain energies and impact energies	109
4.5	Observations of specimens after Impact Event	116
4.6	Table showing estimated damage areas from X-Radiographs	125
4.7	Damage Observations made from X-Rays of damaged samples	126
4.8	Material Properties for the Impactor and Composite for Hertzian Analysis	141
4.9	Indentaion measurements and calculated Contact Forces	141
5.1	Summary of Samples and Measured Impact Velocity and Energy Values for 10cm drops on Thin Flexible Composite Samples with Ideal Calculated Values	149
5.2	Summary of Samples and Measured Impact Velocity and Energy Values for 20cm drops on Thin Flexible Composite Samples with Ideal Calculated Values	150
5.3	Summary of Samples and Measured Impact Velocity and Energy Values for 30cm drops on Thin Flexible Composite Samples with Ideal Calculated Values	151
5.4	Summary of Samples and Measured Impact Velocity and Energy Values for 40cm drops on Thin Flexible Composite Samples with Ideal Calculated Values	152
5.5	Summary of Samples and Measured Impact Velocity and Energy Values for 50cm drops on Thin Flexible Composite Samples with Ideal Calculated Values	153
5.6	Table showing the calculated values for energy absorbed during impact using hysteresis loop shown in Force vs Displacement curves.	188
6.1	Table showing the different impact conditions used for this investigation	193
6.2	Table showing a comparison of the calculated and measured composite stiffness	206
7.1	Figures for critical indentation values and stiffness reduction factors used for the modelling the effects of damage on the high-energy impact of Specimen Type A	244
7.2	Figures for critical indentation values and stiffness reduction factors used for the modelling the effects of damage on the high-energy impact of Specimen Type	246

1. Introduction

In a continuing quest for the improved performance in materials, the criteria include less weight more strength and lower cost, existing materials are reaching their limits. Therefore new materials are often used to replace existing materials in their current applications (Matthews and Rawlings 1994). With their stiffness, strength and low weight, different types of composites have found many applications. This includes their use in the aerospace and other technologically advanced industries that have very demanding material requirements. If the toughness of these composites could be further improved, then, there would be many more applications for these materials. Susceptibility to impact damage, due to composites having a low strength in the thickness direction (Abrate 1998), is a particular problem and continues to be so and this requires careful and ingenious design of products to minimise the severity of impact damage to composite materials used.

Impacting objects, depending upon their size, mass, hardness and shape can first compact and break up the contact site of the composite material. Then, if the composite is deformed, through thickness damage can occur of several different types and degree. The extent of through thickness damage can range from very minor and undetectable to the naked eye to catastrophic and in some cases, a clean hole can be punched through the material by the impacting object. Much depends upon the type and lay up of the fibres, the material's thickness and other dimensions. Also, the way the composite is supported and held in a structure and if the impacts are direct or glancing.

A difficulty, for example, when designing a composite panel that is to be part of a stressed structure, which can be subject to impacts, is to be able to assess the likelihood of inflicted damage threatening the integrity of the structure. A point is often there are other design requirements dictating the weight, the shape and the extent the panel can be reinforced and supported. Within these constraints, the design panel can be susceptible to impact damage in a variety of ways and places depending upon the point of contact between impactor and panel so the type and degree of damage for the same impact conditions can vary. Also, assessing the degree of

damage inflicted can be difficult and particularly so if access to the rear of the panel is not possible. A difficulty, then, can be that the extent of damage of the contact site can belie the extent of the through thickness damage. Hence, it is often necessary to construct a trial installation to make damage assessments.

Therefore much work has been done on understanding exactly what goes on during an impact event. Investigators have looked at various area of the impact event. These include the response of the composite when impacted, damage that occurs, damage initiation, damage propagation, damage detection and post impact properties. Investigators have also looked into how changing various factors, such as impact energy, impactor mass, impact velocity, geometry etc, will effect the above areas of interest.

Numerical and analytical analyses have also been used to model and predict the various events that would occur in a composite when subjected to impact (Abrate 1998). The trend for using these methods of prediction is that actual testing of composite materials can only be really performed on coupon-sized specimens to be economically viable. The problem with this is scaling up from a coupon to an actual structure and if what is seen in the test coupon actually occurs in a large structure. Therefore being able to predict what occurs in a large composite structure becomes important. This type of analysis has been used to predict the impact response and the damage, both nature and amount, that occurs under different impact conditions, and hence predictions of post impact properties can also be made.

Work has also been performed on producing tough composite systems. Investigators have looked into a number of ways of doing this, from engineering the lay-up to using tougher resins for the matrix (i.e. toughened epoxy systems or crystalline thermoplastics) or tougher reinforcing fibres. There has also been work performed on improving a composites impact tolerance by interleaving, in which layers of pure resin are interleaved between layers of pre-preg during lay-up.

The interest in this study is to assess the factors affecting the inherent tolerance of composite panels to impact damage. This is for flat and curved panels of different thickness and other dimensions. The panels are held lightly by grips so that the panels

are not unduly constrained during the impact. The aim of this study is to provide impact data relating to different impact conditions and their effect on the static and dynamic response of panels. This is to range from damage being confined to the contact surface to different degrees of through thickness damage. This is to obtain Force, Time and Displacement related to C-Scan and X-Ray records of the inflicted damage. Also, to model these impact damage processes to assist in the analysis of impact failure processes.

2. Literature Review

This chapter will be concerned with the background information required to understand the field of impact analysis in composite materials. The theory and the background will be covered with the areas of contact and damage initiation and progression being of main concern. The recent work that has been performed in this field will also be reviewed and will be the basis for the rest of the reported research.

2.1 Impact

Firstly, in order to understand an impact event, what occurs during and after the actual impact takes place must be understood. A great deal of this understanding will depend on the type of impact that the composite is experiencing. Therefore, the different types of impacts that can occur need to be defined and explained along with the immediate response to impact and the subsequent propagation of the energy involved in such an event.

2.1.1 Impact Definitions

The different types of impact need to be defined; the problem with this is that there seem to be a lot of discrepancy between different authors on the description of impact types. The following have all been used as descriptions for different types of impacts (Abrate 1991):

Low Velocity Impacts:
a) Impactor speeds of less than 100m/s.
b) Impacts where the entire structure deforms as waves propagate to the boundary and are reflected back several times during the contact duration.

High Velocity Impact:
a) Impacts where complete penetration of the target is achieved.

	b) When the deformation of the structure is localized in a small zone surrounding the contact area during the duration of contact.
Hypervelocity Impacts:	Impact speeds of greater than 1km/s.
Ballistic Impact:	Impacts, which involve complete penetration of the specimen.

As can be seen the definitions used for impacts are mainly based around the velocity in which the impactor strikes the structure or specimen. However, what is of main concern is the actual energy of the impact that occurs. This will also incorporate the mass of the impactor involved in the event. The mass and the velocity of the impactor can further categorise impact events. The two extremes of this are:

High Mass / Low Velocity (HM/LV):	Simulates tool drop impacts.
Low Mass / High Velocity (LM/HV):	Simulates impacts akin to runway/track debris

Impacts in between these two extremes are hard to categorise and are usually termed to be intermediate impacts and the variation within this category is huge.

2.1.2 The Impact Event

In order to understand an impact event, what occurs when and after an impactor makes contact with a composite structure must be understood. This will allow for the full contact force history to be determined. This will mainly involve two separate areas, what actually occurs at the point of contact (contact mechanics) and then what happens subsequently (impact dynamics).

2.1.2.1 Contact Mechanics

Here what occurs at the point when an object makes contact with a structure, which is needed in order to accurately predict the contact force history of an impact event, is

analysed. Local deformations at the contact area must be accounted for first in order for analysis to be accurate (Abrate 1998). Local deformation is usually in the form of indentation and this is defined as the difference between the displacement of the projectile and that of the back face of the laminate.

A viable way to look at these indentations is to consider the impactor and the structure to be two solids in contact and the impact problem can then be analysed as a dynamic contact problem. However this method is computationally expensive and cannot describe the effect of permanent deformation and local; damage on the unloading process. The unloading part of the process can be modelled using experimentally determined contact laws. Therefore to predict the entire contact force history of an impact event and the overall deformation of the target the use of a detailed model of the contact region is not necessary.

One of the common simple relationships used for the analysis of impact of composite materials is one relating the contact force and the indentation devised by Timoshenko known as the contact law. Even though an impact event is a highly dynamic event, where many of the targets vibration modes are excited, statically determined contact laws can be used in the analysis of low velocity impact events as strain rate and wave propagation effects are negligible in the commonly used material systems. In many cases the contact area is small and the behaviour is similar to that observed during the indentation of a half space. The indentation that occurs is independent of the overall deflection of the structure being impacted. Contact mechanics provide results, which are used to model the indentation of composites during impact events.

To begin with the contact between two isotropic elastic bodies need to be looked at. Hertz first pioneered the pioneering theory for this type of investigation and many detailed accounts of this are present (Abrate 1998). The essential results that come from the Hertz law are as follows. For two isotropic bodies of revolution (*Figure 2.1*) contact occurs in a circular zone of radius a in which the pressure varies according to the following relationship:

$$p = p_0\left[1-\left(\frac{r}{a}\right)^2\right]^{\frac{1}{2}} \quad (2.1)$$

where p_0 s the maximum contact pressure at the centre of the contact zone and r is the radial position of an arbitrary point in the contact zone.

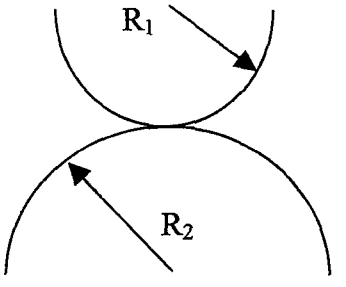


Figure 2.1: Two bodies of revolution for Hertzian analysis of contact

Now by defining the two parameters R and E as:

$$\frac{1}{R} = \frac{1}{R_1} + \frac{1}{R_2} \quad (2.2)$$

$$\frac{1}{E} = \frac{1-\nu_1^2}{E_1} + \frac{1-\nu_2^2}{E_2} \quad (2.3)$$

Where R_1 and R_2 are the radii of curvature of the two bodies, whilst the Young's Modulus and Poisson's ratio of the two bodies are E_1, ν_1 and E_2, ν_2 respectively, with the subscripts 1 being for the indentor and subscript two used for the target. From these the following expressions for the radius of the contact zone a, the relative displacement α and the maximum contact pressure are given as follows:

$$a = \left(3\frac{PR}{4E}\right)^{\frac{1}{3}} \quad (2.4)$$

$$\alpha = \frac{a^3}{R} = \left(\frac{9P^2}{16RE^2}\right)^{\frac{1}{3}} \quad (2.5)$$

$$p_0 = \frac{3P}{2\pi a^2} = \left(\frac{6PE^2}{\pi^3 R^2}\right)^{\frac{1}{3}} \quad (2.6)$$

The force indentation law is then expressed as

$$P = k\alpha^{\frac{3}{2}} \quad (2.7)$$

where P is the contact force, α is the indentation, and the contact stiffness k is given by:

$$k = \frac{4}{3}ER^{\frac{1}{2}} \quad (2.8)$$

Equation 2.7 is known as the Hertz Contact Law, and has been found to apply to a wide range of cases, even if the assumptions used in the derivation are not satisfied. This can be seen in the application of this law with respect to laminated composites, as these are not homogenous and isotropic materials. In the case of the impact of composite materials, permanent deformations are introduced in the contact zone, even at relatively low force levels. However, the material is still assumed to be linear elastic in the analysis. Damage in the form of matrix cracks, fibre fracture and inter-ply delaminations can also be introduced into the contact zone, but still the contact law follows. This basic contact law is the basis of most studies involving impact and as it can be related to composites is an ideal starting point for understanding the theory behind the phenomenon. Although this law is associated with static cases, it has been shown that it can be successfully applied to impact situations (Goldsmith 1960), and has been used at impact velocities up to 500m/s in dynamic situations

(Johnson 1985). In the case of laminated polymer composites this theory holds for impacts up to 200 m/s at the point of impact (Sierakowski and Chatvurvedi 1997). Wu and Yen (1994) also showed that this theory works in curved laminated composites as long as the plate curvature is small.

However the situation becomes a lot more complex when we take into consideration the permanent deformations and the actual nature and behaviour of a laminated composite.

The indentation of a laminated composite plate has been looked at experimentally by many authors (Yang and Sun 1982, Tan and Sun 1985, Gu and Sun 1987,). It was found that during impact the contact force increases to a maximum value and then reverts back to zero. In many cases tests showed that multiple impacts and reloading occur, therefore, contacts laws should include unloading and reloading phases to give a more accurate picture of the impact event.

For the first loading phase the contact law given by Equation 2.7 is followed closely. Here the parameter k is usually determined experimentally, or it can be estimated using Equation 2.8, if the required parameters are known (note that in this case the Poisson's Ratio of the composite is taken to be zero. However this is only accurate for the loading phase as permanent indentations are introduced even at relatively low loading levels in composite laminates. These permanent indentations will cause the unloading phase of the process to be significantly different from that of the loading phase.

Work by Crook (1952) suggested the following contact law during the unloading phase:

$$P = P_m[(\alpha - \alpha_0)/(\alpha_m - \alpha_0)]^{2.5} \quad (2.9)$$

where P_m is the maximum force reached before unloading occurs, α is the indentation that occurs, α_m is the maximum indentation and α_0 is the permanent indentation. α_0 is

zero when the maximum indentation remains below the critical value α_{cr}. When $\alpha_m > \alpha_{cr}$,

$$\alpha_0 = \alpha_m \left[1 - (\alpha_{cr} / \alpha_m)^{\frac{2}{5}} \right] \quad (2.10)$$

During subsequent reloading, the corresponding reloading curve is distinct from the unloading curve but will always return to same point as the beginning of the unloading curve. The corresponding unloading curve can be modelled by the following equation:

$$P = P_m [(\alpha - \alpha_0)/(\alpha_m - \alpha_0)]^{\frac{3}{2}} \quad (2.11)$$

The parameter α_0 does not necessarily correspond to the permanent indentation of the laminate. α_0 is selected so that Equation 2.11 fits the experimental unloading using a least squares method. α_0 is related to the actual permanent indentation, α_p, and the maximum indentation, α_m, by the following relationship during the loading phase:

$$\alpha_0 = \beta(\alpha_m - \alpha_p) \quad (2.12)$$

when $\alpha_m > \alpha_{cr}$; otherwise $\alpha_0 = 0$. The permanent indentation and the parameter β need to be determined experimentally. However this would require a large number of experiments to be performed, whereas if Equation 2.10 were used, then only a single unloading curve would be required to determine α_{cr}.

In composites, permanent indentations are introduced when the indentation exceeds a small critical value. At the same time the material behaviour in the transverse direction is governed by the matrix properties, therefore plastic behaviour can be expected. Firstly the material is thought to behave elastically until the critical indentation is reached. Then the contact area divides into two zones, the plastic zone and the elastic zone, as the loading increases a new contact law is obtained.

Firstly consider a laminate of height h, which is supported by a rigid structure and indented by a rigid sphere of radius R_i. The indentation is assumed to occur as if the material directly under the indenter is under uni-axial compression. The indentation α can be written in terms of the radius of the indentor R_i, and the contact radius R_c. The equation is as follows:

$$\alpha = R_i - \left(R_i^2 - R_c^2\right)^{\frac{1}{2}} \quad (2.13)$$

The contact radius itself is expressed as follows:

$$R_c = \left(2\alpha R_i - \alpha^2\right)^{\frac{1}{2}} \quad (2.14)$$

The indentation is usually much small than the radius of the indentor, and hence the second term on the right hand side of Equation 2.14 can be neglected and the Equation becomes:

$$R_c = \left(2\alpha R_i\right)^{\frac{1}{2}} \quad (2.15)$$

The displacements under he indentor can be written as:

$$\delta(r) = \alpha - R_i\left[1 - \left(1 - \left(\frac{r}{R_i}\right)^2\right)^{\frac{1}{2}}\right]. \quad (2.16)$$

With small indentations the contact radius is much smaller that that of the indentor radius, so the bracketed term in Equation 2.16 can be simplified so that the Equation now becomes:

$$\delta(r) = \alpha - \frac{r^2}{2R_i}. \quad (2.17)$$

Assuming that the transverse normal strain is uniform through the thickness and is given by $\varepsilon_{zz} = \delta(r)/h$, and also assuming that the material is elastic, the contact force can be given by:

$$P = \frac{2\pi E}{h} \int_0^{R_c} \delta(r) r dr \quad (2.18)$$

where E is the elastic modulus in the transverse direction. Now using Equations 2.16 and 2.17, Equation 2.18 gives the following contact law:

$$P = \frac{\pi E R_i}{h} \alpha^2 \quad (2.19)$$

This model therefore indicates that the contact force increases with α^2 instead of $\alpha^{3/2}$, as predicted by the Hertz law of contact. Therefore Hertzian behaviour is only a rough indication of what can happen during impact, and can only really be used as a guideline to the impact behaviour of laminated composites. The law fails when, as in the case of laminated composites, when permanent deformation occurs during impact and the material does not behave in an homogenous and isotropic fashion.

Permanent indentations are often observed even at very low values of the contact force. These effects need to be accounted for and can be done by assuming that in the transverse direction the stress-strain behaviour of the composite is elastoplactic. As larger deformations are present at the centre of the contact zone, stresses will reach the yield strength in the centre and the contact area will be divided into two zones, the plastic zone of radius R_p, and an elastic zone between R_p and R_c. At the junction between these two zones, the stress is equal to the strength of the material Z_c, therefore gives the following:

$$Z_c = \frac{E}{h} \delta(R_p) \quad (2.20)$$

From the use of Equation 2.17 the radius of the plastic zone is given by:

$$R_p = \left[2R_i \left(\alpha - \frac{Z_c h}{E} \right) \right]^{\frac{1}{2}} \quad (2.21)$$

Now as long as the indentation, α, is larger than the critical indentation then:

$$\alpha_{cr} = \frac{Z_c h}{E} \quad (2.22)$$

Yang and Sun (1982) gave contact laws for both the loading and unloading phases of impact. These contact laws are as follows:

For the loading phase: $P = \pi R_i Z_c (2\alpha - \alpha_{cr})$ when $\alpha > \alpha_{cr}$ (2.23)

For the unloading phase: $P = \frac{\pi R_i E}{h} (\alpha^2 - \alpha_o^2)$ when $\alpha > \alpha_o$ (2.23)

Swanson and Rezaee (1990) showed that the Hertz law can adequately model the loading phase, however for large loads (greater than 36,000 N) the contact law will significantly deviates from that given by Hertz during the loading phase of the indentation process. This is due to severe damage being introduced during the indentation process. When the target is back-supported by a hardened steel block, it was found that the indentor penetrates more than half the thickness of the laminate. However the elasto-plastic model fits the data provided, showing that at these levels of load this is a more accurate model.

Christoforou and Yigit (1994) modelled the response of a thin composite laminate to impact using a static contact law, which incorporated damage effects due to local contact stresses. They accounted for damage during the unloading phase rather than

the loading phase as was previously done, and developed a more reasonable and complete picture of an impact event concerning a composite laminate.

Therefore from the above contact theory it can be seen that contact during the impact of a composite laminate can be looked at in many ways. The most basic being using Hertz Theory, this gives a general picture of the impact event, but assumes that a composite laminate behaves like a isotropic material and hence fails when damage and unloading are taken into account. However it can still adequately model the loading phase of the event up to a certain level of force.

Many authors have used the Hertzian Contact Law as the basis of analytical and numerical modelling to predict impact responses of composite materials. Yigit and Christoforou (1995) found that a linearised contact law based on an elastic-plastic contact yielded excellent results for impact response in composite materials. They also identified a parameter that is the ratio of the maximum impact force from dynamic simulation to the one obtained from a half space analysis could be used to characterise the type of impact response (i.e. locally dominated, quasi static or dynamic) would occur. Wu and Shyu (1993) found that the strain history at low velocity impacts are very similar to those found in contact tests except that vibrations were observed in the actual impact tests. Pierson and Vaziri (1996) using a model combining shear deformation, rotary inertia and non-linear Hertzian contact obtain predictions that agreed well with both experimental drop weight and gas gun impacts. Christoforou and Yigit (1998) normalised the governing equations and were able to identify the key parameters, which govern the transition from locally dominated to globally dominated responses.

2.1.2.2 Contact Dynamics

In order to gain some understanding into the effect of foreign object impact on a structure, one of the first steps is to predict its dynamic response. Such a prediction is made using an appropriate mathematical model, which accounts for the motion of the projectile, the overall motion of the target and the local deformations in the area

surrounding the impact point. Firstly a particular theory, beam, plate or shell depending on the geometry of the target, is selected followed by the inclusion of local deformation in the through thickness direction using an appropriate contact law. With low velocity impact, small amounts of damage are usually introduced to a small zone surrounding the point of contact, however this damage usually does not affect the structures dynamic properties. Therefore, impact dynamics analyses does not attempt to model damage that develops during an impact event (Abrate 1998).

The structural theory of choice is selected with careful consideration of the possible complicating factors in mind, such as transverse shear deformation and rotary inertia. Each type of structure has a selection of structural theories to select from, for example with beams possible theories that can be selected include the Timoshenko beam theory, the Bernoulli-Euler beam theory amongst others. With shells and plates the theories available can also model the structure as a two or three-dimensional solid. In some special cases exact solutions are available for structures subjected to dynamic loading, and these solutions can be used effectively. However in general approximate solutions must be sought.

For the object of this report only beam theories will be discussed as they relate closely to the work of interest. However detailed descriptions of plate and shell theories can be found in the book by Abrate (1998).

Beam theories

The following are the available beam theories that can be used in dynamic analysis. Here the general assumptions for each theory and how they are used will be explained, as for the complex mathematics for these theories, these are detailed in the book by Abrate (1998, 0-521-47389-6).

Uniform Loading of a Beam.

This theory is a two dimensional elasticity problem without any assumptions for a particular beam theory. This theory is very useful in order to bring a general

understanding into the behaviour of beams, the assumptions made in beam theories and the limitations of each theory.

Higher Order Beam Theory

The development of this theory is based on two hypotheses:

H1. *The transverse shear stain vanishes on the top and bottom surfaces and follows a parabolic distribution through the thickness.*

H2. *The transverse normal strain can be neglected*

Timoshenko Beam Theory

This is also known as the first order shear deformation theory. With this theory the transverse normal strain is neglected (H2) and the following assumption is made instead of H1:

H1'. *The transverse shear strain is assumed to be uniformly distributed over the cross section.*

Bernoulli-Euler Beam Theory

This theory has the assumption that H1 is replaced by:

H1''. *The transverse normal shear strain is assumed to be negligible.*

Recovery of Accurate Results from Beam Models

It is possible to use the simpler elementary beam theory to determine the axial stress and then subsequently use the result to determine the shear stresses from the equations of equilibrium of two-dimensional elasticity. An example of this is the case of a simply supported beam under uniform loading. In this case the axial stress can be

predicted by the Bernoulli-Euler beam theory. The complex mathematics involved are detailed in the book by Abrate (1998).

Harmonic Wave Propagation

The consideration of the propagation of free harmonic waves is needed in order to compare the dynamic behaviour of beams described by the three above mentioned beam theories.

Free Vibration of Beams

Another method of studying the dynamics of various beam theories is to study the free vibration of finite beams. The natural frequencies of a simply supported beam of length L are identical to the frequencies of free harmonic waves with wave numbers $k = i\pi/L$. This type of study on harmonic wave propagation has shown that there is little difference between the Timoshenko Beam theory and that of the higher order theory.

Beam Theory Summary

Beam theories are based on assumptions, which are aimed at reducing the three-dimensional elasticity problem into a one-dimensional problem. The three most commonly used theories are the Timoshenko, the Bernoulli-Euler, and the higher order theory.

Hamilton's Principle was used, in a consistent way, to derive the equations of motion and the boundary conditions for each theory. The validity of the assumptions made for each of the theories can be evaluated by considering the problem of a simply supported beam subjected to a uniformly distributed load. This showed that for slender beams, the simplest of the three theories, the Bernoulli-Euler theory, is the most accurate. Whilst for short beams the Timoshenko Theory is required as it accounts for transverse shear deformations. Analysis of harmonic wave propagation in beams shows that the higher order theory gives results close to those predicted by

the Timoshenko Theory. This shows that the higher level of complexity in the theory is not justified by a better set of results. The importance of transverse shear deformation and rotary inertia on the impact of beams can be shown using free vibration analysis. The effects of large deformations on beams can be studied by considering the large amplitude vibration of a simply supported beam. This shows that the as long as the amplitude remains small in relation to the radius of gyration of the cross section, non-linear effects are negligible.

The beam theories discussed here are often used in the development of mathematical models for studying the impact dynamics involved in impact tests on beam specimens. On top of that the ideas around the assumptions that have been made concerning the effects of shear deformation and rotary inertia can be directly applied to the development of plate and shell theories.

Plate Theories

The two factors mentioned above, shear deformation and rotary inertia, are expected to have similar effects on the behavior of plates, especially those constructed from composite materials. There are two main plate theories that are available. Firstly there is the first order shear deformation theory (FSDT) also known as the Mindlin or Mindlin-Roessnier plate theory, which is in effect an extension Timoshenko beam theory. The other being for thin plates where shear deformation and rotary inertia effects are small and the theory can be effectively reduced to classic plate theory (CPT), which in turn is an equivalent of the Bernoulli-Euler beam theory discussed above. This are discussed in more detail along with the complex mathematics involved in the book by Abrate (1998) along with higher order plate theories.

Impact Models

There are many mathematical models that exist which are used to study the impact of a structure by a foreign object. For example it is possible, in certain cases, to accurately model the contact force history using an equivalent system of springs and masses. The energy balance approach can be used when the structure behaves quasi-

statically. The energy balance approach states that as the contact force reaches a maximum, the sum of the strain energy in the structure and the energy required for indentation is equal to the initial kinetic energy of the projectile. This energy balance approach is useful when the interest is more in the maximum contact force rather than the complete contact force history. There are also more sophisticated models available for instances where the dynamics of the structure need to be accurately accounted for (Abrate 1991).

Spring Mass Models

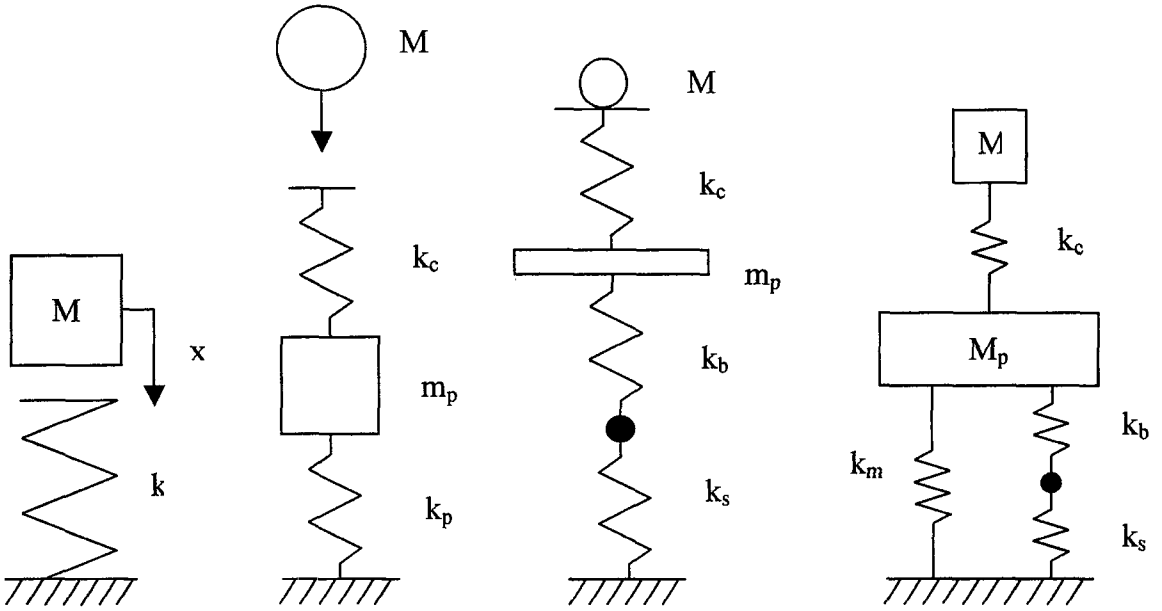
These types of models are simple yet provide accurate solutions to some types of impact that are often encountered during tests on small test specimens. These can come in various forms, from simply consisting of a single mass and a single spring (Caprino et al. 1984) to more complex models consisting of a number of masses and springs (Lal 1983 (b), Shivakumar et al. 1985, Sjoblem et al. 1988). Examples of these are shown in *Figure 2.2*. The complexity of the models that have been presented depended on what exactly the authors were including in the model that they set up. For example Caprino et al (1984) used a simple single degree model (*Figure 2.2(a)*) to analyse the drop weight impact of small glass cloth-polyester panels. The spring constant k in this model represented the static rigidity of the panel at the impact point. Sjoblem (1988) used a two-degree freedom model (see *Figure 2.2(b)*), where the two spring constants, K_p and K_c, represented the rigidity of the plate and the contact rigidity respectively. Lal (1983) used three springs in his model (see *Figure 2.2(c)*) to represent the flexural, shear and indentation stiffness. Shivakumar et al (1985) used a model that contained 4 springs to analyse the impact of a circular plate by a sphere (*Figure 2.2(d)*). The four springs used represented bending, shear, membrane and contact rigidities. This is considered to be the most complete model that has been used (Abrate 1998).

Energy Balance Models

The spring mass models mentioned above are used for the measurement of the entire contact history of the impact event (both the contact force and the displacement

involved). How ever in general, only information on the maximum contact force and the duration of contact is needed, which can be determined in a more efficient manner using energy balance models.

This type of model assumes that the structure being impacted behaves quasi-statically. The initial kinetic energy of the projectile is used to deform the structure that it impacts. With quasi-static behavior, when the structure reaches its maximum deflection the velocity of the projectile has decreased to zero and the initial kinetic energy has been used to deform the structure. This deformation will involve bending and shear deformation, and for larger structure will also incorporate membrane stiffening effects. Local deformations within the contact zone are also considered.



Figures 2.2: Spring mass models. (a) Single degree of freedom model (Caprino 1984); (b) Two degree freedom of model (Sjoblom 1988); (c) Two degree of freedom, three spring impact dynamics model (Lal 1983(b)); (d) Two degree of freedom model with two masses and four springs (Shivakumar et al. 1985)

The energy balance approach equates the initial kinetic energy of the projectile with the sum of the strain energy in the structure and the energy required for indentation. Therefore the resulting energy balance equation can be written as:

$$\frac{1}{2}MV^2 = E_b + E_s + E_m + E_c \quad (2.24)$$

Where the subscripts *b, s* and *m* refer to bending, shear and membrane components of the structural deformation, whilst E_c is the energy stored in the contact region during indentation. However essentially it is possible using this approach to calculate the maximum contact force using the following equation:

$$F = \left(\frac{5}{4}\right)^{\frac{3}{5}} \left\langle M^3 V^6 n^6 \right\rangle^{\frac{1}{5}} \quad (2.25)$$

Whilst the contact duration can be calculated from this following equation:

$$T_c = 3.2145 \left\langle M^2 V^{-1} n^{-2} \right\rangle^{\frac{1}{5}} \quad (2.26)$$

The energy balance approach has been used extensively for the investigation of various impact events (Abrate 1991, Christoforou et al. 1989). Excellent agreement between the energy balance approach and numerical modeling has been shown.

With the use of spring mass modelling and energy balance approaches extensive work has been performed. Olsson (1992(a)) used closed form solutions to predict the impact response of composite laminates, and then went on to modify this in order to model the response of sandwich structures (Olsson and McManus 1996, Olsson 2002), the response for large mass impacts (Olsson 2001) and the response of small mass impacts (Olsson 2003).

2.1.3 Dynamic Response of Composites to an Impact Event

2.1.3.1 Dynamic Properties of Composites

The impact phenomenon is classified as a dynamic event where the material remains contiguous (Sierakowski and Chaturvedi 1997). To understand the collision between the two impacting bodies requires the knowledge of the propagation of stress waves through the material and the constitutive equation for the material itself. The equation is a mathematical description defining the relationship between stress, strain and the time derivatives of stress and strain.

For the development of the constitutive equation for any material system it is essential that the dynamic properties of the material are known. This task is complicated enough for single phase materials (i.e. metals), but in the case of composites there is the added complications of directional dependence of the materials properties due to anisotropy of the material system as well as having to take into account matrix material and environmental effects.

Dynamic properties are difficult to determine, as there are several factors that need to be considered. These include properties that are functions of loading rate, the initiation and growth of damage during loading and the distinction between material and structural response. The structural response will depend on the geometry, loading point and the response of the material. Therefore in order to find the material response it is necessary to separate it from the general response of the structure. These complexities require an overall study of the interactive nature of dynamic events occurring during a loading process. For example, in order to assess the dynamic properties the stress wave propagation and the material constitutive equations must be known. However at the same time in order to understand stress wave propagation, the dynamic properties, which were the subject of the initial investigation, are required. Therefore in order to understand and quantify dynamic effects it is necessary to synthesize the knowledge of stress wave propagation,

material constitutive equations and the dynamic properties. The three aspects are essentially interactive (see *Figure 2.3*).

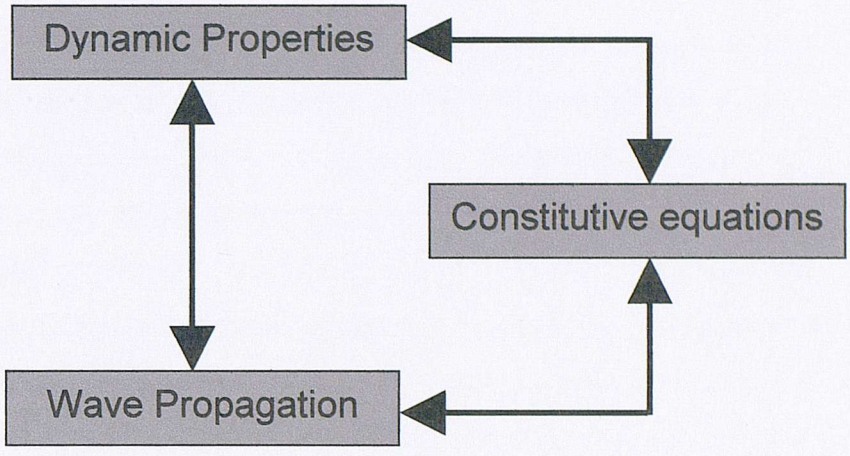


Figure 2.3: Interactive Dynamic Effects (Sierakowski and Chaturvedi (1997))

2.1.3.2 Wave Motion in Composites

Composite system properties, especially the thermoplastic ones, are sometimes evaluated experimentally using a lamina as a basic specimen and then using the results as a global picture of the system. Lamina can be considered to be the building blocks for analyzing static and dynamic properties of structures, as these tend to be made from laminates, which consist of a series of lamina stacked together in an order designed for a particular purpose. However this approach has many drawbacks in dynamic events, especially ones when the microstructure begins to influence the wave motion within the lamina. Phenomena such as wave dispersion, scattering and frequency filtering cannot be explained via idealizing the lamina as a homogenous material, but requires analysis as an anisotropic material. In addition in the case of laminates there is also another microstructure, the one that exists between lamina, which also needs to be taken into consideration.

Many authors have investigated various aspects of wave motion, both transient and steady state, either experimentally or theoretically (Ting 1980, Gibson 1990). Various theories have therefore been proposed, ranging from simple approximations to complex and very sophisticated models.

Theoretical theories can be split into the following categories (Sierakowski and Chatuevedi 1997):

- **Effective modulus theories:** theories based upon the primary assumption that the wave motion of the composite can be analysed by treating the composite as a homogenous anisotropic material. Therefore the constituent elastic properties are replaced by the geometrically weighted averages of the constituent properties.
- **Effective stiffness theories:** continuum theories that take into consideration the influence of the fibre and matrix phases. Typically the fibres and the matrix are considered to be linear elastic, isotropic and homogenous, and their influences are accounted for through their assumed approximate displacements.
- **Elasticity theories with microstructure:** these theories are used when the continuum (i.e. the composite) does not have a periodic microstructure, provided the matrix behaves in an isotropic, elastic fashion. This type of theory involves consider a unit cell as a building block with material constants including moduli and volume fractions.
- **Mixture theories:** with this type of theory the different phases are allowed to undergo individual deformations. The constitutive formulation then requires the superposition of the components. These models can deal with both transient and harmonic waves within composites, and can be extended to include non-linear effects.
- **Continuous theories based upon asymptotic expansions:** micro mechanical theories in that they provide information on stress and displacement distributions within the components. Useful for both steady state and transient response, can also be extended to include non-linear and non-periodic composites.
- **Discrete continuum theories:** defines the displacement field in the form of a two-truncated Taylor series for each layer of a periodic composite. Continuity conditions at the interface are so that differential-difference equations are obtained as the governing equations.

- **Lattice type theories:** the uniform nature of composites in the fibre direction, waves moving in this direction are channelled by the fibres, which act as a wave guide, whilst they hinder waves in the normal direction. Lattice type theories model the fibres as long slender structural elements with the matrix considered to be a system of strings with a given stiffness.
- **Other theories:** Many other authors have investigated the phenomenon using theories that do not fall into the above categories. These techniques include variational methods; methods based on viscoelastic analogy; theories based upon hydrodynamic concepts for analysis of compressive block loading; and various statistically based models.

All the above theories have been developed using specific assumptions and hence each of them will have their merits and drawbacks (Ting 1980). The Effective Modulus Theories yield satisfactory results under static loading for certain geometries. However huge shortcomings come into play when it applied to wave propagation in all forms of geometry. The main reason for this is that these theories are unable to reproduce the dispersion and attenuation observed in composites. These types of effects become increasingly important when the wavelengths are of the same order as the composite micro-dimensions.

This led onto the development of Effective Stiffness Theories. However the accuracy of the Effective Stiffness theories depended greatly on the series expansions of the displacement within the layer, which in turn depended greatly on the thickness of the specimen. Higher order approximations can be obtained using this type of theory, however entire derivations from the beginning are required. Applying this to transient problems requires the solving of the resultant differential equations, of which there are 12 for the lowest order of approximation, making this a rather complex theory to use.

Mixture theories encounter problems when being applied to composite materials, as it is difficult to specify the interactions between the constituents on the basis of the knowledge of the geometry and constitutive relationship of the individual constituents. The main problem with improving this theory lays in the assumption

that the two constituents coexist and are allowed to move independently even though in reality there is perfect bonding between the two. Satisfactory results can be obtained for a bi-laminate plate, however a suitable assumption for the interaction between the constituents still poses a problem.

Interacting continua theories, which are based on asymptotic expansion, have many useful features. For example it is easy to improve accuracy by incorporating higher order terms. They can also be used for either steady state or transient response of composites. However although it does allow the use of higher order theories, there is a difficulty in satisfying the initial and boundary conditions for the higher order differential equations, and hence limits on the application of such theories.

As can be seen theoretical approaches to wave propagation depend greatly on the theory developed and the assumptions made during the set up stages. These assumptions give the theory it advantages and disadvantages. Each theory has conditions it is most suitable for, however the more complex theory does not necessarily produce the best results for a given situation. Accuracy depends greatly on assumptions made for the theory. After all the actual nature of a composite makes wave propagation analysis difficult.

2.1.3.3 Wave Motions in Composites under Impact Loading

The energy that is initially transmitted into an object during impact will propagate through the object in the form of stress waves. At high speeds an impact will involve the formation of a crater or even complete penetration at the impact area. Damage away from the impact site is a result of the reflection of stress waves and focusing due to changes in geometry. It has also been observed that under high strain rates (i.e. high velocity impact) materials will exhibit a higher strength and a lower ductility. This type of evidence validates the use of elastic wave analysis for the determination of pre-fracture stresses caused by impact events. Also note that even if plastic waves pre-dominate, elastic precursor waves will bound the stressed impact zone.

Wave motion in composites under transverse loading is composed of five separate waves, two relate to in-plane motion and three relate to flexural plate motions. Moon (Moon 1972) gives an extensive run through of the calculations involved in determining the velocity and wave surfaces involved when an anisotropic plate in under transverse loading. He uses a modified version of Mindlin's approximate theory of plates and shows that both extensional and bending waves are produced in an anisotropic plate when subjected to transverse impact.

Experimental work on various types of specimen and using various projectiles and velocities have shown that the types and velocities of the waves induced depends greatly on the test conditions. Early work in this area (Ross and Sierakowski 1975) looked at how the nature of waves produced in a composite using various methods of wave inducement. Waves were introduced either ultrasonically or via an impact event and elastic waves speeds of waves propagating in one of the principal material directions could be determined in this fashion. Longitudinal wave speeds can be calculated using the rule of mixtures. Longitudinal wave speeds in transversely reinforced composites can also be determined using the transverse modulus equations and the corresponding basic methods for determining longitudinal waves.

More recently, Takeda et al. (1981) reviewed a number of investigations on the types of waves induced by impact. Elastic wave propagation in boron/epoxy and graphite/epoxy laminates impacted by a silicon rubber projectile is dominated by a flexural wave propagating at different velocities in different directions for $(0°)_{16}$ and $[(0°)_2/\pm 45°]_{2s}$ lay ups. At the same time membrane effects were predominant in tests with large impact velocity to plate bending stiffness ratio and were flexible enough to allow deflections comparable with the plate thickness. With their own experimental work they found that when glass reinforced laminates were impacted by a blunt headed impactor, the predominant wave present was a flexural one within a velocity range of 30 – 40m/s. Embedded strain gauges were used to characterize the nature of the waves induced. They firstly detected a very small tensile wave, which arrives at both surfaces. On the front face, a tensile component of the oncoming flexural wave was detected, followed by a large compressive component of the same wave. The

largest amplitude of the flexural should be the most important factor when considering the resultant delamination and fracture within the plate.

They measured the velocity of the largest amplitude and at a distance of 3.81cm from the center of the plate the average velocities were:

290 m/s in 0° direction
225 m/s in 90° direction

They also found that bending strains were larger at points further away from the centre of the plate, which coincided with a significant decrease in the wave velocity. They also found that both wave velocities and strain amplitudes exhibit a directional dependence.

Other investigators have looked at how changing features of the impact event (i.e. impactor shape) effects the dynamic response of a composite plate. Kim and Goo (1997) looked at this problem. They used an algorithm approach, and considered the effects of impactor shape on the quasi-static contact behavior of composite plates. They also looked at the response of composite laminates due to transverse impact according to the shape of the impactor. They found that the blunter impactors produced a higher contact force for static indentation. Whilst for dynamic situations, blunt impactors raised the maximum impact force and elongatied the duration time.

Experimental investigations into wave motion in structures due to impact loading can be broadly classified into 3 categories. These categories are based upon the wave shape and amplitude and are as follows:

- Low-amplitude sinusoidal waves or ultra-sonic waves
- Low-amplitude transient waves
- High amplitude transient waves

Several experimental methods have been developed specifically for the study of wave motions in composite structures. These methods include the generation and

monitoring of waves under the above categories. For example ultrasonics (see Section 3.3.1) has been successfully used for the characterization of damage in composites. Many experimental methods have been developed for introducing waves into structures. Low amplitude waves can be introduced using mechanical strikers, small charge explosives and shock tubes. High amplitude waves on the other hand can be generated using exploding foils, higher order explosives and fly plate type devices.

The presence and types of waves in a composite have been looked at using experimental methods that utilize strain gauges that are mounted on the surface of the specimen and at the interlaminar planes. Impacts introduced tend to be of low energy so as to avoid damage within the composite. The transient records taken from the strain gauges can then be analysed to identify wave characteristics (wave velocity, wave type, peak strain, strain rates etc.).

Takeda et al (1981) performed wave motion studies due to localized impact and found correlations with transverse matrix cracking and delamination damage in composites. They also found strain waves that were symmetrical to each other, evidence that their plates were in flexural motion during impact, and hence membrane effects are negligible. They also concluded that transverse matrix cracks on the impacted surface were generated by the tensile stresses due to the leading part of the transient flexural wave generated immediately after impact.

Therefore it seems that wave motions caused by an impact event causes the onset of impact damage, as both experimentally and theoretically the motion of the induced waves in a composite can be related to the actual damage within the impacted structure.

2.2. Impact Damage

Damage in composites caused by the impact of a foreign object can be have many forms, but the most common are inter-ply delaminations, fibre fracture, and matrix

cracking (Matthews and Rawlings 1994, Abrate 1998, Abrate 1991and 1994). More often than not the actual damage area will consist of a combination of the different types of damage. Firstly the different types of damage need to be defined before the problem can be looked at in greater detail (Richardson and Wisheart 1996).

Matrix Cracking:	cracking in the polymer matrix that occurs between the fibres
Delaminations:	fracture caused by the debonding between plies within the laminate, these are of most concern as they significantly reduce the strength of the laminated composite.
Fibre Fracture:	the fracture of the reinforcing fibres
Penetration:	Impactor completely perforates the impacted surface

Many investigations have been conducted to determine the exact nature of the damage that occurs, how this damage accumulates and it's exact sequence, and how various parameters, such as impactor shape and size, can effect the above. There are other important parameters, such as damage initiation and perforation threshold energy values, which are important when designing against, drop toll and debris impact.

In order to investigate impact damage, test methods that can simulate impact events are used. Several test methods have been used in impact studies (Abrate 1991, Gary and Zhoa 2000). There are many methods available for testing, as there are several factors that can affect the response of a structure to an impact event. The main factor usually is the initial impact velocity, however factors such as mass and velocity will also play a large part in the overall response of the structure. For example a large mass traveling at a low velocity may not cause the same amount of damage as a small mass traveling at a high velocity even though their kinetic energy is the same. In one case the impact event may cause an overall response in the structure, whilst the other may cause a more localised response at the impact point. Therefore the choice of test method must be appropriate for simulating the required type of impact.

At present there are two main types of apparatus used by investigators for impact studies, and they simulate the two main impact situations that are of interest. First there is the use of a gas gun set up. This set up allows impact events that involve projectiles of low mass (small) traveling at a high velocity which simulate situations such as runway debris impact during aircraft take off. The other common method used for impact testing is the drop weight tester. This method allows high masses traveling at low velocities to be investigated. These situations simulate events such as accidental tool drops on structures during routine maintenance. Apart from these two popular methods investigators have also used other forms of impact testing. These include pendulum style systems, cantilever impactors (Lal (1983(a) and 1984) and the Hopkinson pressure bar technique (Stout et al. 1999) and it's variations (Gary and Zhoa 2000). Beks (1996) used a 'mouse trap' impact machine, which was essentially a variation of the cantilever impact method.

Damage as mentioned before tends to consist of matrix cracking, delaminations and fibre breakage, which all tend to be internal to the structure and cannot be detected simply by inspecting the surface of the specimen. Specific techniques are required in order for investigators to actually determine the damage that occurs within a composite. There are two categories of techniques that are used, non-destructive and destructive. Non-destructive techniques are used when detecting the presence of impact induced damage and also preserving the specimen, which allows for further testing of the specimen. Whilst destructive techniques provide detailed information on the actual damage induced, provided that the location of damage is known, but will destroy the sample in the process (Abrate 1998).

The non-destructive techniques that have been employed are C-Scan Ultrasonics and X-Radiography. Work has been performed using ultrasonics for the detection of impact damage in composites (Cantwell and Morton 1985, Cantwell 1988, Aymerich and Meili 2000), in which both delaminations and matrix cracking were observed. Cantwell and Morton (1989(a)) used X-Radiography to show the presence of separate delaminations within a specimen and compared it to C-Scans where only a damaged area is shown. However neither of these techniques can give a good indication in how the damage behaves through the thickness of the specimen. When a more detailed

knowledge of the through thickness damage is required destructive techniques such as sectioning and microscopy (both light and electron) and de-plying would be used. Cantwell (1988) used these techniques in conjunction with non-destructive techniques to assess the damage in impacted CFRP laminates. Cantwell and Morton (1992) give descriptions of all the above damage detection techniques as well as others which are not as commonly used along with their advantages and disadvantages for detecting all types of damage.

2.2.1 Low Velocity Impact Damage Development

The main modes of failure due to impact, as mentioned previously are matrix cracking, delaminations, fibre failure and penetration. Much work has been performed in order to understand damage patterns that occur due to foreign object impact, and in determining the sequence in which damage accumulates. Cairns and Lagace (1992) developed a design methodology for the treatment of composites under impact. They treated the behaviour of composites under impact as the sequential effect of a number of events. This allowed them to develop a design methodology where the analysis for the impact of composites can be performed in stages.

Investigations like this can have been performed by either experimental observations or by predictive methods such as finite element analysis. Experimental investigations have shown various aspects of impact damage and its development and accumulation. A majority of work in this area has concentrated on low energy testing with in the 1-5J range. A lot about matrix damage and delaminations has been learned from such investigations.

Matrix damage tends to be the first type of damage induced by low energy transverse impact (Abrate 1994). This type of damage usually takes the form of matrix cracking and/or fibre matrix debonding. These occur due to property mismatches between the fibre and the matrix and tend to be orientated in planes parallel to the fibre direction. After impact there tend to be a complex pattern of matrix cracks, which are very difficult to predict accurately. There are in fact two types of matrix cracks that have

been identified (Abrate 1991 and 1994). These are tensile and shear cracks; schematics of these types of cracks are shown in *Figure 2.4*. Matrix cracks that occur in the upper and middle layers start at the edges of the impactor. These are known as shear cracks and are caused by high transverse shear stresses (Abrate 1991, Richardson and Wisheart 1996). These tend to be at an angle of approximately 45°. These shear stresses are related to the contact force and contact area (*Figure 2.4(b)*). The other type of crack is known as a bending or tensile crack. These occur on the bottom layer so the laminate being impacted and are due to high tensile bending stresses and tend to be vertical (*Figure 2.4(b)*). The bending stress is closely related to the flexural response of the laminate.

The type of matrix crack that occurs depends greatly on the global structure of the composite. For long thin specimens bending/tensile cracks occur in the lower surface of the specimen due to excess transverse deflection and subsequent membrane effects predominate. On the other hand short thick specimens tend to be stiffer and hence will cause higher peak contact forces, which induce transverse shear cracks under the impactor in the upper layer.

Early investigations were concentrated on the understanding of delamination patterns and how they are developed. Delaminations are cracks that run in the resin rich area between plies (Richardson and Wisheart 1996). Delaminations always occur between two layers with different fibre orientations, never between two layers of the same orientation. Several investigations have resulted in detailed maps of delamination areas caused by an impact event. Delamination shapes are shown to be oblong or 'peanut-shaped', with the shape's major axis orientated in the fibre direction of the lower ply at that interface. Lui (1988) explained that delamination was a result of bending stiffness mismatches between adjacent layers. Both experiment and analysis showed that plates tend to bend concave in the fibre direction and convex in the transverse direction causing bending induced stresses, which are the major cause of such damage. He also showed that the greater the mismatch between the two layers (0/90 being the worst case scenario), the greater the delamination area will be. However this is also affected by other parameters such as material properties, stacking sequence and the thickness of the laminate.

In general the first phase of impact damage usually consists of the shearing out of a 'generator' strip in the first layer, except in the cases where the velocity is very low. This strip is parallel to the fibre direction and has a width equal to the diameter of the impactor. Up until the point when the fibres fracture, this strip is pushed down by the impactor and subsequently loads the second layer. This initiates interlaminar separation between layers 1 and 2, hence causing a delamination. The fibres in the first layer will fracture either due to shearing actions caused by high velocity impacts or by high tensile stresses which are a result of this layer being pushed through. After the breaking of the fibres in the first layer the process is continued as it repeats by the forming of a 'generator' strip in the second layer and so on. Sierakowski et al. (1976) also looked at failure modes in glass-epoxy composites plates impacted by blunt ended impactors and observed a sequential delamination mode. Takeda et al (1982 (b)) measured the velocity of this generator strip and found it to be higher than that of the measured delamination-crack propagation velocity hence confirming that the assumption of the generator strip initiating damage.

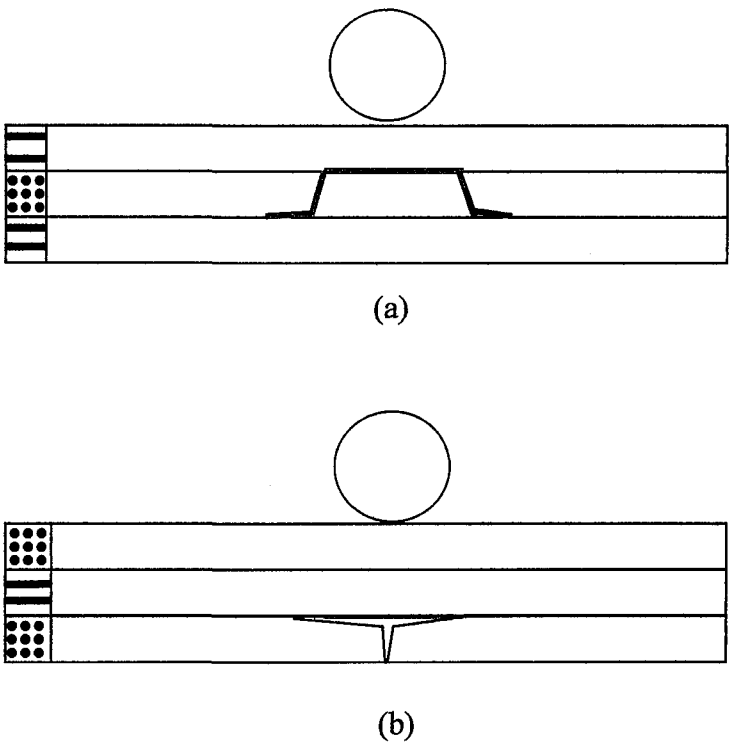


Figure 2.4: The two types of matrix cracking: (a)shear crack; (b)bending or tensile crack

Ross and Sierakowski (1973) studied the damage inflicted onto a composite plate by a blunt ended impactor. Using visual means with a strong light source, they observed significant areas of delaminations. Cristescu et al. (1975) described the failure mechanisms in composite plates impacted by a blunt ended impactor. In their five layer glass-epoxy laminates, they found four distinct delamination areas.

Lui and Malvern (1987) showed several interesting features concerning matrix cracking patterns working on (0, 90, 0) laminates. They showed that cracks were orientated in the fibre direction, and on the impacted surface this pattern could be divided into three zones. The central zone coincides with the delamination on the second interface, however if there is no delamination at this surface then this zone does not exist. The other two zones are wing zones, which are bounded by the diagonals of the plate. On the non-impacted surface the matrix cracks run parallel to the fibres from one edge to the other, apart from the central zone where the cracks are interrupted in the same area as that of the delamination on the second interface. In the internal lamina, 45° cracks were present in an area corresponding to the delamination at the first interface, whilst 90° cracks were observed in the remaining area, which corresponds to the delamination at the second interface. The authors also gave explanations to what caused the matrix cracks. The cracks on the non-impacted surface layer are caused by tensile stresses due to bending during the first quarter of flexural vibration, whilst cracks on the impacted surface layer are caused by the tensile loading portion of the transient wave.

Wang and Karihaloo (1997) found that multi-directional laminates under transverse low velocity impact tend to suffer a considerable amount of delamination damage. The intensity of the damage found depended on the difference in the ply angles above and below the interface. They also looked at the role which matrix cracks have in triggering delaminations using a fracture mechanics based model, and on the influence of the variation of ply angles in adjacent plies on delamination cracking. Their analysis showed that with a composite containing a transverse interply crack, the crack-induced interfacial principal tensile stress is at a maximum when the difference between the ply angles across the interface is at 90°, and is at a minimum when the difference is 40°.

With these two forms of damage identified, their relationship to each other was the next step in investigations. Delaminations caused by transverse impact will only occur after threshold energy has been reached, and it has often been observed that delamination only occurs in the presence of a matrix crack (Richardson and Wisheart 1996).

Results from work performed by Takeda et al (1981) on the impact on composites due to various shaped impactors, showed the presence of transverse matrix cracks in the damage area for the first time. It was also suggested that transverse matrix cracking was caused by the tensile stresses developed by membrane action due to large tensile transverse displacements during the impact event. Further work by Takeda et al. (1982(a)) presented microscopic observations showing the presence of both delaminations and matrix cracking. The observations also showed that there were two distinct types of cracking present. There were cracks that were perpendicular to the interface with no delaminations nearby, whilst others grew obliquely and were subsequently followed by delaminations. This work also showed that delaminations do not always run precisely in the interface region, but can run slightly either side. Other work (Wu and Springer 1988) performed on transverse impact also showed the presence of both normal and inclined matrix cracks.

Joshi and Sun (1985) worked on delamination and crack interaction for 0/90/0 laminates due to transverse impact loading. They identified critical matrix cracks, which are ones that go on to induce delaminations. The two types of cracks already established will initiate their separate delaminations in their own way. When the inclined shear cracks in the upper surface reach an interface there are halted by the change in fibre direction and as a result can only continue to propagate between the layers hence forming a delamination. The continued growth of these delaminations is constrained by the existing transverse cracks within the matrix. On the other hand bending/tensile cracks are vertical and are thought to initiate the lower delaminations and have no growth restrictions.

Lagace and Wolf (1995) worked on the impact of several different laminated composite systems. They found that for laminates constructed from unidirectional

pre-preg tape, the incipient damage is in the form of matrix cracks. These cracks are then followed by delaminations at the cracked ply interface. They also found that this damage mode does not change when the material system is changed (i.e. woven fabrics).

Much more work has been performed trying to explain the mechanisms behind matrix crack induced delaminations. Choi at al (1991 (a) and (b)) and Chang et al. (1990) performed a serious of line loading; low velocity experiments and showed the typical damage pattern shown in *Figure 2.5* in 0/90/0 laminates. Choi and Chang (1992) then went on to use finite element analysis to study the stresses in the immediate vicinity of the cracks. They found that the delaminations are initiated as a mode I fracture process as a result of very high out-of-plane normal stresses caused by the presence of the matrix cracks and the high interlaminar shear stresses present along the interface. Garg (1998) on the other hand proposed that delaminations of this sort were initiated by the development of the interlaminar normal and shear stresses at the interfaces.

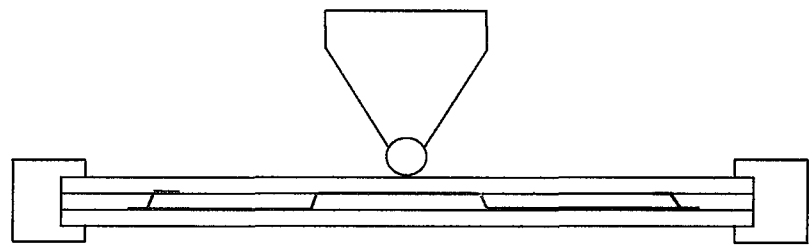


Figure 2.5: Typical Matrix crack and delamination pattern from line load impact on a 0/90/0 composite

Lui et al (1993) used an analytical model to study the interaction of the damage mechanisms based on fracture mechanics. They found that both bending and shear cracks can initiate delaminations. However delaminations caused by shear cracks are unstable, whilst bending/tensile cracks grow in a stable manner and this growth is proportional to the applied load. Collombet et al (1997) worked on $(0_n/90_m/0_n)$ laminates and found cracking in the 90° and delaminations at the interface between two cracked layers at impact energies of around 3J. They also observed that delaminations only appear if the layers on each side of the interface are cracked, and

that the delaminations extend in the areas where the layer furtherest away from the impact location is cracked. De Moura and Marques (2002) showed that the size of delaminations increases from the interface near the impacted surface to the interfaces near to the opposite surface.

Lee and Zahuta (1991) used instrumented impact tests and found that delaminations would suddenly appear only when the impact force had reached and surpassed a threshold energy value. This threshold energy is dependent on the laminate fracture toughness. Increasing the force led to increase in the damage area until fibre breakage occurs which leads to a leveling off in force. They found evidence that the laminate fracture toughness also affected the level off force. Fibre damage also acts to absorb energy and allow further delamination growth. Schoeppner and Abrate (2000) showed that there is significant evidence that a delamination threshold load occurs, which is defined as the load level at which there is a sudden drop in the load-time or load displacement plot for the impact event. This drop corresponds to a loss of stiffness to the in the impacted specimen at the laminate level. Davies et al. (2000) successfully predicted threshold impact energy for the formation of delaminations in plates with simply supported or clamped boundary conditions, using a combination of an energy-balance model and a force-driven model.

With an understanding of the initiation of delaminations from matrix cracks, investigators then went on to look at the development of delaminations. Choi and Chang (1992) stated that the growth of delaminations is determined by interlaminar longitudinal stress and transverse in-plane stress in the layer below the delaminated interface, and by interlaminar transverse shear stress in the layer above the interface. Razi and Kobayashi (1993) used numerical simulation to model impact induced delaminations. They found that mode II fracture was the dominant failure mode for propagation of a delamination. Olsson et al. (1996) looked at delamination growth in different coupon tests and studied the relationship between the delamination criticality growth rate and acoustic emission.

This allows a picture of how the damage progresses through a laminate. Most explanations tend towards matrix cracking being the initial form of damage and these

then lead onto the development of delaminations (Matthews and Rawlings 1994). Matrix cracks are induced by the initial impact, these grow until they reach a ply interface at which point they induce a delamination between the two plies. Matrix cracks then progress from these delaminations into the next layer and onto the next ply interface and subsequently the next delamination. However the position of the first impact induced matrix crack will depend on the thickness of the laminate. In thick laminates, the first matrix crack occurs in the first layer that is impacted due to localised contact stresses. The damage then progresses downwards from the top layer resulting in a pine tree formation (see *Figure 2.6(a)*). On the other hand thin laminates tend to bend on impact. These bending stresses on the back surface result in the first matrix cracks being induced in the bottom layer of the laminate and the damage pattern of matrix cracks and delaminations progress from the bottom layer upwards resulting in a reverse pine tree pattern (see *Figure 2.6 (b)*).

Morita et al (1997) performed drop weight and gas gun impact tests on Carbon Fibre/PEEK and Carbon Fibre/toughened epoxy laminates. They found that both low and high velocity impacts showed the same damage state consisting of delaminations connected by matrix cracks. Cross sections showed a characteristic cone of damage, whose apex is at the impact surface with a widening base as it travels through the thickness of the sample. The size of these 'cones' is dependent on the impact velocity, material system and stacking sequence.

Many authors have used analytical and numerical modelling to predict the damage that occurs in a composite under impact loading. Clark (1989) proposed a model, which was capable of explaining the preferential occurrence of delaminations at certain interfaces as well as characteristics of impact damage such as relative sizes of delaminations and the occurrence of prominent delamination and cracking features. Davies and Zhang (1995) showed that modelling internal damage in carbon composite structures requires the incorporation of non-linear behaviour due to both gross deformations and in-plane material degradation in order to achieve results comparable with experimental data. Duan and Ye (2002) used a three dimensional contact model with friction in finite element analysis, which used the Coulomb friction law to control sliding and friction to model the oblique impact of a cubic block on a thick

laminate plate. Their predicted results for delaminations were accurate when compared to X-Radiographs of a tested sample. Zhang et al. (2003) adequately predicted large deflections and delamination behaviour, in comparison with existing analytical and experimental results, using a model, which incorporates a stress based criteria and a fracture mechanics based criteria for predicting delamination initiation and propagation respectively.

Stout et al. (1999) found that matrix cracks and delaminations occurred at a ratio of 3:1 and that their combined length ratio of matrix cracks to delamination was unity. They also observed that the composites effective modulus decreased rapidly with small amounts of initial damage, whilst subsequent increases in damage decreased the effective modulus at a much lower rate. Pavier and Clark (1995) used artificial damage to investigate the effects of damage on residual properties. They found that in tension the reduction in strength is due entirely to fibre cracks, whilst in compression the reduction is caused by the redistribution of stress leading to buckling of delaminated plies.

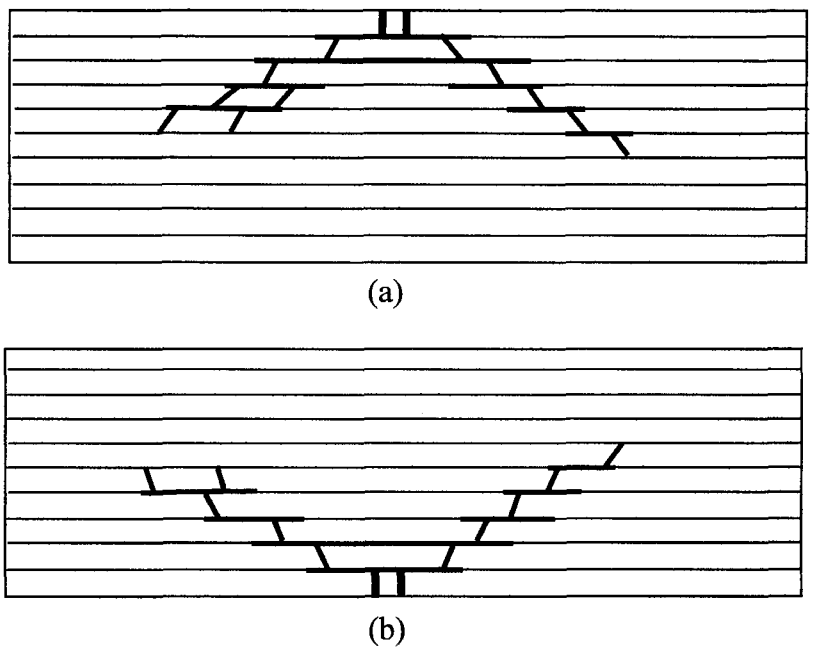


Figure 2.6: Pine Tree (a) and Reverse Pine Tree (b) damage patterns.

Fibre failure on the other hand is a damage mode that tends to occur later on in the fracture process compared to matrix cracking and delamination (Richardson and Wisheart (1996), Cantwell and Morton (1991)). Less information is available on this type of damage as research is generally performed on low velocity impact. However this type of failure occurs under the impactor due to local high stresses and indentation effects. They can also occur on the non-impacted surface due to high bending stresses. The degree of fibre failure depends on the span to thickness ratio and on how much the energy for damage initiation has been exceeded. Fibre fracture occurs in a small central region of an impact damage (Olsson et al. 2000). Fibre failure is recognized as the precursor to penetration failure due to impact.

The final type of damage that can occur with impact is penetration damage. This is a macroscopic mode of failure and occurs when fibre failure reaches a critical level at which the impactor can completely penetrate the material (Richardson and Wisheart 1996). Mines et al. (1999) looked at perforation behaviour of woven fabrics and z-pinned samples and found that at these type of velocities all types of construction behave in a similar manner. Chen et al. (1997) described a model for the prediction of impact damage caused by impact of a cube shaped projectile at a velocity of 2km/s. They found that at these velocities perforation of the whole thickness of the specimen would occur along with large areas of delamination damage on the rear face of the specimen. Although this type of damage is usually associated with the ballistic range of impact, some work on this subject has been performed in the low velocity range. Cantwell and Morton (1989(a)) found that the threshold energy for penetration rises rapidly with specimen thickness for Carbon Fibre Reinforced Polymers (CFRP). They also looked at the energy involved with a process known as shear out, in which the removal of a shear plug occurs. They found that shear out is a major energy absorption mode when it occurs during impact (≈50 – 60% depending on plate thickness). DeLuca et al. (1997) performed impact tests with velocities up to 4000 ft/s on GFR composites using fragments with lengths of up to 3.0 inches. They found that fragment penetration reached up to 91% of the thickness of the specimen and that the damage volume is independent of panel dimensions and depends only on impact fragment size and strike velocity. Composites would experience these types of

impacts and damage when used in application such as multi-wall structures for the protection of spacecraft against orbital debris (Schonberg 2000).

Beks (1996) reported impact response and damage in composite laminates under large and small mass impacts. The results showed that small mass impacts resulted in larger damage areas than large mass impacts and impact durations are extended with growing damage. Bland (2000) looked at the difference in damage behaviour in Low Mass/High Velocity (LM/HV) impacts and High Mass/Low Velocity (HM/LV) impacts. They found that in HM/LV cases, the delamination area increases with increasing impact energy, whilst with LM/HV the delamination area increases with increasing impact energy up to perforation and after decreases with increasing impact energy. HM/LV produces less delamination area than LM/HV for the same impact energies. LM/HV caused delamination areas, which were not affected by specimen span. Very different delamination patterns are shown by flexure dominated (HM/LV) impacts and through thickness stress wave dominated (LM/HV) impacts.

The importance of impact damage is in the affect it has on the performance of composites especially in the reduction of mechanical properties. Impact damage may affect structural failure in several ways that include: delamination growth from the buckling of the sub-laminate and/or panel; reduced panel buckling load caused by the presence of damage; and in-plane failure due to stress concentrations at the damage areas (Olsson 1999). Damage in the form of fibre fracture reduces both tensile and compressive strength (Olsson et al. 2000). Lal (1983) performed work on the residual strength of laminates subjected to impact at increasing levels of impact energy and also proposed a model which gave results which showed the same trends as experimental data. Tracy and Pardoen (1988) showed that delamination damage reduces the three-point bend stiffness of composites by around 34%. Jones et al. (1988) reviews and analysis the procedures and techniques used for assessing impact damaged composite laminate for use in through life support of damaged composites.

2.3 The Factors that Effect The Impact Response and Impact Damage Development in Composite Materials

The main types of damage in composites caused by an impact event and how this damage is initiated has been outlined above. However the way in which a composite responds to impact and consequently the damage caused by an impact event can be affected by many factors. These range from the impact conditions (i.e. impact energy, impactor shape etc) to the actual material (i.e. stacking sequence, material constituents, target geometry, etc.).

2.3.1 Effects of Impact Conditions

The impact energy involved in an impact event can be varied by varying one of two factors, either the impactor mass or the impact velocity. In experiments in which only the velocity of the impactor is the only variable it has been shown that there is a threshold velocity at which no detectable damage occurs (Abrate 1991). Above this threshold velocity no surface damage is detected except maybe a small indentation at the contact point, but below the surface significant internal damage occurs, which includes matrix cracking and delaminations. As the velocity increases to a certain level, surface damage will occur due to fibre breakage being introduced. Finally at very high levels of speed the target does not have enough time to deform and the projectile will perforate the target, leaving a clean hole in the target.

Cantwell and Morton (1989(b)) performed a series of low (using a drop weight set up) and high velocity tests (utilising a gas gun set-up) on CFRP laminates. They found that decreasing the impactor mass resulted in greater levels of incurred damage. It was believed that a light fast moving projectile produced a very localised target response in which in the incident energy of the projectile is dissipated immediately adjacent to the point of impact via the shearing of the fibres.

Robinson and Davies (1992) performed tests in which they varied the impactor mass. They found that for a given specimen size the damage induced by low velocity impact with a varying impactor mass was a function of impact energy alone rather than a function of either impactor mass or velocity. They also found that the peak force correlated with impact energy independent of the impactor mass, which indicated that low velocity impact in this case was a quasi-static process.

Another factor that can change the impact response of a composite is the shape of the actual impactor. The two main types of impactors used in experimental work are spherical and flat-ended impactors. For spherical impactors it has been shown that the contact force-deformation relationship follows a law similar to that of a Hertz analysis for isotropic materials (Chrisoforou 1993). However there are a few uncertainties regarding using the Hertzian contact of a sphere and a half space when applied to thin laminates. The initial stages of loading, during which the contact radius is small compared to the laminate thickness the Hertzian analysis should be adequate, however higher loads cause extensive damage in the contact zone which becomes a major factor in the way the material responds to impact.

Zhou (1995) looked at the damage mechanisms in woven fabric composites due to a flat-ended impactor. He identified two additional damage mechanisms that were associated with the use of a flat-ended impactor. The first of these being surface micro-buckling, which is due to local compression failure at fibre crossovers due to the lack of local support on the impact surface and occurs along the fibre direction in the shape of a cross. The second additional damage mechanism is fibre shear out and is typical of impact by a flat-ended impactor. He also showed that as the incident kinetic energy increases, extensive delamination is generated.

It can be seen by the work of the above two authors that the shape of the impactor does have an effect on the damage that occurs in an impact event.

2.3.2 Effects of Material Constituents

Fibre reinforced composites have two major constituents, the fibres and the matrix, and incorporates what is known as the inter-phase region, which is essentially the area of bond between the two major constituents (Matthews and Rawlings 1994). The properties of all three of these affect the threshold energies and stresses for the initiation of failure modes in impact events.

2.3.2.1 Fibres

The fibres are the main load bearing constituent in a composite and hence provide the composite with a majority of its strength and stiffness. The most popular fibres used in composites are carbon, glass and Kevlar. Each of these fibres has their own set of unique properties and also has their own different grades (Richardson and Wisheart 1996). Carbon fibres are the most widely used fibres in the aircraft and high performance industries, and also have many structural applications. This is due to their high strength and stiffness, although they are the most brittle of the three types with a strain to failure of only 0.5 – 2.4%. Glass fibres on the other hand have a lower strength and stiffness values compared to carbon fibres, but however do have better strain to failure values (≈3.2%) and are less expensive. Kevlar fibres have mechanical properties in between glass and carbon fibres.

For impact resistance the main property that is required from a fibre is the ability to store energy elastically (i.e. fibre strain energy) (Abrate 1991, Richardson and Wisheart 1996). Higher fibre failure strains, with the same elastic modulus, will result in higher energy absorption capacity. The higher the capacity to absorb energy results in less fibre breakage. This will also reduce secondary matrix damage, which occurs after initial fibre failure. This property corresponds to the area under the fibre's stress-strain curve, which is dictated by its modulus and failure strain. Therefore it follows that E-Glass fibres can absorb significantly more energy than carbon fibres, hence making them more resistant to impact damage. Hybrid composites utilising either Kevlar or Glass fibres in conjunction with carbon fibres are

found to further improve impact resistance. However there are mismatches between the fibres, which causes difficulties in hybrid design.

Cantwell et al (1986) performed a series of low velocity tests on composites reinforced with Hercules AS4 high strain carbon fibres. These fibres have a mean tensile strength of 3.59 GPa, an elastic modulus of 235 GPa, a strain to failure of 1.53% and a fibre diameter of 7.0 μm. They found that the damage size was significantly less than that observed in CFRP reinforced with standard carbon fibres with a mean tensile strength of 2.70 GPa, an elastic modulus of 235 GPa, a strain to failure of 1.14% and a fibre diameter of 7.7μm. From the data shown, it can be seen that both types of fibres had the same modulus hence the increase in strength and decrease in damage area corresponds to the increase in failure strain.

2.3.2.2 Matrix

The matrix in a composite has several key functions: it transfers the load to the fibres; protects the fibres from damaging themselves; and aligns and stabilizes the fibres. Strain to failure is again the main material property here. It is recognised that an increase in strain to failure of the matrix leads to better residual properties as a result of a better resistance to impact loads (Abrate 1991). When deflections become greater than one half of the specimen thickness, a significant fraction of the load is carried by membrane action. The maximum load or maximum energy to failure of the resin becomes a measure of the amount of in-plane stress that can be generated before failure.

The most comprehensively used matrix materials at the moment in high performance reinforced plastic composites are thermoset polymers; especially epoxy resins (Richardson and Wisheart 1996). They meet the hot/wet compressive strength requirements. However epoxy resins are brittle and hence have poor resistance to crack growth, which is essentially what a delamination in a layered composite is. Attempts to reduce matrix damage and increase interlaminar fracture toughness in epoxy composites have involved incorporating plasticizing modifiers, or adding rubber or thermoplastic particles to the resin. However attempts like these to increase

strain capability and interlaminar fracture toughness will reduce the mechanical properties of the resin and its performance at high temperatures. Also improvements to the pure matrix are never fully transferred to the composite due to the presence of the brittle fibres (Abrate 1991, Richardson and Wisheart 1996).

The possibility of using other materials for the matrix has also been looked at. The main alternative matrix materials at the moment are thermoplastics, with polyetheretherketone (PEEK) being the one being investigated most. They provide a significant increase in fracture toughness compared to thermosets, but on the other hand have low thermal stability, poor chemical resistance, poor fibre matrix interfacial bonding and have poor creep resistance (Richardson and Wisheart 1996). Dorey et al. (1985) performed tests on laminates with epoxy and PEEK matrices. They found that PEEK laminates showed a visible indentation on the surface after impact, this being evidence of plastic deformation, and they found compressive cracks on the surface fibres of these laminates, where as no evidence of surface damage was visible on the epoxy laminates. Microscopic observations of the two types of laminates showed that there was significantly less delamination damage in the PEEK laminates than in the epoxy laminates, which results in higher residual properties.

Morton and Godwin (1989) tested composites with a toughened epoxy matrix and a PEEK matrix in the form of both short beams and as a diaphragm supported between two 130mm rings. They found that in short beam form visible damage occurred at much the same incident impact energy regardless of material. The PEEK matrix composite showed signs of fibre breakage but little delamination. They also observed that rear face damage occurred later in the PEEK specimen in comparison with the toughened epoxy.

Another method of increasing the matrix resistance to fracture is by including a thin discrete layer of very tough, high shear strain resin (Richardson and Wisheart 1996). These are known as interleaf systems. In general such systems develop less delaminations and yield higher residual properties. However these systems have the downside of raising the resin content of the composite system and hence lowering the modulus and increasing the composites sensitivity to environmental conditions.

Therefore from the above it can be seen that improving the matrix materials resistance to fracture can go a long way to improving the overall composites impact resistance.

2.3.2.3 The Interphase Region

The interphase region is between the fibre and the matrix is a very important part of the composite structure. This region can affect the failure mode that occurs at any given load. For example poor adhesion between the two constituents result in failures at low transverse stresses leaving more or less clean fibres (Richardson and Wisheart 1996). Fibre finishes and matrix properties significantly affect the interfacial shear strength between the two phases. Usually carbon fibres are treated by an oxidative process in order to improve adhesion between itself and the matrix material, whilst glass fibres are often treated using a coupling agent. The bond strength can be manipulated to provide greater impact tolerance by absorbing energy within this interphase region. Peiffer (1979) showed that for glass-epoxy composites, impact resistance could be significantly improved by introducing a rubbery interface between the fibre and the matrix. The properties of the composite are dependent, however, on both the thickness of this interlayer and its glass transition temperature. Often than not manipulating this interphase region will reduce the overall mechanical properties of the composite.

2.3.3 Effects of Stacking Sequence

Ross and Sierkowski (1973) were the first to identify the importance of stacking sequence on the impact resistance of laminates. In unidirectional laminates no delaminations occur due to fibres all being aligned in the same direction. For two plates, both of the same thickness, but with a different stacking sequence, the one with the greater difference of angle between adjacent layers will develop the greater delamination area. At the same time increasing the thickness of each layer will also lead to the increase in number of delaminations. Increasing the difference between the longitudinal and transverse moduli (by manipulating the stacking sequence) of the

material leads to higher bending stiffness mismatches hence creating increased delaminations.

Cantwell and Morton (1985) performed a series of tests on a number of stacking sequences. They found that at low incident energies the location of the damage induced depends on the target stiffness. In thin laminates, which are flexible, damage initiated in the lower ply due to the flexural action of the beam. In stiffer, thicker targets, damage begins at the uppermost layers and is due to large contact stresses.

Fuoss et al. (1998 (a) and (b)) undertook predictive methods for determining effects of change in stacking sequence on the impact damage resistance of composites. They firstly found that a Finite Element Model using quasi-static analysis was suitable for predicting internal damage trends for low velocity impact. They found that the internal damage was related to stress state within the laminate before damage initiation. They successfully investigated the key stacking sequence parameters, which included interface angle (the angular difference in fibre orientation between the two layers within an interface), ply orientation and ply grouping, and developed a set of design guidelines for improving impact damage resistance (Fouss et al. 1998(a)).

These guidelines are as follows:

- avoid ply grouping
- avoid stacking adjacent plies in similar orientations especially at interface angles below 45°
- avoid using multiple interface angles to stack plies
- Give attention to the orientation of plies relative to plate boundaries. For rectangular plates, the following guidelines were recommended:
    - for stacking sequences maintaining an interface angle of 45°, start the stacking sequence with the first ply orientated along the shortest dimension, in this case the width
    - for stacking sequences maintaining an interface angle of 90°, start the stacking sequence with the first ply orientated at ±45° to the width of the plate

They then went on to use a parameter based on bending strain for predicting impact damage resistance of a composite with respect to changes in stacking sequence (Fouss et al. 1998(b)). The method was evaluated by ranking composites for damage resistance using this proposed parameter and comparing the results with existing experimental and numerical results. The results agreed well with experimental measurements of the topographical damage area.

Work by Baker et al (1985) showed that there were two main effects that laminate stacking sequence has. Firstly laminates with 0° outer plies were more weakened by delaminations than those with ±45° on the outer layers. Also in general, laminates that are woven ±45° plies showed better delamination resistance than laminates of unidirectional ±45° plies. This seems to indicate that ±45° orientation have a better resistance to delaminations, however laminates of solely this orientation would sacrifice mechanical properties for impact resistance, therefore the use of ±45° outer layers can be a method of improving impact resistance whilst retaining laminate mechanical properties.

De Freitas et al (2000) used a combination of drop weight test and numerical analysis to investigate the mechanisms of damage growth on two stacking sequences and two different carbon/epoxy composite systems. They found that the delaminated area depends on the number of interfaces between plies, and two failure mechanisms were recognised, both influenced by the stacking sequence and the thickness of the specimen.

However damage initiation is matrix and interface dependent and therefore has no or little dependence on the stacking sequence. Therefore manipulating the stacking sequence only allows for the prevention of damage development and not the actual resistance to damage being induced. However at the same time the peak load reached during impact is strongly dependent on the laminate stacking sequence.

2.3.4 Effects of Target Geometry

Geometrical effects can take many forms, from size effects (thickness, length and width) to target shape. Much work has been performed on the effect that changing the composite geometry has on the impact properties of

Cantwell and Morton (1985) studied the influence of target bending stiffness on low velocity impact damage. They found that the change in target stiffness has a great effect on the damage development. They showed that target stiffness was a dominant parameter. Flexible targets showed a reverse pine tree damage pattern, whilst damage in stiffer targets developed in a pine tree effect. They also showed that at intermediate velocities damage in flexible target originated from high contact stresses at the impact point and both types of damage development can be seen. They also found that there was an optimum thickness, at which damage initiates simultaneously which gives the highest resistance to damage initiation. Their results from two sets of experiments (Razi and Kobayashi 1993, Cantwell 1988) for low and high velocity impacts with the same specimen and boundary conditions showed the same trends but low velocity tests showed higher threshold energies.

Cantwell's (1988) high velocity work showed that changing the targets stiffness either by changing the thickness or the stacking sequence changed the mode of initial failure in the specimens. Changing the geometry led to significant increases in the perforation threshold energy. Damage in a circular plate was roughly the same as that of beam like and rectangular shaped specimens. Also increasing the surface area of the specimen by varying the length and width did not alter the amount of damage incurred by high velocity impact loading. He concluded that it is possible to reproduce damage levels incurred in operational structures in small test specimens.

Later work by Cantwell and Morton (1989(a)) on low velocity tests showed that damage development after initial initiation depends strongly on the ability of the structure to absorb energy elastically. Their tests on circular plates showed that under certain conditions they are capable of absorbing less energy than small simple beam-like specimens. Therefore this shows that simple target configurations don't

necessarily predict the mode of failure in more complex structures, and in some instances can indicate an optimistic prediction of the response of operational components.

Found et al (1997) looked at the static indentation and impact behaviour in 3 and 9 ply CFRP panels, which were circularly clamped with different diameter rings. They found that the maximum static force was similar for all conditions. However in 3 ply specimens increasing the panel size only affected the threshold for perforation. Whilst in 9 ply specimens an increase in the panel size led to a reduction in the delamination area and back face cracking. This indicates that increase in size (both thickness and surface area) leads to better impact damage resistance.

Morton and Cantwell (1989) showed that changing the testing arrangement from a short beam configuration to a diaphragm set-up changed the onset of visible damage. In the short beam configuration both a toughened epoxy matrix and a PEEK matrix showed no difference in when the onset of visible damage occurred, whilst in the diaphragm set-up the PEEK matrix showed signs of visible damage first.

Lui et al (1998) looked at a range of impacts ranging from sub perforation to perforation as well as various in-plane dimensions and thickness. Their experimental results showed that the influence of target thickness was much greater than the influence of in-plane dimensions. They suggested that as thickness effects are of greater influence, bending rigidity would be an important element for perforation analysis. They also concluded that perforation was the most important damage stage in composite laminates subjected to impact. This was due to the fact that impact characteristics and mechanical properties degradation became stable once perforation takes place. As this is the case delaminations therefore become the important role in impact energy absorption and mechanical properties degradation.

Lui (1994) used analytical and computational methods to model damage initiation and growth in thick sectioned composites. They found that damage in thick sectioned composites may be initiated in the layer right below the indentor due to the compressive load or by the interior shear matrix cracks due to transverse shear. They

also found that the delamination induced by shear cracks is dominated by fracture modes II and III for growth in thick sectioned composites due to indentation loading. Zhou (1996) used static tests to show the behaviour of damage in thick laminates and found that their behaviour is dominated by the onset of delamination, it's propagation and fibre shear out which is a measure of the laminate load bearing capability. Increasing the laminate thickness increases the load level of the incipient delamination and is proportional to that of the load bearing capability.

From the above it can be seen that a majority of impact tests are performed on flat coupons in beam or plate format, either clamped or simply supported. However composite components usually have more complex geometries, and in reality the response of stiffened panels would be more important. Work has tended toward the understanding of impacts in shaped and stiffened composite structures.

It has been shown that the energy required to cause Barely Visible Impact Damage (BVID) in stiffened composite structures drops significantly near stiffeners, as the structure is less compliant in this area. Damage around these type of areas spread asymmetrically as they are areas of non-uniform stiffness (Richardson and Wisheart 1996). Wiggenraad et al. (1999) impacted heavily loaded, stiffened composite wing panels, and showed that damage is very different when the specimen is impacted in the skin region, near the edge of the stiffener and actually at the stiffener.

Wardle and Lagace (1997) found that the behaviour of convex shells under both static and dynamic (impact) transverse loading is very different from what occurs in flat plates. They proposed that a structural instability occurs in convex shells which allows the shell to dissipate energy through structural deformation hence improving the impact damage resiistance. Kim et al (1997) used a three dimensional finite element model to model the impact behaviour in composites laminates with increasing levels of curvature. The model showed that as curvature increases the maximum impact force increases at the same impact velocity and that delamination patterns have the same tendency as plates, but the delaminated areas widen with increasing curvature. Work on curved structures lead on to work on practical uses of composites. Kostopuolos et al. (2002) modelled the effect of composite stiffness and

the damage development during impact on the dynamic response of composite motorcycle helmets, and found that shell systems with lower shear performance provides additional energy absorbing mechanisms leading to better crashworthiness in motorcycle helmets.

3. Materials and Experimental Procedures

This chapter describes the experimental techniques, equipment and materials used for the research presented in this thesis. The aim was to establish basic relationships between material properties, parameters and damage incurred during various levels of impact event. This made it necessary to devise experimental techniques that were different from the existing standard test procedures. The main interest in this research is to study the damage inflicted on curved composite panels subject to different types of impact. To complement this work on curved panels, a range of other studies were made including impacting flexible panels and flat panels with suitable fixtures and clamping arrangements so that there could be meaningful comparisons between the different studies and impact conditions for the different materials studied.

The main factors of interest were the effect of shape, size and flexibility of the composite panels as to their ability to absorb impact energy and the relationship of this to the level of damage inflicted for the different impact events. The study of inflicted damage included that developed at the contact site between impactor and specimen, through thickness damage, far-surface damage and that occurring at the specimen supports. To be noted for the materials studied, their shape, flexibility, structural stiffness and other parameters affect the ability of the different specimens to deform when impacted and this could have a significant effect on the level of energy absorbed at different stages of the impact event. Experimental methods were required, therefore, to observe the dynamic behaviour of the specimens throughout the impact event and high-speed photographic sequences were recorded for this purpose. This experimental arrangement provided for capturing the entire impact event from the approach of the projectile to the target, initial impact, changing deformation of the target, bounce of the target off the specimen and the following sequences of re-contact and bounce of the projectile.

Non-destructive techniques including X-Radiography and Ultra-Sonic C-Scanning were used to study the different degrees and extent of damage inflicted on specimens by the different impacts. Sectioning and detailed microscopy was also used to study

the disturbance of the material about the damage zones and how these damage zones varied for different impact conditions, specimen material and its shape. Whenever possible, the impact sequence of the damage was related to the different phases of the impact event.

3.1. Materials

The materials used for this PhD research were chosen after consulting users of the material as to the impact information in which they were particularly interested. Limiting factors in covering all that was required were mainly the time and effort available. Also, it was not always possible to obtain materials of all the shapes requested and this added to the experimental work needed to obtain the required information. Three main types of composite laminate were obtained and used for this research namely curved, flexible and flat laminates. A description of the materials used will be given here, including the composite system, lay-up stacking sequence and test specimen sizes. Stacking sequences are quoted in standard convention, for example $[(a/b/c)_n]_s$, where a, b and c are fibre directions, n is a repetition number and s denotes symmetry. *Figure 3.1* shows the direction of the fibres as quoted. Therefore, if the following stacking sequence is quoted $[(45/0/90)_2]_s$ the actual stacking sequence of fibre directions will be as follows 45,0,90,45,0,90,90,0,45,90,0,45. The laminate panels that were used were either supplied in sheet form or sections from contoured material.

3.1.1. Curved Laminates

The curved composite panels had a 2m radius of curvature in one direction only. These specimens were obtained from material shaped for use in airframes and provided by QuinetiQ (formerly known as DERA, Farnborough).

The composite system used for these panels was T800 carbon fibres in 924 Epoxy Resin. The original pre-preg material was supplied by HEXCEL. The stacking

sequence used was $[(\pm 45/0/90)_s]_4$, hence giving a quasi-isotropic laminate. With each layer being 0.125 mm thick, this produced a laminate with a thickness of 4 mm.

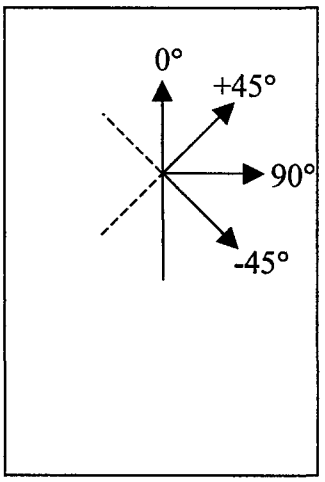


Figure 3.1: Standard convention for fibre direction notation in a composite laminate

Samples were cut to a size of 40 x 120 mm in two different orientations so that the main curvature was either longitudinal (along the 120 mm side) or transverse (along the 40 mm side). Schematics of these two different sample orientations are shown in *Figure 3.2*.

3.1.2. Flexible Thin Laminates

These panels were used to investigate the effects of flexibility on the level of damage incurred during an impact event. These samples were obtained from material being used by BAE Systems in their products.

The flexible materials used both employed PPS as the matrix material and to achieve different flexibility, carbon and glass fibres were used. The use of different fibres also affected the damage and energy absorption properties of the two materials. This was a complication that needed to be taken into account in the analysis of the results. This is very much the situation users of flexible materials need to consider. The specifications for the panels that were received are as follows:

Panel A: ***Fibredux 924C-833-42***

Carbon fibre Fabric: T300 Fibres – Specification: RMS 8050 Toray 5 Harness Satin Weave with T300 3K rovings

Lay-up: $[(0)_4]_s$

Panel Thickness: 0.315mm

Size: 300 x 300

Panel B: ***Fibredux 924C-20982-37***

R Glass Fibre Fabric

Weave unknown

Lay-up: $[(0)_5]_s$

Panel Thickness: 0.197mm

Size: 300 x 300

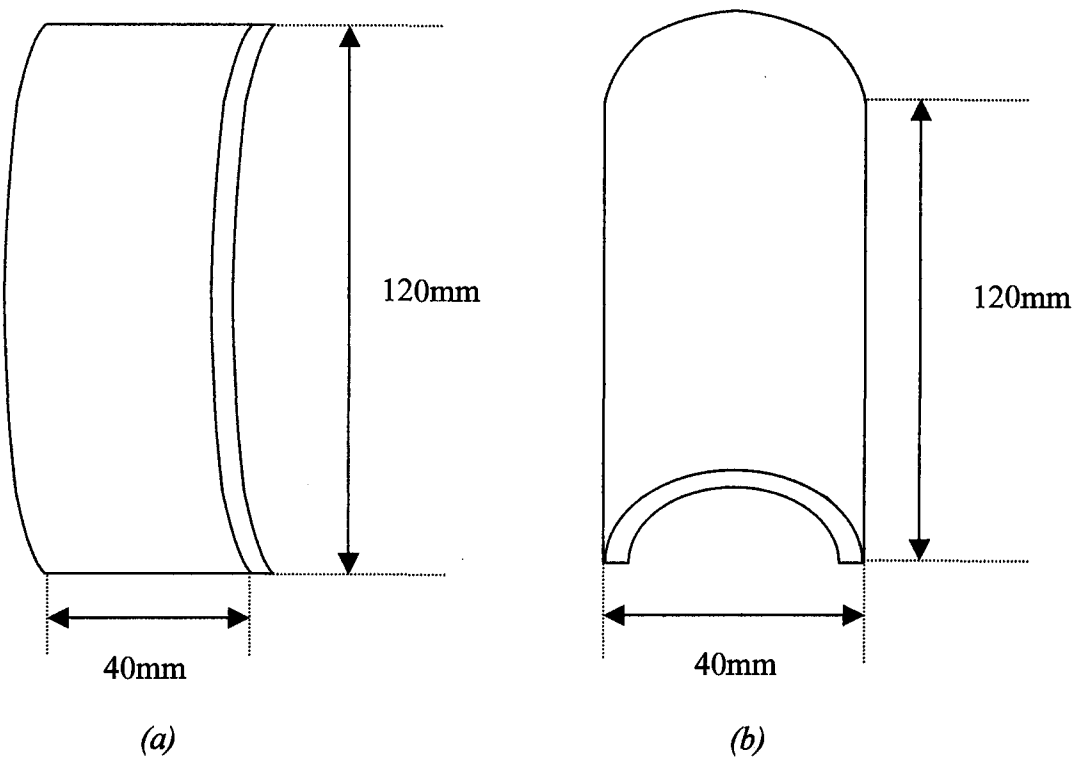


Figure 3.2: Schematics of the two different sample orientations for the curved specimens: (a) Longitudinal Curvature; (b) Transverse Curvature

These panels were then cut using a wet diamond coated circular saw. Two specimen dimensions were cut, 120 x 40 mm and 160 x 40 mm. These sizes were used in order to maximize the number of samples that could be produced from the size of panel obtainable. This, with the two different fibre types, gave four different levels of flexibility to be evaluated.

3.1.3. Laminates for Thickness and Size Effects

The samples studied were carbon fibre reinforced epoxy laminates as used by the aerospace and other advanced industries in their products. The fibre pre-preg used here was AS4 carbon fibres in an 8552 epoxy resin matrix. Two thicknesses were used and both used quasi-isotropic lay up sequences. The first thickness used was 4 mm and the stacking sequence for these was $[(\pm 45/0/90)_2]_S$. The other thickness used here was 10 mm and their stacking sequence was $[(\pm 45/0/-45/90)_5]_S$.

As well as having two thicknesses, samples were cut so that both length and width were varied so that the effect of varying all the dimensional variables could be considered. A list of the different sample dimensions used in this part of the research is shown in *Table 3.1.*

Panel	Thickness (mm)	Length (mm)	Width (mm)
A	4	150	80
B	10	150	80
C	10	150	60
D	10	150	40
E	10	120	80
F	10	120	60
G	10	120	40

Table 3.1: Dimensions for Panels used in Thickness and Size Effect Investigation.

3.1.4 Materials Sectioning

Of the three sets of materials referred to above only the curved laminates could be obtained in the needed size. Both the flexible panels and the thick laminates came in large panels that required sectioning into the required sizes. This was performed using the BENETEC Ltd. Series 500 Composite Plate Saw. This is a 'wet saw', with a diamond coated saw wheel and a constant flow of water based lubricant. This saw necessarily cuts at a slow rate. This was for two reasons, firstly so that no overheating occurs and secondly so that the lubricant is able to wash away effectively the carbon fibre dust produced during the cutting process.

The machine is automated so that once the cut line was set, the 'wet saw' performed the required cutting at the defined rate and length.

3.2. Experimental Procedures

This section of the chapter details all the experimental procedures that were involved in this project. This will include experimental set-ups and methodology.

3.2.1. Clamping Unit and Arrangements

The same main clamping unit was used in all of the three investigations but the gripping fixtures were slightly different to provide for different boundary conditions needed to achieve specific specimen behaviour of interest. Brief description of the fixtures and the clamping unit will be given here along with schematics of the units.

Main Clamping Unit:

Figure 3.3 shows a schematic of the main clamping unit as used to secure the samples in place for the impact experiments. This same clamping unit was secured appropriately to the drop weight or gas gun equipment. For the drop weight

experiments, the upper plate of the clamping unit was removed to provide clear passage to the specimen for the drop weight impactor. For the gas gun impact experiments an additional plate, with an aperture at the centre, was required in front of the clamping unit. This was so as to allow only the a 3 mm diameter free flight impactor to gain access to the specimen by obstructing the passage for the sabot and other free flight fragments that may be accompanying the impactor.

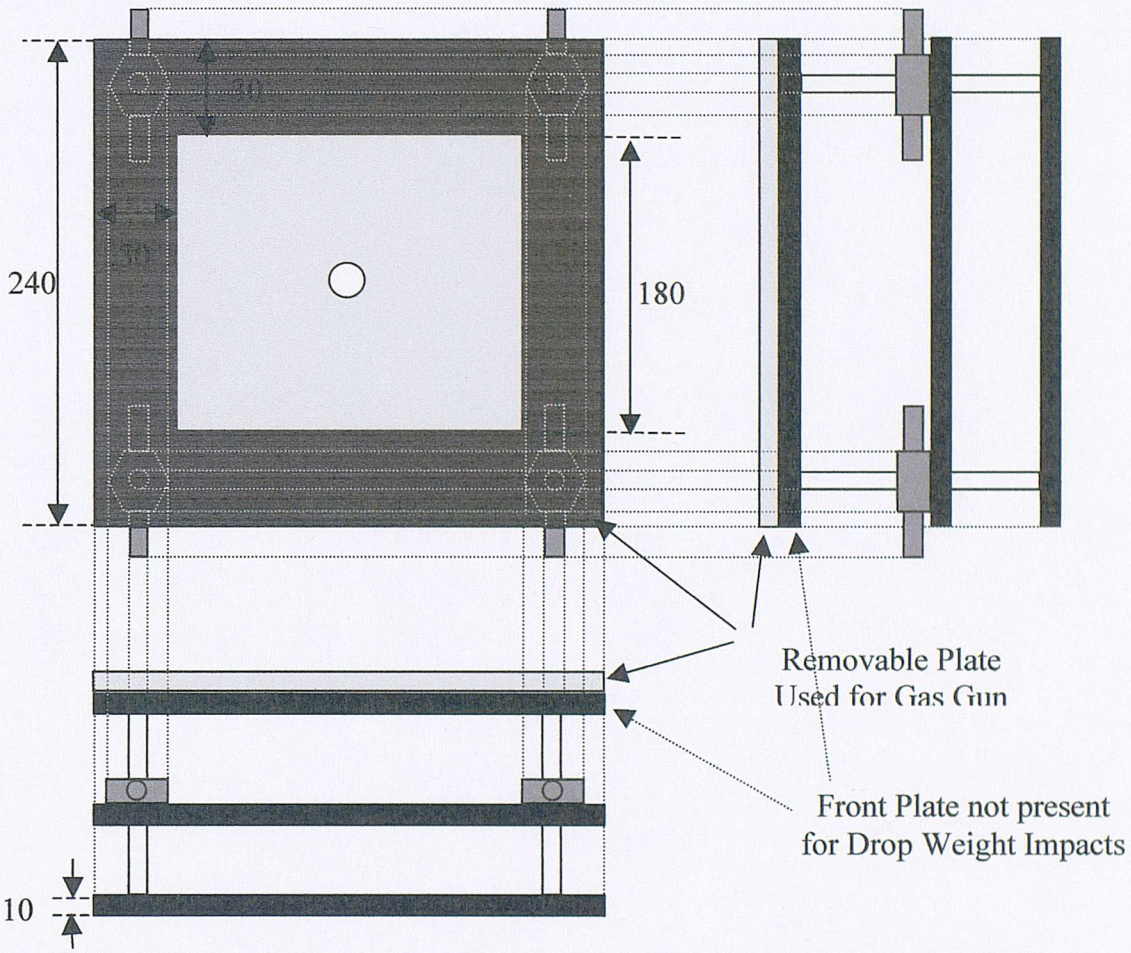


Figure 3.3: Schematic Drawing of the main Clamping Unit (Measurement in mm, not to scale)

Fixtures:

The different specimens were secured into fixtures that were designed that allowed them to have the required degrees of freedom to respond appropriately for the different impact experiments.

For the impacting of the curved composite laminates, the interest was how the initial and changing shape of the specimen affected its dynamic behaviour and inflicted damage during the impact event. Also, the effect on the overall damage suffered by the material specimen at the end of the impact event was of importance. Hence it was important to keep the specimen in a state in which it was free to respond fully to an impact. It was found that if the specimen is simply supported at the shorter of the two main dimensions, as shown in *Figure 3.4,* the curved specimen dynamic response was not constrained by the fixture. This is providing the grooves in which the specimen was located accommodated well the curvature of the specimen and allowed a small amount of free movement.

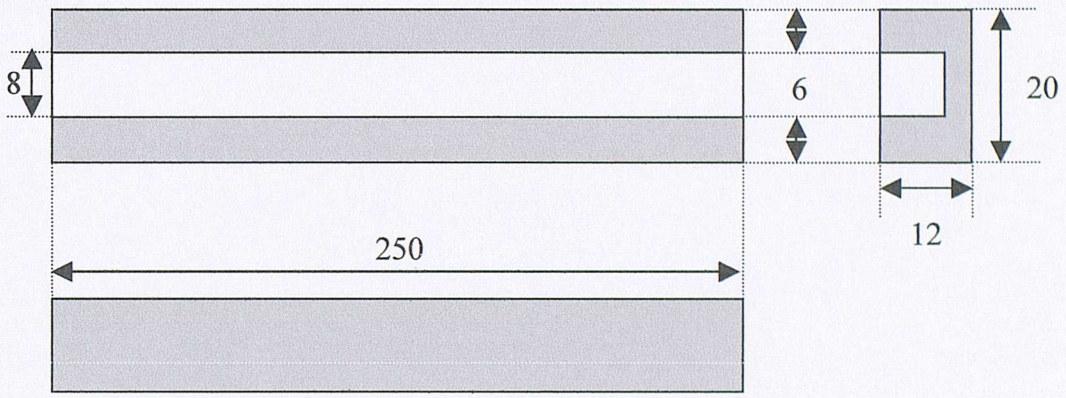


Figure 3.4: Schematic with dimension for one of the two grooved supports used for holding the curved laminates for impact testing (in mm not to scale).

The specimen fixtures for investigating the impact behaviour of thin flexible composite material, as to size and other effects of interest, require that the two ends of the specimens need to be rigidly held. Therefore, for both of these investigations, the samples were clamped securely at both ends using a set of clamps as shown in *Figure 3.5.*

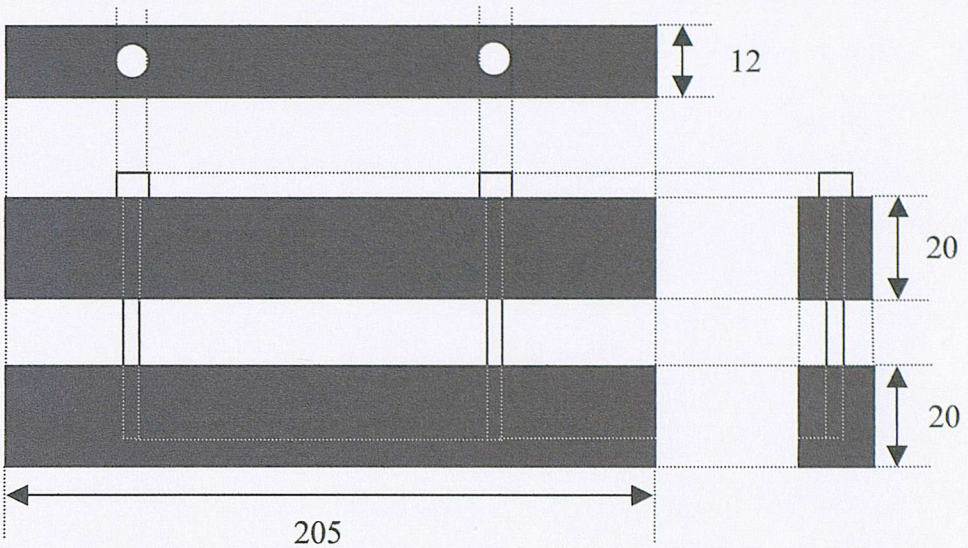


Figure 3.5: Schematic of one of the two end clamping supports for impact testing of both flexible and thick laminates (in mm not to scale).

3.2.2. Instrumentation

High-speed photography was used to capture the impact event. This was so the dynamic behaviour and visual evidence of inflicted damage, at different stages of the impact event, could be related. These data are also needed, with post impact studies of through thickness and other damage, to arrive at an impact damage history for each of the studies. The following provides information on the system used for the high-speed photography, including the camera's capability and how it was set up for use with the impact studies presented.

The camera used for this research project was the Hadland Imacon 468, provided by the EPSRC Instrument Loan Pool at the Rutherford Appleton Laboratory. This camera can take pictures at rates from 1000 fps (frames per second) up to 100 million fps, which is controlled by the minimum time delay between each frame, in this case 10 ns. However, the camera can only capture 8 pictures for each event. Each picture can be individually set so that the exposure of each channel and the inter-frame time between each channel can be completely independent of each other. This allowed precise points of the impact event to be recorded by adjusting the time at which each frame was taken after the triggering event. It was also possible to adjust the

brightness of each frame by varying the exposure time. This was especially helpful when using the system with the gas gun, as the illumination needed to be by flashlights and in order to achieve a good quality picture, the exposure had to be increased with each advancing frame. In these studies it was decided that, when possible, the eight images recorded would include the incoming projectile, the contact point, the response of the sample to the impact event and the rebound of the projectile.

A 266 MHz computer running Windows 95 controls the system. The computer is connected to two monitors; one displays the system software for control changes and the other monitor displays captured images. The images can be analysed aided by the dedicated DRS Hadland's software provided. *Figure 3.6* is a photograph of the assembled system.

The high-speed camera system is triggered by the interruption of a laser beam by the impacting projectile and the filming sequence is started and this includes the appropriate timing control of flashlight from the delay time settings. By calibrating the camera system the free flight velocity of the impactor can be derived from markers on the films capturing the impact event.

The twin laser beam triggering system also had a secondary purpose. It was connected to an oscilloscope, which allowed the time period between the breaking of the two beams to be recorded. Knowing the fixed distance between the two beams and this recorded time period allowed for a second method of obtaining the velocity of the incoming projectile.

Figure 3.7 shows a schematic arrangement of the instrumented gas gun equipment. To achieve a conveniently compact arrangement the camera was focused onto the impact target by using a mirror. To improve the quality of the film, as much as possible, the equipment was painted matt black. The projectiles were painted white and the sides of target specimens facing the camera were painted white and marked with thin black lines every 20mm across the thickness of the specimen. This helped to observe better the free flight of the impactor and the bounce of the impactor off the target specimen. Also the related changing deformation of the specimens during the impact.

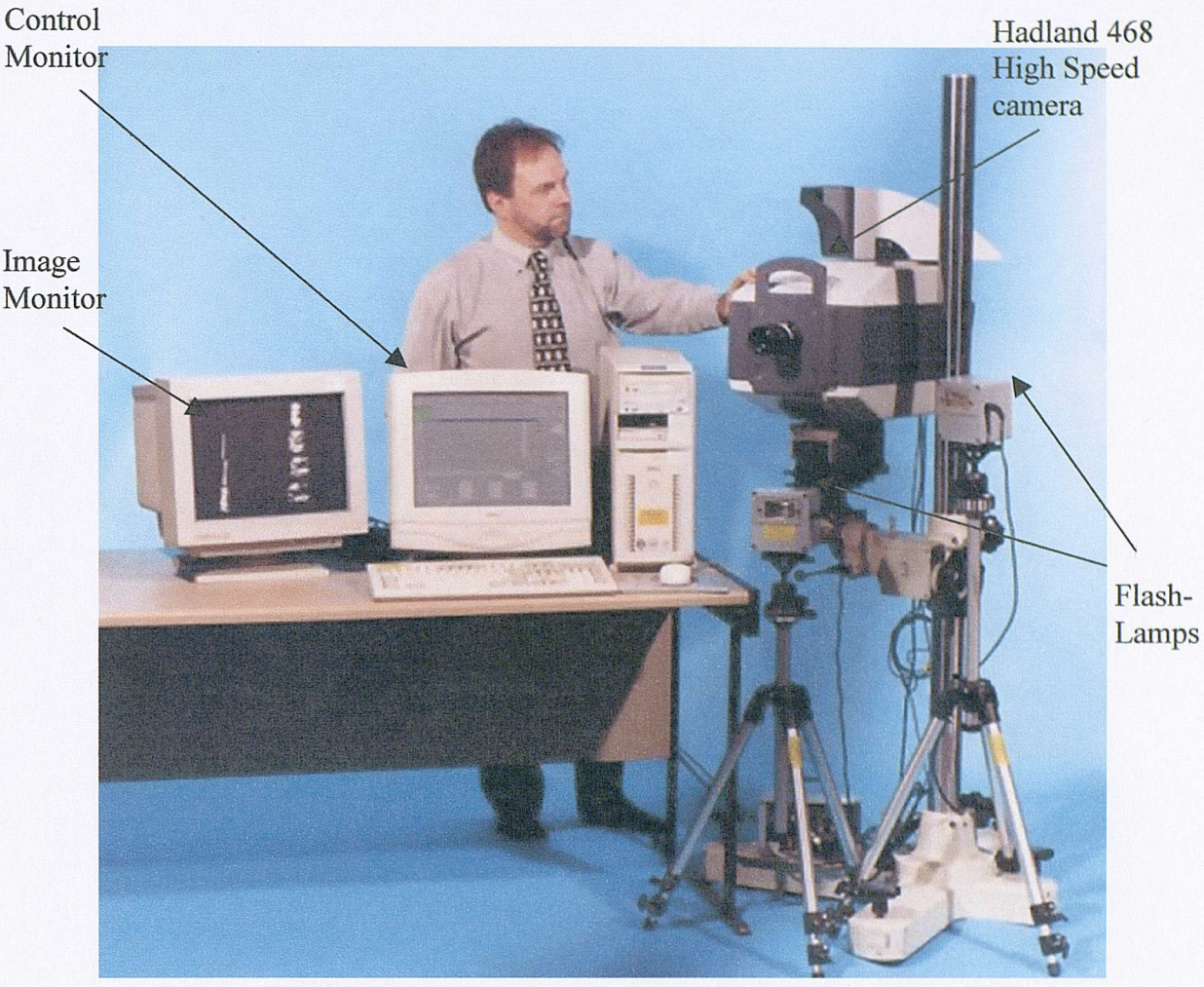


Figure 3.6: The Hadland 468 High Speed Camera System as borrowed from the EPSRC Instrument Loan Pool (picture taken from www.eip.rl.ac.uk)

Figure 3.8 illustrates the simple setting up procedure prior to the use of the camera to capture images of the impact of specimens. This was to use a carefully marked white card with vertical and horizontal lines, as shown, to calibrate the dimension of the images on the high-speed photographs recording the impact events.

When the camera was used for drop weight impact experiments different lighting arrangements were needed. Instead of flashlights, diffused back lighting was used, together with some additional side lighting, to achieve good illumination of the specimen in the drop weight fixture. Several adjustments were needed positioning the lighting to reduce glare and other photographic problems. Figure 3.9 shows a

schematic of the drop weight experimental configuration and Figure 3.10 shows the dimension calibration used.

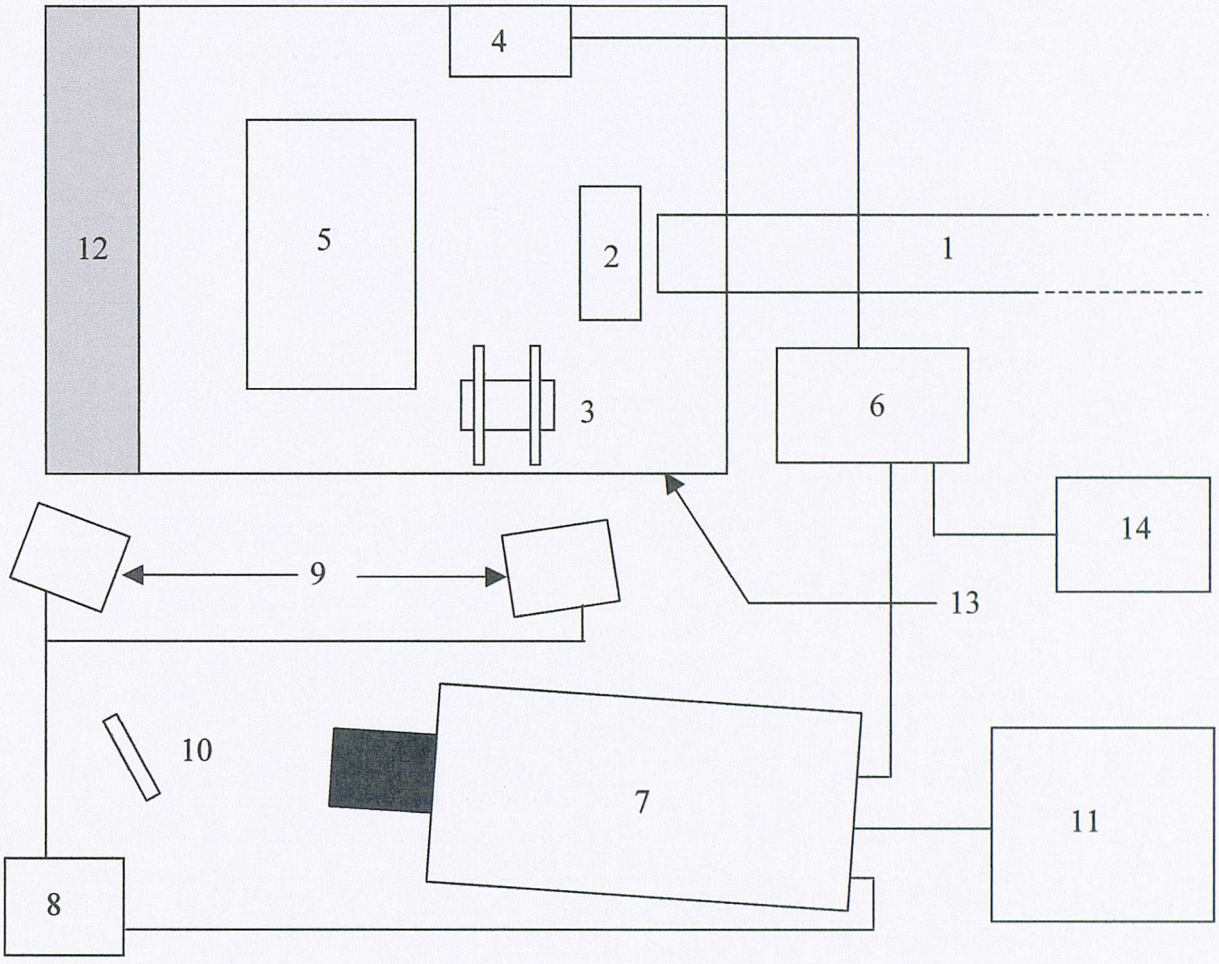


Figure 3.7: Schematic of the entire test set up. 1) Gun barrel; 2) Sabots stripper; 3) Light Pens; 4) Trigger Sensors; 5) Clamping Structure; 6) Trigger System; 7) High Speed Camera; 8) Flash Trigger; 9) Flash Lamps; 10) Mirror; 11) Computer; 12) Sand Bags; 13) Observation Window; 14) Oscilloscope.

The calibration method used for the drop weight set up was slightly different. *Figure 3.10* show a typical image taken from a sequence whilst using the drop weight facility. As can be seen there are two protruding metal spokes which are part of the main clamping unit. The fixed distance between the two spokes was measured and was inputted into the calibration step for the Hadlands Software.

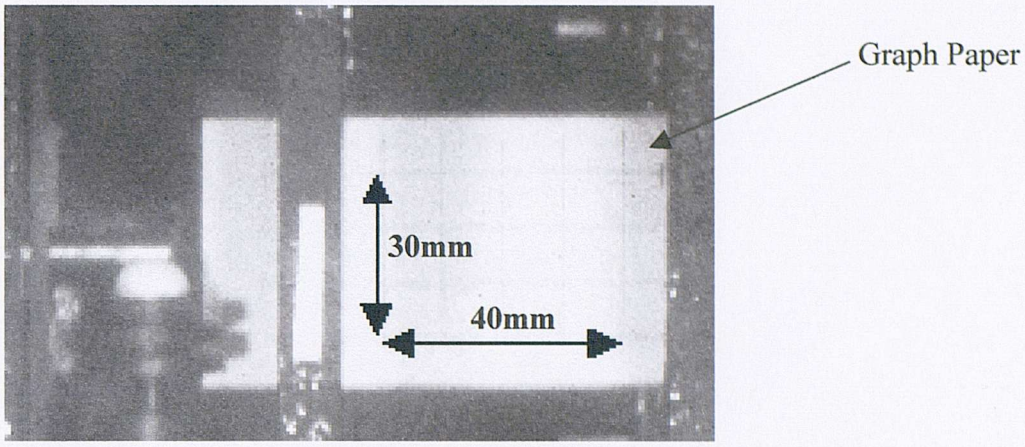


Figure 3.8: Example of a calibration picture taken using the gas gun set-up, from which base measurements of distance were provided to the Hadlands Software for the distance and velocity measurement to be calculated.

3.2.3 Impact Tests.

Two types of experimental equipment were used in this study namely; a Gas Gun Impact system and a Drop Weight Impact facility. The gas gun was used for investigating impact damage to curved composite laminates and the drop weight facility employed for impact research of flexible panels and thick panels. The following describes the use of these experimental systems in this study.

3.2.3.1 Gas-Gun Impact Experiments

In preparation for the use of the gas-gun its reservoir was charged with nitrogen up to 30 bar from a storage bottle. A safety valve system is incorporated to prevent overcharging and provide for the safe release of gas from the reservoir. A calibrated pressure transducer and a digital display measure the pressure of the installed gas. A fast acting solenoid valve controls the discharging of the reservoir gas into the gun barrel to propel the projectile. A schematic of the gas gun apparatus is shown in *Figure 3.11*.

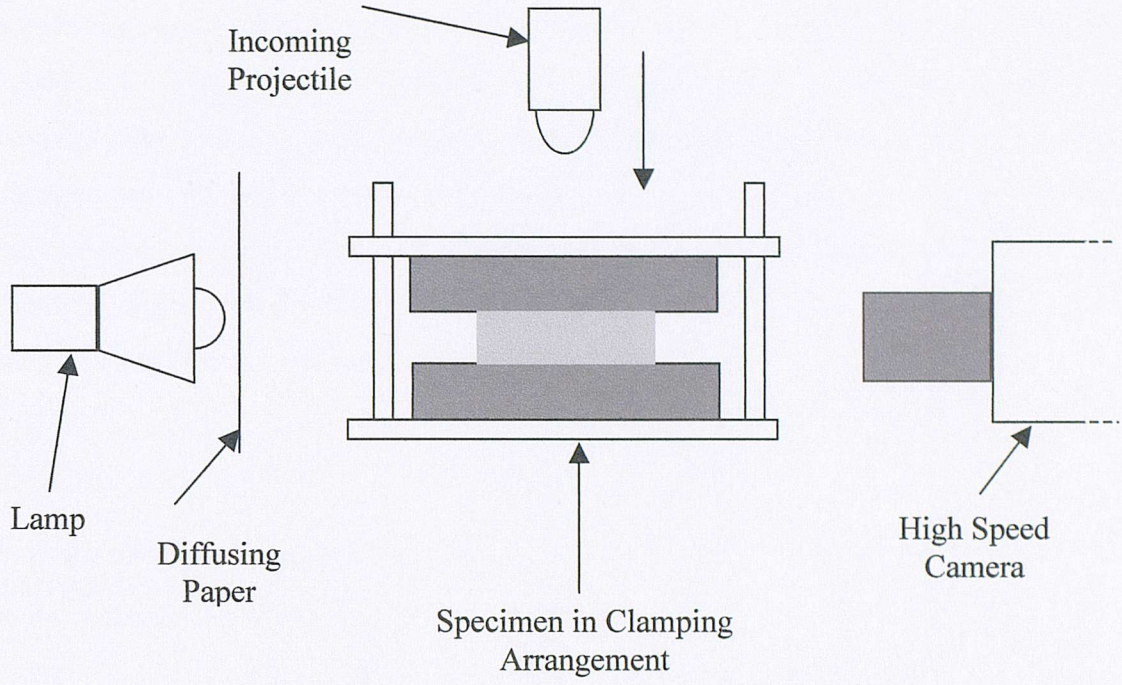


Figure 3.9: Schematic of camera and lighting set up when used during Drop Weight Tests.

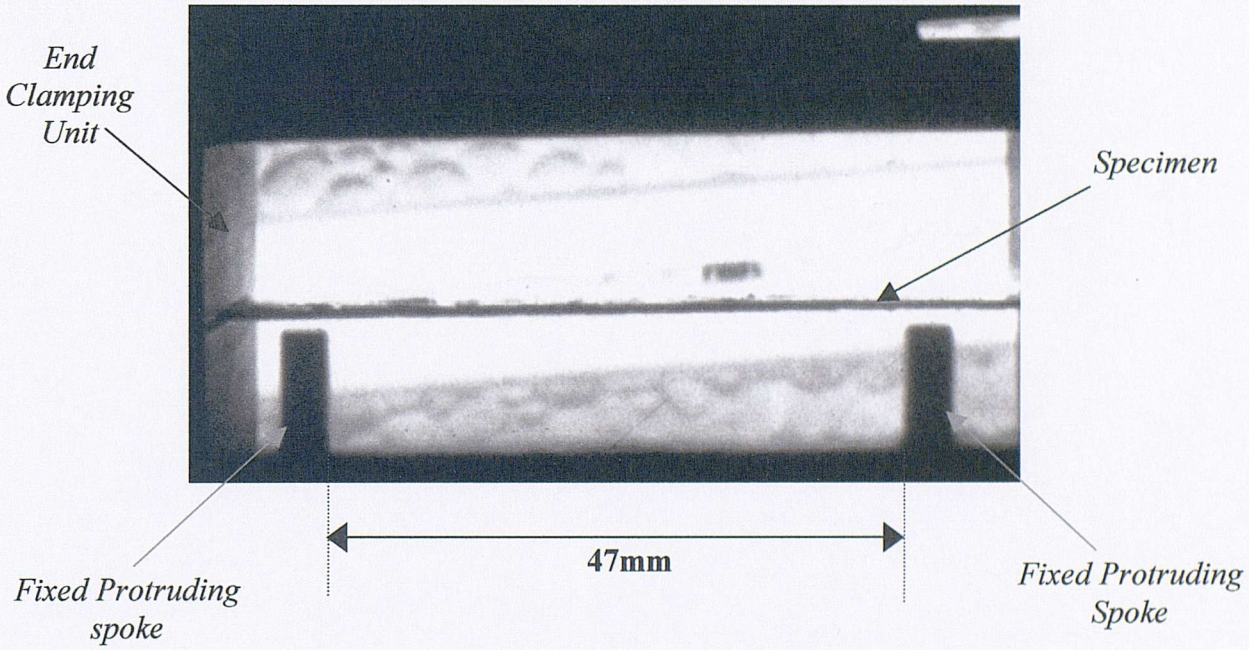


Figure 3.10: A typical image from drop weight testing with the distance and points used for calibration of the system.

The gun barrel has a length 3 m and an inner bore diameter of 32 mm. An injection-moulded polypropylene sabot (nominal mass of 6.4g ± 0.1 g) was used as shown in *Figure 3.12*. For these low mass high velocity studies the projectile was a 6.35mm diameter steel ball but a wide range of projectile masses can be used with this sabot arrangement. The sabot stripper used was a 5 kg steel block with a clearance hole for the free passage of the steel ball. The shape of the strippers contact face with the impacting sabot provided for a neat clean removal of the sabot. A schematic of the sabot stripper action is shown in *Figure 3.13*.

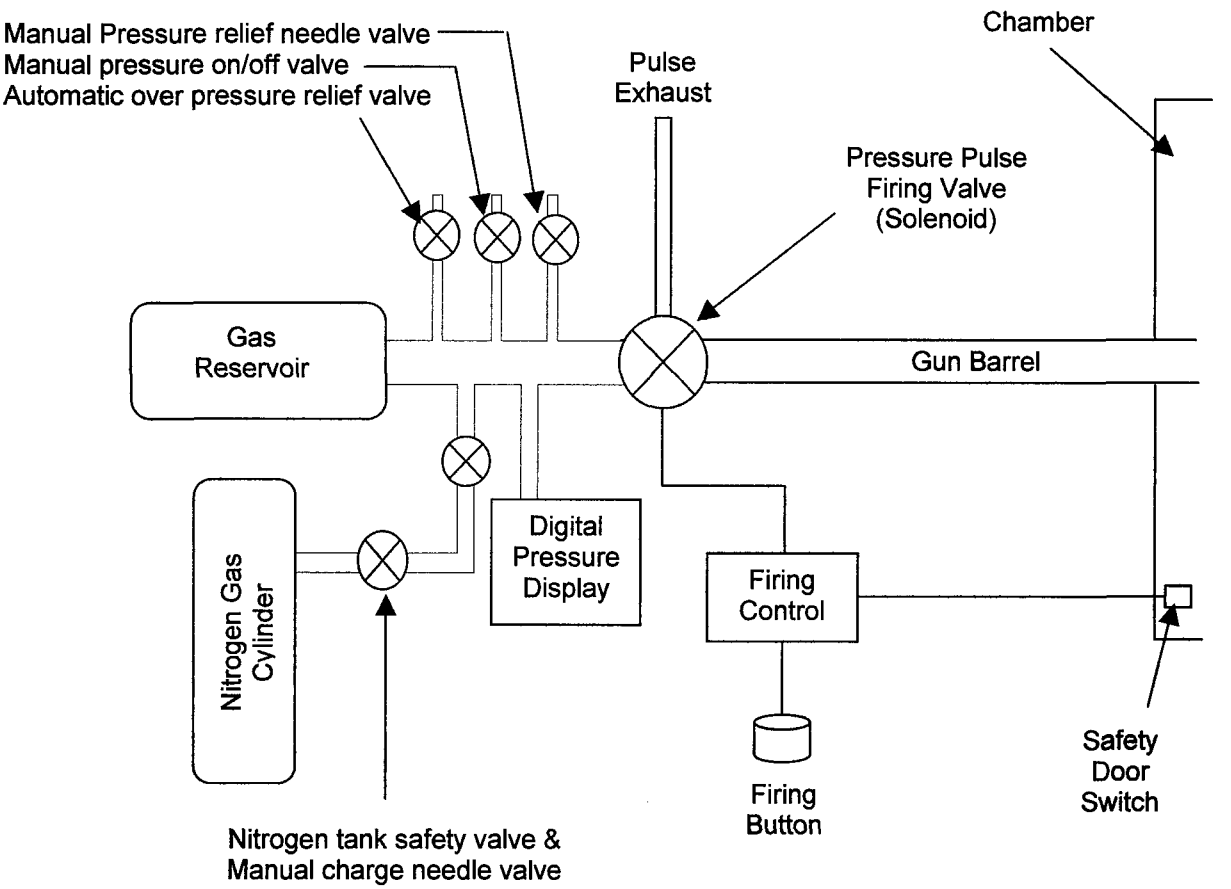


Figure 3.11: Schematic of the main Gas-Gun components

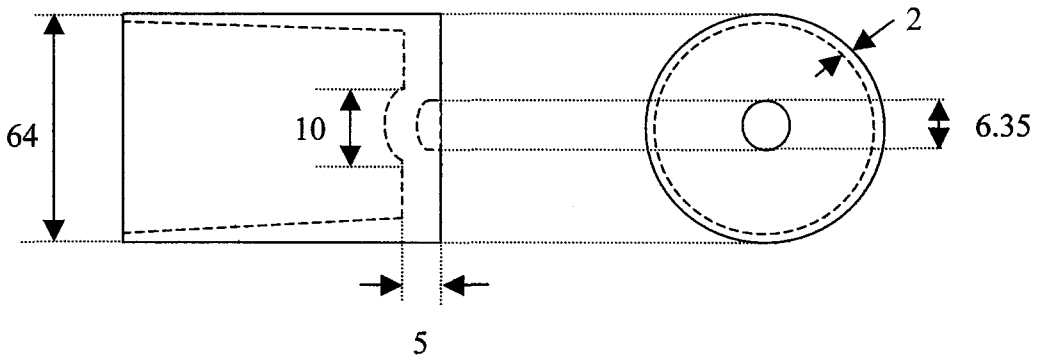


Figure 3.12: Schematic, with dimensions, of an injection-moulded sabot (in mm. Not to Scale)

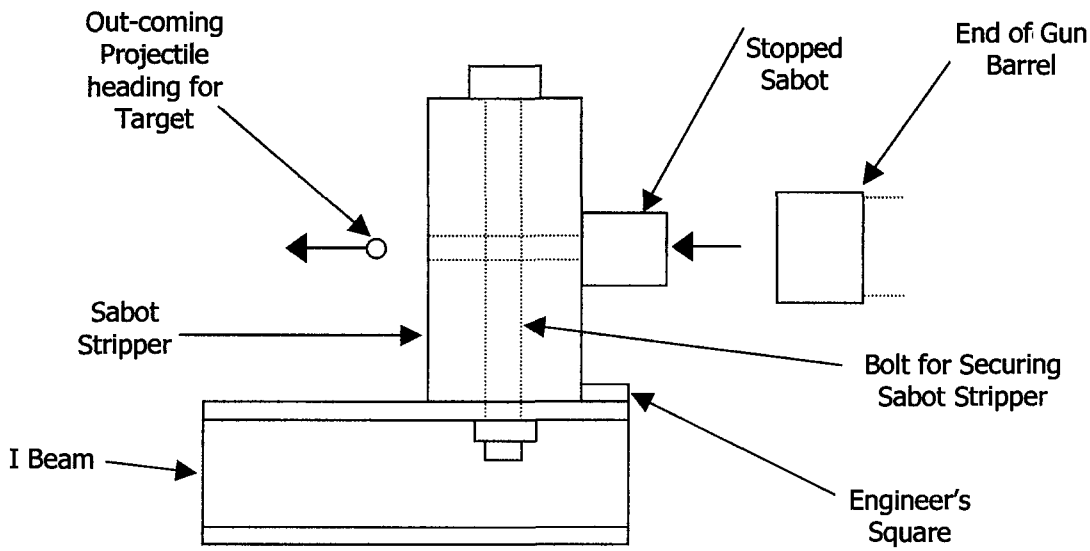


Figure 3.13: Schematic of the role the sabot stripper plays in gas gun impact involving ball bearing projectiles.

3.2.3.2 Drop Weight Impact Experiments

Drop Weight Impact experiments were used when investigating the impact behaviour of the flexible and the thick composite laminates. These experiments were conducted

on a drop weight tower with a 3 m guide rail and a 1.55 kg drop weight with a hemi-spherical indentor attached. The tower did not have an auto-release mechanism and drops were released manually. The low friction guide rails provided for a clean fast drop without unwanted vibrations. Care was taken to attach rigidly the specimen fixture to the heavy drop weight platform so as to avoid interfering vibrations. The laser beam triggering system was placed 20 mm from the impact surface of the specimen. Close to the point of striker impact a projector velocity sensor device was located. The output from this sensor and those in the load cell located in the drop weight head was fed into the instrumentation computer to obtain plots of Velocity-Time, Displacement-Time and Force-Displacement related to the impact behaviour of the impacted specimens. These arrangements are illustrated in *Figure 3.14.*

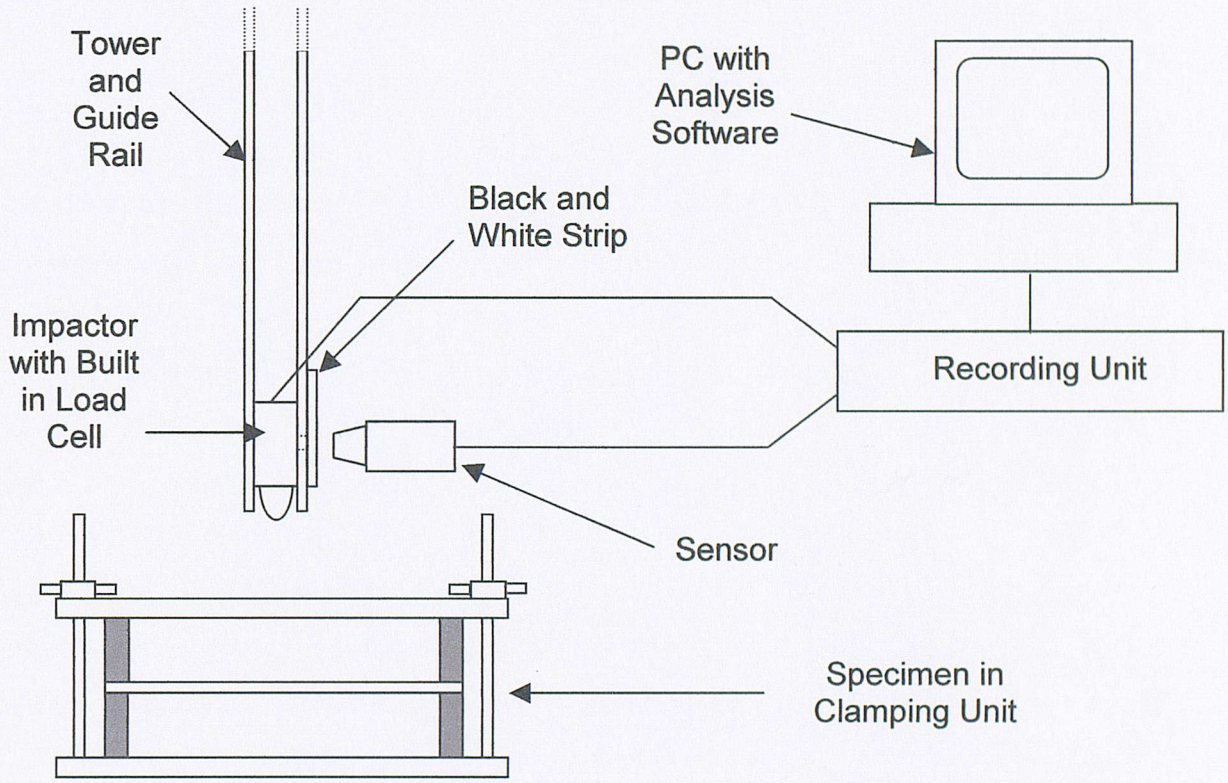


Figure 3.14: Schematic of Drop Weight Tower set up for Impact Testing. The sensor shown records the passing of the black and white strip and converts it into a time base measurement. The black and white strip itself has equidistant and equal sized black and white sections on it.

With some experiments it was necessary to be able to capture, with the high-speed camera, a sequence of frames starting with showing the free flight of the projectile and ending with the projectile bouncing off the target. This and other demanding experimental requirements needed some fine adjustments to be made and development of needed expertise.

3.2.4 Post Impact Analysis

After Impact tests were performed several methods were used to analyze the level of damage inflicted on the impacted specimens. The methods included X-Radiography, Ultrasonic C-Scan and Scanning Electron Microscopy (SEM). The following describe the techniques used, including any sample preparation where necessary.

3.2.4.1. X-Radiography

X-radiography techniques were used to analyse the damage inflicted on the curved composite laminates subjected to gas-gun impacts. The penetrant used was a zinc-iodide/isopropanol solution. The specimens were immersed in this solution and left for 24 hours before having the excess solution drained off for a further 3 hours. They were then placed into an X-Ray cabinet (Faxitron X-ray Systems Model 43084N) on top of a Polaroid film and exposed to X-rays. The optimum voltage and exposure time for these specimens was found to be 20 kV for 10 minutes. This technique provided for good assessments of the spread of delamination damage. However, the radiographs are difficult, if impossible, to interpret in terms of through thickness damage as to the location and degree of damage at each thickness level.

In order to obtain a X-radiograph, the tested sample needs to have a broken surface through which an appropriate penetrant can be injected. This penetrant then, through capillary action, travels to the limits of any delaminations and hence marks out the edge and hence the shape and size of the delaminations. The gas gun impacted curved specimens all experienced penetration of the projectile on the surface layer and hence

all had a site from which the penetrant could enter the specimen and 'mark out' the damage.

3.2.4.2 Ultrasonic C-Scan

All of the impacted samples were also subjected to Ultrasonic C-Scan analysis to obtain additional information as to the size of the damaged area. A Meccasonics ultrasonic unit was used in conjunction with a D320 display unit. The samples were immersed in a water bath and supported on square cross section metal rods at either end. The probe is then passed across the entire specimen and a broad picture of the damage area is obtained. Good correlation between X-Radiography and Ultrasonic C Scan was achieved as to the general dimension of the damage zone.

3.2.4.3 Scanning Electron Microscopy

Scanning Electron Microscopy (SEM) was used to obtain a better understanding of the damage distribution through the thickness of the impacted curved composite laminates. This required considerable care in sectioning, mounting and polishing the specimen. The sectioning of the specimens was as shown in *Figure 3.15* using a diamond coated cutting wheel. In the cases where the impact damage was extensive, so that there was a risk of specimen break up during sectioning, the specimens were encapsulated in a polyester moulding.

These mounted specimens were then polished using a Struers Rotopol 21 polishing unit that had programmable feed device to supply polishing agents and lubricants at the required rate This system consisted of two grinding polishing disc holders with interchangeable discs for each polishing stage. Between each stage the specimens were rinsed with water to remove any surface grit and to avoid cross contamination from the previous stage. The specimen holder rotated independently of the polishing discs. The grinding and polishing details are given in *Table 3.2*. The time for the first polishing stage was varied to achieve an entirely full flat specimen surface to be polished for viewing. This was needed because of the curvature of the specimens.

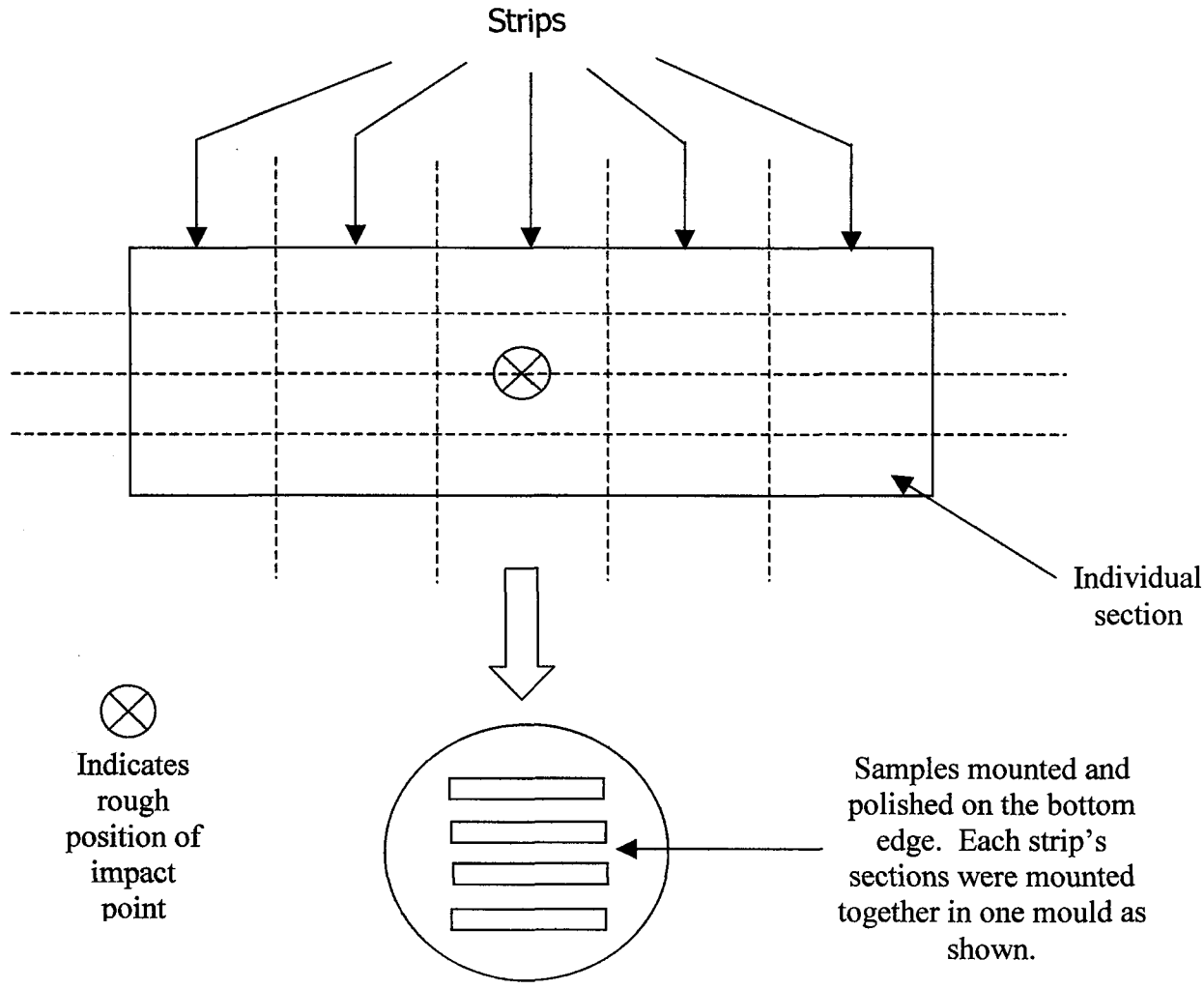


Figure 3.15: Diagram showing how each sample was sectioned for microscopy. Note that the two end 'strips' were not fully sectioned, as X-radiographs did not show enough significant damage in these areas.

After being polished, the specimens were then coated with a thin film of gold ready for the SEM study. This was performed in a ScanCoat machine. The specimens were placed in a vacuum and left for 70 seconds under the cold coating beam. Each specimen was coated separately and subjected to microscope examination immediately after coating was applied. This was to avoid the effects of the coating agents reacting with the polyester mounting resin and affecting the quality of image obtained. To provide good conduction through the sample a layer of conducting silver paint was applied between the sample and the holding plate in the SEM.

The following setting were used in the SEM:

Accelerating Voltage: 20 kV

Working Distance: 6 mm

The working distance being that between the electron beam emitter and the surface of the sample being viewed.

Pictures were then taken at a magnification of 50 times. The areas photographed were the impact point, the progression of damage directly below impact point, delamination growth through the specimen and damage observed along the back face of the specimen. The separate images were taken so that they could be overlapped to provide a full picture of the damage inflicted on the specimen.

	Stage 1	Stage 2	Stage 3	Stage 4	Stage 5
Base Disc	MD Piano	MD Piano	MD Dur	MD Dur	MD Nap
Grit	220	1200	-	-	-
Medium	-	-	DP Susp P 6μ	DP Susp P 3μ	OP-U 0.06μ
Lubricant	Water	Water	DP Green	DP Red	-
Force (N)	30	30	40	40	30
Revs (per min)	300	300	150	150	150
Time (min)	2:30*	2:00	5:00	5:00	2:00
Dose Rate	-	-	8	8	5
Lubricant Rate	-	-	6	5	-

*Table 3.2: Table showing the grinding and polishing regime for sectioned samples for SEM analysis. Note that the rotation direction of the disc and sample holder were in the same direction. * This was a guideline time, the first grinding stage was used until all the edges of the sections were flat with the mould therefore an increased amount of time was common.*

4 Impact of Curved Carbon Fibre Composite Laminates

This research relates to the impact damage that can be suffered by curved composite panels. Valuable information has been published as to the impact damage that can be inflicted onto flat composite specimens (Abrate 1991, 1994, 1998 and Mattthews and Rawlings 1994) but often materials need to be used in curved and more complex shapes. As revealed in this study, composite panels that are only slightly curved can have a different dynamic response and suffer different degrees of damage depending upon the curvature and its orientation with respect to the impact. This to be expected as the impact stiffness of curved specimens differs depending upon their orientation but less well known is the effect on the damage that can be inflicted on specimens so shaped. An impact normal to the nearly flat crown of a gently curved specimen would be a glancing blow on its sloping sides. It follows that a full study of the level of possible inflicted impact damage on curved or other contoured panels would require very extensive research than is not possible within this study. However, the research presented in the following chapter regarding the damage inflicted by impacts directed onto the crown of the curved panel is a logical first research step to be taken.

4.1 Aims and Objectives

The main aim is to study the history of damage inflicted on curved specimens by an impactor. This investigation looks at how differing impact conditions changes the damage that develops during an impact event within a curved composite laminate. Factors that were investigated included wether the curvature was of a convex or concave nature, both of which would occur within a shaped composite structure. The actual direction of the curvature was also varied from being in the longitudinal direction to being in the transverse direction. Finally two different impact energies were used to show how much change in severity of impact damage could be caused by an increase in only an increase in the velocity of the incoming projectile.

4.2 Procedure

These investigations were performed using a gas gun impactor in conjunction with the Hadlands 486 high-speed camera. This provided for the impact event to be recorded showing the changing dynamic reaction of the specimen during the impact sequence and the progressive development of delamination and other damage during the course of the impact. Spherical steel balls with a diameter of 6 mm were projected at the curved samples at two firing pressures of 5 and 8 bar to give impact velocities of approximately 150 m/s and 190 m/s respectively. Post impact damage was assessed firstly with X-Radiography in order to get a general picture of the extent of damage. To assess the damage through the thickness of the laminate, the sample was sectioned, polished and studied using Scanning Electron Microscopy. This was to assess the severity of the damage as it progressed through the specimen during the impact.

4.2.1 Experimental Details

The general experimental arrangements have been given in Section 3.2. More detailed information is given below. For each impact study, several specimens were used for repeat experiments to confirm results and to obtain sufficient specimens for damage analyses. For good consistent data, the dimensions of the curved samples need to be carefully controlled and located in the grooved support fixtures as identically as possible. It was important that the groove accommodated the curving end of the specimens a little free clearance (See *Figure 3.4*) so that any flexure of the specimen was allowed. For impacting pairs of specimens, one on its convex side and the other on its concave side, care was taken to achieve closely related impact contact points on each side of the specimen. With the different orientations of the specimen, there were 8 different impact conditions in total that were required.

Achieving the appropriate level of illumination so as to capture the progress of the high velocity steel ball and to be able to observe the movement of the impacted target and to see the start and development of the impact damage required development of the photographic technique with several trial firings. The edge of the specimen to be

viewed by the camera was painted white and marked with black graduation lines, which were 20 mm apart. As well being useful for capturing the response of the specimen to the Impact event, the marked specimen side was also of assistance when calibrating the system.. For each firing, eight photographic frames were obtained and these captured the free flight of the incoming projectile in the first two frames to determine its velocity. The other six frames were used to capture the closure of the projectile with the target, the deformation of the target and the progressive delamination and damage to the specimen as seen from an edge on view of the specimen.

Because of the illumination problems, photographing the free flight of the steel ball proved to be a problem with some firings as to be expected with this type of experimentation. Therefore, only when the free flight velocity of the steel ball could be measured from the high-speed photographs and the twin laser beam-measuring device are records made in *Tables 4.1* and *4.2*. It was important was to obtain sufficient number of reliable recordings for damage assessments to be made. However, for completeness, all specimens impacted are shown in *Tables 4.1* and *4.2*. The confirmed projectile velocities were used to calculate the impact energy of the event using the kinetic energy equation, $E = \frac{1}{2}mv^2$.

Post impact examination was started with careful removal of the damage specimen from the experimental rig and photographs taken to show visual damage to the front, rear and side views of the specimens. Having obtained these initial photographic records, the following detailed study was made.

Two X-Radiographic studies were made employing different penetrants to obtain a variation of image discrimination. Specimens were taken of each impact condition and were subjected to these two different techniques for X-Ray analysis. Firstly, negative photographs were taken using di-iodomethane as a penetrant. Secondly, the penetrant used was Zinc iodide/isopropanol penetrant (refer to Section 3.2.4.1 for exact details of the procedure used). These X-Ray pictures showed the general and more detailed level of damage. Scanning Electron Microscopy (SEM) was then used

to study the through thickness damage of impacted specimens. This required appropriate sectioning and preparation of the specimens.

Sample Number	Front Face Curvature	Gas-Gun Pressure (bar)	Velocity (m/s)	Impact Energy (J)
LC1	Convex	5	-	-
LC2	Convex	5	-	-
LC3	Convex	5	137	9.4
LC4	Convex	5	-	-
LC5	Convex	5	143	10.2
LC6	Convex	5	138	9.5
LC7	Convex	8	-	-
LC8	Convex	8	-	-
LC9	Convex	8	188	17.6
LC10	Convex	8	-	-
LC11	Convex	8	-	-
LC12	Convex	8	185	17.2
LC13	Concave	5	-	-
LC14	Concave	5	159	12.6
LC15	Concave	5	153	11.7
LC16	Concave	8	196	19.2
LC17	Concave	8	191	18.2
LC18	Concave	8	-	-

Table 4.1: Table showing samples and their impact conditions for samples containing a longitudinal curvature.

The sectioning was performed as detailed in Section 3.2.4.3. The individual sections were 20 mm x 10 mm in size. Each strip of sections was mounted together onto one 40 mm diameter mould with each section was secured on its bottom edge, i.e. the side which corresponds to the same side as the whitened side of the full specimen. Each mounted strip of sections was subjected to the grinding and polishing as previously explained.

The central strip containing the impact site being of most interest was studied in the SEM. The objective in this part of the analysis was to show the damage through the

thickness of the sample and to assess how this damage progressed through the sample and to relate this to the high-speed camera sequences. The micrographs showed the impact site and the area immediately below the impact site stretching to the back face of the specimen. Obtaining micrographs showing the back face of the specimen from the area immediately below the impact site to one edge of the specimen followed this study. Micrographs were also taken of the delamination that stretched to the edge of the strip. In addition, any other areas of interest were studied and the results shown below.

Sample Number	Front Face Curvature	Gas-Gun Pressure (bar)	Velocity (m/s)	Impact Energy (J)
TC1	Convex	5	-	-
TC2	Convex	5	-	-
TC3	Convex	5	146	10.7
TC4	Convex	5	-	-
TC5	Convex	5	154	11.9
TC6	Convex	5	163	
TC7	Concave	5	-	-
TC8	Concave	5	161	13.4
TC9	Convex	8	-	-
TC10	Convex	8	-	-
TC11	Convex	8	186	17.3
TC12	Convex	8	175	15.3
TC13	Concave	8	-	-
TC14	Concave	8	181	16.4
TC15	Concave	8	-	-
TC16	Concave	8	180	16.2

Table 4.2: Table showing samples and their impact conditions for samples with a transverse curvature

4.3 Results

A great deal of investigations were made as explained above and in presenting the results, only the significantly informative data is given below. A generally informative example of each type of results is shown with areas of interest identified. This is followed by results that show more details of interest.

4.3.1 High Speed Photography

In order to be able to see properly what is shown in these sequences, a sample frame from one sequence is shown in *Figure 4.1*, which shows the specimen before impact, and the significant features are labelled. *Figure 4.2* is a frame taken from a sequence showing a specimen after impact and shows the specimen responding to the impact when delaminations to the edge of the specimen have started. These frames give a brief appreciation of how the delaminations move through the thickness of the specimen. This is typical in all the impact damage studied in this research namely for the delaminations to start from the centre of the specimen and progress towards the back of the specimen depending on the impact stresses. *Figure 4.3* shows the deformation of the specimen that can be related to the inflicted damage. The ability of the specimen to flex in order to absorb a degree of the impact energy can be seen and this ability to flex will be shown to have a great effect on the amount of impact damage that is incurred by the specimen. This ability to flex is shown to be linked with the specimen's orientation.

Figures 4.4 to 4.11 show a selection of the high-speed sequences that were taken, one for each impact condition studied. To be noted is that the corresponding specimens from these sequences were the ones that were taken for post impact analysis to provide continuity in the analysis of the data. For each high-speed photographic sequence, notes are provided as to what is seen in terms of the specimen response to the impact event in Table 4.3. The order of the photographs in the sequence shown start from the top left moving downwards and towards the right with the bottom right

hand image being the final one. The frame numbers are given in the bottom right hand corner of each separate image.

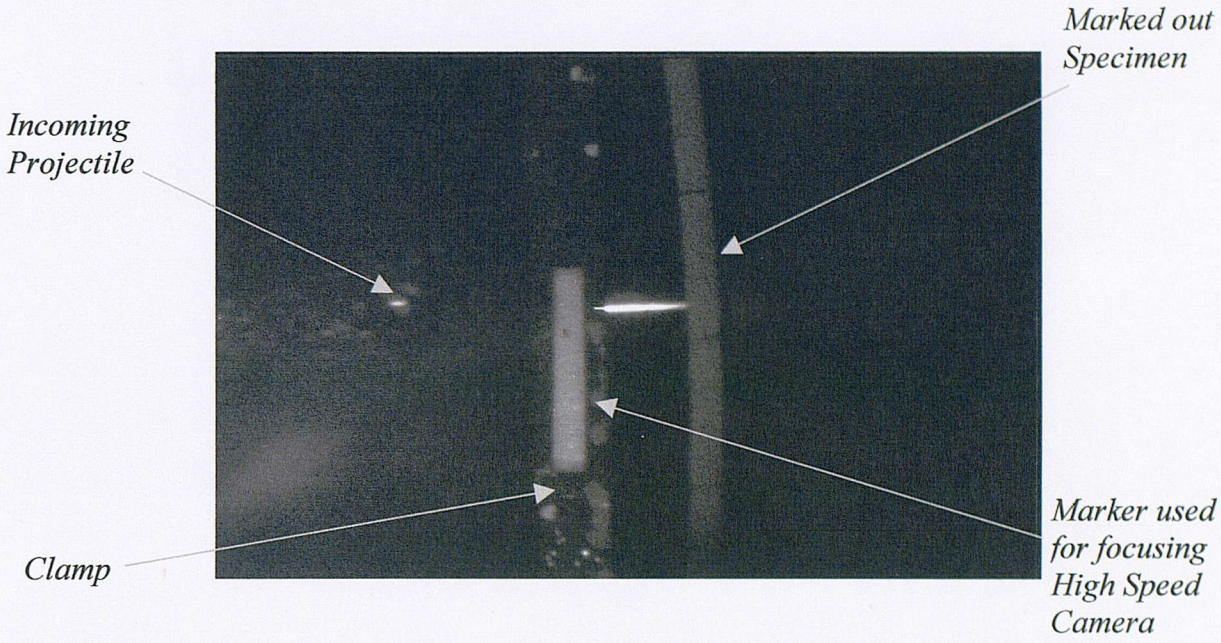


Figure 4.1: A frame from a typical High Speed Photography sequence showing the specimen at rest, a section of the clamp and the incoming ball bearing projectile.

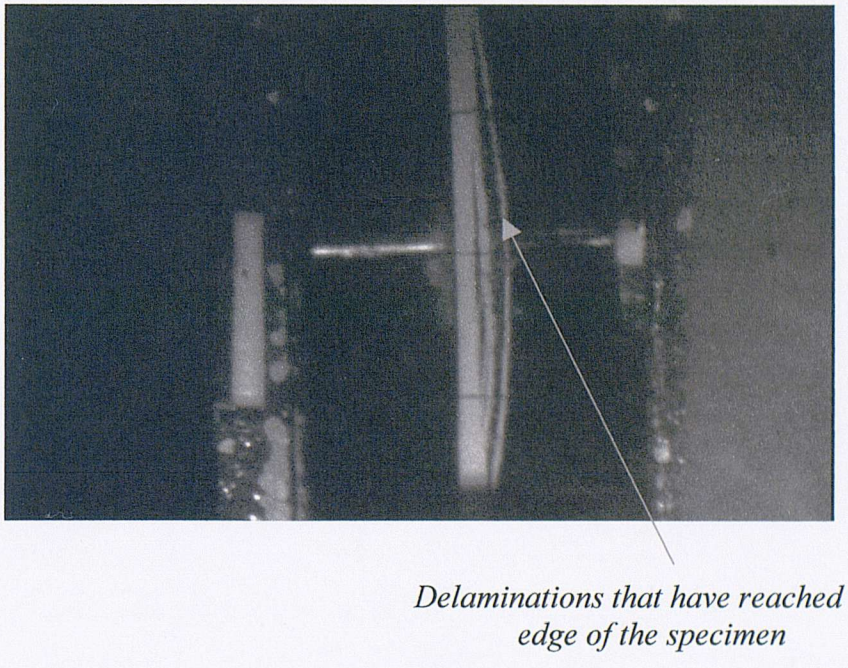


Figure 4.2: A frame selection showing the response of the specimen to the impact event and delaninations that have reached the edge of the specimen.



(a) (b)

Figure 4.3: Two frames taken from the same sequence showing the ability of the specimen to flex during the impact event. In (a) the specimen is at rest. In (b) the specimen has been impacted and it can be seen that the specimen has flexed to a straighter shape due to the impact event. Damage can also be seen to be coming through the centre of the thickness of the specimen.

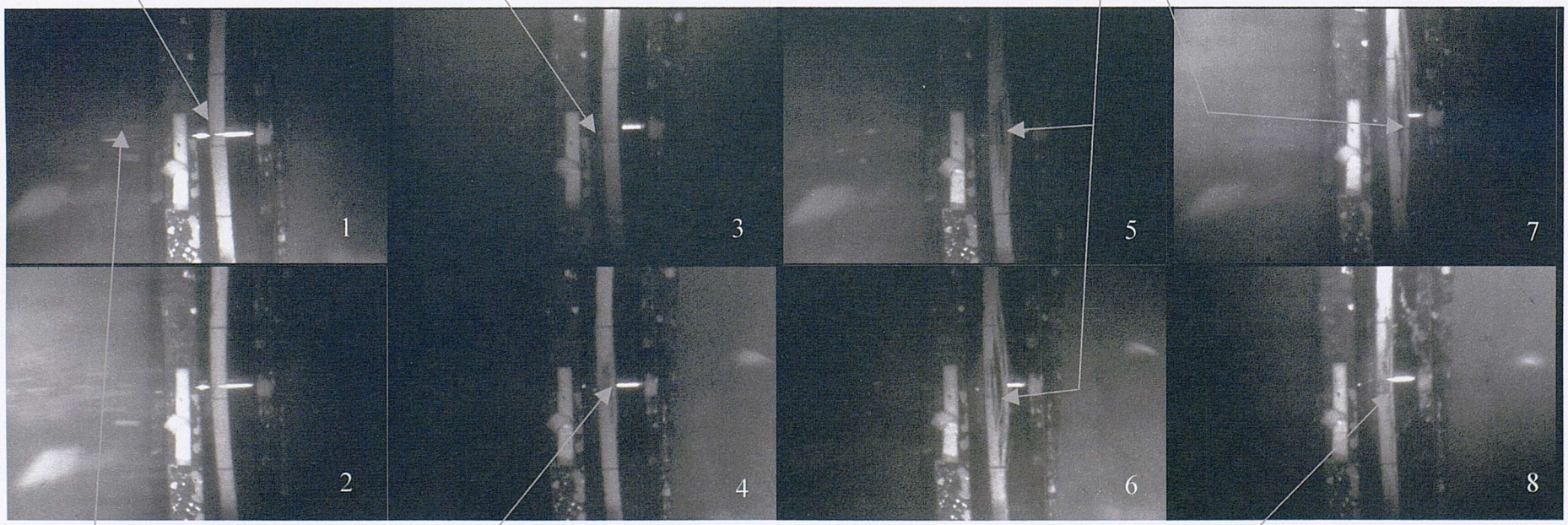
In all impact there are a few common occurrences that can be seen in the high-speed photographic sequences. Notably, the damage that is first seen occurs in the centre of the thickness of the specimen, and progresses towards the back-face of the specimen. However, it is noted that this progression is only for the visible damage from the side view, the initiation of damage internally cannot be determined from these high-speed photographs.

For the specimens with the longitudinal curvature and convex front impact face, a side view of the specimen shows well the protruding fracture damage from the rear surface (*Figures 4.4 and 4.5*). The damage appears to start at the centre of the thickness and then the delaminations propagate to the specimen edges. This evident for both 5 and 8 bar pressure impacts (impact velocity ca. 150 m/s and 190 m/s respectively). It gets to the point were the layers towards the back that have become delaminated, flip outwards due to the continuing impact event. In the 8 bar impact case the back layers appear as though they have separated along the whole length of the laminate, with only the supports (which are out of view) keeping these layers attached to the rest of the specimen.

Longitudinal specimens with a concave front-face, show less damage than specimens with the convex front-face. In the 5 bar impact case (impact velocity ca. 150 m/s), the damage that reaches the sides can just be made out and only near the end of the impact event can cracks in the white paint be seen, although the crack near to the back of the specimen can be seen to reach a fair length along the specimen (*Figure 4.6*). At 8 bar (impact velocity ca. 190 m/s), the damage is more extensive, and the back layers can be seen to separate from the rest of the specimen, but not as extensively as in the convex front-face impact case, and relax back to more or less the same position as where there started at (*Figure 4.7*). The difference between the convex front face impact and concave front face impact is that with the convex impact case, there is a propensity for the specimen to buckle and this increases the damage propagation.

For the transverse specimens (both with convex and concave front-faces), the high-speed photographs of the specimen edge are straight and the damage protrusions tend to be partly hidden. With the transverse curvature impacts, for the convex impact case, the damage protruding from the rear of the surface was partly obscured and for the concave impact case, a difficulty was that the instant of contact between impactor and specimen was partly obscured. More reliance, therefore, in understanding the impact damage effects was on the post-impact analysis. The damage from the high-speed photographic sequences showed that the specimens flexed before noticeable impact damage could be seen (*Figures 4.8, 4.9, 4.10 and 4.11*). Damage, like the longitudinal specimens, appeared to begin at the centre and progresses towards the back of the specimen.

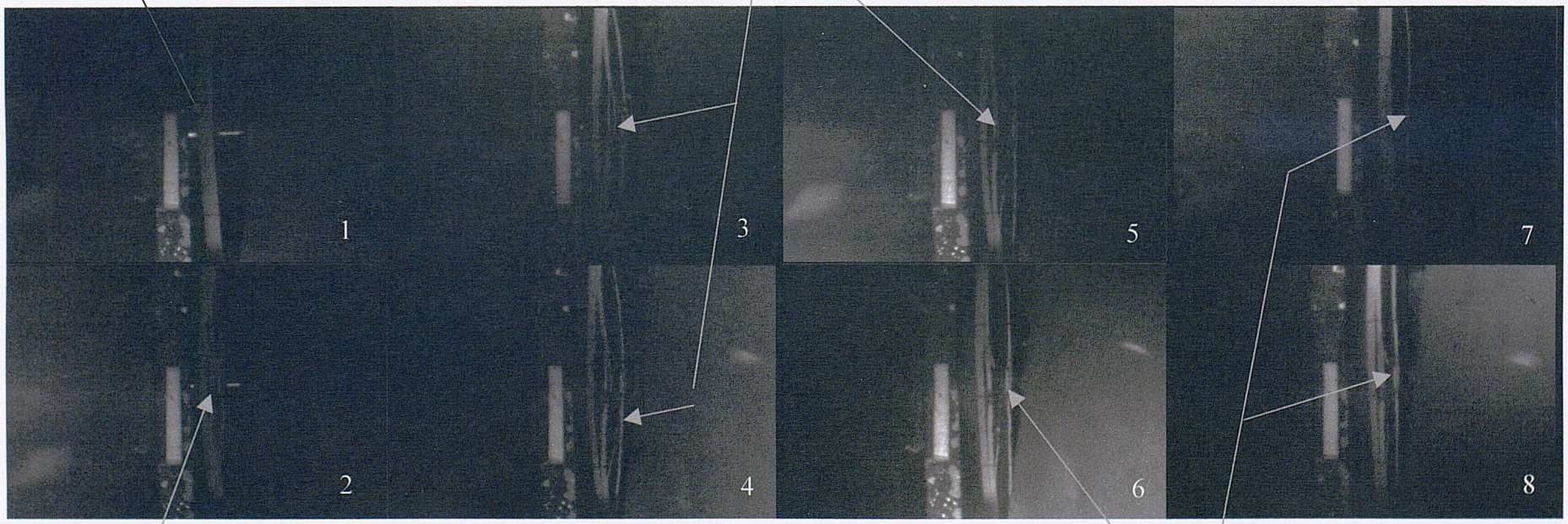
For the transverse curvature convex impact face, the progression of damage with a 5 bar impact is only slight during the flexing. The damage begins at the centre and stretches along the length, and no damage is evident towards the back-face (*Figure 4.8*). When the specimen has relaxed the crack is still evident at the centre of the thickness. At 8 bar however, during the latter stages of the flexing the layers towards the back of the specimen come apart and this separation stretches to a great portion of the specimen, and on relaxing these layers tend to return to more or less their original place, bearing in mind the damage that has been caused (*Figure 4.9*).



Frame No.	1	2	3	4	5	6	7	8
Frame Setting (mS)	0.9	1.0	1.1	1.125	1.15	1.175	1.2	1.3
Exposure Time (μS)	25	25	15	15	15	15	25	25

Pressure: *5 Bar* *Projectile:* *1 g Steel Ball Bearing*
Velocity: *143 m/s* *Impact Energy:* *10.2 J*

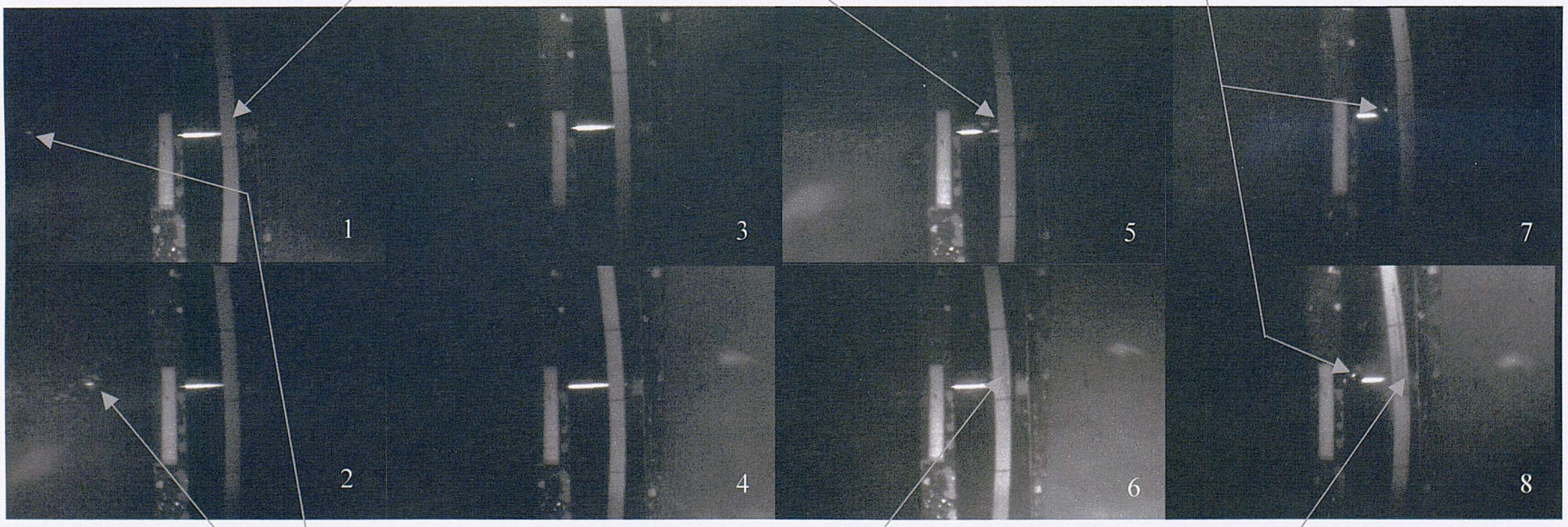
Figure 4.4: High Speed Photography Sequence for Specimen LC6, Longitudinal Curvature, Convex Front Face at 5 Bar Pressure.



Frame No.	1	2	3	4	5	6	7	8
Frame Setting (mS)	0.6	0.7	0.75	0.8	0.85	0.9	1.0	1.1
Exposure Time (μS)	10	10	10	11	12	13	14	15

Pressure: *8 Bar* *Projectile:* *1 g Steel Ball Bearing*
Velocity: *188 m/s* *Impact Energy:* *17.6 J*

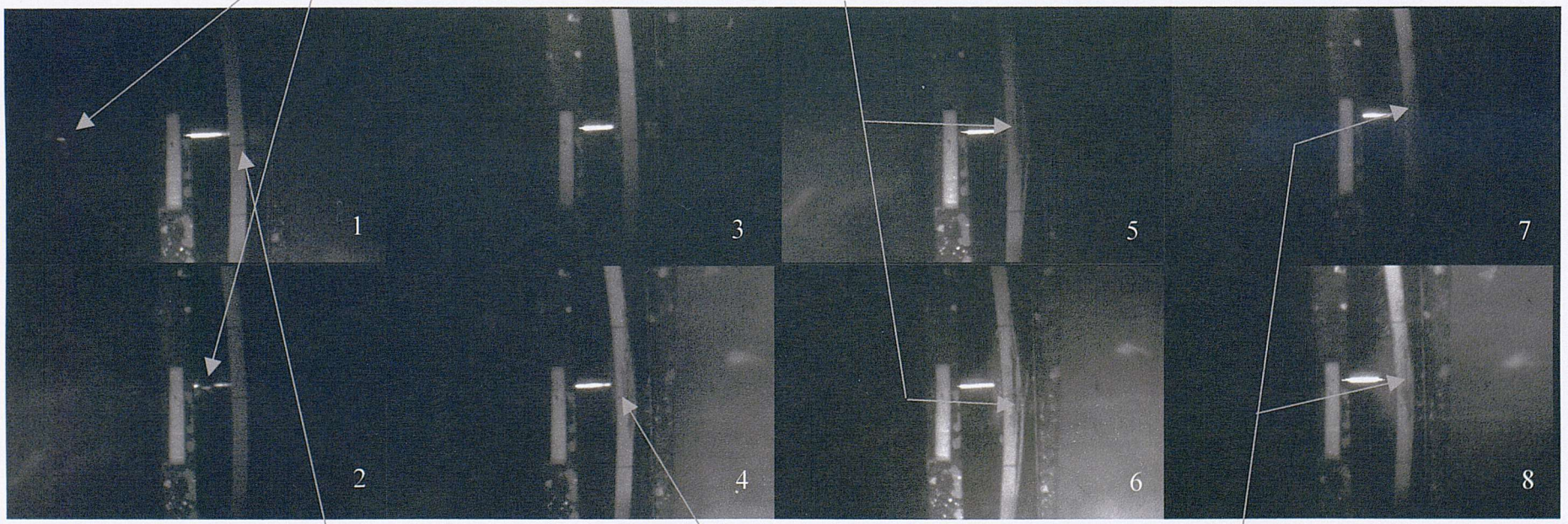
Figure 4.5: High Speed Photography Sequence for Specimen LC11, Longitudinal Curvature, Convex Front Face at 8 Bar Pressure.



Frame No.	1	2	3	4	5	6	7	8
Frame Setting (mS)	0.8	0.9	0.95	1.0	1.1	1.15	1.25	1.50
Exposure Time (μS)	10	10	10	11	12	13	14	15

Pressure: *5 Bar* *Projectile:* *1 g Steel Ball Bearing*
Velocity: *153 m/s* *Impact Energy:* *11.8 J*

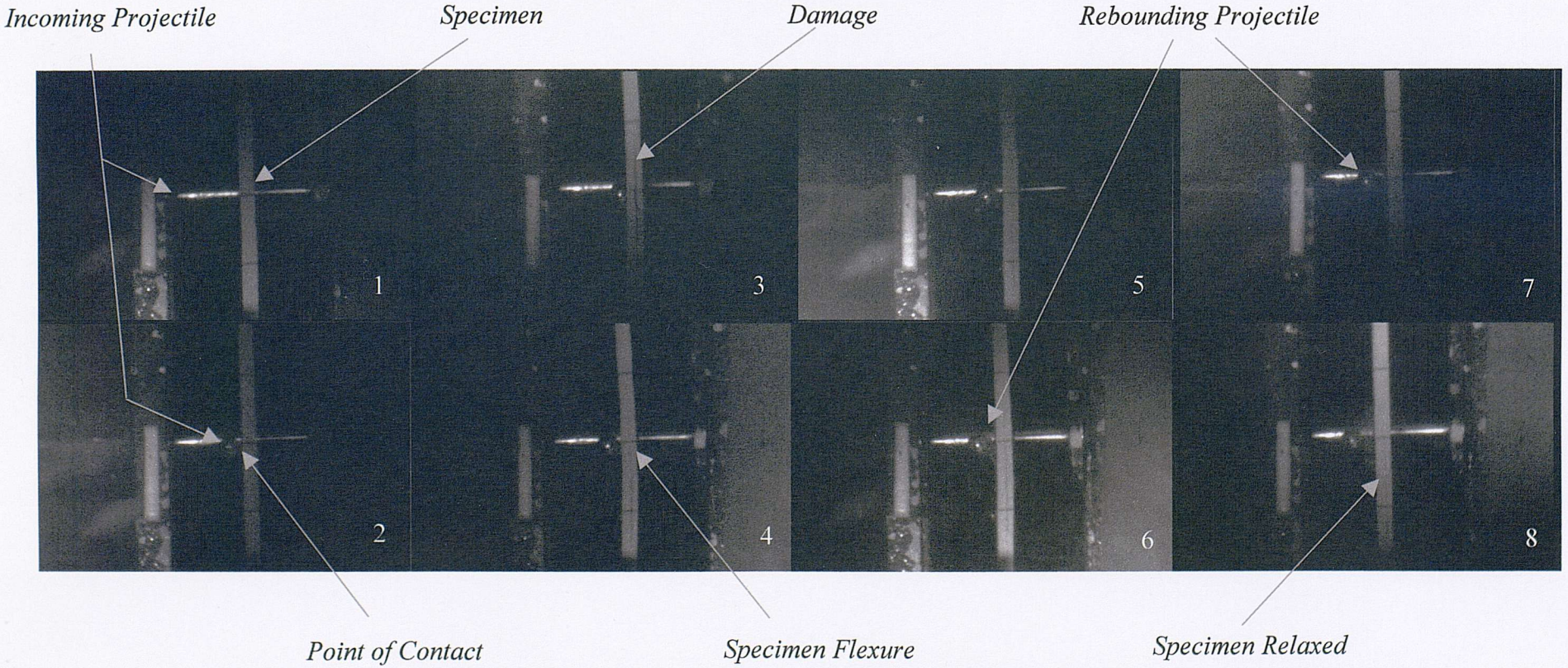
Figure 4.6: High Speed Photography Sequence for Specimen LC15, Longitudinal Curvature, Concave Front Face at 5 Bar Pressure.



Frame No.	1	2	3	4	5	6	7	8
Frame Setting (mS)	0.7	0.9	0.95	0.975	1.0	1.025	1.05	1.15
Exposure Time (μS)	10	10	10	11	12	13	14	15

Pressure: *8 Bar* *Projectile:* *1 g Steel Ball Bearing*
Velocity: *188 m/s* *Impact Energy:* *17.6 J*

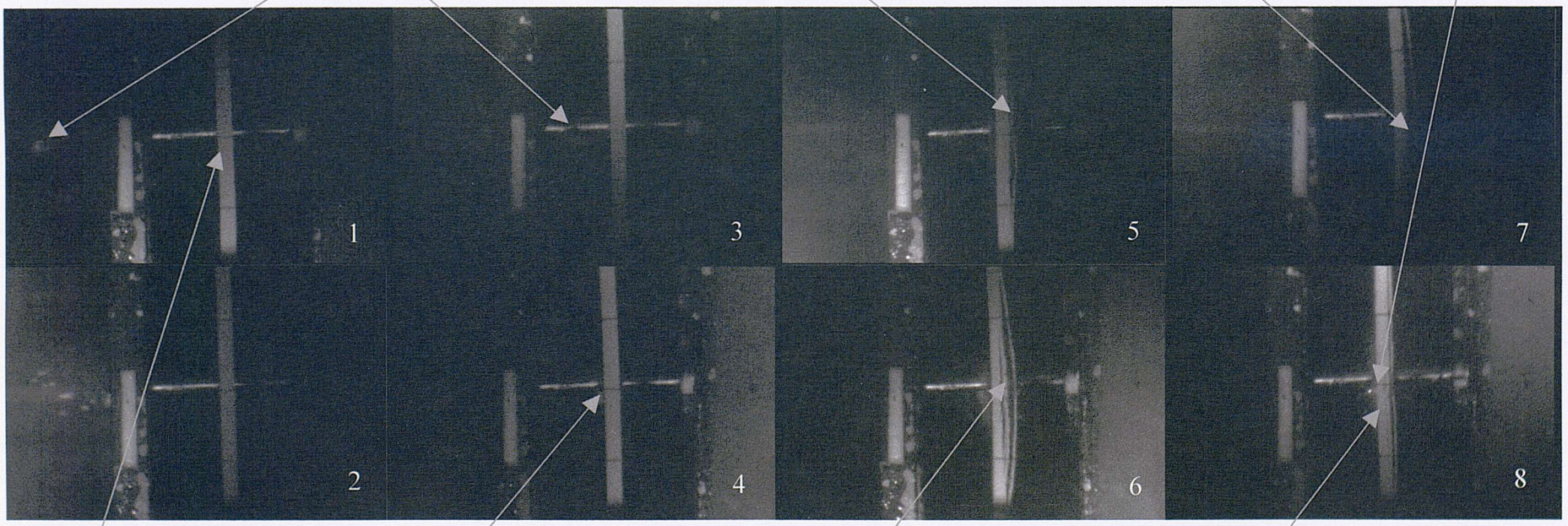
Figure 4.7: High Speed Photography Sequence for Specimen LC18 Longitudinal Curvature concave Front Face at 8 Bar Pressure.



Frame No.	1	2	3	4	5	6	7	8
Frame Setting (mS)	0.9	1.0	1.1	1.2	1.25	1.3	1.35	1.4
Exposure Time (μS)	10	10	10	11	12	13	14	15

Pressure: *5 bar* *Projectile:* *1 g Steel Ball Bearing*
Velocity: *164 m/s* *Impact Energy:* *14.0 J*

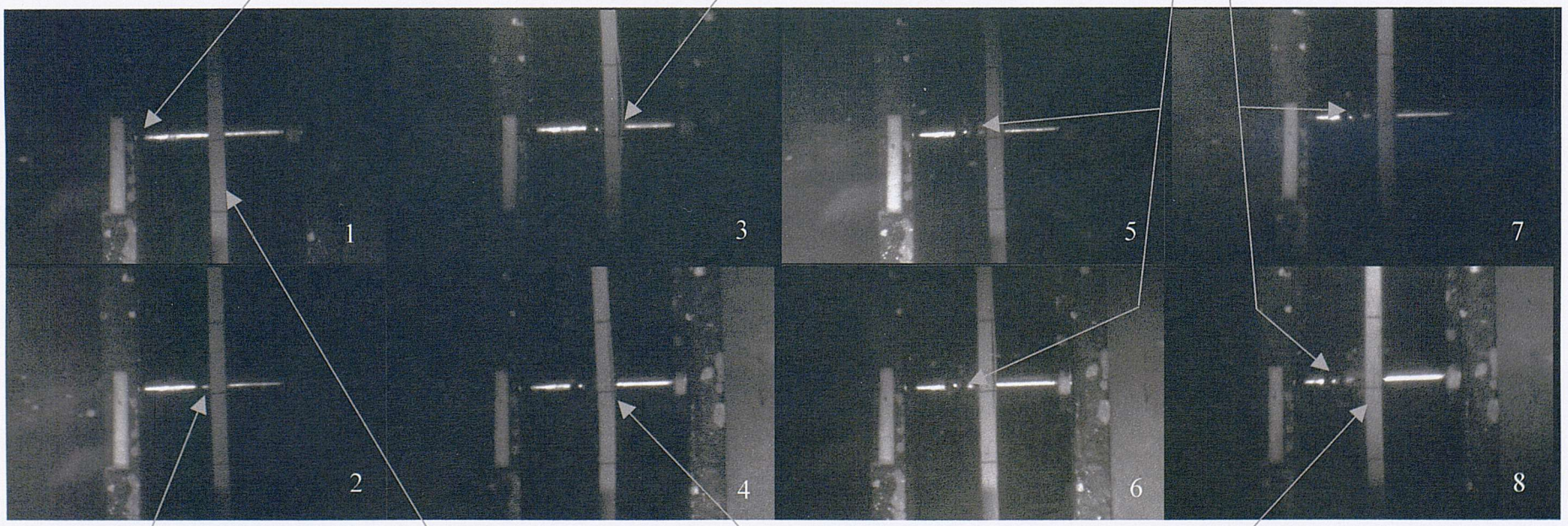
Figure 4.8: High Speed Photography Sequence for Specimen TC6 Transverse Curvature Convex Front Face at 5 Bar Pressure.



Frame No.	1	2	3	4	5	6	7	8
Frame Setting (mS)	0.6	0.7	0.8	0.85	0.9	0.95	1.0	1.2
Exposure Time (μS)	10	10	10	11	12	13	14	15

Pressure: *8 Bar* *Projectile:* *1 g Steel Ball Bearing*
Velocity: *186 m/s* *Impact Energy:* *18.2 J*

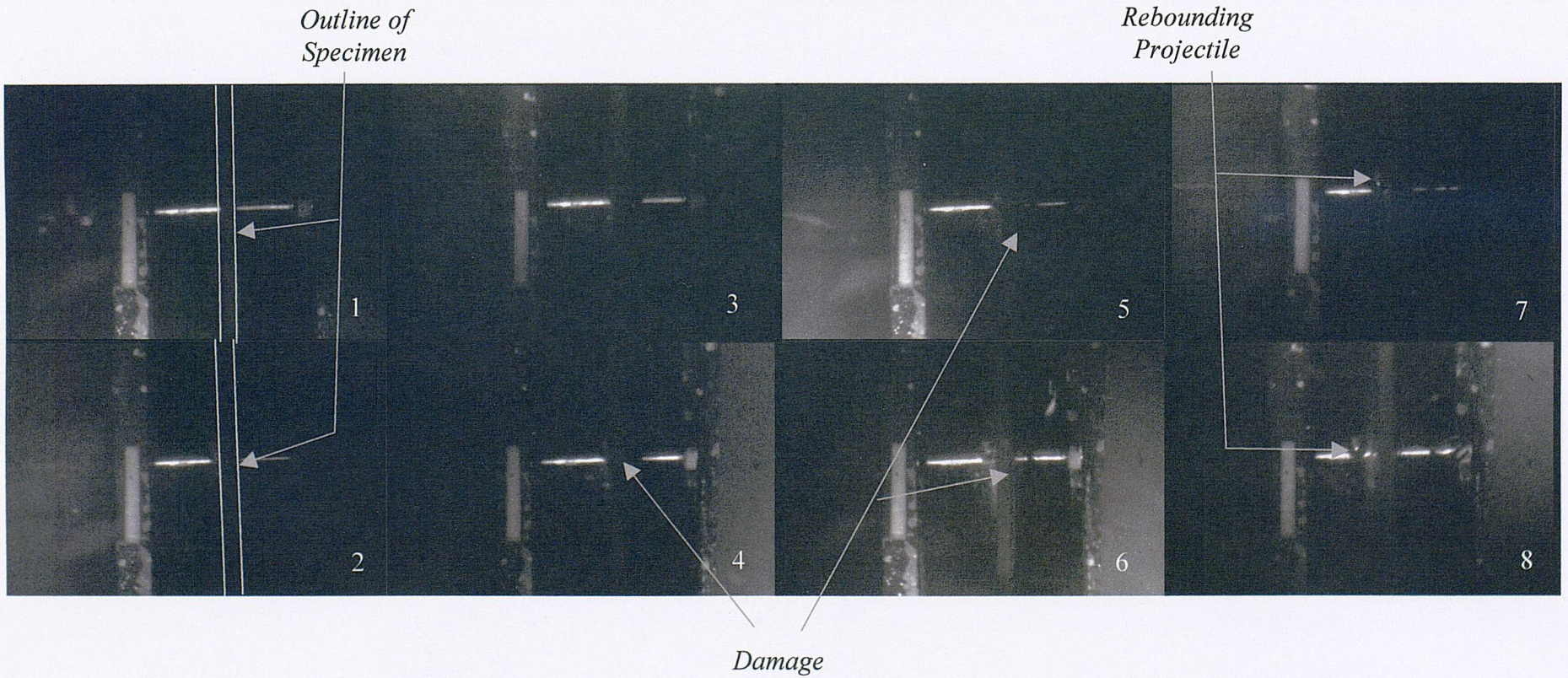
Figure 4.9: High Speed Photography Sequence for Specimen TC11 Transverse Curvature Convex Front Face at 8 Bar Pressure.



Frame No.	1	2	3	4	5	6	7	8
Frame Setting (mS)	0.9	1.0	1.1	1.2	1.25	1.3	1.35	1.4
Exposure Time (μS)	10	10	10	11	12	13	14	15

Pressure:	*5 Bar*	*Projectile:*	*1 g Steel Ball Bearing*
Velocity:	*161 m/s*	*Impact Energy:*	*13.7 J*
Rebound Velocity:	*37 m/s*	*Rebound Energy:*	*0.68 J*

Figure 4.10: High Speed Photography Sequence for Specimen TC7 Transverse Curvature Concave Front Face at 5 Bar Pressure.



Frame No.	1	2	3	4	5	6	7	8
Frame Setting (mS)	0.9	1.0	1.1	1.2	1.25	1.3	1.35	1.4
Exposure Time (μS)	10	10	10	11	12	13	14	15

Pressure: *8 Bar* *Projectile:* *1 g Steel Ball Bearing*
Velocity: *189 m/s* *Impact Energy:* *17.9 J*
NB: Whitened surface not in view as specimen is the wrong way round.

Figure 4.11: High Speed Photography Sequence for Specimen TC15 Transverse Curvature Concave Front Face at 8 Bar Pressure.

	Impact Pressure (bar)	Curvature	Front Face	Observations
LC6	5.0	Longitudinal	Convex	Contact occurs in frame 3. Damage can be seen from Frame 4. Damage (in the form of delaminations) begins from the centre of the specimen and progresses towards the back face. Damage seems to spread further along the specimen towards the back face. Damage reaches maximum in Frame 6 and relaxes in Frames 7 and 8.
LC11	8.0	Longitudinal	Convex	Impact occurs between Frames 1 and 2. Damage again starts from the centre of the specimen and progresses toward the back face. Delaminations are more extensive and the back layers flex out causing delaminations to travel along the length along the specimen. Damage begins to relax in Frame 5, but not fully relaxed by Frame 8.
LC15	5.0	Longitudinal	Concave	Impact occurs between Frames 5 and 6. Damage again begins from the centre of the specimen, but does not seem to be as extensive as can be seen in LC6. However, examination of the specimen after impact shows that damage extends as far as in LC6 and back face splitting can also be seen.
LC18	8.0	Longitudinal	Concave	Impact occurs around Frame 3. Damage begins from centre and progresses towards the back face of the specimen. The degree of delamination does not seem to be as extensive as those shown in LC11. Relaxation of damage begins after Frame 6 and is fully relaxed by Frame 8.
TC6	5.0	Transverse	Convex	Impact occurs between Frames 2 and 3. Damage is already visible in Frame 3 in the form a large delamination in the centre of the specimen. The specimen can be seen to bend back due to the impact. Not much damage development can be seen. However the relaxation of the bending can be seen and the specimen is fully relaxed by Frame 8.
TC11	8.0	Transverse	Convex	Impact occurs between Frames 3 and 4. Specimen can be seen to flex in Frame 4 due to the impact. Delaminations start from the centre and progress towards the back of the specimen. Specimen is almost fully relaxed by Frame 8.
TC7	5.0	Transverse	Concave	Impact occurs between Frames 2 and 3. First delamination evidence seems to be towards to the back of the specimen and signs of damage at the centre occur later. Specimen flexes due to impact and is fully relaxed by Frame 8.
TC16	8.0	Transverse	Concave	Impact occurs in Frame 3. Delamination can be seen; this propagates along the length of the specimen with lots of flexing. The projectile can be seen to embed itself into the specimen during the event and rebound out of the specimen. Relaxation begins in Frame 5 and specimen is fully relaxed by Frame 8.

Table 4.3: Damage Observations made from high-speed photographic sequences.

For the concave front-face impact specimens at 5 bar, the observable cracking can only just be seen at the back face, during the beginning stages of the flexure of the specimen and this crack does not appear to stretch as far compared to the convex front-face case (*Figure 4.10*). At 8 bar, the damage yet again seems to be more evident towards the back-face of the specimen and the back layers more clearly separate from the rest of the specimen and do relax back towards the latter stages of the sequence (*Figure 4.11*).

From the high speed photograph sequences estimations of the amount of deflection caused by the impact can be taken. Using these estimations for the deflection of each specimen and assuming relative flat plate conditions, due to the low radius of curvature for the panel, the elastic strain energy can be calculated using Equations 4.1 and 4.2 (Ashby and Jones (1980)), where U is the elastic strain energy, k the stiffness of the composite, δ the deflection, E is the modulus of the composite, w, t and l the width, thickness and length of the specimen respectively.

$$U = \frac{k\delta^2}{2} \qquad (4.1)$$

where:

$$k = \frac{Ewt^3}{0.25l^3} \qquad (4.2)$$

Table 4.4 shows the estimated deflection values (δ) and the resultant calculated elastic strain energies along with the impact energies for each impact. It can be seen from these figures that the impact energy that is absorbed in the form of elastic strain energy due to deformation is very small in comparison with actual incoming impact energy. The figures also show that the transverse curvature specimens show roughly the same level of elastic strain energy regardless if they are in the concave or convex orientation showing that the curvature is small enough that the behaviour of the two orientations do not differ. This would suggest that deformation alone has only a limited level of energy absorption capability.

E = 140 GPa w = 40mm l = 120mm t = 4mm $\therefore$ k = 830kN/m								
Specimen	**LC6**	**LC11**	**LC15**	**LC18**	**TC6**	**TC11**	**TC7**	**TC16**
Impact Velocity (m/s)	143	188	153	188	164	186	161	189
δ (mm)	0.47	1.25	0.31	0.63	0.69	0.78	0.75	0.75
U (J)	0.09	0.65	0.04	0.16	0.20	0.25	0.23	0.23
Impact Energy (J)	10.2	17.6	11.8	17.6	14.0	18.2	13.7	17.9

Table 4.4: Table showing estimated deflections calculated elastic strain energies and impact energies.

4.3.2 Post-Impact Photographs

For damage analysis, the post-impact photographs correspond to the high-speed photographic sequences. The photographs taken after impact show the type and extent of damage that would be seen by the naked eye when examining damage to working structures. The types of post-impact damage that can be recognised using the naked eye are shown in *Figure 4.12*, these include sample penetration, delamination damage, back face spalling, ply splitting and indentation protrusion on the back face.

Here the description of the different types of damage that were seen will be given as to further understand what is described:

Delamination: *Damage in which areas where plies have come apart from each other.*

Ply Splits: *Damage in which a ply is broken between adjacent fibres and splits apart.*

Back Face Spalling: *Damage which occurs on the back face of the specimen, in which areas of that ply have come apart from the specimen.*

Indentation: *An area on the impact contact surface where the projectile has penetrated the surface.*

Back Face Protrusion: *An area where the projectile has caused a bulge under the impact point due to penetration of the projectile and crushing of the plies under the impact point.*

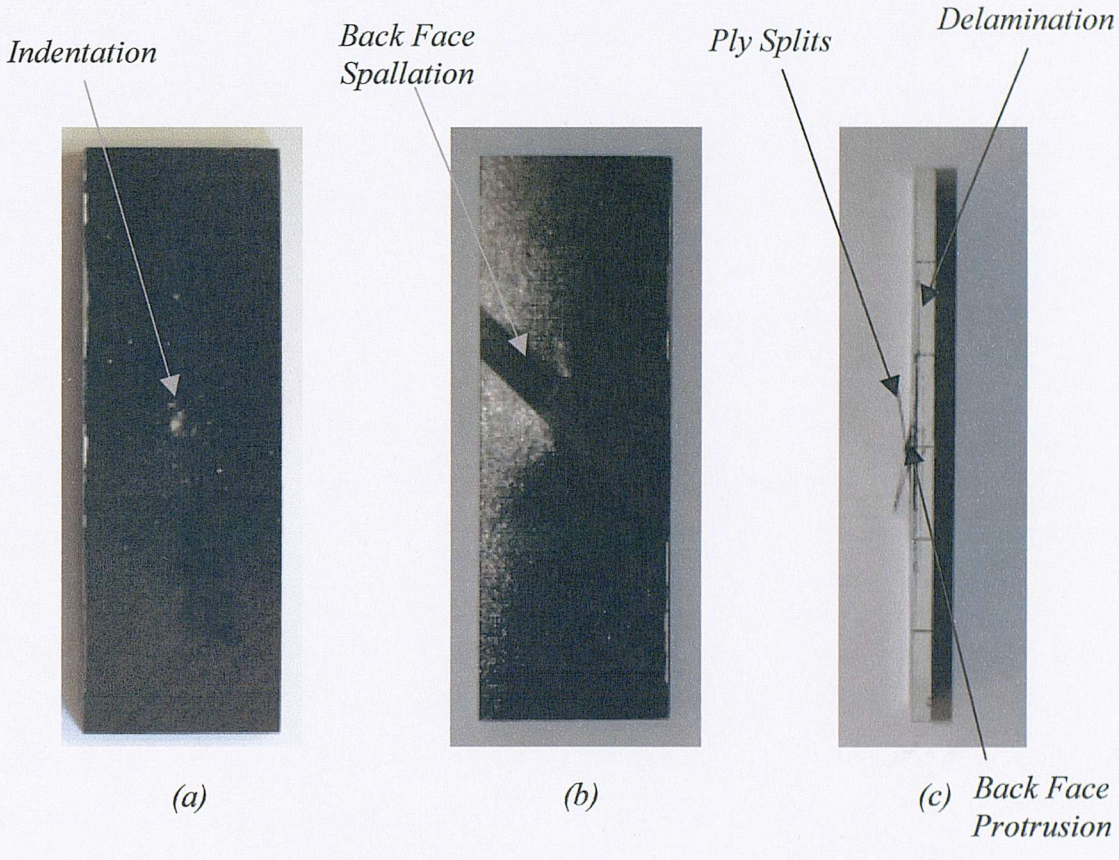


Figure 4.12: Typical types of damage that can be seen by the naked eye from the post impact photographs of specimens in the three views that image were taken in: (a) Front View; (b) Back View; (c) Side View.

Figures 4.13 through to *4.20* show the still photographs taken of the specimens (corresponding to the high speed photography sequences) in which areas of damage have been highlighted. Summary points on these post-impact photographs are brought together with the findings from the X-radiography in *Table 4.5* (see Section 4.3.3).

When looking at the specimens after the impact event a good deal about the extent of the damage that the impact event has caused can be seen. At both these impact pressures, on all the specimens, the projectile has caused an indentation at the contact point. Also the cracks seen by the HSC sequences are evident on examining the specimen after impact. Back face damage can also be seen.

At the impact points, similar features occur in all the specimens. At a 5 bar firing pressure (impact velocity ca. 150 m/s), the indentations are slight but evident, with visible fibre breakage and in the top layers there is evidence of the plies being crushed. At 8 bar firing pressure (impact velocity ca. 190 m/s respectively), the indentation is far deeper and reaches at least half way into the specimen with extensive fibre breakage and lots of plies having been crushed.

With the longitudinal specimens with the convex front-face, the cracks were extensive on the side, with the cracks towards the back-face having stretched much further along the specimen. On the back face, with the 5 bar impact (impact velocity ca. 150 m/s), ply splitting can be seen immediately behind the impact point. For the 8 bar impact (impact velocity ca. 190 m/s respectively), there was a bulge corresponding to the shape of the projectile on the back-face. Spalling behind the impact point occurs and ply splitting further away from the impact point had also occurred. With the concave front face for a 5 bar impact, the damage evident is similar to that with the convex front face at the same pressure. For an 8 bar impact, similar damage can be seen at the back-face as with the convex front face, however, notably this time the area of the bulge contained multiple split plies and fibre breakage. With the two 8 bar pressure impacts, the areas where ply splitting is most evident are on the back face where the ply material has nearly separated from the specimen.

The transverse specimens cracks are evident along the centre line on all specimens, however the extent of the damage observed is far less than that in the longitudinal specimens. At 5 bar only the centre line cracks visible along the sides. On the back face of the specimens there are ply splits, however the split area on the concave front face begins to spall off the specimen.

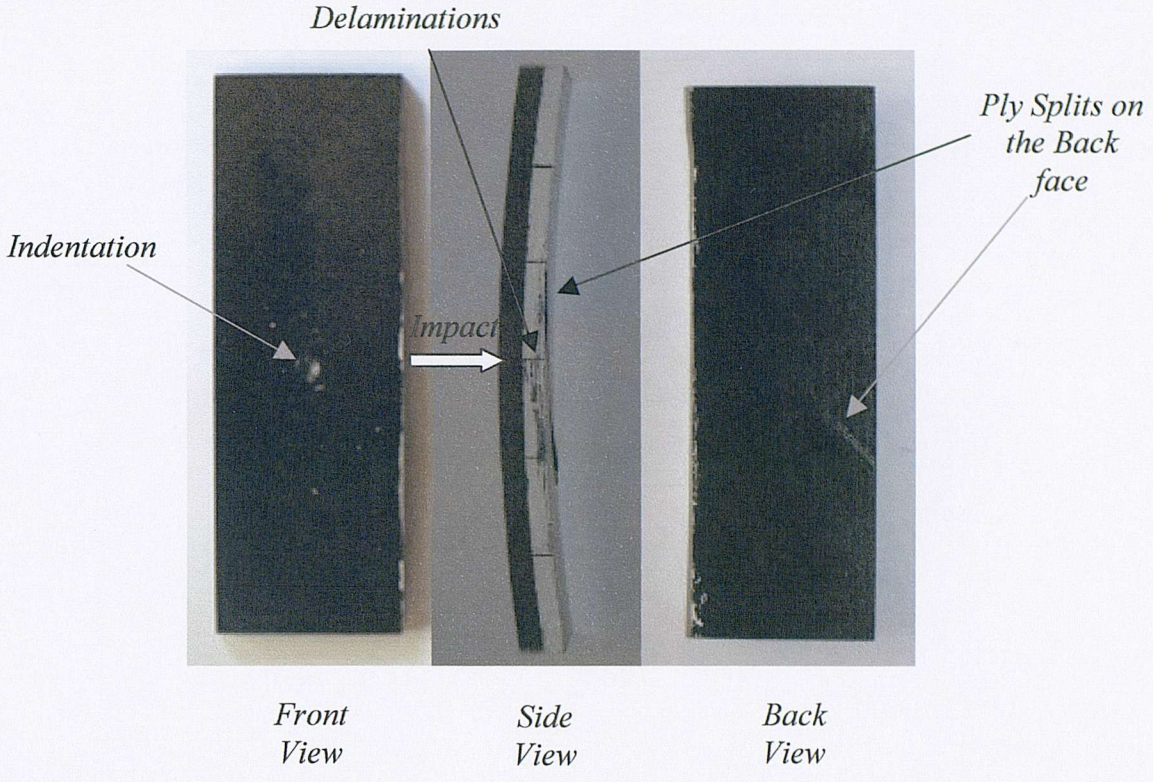


Figure 4.13: Post-impact Photograph of Specimen LC6: Longitudinal Curvature Convex Front Face at 5 Bar Pressure.

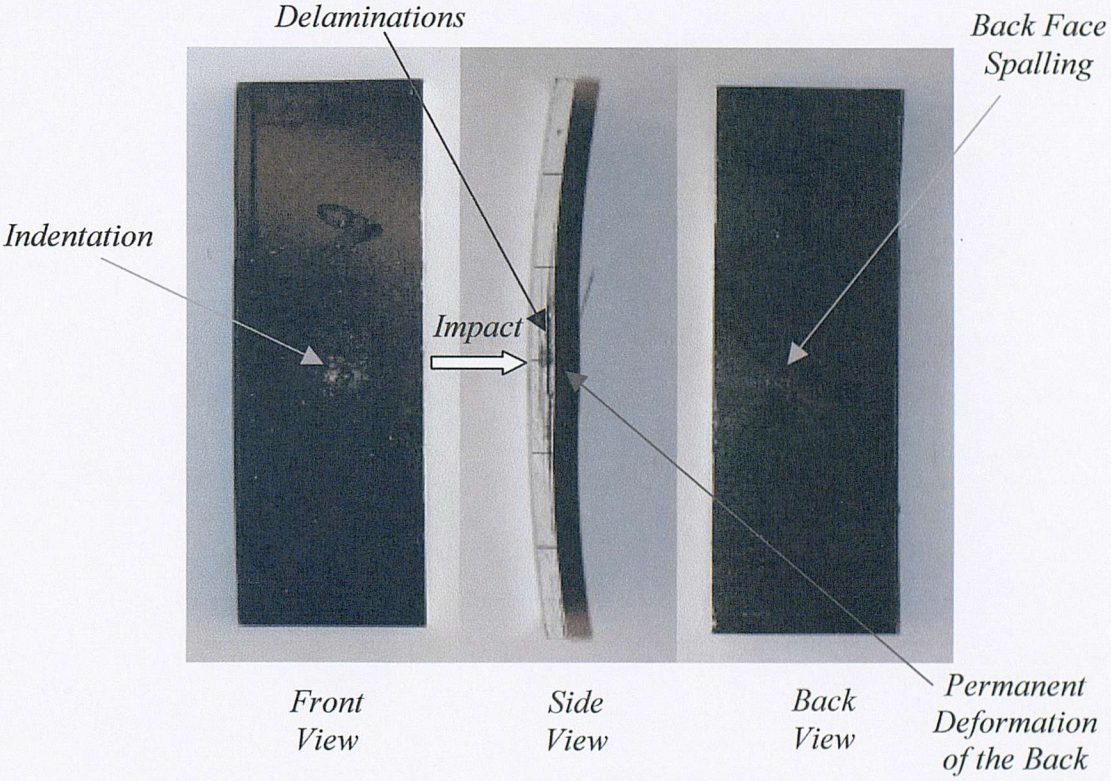


Figure 4.14: Post-impact Photograph of Specimen LC11: Longitudinal Curvature Convex Front Face at 8 Bar Pressure.

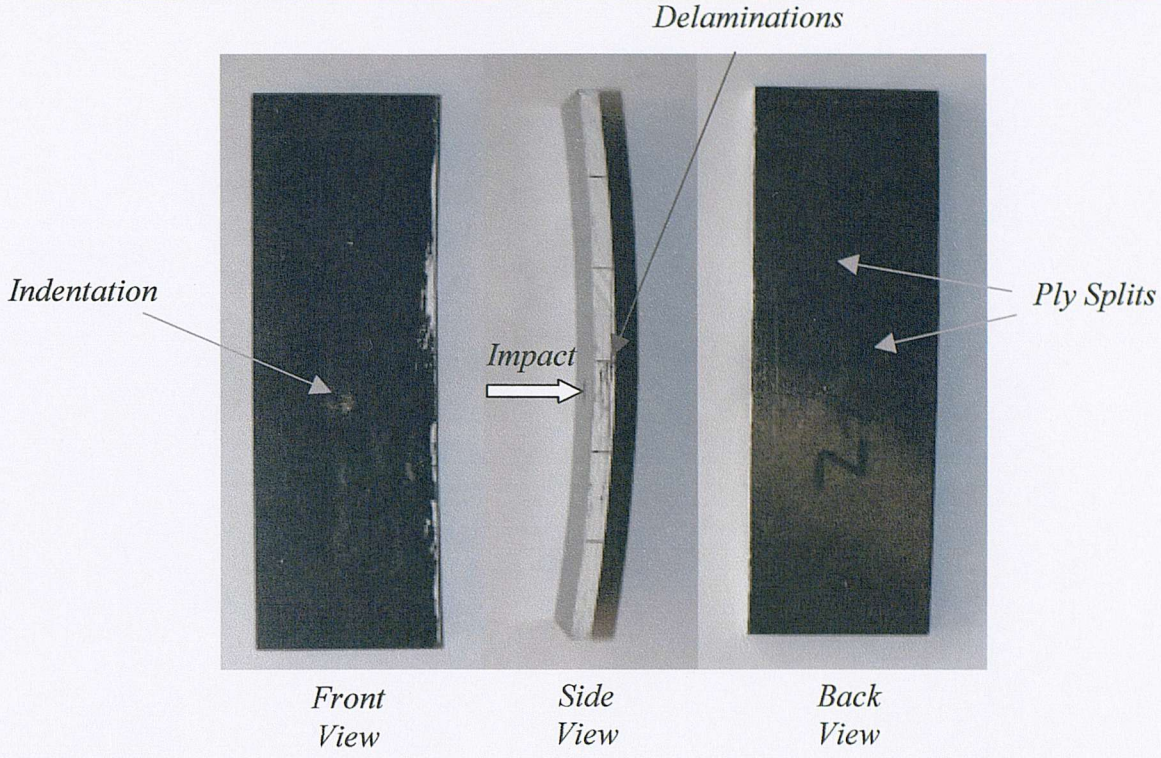


Figure 4.15: Post-impact Photograph of Specimen LC15: Longitudinal Curvature Concave Front Face at 5 Bar Pressure.

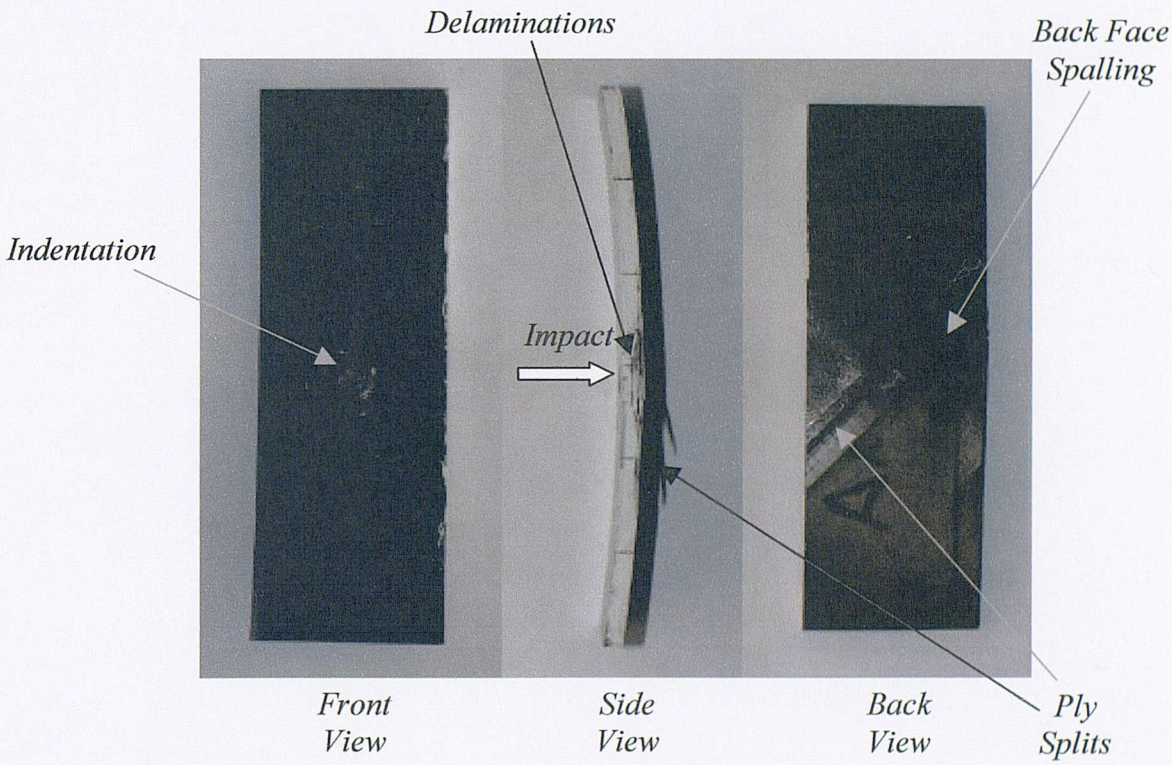


Figure 4.16: Post-impact Photograph of Specimen LC18: Longitudinal Curvature Concave Front Face at 8 Bar Pressure.

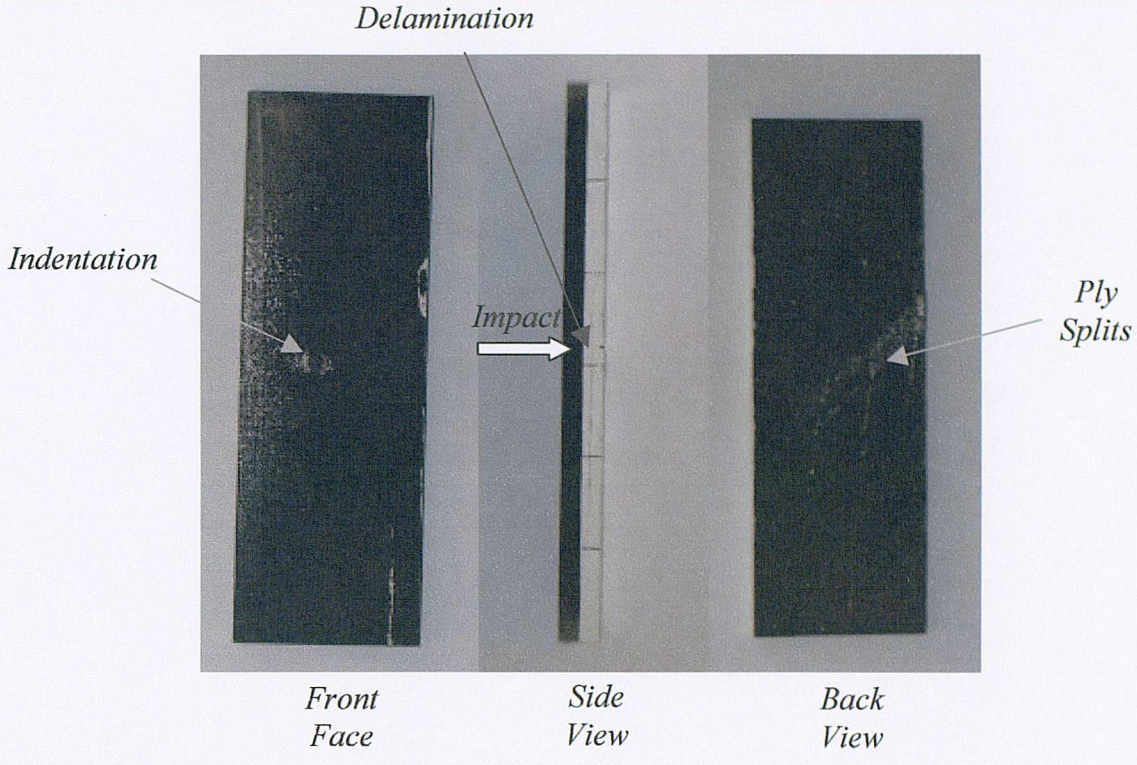


Figure 4.17: Post-impact Photograph of Specimen TC6: Transverse Curvature Convex Front Face at 5 Bar Pressure.

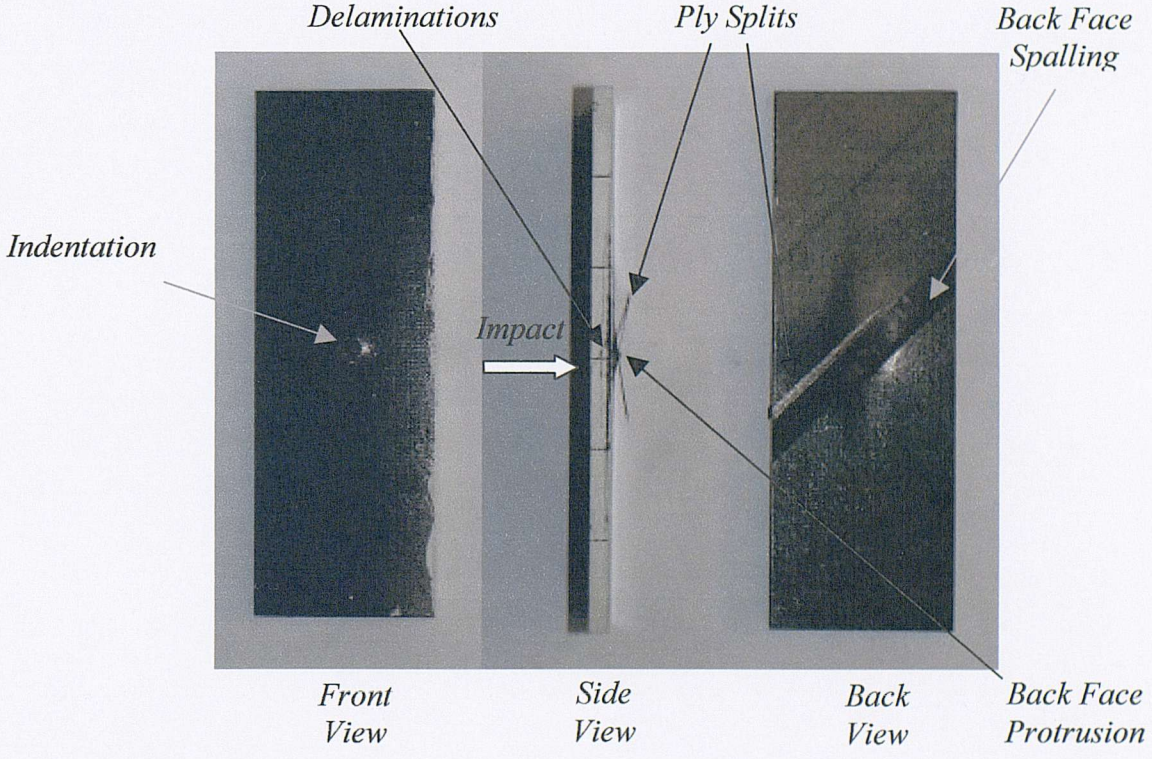


Figure 4.18: Post-impact Photograph of Specimen TC11: Transverse Curvature Convex Front Face at 8 Bar Pressure.

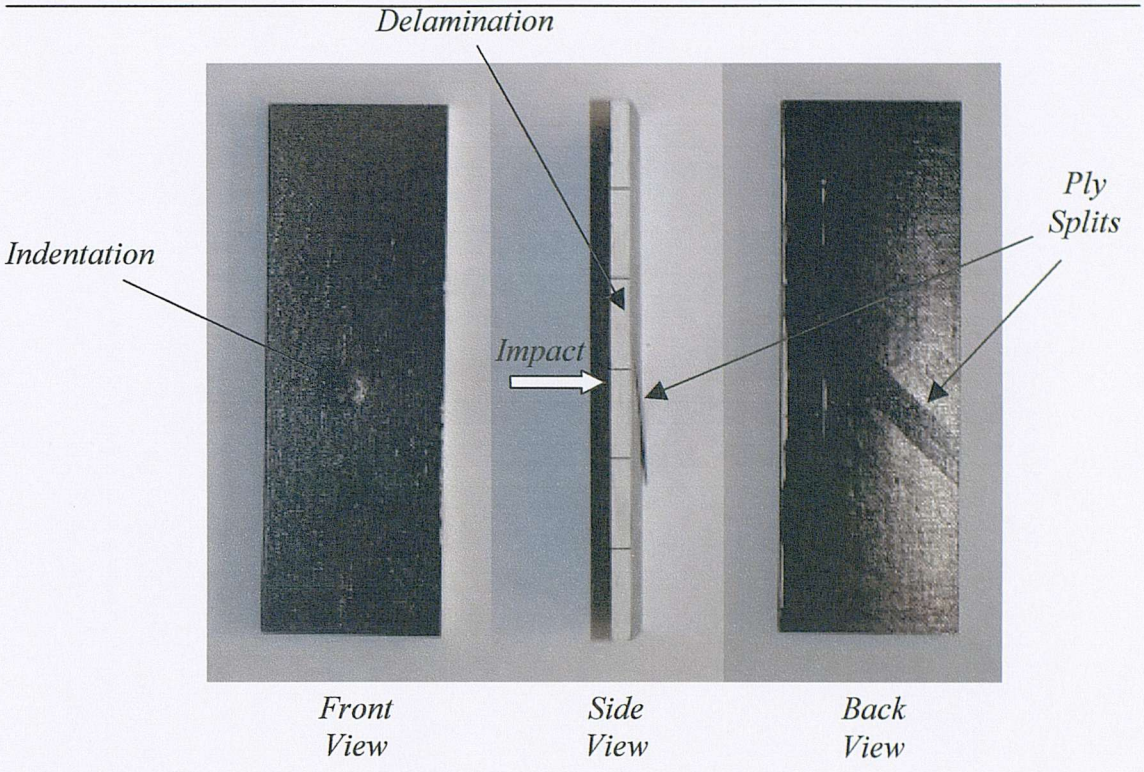


Figure 4.19: Post-impact Photograph of Specimen TC7: Transverse Curvature Concave Front Face at 5 Bar Pressure.

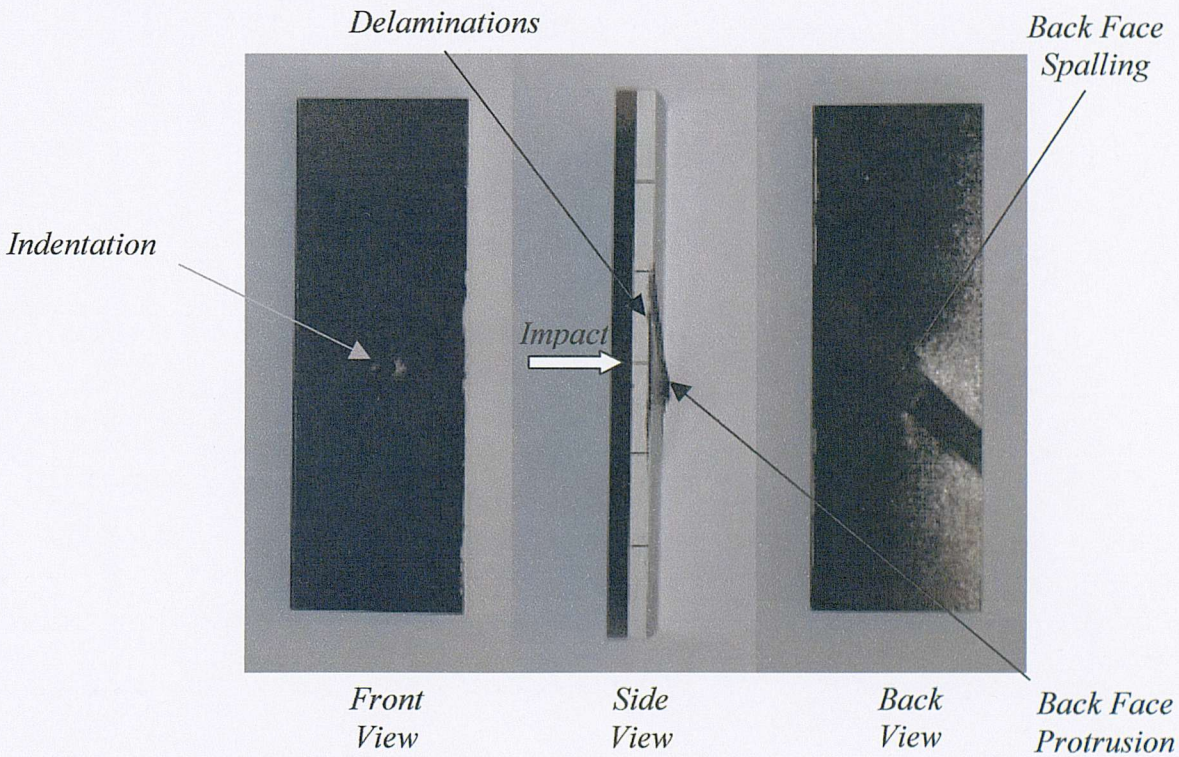


Figure 4.20: Post-impact Photograph of Specimen TC16: Transverse Curvature Concave Front Face at 8 Bar Pressure.

	Impact Pressure (bar)	Curvature	Front Face	Observations
LC6	5.0	Longitudinal	Convex	Indent the size of the projectile is evident on the front face, with fibre breakage and crushed plies visible. Cracks from delaminations to the edges are visible on painted side of specimen. Ply splitting on the back face, generated from the impact point.
LC11	8.0	Longitudinal	Convex	Deep indent at impact point. Fibres broken and top plies are crushed and broken by the projectile. Large cracks visible on both painted and unpainted side, with one reaching the end of the specimen. Indent visible on the back face along with back face spalling and ply splitting at impact point.
LC15	5.0	Longitudinal	Concave	Projectile shaped indent on font face and evidence of top plies being crushed and fibres being broken. Cracks visible on side, staring around a third into the thickness and progressing to the back and increasing in size. Ply splitting on the back face at the impact area.
LC18	8.0	Longitudinal	Concave	Crushed indent at impact point. Side view shows cracks beginning from center progressing to the back face and are visible from both sides (painted and unpainted). Indent visible on back face with bulge, back face spalling, fibre and ply breakage visible.
TC6	5.0	Transverse	Convex	Indent at impact point with visible fibre breakage and ply crushing and evidence of relaxation. One large crack visible on the painted side of the specimen. Ply splits visible on the back face at the impact area.
TC11	8.0	Transverse	Convex	Deep indent at impact point with obvious fibre breakage and ply crushing visible. Along the thickness cracks along the center and near the back face of the specimen visible on both sides. Spalling and ply splits on the back face, with a visible indent and extensive damage around it.
TC7	5.0	Transverse	Concave	Indent at impact point, visible fibre breakage, ply crushing and evidence of relaxing of the crushing behaviour. Slight cracks visible on either side and are from the center of the thickness going towards the back surface. Beginnings of spalling visible with ply splits.
TC16	8.0	Transverse	Concave	Crushed indent at the impact point. Huge cracks visible towards the back face of the specimen from side views. Indent visible on the back face, bulging and breaking through the back layer of the specimen. Spalling evident on the back face along with ply splits.

Table 4.5: Observations of specimens after Impact Event.

At 8 bar pressure, projectile shape bulges are evident on the back face, along with spalling of the area immediately behind the impact point. Lots of fibre breakage is also evident in this area. Also parts of the split back ply are beginning to spall off. Also, from the side view, cracks representing delaminations are also seen towards the back of the specimen. It is also to be noted that from the observation of the impacted specimens it seems that the specimens with the convex front-face are more heavily damaged when compared to the corresponding specimens with a concave front-face.

As can be seen there is only limited information that can be obtained from observing the impacted specimens. Only damage on the surface can be seen, however it is the damage that lies underneath the surface that causes the majority of post-impact problems in the use of composites in engineering applications. Therefore, it is of importance that the extent of the internal damage can be assessed. In order to perform this more intricate analysis, X-Radiography and other techniques are required.

4.3.3 X-Radiography

In order to understand the internal damage that has occurred due to the impact event the method of X-Radiography was used. This method relies on the penetrant that is used to highlight the damage within the specimen, therefore two different penetrants were used in order to determine the depth of the damage. The two different penetrants used were firstly di-iodomethane, a organic based penetrant which has the advantage of evaporating at room temperature and therefore will remove itself from the specimen in due course. Secondly, the more traditional zinc-iodide/isopropanol solution was used. An example of each of the X-Radiographs using the two different penetrants is shown in *Figure 4.21* with all the highlights and damage types shown.

It can be seen that the two different penetrants used in general highlight the same damage areas, however the finer details can differ. The di-iodomethane penetrant highlights the edge of the delaminations a lot clearer than the traditional Zinc Iodide/ Isopropanol solution. The Zinc Iodide solution gives a clearer picture of the damage that occurs just below the impact point, and details of delamintauion and ply splits in

this area can be better identified, whilst the di-iodomethane solution can only show a general region of damage as it is unable to clearly outline separate parts of an intensely damaged area. This main difference could be due to the viscosity of the two penetrants. Di-iodomethane is the lower viscosity of the two and therefore the capillary action that draws the penetrant into the delaminations has a greater effect and therefore can draw it to the extremities of the damaged area a lot easier and hence this particular penetrant gives a clearer picture of the outer edges of the damaged area. The Zinc Iodide solution being the higher viscosity of the two does not show the extremities as well, however it is able to highlight the extensive damage under the impact point.

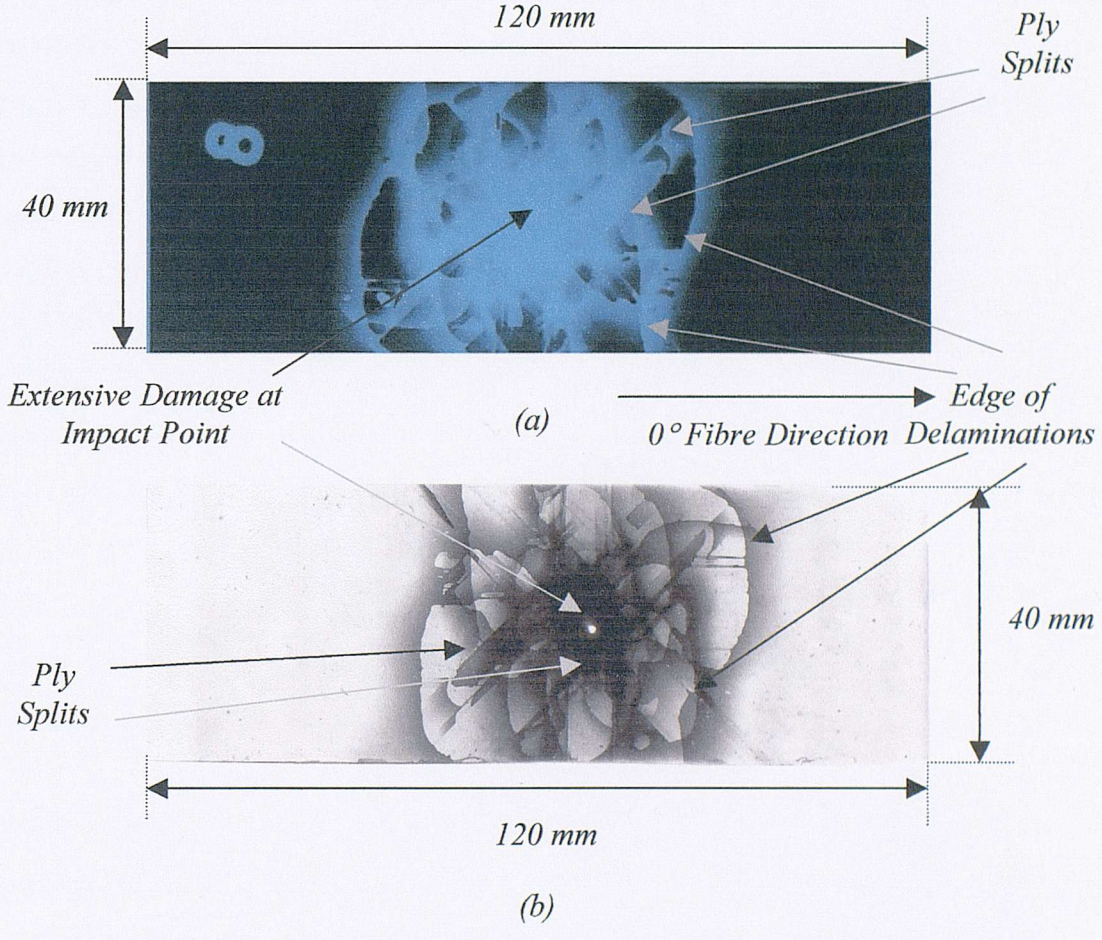


Figure 4.21: An example of an X-Radiograph with the types of Damage that can be identified: (a) X-Radiograph using di-iodomethane as a penetrant; (b) X-Radiograph using zinc iodide/isopropanol solution as a penetrant.

Figures 4.22 – 4.29 show the X-Radiographs for the eight specimens that have been investigated.

Table 4.7 summarises the damage and details that have been observed from the X-Radiographs. The delaminations tend to have an oval peanut shape whilst ply splitting and deplying are represented by the lined areas in the 4 ply orientation directions. The damage at the impact point is so intense that that particular area is very blurred in the radiographs.

With the specimens of longitudinal curvature, the convex front-faced specimens seem to incur much more damage than the concave front-faced specimens. At 5 bar firing pressure (impact velocity ca. 150 m/s) the convex front-faced specimen has intense damage at the impact point, with damage growing along and across the specimen (*Figure 4.22*). Studying the 8 bar specimen (impact velocity ca. 190 m/s), the damage has grown a great deal along the specimen and the total damage area covers around 80-85% of the specimen, making it the most damaged specimen of the lot (*Figure 4.23*). The damage that occurs in the concave front face specimens seems to grow mainly in the transverse direction, and is concentrated across the centre of the specimen. The 5 bar longitudinal specimen with a concave front-face (impact velocity ca. 150 m/s) seems to be the least damaged of all the specimens (*Figure 4.24*). There is an increase in damage intensity for the 8 bar longitudinal specimen with a concave front-face (impact velocity ca. 150 m/s) as would be expected, however the concentration of damage in the 90° directions is marked in the 8 bar specimen (*Figure 4.25*).

With the specimens of transverse curvature, for a 5 bar firing pressure (impact velocity ca. 150 m/s), the damage incurred with a convex front-face seems to incur the greatest amount of damage amongst all the specimens at 5 bar (*Figure 4.26*). The damage area for this condition is around 60% of the specimen. The damage also seems to be more on one side of the specimen. However, this can be attributed to the impact being not totally central.

The damage in the 8 bar impact (impact velocity ca. 190 m/s) of the convex front-face transverse specimen shows a greater amount of delamination than the 5 bar specimen, however this increase in delamination has not stretched the whole length of the specimen, but has grown in the transverse direction so reaching to the sides of the specimen (*Figure 4.27*).

The same trend in damage observed can be seen in the concave front-face transverse specimens. But the damage is not as intense as it is in the convex front-face cases (*Figures 4.28 & 4.29*), with the damage only covering roughly 30-40% of the specimen.

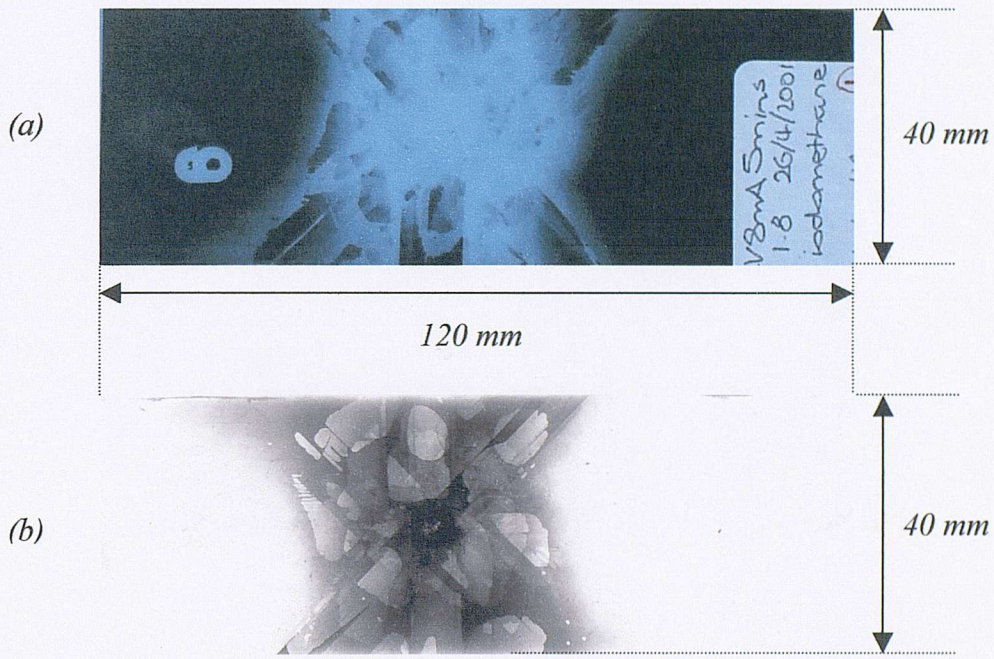


Figure 4.22: X-Radiographs for Specimen LC6 (Longitudinal Curvature Convex Front Face at 5 Bar Firing Pressure): (a) Di-Iodomethane Penetrant; (b) Zinc Iodide/Isopropanol Penetrant.

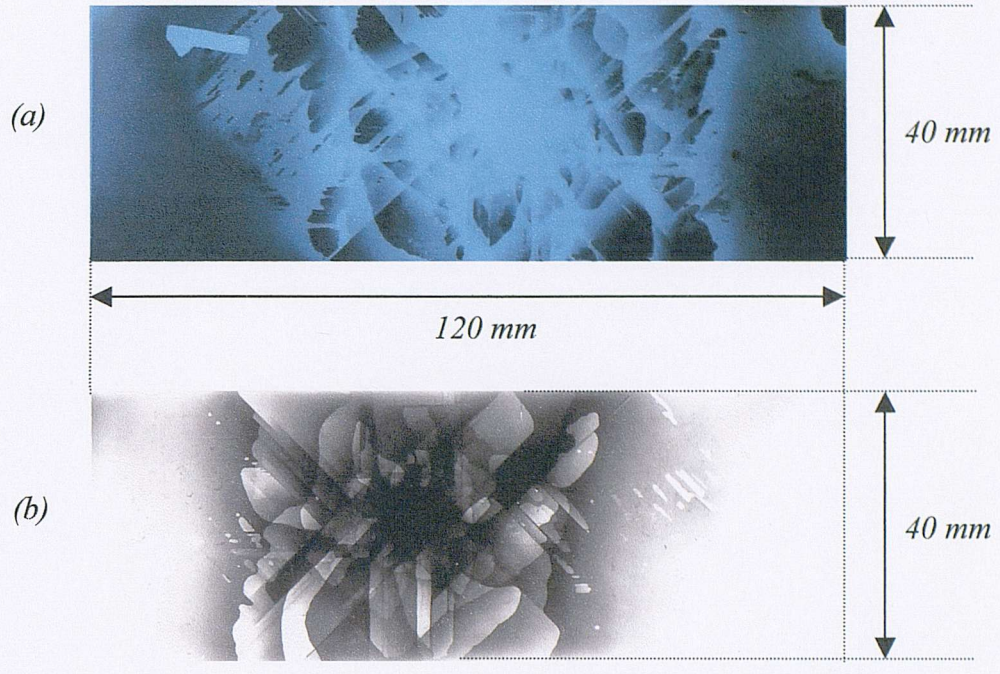


Figure 4.23: X-Radiographs for Specimen LC11 (Longitudinal Curvature Convex Front Face at 8 Bar Firing Pressure): (a) Di-Iodomethane Penetrant;(b) Zinc Iodide/Isopropanol Penetrant.

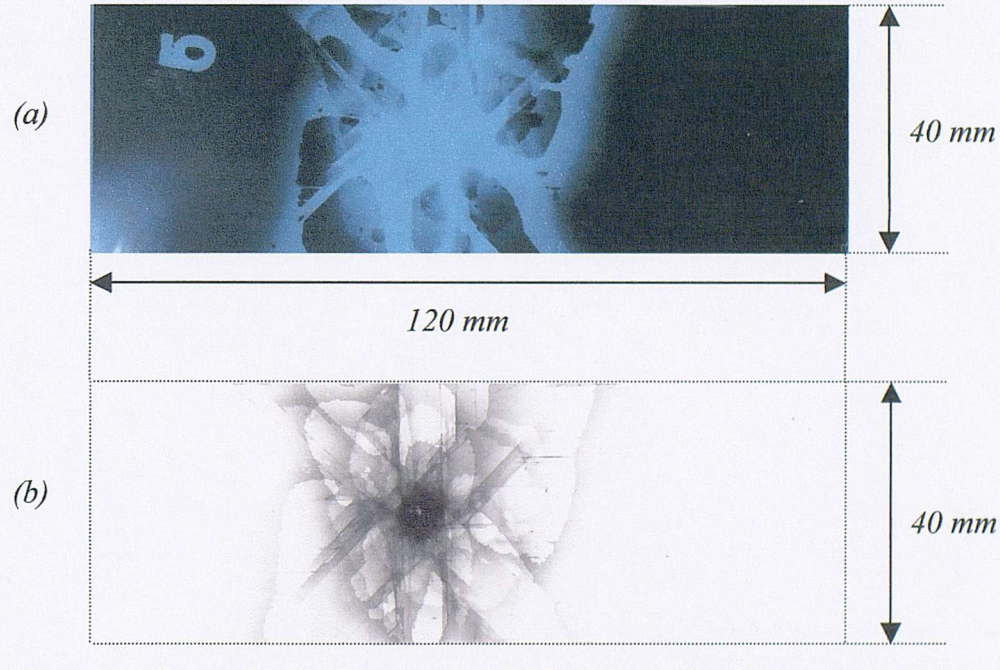


Figure 4.24: X-Radiographs for Specimen LC15 (Longitudinal Curvature Concave Front Face at 5 Bar Firing Pressure): (a) Di-Iodomethane Penetrant; (b) Zinc Iodid/Isopropanol Penetrant

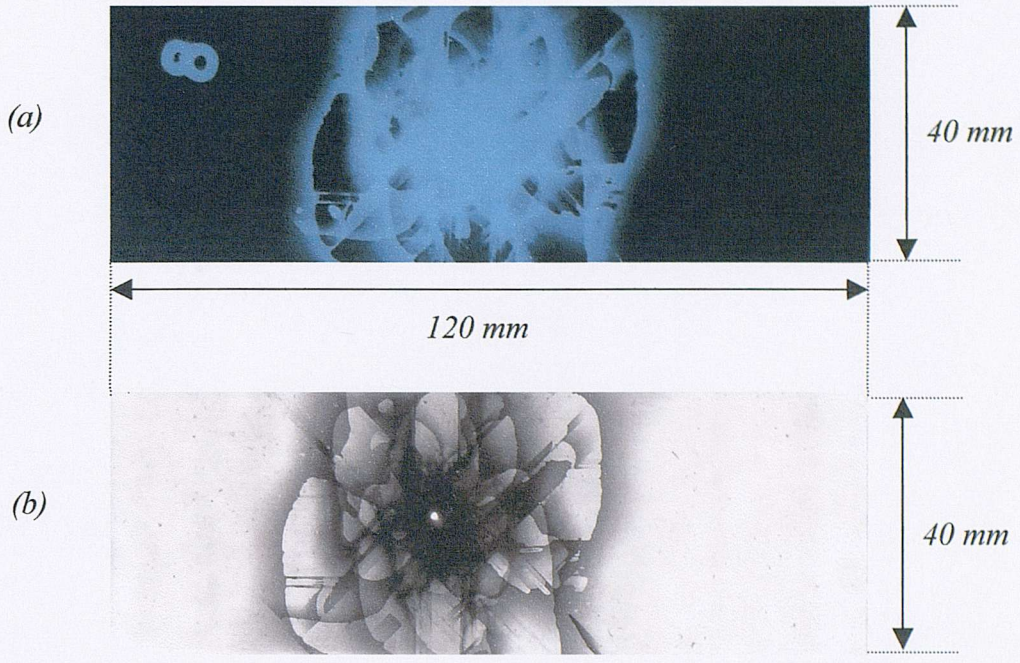


Figure 4.25: X-Radiographs For Specimen LC18 (Longitudinal Curvature Concave Front Face at 8 Bar Firing Pressure): a) Di-Iodomethane Penetrant; (b) Zinc Iodide/Isopropanol Penetrant

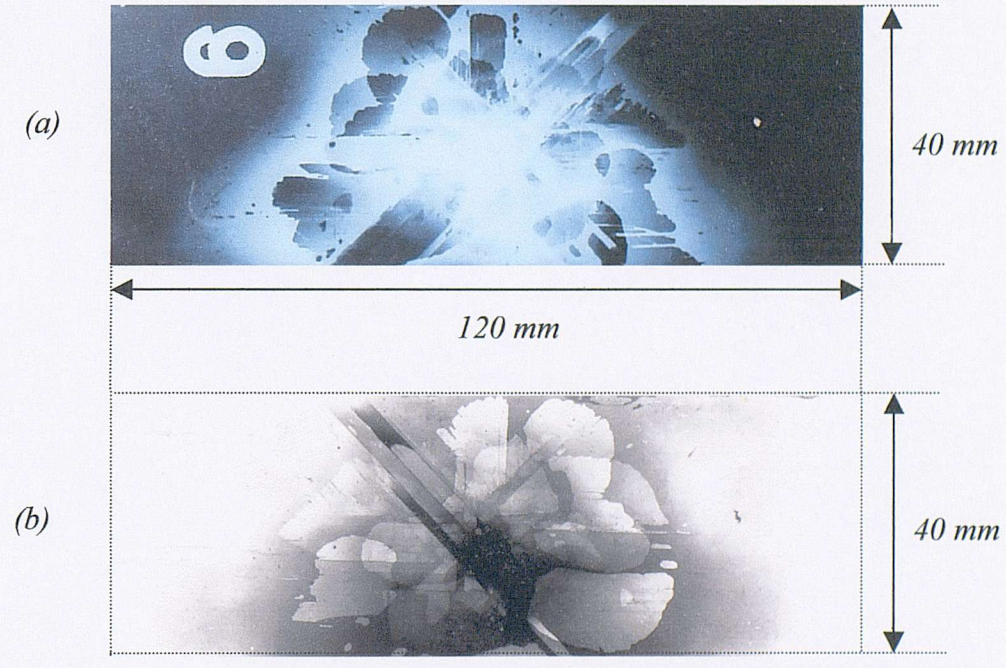


Figure 4.26: X-Radiographs for Specimen TC6 (Transverse Curvature Convex Front Face at 5 Bar Firing Pressure): (a) Di-Iodomethane Penetrant; (b) Zinc Iodide/Isopropanol Penetrant

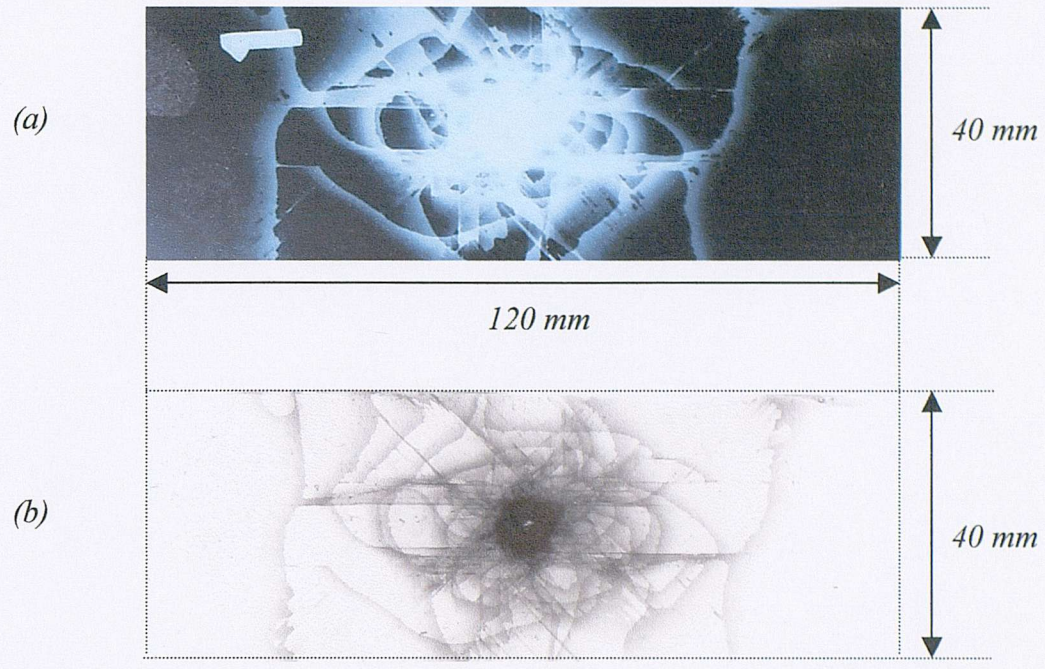


Figure 4.27: X-Radiographs for Specimen TC11 (Transverse Curvature Convex Front Face at 8 Bar Firing Pressure): (a) Di-Iodomethane Penetrant; (b) Zinc Iodide/Isopropanol Penetrant.

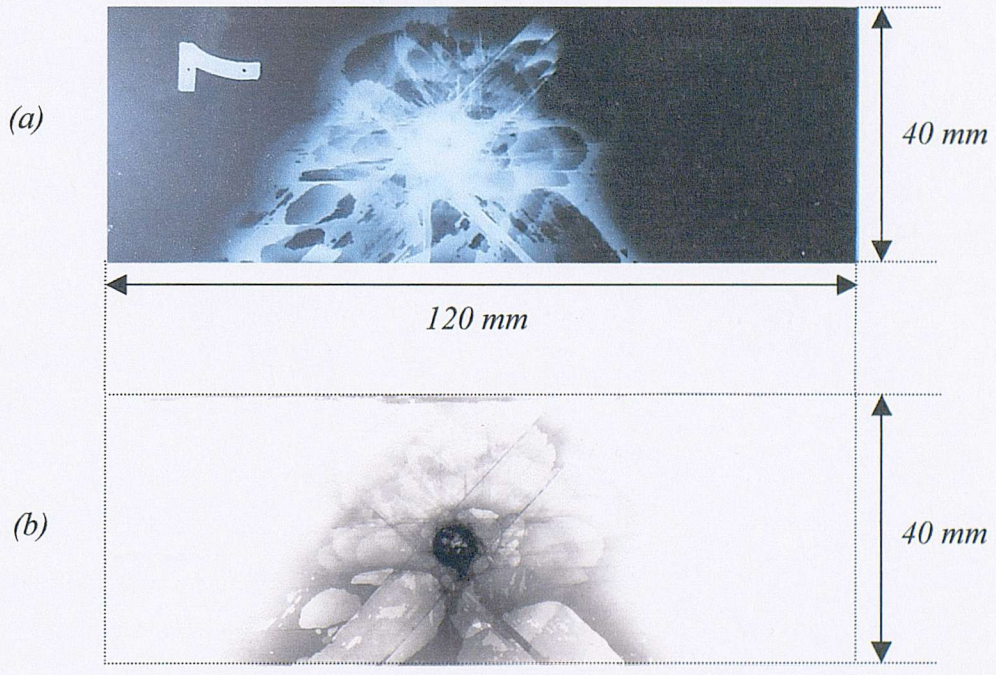


Figure 4.28: X-Radiograph for Specimen TC7 (Transverse Curvature Concave Front Face at 5 Bar Firing Pressure): (a) Di-Iodomethane Penetrant; (b) Zinc Iodide/Isopropanol Penetrant.

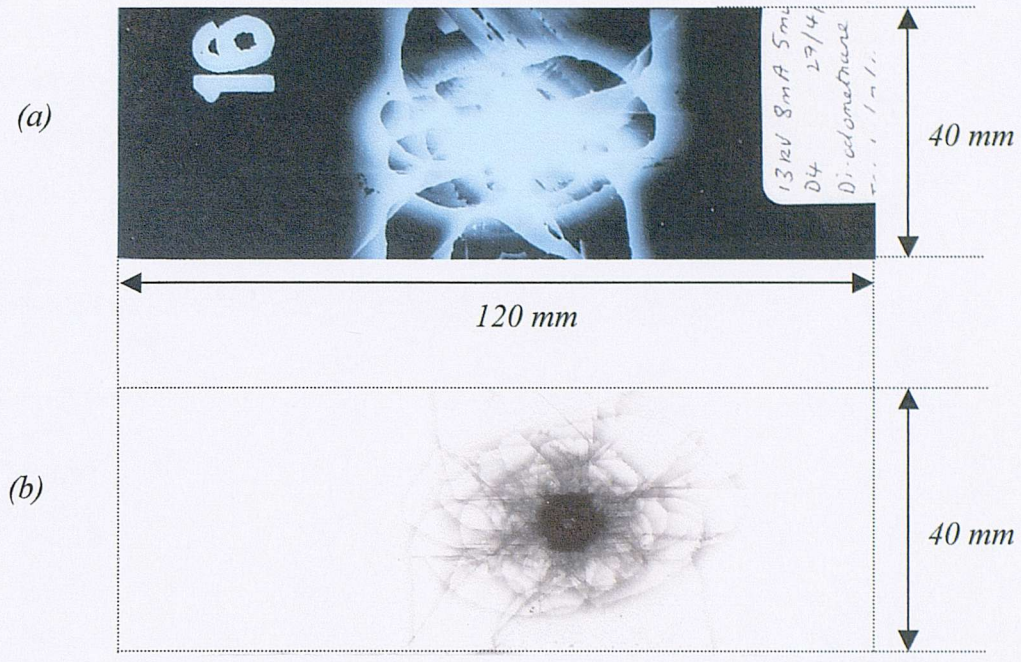


Figure 4.29: X-Radiographs for Specimen TC16 (Transverse Curvature Concave Front Face at 8 Bar Firing Pressure): (a) Di-Iodomethane Penetrant; (b) Zinc Iodide/Isopropanol Penetrant.

Using simple length and with measurements of the damage highlighted, estimations of the 2-dimensional damage area are made. Area formulae for either a rectangle or an ellipse were used depending on the resemblance shown by the X-Radiograph. For the cases where an elliptical damage area was assumed the length and width measurements were taken in the orientation of the ellipse itself. The estimated sizes of the damaged areas are shown in *Table 4.5,* the formula used in each case is indicated in the area column.

The figures shown in *Table 4.6* and *Figure 4.22* indicate that the 2D damage areas, as would be expected, increase in size when the impact energy is increased. However it must be noted that these areas are 2 dimensional and the extent of the damage through the thickness of the sample cannot be judged by these figures. As can be seen when comparing he damage area for LC15 and LC18, the increase in impact velocity for this arrangement has caused a decrease in the 2D damage area. However when comparing the two actual X-Radiograph images it can be seen that the damage in

LC18 is far more extensive, especially at the impact point, than that in LC15 and this must be attributed to the increase in through thickness damage with the increase of impact energy. The differences in the through thickness damage is shown in Section 4.3.4 where SEM micrographs are used to show how damage progresses through the thickness of the samples.

Specimen	Damage Length (mm)	Damage Width (mm)	Damage Area (mm^2)*
LC6	55.02	40	2200.8 (R)
LC11	69.43	40	2777.2 (R)
LC15	53.71	40	2148.4 (R)
LC18	64.19	51.09	1717.1 (E)
TC6	66.81	37.64	1975.1(E)
TC11	72.05	40	2882 (R)
TC7	45.85	35.29	1270.8(E)
TC16	43.23	40	1729.2 (R)

*Table 4.6: Table showing estimated damage areas from X-Radiographs (*R = assumed rectangular shape, E = assumed elliptical shape).*

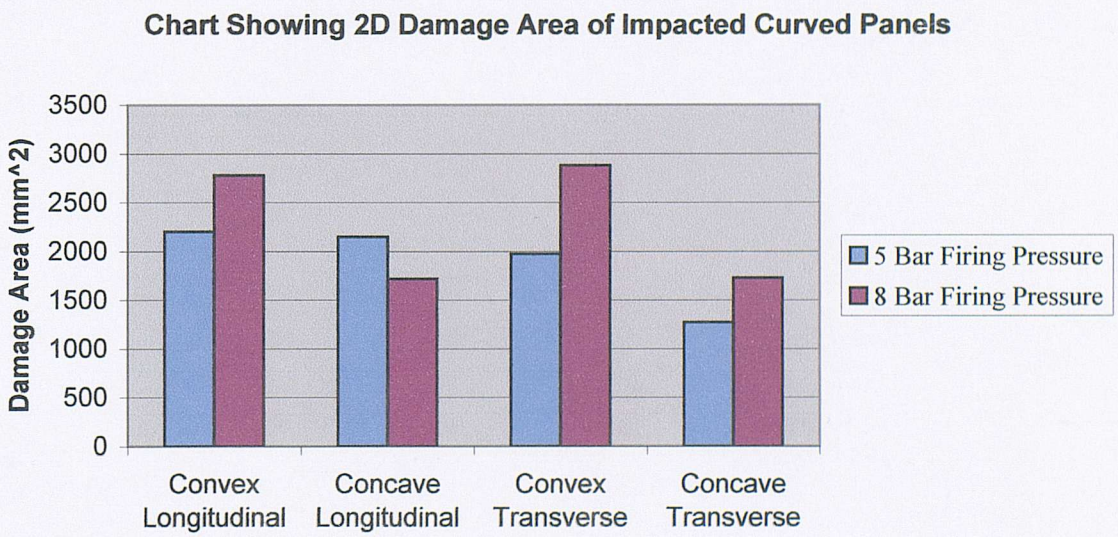


Figure 4.30: Chart Showing Damage Area of Impacted Curved Composite Panels.

	Impact Pressure (bar)	Curvature	Front Face	Observations
LC6	5.0	Longitudinal	Convex	Delamination areas visible throughout the specimen with typical peanut shapes. Ply splitting can be seen but are mainly in the ±45° directions. Limited de-plying in the 90° direction can also be seen near the central part of the specimen. Damage area covers roughly the central 50% of the specimen.
LC11	8.0	Longitudinal	Convex	As above but far more extensive. The damage area covers around 80% of the specimen. Definite de-plying in the 90° direction around the central part of the specimen as well as visible deply and splitting in the 0° direction. Damage seems to spread towards the outside of the specimen via the ±45° directions.
LC15	5.0	Longitudinal	Concave	Damage is concentrated at the central part of the specimen. Consists mainly of delaminations. Ply splitting and de plying are shown in the ±45° and 90° directions.
LC18	8.0	Longitudinal	Concave	Same as for LC15, but more extensive and still concentrated around the center of the specimen. Also includes limited 0° ply splitting and de-plying. Damage seems to spread towards the outside of the specimen via the ±45° directions.
TC6	5.0	Transverse	Convex	Peanut shaped delamination areas can be observed, damage does not seem to be that concentrated. Ply splits can be seen in all 4 directions.
TC11	8.0	Transverse	Convex	Delamination areas can be seen to stretch to the sides of the specimens, and progression seems to be in the 90° direction. Most delamination areas seem to be in the 0° and 90° directions, as so ply splits and de-ply areas. Much more extensive damage than in TC6.
TC7	5.0	Transverse	Concave	Damage concentrated in the center of the specimen, but does not seem to be very extensive. Delamination areas don't seem as large as for the other specimens. However extensive splitting can be observed in all 4 directions.
TC16	8.0	Transverse	Concave	Damage concentrated in the center of the specimen. Covers around 30% of the specimen. Evidence that progression is along the 90° direction is evident. Main splitting and de-plying directions seem to be the ±45° directions, with limited evidence in the 0° and 90° directions.

Table 4.7: Damage Observations made from X-Rays of damaged samples.

4.3.4 Scanning Electron Microscopy

Although the X-Radiographs give a good idea of the spread of the damage in the impacted specimens they are unable to show how the damage progresses through the thickness of the specimen, and at which level of the thickness of the specimen the delaminations occur. The progression of damage in the specimen and the way the damage occurs through the thickness, both in the form of delaminations and matrix cracking, needs to be seen in order to understand the likely path of damage development. Therefore the specimens were sectioned, mounted, polished and prepared for examination (details for this procedure are given in Section 3.2.4.3).

The order in which these micrographs were taken was in a way in which certain aspects of the damage were studied. Firstly, the damage at and immediately below the impact point was assessed. Then, the damage was followed through the specimen until the rear face of the specimen was reached. The rear face was examined and the growth of delaminations was followed to where they were initiated. *Figure 4.31* shows a typical micrograph and gives the types of damage that can be shown using this method.

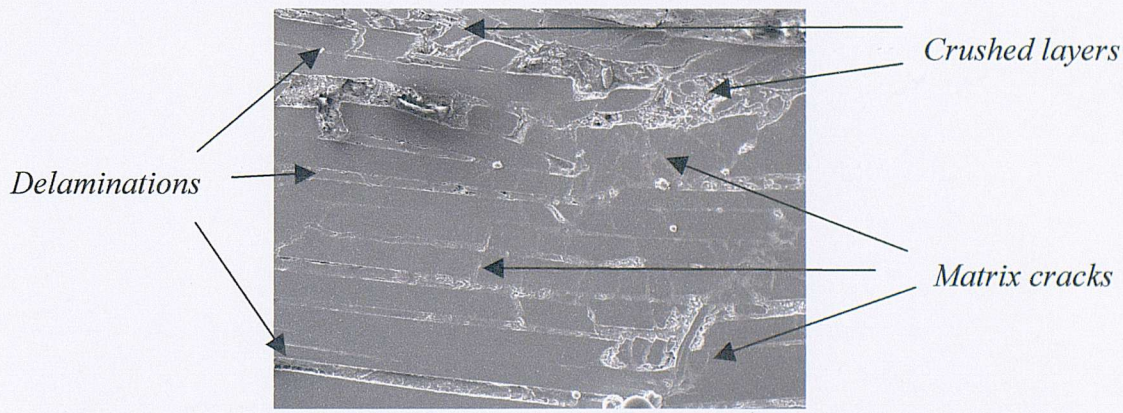


Figure 4.31: Typical micrograph with details of damage that can be viewed using electron microscopy.

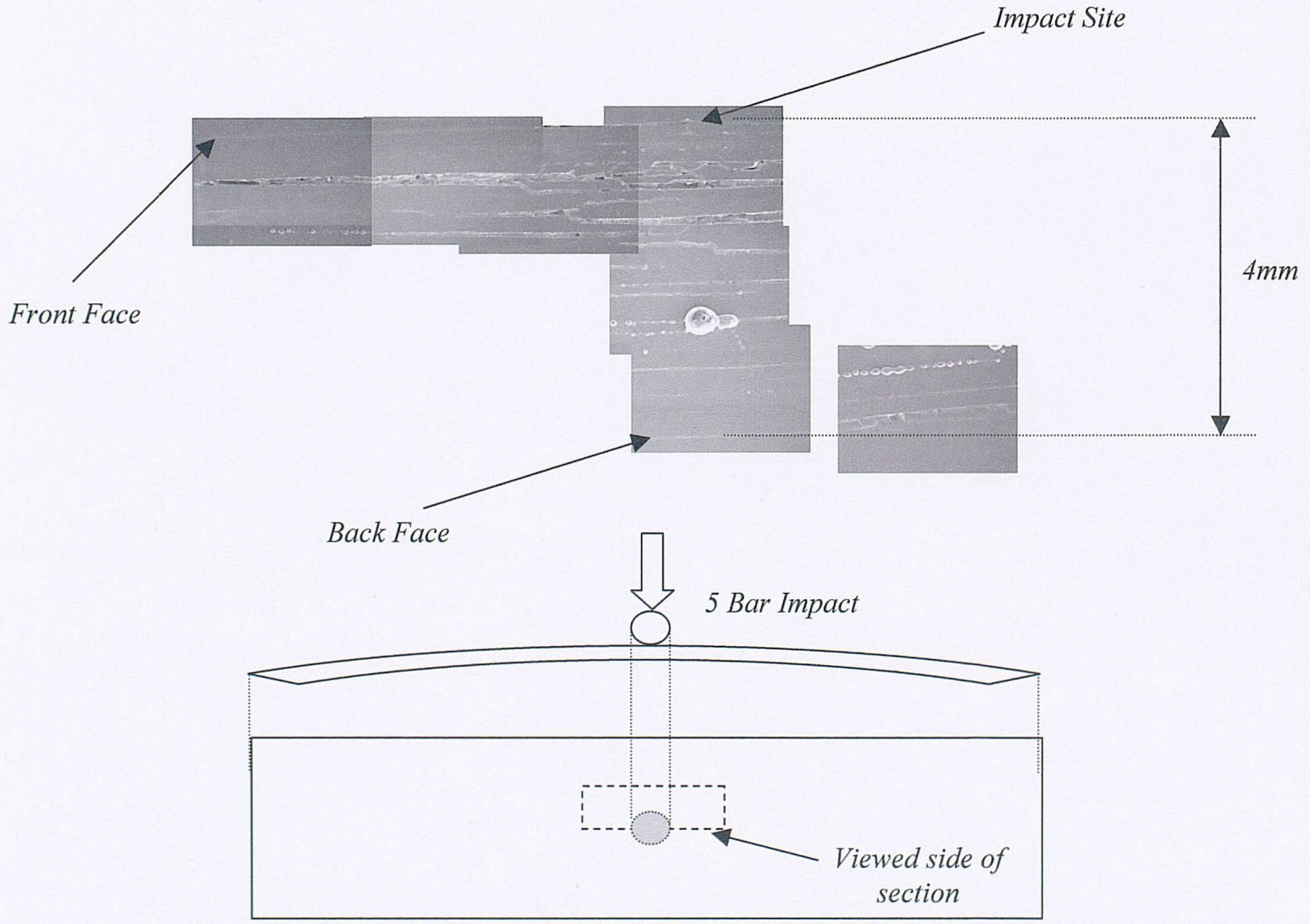


Figure 4.32: Amalgam of Micrographs for Specimen LC6 (Longitudinal Curvature with Convex Impact Face at 5 bar firing pressure).

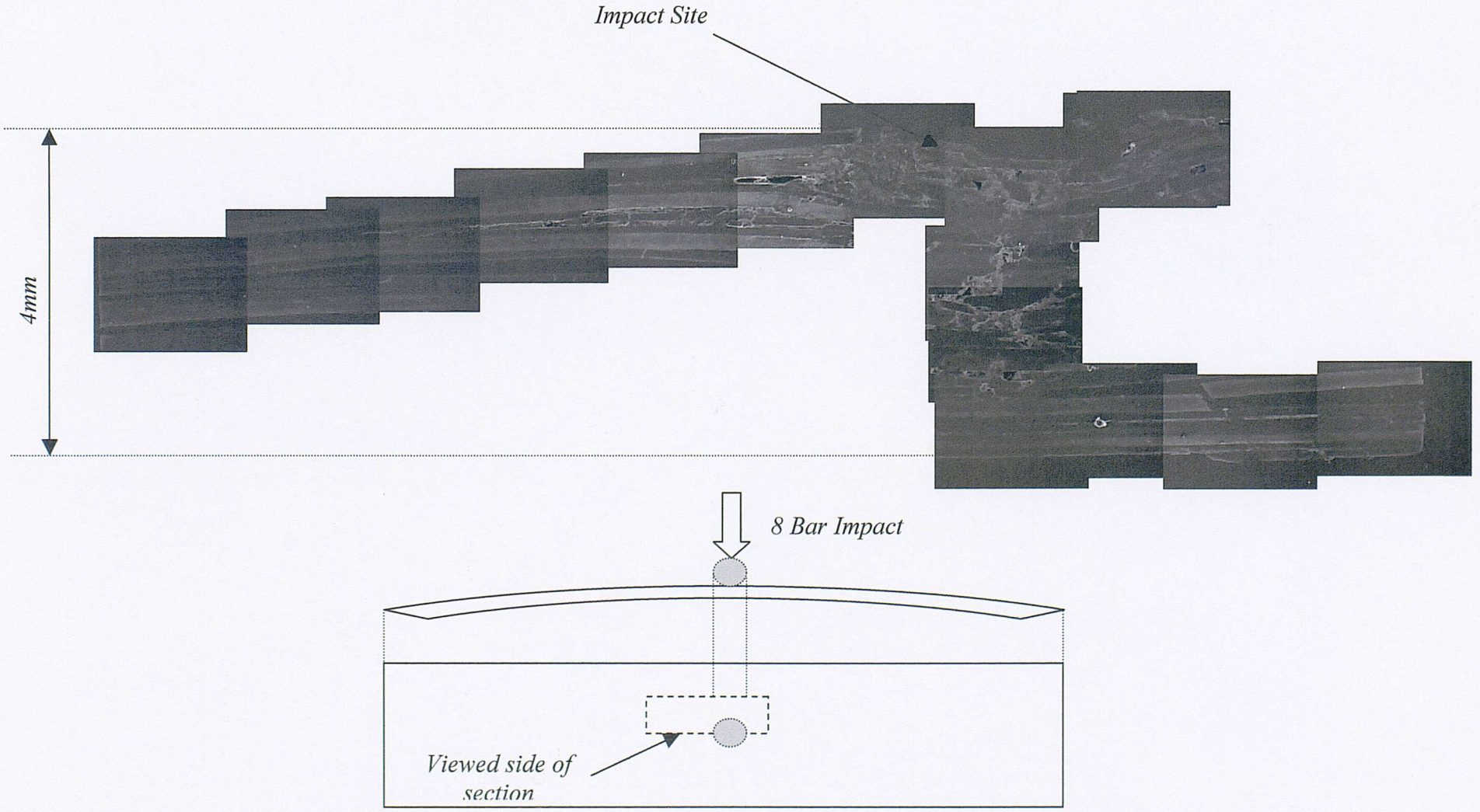


Figure 4.33: Amalgam of micrographs for Specimen LC11(Longitudinal Curvature with Convex Impact Face at 8 bar firing pressure).

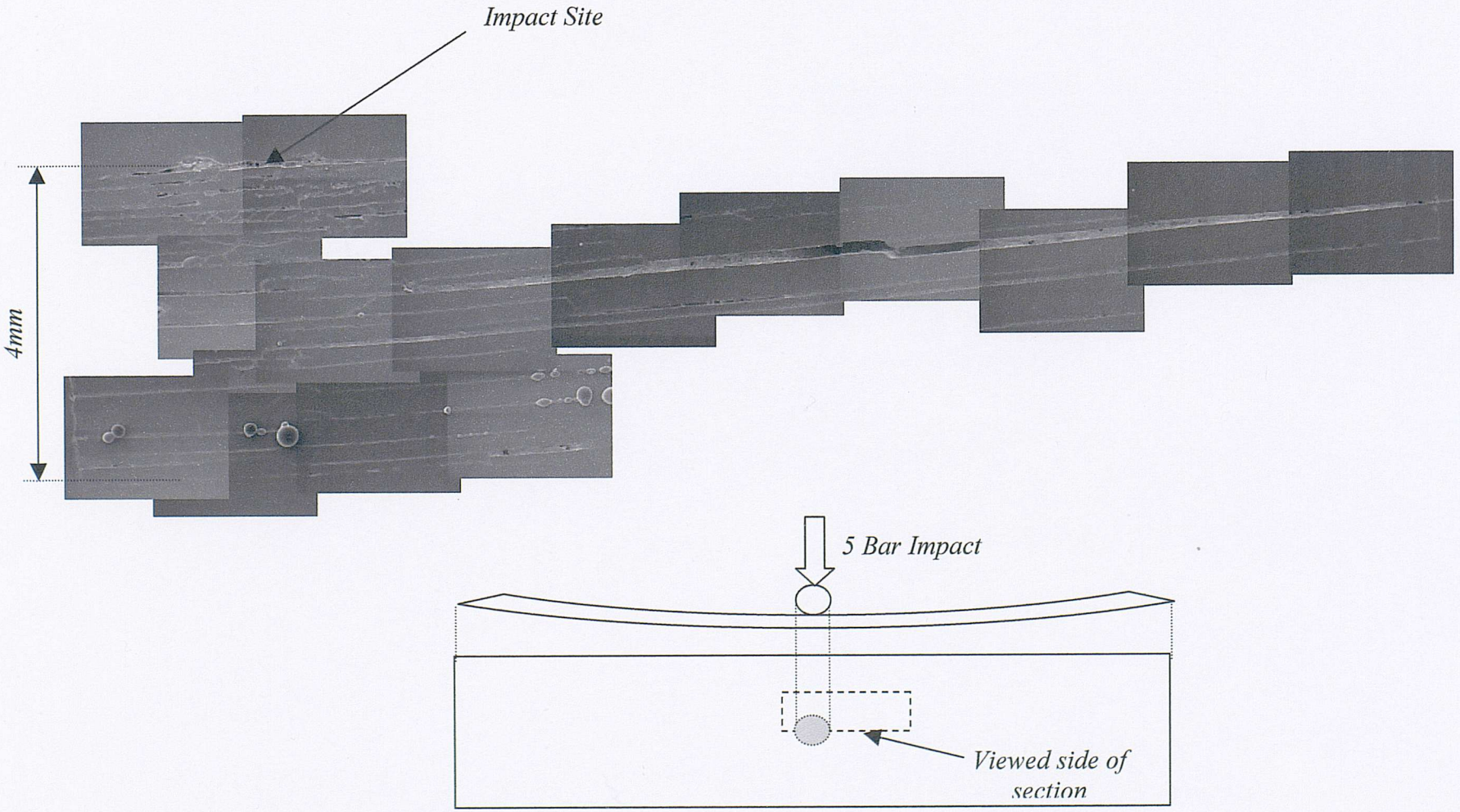


Figure 4.34: Amalgam of Micrographs for Specimen LC15 (Longitudinal Curvature with Concave Impact Face at 5 bar firing pressure).

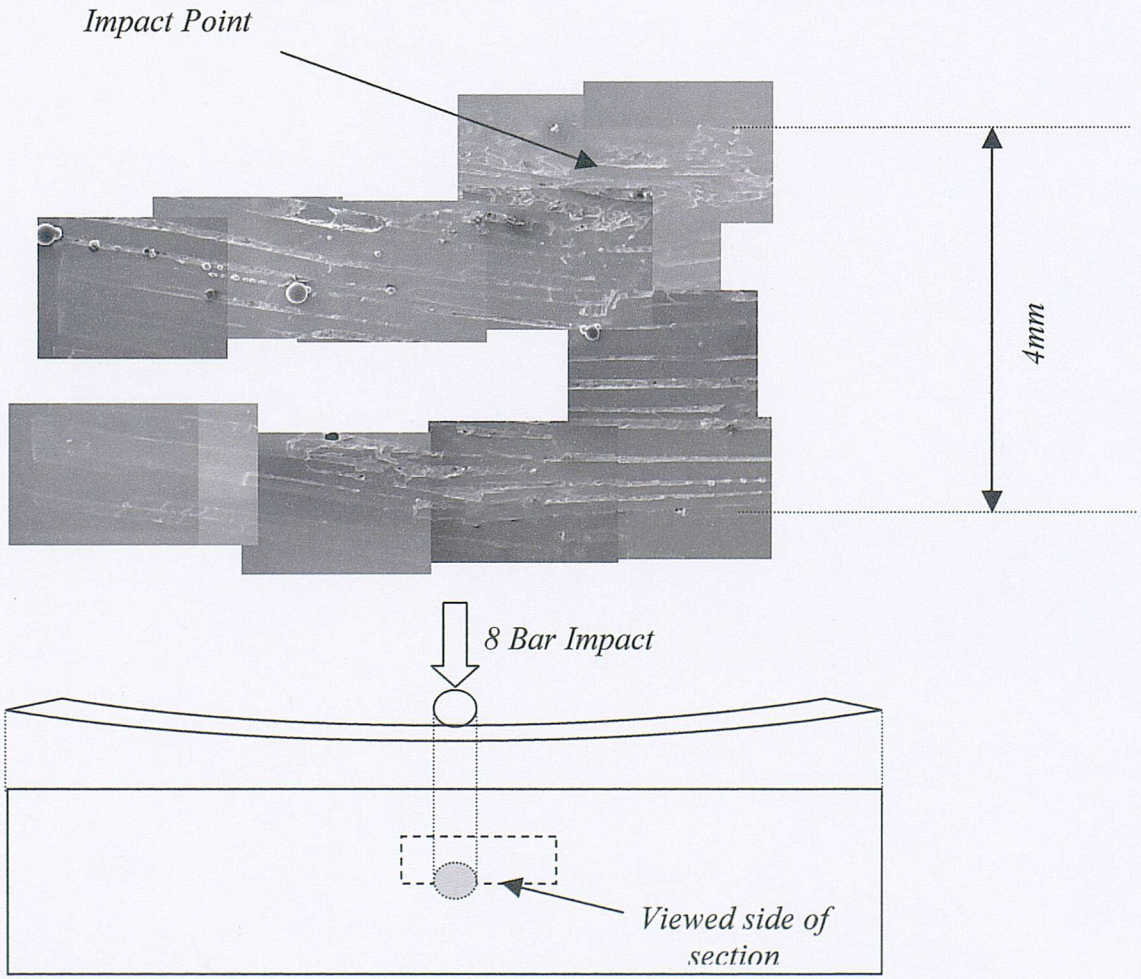


Figure 4.35: Amalgam of Micrographs for Specimen LC18 (Longitudinal Curvature with Concave Impact Face at 8 bar firing pressure).

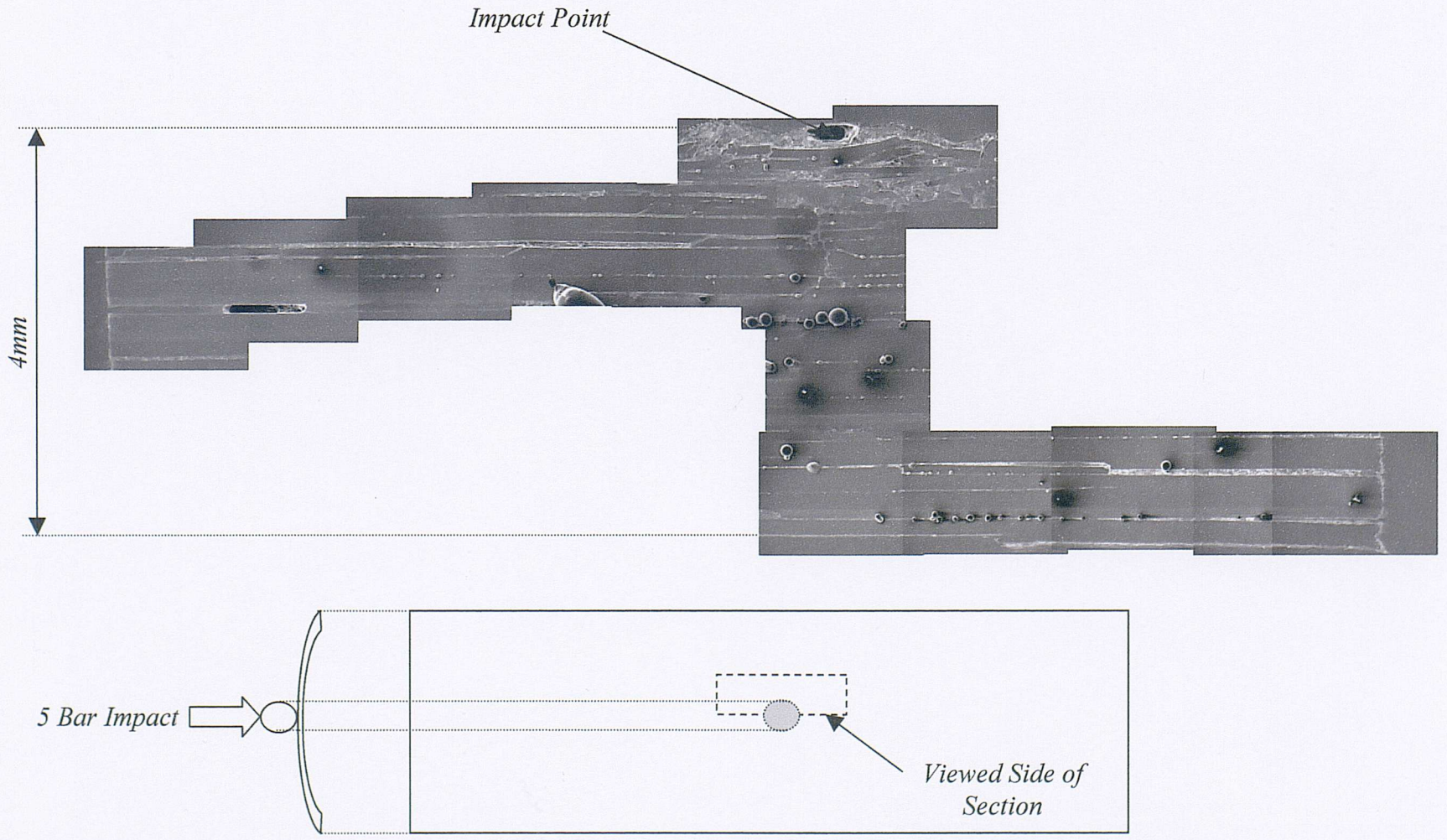


Figure 4.36: Amalgam of Micrographs for Specimen TC6 (Transverse Curvature with Convex Impact Face at 5 bar firing pressure).

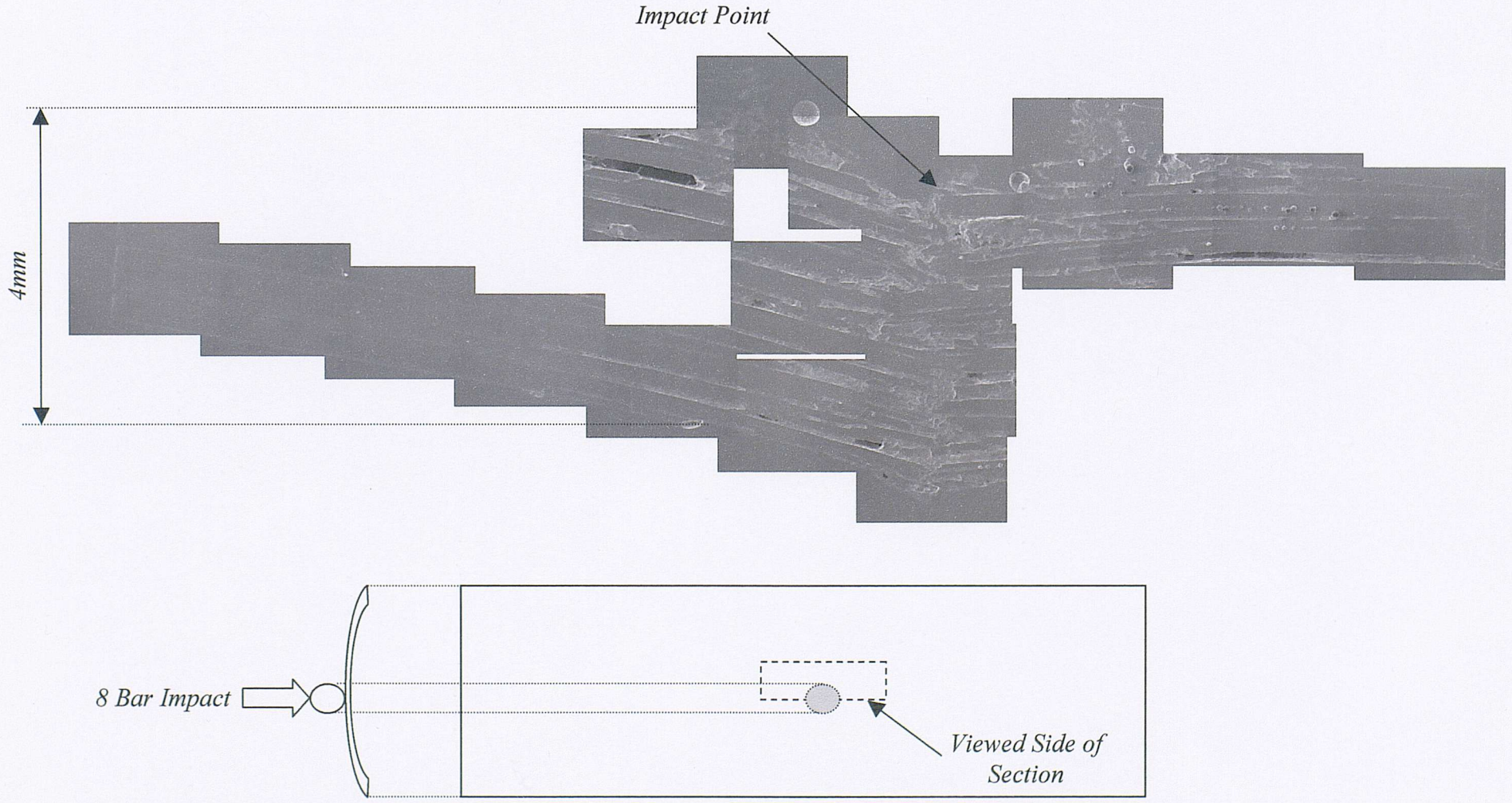


Figure 4.37: Amalgam of Micrographs for Specimen TC11 (Transverse Curvature with Convex Impact Face at 8 bar firing pressure).

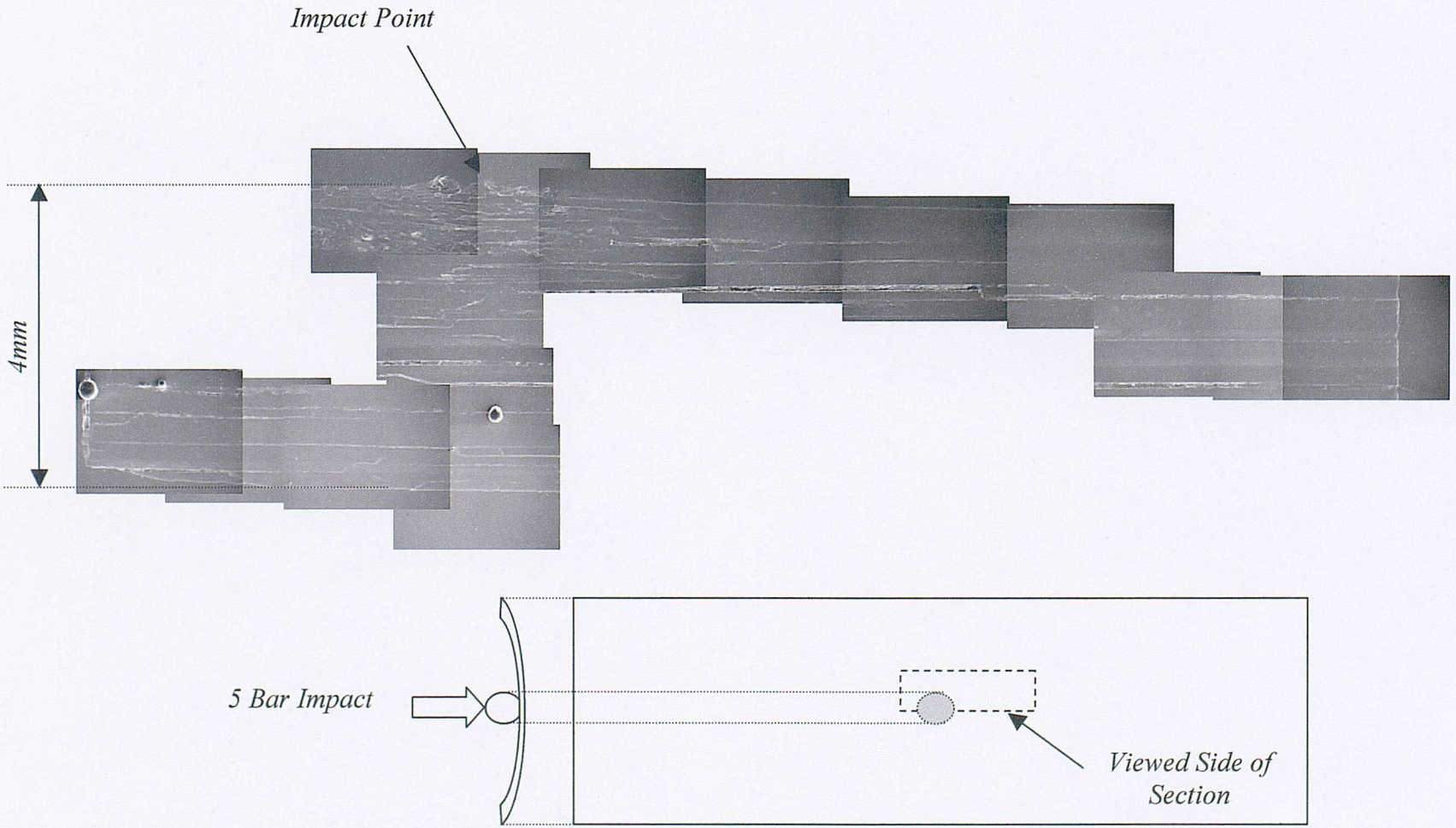


Figure 4.38: Amalgam of Micrographs for Specimen TC7 (Transverse Curvature with Concave Impact Face at 5 bar firing pressure).

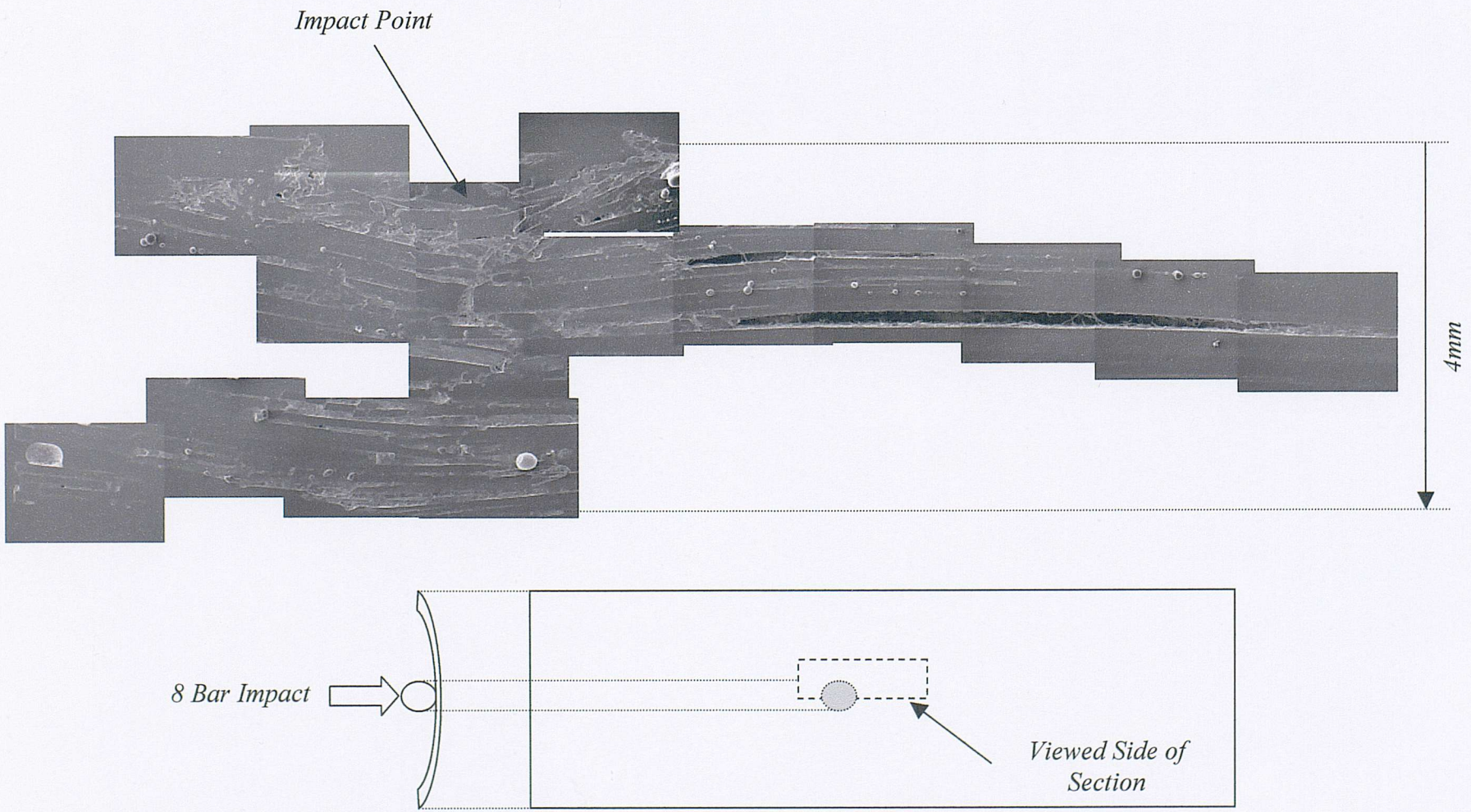


Figure 4.39: Amalgam of Micrographs for Specimen TC16 (Transverse Curvature with Convex Impact Face at 8 bar firing pressure).

All the individual micrographs are listed in Appendix 2, whilst the amalgams of the micrographs taken for each specimen are shown in *Figures 4.32 – 4.39* with details of important features highlighted.

From these figures it can be seen that at these particular impact velocities, there is enough energy involved to be able to break the surface of the impacted face and cause extensive damage immediately below the surface. The indentation seems to be caused by the breaking of the surface layer at either side of the projectile and then the compaction of the layers immediately under the impact site. This can be seen by the relatively unbroken ply being driven into the specimen and the crushed plies on either side. The layers immediately below the impact points contain a lot of crushed layers, this can be seen from the high density of matrix cracking and delaminations and broken layers compacted together (see *Figure 4.40*). Now looking in the this area and comparing the actual impact sites between the different firing pressures, the actual level of initial contact damage, in terms of the indent caused, it can be seen that with a firing pressure of 5 bar impacts the actual indent is only very slight, whilst at 8 Bar firing pressure impacts the indent is a lot more significant. This comparison is shown in *Figure 4.41* where the impact sites of the longitudinal curvature with a concave front face specimens are shown.

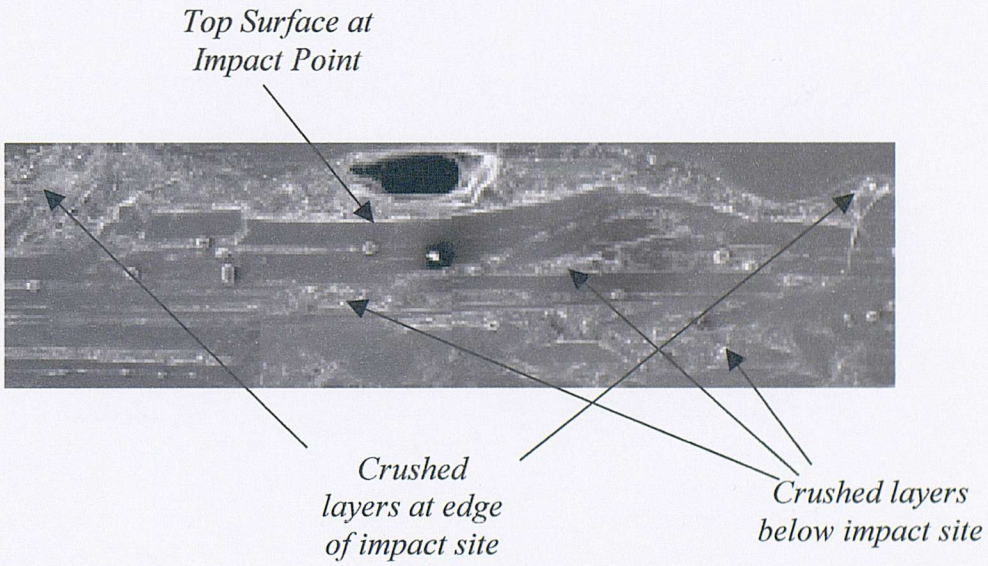


Figure 4.30: Impact site of Specimen TC6 showing damage at the impact site and it's immediate surroundings

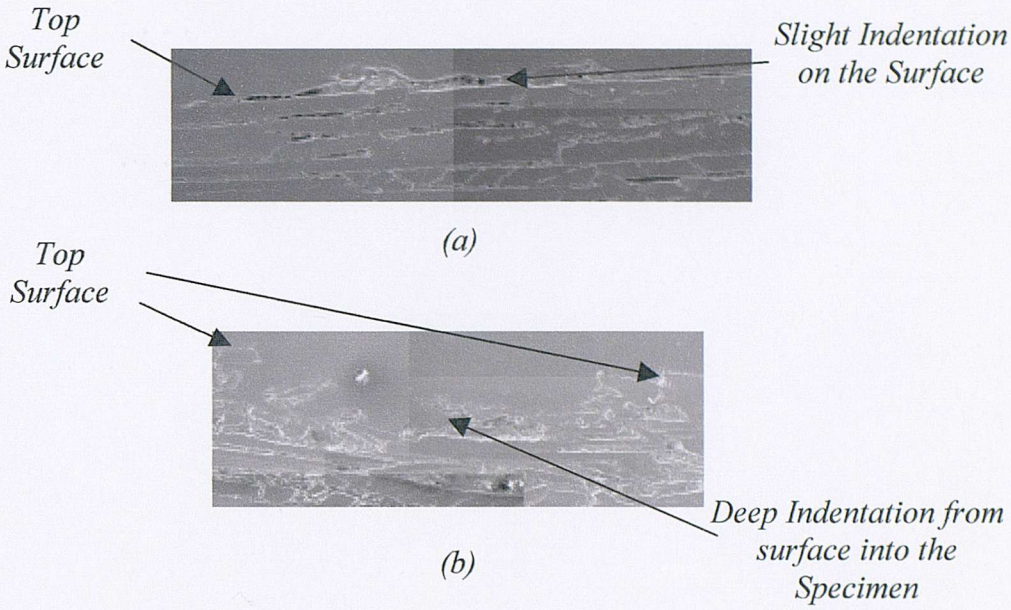


Figure 4.41: A comparison of the difference in depth of initial indent caused by a 5 and 8 Bar firing pressure impact: (a) 5 Bar Impact; (b) 8 Bar Impact.

A comparison of the difference in depth of this crushed impact area between a typical 5 bar and 8 bar firing pressure impact is shown in *Figure 4.43*. It can be seen that the increase in impact energy due to this increase in impact pressure causes a large increases in the level of penetration and crushing caused by the projectile. With the 8 bar impacts (velocity ca. 190 m/s) this crushing behaviour can be seen to extend to at least half of the way through the thickness of the specimen compared to only the top surface layers being effected in the 5 bar impact.

Looking at this crushed area more closely and comparing the different impact conditions it can be seen that the orientation with the greatest crushed area in both the 5 Bar and 8 Bar impacts was the transverse curvature with a convex front face. In the case of the 8 Bar impact in this orientation this zone actually reaches the back face, as can be seen in *Figure 4.43*.

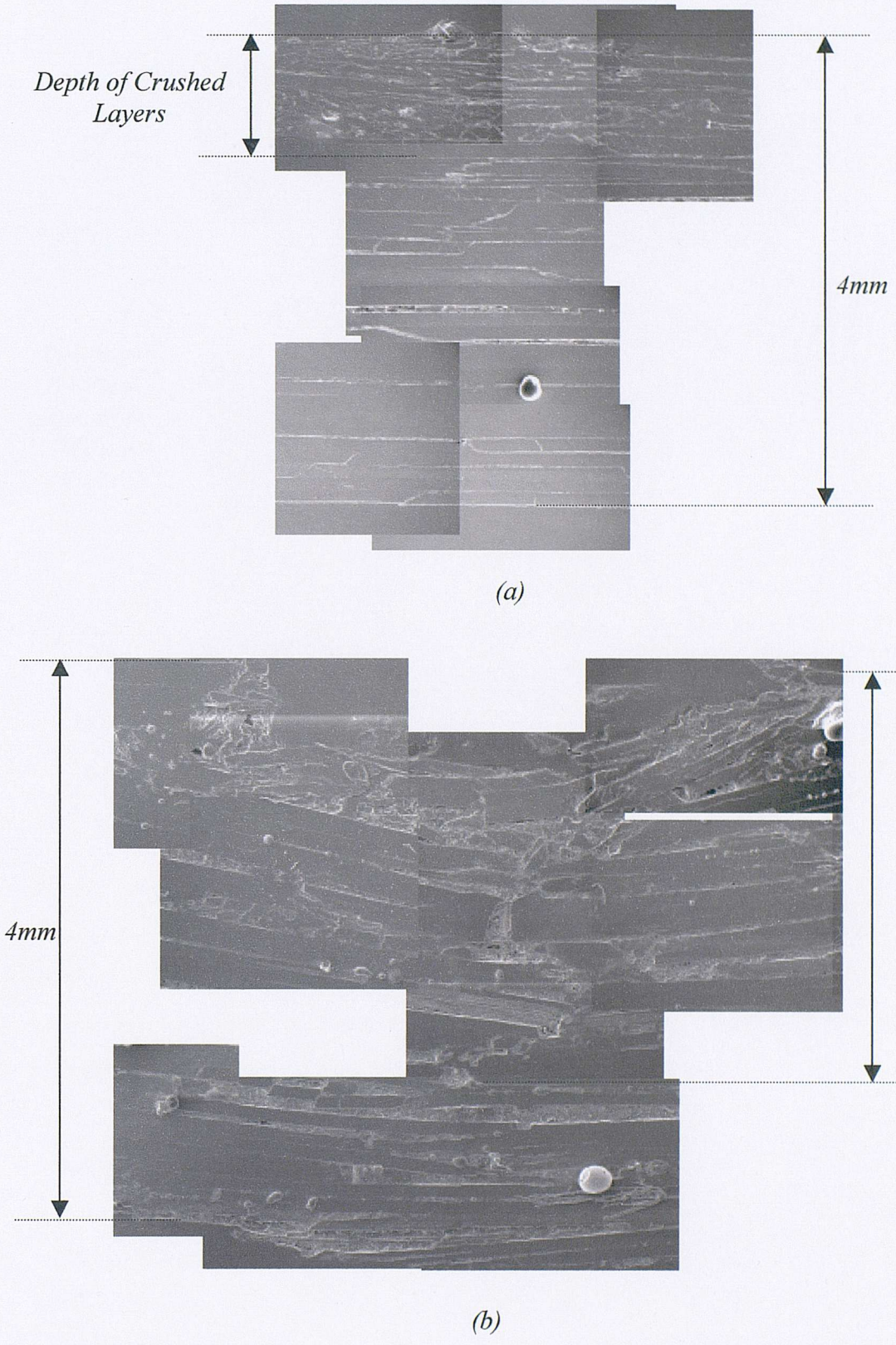


Figure 4.42: Impact areas for Specimens TC7 (a) and TC16 (b) showing the increase in depth of the crushed area directly under the impact site.

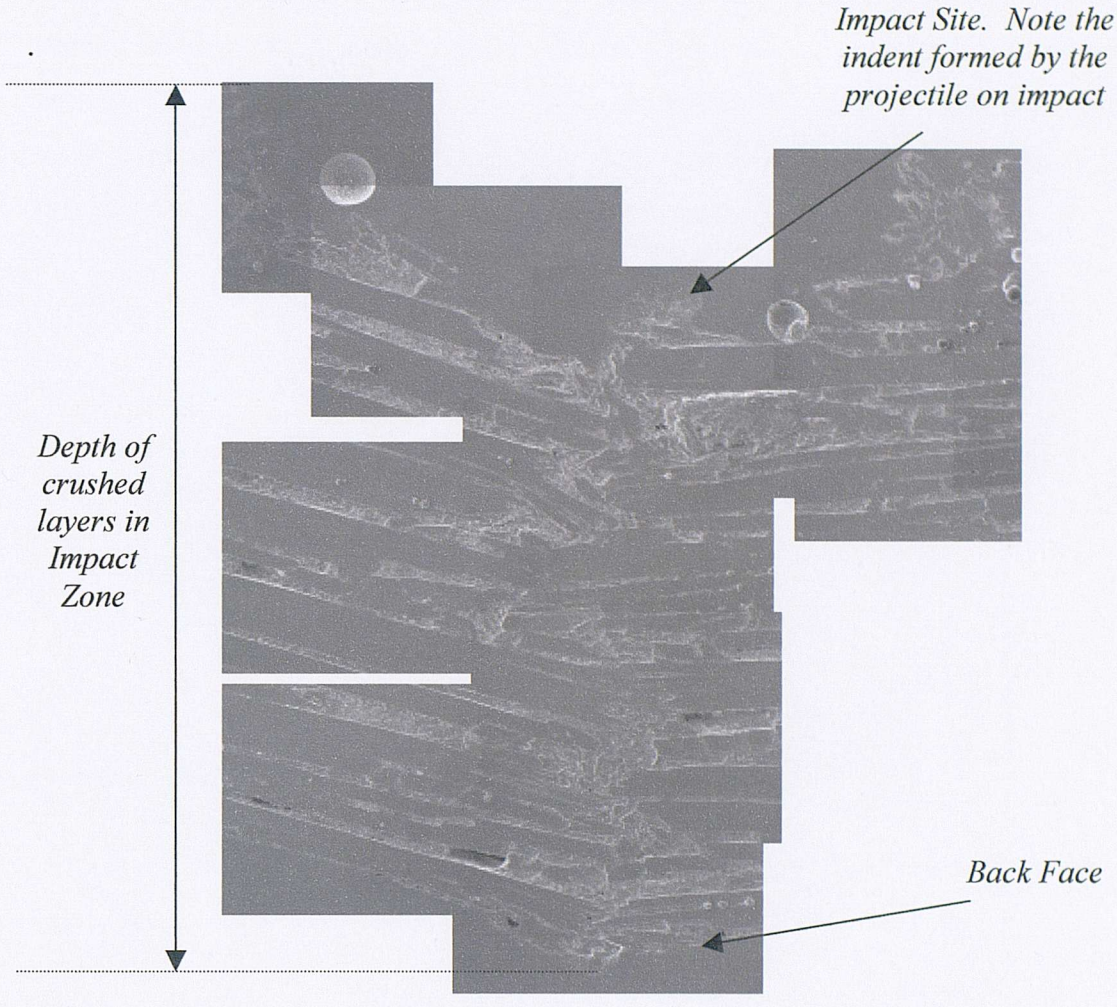


Figure 4.43: The central impact zone from Specimen TC6, Transverse curvature impacted on the convex face at 8 bar firing pressure. The Impact zone can be seen to run all the way through the specimen thickness and reach the back face of the specimen. Also shows how the delamination damage in the specimen originates from this impact zone.

Many delaminations can also be seen to originate from this central crushed area (see *Figure 4.43*). The largest of these delaminations tend to reach all the way to the edge of the specimen. These delaminations can also be seen to initiate matrix cracking and particularly as the delaminations approach the edge of the specimen. This phenomenon either arrests the delamination growth or produces further delaminations in the adjacent ply interfaces.

When looking at the rear surface of the specimen, it can be seen that there is damage present in the form of matrix cracks. At the higher firing pressure of 8 bar (impact velocity 190 m/s), back face spalling can also be observed. This was either in the case where sections of the rear plies had been fully removed from the specimen or where they have become partially detached, as shown in *Figure 4.44*.

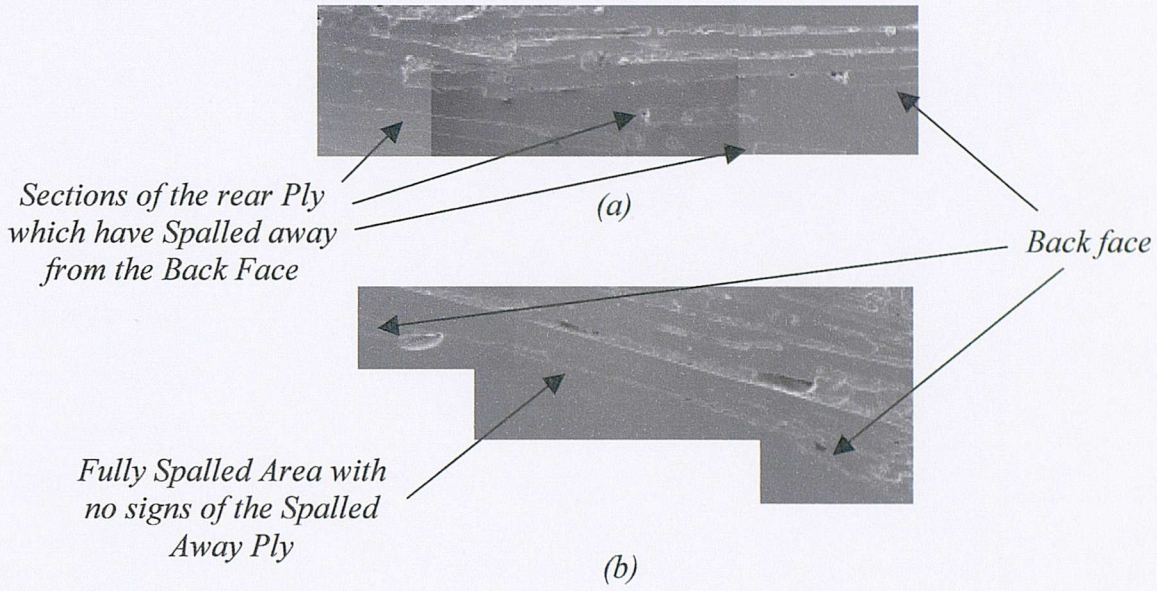


Figure 4.44: Sections of micrographs taken from 8 Bar Firing Pressure Impacts of Specimens TC11 and LC18 showing the two different types of back face spalling, (b) Partial Spalling when the spalled ply is still attached to the specimen; (a) Fully Spalled where the spalled ply has come fully apart from the specimen

The patterns of damage indicate that both typical pine tree and reverse pine tree damage patterns are in evidence. Pine tree damage formation originating from compression failure of the layers directly below the impact point and the reverse pine tree damage formation being initiated from the tension failure of the rear-face of the specimen.

From the amalgamated SEM micrographs an estimates of the actual indentation caused by the impacts can be taken. Using these indentation estimations and Hertz Theory the actual contact forces for each impact can be calculated. Using *Equations 2.2, 2.3, 2.7* and *2.8* (Johnson 1985) and required material properties shown of both

the impactor the composite shown in *Table 4.8* the values in *Table 4.9* were calculated.

	E (GPa)	*v*	***R (mm)***
Impactor (Steel)	210	0.29	3
Composite (CFRP)	140	0.3	

Table 4.8: Material Properties for the Impactor and Composite for Hertzian Analysis

Specimen	**LC6**	**LC11**	**LC15**	**LC18**	**TC6**	**TC11**	**TC7**	**TC16**
Impact Velocity (m/s)	143	188	153	188	164	186	161	189
Indentation (mm)	0.073	0.4	0.18	0.36	0.036	1.31	0.073	0.65
Contact Force (N)	148.8	1909.1	576.3	1630.0	51.6	11314.7	148.8	3954.6

Table 4.9: Indentaion measurements and calculated Contact Forces.

These contact force values show that the higher impact velocity cause a higher level of contact force. Contact force is greater in the concave orientations and when the curvature is in the transverse direction and this is due to the different curvatures and orientations affecting the level of indentation that is allowed to occur. This clearly shows that the orientation and the direction of the present curvature have a great effect on the level of contact force that occurs in a curved specimen.

4.4 Discussion

Using the high speed photography sequences and measuring an estimation of the level of deflection that occurs during the impact event, elastic strain energy was calculated. The figures show that the elastic strain energy is only a small proportion of the actual

projectiles incoming impact energy. Therefore showing that the energy that can absorbed through the deflection of the specimen is only very small.

Initially from the high speed sequences and the X-Radiographs a general picture of how the level of damage incurred was affected by the orientation of curvature and the conditions of the impact event. These initial observations from the X-radiographs and post impact images indicate that damage intensity in the specimens tested is in the following order:

1) Longitudinal Curvature with a convex front-face,
2) Transverse Curvature with a convex front-face,
3) Transverse Curvature with a concave front-face,
4) Longitudinal Curvature with a concave front-face.

An increase in firing pressure giving an increase of impact velocity from 150 m/s to 190 m/s increases the amount of damage that a specimen orientation incurs.

The indications are that there is not a simple relationship between the energy absorbed in flexing the target specimen and the energy consumed by the damage processes. Much depends upon the structure of the composite, its dimensions and the toughness of its fibre components, the host material and the bonding of all these together. Not to be overlooked is that as damage occurs and where so the flexure and dynamic response of the material appropriately changes. However, the ability of the specimen to flex clearly has a notable effect on the pattern of damage that is inflicted. This is evident as the longitudinally curved specimen with its convex side at the front (the most highly damaged orientation), has less ability to flex due to the constraints of the support arrangement. Without flexure as an energy absorption and dissipation mode, the impact energy can only be dissipated through the formation of damage. In comparison the least damaged orientation, longitudinal curvature with a concave front-face, has the most ability to flex, as the support arrangement allows the specimen greater freedom to deform so absorbing energy.

The damage can also be seen to grow in the direction of the curvature. This can be seen by the increase in damage for each orientation for an impact velocity 150 m/s (5 bar impact) to an impact velocity 190 m/s (8 bar impact). As expected the damage in this jump increases, but the damage area increases in the longitudinal direction in the specimens with a longitudinal curvature and in the transverse direction in the specimens with a transverse curvature.

As all the specimens show the ability to deform in flexure, damage initiation (i.e. first initial matrix crack) should form on the rear face and grow in a reverse pine tree formation as reported (Abrate 1998, Matthews and Rawlings 1994). This is reinforced by the first evidence of delamination, from side views of the specimens, in all specimens being towards the centre. However, if this was the case, further delamintions should occur towards the front face of the specimen, but in these cases the subsequent delaminations evidence at the sides of the specimen occur towards the back. This could be due to the effects of the impactor and the flexure of the specimen causing the existing internal delaminations at the back of the specimen to grow. However, the extent of the overall damage cannot be determined by X-Radiography alone, and a complete picture of the damage development cannot be determined.

Therefore, the specimens were subjected to the sectioning and electron microscopy study in order to develop a clearer picture of how the damage looks through the thickness of the specimen.

The micrographs that were taken show that damage is present throughout the thickness of the sample within the section immediately under the impact site. The most intense area of damage is, as would be expected, immediately under the impact point. The first detail that can be noticed immediately is that the change from an impact velocity of 150 to 190 m/s causes a substantial change in size of the impact zone under the impact point. At all the 150 m/s impacts, the impact zone is shallow and not much ply crushing is evident in this zone. However, when the impact velocity is increased to 190 m/s, the impact zone increases in depth significantly and lot more crushed plies are evident. The plies in the impact zone can also be seen to have 'caved in' under the impact site. The plies have broken and deformed with the

embedding projectile and produced the visible indentation. Comparing the size of the zones between the 5 bar and 8 bar impact pressures it can be seen that both the depth and width of the impact zone increases by roughly 100% in size between the two impact experimental cases (150 m/s and 190 m/s). Therefore, it can be shown that the increase in impact energy between the two pressures used can cause a large change in the level of damage caused in the impact zone.

Using the micrographs and estimating the size of the indentation that occurs due to the performed impacts contact forces were calculated. The figures calculated show that contact forces are higher in specimens with the curvature in the transverse direction and when the curvature is in the concave orientation. This suggests that the more compliable the orientation and curvature direction the higher the contact force that occurs during the impact.

When examining the pattern of damage more closely it can be seen that if the immediate intense crushed area is overlooked and the area immediately below this is studied. It can be seen that matrix-cracking patterns indicate that the initiation of damage here is caused by compression failure in this zone. However, when the rear face is viewed, the matrix cracking suggests that the damage is initiated from tension failure. Therefore, with both types of initiation present it can be suggested that the behaviour of the sample in reaction to the impact events under these conditions causes damage to initiate from both compression and tension failure on both sides for the specimen. The level of flexure that happens in these impacts show that tension failure is very likely to have initiated damage, whilst at the same time the indentation and crushed layers at the impact site also suggest compression failure initiation at the impact site.

Now looking at the impact zone in closer detail it can be seen that this area not only contains huge amounts of crushed composite, it is an area which initiates many of the delaminations that grow and lead to further damage initiation away from the impact site. The largest delaminations can also be seen to be around the centre of the thickness of the specimen. These delaminations do seem to be initiated around the impact site, however when looking at the 'largest' delamination and comparing it for

the two different impact velocities, the delaminations in the specimens impacted at 150 m/s are initiated slightly below the impact zone whilst the ones in the specimens impacted at 190 m/s are initiated earlier in the impact zone. However, both these location seem to be roughly near the centre line of the specimen thickness.

With this in mind and the previous point of the possibility of both compression failure and tension failure initiating the damage pattern it seems that the nature of these impacts and the response of the specimen causes simultaneous damage initiation under the impact point and at the rear face. Both these sites initiate damage in their corresponding pine tree and reverse pine tree formations respectively, and these damage patterns progress towards the centre of the specimen where they both coalesce and hence cause the largest delamination to occur around the central region of the specimen.

When comparing this theory with the high-speed photographic sequences, which show delaminations near the thickness centre line and then delaminations occur towards the rear face as the impact event progresses, there is little evidence of delaminations at the front face. This seems to show that after the two damage formations merge; the pine tree formation caused by the compression failure initiation from the impact point takes over and becomes the dominant damage progression path. Therefore, it can be said that although both textbook damage progression paths are evident, the more dominant one, under these condition, seems to be the pine tree formation. This could be due to the change in shape of the specimen, due to the increasing flexure of the specimen, as part of the impact event. If the damage follows the curvature of the specimen, as assumed above, then it follows on that the change in shape caused by the flexure and the relaxation from flexure arrests the tension initiated damage progression travelling from the back face. This damage progressing from the back face encounters an easier progression path when the specimen is in flexure, when the curvature promotes damage progression travelling in this direction. However when the specimen relaxes the specimen returns to a shape that encourages damage to progress from the front face and hence damage from the front face carries on towards the back face, and the damage in the other direction arrests.

This shows that although the flexure of the specimen absorbs only a small amount of the impact energy, damage development is a much the dominant form of energy absorption. Therefore although the elastic strain energy calculations

Firstly it can be seen that in this case, as with most cases, several damage investigation methods are required in order to get a comprehensive understanding of the damage that accumulates within a composite laminate due an impact event. It is also necessary to view the specimen using the destructive microscopy technique in order to be able to see the important matrix cracking which is required in order to be able to explain the possible sequences in which damage occurs.

5 Impact of Thin Flexible Composite Panals

After the discovery in the previous section of work that the stiffer the orientation of the curved sample the more damage occurs as a result to an impact event. This relationship between orientation and stiffness has a direct effect on the level of damage caused by an impact event due to the level of flexibility allowed. Therefore the following work was performed in order to show the importance of flexibility as an energy absorbing mechanism and impact damage limitation route.

5.1 Aims and Objectives

The main aim in this section is to show how differing levels of flexibility within a composite system affects the level of damage incurred during an impact event. It was also of importance to see how the difference in flexibility affected the behaviour of the panel, and then to see how this difference in behaviour in turn affected the level of damage that occurs due to the impact events. Therefore a series of impact tests were performed on a series of composite samples with varying levels of flexibility to show the importance of this behaviour with respect to the impact of composite materials in general. The investigation also looked at the effects of changing the flexibility of the material by changing it's constituents and by changing the samples dimensions.

5.2 Procedure

Firstly to ensure that a great enough degree of flexibility could be induced during the impact event to actually show the affect intended, thin (<1mm) composite panels were used for this investigation.

The level of flexibility within the samples was altered in two ways. Firstly the constituent material was changed. Two types of composite (see Section 3.1.2 for precise material specifications) were used, the differing factor being the types of fibre

used in the material. Both were based on a PPS matrix, one with woven carbon fibres the other with woven R-glass fibres. The difference in the fibre used in these composites gives a distinct difference in the stiffness of the panels, with the carbon fibre panel naturally having the higher stiffness than the glass fibre composite due to the difference in nature of the two types of fibres. Secondly the dimensions were changed. Two different lengths of specimen were also used which varied the flexibility as the longer the specimen the more flexible it is.

These samples were subjected to a series of Drop Weight Impact tests, in conjunction with High Speed Photography to capture the specimen reactions to the impact tests. A hemi-spherical indentor of mass 1.55kg was dropped from heights of 10, 20, 30, 40 and 50cm. The Drop Weight Tower also produced data for a Force-Time trace, which was then manipulated to produce Velocity-Time, Displacement-Time and Force-Displacement traces using a spreadsheet. This allowed for the impact event and the behaviour during the event to be understood better. After testing, the samples were subjected to Ultrasonic C-Scans to assess the level of damage caused by the impact events.

5.2.1 Experimental Details

The general details of the experimental procedures are given in Section 3.2. More precise details of the exact set-ups for this investigation will be given with reference to the general details given previously. The exact set up for the equipment for this investigation is shown in *Figure 3.9*, which shows the back lighting set-up and *Figure 3.14*, which shows the tower and the data recording equipment.

The samples were held in at either end by the clamps shown in *Figure 3.5* which were in turn held in the main clamping unit shown in *Figure 3.3*. The removable plate and the front most plate in the main unit were not used, this was to allow the drop weight indentor a free a path as possible to the actual specimen. The main clamp was in turn clamped tightly onto the main frame work of the drop weight tower using two large G-Clamps. This was in order to secure the clamping unit so that it was not allowed to

move as a reaction to the impact event and hence trying to maximize the level of impact energy directly transferred to impacted sample. The indentor was held at the required height by hand and then dropped and caught as it rebounded back off the specimen.

Specimen	Fibre Type	Specimen Size (mm)	Measured Velocity (m/s)	Impact Energy (J)
CPPS1	Carbon	120x40	1.35	1.41
CPPS2	Carbon	120x40	1.25	1.21
CPPS3	Carbon	120x40	1.47	1.67
CPPS4	Carbon	120x40	1.41	1.54
GPPS1	R-Glass	120x40	1.37	1.45
GPPS2	R-Glass	120x40	1.24	1.19
GPPS3	R-Glass	120x40	1.38	1.48
GPPS4	R-Glass	120x40	1.43	1.58
1CPPS1	Carbon	160x40	1.40	1.52
1CPPS2	Carbon	160x40	1.46	1.65
1GPPS1	R-Glass	160x40	1.33	1.37
1GPPS2	R-Glass	160x40	-	-
1GPPS3	R-Glass	160x40	1.44	1.61

Note: No Values for Specimen 1GPPS2 as equipment was not triggered for this test, no images or drop weight traces available.

Calculated Velocity = 1.40 m/s Ideal Impact Energy = 1.52 J

Table 5.1: Summary of Samples and Measured Impact Velocity and Energy Values for 10cm drops on Thin Flexible Composite Samples with Ideal Calculated Values.

The same laser pen triggering system was used here to trigger the operation of the High Speed Camera. In this case a back lighting method was used as the lighting source for the camera as the delay between the breaking of the laser beam and the

actual impact event was greater than the light period emitted by the flash lamps used in the gas-gun arrangement. Therefore the images captured by the camera were the back lit shadow of the actual event. Due to the limitation of the amount of available specimens, as many samples for each condition that could be were tested (no more than 3 in most cases). All the High Speed Photography sequences and their relevant settings for this investigation are given in Appendix 3. Tables 5.1 to 5.5 give the details of the actual impact events.

Specimen	Fibre Type	Specimen Size (mm)	Measured Velocity (m/s)	Impact Energy (J)
CPPS5	Carbon	120x40	1.85	2.65
CPPS6	Carbon	120x40	1.95	2.95
CPPS&	Carbon	120x40	1.97	3.01
GPPS5	R-Glass	120x40	1.92	2.86
GPPS6	R-Glass	120x40	1.93	2.89
GPPS7	R-Glass	120x40	1.94	2.92
1CPPS3	Carbon	160x40	1.88	2.74
1CPPS4	Carbon	160x40	1.92	2.86
1CPPS5	Carbon	160x40	1.98	3.04
1GPPS4	R-Glass	160x40	1.99	3.07
1GPPS5	R-Glass	160x40	2.01	3.13
1GPPS6	R-Glass	160x40	1.87	2.71

Ideal Impact Velocity = 1.98 m/s Ideal Impact Energy = 3.04 J

Table 5.2: Summary of Samples and Measured Impact Velocity and Energy Values for 20cm drops on Thin Flexible Composite Samples with Ideal Calculated Values.

The velocities in this case were measured using the HSC images, using a frame containing the impactor and the frame showing as close to initial contact as possible, and calculated using the following equation:

$$v = \sqrt{2hG}$$

which is taken from equating standard potential and kinetic energy equations, where v is the velocity, h is the drop height and G is acceleration dues to gravity. Note that the slight variations that occur in the velocities taken from the HSC sequences are mainly due to either the initial positioning of the height of the indentor being as close to the required height on the tower as possible and the difficulties encountered trying to capture the exact impact point in one of the 8 framed images. The ideal impact energy fro each drop height was calculated using the potential energy equation, $E = mGh$, whilst energies for each test were calculated using the measured impact velocity and the kinetic energy equation, $E = 1/2\ mv^2$.

Specimen	Fibre Type	Specimen Size (mm)	Measured Velocity (m/s)	Impact Energy (J)
CPPS8	Carbon	120x40	2.40	4.46
CPPS9	Carbon	120x40	2.46	4.69
CPPS10	Carbon	120x40	2.39	4.43
GPPS8	R-Glass	120x40	2.40	4.46
GPPS9	R-Glass	120x40	2.44	4.61
GPPS10	R-Glass	120x40	2.39	4.43
1CPPS6	Carbon	160x40	2.44	4.61
1CPPS7	Carbon	160x40	2.39	4.43
1CPPS8	Carbon	160x40	2.40	4.46
1GPPS7	R-Glass	160x40	2.39	4.43
1GPPS8	R-Glass	160x40	2.45	4.84
1GPPS9	R-Glass	160x40	2.40	4.46
1GPPS10	R-Glass	160x40	2.41	4.50

Ideal Impact Velocity = 2.43 m/s Ideal Impact Energy = 4.56 J

Table 5.3: Summary of Samples and Measured Impact Velocity and Energy Values for 30cm drops on Thin Flexible Composite Samples with Ideal Calculated Values.

Specimen	Fibre Type	Specimen Size (mm)	Measured Velocity (m/s)	Impact Energy (J)
CPPS11	Carbon	120x40	2.81	6.12
CPPS12	Carbon	120x40	2.83	6.21
CPPS13	Carbon	120x40	2.79	6.03
GPPS12	R-Glass	120x40	2.78	5.99
GPPS13	R-Glass	120x40	2.80	6.08
GPPS14	R-Glass	120x40	2.83	6.21
1CPPS9	Carbon	160x40	2.75	5.86
1CPPS10	Carbon	160x40	2.81	6.12
1CPPS11	Carbon	160x40	2.79	6.03
1GPPS10	R-Glass	160x40	2.77	5.95
1GPPS11	R-Glass	160x40	2.81	6.12
1GPPS12	R-Glass	160x40	2.82	6.16
1GPPS13	R-Glass	160x40	2.77	5.95

Ideal Impact Velocity = 2.80 m/s Ideal Impact Energy = 6.08 J

Table 5.4: Summary of Samples and Measured Impact Velocity and Energy Values for 40cm drops on Thin Flexible Composite Samples with Ideal Calculated Values.

After impact the specimen were assessed for damage using ultrasonic C-Scan. This method was selected for this investigation as the low thickness of the samples resulted in a limited number of actual plies (no more than 2) being involved and a clear picture of the layer by layer delamination damage was deemed unnecessary. The C-Scan results provided a good indication of the shape and size of the damage that allowed a comparison between the different specimens and impact conditions. The C-Scan images taken for all the specimens are shown in Appendix 4.

The recorded Force-Time data was inputted into a spreadsheet and used to produce a Force-Time trace, which described the behaviour of the Force inflicted onto the specimen during the impact event. The data was then further manipulated using the

trapezium integration rule twice. The first integration produced a Velocity-Time trace showing the change in velocity of the impactor during the impact event. The second integration produces a Displacement-Time trace, this shows the amount of and change of displacement that occurs and is an indication of the level of deformation that occurs during the entire impact event. Finally using the data already produced a Force-Displacement trace was produced fro which the relationship between the force applied and the amount of displacement that occurs can be seen and in addition stiffness properties can also be assessed.

Specimen	Fibre Type	Specimen Size (mm)	Measured Velocity (m/s)	Impact Energy (J)
CPPS14	Carbon	120x40	3.12	7.54
CPPS15	Carbon	120x40	3.16	7.74
CPPS16	Carbon	120x40	3.10	7.45
GPPS14	R-Glass	120x40	3.14	7.60
GPPS15	R-Glass	120x40	3.09	7.40
GPPS16	R-Glass	120x40	3.17	7.79
1CPPS12	Carbon	160x40	3.11	7.50
1CPPS13	Carbon	160x40	3.14	7.60
1CPPS14	Carbon	160x40	3.16	7.74
1GPPS14	R-Glass	160x40	3.11	7.50
1GPPS15	R-Glass	160x40	3.12	7.54
1GPPS16	R-Glass	160x40	3.19	7.89
1GPPS17	R-Glass	160x40	3.12	7.54

Ideal Impact Velocity = 3.14 m/s Ideal Impact Energy = 7.60 J

Table 5.5: Summary of Samples and Measured Impact Velocity and Energy Values for 50cm drops on Thin Flexible Composite Samples with Ideal Calculated Values.

5.3 Results

The results obtained from this section of work will be presented in this section. As with the previous study the amount of data produced is high, therefore representative data for each impact condition will be presented and then discussed. At the start of each set of results a general example will be shown first, with the areas of importance highlighted. These will then be followed by the representative results with details of interest highlighted for further discussion.

5.3.1 High Speed Photography

As with the previous investigation it is necessary to firstly highlight some of the more prominent features, which in turn are the ones of most interest in the analysis of the results of this section, of the impact event that the High Speed Photography sequences can capture. *Figure 5.1* shows a typical frame from one of the recorded sequences. This particular frame is pre impact and shows the incoming projectile and the thin laminate clamped within the main clamping unit. The end clamping units can also be seen in this image, however in the case of the sequences for the longer specimens this is not the case as they are just out of the viewing plane of the camera.

Figure 5.2 shows another typical frame from one of the high speed sequences, this time it is one that is post-contact and shows the specimen deforming as a consequence of the impact event. It is this deformation and the change in the amount of deflection due to the degree of flexibility that is allowed that is of interest in this study.

Not only was the response of the specimen looked at but also the level of deformation. The measurement used to ascertain the level of deformation was the actual distance away from the resting level of the specimen that that the peak of the bowed area of the specimen reaches. This was measured using the built in software on the High Speed Camera by using two frames from the sequence, one with the specimen at rest and the other as close to the peak of the specimen bowing as possible. This is a very rough estimate as it is impossible to be certain if the second frame used for this

measurement was actually the peak point. However this measured value will be compared to the peak displacement values that will be obtained from the analysis of the Force-Time data obtained from the drop weight tower set-up.

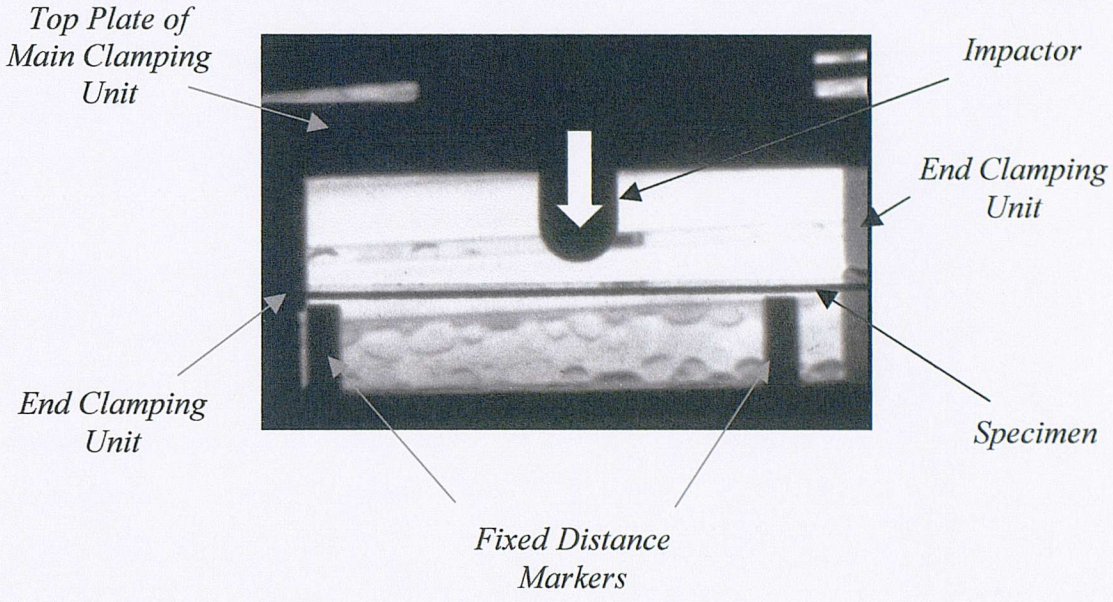


Figure 5.1: A typical pre-impact frame from a High Speed Sequence for the impact of a thin flexible laminate.

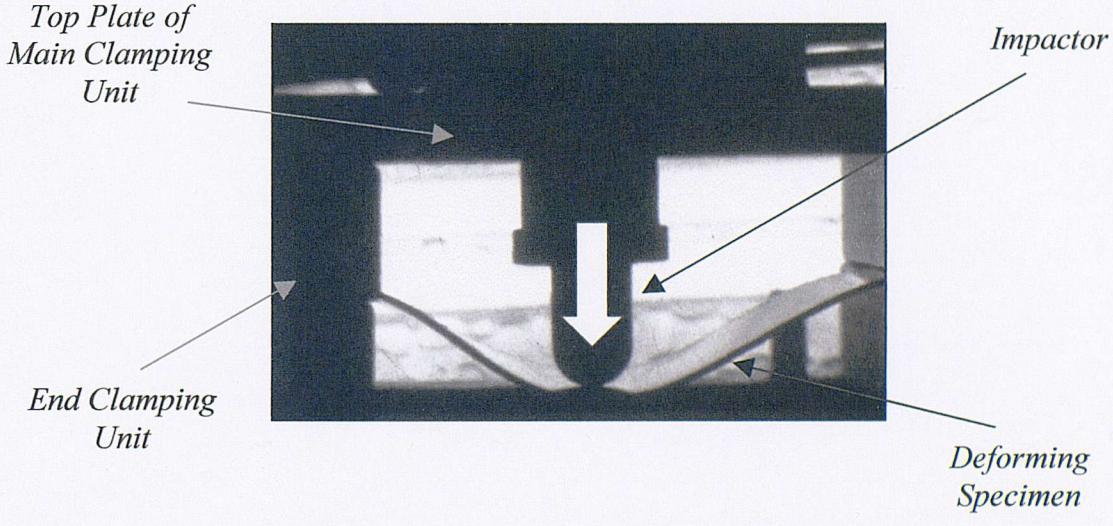
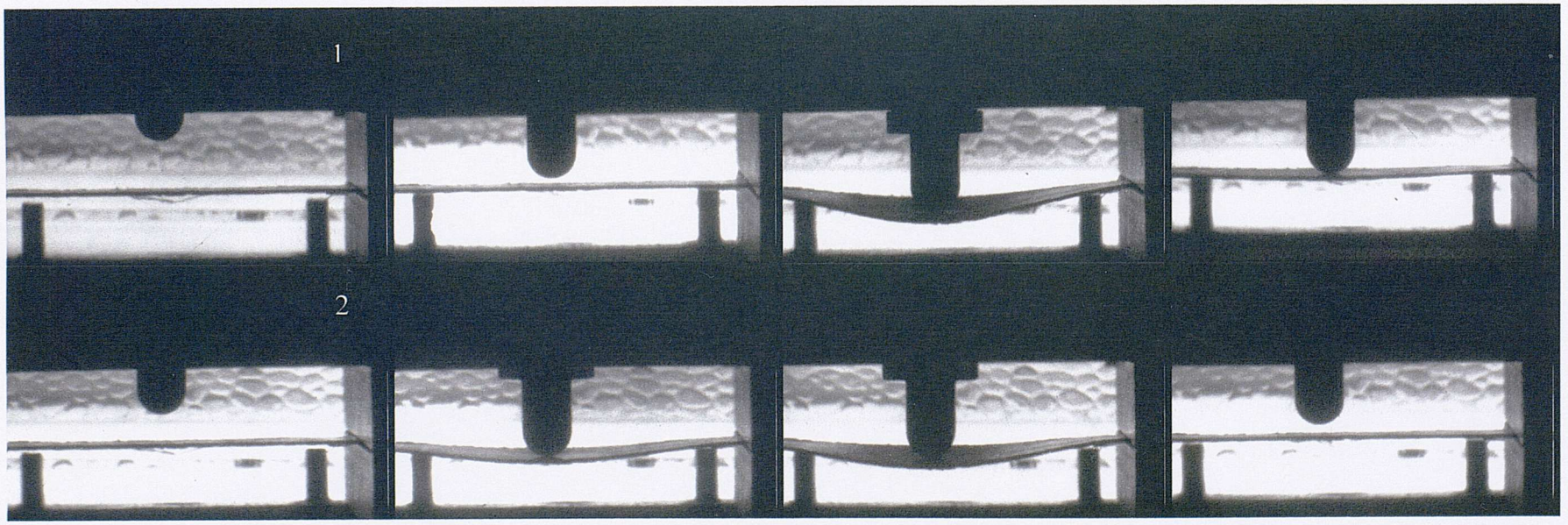


Figure 5.2: A typical post impact frame from the High Speed sequence showing the deforming thin flexible panel

Figures 5.3 to 5.12 show High Speed Photography sequences for all the impacts performed on the shorter specimens with dimensions of 120mm x 40mm. There is one sequence shown for each material at each different drop height. *Figure 5.3-5.7* being sequences for the Carbon Fibre Specimens and *Figures 5.8-5.12* being the ones for the R-Glass Fibre specimens. Also included are the camera settings for image capturing and the measured estimate of the maximum displacement of the specimen as well as the actual frames used for that particular measurement. Note each frame number is given in the top right hand corner of the said frame.

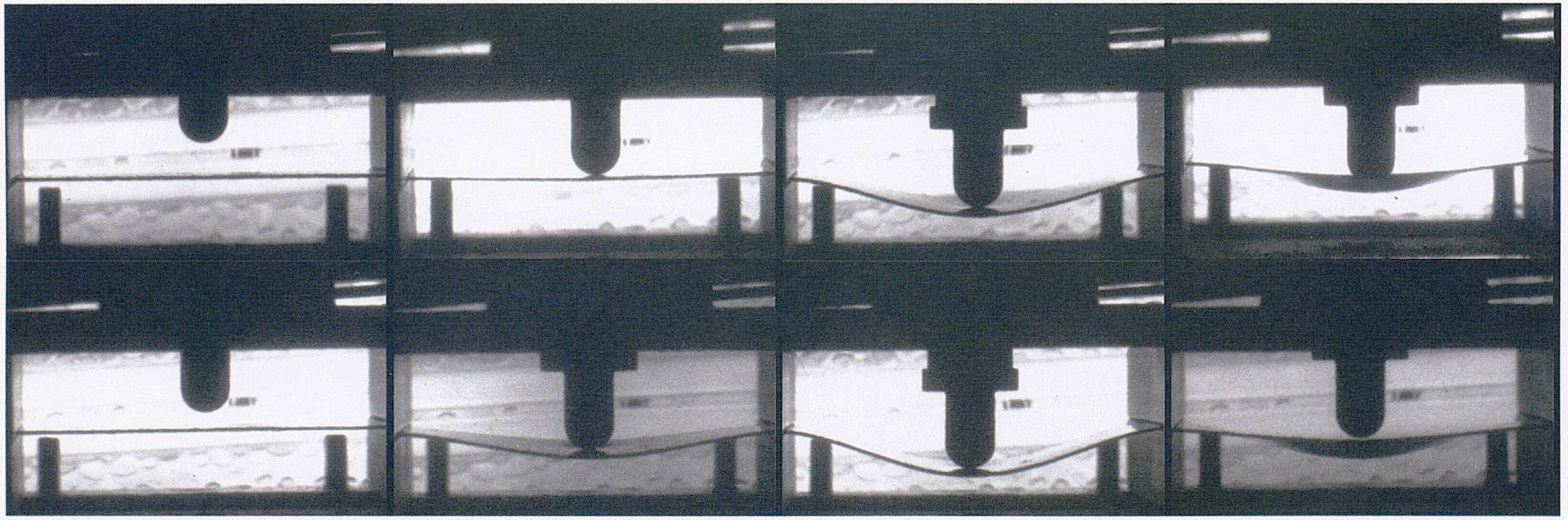
Now when looking at this set of sequences it can be seen that the specimens are thin and flexible enough to deform in order to absorb the incoming impact energy, even at the lowest drop height of 0.1m. As the drop height is increased the level of this deformation increases. At the lower drop heights the specimen relaxes after the impact event and returns back to it's original position. However it seems that there is a point where the deformation caused is so great that the stored elastic energy within the sample cannot return the specimen back to it's original position and the specimen remains deformed within the clamping arrangement after the impact event (see *Figures 5.6, 5.11 and 5.12*). However when these samples were released from the clamping arrangement they relaxed further and returned to being a flat specimen.



Frame No.	1	2	3	4	5	6	7	8
Frame Setting (mS)	40	45	50	55	60	65	70	75
Exposure Time (μS)	150	150	150	150	150	150	150	150

Drop Height:	*0.1m*	*Projectile:*	*1.55kg Hemi-spherical Indentor*
Ideal Impact Velocity:	*1.4m/s*	*Ideal Impact Energy:*	*1.52J*
Measured Impact Velocity:	*1.35m/s*	*Calculated Impact Energy:*	*1.41J*
Maximum Displacement:	*2.95mm*	*Frames Used:*	*1 and 5*

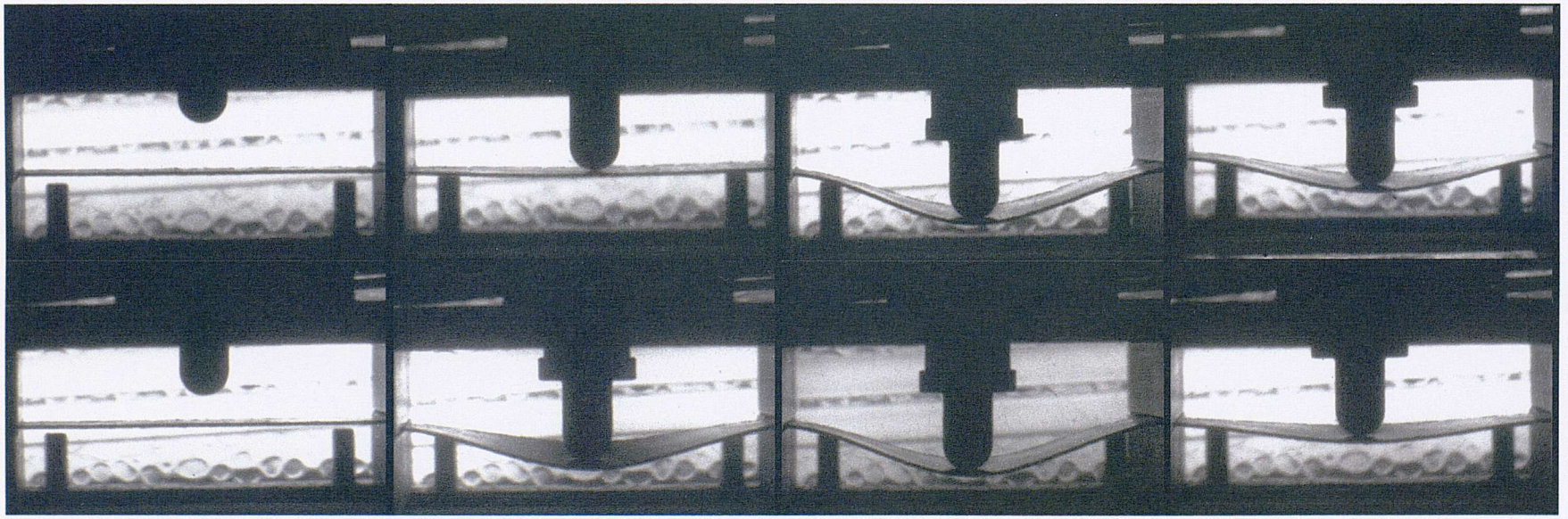
Figure 5.3: High Speed Photography Sequence for Specimen CPPS1, 0.1m Drop on a 120mm x 40mm Carbon Fibre Flexible Specimen



Frame No.	1	2	3	4	5	6	7	8
Frame Setting (mS)	25	27.5	30	32.5	35	40	47.5	52.5
Exposure Time (μS)	150	150	150	150	150	150	150	150

Drop Height:	*0.2m*	*Projectile:*	*1.55kg Hemi-spherical Indentor*
Ideal Impact Velocity:	*1.98m/s*	*Ideal Impact Energy:*	*3.04J*
Measured Impact Velocity:	*1.97m/s*	*Calculated Impact Energy:*	*3.01J*
Maximum Displacement:	*4.65mm*	*Frames Used:*	*1 and 5*

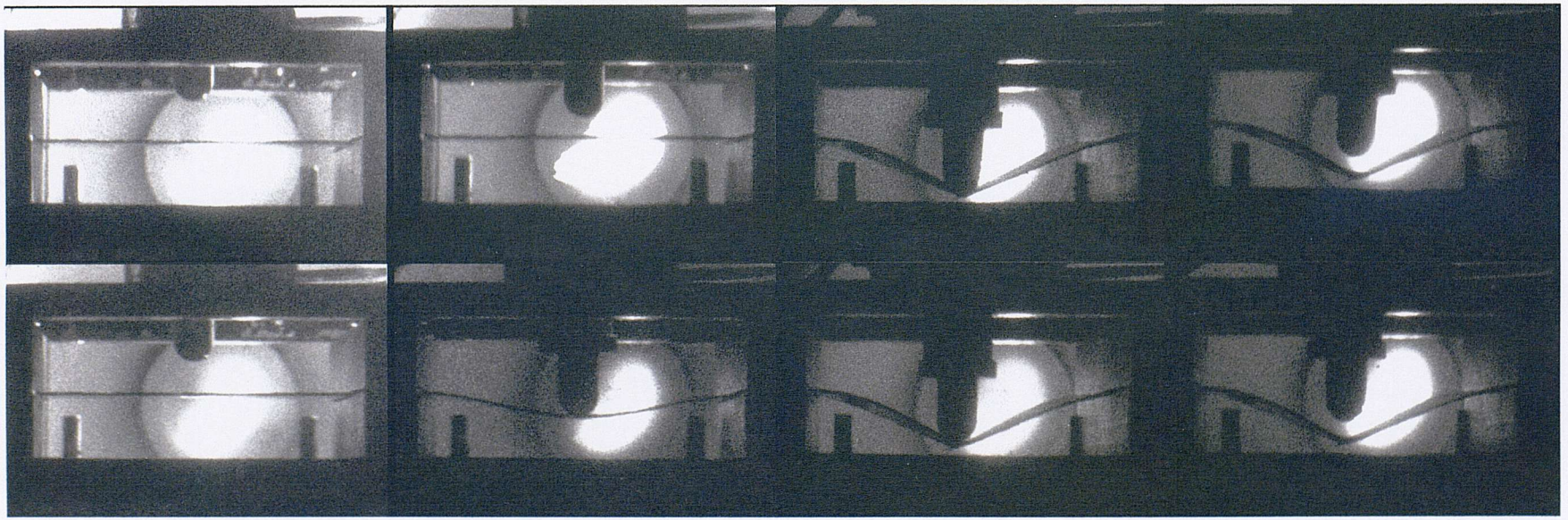
Figure 5.4: High Speed Photography Sequence for Specimen CPPS7, 0.2m Drop on a 120mm x 40mm Carbon Fibre Flexible Specimen



Frame No.	1	2	3	4	5	6	7	8
Frame Setting (mS)	20	22.5	26	30	35	37.5	45	50
Exposure Time (μS)	150	150	150	150	150	150	150	150

Drop Height:	*0.3m*	*Projectile:*	*1.55kg Hemi-spherical Indentor*
Ideal Impact Velocity:	*2.43m/s*	*Ideal Impact Energy:*	*4.56J*
Measured Impact Velocity:	*2.46m/s*	*Calculated Impact Energy:*	*4.69J*
Maximum Displacement:	*4.34mm*	*Frames Used:*	*1 and 5*

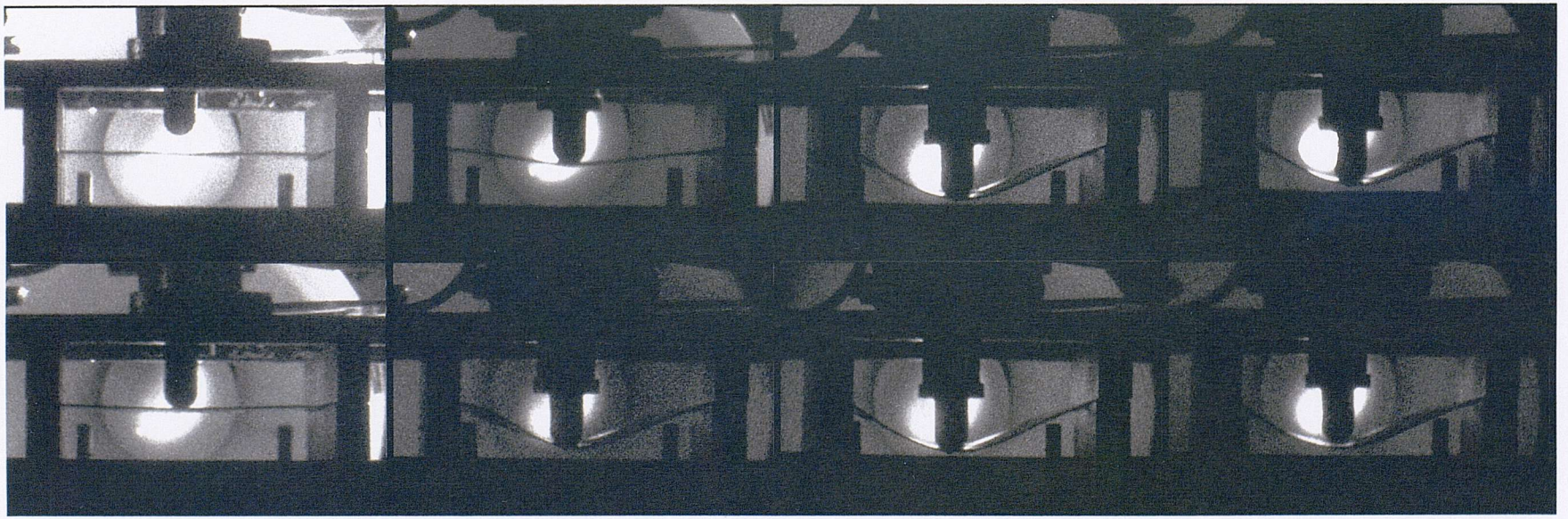
Figure 5.5: High Speed Photography Sequence for Specimen CPPS9, 0.3m Drop on a 120mm x 40mm Carbon Fibre Flexible Specimen



Frame No.	1	2	3	4	5	6	7	8
Frame Setting (mS)	10	11	12.5	17.5	25	30	52.5	55
Exposure Time (μS)	6	6	6	6	6	6	6	6

Drop Height:	*0.4m*	*Projectile:*	*1.55kg Hemi-spherical Indentor*
Ideal Impact Velocity:	*2.80m/s*	*Ideal Impact Energy:*	*6.08J*
Measured Impact Velocity:	*2.79m/s*	*Calculated Impact Energy:*	*6.03J*
Maximum Displacement:	*6.95mm*	*Frames Used:*	*1 and 6*

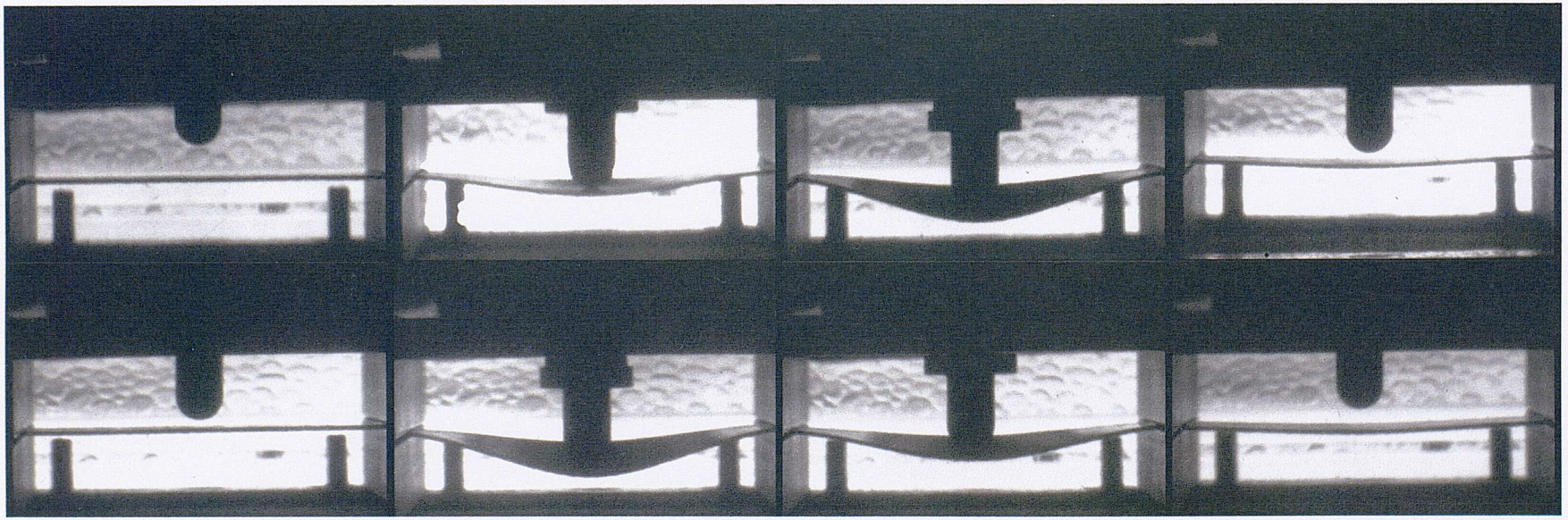
Figure 5.6: High Speed Photography Sequence for Specimen CPPS13, 0.4m Drop on a 120mm x 40mm Carbon Fibre Flexible Specimen



Frame No.	1	2	3	4	5	6	7	8
Frame Setting (mS)	6	8.5	10	15	18	19	20	27.5
Exposure Time (μS)	6	6	6	6	6	6	6	6

Drop Height:	*0.5m*	*Projectile:*	*1.55kg Hemi-spherical Indentor*
Ideal Impact Velocity:	*3.14m/s*	*Ideal Impact Energy:*	*7.60J*
Measured Impact Velocity:	*3.10m/s*	*Calculated Impact Energy:*	*7.45J*
Maximum Displacement:	*6.29mm*	*Frames Used:*	*1 and 6*

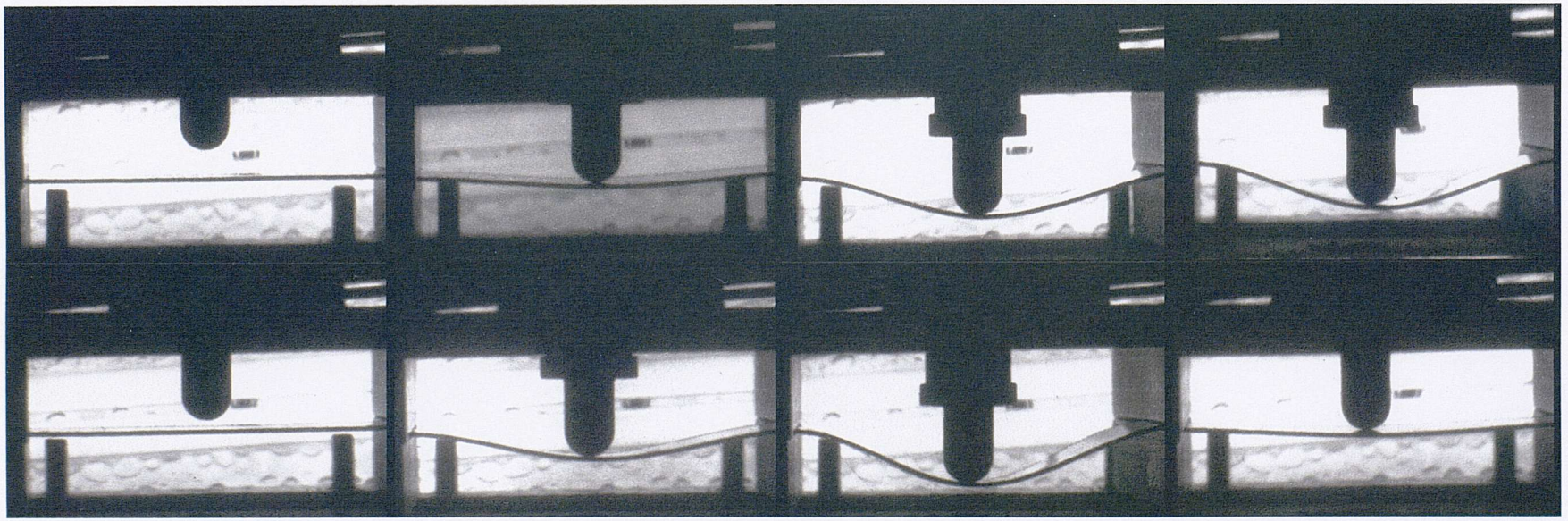
Figure 5.7: High Speed Photography Sequence for Specimen CPPS16, 0.5m Drop on a 120mm x 40mm Carbon Fibre Flexible Specimen



Frame No.	1	2	3	4	5	6	7	8
Frame Setting (mS)	40	45	50	55	60	65	75	80
Exposure Time (μS)	150	150	150	150	150	150	150	150

Drop Height:	*0.1m*	*Projectile:*	*1.55kg Hemi-spherical Indentor*
Ideal Impact Velocity:	*1.4m/s*	*Ideal Impact Energy:*	*1.52J*
Measured Impact Velocity:	*1.38m/s*	*Calculated Impact Energy:*	*1.48J*
Maximum Displacement:	*4.65mm*	*Frames Used:*	*1 and 5*

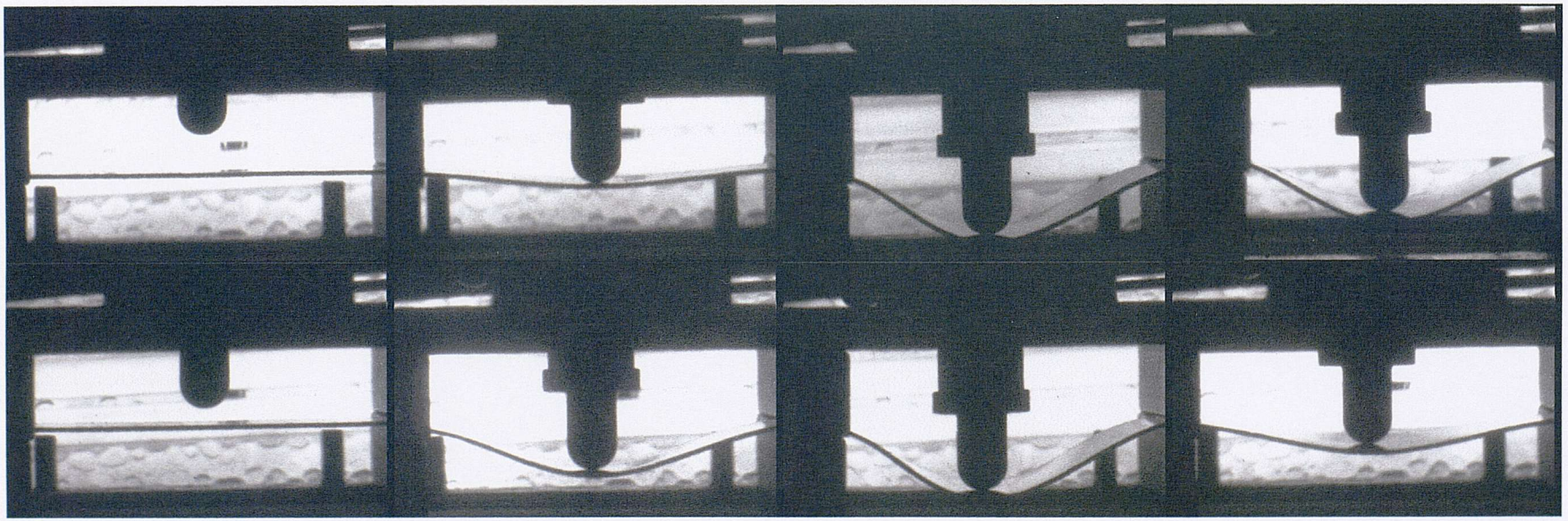
Figure 5.8: High Speed Photography Sequence for Specimen GPPS3, 0.1m Drop on a 120mm x 40mm Glass Fibre Flexible Specimen



Frame No.	1	2	3	4	5	6	7	8
Frame Setting (mS)	25	27.5	30	32.5	35	40	47.5	52.5
Exposure Time (μS)	150	150	150	150	150	150	150	150

Drop Height:	*0.2m*	*Projectile:*	*1.55kg Hemi-spherical Indentor*
Ideal Impact Velocity:	*1.98m/s*	*Ideal Impact Energy:*	*3.04J*
Measured Impact Velocity:	*1.94m/s*	*Calculated Impact Energy:*	*2.92J*
Maximum Displacement:	*5.03mm*	*Frames Used:*	*1 and 6*

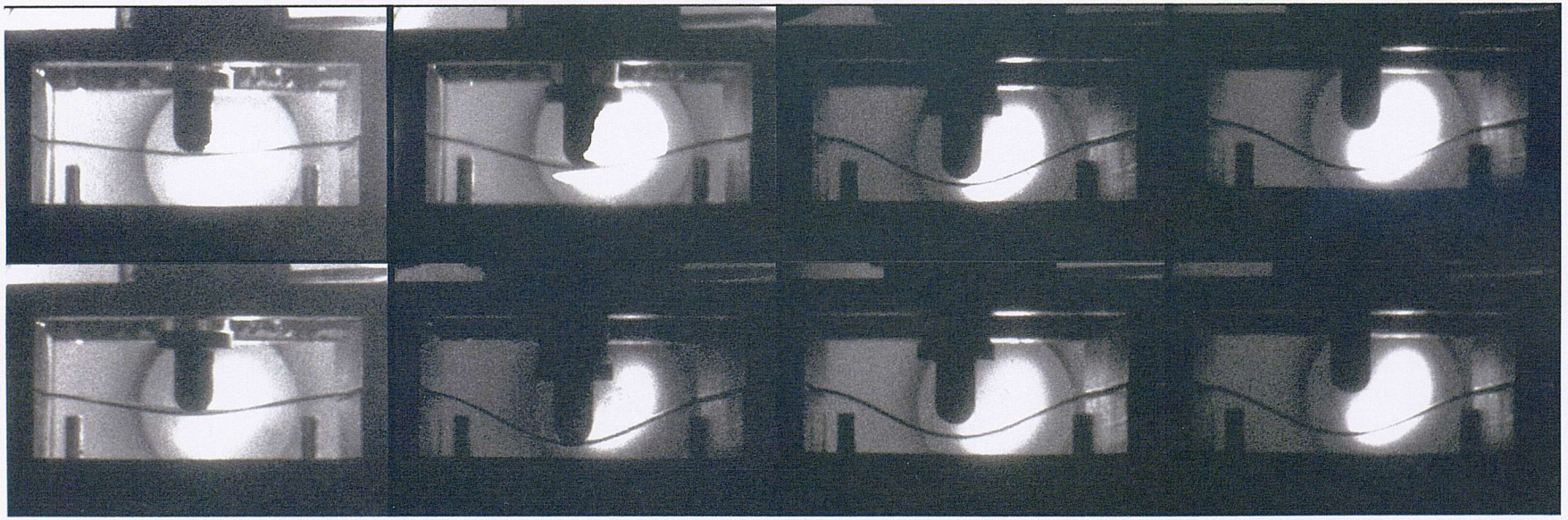
Figure 5.9: High Speed Photography Sequence for Specimen GPPS7, 0.2m Drop on a 120mm x 40mm Glass Fibre Flexible Specimen



Frame No.	1	2	3	4	5	6	7	8
Frame Setting (mS)	20	22.5	26	30	35	37.5	42.5	50
Exposure Time (μS)	150	150	150	150	150	150	150	150

Drop Height:	*0.3m*	*Projectile:*	*1.55kg Hemi-spherical Indentor*
Ideal Impact Velocity:	*2.43m/s*	*Ideal Impact Energy:*	*4.56J*
Measured Impact Velocity:	*2.40m/s*	*Calculated Impact Energy:*	*4.61J*
Maximum Displacement:	*6.47mm*	*Frames Used:*	*1 and 6*

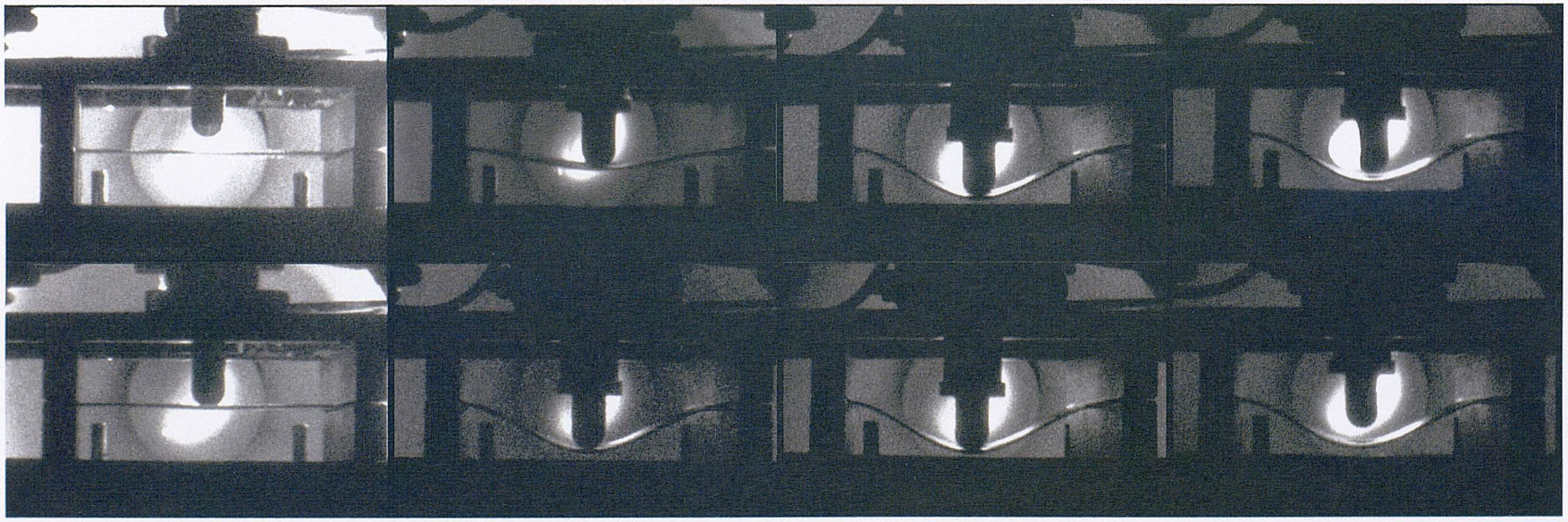
Figure 5.10: High Speed Photography Sequence for Specimen GPPS9, 0.3m Drop on a 120mm x 40mm Glass Fibre Flexible Specimen



Frame No.	1	2	3	4	5	6	7	8
Frame Setting (mS)	10	11	12.5	17.5	25	30	52.5	55
Exposure Time (μS)	6	6	6	6	6	6	6	6

Drop Height:	*0.4m*	*Projectile:*	*1.55kg Hemi-spherical Indentor*
Ideal Impact Velocity:	*2.80m/s*	*Ideal Impact Energy:*	*6.08J*
Measured Impact Velocity:	*2.78m/s*	*Calculated Impact Energy:*	*5.99J*
Maximum Displacement:	*7.57mm*	*Frames Used:*	*1 and 4*

Figure 5.11: High Speed Photography Sequence for Specimen GPPS12, 0.4m Drop on a 120mm x 40mm Glass Fibre Flexible Specimen



Frame No.	1	2	3	4	5	6	7	8
Frame Setting (mS)	6	8	10	15	16	18	25	35
Exposure Time (μS)	6	6	6	6	6	6	6	6

Drop Height:	*0.5m*	*Projectile:*	*1.55kg Hemi-spherical Indentor*
Ideal Impact Velocity:	*3.10m/s*	*Ideal Impact Energy:*	*7.60J*
Measured Impact Velocity:	*3.17m/s*	*Calculated Impact Energy:*	*7.79J*
Maximum Displacement:	*7.57mm*	*Frames Used:*	*1 and 6*

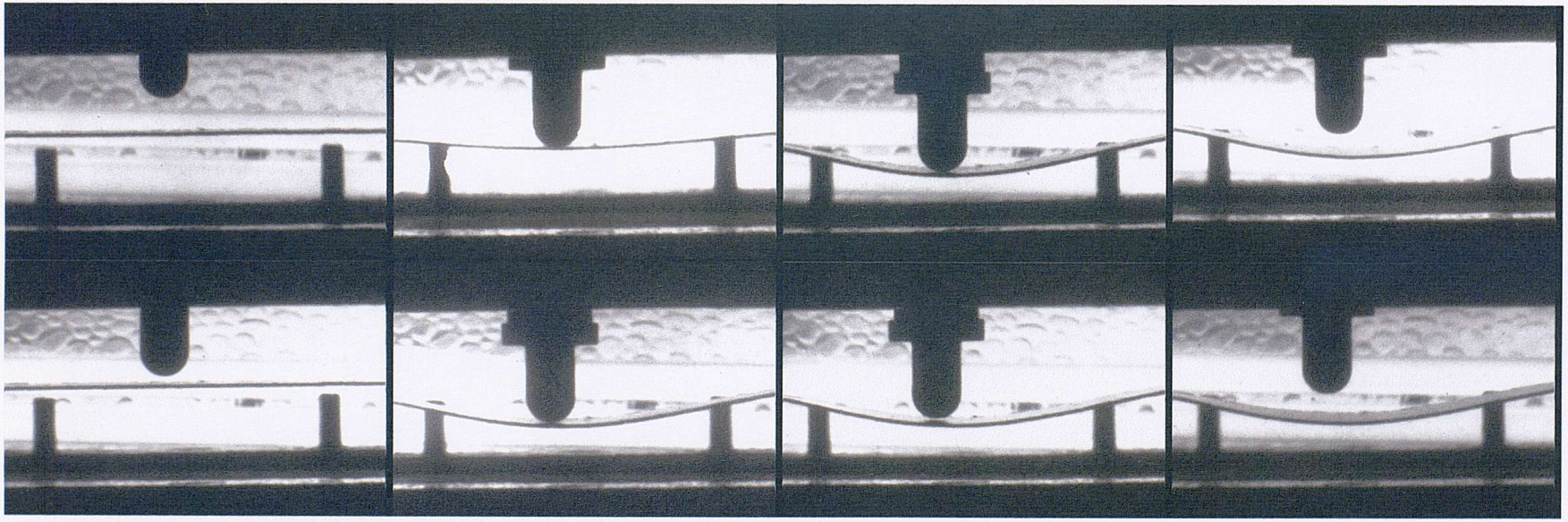
Figure 5.12: High Speed Photography Sequence for Specimen GPPS16, 0.5m Drop on a 120mm x 40mm Glass Fibre Flexible Specimen

Figure 5.6 shows the specimen forming a slight 'V' shape due to the impact event. This corresponds to a crack being observed across the specimen in line with the impact point when the specimen was released from the clamp.

When observing these for visible damage specimens after impact, there are no signs of any damage within the specimens that had been impacted from a 0.1m and 0.2m drop height. However from a 0.3m drop height onwards the specimens begin to show signs of visible damage. At a drop height of 0.3m the Carbon Fibre specimens show signs of fibre breakage and rear ply splitting, however in the case of the R-Glass Samples only a slight indent on at the impact point can be seen. At a 0.4m drop height the Carbon Fibre specimens begin to show obvious cracking on the back face at a position corresponding to the impact site on the front face. The R-Glass fibre begin to show signs of splitting on the back face. At a 0.5m drop height, the back face of the Carbon fibre specimens contain splits across the specimen and bulges at the impact point. In one case, Specimen CPPS16 the specimen snaps at one end along the end clamping unit. As for the R-Glass Fibre specimens, fibre and ply splitting can be observed on the back face along a line directly below the impact point. In some cases a depression can be observed at the impact point with trace signs of fibre crushing also being observed within this depression.

Figures 5.13 to 5.22 show the High Speed Photography sequences for the impact on the longer, 160mm x 40mm specimens. Again one for each specimen at each drop height is shown. Figure 5.13-5.17 show the Carbon Fibre Specimens and *Figures 5.18-5.22* show the R-Glass Fibre Specimens. The same information is provided along with the sequences as before. Also given are the measured maximum deflections taken from the sequences with the frames that were used for these measurements.

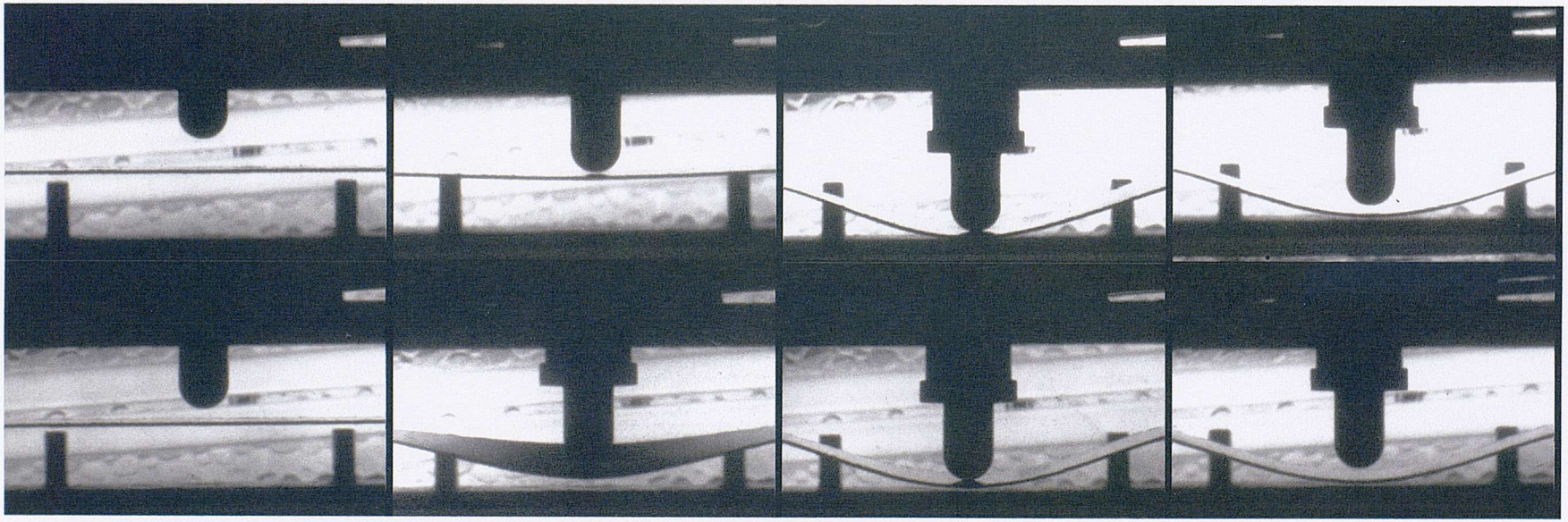
Firstly when observing the sequences it can be seen that the specimens remained deformed within the clamps after the impact event at the first drop height of 0.1m, unlike the shorter specimens, which retained enough energy to return to it's original shape at such a drop height.



Frame No.	1	2	3	4	5	6	7	8
Frame Setting (mS)	40	45	50	55	60	65	75	80
Exposure Time (μS)	150	150	150	150	150	150	150	150

Drop Height:	*0.1m*	*Projectile:*	*1.55kg Hemi-spherical Indentor*
Ideal Impact Velocity:	*1.40m/s*	*Ideal Impact Energy:*	*1.52J*
Measured Impact Velocity:	*1.40m/s*	*Calculated Impact Energy:*	*1.52J*
Maximum Displacement:	*5.08mm*	*Frames Used:*	*1 and 5*

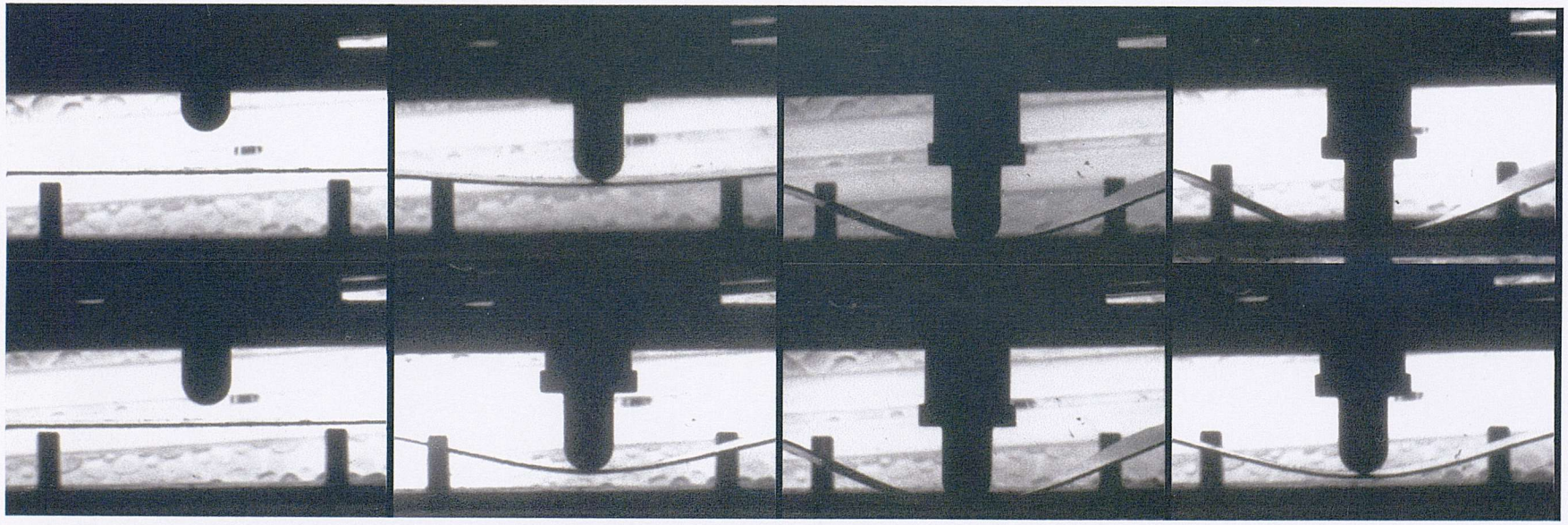
Figure 5.13: High Speed Photography Sequence for Specimen 1CPPS1, 0.1m Drop on a 160mm x 40mm Carbon Fibre Flexible Laminate



Frame No.	1	2	3	4	5	6	7	8
Frame Setting (mS)	25	27.5	30	35	42.5	47.5	52.5	55
Exposure Time (μS)	150	150	150	150	150	150	150	150

Drop Height:	*0.2m*	*Projectile:*	*1.55kg Hemi-spherical Indentor*
Ideal Impact Velocity:	*1.98m/s*	*Ideal Impact Energy:*	*3.04J*
Measured Impact Velocity:	*1.98m/s*	*Calculated Impact Energy:*	*3.04J*
Maximum Displacement:	*6.38mm*	*Frames Used:*	*1 and 5*

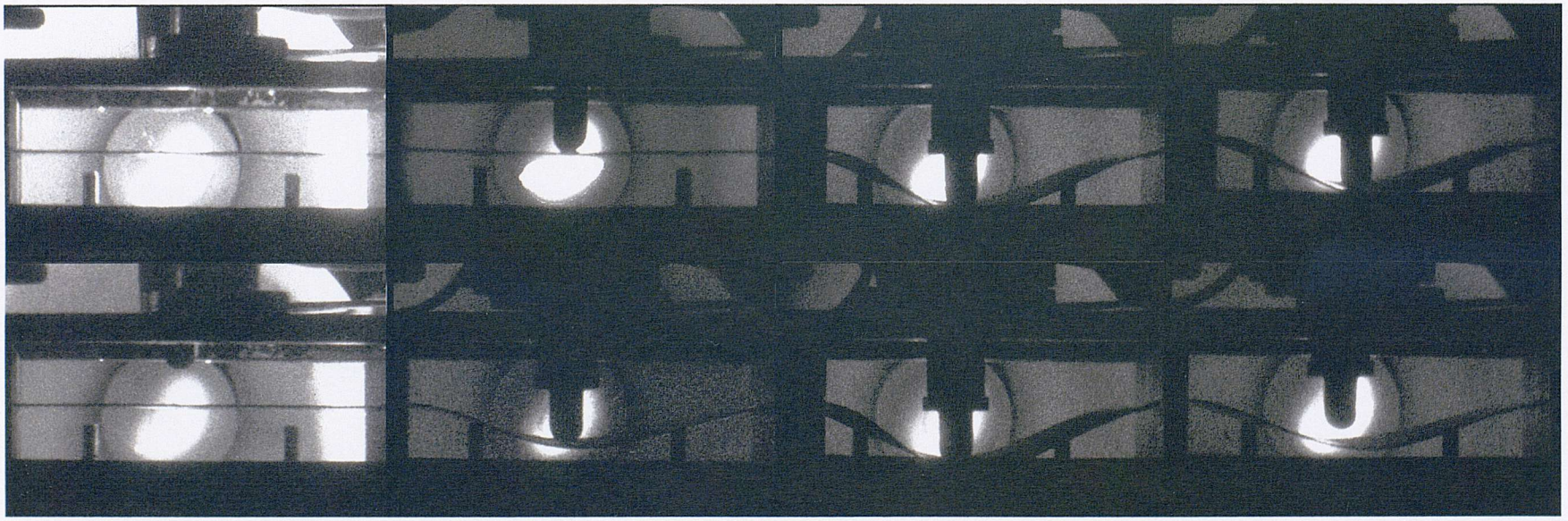
Figure 5.14: High Speed Photography Sequence for Specimen 1CPPS3, 0.2m Drop on a 160mm x 40mm Carbon Fibre Flexible Laminate



Frame No.	1	2	3	4	5	6	7	8
Frame Setting (mS)	20	22.5	26	30	35	37.5	42.5	52.5
Exposure Time (μS)	150	150	150	150	150	150	150	150

Drop Height:	*0.3m*	*Projectile:*	*1.55kg Hemi-spherical Indentor*
Ideal Impact Velocity:	*2.43m/s*	*Ideal Impact Energy:*	*4.56J*
Measured Impact Velocity:	*2.44m/s*	*Calculated Impact Energy:*	*4.61J*
Maximum Displacement:	*6.89mm*	*Frames Used:*	*1 and 6*

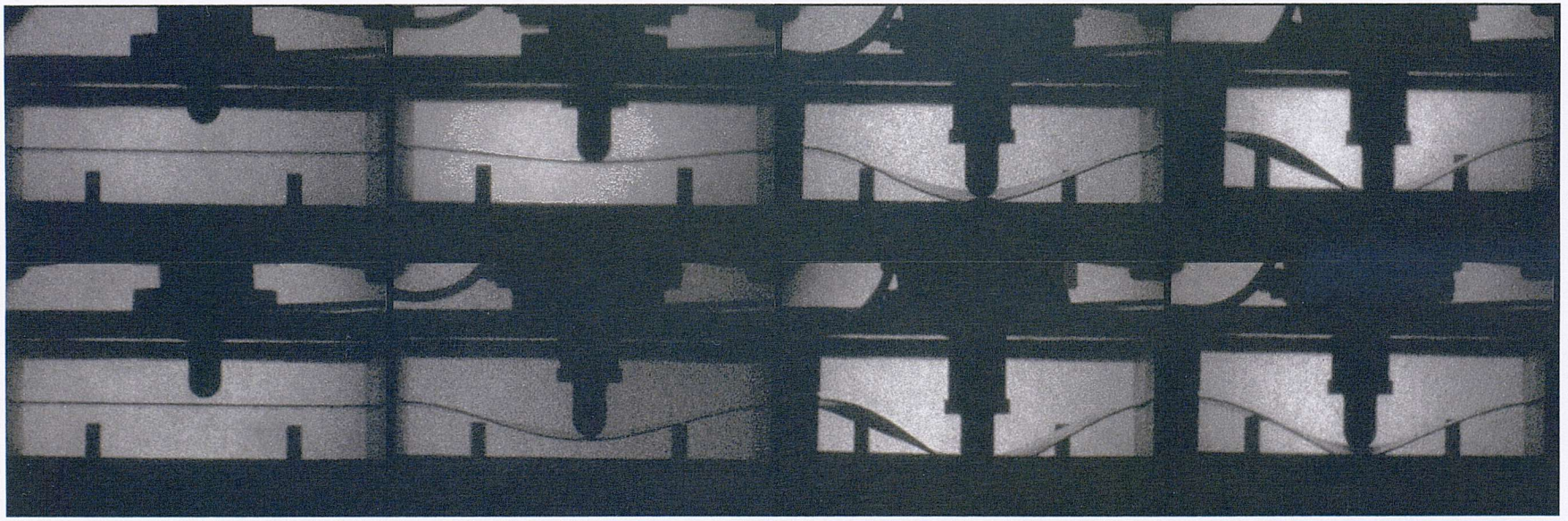
Figure 5.15: High Speed Photography Sequence for Specimen 1CPPS6, 0.3m Drop on a 160mm x 40mm Carbon Fibre Flexible Laminate



Frame No.	1	2	3	4	5	6	7	8
Frame Setting (mS)	7.5	9.5	15	20	25	27.5	37.5	52.5
Exposure Time (μS)	6	6	6	6	6	6	6	6

Drop Height:	*0.4m*	*Projectile:*	*1.55kg Hemi-spherical Indentor*
Ideal Impact Velocity:	*2.80m/s*	*Ideal Impact Energy:*	*6.08J*
Measured Impact Velocity:	*2.79m/s*	*Calculated Impact Energy:*	*6.03J*
Maximum Displacement:	*7.54mm*	*Frames Used:*	*1 and 6*

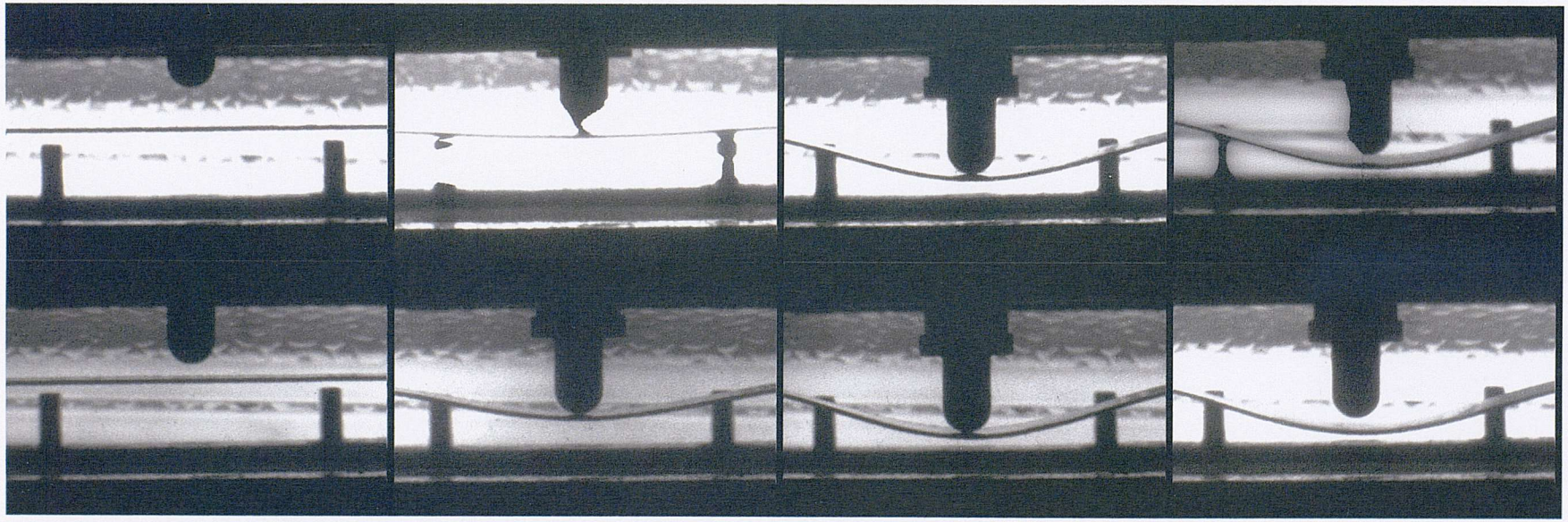
Figure 5.16: High Speed Photography Sequence for Specimen 1CPPS11, 0.4m Drop on a 160mm x 40mm Carbon Fibre Flexible Laminate



Frame No.	1	2	3	4	5	6	7	8
Frame Setting (mS)	10	12.5	15	17.5	20	25	30	45
Exposure Time (μS)	40	40	40	40	40	40	40	40

Drop Height:	*0.5m*	*Projectile:*	*1.55kg Hemi-spherical Indentor*
Ideal Impact Velocity:	*3.14m/s*	*Ideal Impact Energy:*	*7.60J*
Measured Impact Velocity:	*3.16m/s*	*Calculated Impact Energy:*	*7.74J*
Maximum Displacement:	*7.00mm*	*Frames Used:*	*1 and 6*

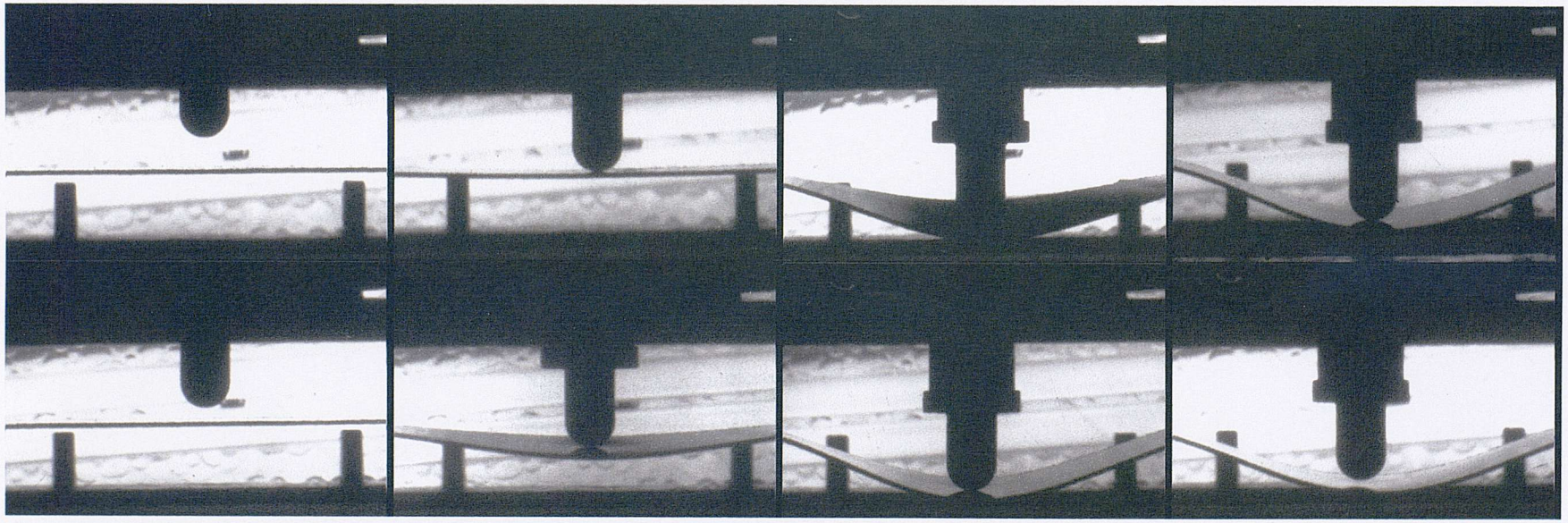
Figure 5.17: High Speed Photography Sequence for Specimen 1CPPS14, 0.5m Drop on a 160mm x 40mm Carbon Fibre Flexible Laminate



Frame No.	1	2	3	4	5	6	7	8
Frame Setting (mS)	40	45	50	55	60	65	75	80
Exposure Time (μS)	150	150	150	150	150	150	150	150

Drop Height:	*0.1m*	*Projectile:*	*1.55kg Hemi-spherical Indentor*
Ideal Impact Velocity:	*1.40m/s*	*Ideal Impact Energy:*	*1.52J*
Measured Impact Velocity:	*1.44m/s*	*Calculated Impact Energy:*	*1.61J*
Maximum Displacement:	*5.75mm*	*Frames Used:*	*1 and 5*

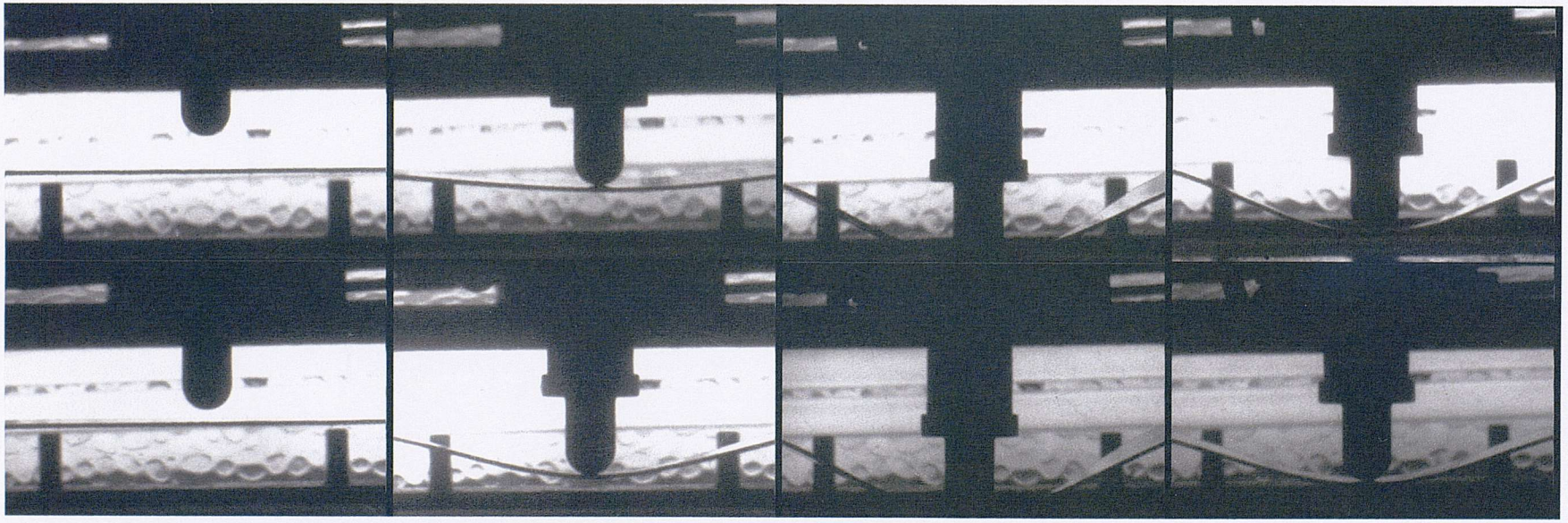
Figure 5.18: High Speed Photography Sequence for Specimen 1GPPS3, 0.1m Drop on a 160mm x 40mm R-Glass Fibre Flexible Laminate



Frame No.	1	2	3	4	5	6	7	8
Frame Setting (mS)	25	27.5	30	32.5	37.5	42.5	50	55
Exposure Time (μS)	150	150	150	150	150	150	150	150

Drop Height:	*0.2m*	*Projectile:*	*1.55kg Hemi-spherical Indentor*
Ideal Impact Velocity:	*1.98m/s*	*Ideal Impact Energy:*	*3.04J*
Measured Impact Velocity:	*1.87m/s*	*Calculated Impact Energy:*	*2.71J*
Maximum Displacement:	*6.68mm*	*Frames Used:*	*1 and 5*

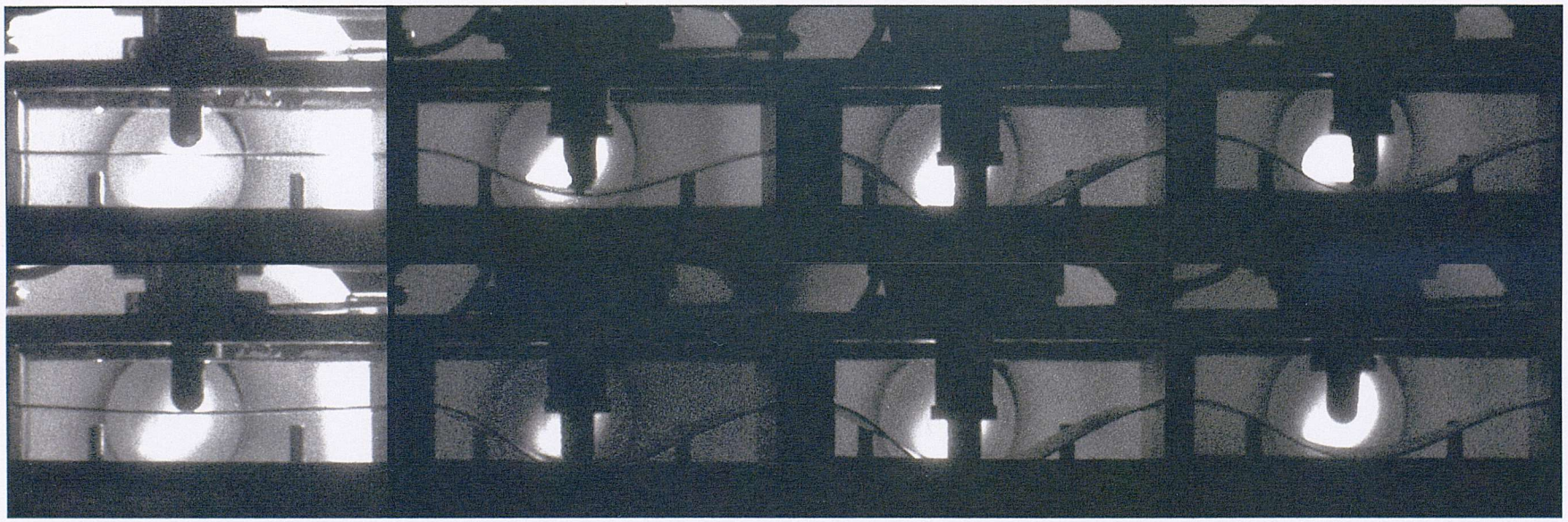
Figure 5.19: High Speed Photography Sequence for Specimen 1GPPS6, 0.2m Drop on a 160mm x 40mm R-Glass Fibre Flexible Laminate



Frame No.	1	2	3	4	5	6	7	8
Frame Setting (mS)	20	22.5	26	30	37.5	45	50	55
Exposure Time (μS)	150	150	150	150	150	150	150	150

Drop Height:	*0.3m*	*Projectile:*	*1.55kg Hemi-spherical Indentor*
Ideal Impact Velocity:	*2.43m/s*	*Ideal Impact Energy:*	*4.56J*
Measured Impact Velocity:	*2.40m/s*	*Calculated Impact Energy:*	*4.46J*
Maximum Displacement:	*8.48mm*	*Frames Used:*	*1 and 6*

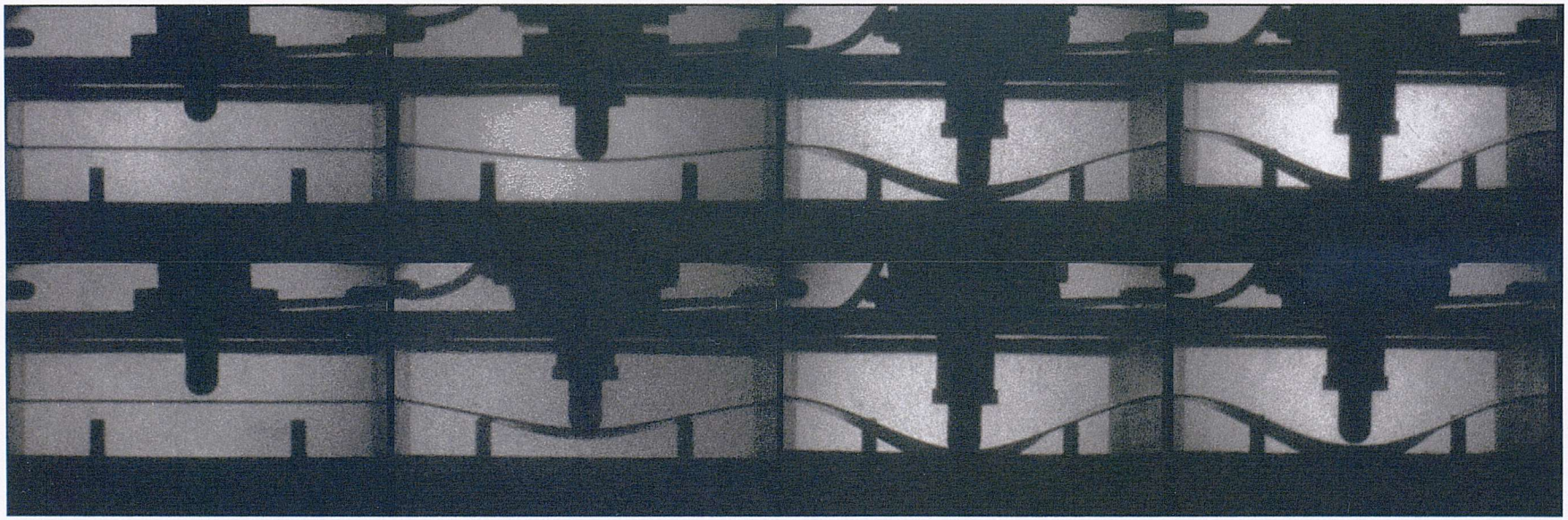
Figure 5.20: High Speed Photography Sequence for Specimen 1GPPS9, 0.3m Drop on a 160mm x 40mm R-Glass Fibre Flexible Laminate



Frame No.	1	2	3	4	5	6	7	8
Frame Setting (mS)	8	9.5	15	20	25	27.5	40	57.5
Exposure Time (μS)	6	6	6	6	6	6	6	6

Drop Height:	*0.4m*	*Projectile:*	*1.55kg Hemi-spherical Indentor*
Ideal Impact Velocity:	*2.80m/s*	*Ideal Impact Energy:*	*6.08J*
Measured Impact Velocity:	*2.77m/s*	*Calculated Impact Energy:*	*5.95J*
Maximum Displacement:	*8.12mm*	*Frames Used:*	*1 and 6*

Figure 5.21: High Speed Photography Sequence for Specimen 1CPPS13, 0.4m Drop on a 160mm x 40mm R-Glass Fibre Flexible Laminate



Frame No.	1	2	3	4	5	6	7	8
Frame Setting (mS)	10	12.5	15	17.5	20	25	30	45
Exposure Time (μS)	40	40	40	40	40	40	40	40

Drop Height:	*0.5m*	*Projectile:*	*1.55kg Hemi-spherical Indentor*
Ideal Impact Velocity:	*3.14m/s*	*Ideal Impact Energy:*	*7.60J*
Measured Impact Velocity:	*3.11m/s*	*Calculated Impact Energy:*	*7.50J*
Maximum Displacement:	*9.13mm*	*Frames Used:*	*1 and 6*

Figure 5.22: High Speed Photography Sequence for Specimen 1CPPS14, 0.5m Drop on a 160mm x 40mm R-Glass Fibre Flexible Laminate

As with before the level of deformation increases with increasing drop height with the R-Glass Specimens deforming more than the Carbon Fibre Specimens at the same drop heights.

No visible signs of damage were recorded for specimens with drop heights of 0.1, 0.2 and 0.3m. At 0.4m drops the Carbon Fibre specimens begin to show signs of damage, whilst the R-Glass Fibre specimens remain with no visible signs of damage. Visible indents can be seen along with signs of the back face beginning to split on the Carbon Fibre Specimens. At the highest drop height of 0.5m both types of specimens show visible signs of damage after the impact event. The Carbon Fibre specimens show visible indents at the impact point and obvious cracking on the back face, whilst the R-Glass Fibre specimens show no signs of damage on the back face but indents at the impact point are visible to the naked eye. The same difference in the behaviour of the two types of specimens is shown here as was shown with the shorter specimens. The R-Glass Fibre specimens are less stiff compared with the Carbon Fibre Specimens and therefore are able to deform a lot more and hence absorb more impact energy leaving less energy to damage the specimen and therefore contain less damage after impact.

Now comparing the behaviour of the two different sized specimens show that with the corresponding material and drop heights the shorter specimen deformed less. Visible damage is shown at lower drop heights in the shorter specimens and more damage is observed in the shorter specimens at the higher drop heights when both sizes of specimen contain visible damage. The length of the specimen affects the amount the specimen can flex and deform. The longer the specimen the easier it is for the specimen to deform, therefore it is fair to say that the shorter specimen is in effect the stiffer of the two under bending conditions. Therefore the less stiff option is able to deform more as a route of impact energy absorption and therefore incurs less damage due to the impact in comparison with the stiffer motion. Hence the shorter specimens show more visible damage in comparison to the equivalent drop height in the longer specimen of the same material.

5.3.2 Ultrasonic C-Scan

For the actual level of damage to be shown the specimen were subjected to Ultrasonic C-Scan. The general details of this technique are given in Section 3.2.4.2. These techniques allowed for a good idea to be obtained of the level of damage that was incurred. The area which the damage occupied would be shown in an obvious different colour to the background of the undamaged areas of the specimen. Although the layer to layer damage could not be shown using this technique it was decided that it not necessary as the results obtained were sufficient enough to show an comparison of the levels of damage within the samples. Also due to the thinness of these samples the layer to layer damage would not divulge much more information than just an indication of the area that the damage occupied. A typical Scan of a sample with damage is shown in *Figure 5.23*.

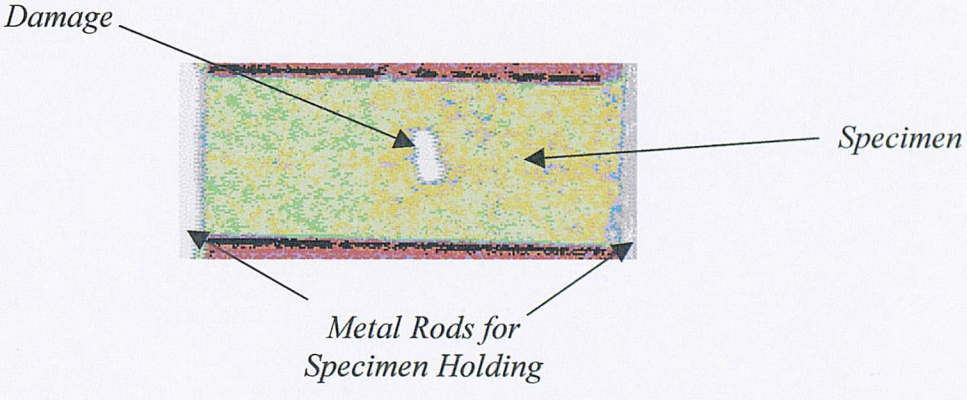


Figure 5.23: Typical C-Scan Image of a damage Thin Flexible Panel (Specimen CPPS8, Carbon Fibre Specimen Impacted from a 0.3m Drop Height)

All the C-Scan Images are given in Appendix 4, however due to the amount of samples that were tested typical images for each condition will be shown here and discussed, plus any other images that show details of interest.

Figures 5.24 and 5.25 show the C-Scan Images for the shorter 120mm x 40mm specimens.

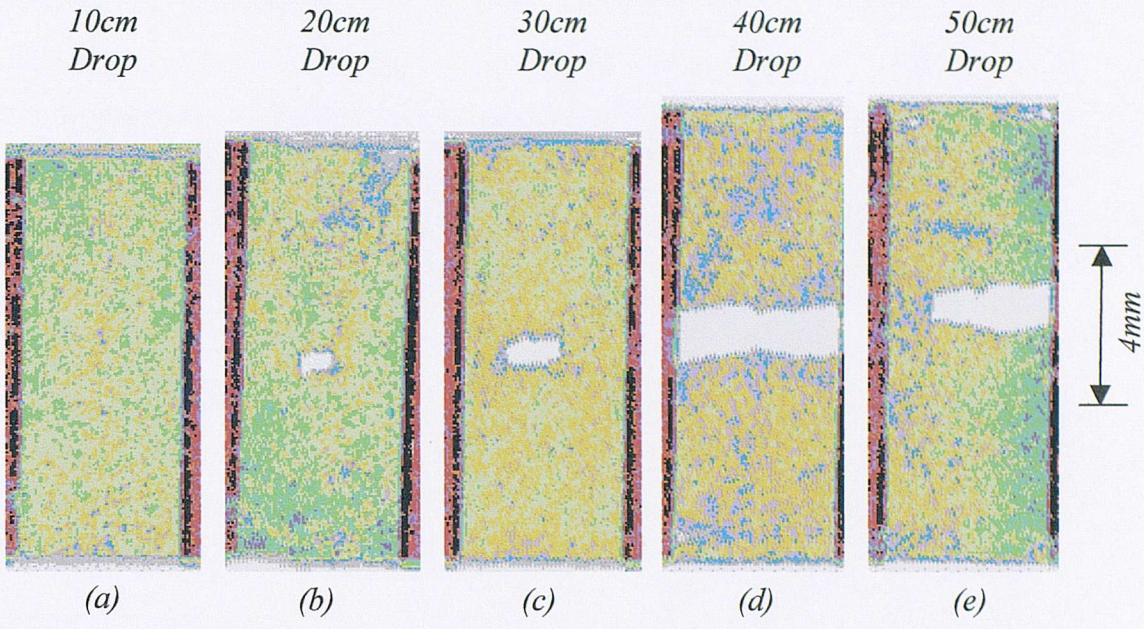


Figure 5.24: C-Scan Images for a selection of the short 120mm x 40mm Carbon Fibre Thin Flexible Laminates: (a) CPPS1; (b) CPPS5; (c) CPPS9; (d) CPPS13; (e) CPPS15

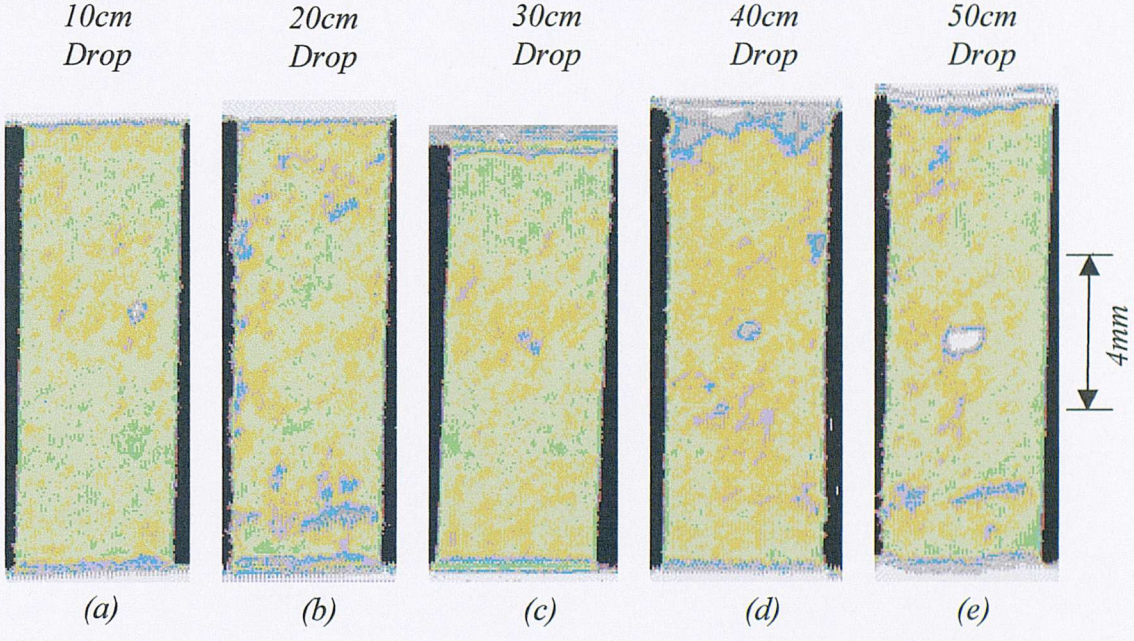


Figure 5.25: C-Scan Images for a selection of the short 120mm x 40mm R-Glass Fibre Thin Flexible Laminates: (a) GPPS3; (b) GPPS5; (c) GPPS9; (d) GPPS13; (e) GPPS16

As can be seen from the above figure the level of damage increases with an increase in drop height. When comparing the two different materials what was indicated in the initial observation of the post impact specimen has been confirmed. The Carbon Fibre specimen incurred a much greater level of damage than the R-Glass Fibre specimen. Thus confirming that the stiffer the material the more damage is incurred due to the less ability it has to deform in order to absorb the impact energy.

With the Carbon Fibre specimens damage can be seen in the 0.2m drop height impact and the damaged area increases with drop height up until the 0.4m drop. Both the 0.2 and 0.3m drop specimen shows a damage area that resembles a typical peanut shaped delamination. This damaged area increases across the specimen rather than concentrically outwards from the impact point, which corresponds to the splitting across the specimen that was observed in the specimens post impact. The C-Scan images show that the damage area in the 0.5m drop seems to have a smaller damaged area than the specimen for the 0.4m drop. This area also is concentrated towards one side of the specimen, this suggests that the actual impact was not central. this also corresponds to the observed damage of the specimen post impact.

Now looking at the R-Glass fibres, there is no damage shown in the 0.12 and 0.2m drops. A slight indication or damage is present roughly around the impact point in the 0.3m drop specimen and this damaged area increases with the further increases in drop height. The damaged area observed in the 0.5m drop specimen is also resembles a peanut shaped delamination.

Figures 5.26 and *5.27* show the selection of typical C-Scan images for the longer 160mm x 40mm As with the shorter specimen the R-Glass Fibre Specimens show less damage at the same drop height impact compared to the Carbon Fibre Specimens. With these longer specimens at the lowest drop heights, 0.1m and 0.2m, there is no damage that can be seen within the C-Scan images in either of the two materials. The Carbon Fibre Specimen begin to show a slight indication of damage at the 0.3 m drop height, and the peanut shaped delamination damage increases in size with the increases in drop height.

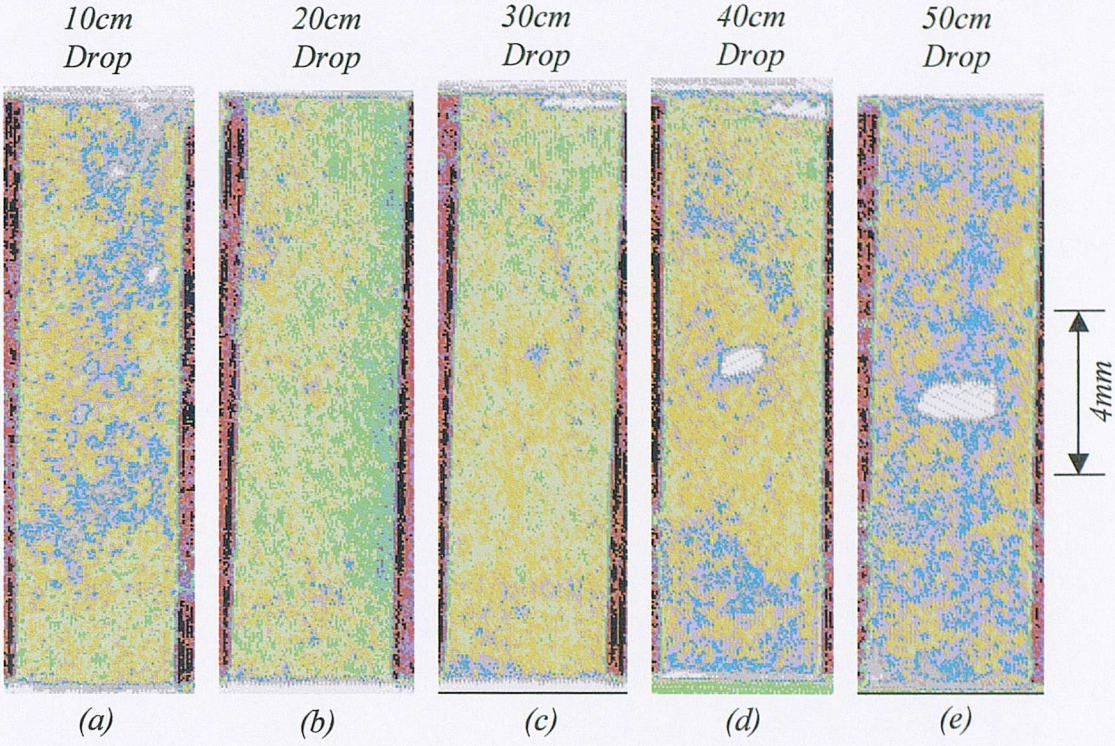


Figure 5.26: C-Scan Images for a selection of the short 160mm x 40mm Carbon Fibre Thin Flexible Laminates: (a) 1CPPS2; (b) 1CPPS4; (c) 1CPPS7; (d) 1CPPS11; (e) 1CPPS12

Looking at the C-Scan images for the R-Glass Specimens only a very slight indication of damage can be seen at the 0.3m drop height. This damage area does increase in size as the drop height increases, however the rate at which it increases is less than that for the Carbon Fibre Specimens. The first indication of damage for both types of specimen is at the 0.3m drop height and the damage areas are roughly the same size. The area then increases at the next two drop height for both types of specimen, however the damage areas in the Carbon fibre specimens are greater in the 0.4m and 0.5m drop heights.

Now when we compare the damage for the same type of specimen but different sizes, once again the damage in the shorter specimens is greater than that in the longer specimens which agrees with the observations taken of the specimens after impact. The images also show that the short R-Glass Specimens incur less damage than the actual long Carbon specimens. This suggests that even with the increase in flexibility

of the longer specimen the Carbon Fibre material is still stiffer and less efficient at absorbing impact energy as the short, stiff R-Glass Fibre specimen.

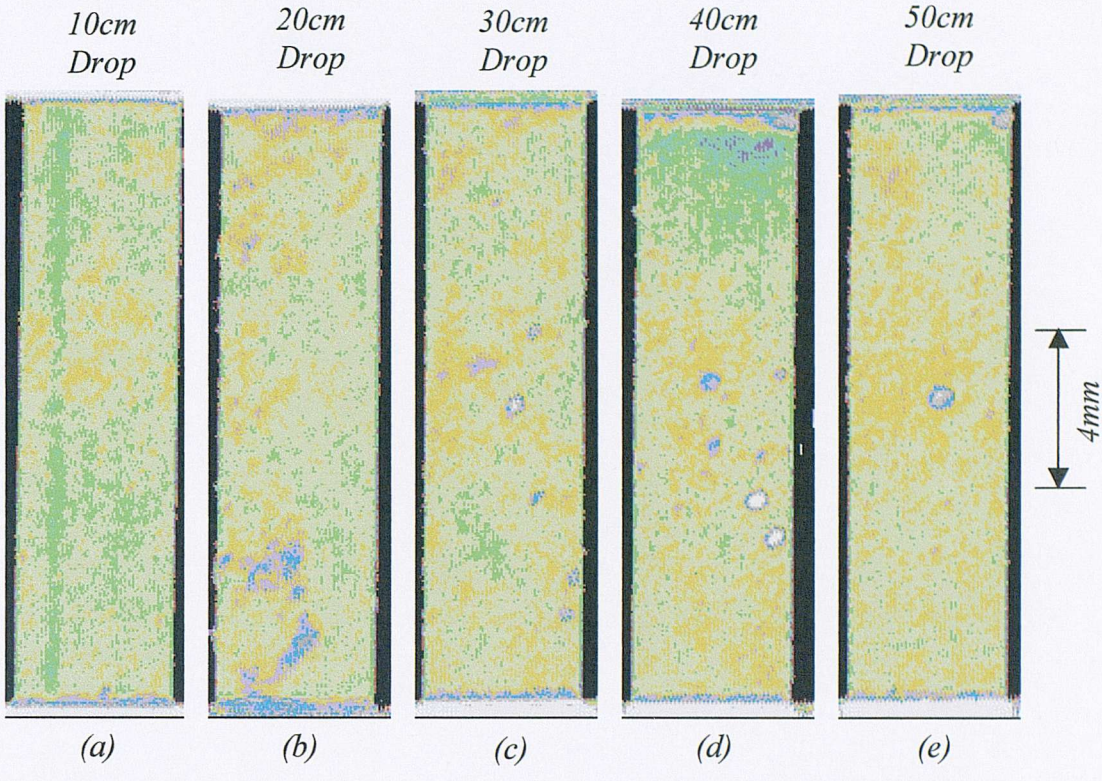


Figure 5.27: C-Scan Images for a selection of the short 160mm x 40mm R-Glass Fibre Thin Flexible Laminates: (a) 1GPPS2; (b) 1GPPS6; (c) 1GPPS7; (d) 1GPPS12; (e) 1GPPS14

During the work one particular Carbon Fibre specimen, when impacted from a height of 0.5m, actually broke along the end clamped area. *Figure 5.28* show the C-Scan image of that particular impacted specimen along with another Carbon Fibre specimen impacted form the same height. It can be seen by comparing the two damaged areas around the impact site that the breaking of the specimen actually absorbed a good portion of the energy that would have caused further damage in the impact area. This shows that damage, as well as specimen deformation, is an impact energy absorbing mechanism.

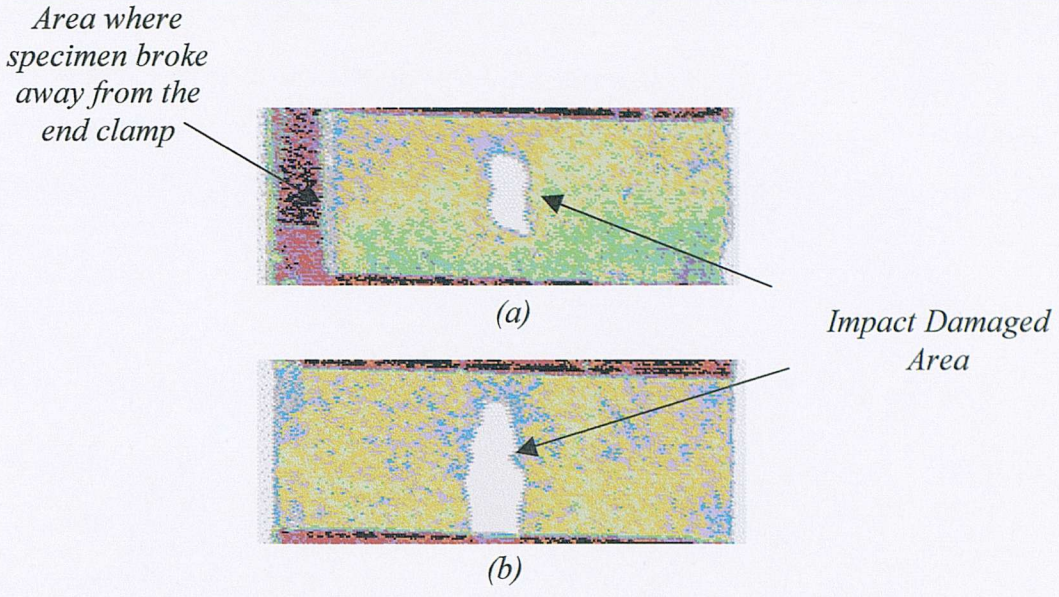


Figure 5.28: A comparison of the damaged area of a carbon Fibre specimen which broke at the clamped end and one which did not from a 0.5m drop height. (a) CPPS16; (b) CPPS14

The results here show that the most intensely damaged specimens are the ones made with Carbon Fibre, showing that they are in general less efficient at absorbing energy in comparison to the R-Glass Specimens.

5.3.3 Drop Weight Data

The data obtained from the Drop Weight Facility was converted into a spreadsheet format and several plots were produced. The data itself came in the form of Force vs Time. However the raw data itself all oscillated around the actual point of interest, hence average data points were produced by using both 40 and 150 data points, and these averaged data points were used to produce the first Force vs Time plot. An example of this plot is given in *Figure 5.29,* which also shows the raw recorded data indicating why this smoothing technique is required in order to analyse this data further. Note the level of noise in the background causing the roughness of the plotted line this was due to the thinness of the specimen not allowing the clear signal to be recorded. It can be seen in the plot that the data does not necessarily begin at the zero point and hence the data was corrected so that the plotted data begins as close to

the zero point as possible. This was necessary in order to carry on with the further analysis of the data. It was also decided that the 40 average points data would be used as they seemed to correspond more closely to what would be expected to occur due to the actual impact event. *Figure 5.30* shows a corrected version of the Force vs Time Data.

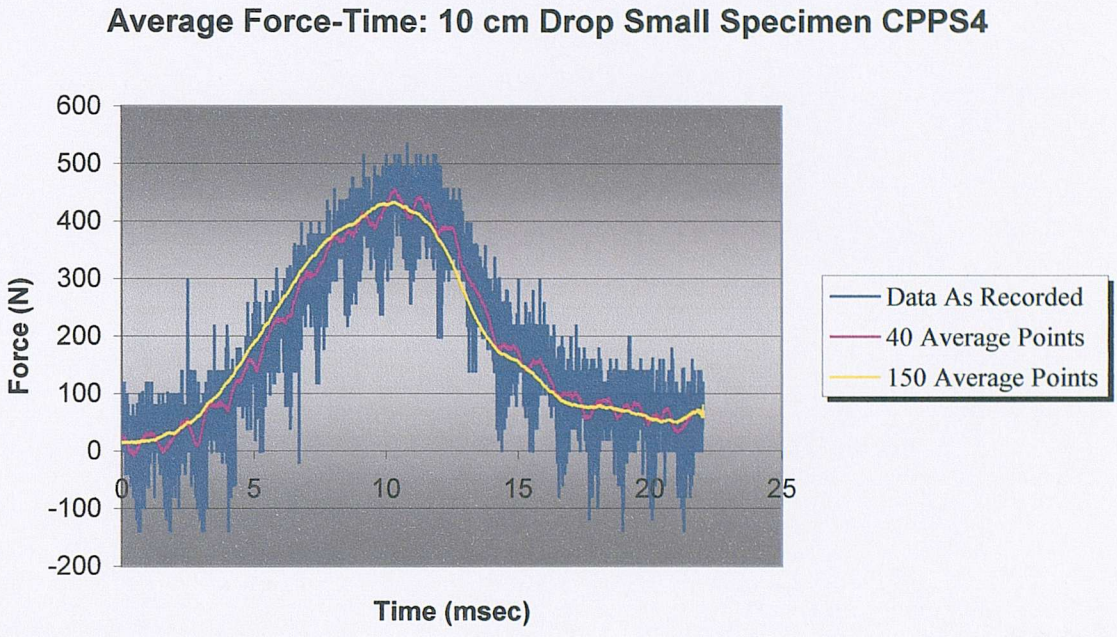


Figure 5.29: Plot showing Force-Time Trace for Specimen Small Specimen CPPS4, 0.1m Drop Height, using 40 and 150 Average Data Points and showing the raw recorded data

Now using the data obtained for the Corrected Force vs Time plot and the Trapezium integration rule, a double integration was performed on the data. The first integration produces a Velocity vs Time Profile, showing the change in velocity of the impactor throughout the impact event. This plot starts with the velocity at impact, which decreases during the impact event until it reaches zero and then goes negative showing an increasing velocity of the rebounding impactor until the actual rebound velocity is reached. The corresponding Velocity vs Time plot for the data shown is given in *Figure 5.31*, along with the impact and rebound velocities marked out.

The second integration gives a Displacement-Time profile, which corresponds to the impactor movement after the initial contact. This is also almost equivalent to the

actual displacement and amount of deformation that occurs in the specimen itself. The peak in this plot shows the maximum displacement that occurs in the specimen during the impact event. *Figure 5.32* shows the corresponding Displacement vs Time Plot for this particular set of data.

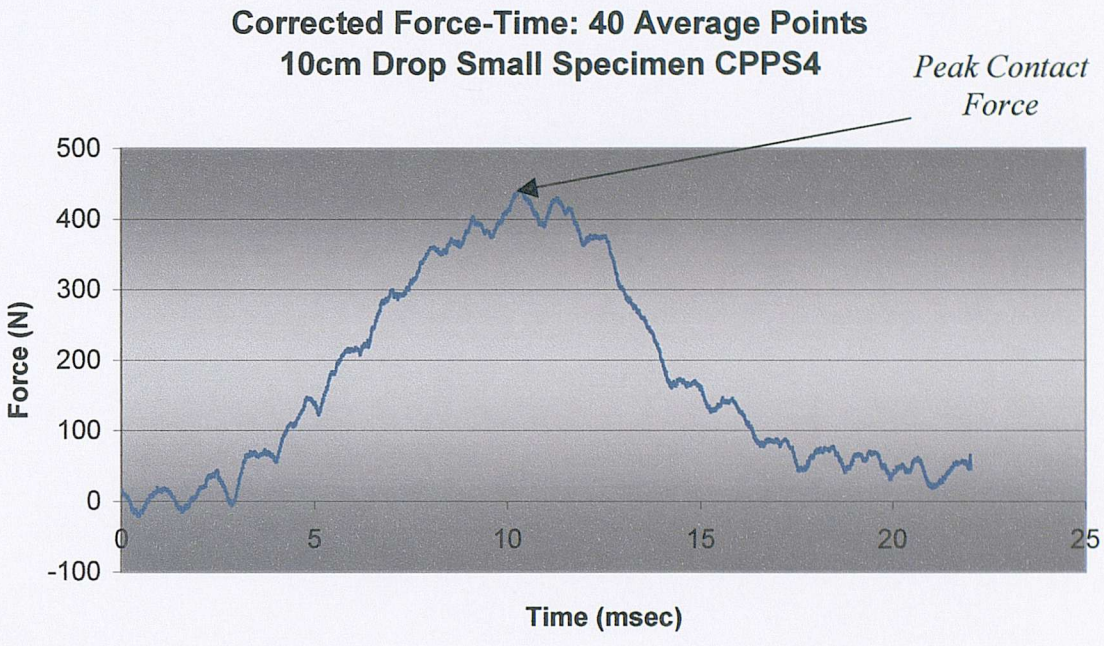


Figure 5.30: Corrected Force-Time Plot using 40 Average Points for Small Specimen CPPS4, 0.1m Drop Height

Finally combining the data produced for the Force-Time Plot and the Displacement vs Time plot a Force-Displacement Plot can be produced. The corresponding Force-Displacement Plot for this set of data is shown in *Figure 5.33*. Due to the nature of this impact event and the relaxation for the specimen the Force-Displacement plots goes back on itself when the displacement decreases after reaching it's maximum. This phenomenon is shown in the plot by using two different colours for the two different regions of the plotted line. The Blue line is for increasing displacement, which corresponds to the actual impact of the specimen. Whilst the pink part of the plot corresponds to a decrease in displacement which in turn corresponds to the rebounding or relaxation part of the impact event.

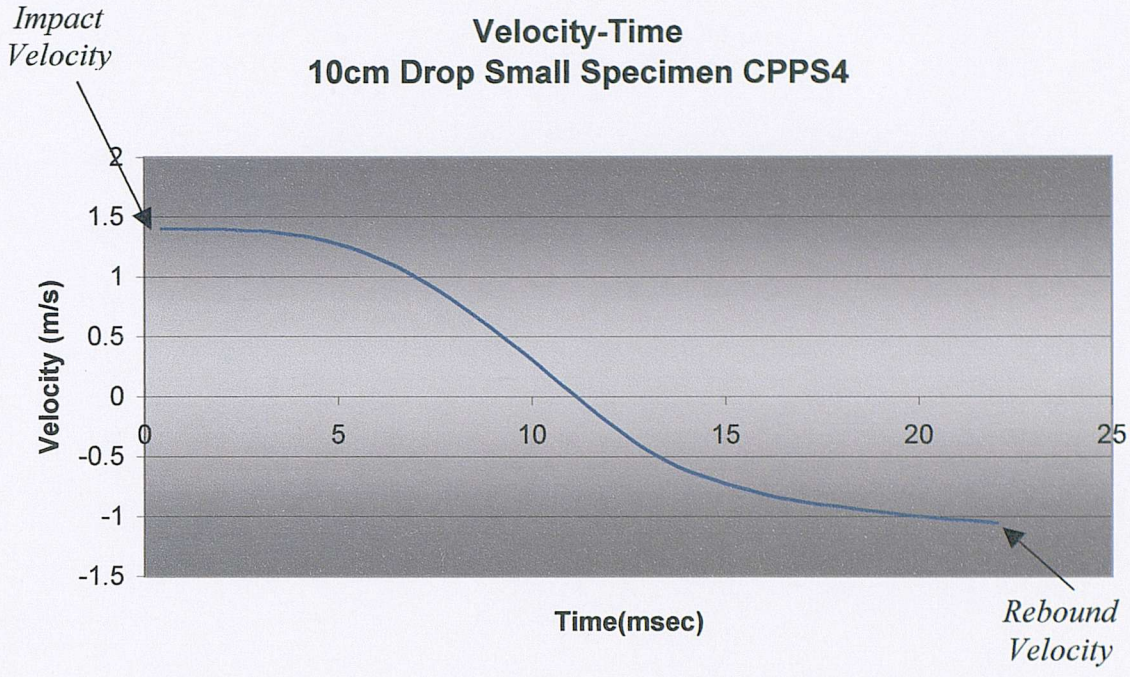


Figure 5.31: Velocity-Time profile for 0.1m Drop on Small Specimen CPPS4

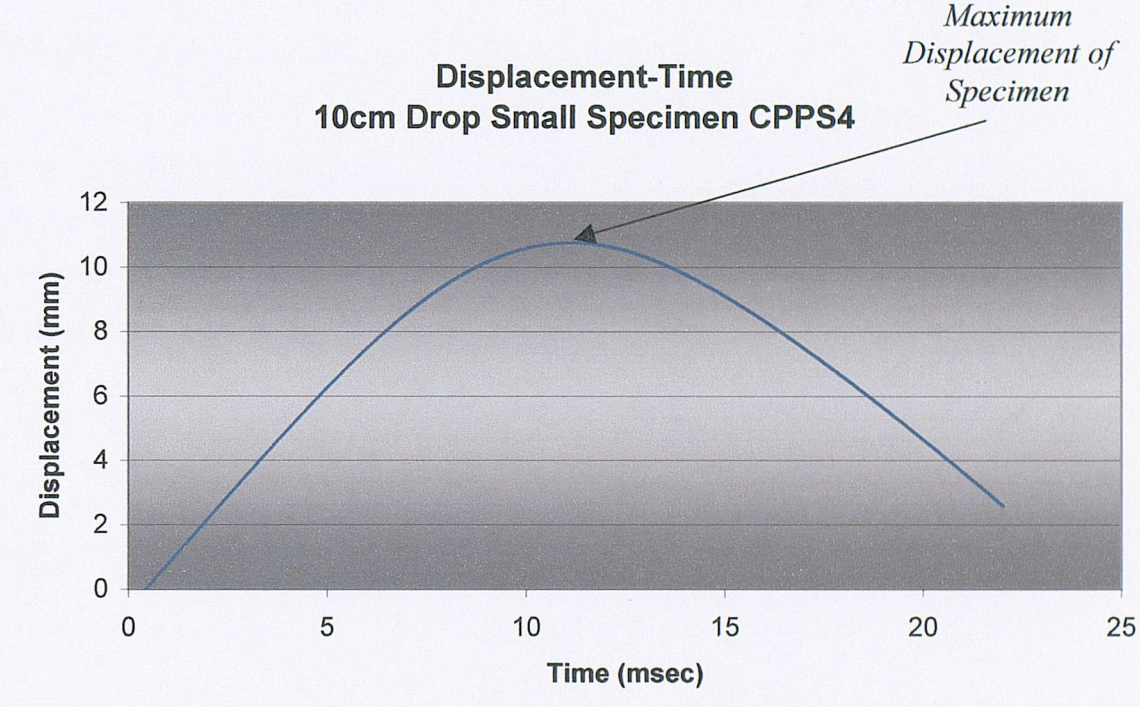


Figure 5.32: Displacement-Time Plot for 0.1m Drop on Small Specimen CPPS4

From these plots a lot of data has been obtained and shall be looked at in turn. Average values for the different parameters of interest have been taken for analysis. The average values were obtained by taking the mean average of the values taken from all the tests that were performed. Firstly the Peak Force data is looked at.

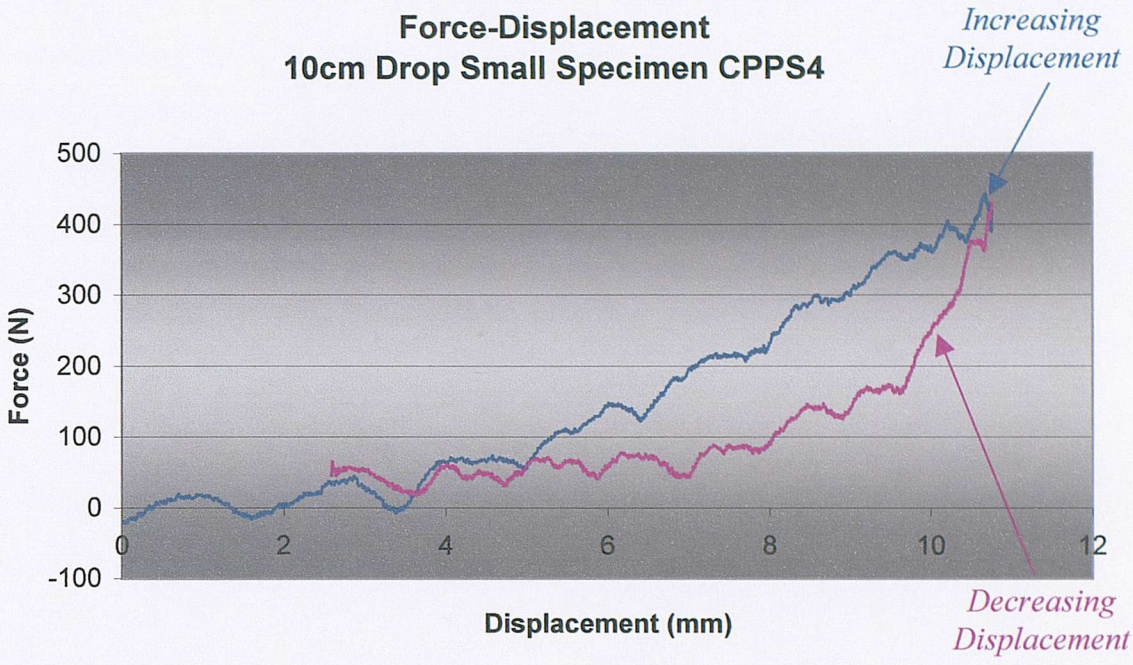


Figure 5.33: Force-Displacement Plot for 0.1m Drop on Specimen CPPS4

Using the corresponding Force vs Displacement plots and the curves representing the increasing and decreasing displacement, the hysteresis loop can be calculated by integrating the two curves and subtracting the integral of the decreasing line from the increasing line. This integral should be a good representation of the level of energy absorbed during the impact event. *Table 5.6* shows the calculated values for energy absorbed by the impact events in this study.

		Energy Absorbed (J)			
Drop Height (cm)	Impact Energy (J)	**Short (120mm) Carbon**	**Long (160mm) Carbon**	**Short (120mm) Glass**	**Long (160mm) Glass**
10	**1.52**	0.70	1.33	1.25	1.19
20	**3.04**	1.00	1.43	1.26	-
30	**4.56**	-	-	3.62	-
40	**6.08**	2.36	5.77	6.01	6.06
50	**7.60**	5.06	7.54	4.69	3.37

Table 5.6: Table showing the calculated values for energy absorbed during impact using hysteresis loop shown in Force vs Displacement curves.

There are values missing for certain impact conditions due to the plots not containing the required loop for calculations. In general however the values show that the more flexible the specimen, whether that is due to the geometry (increase in length equates to an increase in flexibility) or the material constituent (glass fibres rather than carbon fibres), the more energy is absorbed. This correlates with the C-Scan results, which show lower levels of damage in the corresponding specimens types.

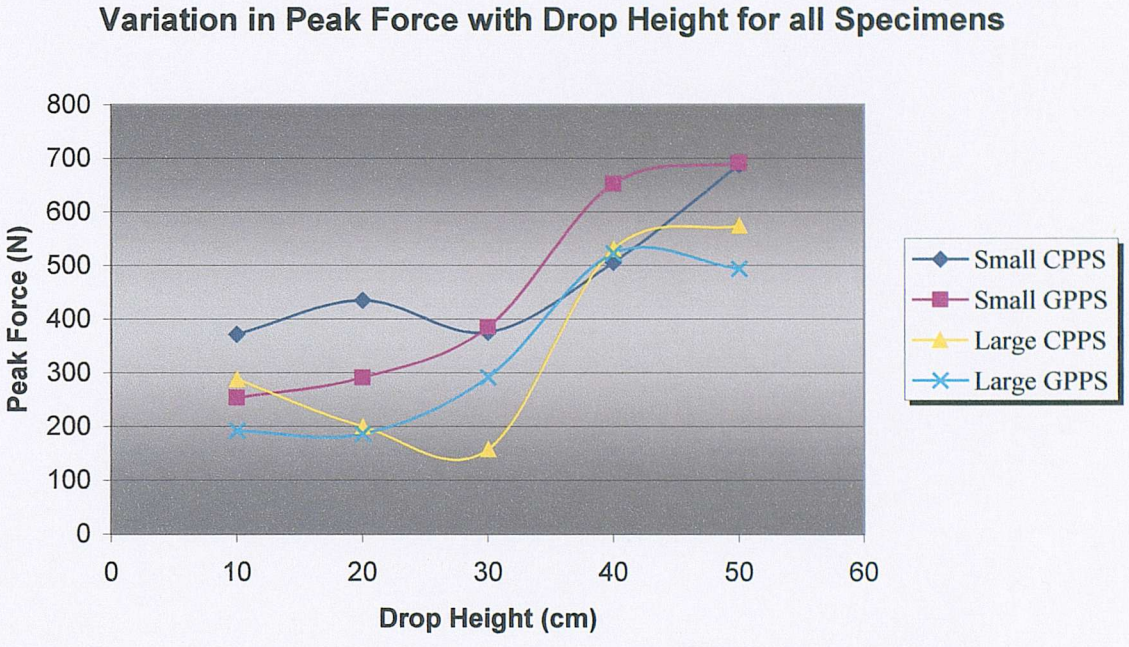


Figure 5.34: Plot showing the variation of Peak Contact Force with Drop height for all 4 types of specimen tested.

Figure 5.34 shows how the Peak Contact Force varies with drop height and how this relationship differs for the 4 different types of specimen. The figure shows that for each type of specimen there seems to be a rate at which the peak contact force increases as depicted by the linear part of the relationship. There seems to be a an impact energy, indicated by the drop height, at which this rate decreases. However a true indication of the behaviour cannot be determined without further tests at higher impact energies were to be performed.

There is also a distinct difference in the shape of curve of this relationship for the two different materials. The peak force for the carbon specimens drops to a minimum before increasing in a linear fashion, whilst the for the R-Glass specimens the peak

force rises immediately but not at a linear rate until a drop height of roughly 0.3m. The levels of peak force are shown to be greater for the carbon fibre specimens in comparison to the R-Glass fibre specimen, which should be expected, as the carbon fibre samples are the stiffer of the two materials. The shorter specimens show a significantly greater peak force in comparison to the longer specimens (a difference of nearly 150N for the carbon specimens and 200N for the R-Glass specimens).

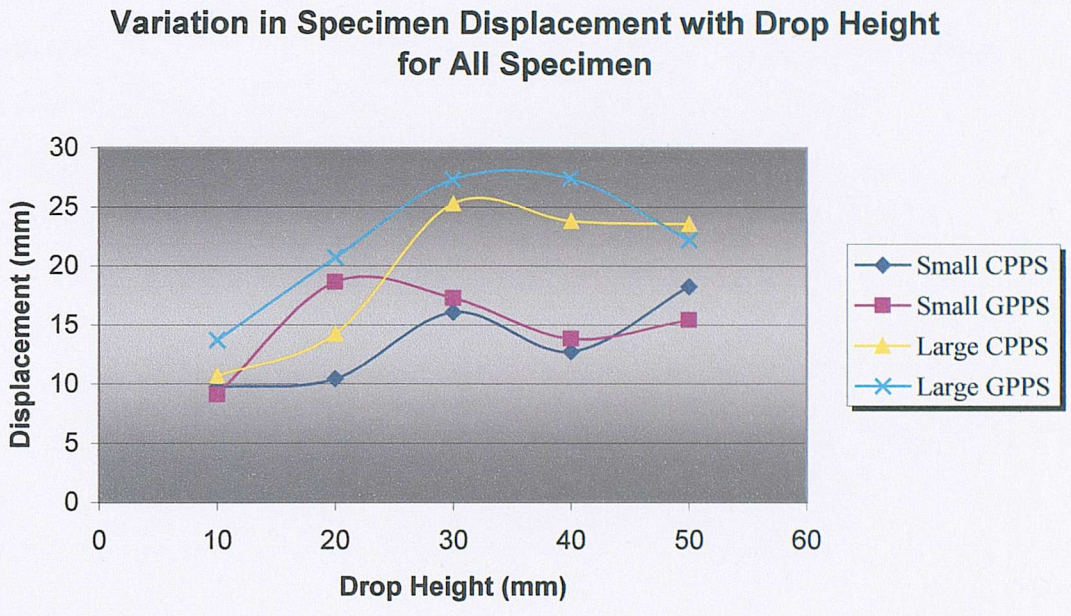


Figure 5.35: Plot showing the variation of Displacement with Drop height for all 4 types of specimen tested.

Figure 5.35 shows how the level of displacement or deformation of the specimen varies with the drop height. The displacement values taken are the ones obtained from the drop weight data, and average values are taken for each drop height. The amount of deflection reflects the actual level of stiffness of the material. The most deflection occurs in the large R-Glass specimens, followed by the large Carbon specimen, the small R-Glass fibre and finally the specimen with the least deflection is the small carbon fibre specimen. However the plot also shows that at the highest drop height, 0.5m, the deflection of the carbon specimens become greater than that of the corresponding sized R-Glass specimen. Previously it has be seen that at this higher drop height the damage levels than occur in the carbon specimens are greater and actually cause cracking and failure on the back face of the sample. Therefore be

surmised that at this drop height due to the failure of the back face the resistance to the impactor is reduced and hence it is able to travel further and hence record a higher level of displacement at such drop heights in comparison to the equivalently sized R-Glass specimen.

5.4 Discussion

It has been shown in these results that the level of flexibility is greatly affected by the constituent fibres and as a result he actual fibre used has a significant effect on the levels of Damage that occurs during impact. Less stiff R-Glass fibre produce the more flexible panel and hence is much superior at absorbing impact energy and incurs less damage than the laminate made from stiff carbon fibres. This is reflected in the levels of damage that were observed in the C-Scans of the impacted samples.

From the results taken from the drop weight impact data it can be seen that the drop height is directly linked with the level of damage that occurs, and from the summary plots it shows that the amount of damage within an impacted sample may have a significant effect on the level of displacement that occurs due to the loss of integrity of the specimen. For example at the high drop heights for the carbon specimens the damage which reaches the back face in the form of a split, the integrity of the specimen drops and hence the impactor can travel further than when impacting from the same drop height on the equivalent sized R-Glass specimens which remain relatively intact and still are able to flex and resist deformation, whilst absorbing energy.

6 Effects of Length, Width and Thickness on the Impact Damage of Composite Laminates

This chapter investigates how the impact damage can be affected by a change in specimen size in all three dimensions i.e. length, width and thickness. It was shown previously (**Chapters 4 and 5**), that flexibility could be used as an energy dissipation route for absorbing impact energy and hence limiting impact damage. Therefore, in this investigation, the interest was in studying how specimen dimensions affect the impact damage that occurs in a composite. It was decided to use specimens of sufficient thickness that a minimal amount of flexure can occur so that as much of the impact energy as possible goes towards creating damage in the specimens.

6.1 Aims and Objectives

The main aim for this chapter is to show how different length, width and thickness in a composite laminate can affect the level of damage that is induced when the laminate is subjected to impact. Therefore, a series of drop weight impact tests were performed on a set of thick composite laminates with varying length, width and thickness and their damage was analysed. Also, the force-time behaviour during the impact event will be analysed to show how the contact force changes with the introduction of damage into the laminate.

6.2 Procedure

With these experiments the specimen arrangement was so that there was little deflection of the specimen that could occur and as a result the absorbed impact energy was given to producing damage. For these experiments, therefore, the force-time data obtained from the instrumented drop weight test could be used directly in the analysis of results. Previously, for the flexible specimens, high-speed photography was

required to monitor the dynamic behaviour of the impacted specimens. C-Scan Ultrasonics was used to assist in the investigation as to the extent and nature of the damage inflicted in the impacted specimens.

As shown in *Table 3.1*, the sizes of the specimens are: A(80x150x4 mm), B(80x150x10 mm), C(60x150x10 mm), D(40x150x10 mm), E(80x120x10 mm), F(60x120x10 mm) and G(40x120x10 mm). Specimens A and B were used to assess the effect of thickness. Specimens B, C, D, E, F and G were used for the investigation into how length and width changes can affect the impact damage that occurs. Three different drop weight conditions were used for these impacts, all with hemispherical impactors but different drop heights and impactor mass. The different conditions that were used are detailed in Table 6.1. Condition α was used only on specimen geometry A and B, which looks at the effect of thickness. Condition β was used on specimen geometry B, C, D, E, F and G; these look at the effects of changing both the length and the width of the specimen. Finally, conditions γ and δ were used on all specimen geometries.

	Condition α	**Condition** β	**Condition** γ	**Condition** δ
Drop Height (m)	0.5	0.6	1.5	1.0
Impactor Mass (kg)	1.55	1.55	1.55	5.4
Impact Energy (J)	7.60	9.12	22.81	52.97
Impact Velocity (m/s)	3.14	3.43	5.43	4.43

Table 6.1: Table showing the different impact conditions used for this investigation.

The first two conditions, α and β, were used to reveal the specimen behaviour in terms of force-time during the impact event when the induced damage is negligible. This provided a comparison reference for other studies when the specimens did suffer impact damage. Conditions γ and δ were used to study the force-time behaviour of the specimens during the infliction of damage by the impactor.

The specimens were clamped with the end clamp units within the main clamping unit, as shown and described in Section 3.2.1. As with the previous drop weight tests, the main clamping unit was secured onto the drop weight tower with two large G-clamps and this minimised any movement of the whole clamping arrangement during the impact event. Repeat identical impacts were performed on each specimen geometry to ensure reproducibility of impact data and damage results.

Force versus Time data was also recorded from the drop weight tests. These were transferred onto a spreadsheet and plotted into graphical form. Once again a double integration was performed so that Velocity versus Time and Displacement versus Time data was obtained. From this data, Force versus Displacement plots were produced. The results obtained show what had occurred during the impact event in terms of changes in the contact force, the impactor's velocity and the displacement of the impactor during its contact with the specimen.

After the impact tests were performed, the laminates were then C-Scanned using the through transmission mode owing to the thickness of the laminates making the pulse echo mode ineffective at mapping out the damage in these specimens.

6.3 Results

From the results obtained, the behaviour during the impact event was studied first to investigate how the behaviour changes during the impact event and when damage is induced, and then how this behaviour is affected by the change in dimensions of the specimen. The effects on the level of damage are then investigated together with how the damage level relates to the impact response.

6.3.1 Drop Weight Data

The first set of impact results data that will be looked at will be the data obtained from the lower mass and lower drop height (α and β), and hence lower impact energy tests.

These will show how changes in dimensions change the behaviour that occurs during the impact event.

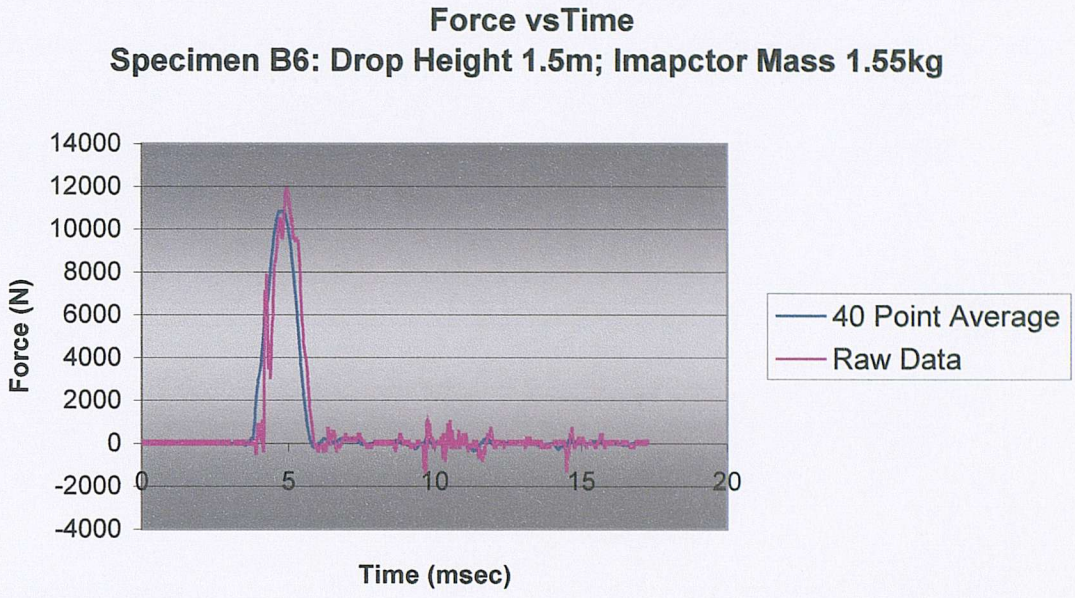


Figure 6.1: Typical Force versus Time Plot for Dimension Change Investigation, here showing both the raw data and the effects of smoothing the curve by averaging 40 points.

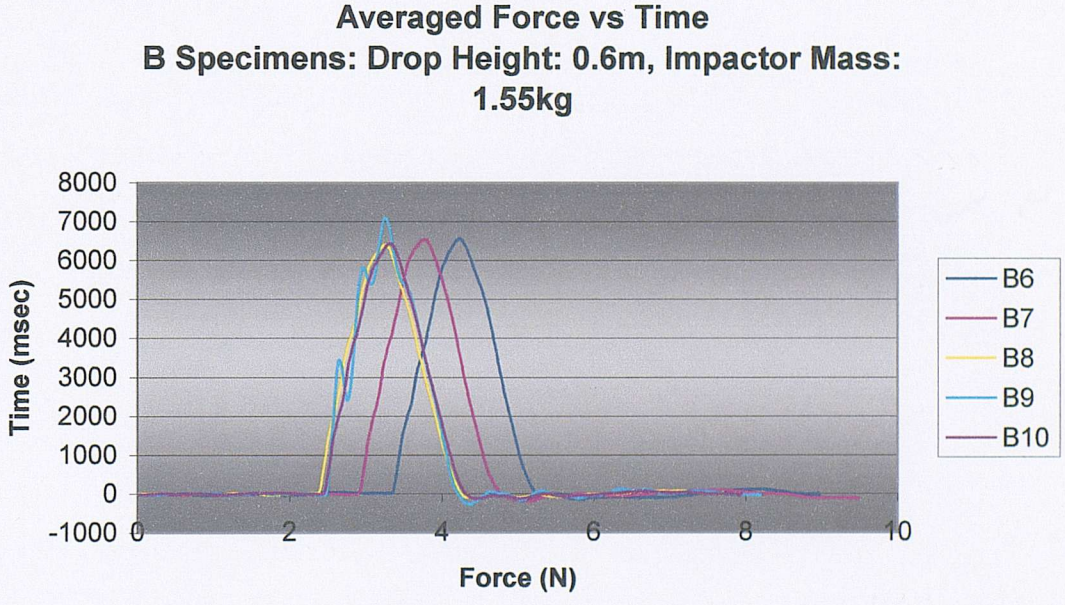


Figure 6.2: Force vs Time plots for all B specimens impacted from a drop height of 0.6m showing the reproducibility of the results obtained from the drop weight testing.

As with the previous chapter the data, small fluctuations were smoothed, by averaging every 40 data points to obtain one data point. Unlike the previous investigation, there is not a lot of background noise involved and hence the resultant Force versus Time plot is a lot smoother. A typical Force versus Time plot for this investigation is shown in *Figure 6.1*. *Figure 6.2* shows the Force vs Time data for all tests performed on Specimen Type B from a drop height of 0.6m, showing the reproducibility of the data acquired from this set of tests. The double integration then allows data for velocity and displacement to be obtained.

6.3.1.1 Changes in Behaviour due to a Change in Dimension

Firstly the change in the actual behaviour of the Force, Velocity and Displacement during an impact event due to a change in dimension will be determined so the low drop height specimens will be studied first.

6.3.1.1.1 Low Drop Height Impacts

Firstly to show how the specimen types react differently to an impact, low drop height impacts were used. A drop height of 0.5m was used with a impactor mass of 1.55kg (Drop Condition α from Table 6.1) to show the behaviour of a change in thickness, whilst a drop height of 0.6m with the same impactor mass (Drop Condition β from Table 6.1) was used for the effects of a change in length and width of the laminate.

Thickness Effects

Figure 6.3 shows a comparison between the Force versus Time plots for specimen dimensions A and B for their low drop height tests. It can seen that the peak contact force has almost a two fold increase due to the increase in the thickness of the laminate. The difference in the slope of the curves also show that the rate of increase and decrease of the contact force is greater in the thicker laminate than it is in the thinner laminate. It can also be seen that the duration of the impact event is longer for

the thin laminate. This indicates that there may be a lot more damage development occurring during the impact of the thin laminate than in the impact of the thick laminate, resulting in a longer period of actual contact between the impactor and the laminate. Also, of note is the difference in the smoothness of the two curves. The steps that occur in these type of curves are due to dynamic oscillations during the impact event. Therefore, it is clear that there are less such oscillations in the impact of the thicker laminate than a thinner one.

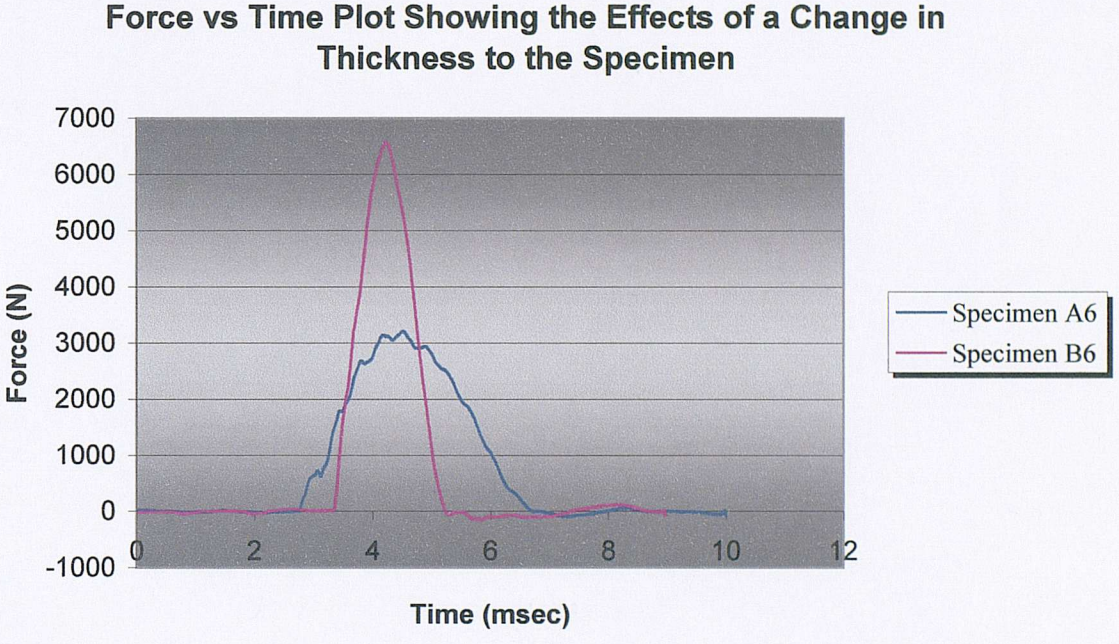


Figure 6.3: Force versus Time Plot showing the Difference in Behaviour due to a change in the Thickness (A: 4mm and B: 10mm) of the Laminate.

Figure 6.4 shows how the velocity profile changes during the impact event of the laminates with the two different thicknesses. There is a difference in the actual initial impact velocity, this could be due human error in the placement of the impactor at the initial drop height and any loss of momentum of the impactor due to friction between the impactor and the guide rails on the drop weight tower. The plot shows a distinct difference between the rates at which the velocity decreases on impact with the thicker laminate having the greater of the two rates. There is also a slight difference

in the rebound velocity. The thicker laminate giving the higher rebound velocity even though its initial impact velocity is lower than that of the thinner laminate.

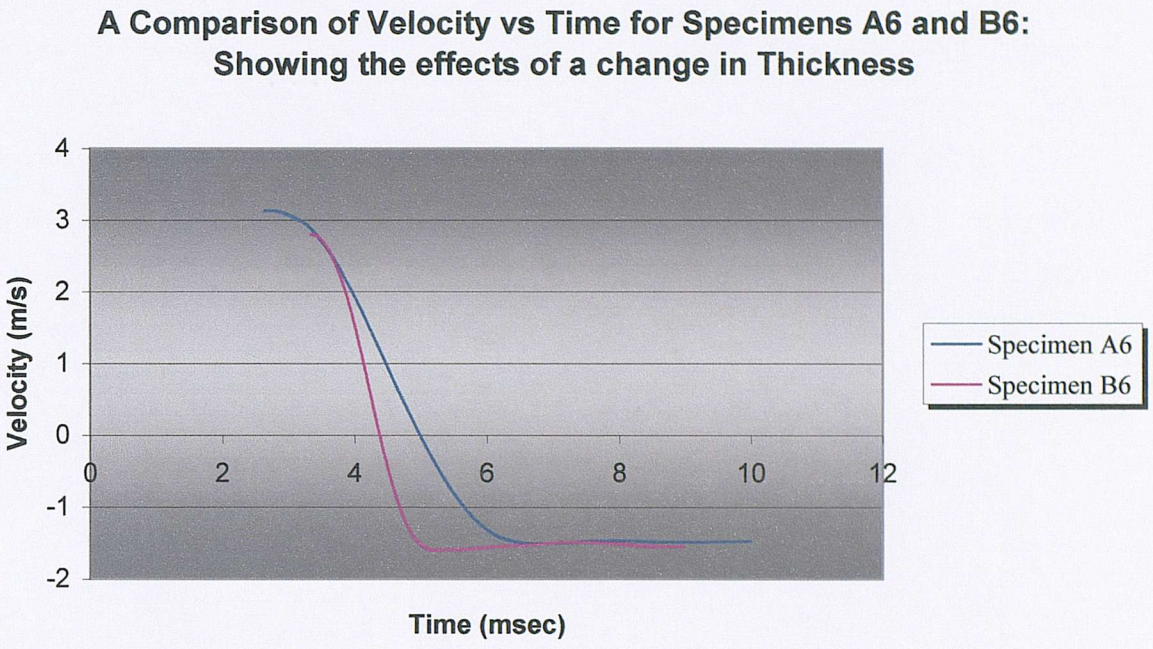


Figure 6.4: Velocity versus Time Plot showing the Difference in Behaviour due to a change in the Thickness (A: 4mm and B: 10mm) of the Laminate.

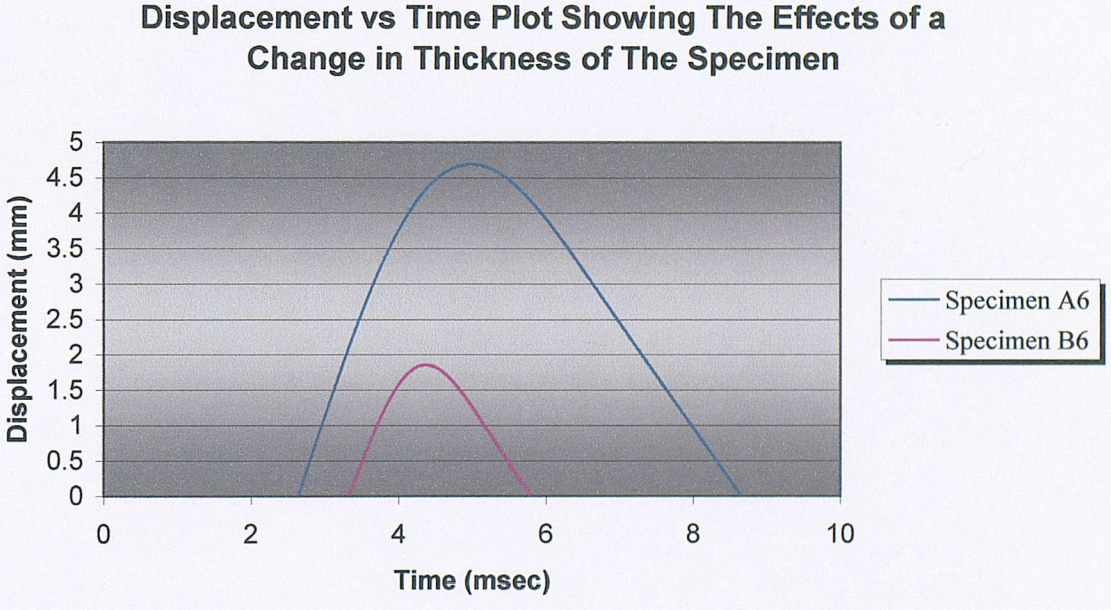


Figure 6.5: Displacement versus Time Plot showing the Difference in Behaviour due to a change in the Thickness (A: 4mm and B: 10mm) of the Laminates.

Figure 6.5 shows a comparison of the impact displacement that occurs in the two different laminates. The displacement is much higher in the thinner laminate than in the thicker one. This larger displacement, of the thin laminate, relates to the flexural response of the specimen. This explains why the impactor rebound velocity is lower in the thinner laminate even though the initial impact velocity was higher. The flexure absorbs impact energy and this has an effect on the amount of energy left to cause rebound and hence the rebound velocity. The rate at which the displacement increases to a peak value and decreases is similar and the displacement returns to zero in these curves showing that no permanent deformation occurs at the end of the impact event.

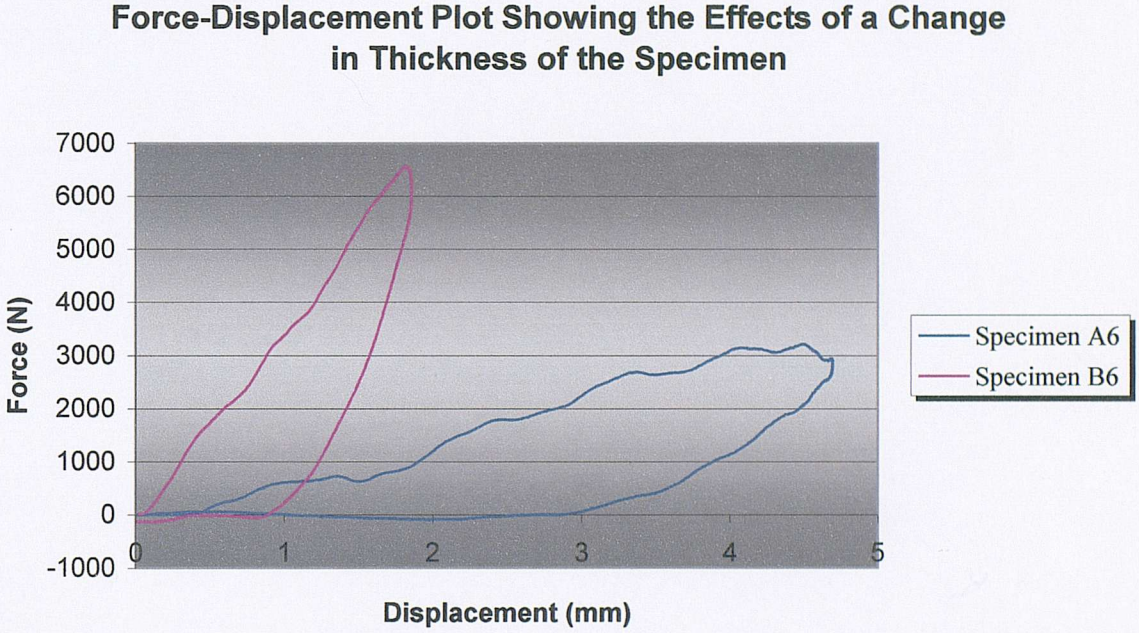


Figure 6.6: Force versus Displacement Plot showing the Difference in Behaviour due to a change in the Thickness (A: 4mm and B: 10mm) of the Laminate.

Figure 6.6 gives a comparison of the two Force versus Displacement curves of specimens of different stiffness due to their different thickness. The area under the curves and their shape are different. Also there are more oscillations on the A6 curve. Comparing the two initial slopes of the curves it can be see that, the thicker laminate has the higher stiffness. Now comparing the entire change of Force with Displacement it can be seen that the thicker laminate has the higher peak contact force and a corresponding higher overall stiffness. The B6 specimen that exhibits the higher

peak contact force shows the lower level of displacement. As a result, the higher stiffness laminate exhibits a higher peak contact force and a lower level of maximum displacement.

Length and Width Effects

The same type of approach as above will be used to investigate how a change in length and width would change the behaviour during the impact event. However, firstly, the different samples need to be differentiated in a manner in which this investigation can be explained. Specimen types B, C and D all have a length of 150mm, with widths 80mm, 60mm and 40mm respectively. Whilst specimen types E, F and G all have a length of 120mm with widths of 80mm, 60mm and 40mm respectively. Therefore, each set of specimen types (B, C, D and E, F, G) can be used to show the effects of a change in width, whilst specimen type pairs B & E, C & F and D & G can be used to show what happens when the length is changed.

Figures 6.7 and *6.8* show how a change in the length and width affects the behaviour of the contact force during the impact event.

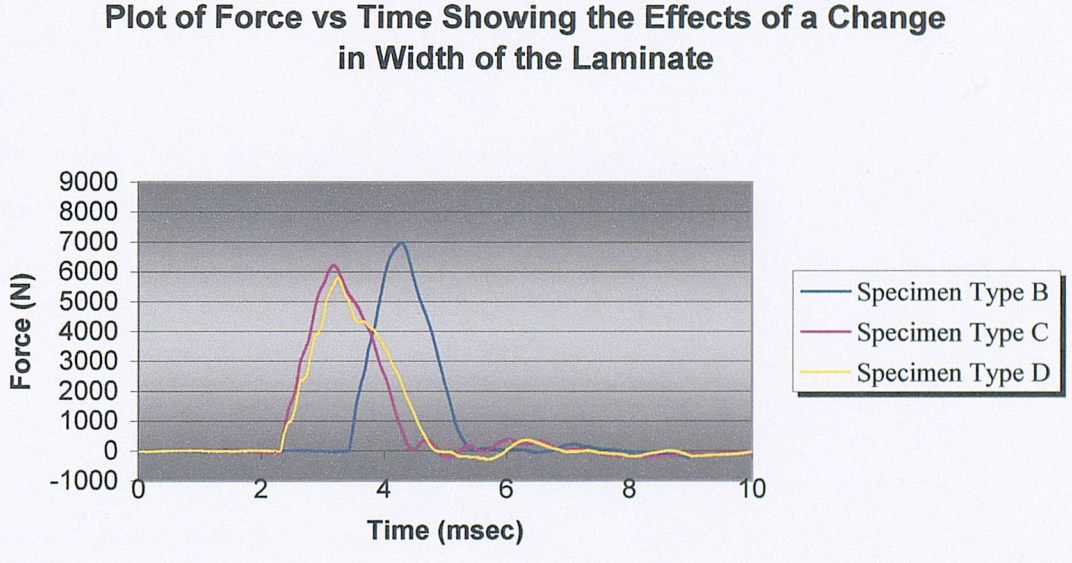


Figure 6.7: Plot of Force versus Time for Specimen Types B, C, and D all of 150mm Length but having widths of 80mm, 60mm and 40mm respectively.

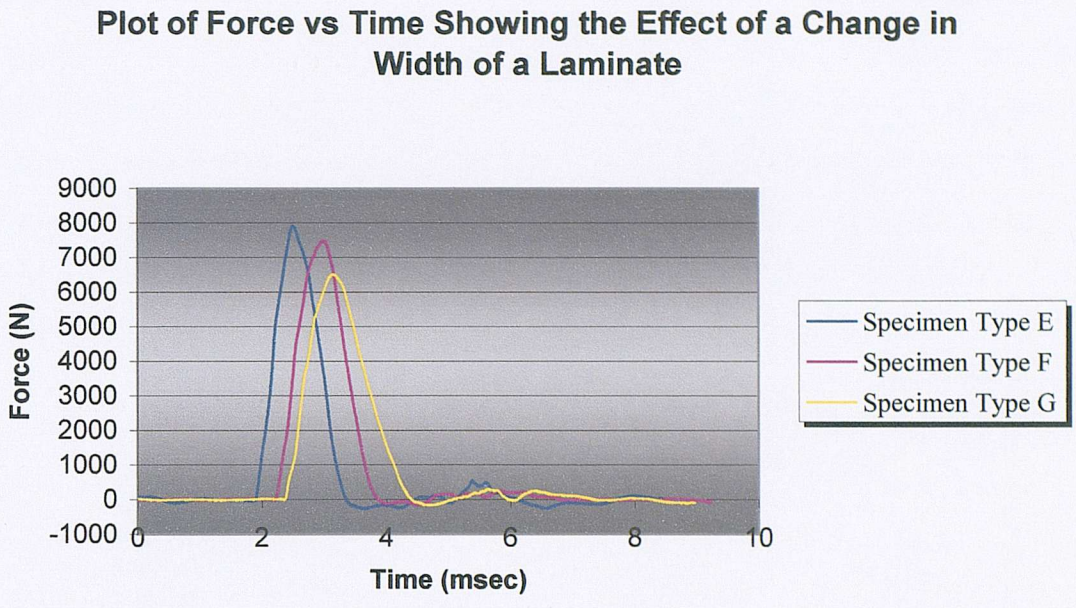


Figure 6.8: Plot of Force versus Time for Specimens Types E, F and G all of 120mm Length but having widths of 80mm, 60mm and 40mm respectively.

First of all the peak contact force decreases with decreasing specimen width, this can be seen in both *Figures 6.7* and *6.8*. Comparing the two plots it can also be seen that the laminates with the shorter length have a higher peak contact force when compared to the corresponding specimen with the same width. For example Specimen Type E (length 120mm) is the same width and thickness as Specimen B (length 150 mm), but its shorter length results in a greater peak contact force.

The period of the peak, which is a direct measurement of the duration of the impact, shows an increase with a decrease in the width of the specimen. When comparing the curves in *Figures 6.7* and *6.8* it can also be seen that a decrease in length results in a shorter period, and therefore causes shorter impact duration.

Figure 6.9 shows how the velocity profile of the impactor changes with these changes in length and width. The initial contact velocity is consistent in this case. The slopes of these plots show that the rate at which rate at which the velocity decreases during contact is roughly the same in all 6 specimen types. The rebound velocity is always a good indication of the level of impact energy absorbed by the specimen, as the more energy absorbed the less energy is available to cause a rebound of the impactor and

hence a lower rebound velocity would be achieved. Here we see the rebound velocity being consistent for the specimen types with a length of 150mm. However when the length drops to 120mm, a variation in the rebound velocity can be seen. The rebound velocity increases with decreasing specimen width, indicating that the narrower the specimen the less energy is absorbed during the impact event. The fact that there is no significant change in rebound velocity in the longer specimens indicates that there may be a threshold length at which this variation with width begins to occur.

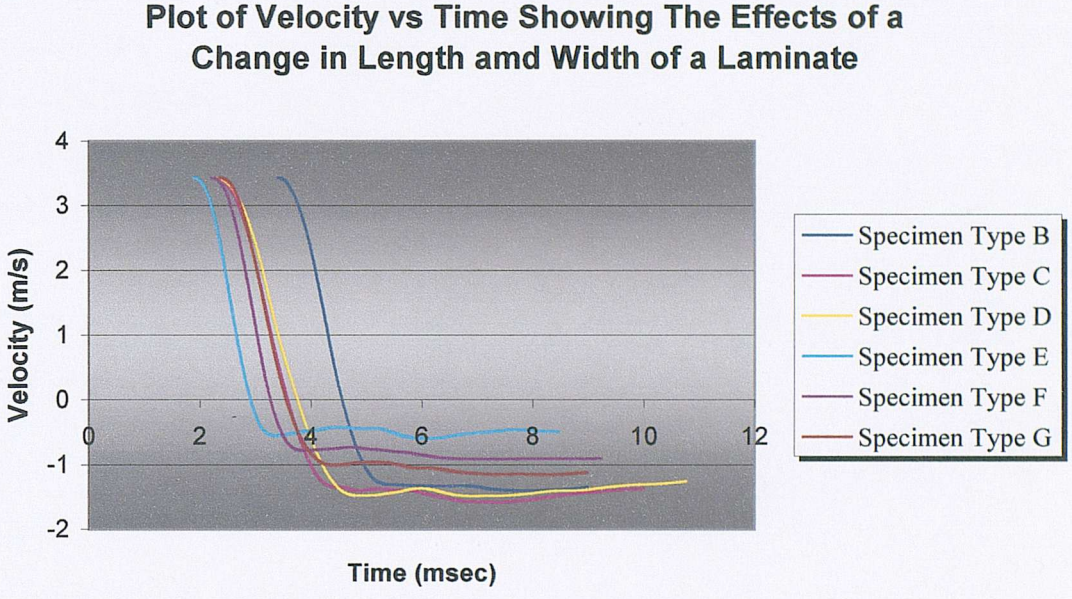


Figure 6.9: Plot showing the changes in the Velocity Profile of the Impactor due to a change in Length (B, C & D: 150mm and E, F & G: 120mm) and Width (B & E: 80mm, C & F: 60mm and D & G: 40mm) of a Laminate.

Looking and comparing at the levels of displacement that are shown in *Figure 6.10*, it can be seen that when comparing the two sets of different length specimens that the longer specimens (B, C and D) show a greater displacement when compared with the shorter specimens (E, F and G). Now comparing the behaviour of the displacement of the longer specimens, it can be seen that a decrease in the width of the specimen causes a increase in the level of displacement that occurs due to the impact event. With the shorter specimen types, type F (60mm width) shows a higher level of displacement than type E (80mm width), which is in agrees with what is seen in the longer specimens. However type G (40mm width) shows a lower level of displacement, in fact it shows the lowest level of displacement when compared to all

the specimen types. Now looking at the rate at which the displacement decreases, it seems to be roughly the same for the group of longer specimen types, but it changes for the shorter specimens. There is a decrease in the rate at which the displacement decreases with decreasing length of specimen.

Finally, studying the Force versus Displacement variation in *Figure 6.11*, it can be seen that the initial slope of the plots are each slightly different due to the effect of length and width on specimen stiffness. As shown previously, the peak contact force increases with increasing width of specimen and increases with decreasing length of specimen. The actual stiffness of each specimen (see *Figure 6.11*) shows that the higher the peak contact force the higher the corresponding stiffness. Studying the plots for specimen types B and G, it is clear that on loading their behaviour is almost identical with both reaching a similar peak contact force. However, the difference in their aspect ratios gives different behaviour when the specimens are unloaded and when the impactor rebounds from the specimen.

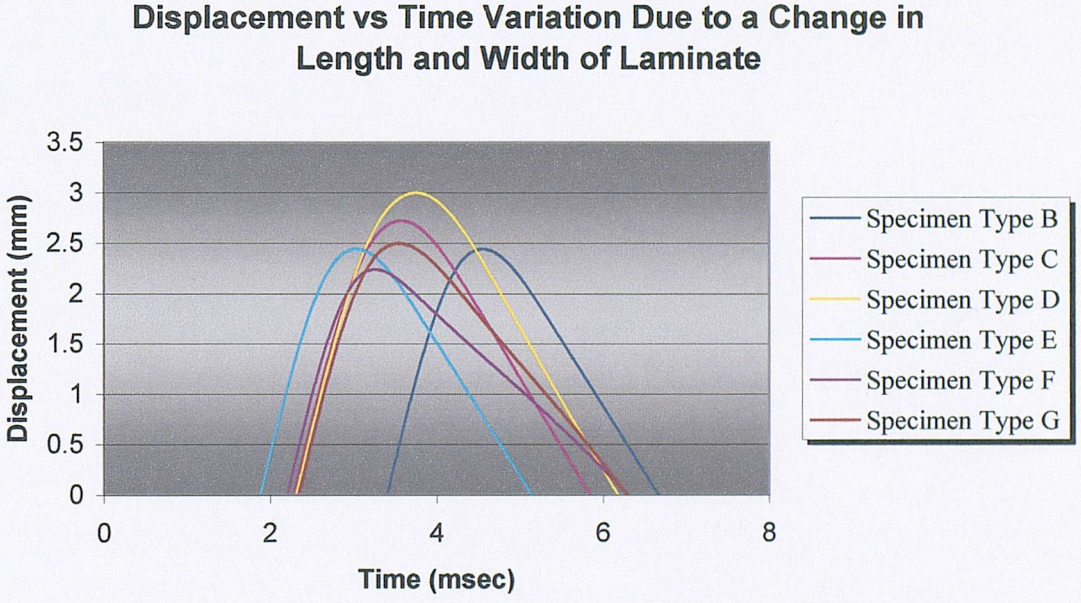


Figure 6.10: Plot showing the change in the Displacement of the Laminate due to a change in Length (B, C & D: 150mm and E, F & G: 120mm) and Width (B & E: 80mm, C & F: 60mm and D & G: 40mm) of a Laminate.

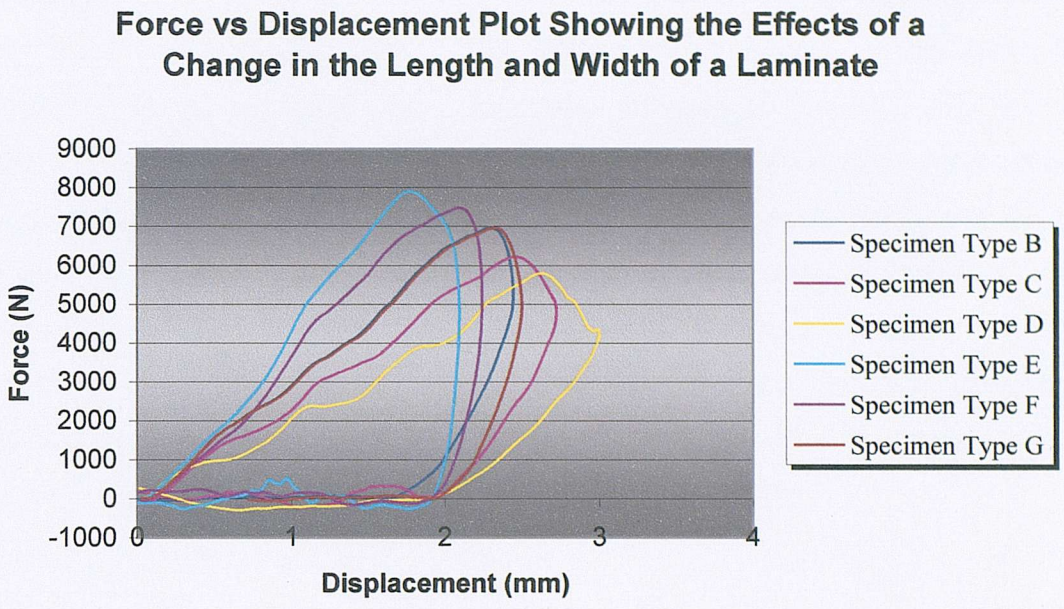


Figure 6.11: Plot Showing the Variation in Force versus Displacement Relationship as an effect of a change in Length (B, C & D: 150mm and E, F & G: 120mm) and Width (B & E: 80mm, C & F: 60mm and D & G: 40mm) of a Laminate.

There is a slightly larger maximum displacement in Specimen G and hence its relaxation takes longer than that of Specimen B.

There is also a relationship that can be seen between the peak contact force and the extent of displacement of the impacted specimen. The higher the peak contact force, then, the lower the level of maximum displacement that occurs. The stiffest of these specimen types studied in this research is E (80x120x10 mm) and the least stiff is D (40x150x10 mm).

6.3.1.1.2 Higher Drop Impacts

In the second stage of this investigation a higher drop was used in order to achieve damage in the specimens and to compare the behaviour of these impacts with that of the lower drop height impacts. The purpose of this was to show the effects of the introduction of damage on the behaviour of the contact force, velocity profile and level of displacement that occurs.

Figure 6.12 shows a plot of Contact Force versus Time for all the samples impacted from a drop of 1.5m using the 1.55kg hemi-spherical impactor. Generally, the increase in drop height raises the peak contact force in all the different specimen types. It can be seen here that the same variations can be seen as before when changing the dimensions of the laminate being impacted. An increase in thickness causes an increase in peak contact force and a decrease in contact duration. The rate at which the contact force increases is also increased. An increase in width gives an increase in peak contact force and a decrease in the contact duration. Finally, a decrease in length gives an increase in peak contact force and a decrease in contact duration.

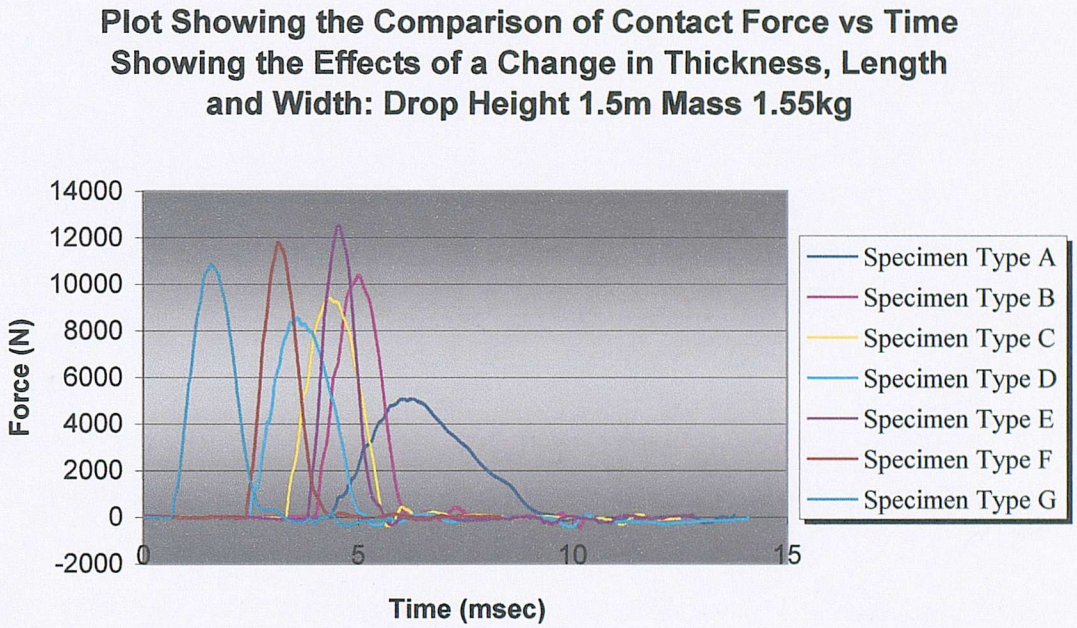


Figure 6.12: Plots of Force versus Time for all specimen types impacted from a drop height of 1.5 m and an Impactor Mass of 1.55kg showing the change in the Thickness (A: 4mm & B: 10mm), Length (B, C & D: 150mm and E, F & G: 120mm) and Width (B & E: 80mm, C & F: 60mm and D & G: 40mm) of the Laminate.

From these plots the stiffness for each of the panels can also be estimated by taking the gradient of the slope of the curve. These values can be compared to those calculated using Equation *4.2*. *Table 6.2* shows a comparison of the calculated stiffness values both from theory and the experimental data.

The figures in *Table 6.2* show that using the gradient of the Force-Displacement graph can produce very accurate values for stiffness in comparison for the figures calculated from theory. However it can also be seen that when the width of the specimen increases the inaccuracy of the experimental data increases. The measured stiffness in Sample A is much greater than the calculated theoretical value, whilst the calculated value for Samples B and E are both under the theoretical values. These inaccuracies maybe due to oscillations that occur in the experimental data and the consequent smoothing that is required for the data to be analysed. The inaccuracy in the values for Specimen A may also be an effect of the difference in th ethickness of the specimen. It can also be seen from the figures in the table as well as *Figure 6.12* that the stiffness of the samples increases with decreasing width of specimen.

Specimen type	**A**	**B**	**C**	**D**	**E**	**F**	**G**
t (mm)	4	10	10	10	10	10	10
w (mm)	80	80	60	40	80	60	40
l (mm)	120	120	120	120	120	120	120
Calculated k (MN/m)	0.850	13.27	9.96	6.64	25.93	19.44	12.96
Experimental k (MN/m)	2.8	10.86	9.41	6.93	17.96	16.8	12.32

Table 6.2: Table showing a comparison of the calculated and measured composite stiffness.

Figure 6.13 shows the velocity profiles of the 1.55kg impactor from a drop height of 1.5m for the impact of all the different specimen types. Firstly, the thin sample can be seen to have the lowest rate of velocity decrease during the impact event and also has the highest rebound velocity of all the specimen types. The slopes of these plots indicate that there is an increase in the rate of velocity decrease with an increase in the width of the laminate. For the longer specimen types (B, C & D: length 150mm), the rebound velocity is roughly the same showing that the energy absorbing characteristics do not change much with a change in width. However when the

velocity profiles for the shorter samples (E, F & G: length 120mm) are studied, an increase in rebound velocity is shown as the width of the laminate decreases (E to G). This agrees with the observations from the velocity profiles for the impacts from the lower drop heights, showing that there is an indication of a threshold length of specimen at which the variation of width notably causes a change in the energy absorption characteristics of the laminate (see later in **Chapter 6**).

Interestingly, the variation in impact behaviour is similar for the high drops to that observed in the lower drop height impacts. The thinnest specimen type shows the greatest level of displacement, which coincides with the samples greater ability to flex when impacted. The displacement behaviour of the thicker laminates show that there is an increase in the level of displacement with a decrease in the width of the specimen. A decrease in length causes a decrease in displacement, which is explained by the fact that the shorter laminates are less flexible. The rate at which the displacement reduces after a peak value has been reached also decreases with the length of the sample.

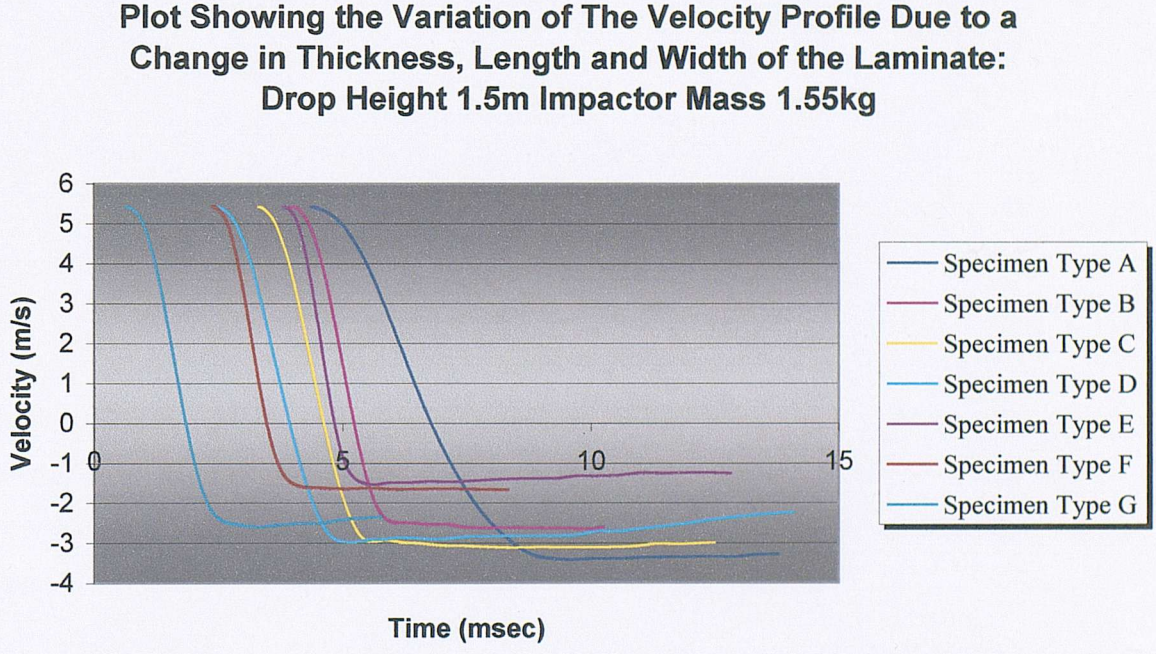


Figure 6.13: Plots of Velocity versus Time showing the Variation of the impactor velocity profile due to a change in the Thickness (A: 4mm & B: 10mm), Length (B, C & D: 150mm and E, F & G: 120mm) and Width (B & E: 80mm, C & F: 60mm and D & G: 40mm) of the Laminate.

The variation of the Force versus Displacement plots for the different specimen types for these drop conditions is shown in *Figure 6.15*. The initial contact stiffness and overall stiffness of the thin (A: 4mm) laminate is the lowest of all the specimen types. For all the thicker (B to G) specimen types the contact stiffness should be similar with the overall stiffness of these panels reducing with decrease in width and increase in length.

These findings similar as those found from the impact data for the lower drop height impacts as to the general shape and form of the plotted data. Hence, the main differences relate to the change in magnitude of the impact forces.

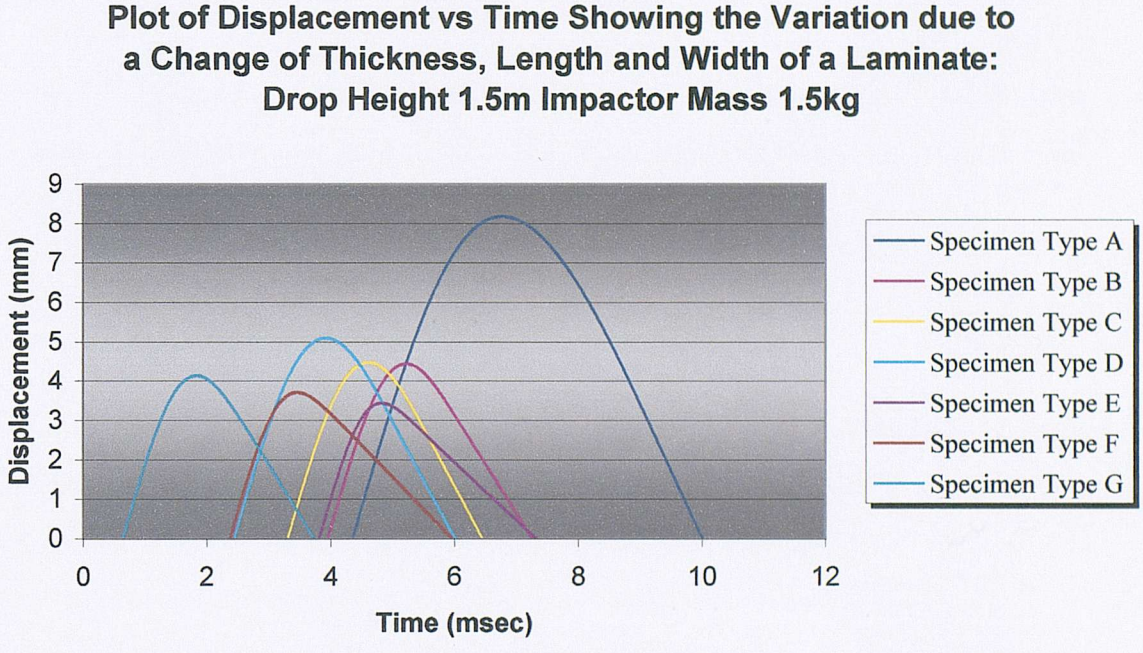


Figure 6.14: Plot of Displacement versus Time Showing the Variation due to a Change in Thickness (A: 4mm & B: 10mm), Length (B, C & D: 150mm and E, F & G: 120mm) and Width (B & E: 80mm, C & F: 60mm and D & G: 40mm) of the Laminate.

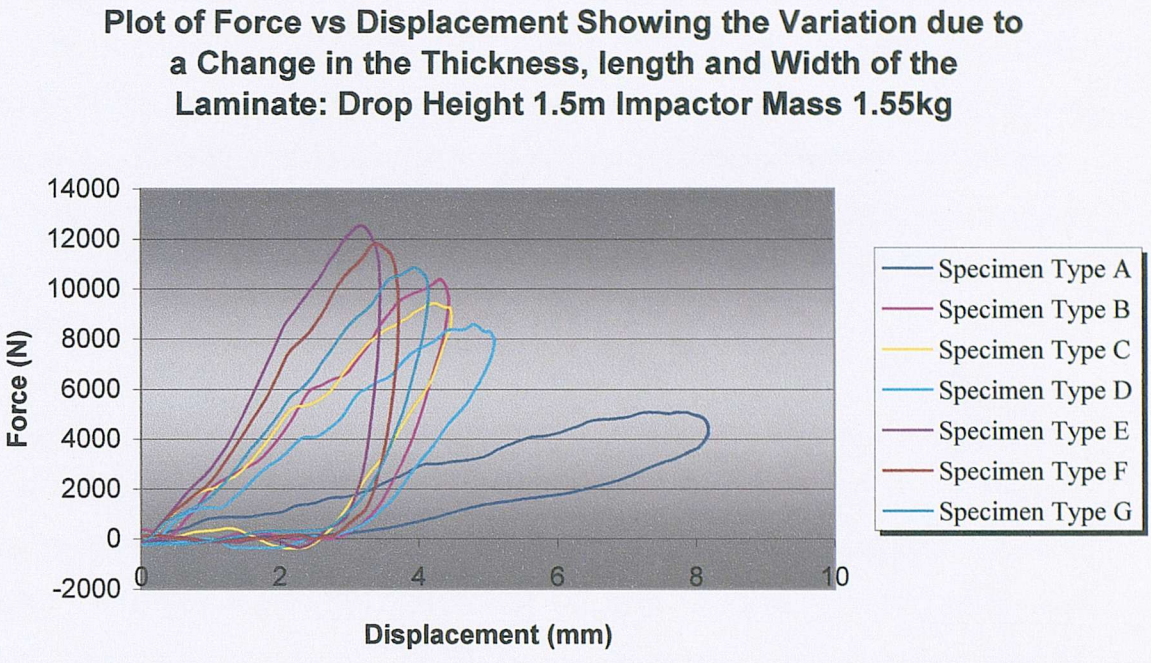


Figure 6.15: Plot of Force- Displacement Showing the Variation in Behaviour due to a change in Thickness , Length (B, C & D: 150mm and E, F & G: 120mm) and Width (B & E: 80mm, C & F: 60mm and D & G: 40mm) of the Laminate.

6.3.1.1.3 Discussion

The main findings in these sets of test data are that they confirm the specimen dimensions significantly influence the impact behaviour of the specimens. However, there can be a threshold length beyond which due to changing flexure behaviour of the specimen, the impact energy absorbed is affected. At both drop heights used (0.5 and 1.5 m), the rebound velocity for the longer specimens (B, C & D: 150mm) shows little change with specimen width indicating that the level of energy absorbed does not vary with specimen width. However, when the length of the specimen is decreased (E, F & G: 120 mm) a variation in the rebound velocity is observed with specimen width. However, the behaviour of the Force versus Time plots (*Figures 6.7*, *6.8* and *6.12*) or the Force versus Displacement plots (*Figures 6.11* and *6.15*) have no significant changes that would indicate any type of damage being inflicted. If damage did occur it would cause a loss of stiffness and would be shown as a distinct step in the loading part of the relevant curve. Therefore, there must be another mechanism that occurs which absorbs energy which results in a change in the rebound velocity.

This indicates that there are optimum conditions of impact when specimens of different shape absorb the maximum energy from given impacts. The contact conditions could vary as the specimen dynamically responds to the initial impact. Also, there could be subsequent contact interference between impactor and specimen, frictional losses at the grip points holding the specimen as well as vibrational and other flexural energy retained in the specimen after the impactor has separated from the specimen.

As mentioned above a change in the rebound velocity of the impactor is an indication of the level of energy that is absorbed by the impact event. The lower the rebound velocity the more energy has been absorbed. The main energy absorbing mechanism should be, in these cases where no damage has been initiated, related to the level of displacement that occurs, as flexure as discussed in previous chapters is a good energy absorbing mechanism. It is interesting to note that when *Figures 6.13* and *6.14* are analysed together, they show that the more displacement that occurs the greater the rebound velocity of the impactor. A similar type of effect occurs at the lower drop height (see *Figure 6.9* and *6.10*).

6.3.1.2 High Energy Drops: Variations in Induced Damage due to Specimen Dimension Changes

High-energy drops were used to ensure that damage would be induced in the specimens so the effects on damage due to a change in specimen dimension could be investigated. The high energy drops were achieved using a 5.4 kg mass, which was dropped from a height of 1m and this resulted in an impact with 52.92J of energy. The level of damage was assessed using Time Of Flight C-Scan. This form of C-Scanning allowed an indication of the depth of the damage that is present. Damage at different levels of the thickness is shown in a different colour on the resulting image. The behaviour was assessed using the Force-Time Data recorded by the experimental equipment and the double integration method as described in the previous section.

6.3.1.2.1 The Effects of a Change in Thickness

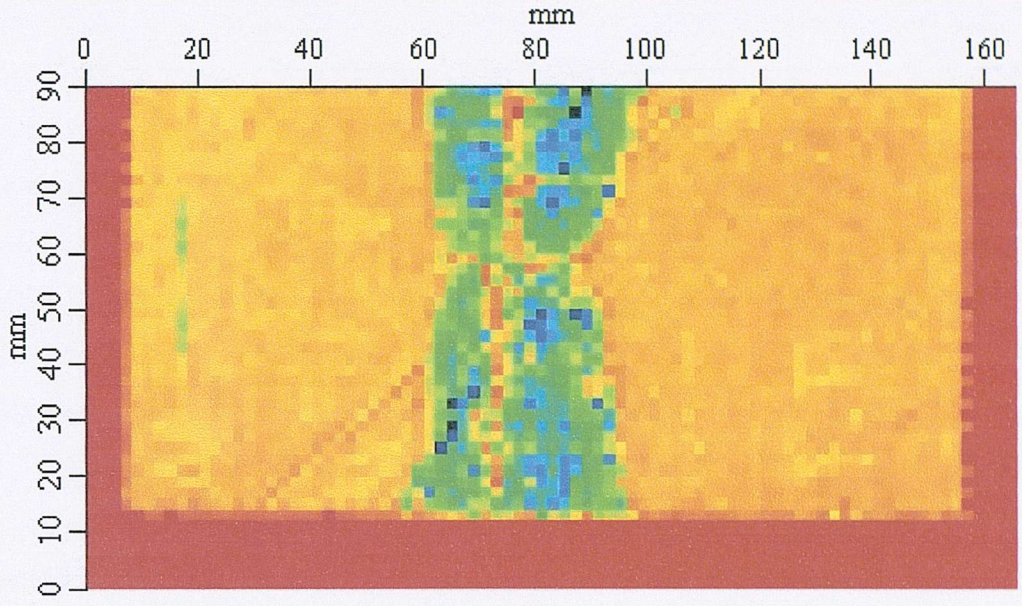
Firstly the effect that changing the thickness of the specimen has on the damage that is induced was studied. A series of Specimen Type A and B samples were impacted using the high-energy drop conditions.

After impact, the difference in the damage induced can be seen with the naked eye. A visible crack was observed on the impacted surface of the Type A specimens (4mm thickness) stretching across the width of the specimen originating from the impact point itself. Type B specimens (10mm thick) had no visible signs of external damage after impact. However, the level of internal damage could not be assessed in this way and hence the Time of Flight C-Scan images were used to see if internal damage had occurred and if so how this internal damage differed between the two different thicknesses.

Time of Flight C-Scanning

Figures 6.16 and *6.17* show the C-Scan images of damage induced in the two different specimen types (A and B). The differences in the damage caused in these impacts can be clearly assessed.

As observed with the naked eye, there is extensive damage in the Type A specimen (4mm thickness) stretching across the width of the specimen and this covers around 40mm of the length of the specimen (see *Figure 6.16*). When comparing this damage to that sustained by the thicker Type B specimen (10mm thickness), the damage is mostly confined to the centre of the specimen (See *Figure 6.17*). Only a nominal amount of damage can be seen directly under the impact site. Therefore, it is clear that a change in thickness can have a dramatic effect on the level of damage that is sustained at these impact energies. The thicker specimen will to a certain degree have a greater stiffness in comparison with the thinner specimen and hence will in theory be able to withstand higher energy impacts without deforming and sustaining any damage and this has been confirmed.



Figures 6.16: Time of Flight C-Scan Image of damage caused by High Energy Impact on Specimen Type A (4mm thickness). The specimen's dimensions are 80 by 150 mm

.

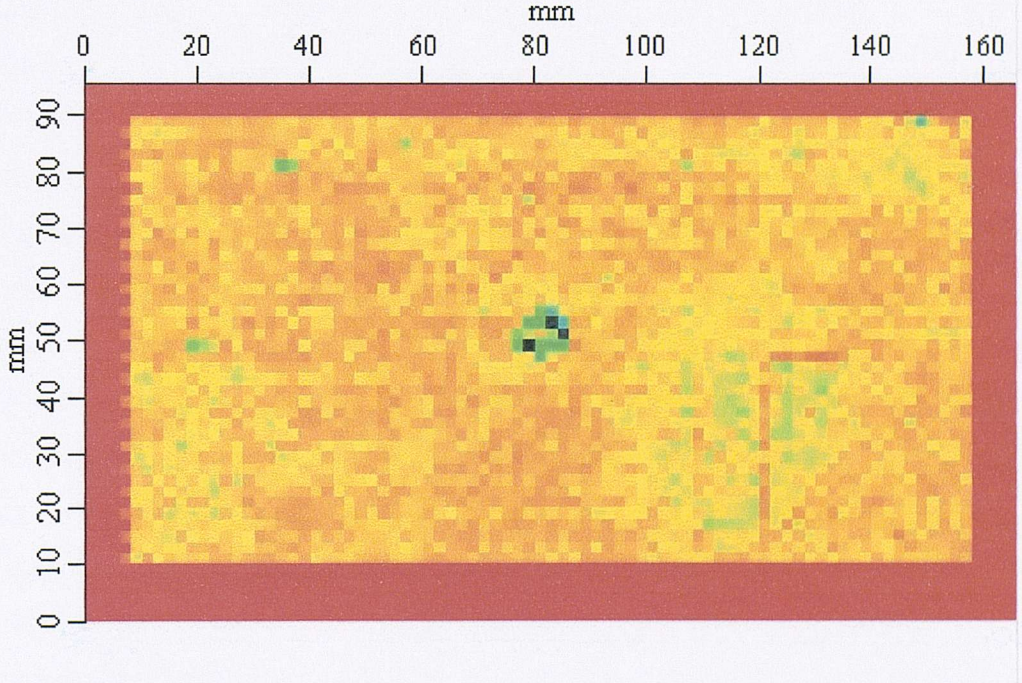


Figure 6.17: Time of Flight C-Scan Image of Damage induced by a High Energy Impact on Specimen Type B (10mm thickness). The specimen's dimensions are 80 by 150 mm.

However, the damage that has occurred in the thinner sample has not shown up, as would be expected, in a flower pattern caused by peanut-shaped delaminations being observed between different plies. A possible explanation for this would be the specimen has flexed under these impact energies, which caused cracking across the width of the specimen to be the dominant damage that is induced. The delamination area that can be seen shows signs of peanut shaped behaviour originating form the impact site. The flexing that is predicted to have occurred seems to have been caused by the delamination damage growing preferentially across the specimen with bending of the specimen hence causing the damage that is seen in *Figure 6.16* where the damage is concentrated across the specimen rather than growing along the specimen length

Force-Time Data

The C-Scan analysis of the damage induced in the specimens with two different thickness showed there to be a distinct difference caused by the change in thickness. The Force-Time data collected from these tests was also studied to see what effects the difference in damage levels have on them, as well as to show how the introduction of damage can affect the Force-Time behaviour.

Figure 6.18 shows a comparison of the Force-Time behaviour between the two different thicknesses (A: 4mm and B: 10mm). A difference in behaviour that can be observed are the peak force values that relate to the different sicknesses of the material (disregarding the initial fluctuation in the force time behaviour shown in *Figure 6.18*). Also, the Force-Time Behaviour is notably different. The thicker Type B specimen shows a clean trace where the force increases steadily to a peak and then decreases steadily from that peak value back to zero. Whilst with the thinner specimen the actual impact event seems to be a lot longer with more erratic rises and falls during that time period presumably as the damage process fluctuates as it progresses through the specimen. The force rises to an initial peak and then generally decays with a succession of smaller peaks for the Type A specimen (thickness 4mm). The indications are that these force fluctuations relate to the failure of individual layers within the composite as they occur. Each drop in force from a peak failure

indicates a layer failing, hence the overall drop in stiffness, resulting in the force dropping as the specimen reloads without the failed layer.

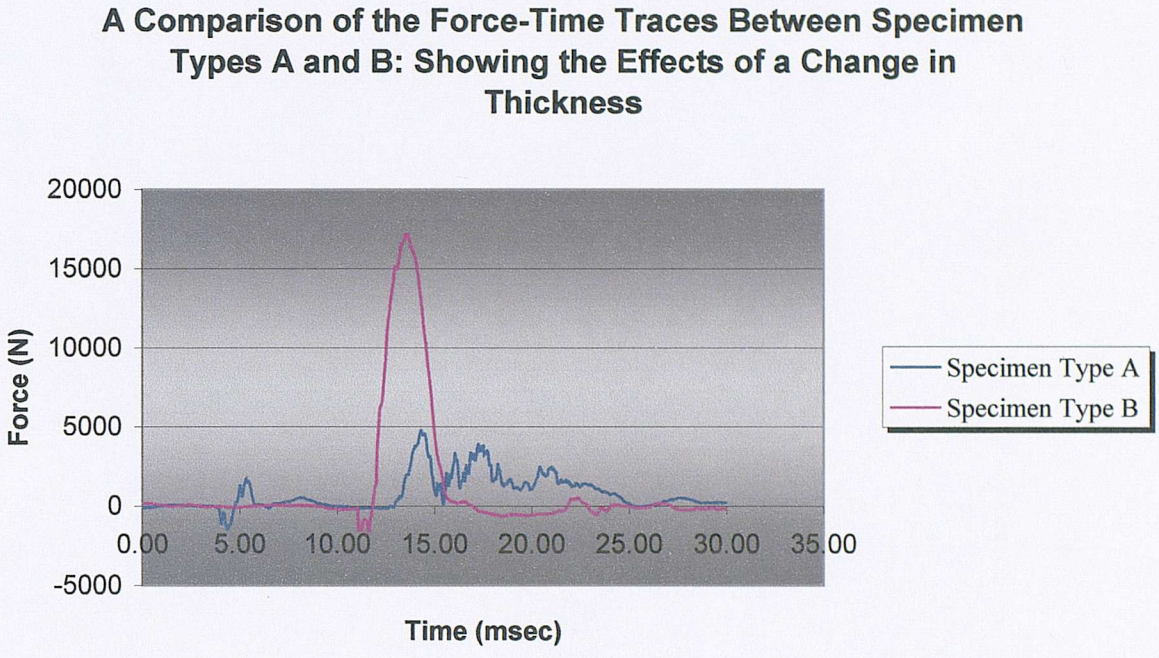


Figure 6.18: A Comparison of the Force-Time Behaviour between Specimen Type A (4mm Thickness) and Specimen Type B (10mm Thickness).

Figure 6.19 shows a comparison of the velocity profiles for these two types of specimen. For specimen Type B (10 mm thickness), the impactor velocity decreases quickly and passes through zero velocity to become negative as its motion is reversed. For specimen Type A, the fall off of the impactor velocity is slower and the greater inflicted damage deprives the specimen of recovery to attempt to repel the impactor. Also, there is a difference in the smoothness of the Velocity-Time curves. Specimen Type A shows three distinct points where the gradient changes, whilst Specimen Type B does not have these sudden gradient changes and the decrease in velocity is relatively smooth. The changes in gradient that occurs in the profile of Specimen Type A occur at the same time references as the peaks in the corresponding Force-Time trace and can therefore be attributed to the same cause, which is the failure of separate layers causing a loss in stiffness of the specimen.

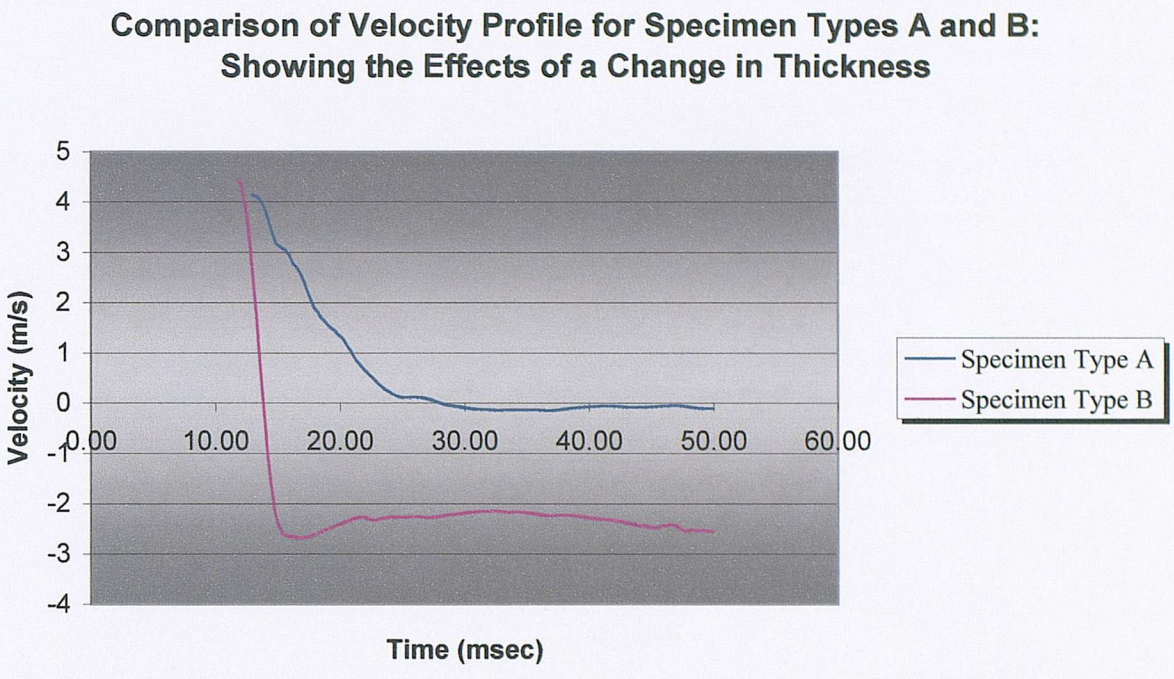


Figure 6.19: A Comparison of the Velocity Profile between Specimen Type A (4mm Thickness) and Specimen Type B (10mm Thickness).

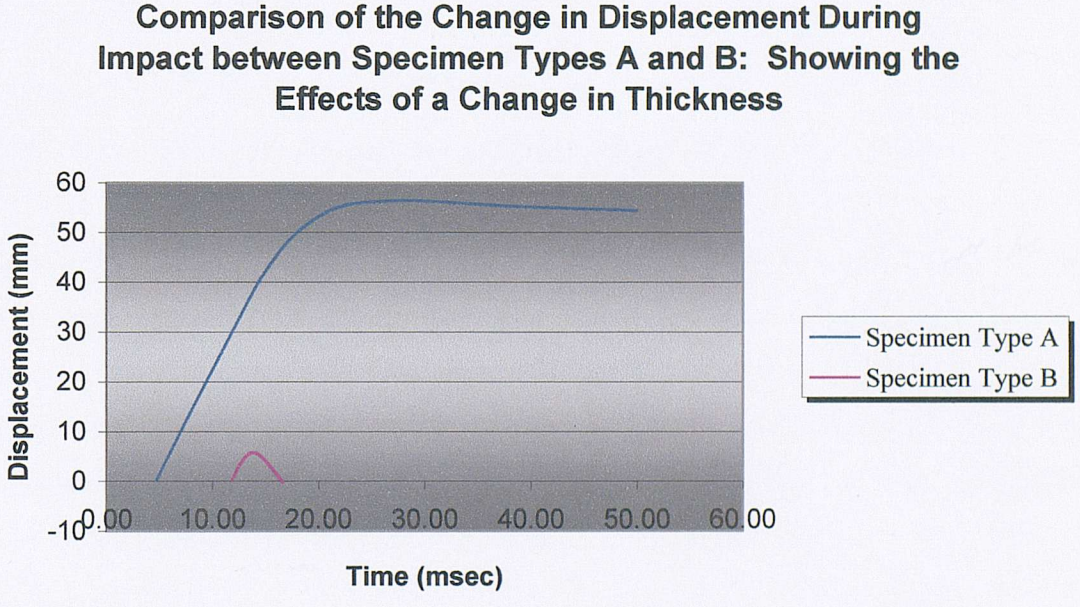


Figure 6.20: A Comparison of the Change in Displacement between Specimen Types A (4mm Thickness) and Specimen Type B (10mm Thickness).

The plots showing the displacement that occurs during the impact event are shown in *Figures 6.20* and *6.21*. The thicker specimen Type B has a small maximum

displacement and recovers its flat shape or nearly so. That is what would be expected as the thicker specimen would be less likely to be able to deform under load due to it's higher stiffness. The level of displacement is also a good indication of the length of the actual impact event. The thinner Type A specimen is deformed and damaged to the extent that it cannot recover its flat shape with the presence of the impactor.

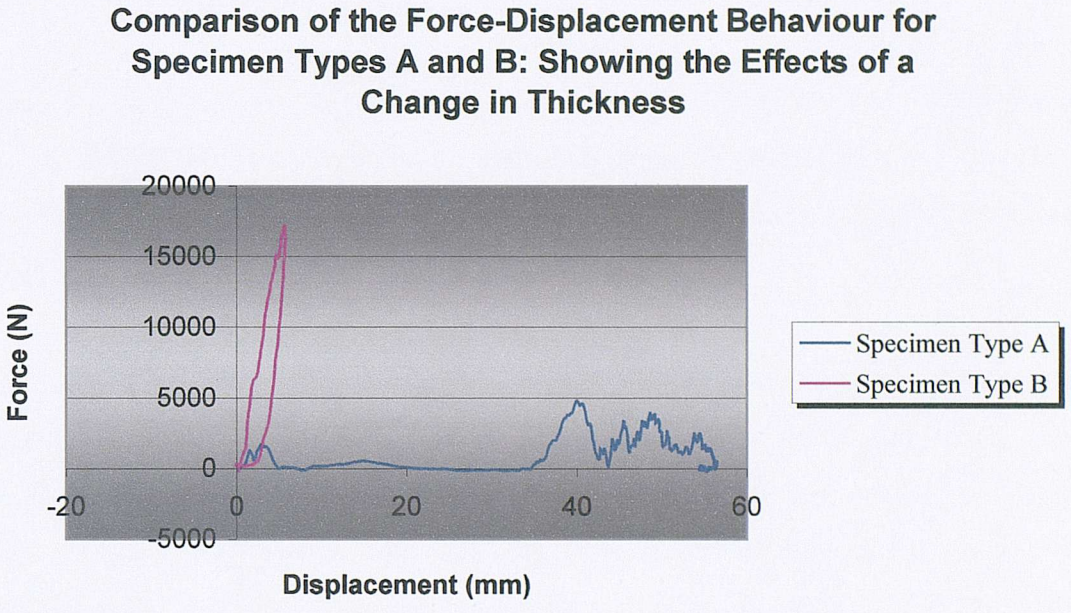


Figure 6.21: A Comparison of the Force-Displacement Behaviour between Specimen Type A (4mm Thickness) and Specimen Type B (10mm Thickness).

The initial stiffness (shown by the gradient of the loading section of the graph) of the two specimen types are very different. The thicker specimen is much stiffer than the thinner one as the gradient of the loading section of the graph indicates. For the thinner specimen, after the initial contact force peaks, the specimen offers little resistance until it is deformed to start the failure processes, then, several force peaks occur in succession as the different failure processes are initiated.

6.3.2.1.2 The Effects of a Change in Length and Width

The impacts of Specimen Types B, C, D, E, F and G will show the effects that a difference in length and width have on the damage that occurs. As mentioned previously Specimen Types B, C and D have a length of 150mm with varying widths

(80, 60 and 40 mm) whilst Specimen Types E, F and G have the same widths as B, C and D respectively but have a length of 120mm. Therefore, the effects of both changing width and length of a specimen on the damage that occurs can be investigated by comparing the damage and the Force-Time behaviour of these specimen types.

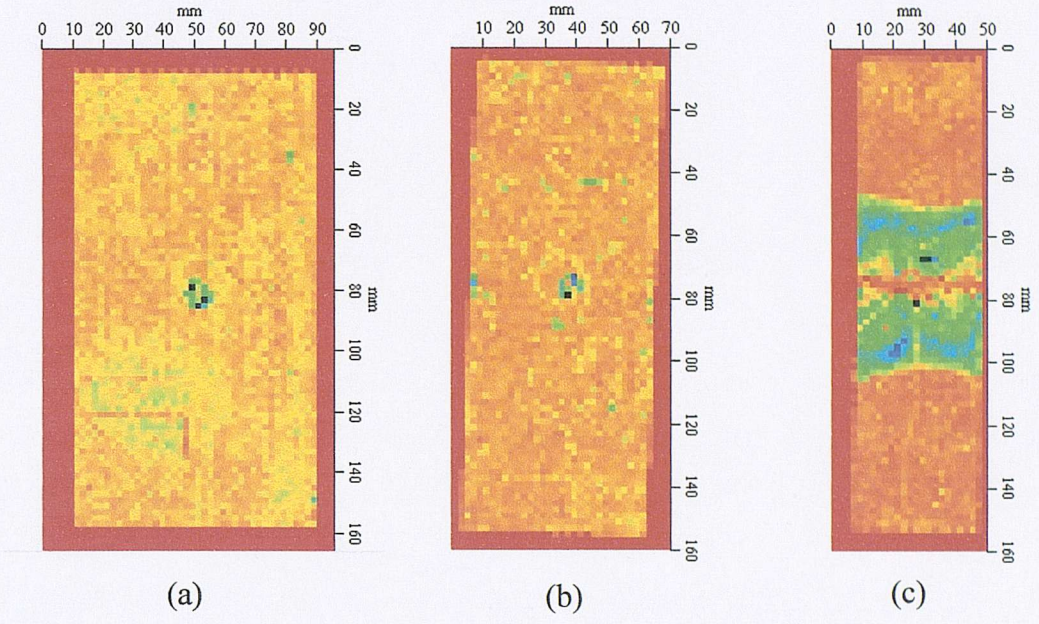
Time of Flight C-Scans

Firstly the damage that has been caused by these high-energy impacts will be shown via the Time of Flight C-Scan images that were taken. *Figure 6.22* typical images of Specimen Types B, C and D and *Figure 6.23* show images representing Specimen Types E, F and G.

When viewing the damage that is present in the 150mm long specimens (B,C and D) it can be seen that only a minimal damage is present in the 80mm and 60mm wide specimens (B and C), and this minimal damage is concentrated around the impact point. The narrowest of the three specimen types, D with a width of 40mm, shows a much larger damage area. The damage in D is concentrated around the centre line of the specimen and spans roughly 55mm of the specimen length. This damage looks to have originated from a crack at the centre of the specimen, which stretches across the specimen and looks to have originated from the impact point.

In comparison the specimens (E, F and G) with a length of 120mm show much greater damage areas. The total area of damage in this plane is roughly circular in shape in E and F with a diameter of 40mm. As with the 150mm specimens, there is no difference in the size of the damage in the specimens with 80mm and 60mm width. However looking at these two damage areas the typical peanut shaped delaminations can be observed in different layers, which are shown by the dark and light blue areas in the image. The 40mm wide specimen (G) shows damage, which as with the 150mm sample stretches across the width of the specimen. Another similarity is that this damage area also seems to show a crack going across the centre line, originating from the impact point. It can also be seen when the damage in Specimen Type G and D are compared (40mm width with a length of 120mm and 150mm respectively) the

main difference is the colour in which the damage is shown. This is an indication that the damage occurs at a different depth within the two specimens, again clearly indicating that the change in length of the specimen causes a clear change in the impact damage that occurs.



(a) (b) (c)

Figure 6.22: Time of Flight C-Scan images for Specimen Types with a length of 150mm: (a) Specimen Type B (80mm width); (b) Specimen Type C (60mm Width); (c) Specimen Type D (40mm Width).

Force-Time Data

With the information of the Time of Flight C-Scan images there is a notable difference in the impact damage that occurs when the length and width of the panel are changed. The Force-Time behaviour will now be considered for these impact conditions. This is to study the changes in behaviour, which occur due to changes in specimen dimensions. Also, how these changes can be related to the damage generated.

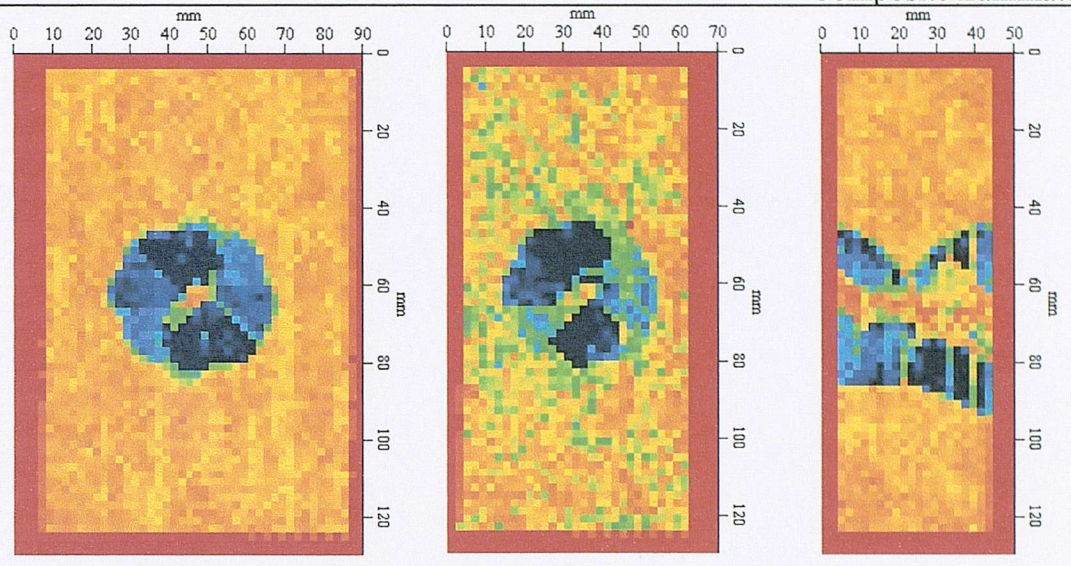


Figure 6.23: Time of Flight C-Scan image for Specimen Types with a length of 120mm: (a) Specimen Type E (80mm Width); (b) Specimen Type F (60mm Width); (c) Specimen Type G (40mm).

Figures 6.24 and *6.25* show the Force-Time Traces for the six different specimen types, they are grouped with respect to their specimen length. These correspond to the damage observed in *Figures 6.22* and *6.23*. The Force-Time plots are similar in shape but reach different heights depending upon the specimen width. For a width of specimen of 80 mm (Type B), the Force-Time curve has clean rise and fall but for widths 60mm and 40mm (Type C and D), the peaks are broken up by fluctuations in force. This is very noticeable for Specimen Type D where the damage extended across the full width of the specimen.

Figure 6.25 shows the Force-Time plots that can be related to the considerable damage revealed by the C-Scans in *Figure 6.23*. The peak of the Force-Time curves in *Figure 6.25* are broken up considerably by many fluctuations in force. For specimen Type G (width 40mm), these peak fluctuations are notably more extensive and this is for the specimen where the damage spread across its full width. Otherwise, the Force-Time curves have a similar shape. It is clear that the reduced height of specimens (120 mm) relates to more damage and more erratic Force-Time traces near their peak values.

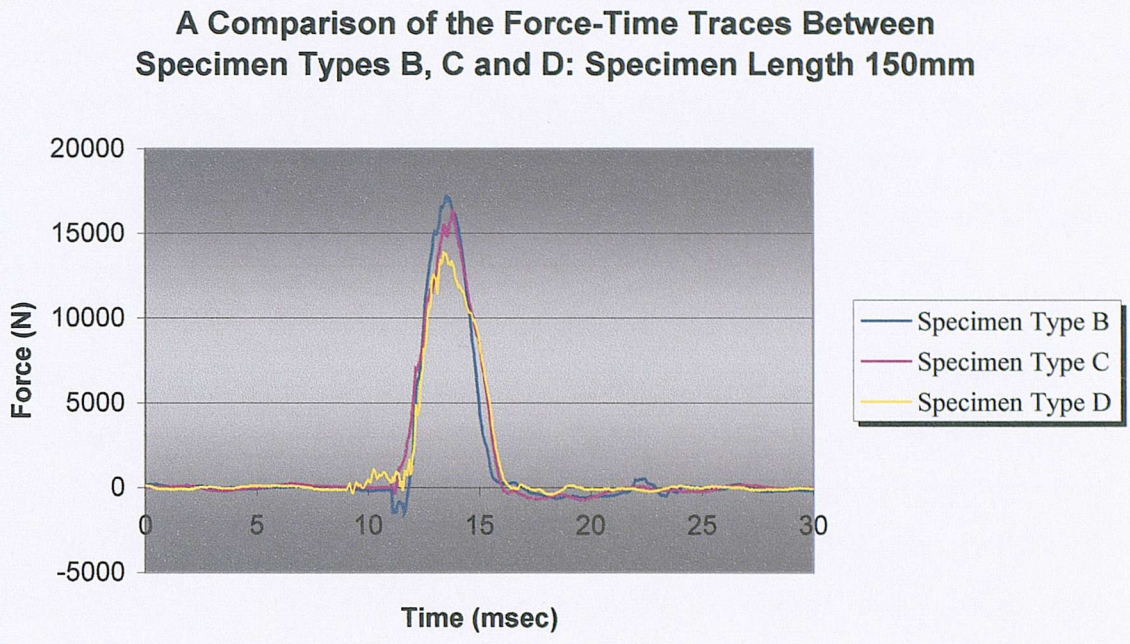


Figure 6.24: Chart showing a comparison of Force-Time Behaviour for Specimen Types B, C and D (Thickness: 10mm, Length: 150mm, Width: 80, 60 & 40mm respectively)

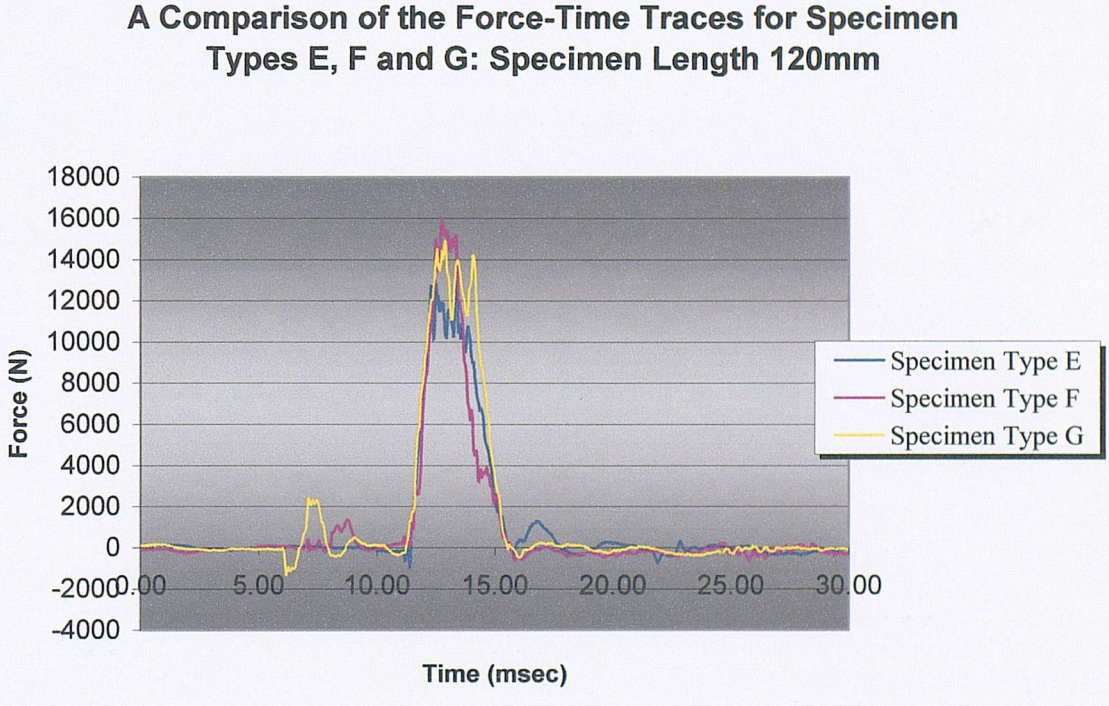


Figure 6.25: Chart Showing a Comparison of the Force-Time Behaviour for Specimen Types E, F and G (Thickness: 10mm, Length: 120mm, Width: 80, 60 & 40mm respectively).

Specimen Type G also shows an increase in Force prior to the main peak, this is common with Specimen Types A and D and the difference between the specimen after impact in these three types is that the top surface is broken and the damage spread right across the width of the specimen. Therefore, this difference in the Force-Time behaviour can confidently be attributed to the difference in the types of damage that are observed.

Comparing *Figures 6.24* and *6.25* with each other it can be seen that the main difference is the level of peak contact force, with specimens of a length of 150mm having a higher peak contact force. The period of the impacts were also longer for the specimens of 120mm in length and this can be attributed to the increase in the level of damage that occurs. There is also a difference in the smoothness of the curves, with the shorter specimens showing oscillations at the peak of the curve, whilst the longer specimens have much smoother peaks. This oscillating behaviour is related to the higher levels of damage that occur in these specimens.

Figures 6.26 and *6.27* show the velocity profiles, for specimen types with a length of 150mm and 120mm respectively. There are two main points that can be idenified by the velocity profiles. Firstly, the rate at which the velocity decreases and secondly, the level of energy that has been absorbed by the specimen that affects the impactor rebound velocity. The lower the rebound velocity the more energy that is absorbed by the specimen.

Figure 6.26 shows the decrease in the velocity of the impactor is similar in all three specimen types with a length of 150mm. Specimen Type D does, however, show a much slower decrease initially, which is due to the initial Force increase in the Force-Time trace. This behaviour is also shown by Specimen Types F and G, which also show the initial increase in the Force-Time Trace. The rebound velocities in the 150mm long specimens are all around about the same indicating that they all absorb roughly the same amount of impact energy. This also indicates the level of impact energy that is absorbed is enough to cause significant damage in the 40mm wide specimen but not in the 80mm and 60mm wide specimens. This indicates that a change in the more narrow a sample the more susceptible it is to impact damage in

comparison to wider samples and can incur greater degrees of damage when being impacted by the same levels of energy.

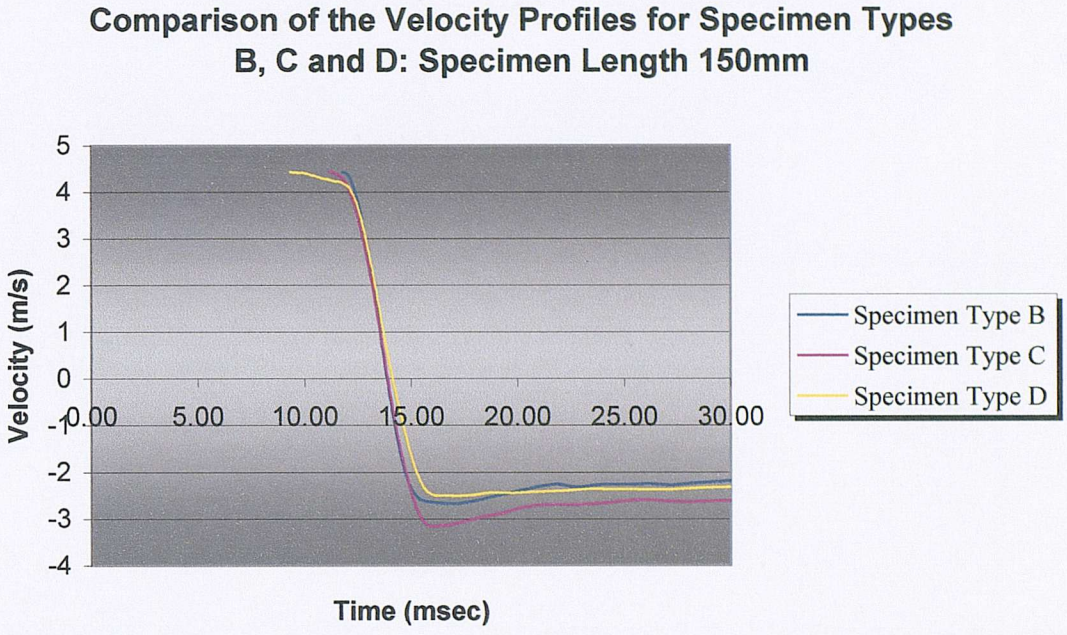


Figure 6.26: Chart Showing a Comparison of the Velocity Profile for Specimen Types B, C and D (Thickness: 10mm, Length: 150mm, Width: 80, 60 & 40mm respectively).

Figure 6.27 shows that the decrease in velocity is fairly constant for all three of the specimen widths. There is also the slow decrease that occurs prior to the main decrease in Specimen Types F and G and this corresponds to a small increase in the force levels in the corresponding Force-Time Traces. The rebound velocities in *Figure 6.27* show a lot of variation in comparison to the rebound velocities shown in *Figure 6.26*. The rebound velocities for the two wider specimens, Type E (80mm) and Type F (60mm) are nearly the same to start with but then differ. In comparison the profile for Specimen Type G shows a much higher rebound velocity, which indicates that less energy has been expended in the specimen during impact. When this is related to the C-Scan images, it can be shown that less energy is required to cause the damage across the width of the specimen than it is to cause the circular pattern of damage in the centre of the specimen in the wider specimens. This indicates that damage across the width is more readily formed in narrower specimen types. This is in agreement with the observations from *Figure 6.26* as more damage

is developed in the narrowest specimen (G: 40mm) by roughly the same level of energy absorbed as the two wider specimens.

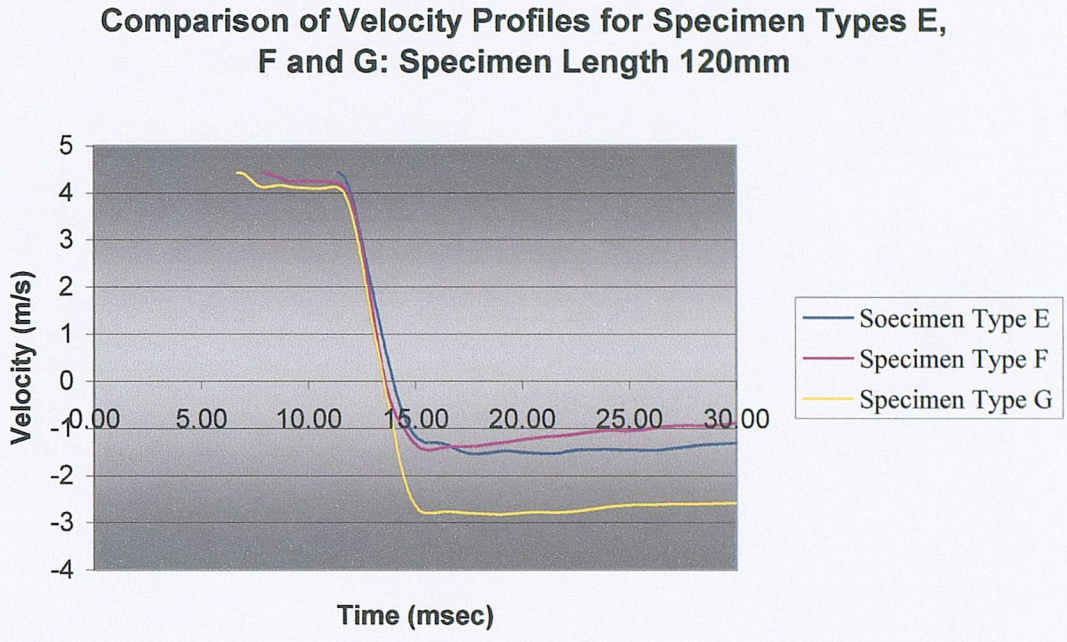


Figure 6.27: Chart Showing a Comparison of the Velocity Profiles for Specimen Types E, F and G (Thickness: 10mm, Length: 120mm, Width: 80, 60 & 40mm respectively).

When the velocity profiles are compared with regards to specimen length it can be seen that, with exception to Type G, the shorter specimens (120mm length) show much lower rebound velocities (roughly 1m/s slower, equivalent to 2.7J of impact energy) in comparison to the longer (150mm length) specimens. This would be not only due to the difference in dimensions as observed previously in this chapter but also due to the higher level of damage that has been caused. The rebound velocity in Specimen Type G is slightly higher than that of Specimen Type D showing that the damage caused in Type G requires less energy than that caused in Type D. The shape of the damage areas are relatively the same but their positioning with regards to the specimen are different, which is shown by the different colour of the highlighted damage areas. The damage in Specimen Type G occurs further away from the surface than that in Type D, which can be observed in the post impact specimen as the delamination that has reached the edge of the specimens occurs closer to the impact surface in Type D. However, the differences in rebound velocity suggest that less

energy is required to cause deep damage in the shorter specimen than it does to cause near surface damage in the longer specimen.

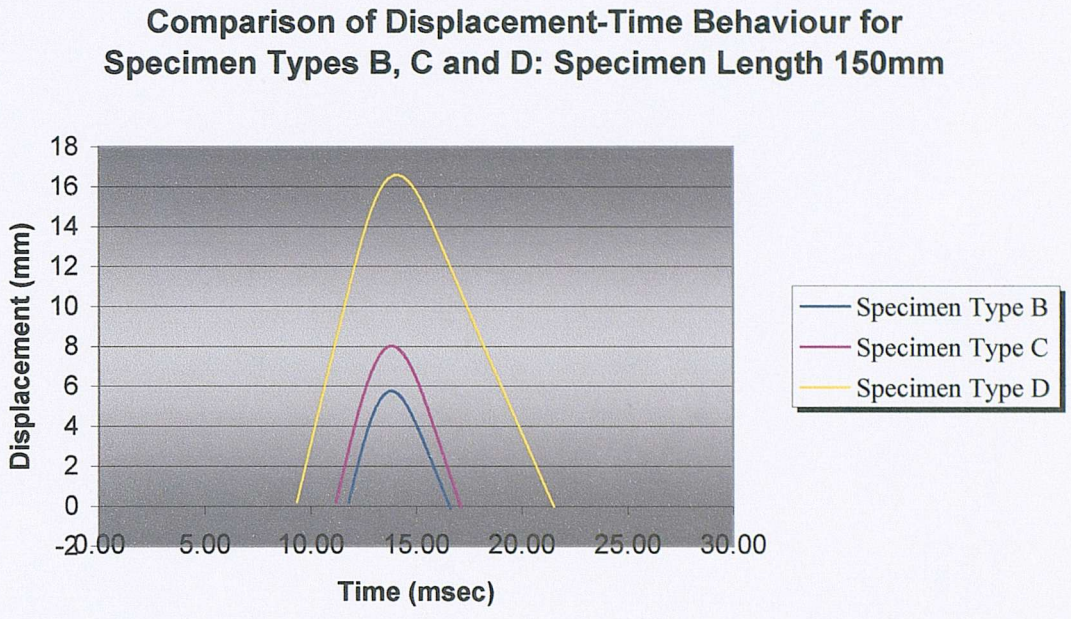


Figure 6.28: Chart Showing a Comparison of the Displacement-Time Behaviour for Specimen Types B, C and D (Thickness: 10mm, Length: 150mm, Width: 80, 60 & 40mm respectively).

The comparisons of the Displacement-Time profiles are shown in *Figures 6.28* and *6.29*. Firstly what can be seen is that with both lengths of specimen the peak displacement value increases with decreasing specimen width, which was shown in the previous sections of this chapter when the behaviour of the specimen under impact were assessed. However, in these cases where damage is caused by the impacts the level of displacement increases dramatically when more damage is present in the specimen. This is shown in *Figure 6.28* where the increase in displacement between the 80mm wide (Type B) specimen and the 60mm wide (Type C) specimen is 2.5mm as would be expected from the previous experiments to occur when the width is decreased. The increase in displacement caused by higher level of damage occurs in the 40mm wide (Type D) specimen results in a much greater increase in displacement (8.5mm) than would be expected by just decreasing the width. Therefore, this large increase in displacement can be attributed to more damage in the specimen.

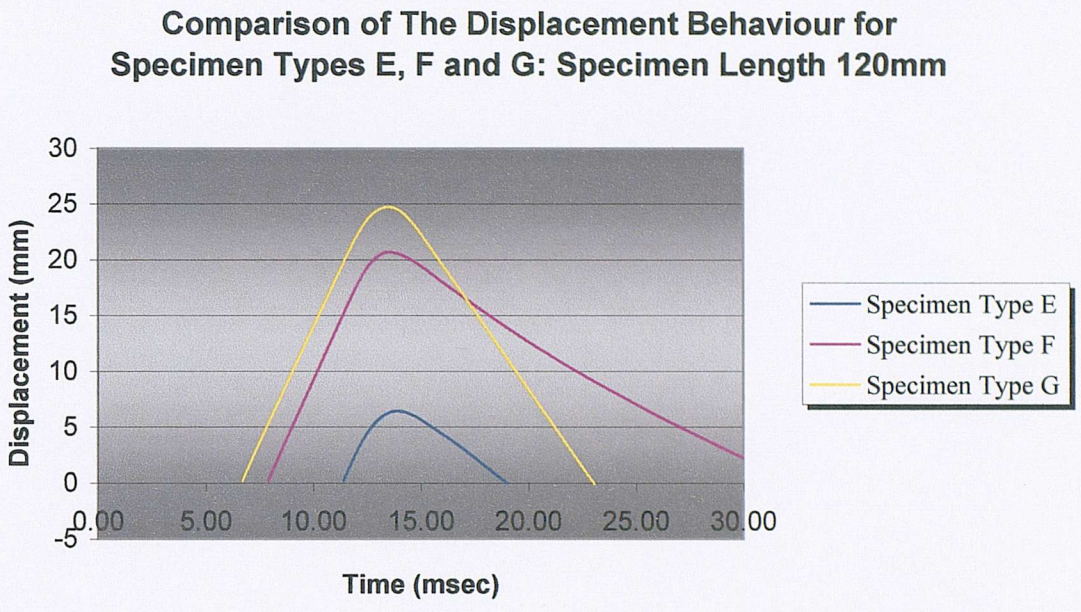


Figure 6.29: Chart Showing a Comparison of the Displacement-Time Behaviour for Specimen Types E, F and G (Thickness: 10mm, Length: 120mm, Width: 80, 60 & 40mm respectively).

Figure 6.29 shows that there is a large displacement increase between the 80mm wide (Type E) and the 60mm wide (Type F) specimens (roughly 15mm), whilst the increase between the 60mm (Type F) and 40mm (Type G) specimens is more like what was observed previously (roughly 4mm). If what was seen in *Figure 6.28* is taken into account then the huge increase in displacement between the 80mm wide and 60mm wide specimen would indicate an increase in the level of damage that occurs, however this is not shown in the C-Scan Images. If the damage is increased between these two specimen types then it could be that the increase in damage is not shown on the C-Scan image, in which case it could be in the form of delaminations, which are masked by the delaminations shown, and an increased level of matrix cracking between the plies. The rate of increase in displacement is the same in all three specimens in this figure, however the rate at which the displacement decreases is not. Types E and F have roughly the rate of displacement decrease, whilst the rate at which the displacement decreases in Type G is much greater. The difference that can be attributed to this is the shape of the damage that has occurred, as in Type G the damage has stretched across the whole width of the specimen whilst in the other two specimen types the damage in concentrated in the centre of the specimen, around the

impact point. However, this change in displacement behaviour when the damage stretches across the specimen is not observed in the longer specimens but the wider specimens in that case do not contain any damage at all and could be the cause of this difference in behaviour.

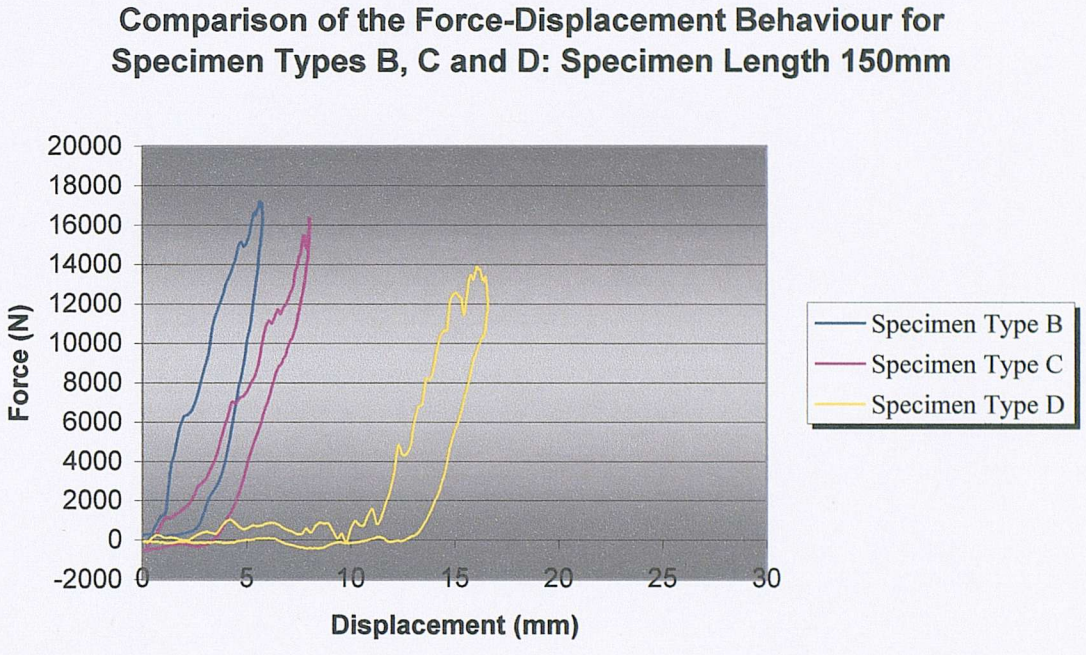


Figure 6.30: Chart Showing a Comparison of the Force-Displacement Behaviour for Specimen Types B, C and D (Thickness: 10mm, Length: 150mm, Width: 80, 60 & 40mm respectively).

Comparing the two sets of specimens with two different lengths (150mm and 120 mm) reveals that the shorter specimens tend to have larger level of displacement in comparison. This also agrees with observations seen in previous sections of this chapter. This is regardless of whether damage is present or the maximum displacement that occurs increases when the width and length is decreased

The Force-Displacement traces for these impacts are shown in *Figures 6.30* and *6.31*. The point revealed again is that the initial displacement is affected by width and length of the specimens and also the damage caused increases the resultant deformation. The higher energy drops generally cause more displacement and a higher level of induced damage and this makes the peak of the Force-Displacement

plot wider. In the cases where there are force increases before the main peak, this gives a second peak that occurs prior to the main peak. This is attributed to some damage occurring that does not affect greatly the specimen as a whole in its impact behaviour.

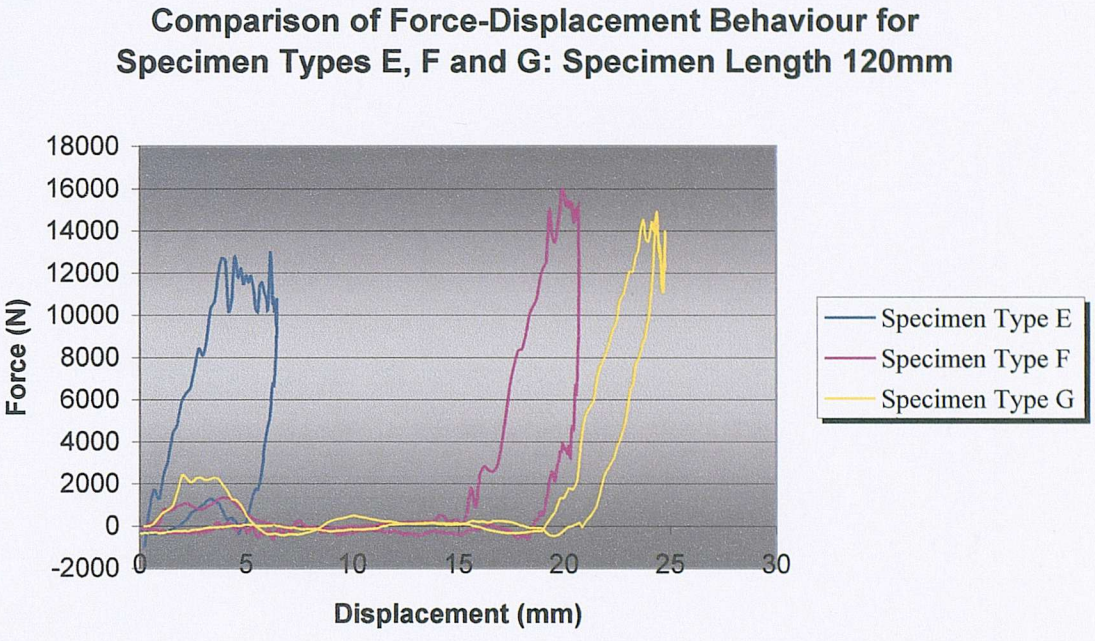


Figure 6.31: Chart Showing a Comparison of the Force-Displacement Behaviour for Specimen Types E, F and G (Thickness: 10mm, Length: 120mm, Width: 80, 60 & 40mm respectively).

6.3.2.1.3 Discussion

A finding of this section is that the damage caused by impacts at these energy levels is significantly affected by the changes in dimensions of the specimen.

A change in thickness of the specimen causes a large difference in the level of damage that occurs. Changing the thickness by 6mm, causes the damage to change from being only slightly evident about the impact point (10mm thickness specimen) to damage that is through the thickness and stretches right across the specimen width (4mm thickness specimen). This is expected as the change in thickness would cause a

considerable change in the stiffness of the sample and would in turn affect the damage tolerance of the material.

Reducing the length of the specimen causes a greater degree of damage to occur, whilst decreasing the width of the specimen also increases the degree of damage. However, with the width changes it seems that there is a threshold width at which the degree of damage actually increases as is shown by the C-Scan images, where the damage in the 80mm and 60mm wide specimens shows the same size of damage area whilst the 40mm wide specimens showed more extensive damage extending across the width. However, later analysis of Force-Time data shows that here is a possibility that damage in some cases does exist but is not revealed by C-Scan imaging.

There is also an indication that much less energy is required to cause damage in narrow samples as in the long specimens more damage is caused by roughly the same level of absorbed energy (indicated by the rebounding velocities) where the shorter specimens showed that more damage is present in the most narrow sample but the energy absorbed is less than that by the wider specimens. The same conclusion can be deduced for a change in the length as, with respect to the rebound velocities, less energy is absorbed by Type G than Type D specimens but the intensity of the damage is increased. Therefore, this shows that less energy is required to cause a greater level of damage when the specimen length is reduced.

7. Modelling the Change in Impact Response due to Damage using Closed Form Solutions

The focus of this chapter is on applying an analytical model to predict the impact response of composite laminates with the inclusion of developing damage during the impact event. Firstly, the background to this model will be discussed and then it will be used to predict impact responses using the same parameters for two of the specimen types that were used in the previous chapter's work on thick laminates and these predictions compared to the experimental responses obtained previously.

7.1. Closed Form Solutions for the Prediction of Impact Response

The first step in understanding the causes and leading to the prevention of impact damage is a basic understanding of the dynamic impact response. Impact duration can strongly influence the response of plates. Long duration impacts cause quasi-static response influenced by plate size and boundary conditions, whilst short duration impacts cause a response that is governed by wave propagation, which is less affected by plate size or boundary conditions. Response types can be dominated by the impactor-plate mass ratio as well as the actual impact velocity (Olsson 2003). Ideally closed form solutions are the desired route for predicting the desired impact response (Olsson 1992(b)). The closed form solution work is based on that performed by Olsson (1992(a), 1998) which has been used to good effect and has more recently been developed to predict small mass impacts (Olsson 2003), large mass impacts (Olsson 2001) and sandwich panels (Olsson and McManus 1996 and Olsson 2002). Olsson' work has all been based on the spring-mass model for contact proposed by Shivakumar et al. (1985), however for the work performed here, the general methods and formulae ar ethat used by Oilsson but the actual model used is a simplified version with the spring representing membrane stiffness being eliminated, resulting in

a two degree of freedom model which was proposd by Lal (1983(b)). The model used for this investigation is shown in *Figure 7.1.*

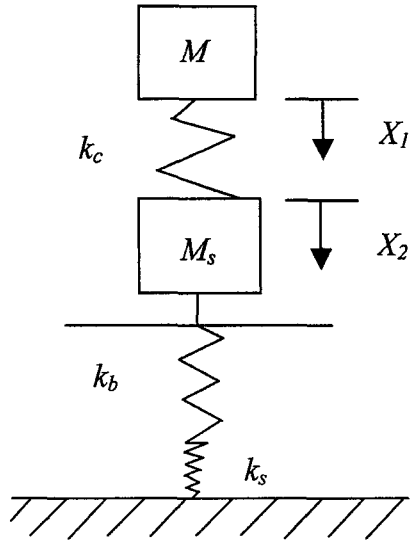


Figure 7.1: Two degree of freedom model for contact proposed by Lal (1983(b)).

M represents the mass of the impactor and M_s represents the mass of the impacted composite specimen. The two masses are connected by a spring representing the contact stiffness of the specimen, k_c. In order to get a more complete picture of the behaviour of the composite being impacted a further arrangement of springs which incorporates the bending stiffness, k_b, and the shear stiffness, k_s. X_1 is the displacement of the impactor whilst X_2 is the displacement of the specimen. This particular model is considered to be the most complete model for the impact response of a composite laminate (Abrate 1992). The equations for force in the above model are as follows:

Force on the Bending / Shear Spring: $F_{bs} = k_{bs} X_2$

Where k_{bs} is found from: $$\frac{1}{k_{bs}} = \frac{1}{k_b} + \frac{1}{k_s}$$

Damping in the Contact Spring: $f_c = d_c \sqrt{(k_c M)}$

Damping in the Spring Arrangement: $f_{bs} = d_{bs} \sqrt{(k_{bs} M_s)}$

Contact Force Relationships: $M\frac{d^2X_1}{dt^2} = -F_c$

$$M_s\frac{d^2X_2}{dt^2} = F_c - k_{bs}X_2 - f_{bs}\frac{dX_2}{dt}$$

Contact Force: $$F_c = k_c(X_1 - X_2)^{\frac{3}{2}} + f_c\left(\frac{dX_1}{dt} - \frac{dX_2}{dt}\right)$$

7.2 The Inclusion of Damage and its Effects on Impact Response

The above equations and model representation of impact response is the basis of the model which will be used in this section of the thesis. The actual model used here will attempt to model the response of the laminate after damage has occurred. The concept behind incorporating the effects of damage is that when damage occurs then the stiffness of the laminate will reduce.

The method in which damage is introduced into the Olsson model, for this study, involves including stiffness reduction factors at particular points during the indenting of the impactor into the laminate. Indentation occurs in this model when the difference in the displacement of the impactor and that of the specimen is positive. In this model there are three specific indentation points set up and at each point a contact stiffness reduction factor can be set. The actual stiffness reduction factors are cumulative, for instance if the stiffness reduction factor at the first critical indentation is set at 0.8 and then the second stiffness reduction factor is set at 0.7, then when the second critical indentation is reached the contact stiffness associated with the laminate would have been reduced to 56% of it's original value. It is the contact stiffness, which is modified as the damage is assumed to be local to the contact area.

7.3 Modelling Method

The model uses the equations given in Section 7.1 in a visual basic programme within Microsoft Excel. Visual Basic Macros generate solutions in the form of cells and the data is exported to the worksheet from which graphical data for Force-Time and Displacement-Time is obtained.

In solving the differential equations for X_1 and X_2, care is taken to use a time step, which was sufficiently small to capture the highest frequency oscillation in force displacement and time. This is typically 1/100 of the shortest time period of excitation. The coupled differential equations were solved using a iterative time marching sequence for this sized time step.

Data that was required to be inputted into this model include the impact velocity, contact stiffness, bending stiffness the reduction factors and the critical indentations at which they were to be activated.

Shear stiffness has been assumed to be a much greater value in comparison to the bending stiffness and thus having a negligible effect on the impact response. The aspect ratios of the sample size deem that the shear effects in the sample become negligible. The damping that occurs in the springs in the model has also been set to a low value (critical damping ratio of about 5%), as the actual intrinsic damping in a composite laminate is low.

Bending stiffness, k_b, and shear stiffness, k_s, values were obtained from performing experimental tests on samples of the Specimen Types (A and B) that are to be modelled. The tests were performed on an Instron 5584 rig using a 50kN load cell and a strain rate of 1mm/min.

For the contact stiffness measurement the composite panel was placed and clamped onto a rigid surface so that only the surface of the sample would be deformed (see *Figure 7.2*). For the bending stiffness the samples were place into the actual clamp that they were held in for the impact tests and loaded in bending until failure occurred

(see *Figure 7.3*). An identical shaped indentor to the one used in the impact tests was used for these tests using the Instron Rig.

The impact velocity to be inputted using the following equation derived from equating potential and kinetic energy equations:

$$v = \sqrt{2gh}$$

where v is the velocity, g is acceleration due to gravity and h is the drop height.

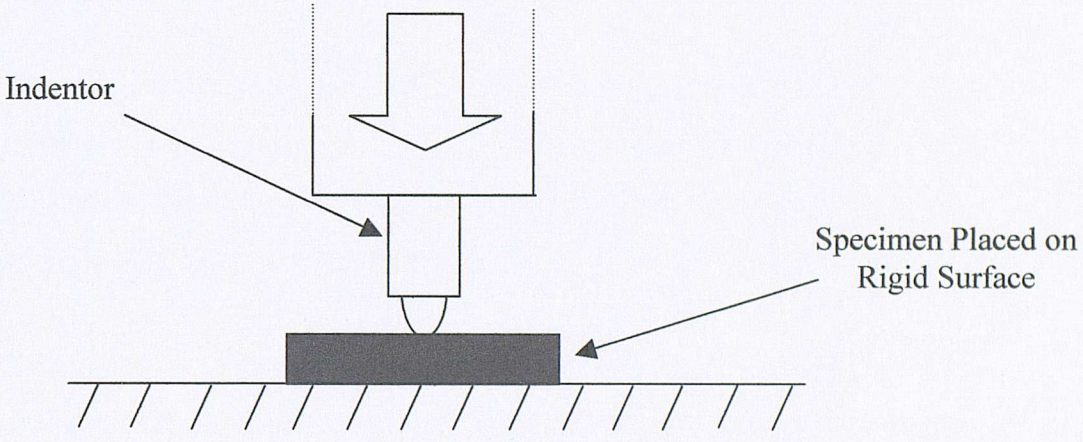


Figure 7.2: Schematic of loading set-up for Contact Stiffness Measurements in the Instron Rig.

The values used for indentation level and stiffness reduction factors were estimates, with the indentation values being influenced by the shape of the indentation-time curve that is presented by the model before damage is introduced. These values are adjusted in order to achieve as close a prediction as possible to the experimental impact response obtained for the specimens.

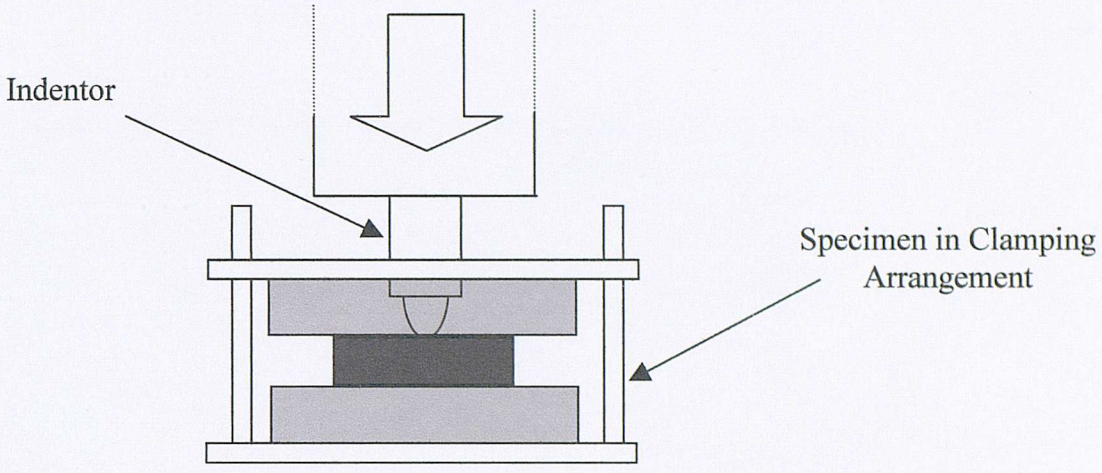


Figure 7.3: Schematic of loading set-up for Bending Stiffness Measurements in the Instron Rig.

Four sets of impact conditions were looked at for the two specimen types that were modelled. Three of the conditions are α, γ and δ from *Table 6.1* in **Chapter 6**. The fourth modelled condition is for a 1.55kg mass being dropped from a height of 1m, for which drop weight tests have been performed.

All the conditions using a 1.55kg drop mass were shown in the previous chapter not to produce any damage in the laminates used. Whilst the Drop condition using the 5.4kg was able to introduce a significant level of damage and the behaviour of the impact response in the form of the Force-Time traces changed significantly. In the cases where no damage is expected the part of the model that introduces damage is switched off and the model was used to predict impact response. In the cases where damage is expected, the damage conditions in the model are switched on and the stiffness reduction factors and their placement are adjusted until a similar response as to that achieved experimentally is predicted.

7.3.1 Input Data

The following is a list of the data that was recorded and used in the modelling:

Specimen Data:	Specimen Type A –	Mass	- 0.077kg
		k_c	- 45.29MN/m
		k_b	- 0.84MN/m
	Specimen Type B –	Mass	- 0.19kg
		k_c	- 33.97MN/m
		k_b	- 4.03MN/m
Impact Conditions:	Condition 1 -	h	- 0.5m
		M	- 1.55kg
	Condition 2 -	h	- 1.0m
		M	- 1.55kg
	Condition 3 -	h	- 1.5m
		M	- 1.55kg
	Condition 4 -	h	- 1.0m
		M	- 5.4kg

7.4 Results

The results obtained from this model are displayed along with the experimental data for the exact same impact conditions. *Figures 7.4, 7.6* and *7.8* show the comparisons of the predicted Force Response for Specimen Type A (80mm x 150mm x 4mm) subjected to impacts concerning a 1.55kg mass dropped from heights of 0.5m, 1.0m and 1.5m respectively. *Figures 7.5, 7.7* and *7.9* show the corresponding comparisons for displacement behaviour for Type A specimens impacted at the same heights.

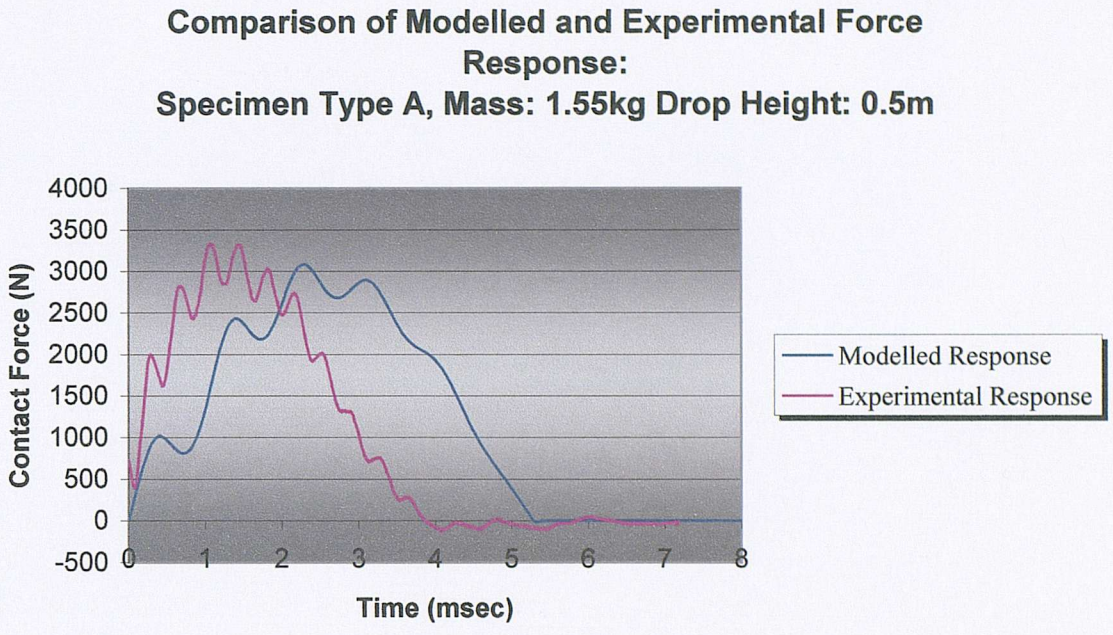


Figure 7.4: Comparison of Modelled and Experimental Force-Time Response for Specimen Type A (80mm x 150mm x 4mm) being impacted by a mass of 1.55kg from a drop height of 0.5m.

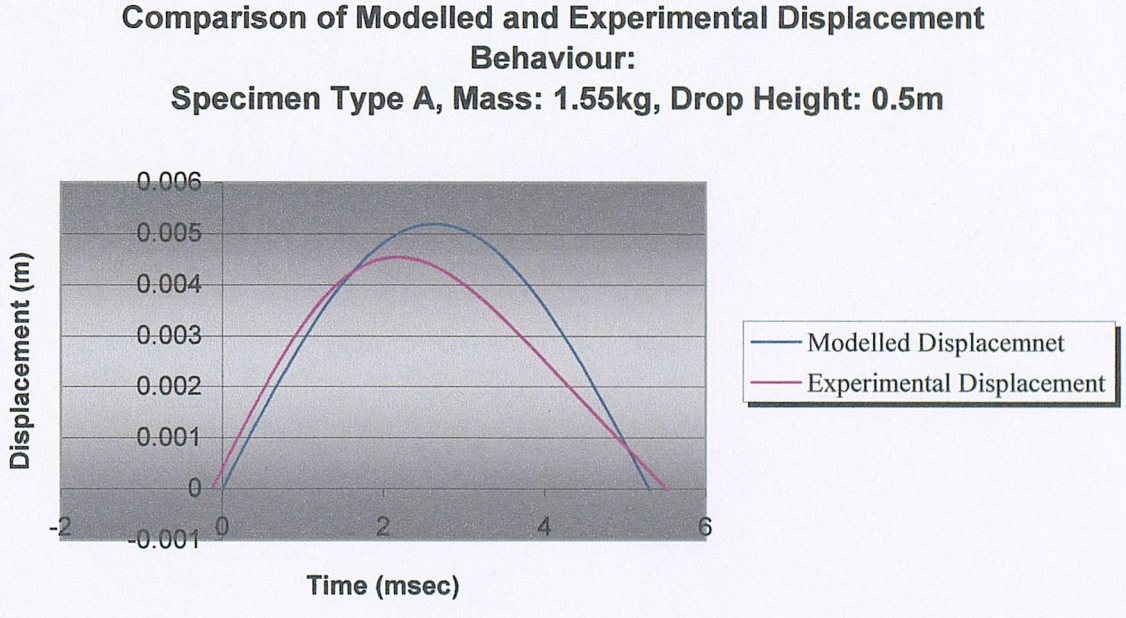


Figure 7.5: Comparison of Modelled and Experimental Impactor Displacement Behaviour for Specimen Type A (80mm x 150mm x 4mm) being impacted by a mass of 1.55kg from a drop height of 0.5m.

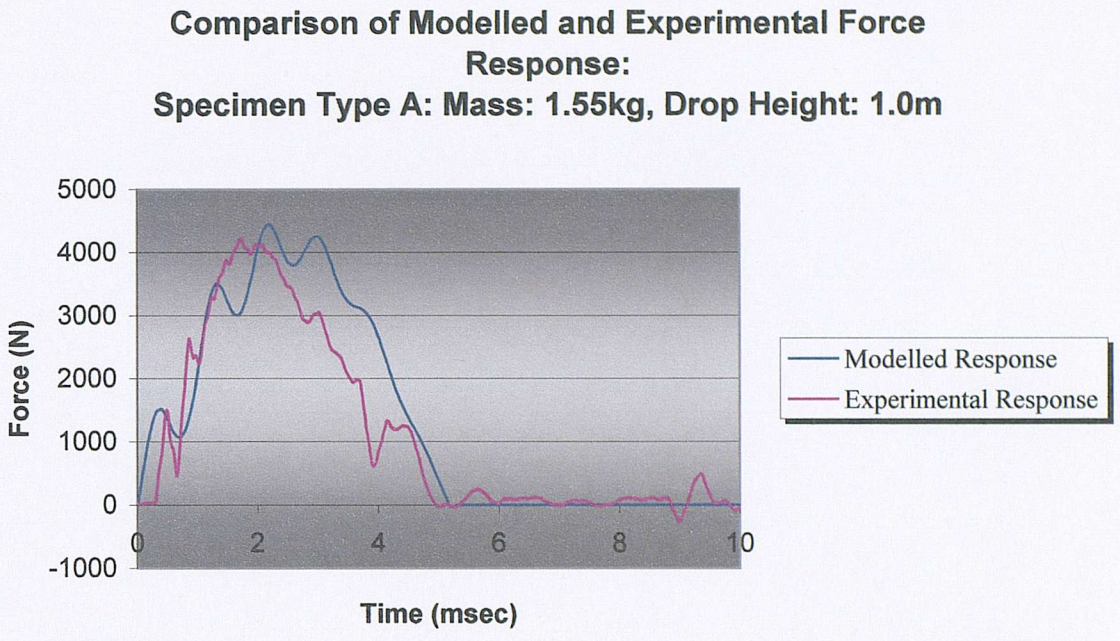


Figure 7.6: Comparison of Modelled and Experimental Force-Time Response for Specimen Type A (80mm x 150mm x 4mm) being impacted by a mass of 1.55kg from a drop height of 1.0m.

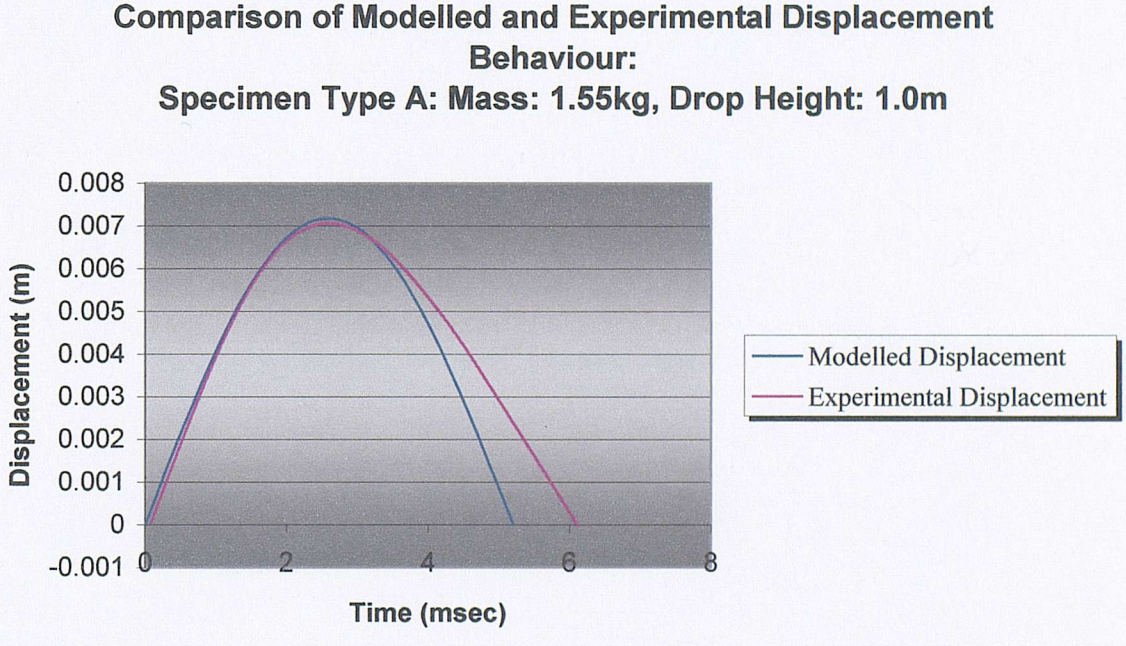


Figure 7.7: Comparison of Modelled and Experimental Impactor Displacement Behaviour for Specimen Type A (80mm x 150mm x 4mm) being impacted by a mass of 1.55kg from a drop height of 1.0m.

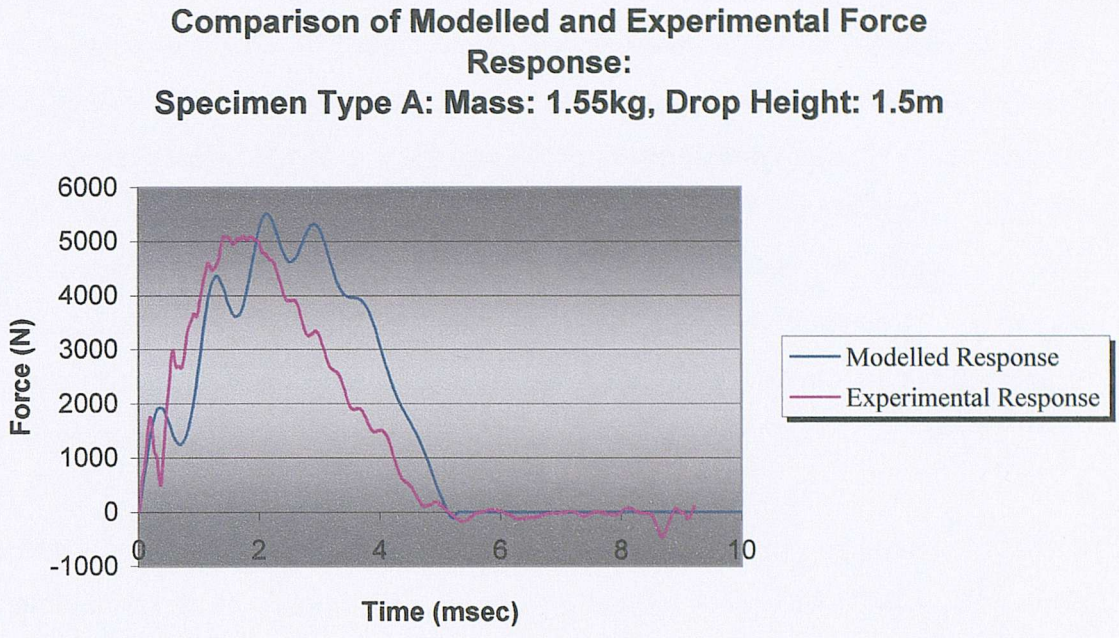


Figure 7.8: Comparison of Modelled and Experimental Force-Time Response for Specimen Type A (80mm x 150mm x 4mm) being impacted by a mass of 1.55kg from a drop height of 1.5m.

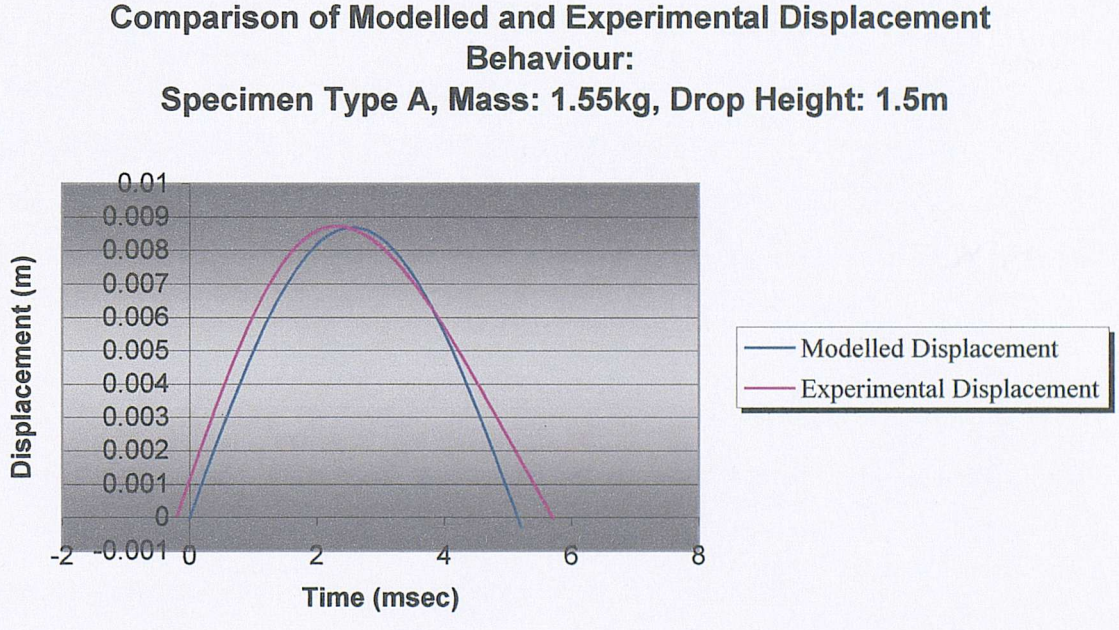


Figure 7.9: Comparison of Modelled and Experimental Impactor Displacement Behaviour for Specimen Type A (80mm x 150mm x 4mm) being impacted by a mass of 1.55kg from a drop height of 1.5m.

When studying the above figures it can be seen that the model gives good predictions of both the impact force response and the displacement behaviour but there are a few points to be explained. Firstly, the model predicts only a small number of oscillations in the Force-Time trace in comparison to the experimental traces. However, the model oscillations do closely correspond to key experimental oscillations. Also, the peak impactor displacements predicted are very close to those recorded experimentally. The rate at which the displacement increases is predicted well but the predicted decrease rate is greater than observed experimentally so the model predicts the displacement behaviour to be in a shorter period of time.

For the 0.5m drop height (See *Figures 7.4* and *7.5*), there are far more oscillations throughout the Force-Time trace. Both the rate of increase and decrease of contact force have been predicted to be much lower than the experimental data, this causes a period of impact to be predicted to be larger than the observed. The predicted peak contact force here is almost 500N lower than is observed in the experimental data. This impact condition is the only one where the peak displacement has been over-predicted (see *Figure 7.5*).

In both the 1.0m and 1.5m drops the peak contact force is predicted to be higher than the observed peaks from the experimental data (see *Figures 7.6* and *7.8*). In both cases the rate of increase of force is predicted well, whilst the rate of decrease is predicted to be higher than the observed, this combined with the over predicted peak force results in a good prediction for the duration of the impact event.

Figures 7.10, 7.12 and *7.14* show the comparisons for the model predicted force response and the experimentally recorded response for specimen type B impacts with a 1.55kg mass at 0.5m, 1.0m and 1.5m respectively. *Figures 7.11, 7.13* and *7.15* show the corresponding comparisons for the displacement behaviour.

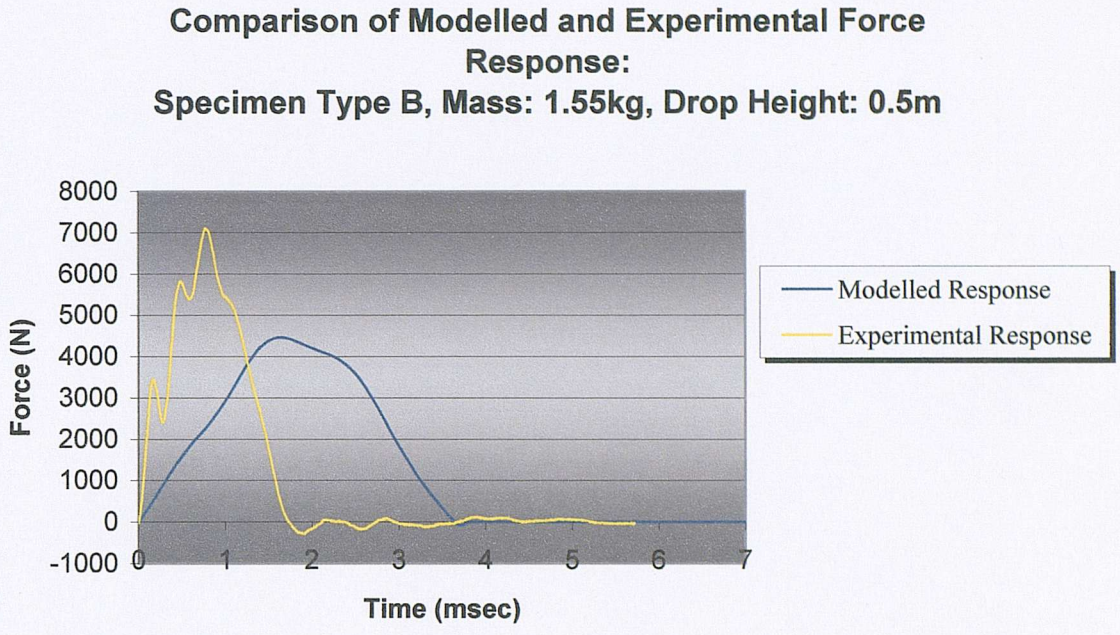


Figure 7.10: Comparison of Modelled and Experimental Force-Time Response for Specimen Type B (80mm x 150mm x 10mm) being impacted by a mass of 1.55kg from a drop height of 0.5 m.

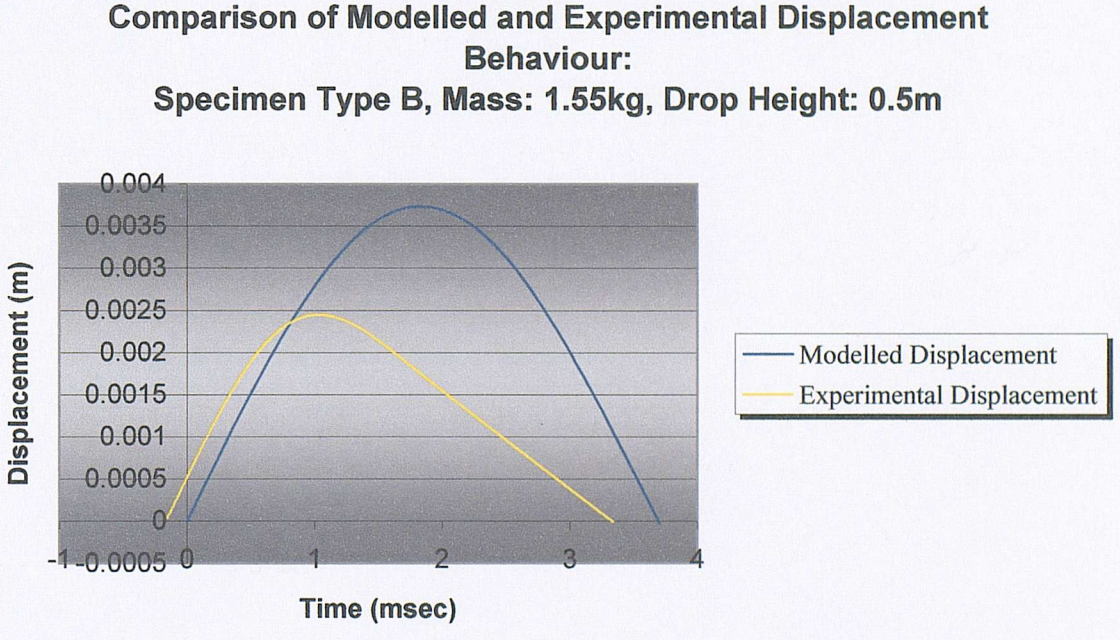


Figure 7.11: Comparison of Modelled and Experimental Impactor Displacement Behaviour for Specimen Type B (80mm x 150mm x 10mm) being impacted by a mass of 1.55kg from a drop height of 0.5m.

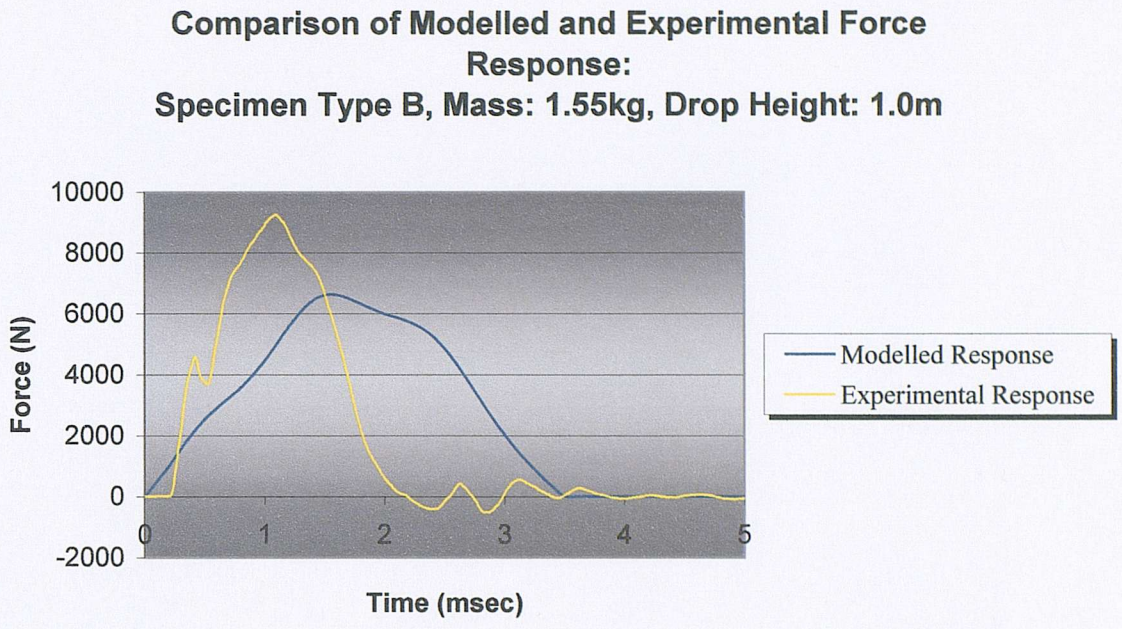


Figure 7.12: Comparison of Modelled and Experimental Force-Time Response for Specimen Type B (80mm x 150mm x 10mm) being impacted by a mass of 1.55kg from a drop height of 1.0m.

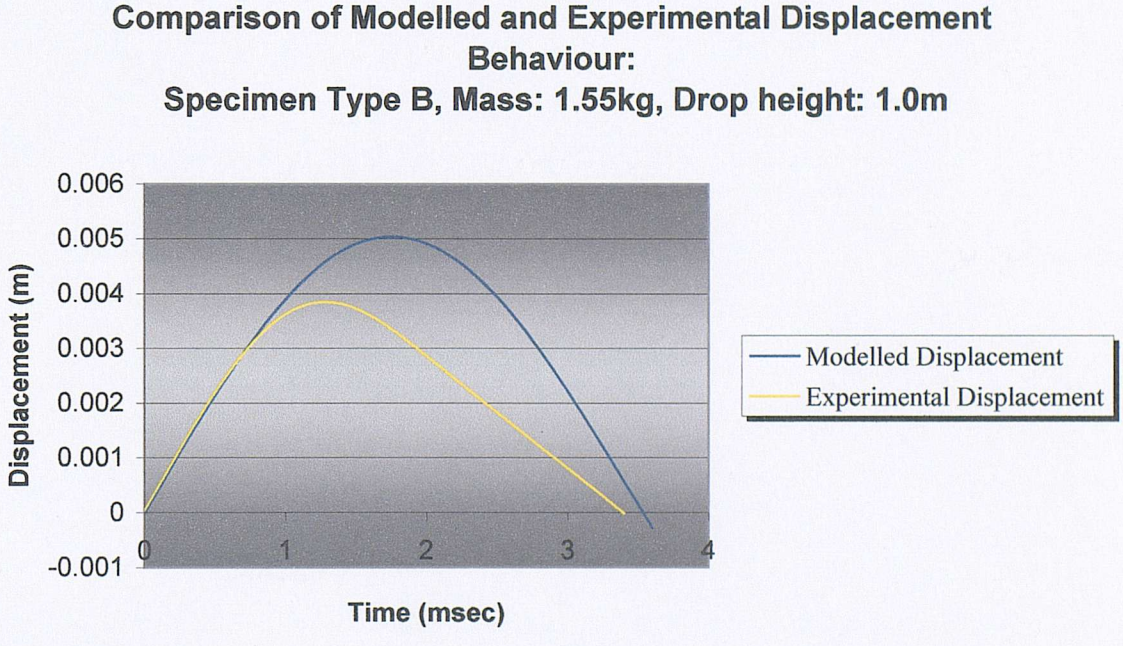


Figure 7.13: Comparison of Modelled and Experimental Impactor Displacement Behaviour for Specimen Type B (80mm x 150mm x 10mm) being impacted by a mass of 1.55kg from a drop height of 1.0m.

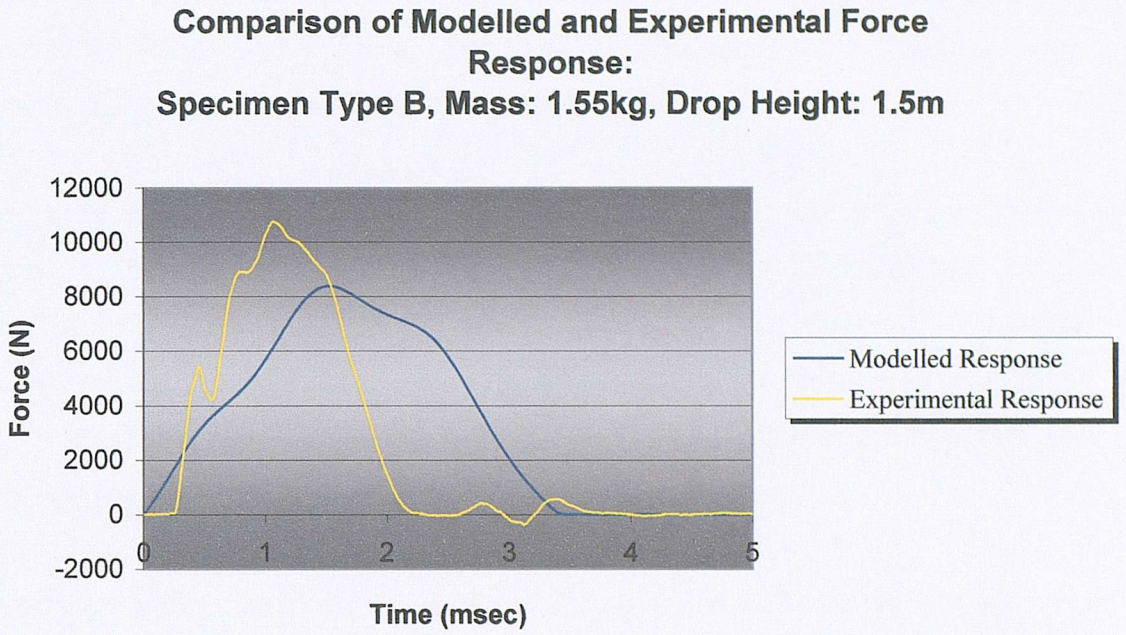


Figure 7.14: Comparison of Modelled and Experimental Force-Time Response for Specimen Type B (80mm x 150mm x 10mm) being impacted by a mass of 1.55kg from a drop height of 1.5m.

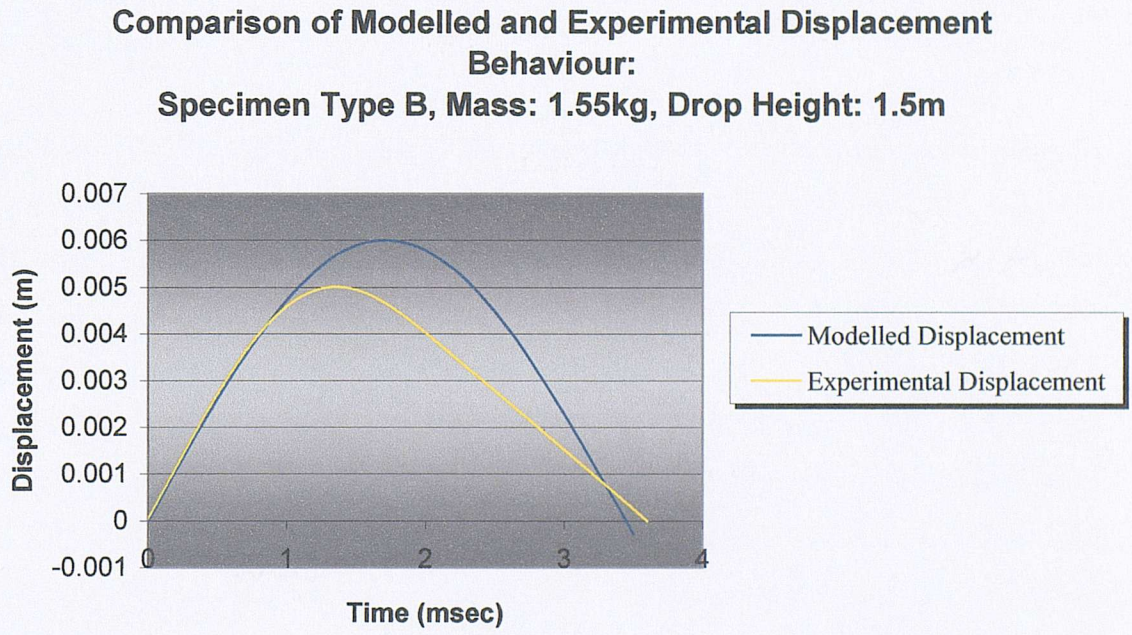


Figure 7.15: Comparison of Modelled and Experimental Impactor Displacement Behaviour for Specimen Type B (80mm x 150mm x 10mm) being impacted by a mass of 1.55kg from a drop height of 1.5m.

The measured contact stiffness, when introduced into the model, greatly under predicts the Force-Time response. There are less oscillations in the observed Force-Time traces in these impacts compared to those for Specimen Type A.

Examining *Figures 7.10, 7.12* and *7.14*, the predicted responses have less oscillations, are smoother, and predict the impact duration to be much longer than in the experimental data. The rates of increase and decrease are well predicted, however the size of the oscillations are greater than that observed in the experimental data, and it is this discrepancy that causes the predicted period of impact to be longer than that seen in the experimental data.

The comparison of the modelled displacement behaviour with the experimental data (see *Figures 7.11, 7.13* and *7.15*) shows that the predicted responses give much higher values for peak displacement than that experimentally observed. However, the period for displacement from these predictions are comparable with those observed by the experimental data. The rate at which the displacement increases is well predicted. The rate of decrease of the displacement is predicted to be much greater than that of the observed data.

As can be seen, the model predicts quite well the impact response of the laminates in studies when they are subjected to impact conditions that do not cause any damage. The model is now modified in order to incorporate the effects of damage on the specimen. As explained previously the effects of damage are modelled in the form of percentage decreases of laminate contact stiffness, due to failure of plies, at set levels of impactor indentation. The impact conditions used corresponds to the high-energy impacts from the previous chapter, which were shown to induce damage within both Specimen Type A and Type B (5.4kg mass dropped at height of 1.0m). The required modelled effects of damage can by altered by adjusting the indentation level at which the stiffness reduction factors occur, and by adjusting the actual stiffness reduction factors themselves.

Table 7.1 shows the inputted damage variables for the model used for predicting the effects of damage in the high-energy impact of Specimen Type A. The values used

for the critical indentations were based on the values given by an un-damaged model, and are all below the peak indentation value. With the third value chosen being very close to the peak value, stiffness reduction factors were adjusted until a good model was produced.

1st Critical Indentation	1st Stiffness Reduction	2nd Critical Indentation	2nd Stiffness Reduction	3rd Critical Indentation	3rd Stiffness Reduction
0.001m	0.7	0.002m	0.7	0.004m	0.25

Table 7.1: Figures for critical indentation values (m) and stiffness reduction factors used for the modelling the effects of damage on the high-energy impact of Specimen Type A.

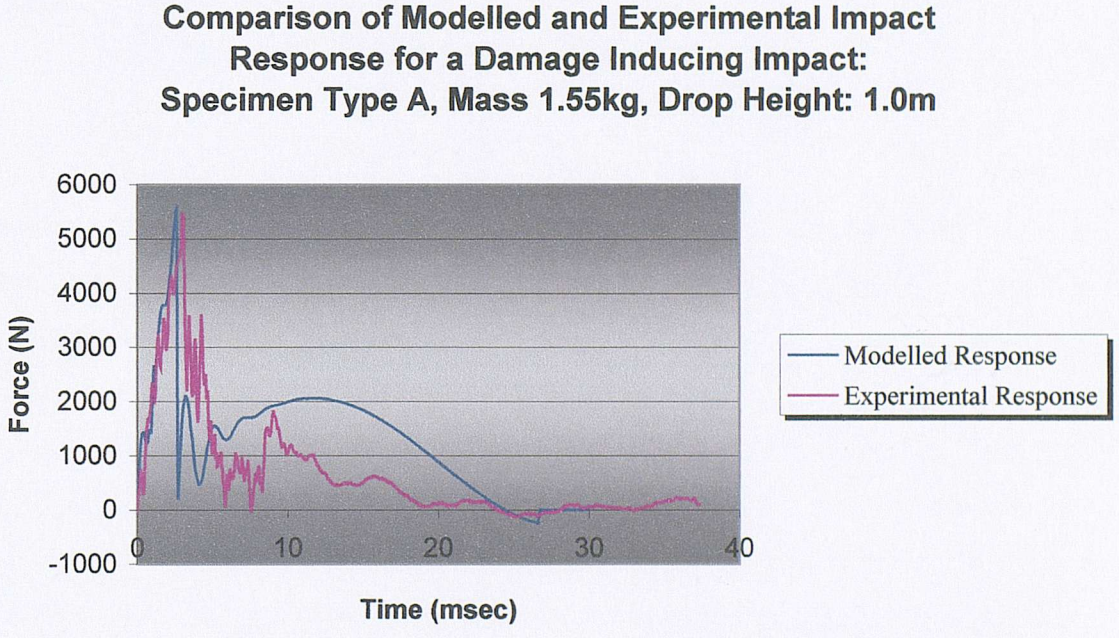


Figure 7.16: Comparison of Modelled and Experimental Force-Time Response for Specimen Type A (80mm x 150mm x 4mm) being impacted by a mass of 5.4kg from a drop height of 1.0m.

Figures 7.16 show the comparison for the modelled with the experimental impact response for the high-energy impact of Specimen Type A. The model predicts well

the actual impact response with peak contact force, period of the event and points at which the force drop and rise agreeing well with experimental data. However, the second peak is predicted at a lower value, and the third peak is predicted to be higher than the experimental peak and decreases in a much more progressive fashion than that which occurs in the recorded data.

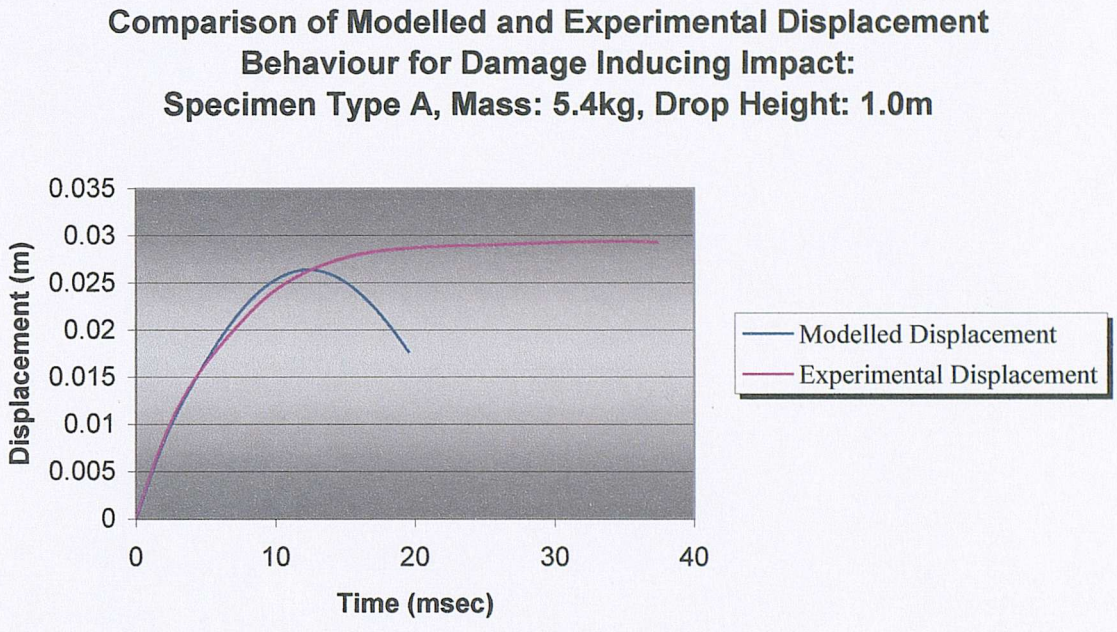


Figure 7.17: Comparison of Modelled and Experimental Impactor Displacement Behaviour for Specimen Type A (80mm x 150mm x 4mm) being impacted by a mass of 5.4kg from a drop height of 1.0m.

Figure 7.17 shows the comparisons for the displacement behaviour in the high-energy impact of Specimen Type A. The immediate difference that is shown is in the fact that the experimental displacement does not return to zero and seems to show some form of asymptotic behaviour indicating that permanent damage may have occurred.

Table 7.2 shows the inputted damage variables for the model used for predicting the affects of damage in the high-energy impact of Specimen Type B. The same principle was used for the selection of the critical indentaion values and the reduction factors.

1st Critical Indentation	1st Stiffness Reduction	2nd Critical Indentation	2nd Stiffness Reduction	3rd Critical Indentation	3rd Stiffness Reduction
0.001m	0.9	0.0015m	0.9	0.0023m	0.9

Table 7.2: Figures for critical indentation values and stiffness reduction factors used for the modelling the effects of damage on the high-energy impact of Specimen Type B (80mm x 150mm x 10mm).

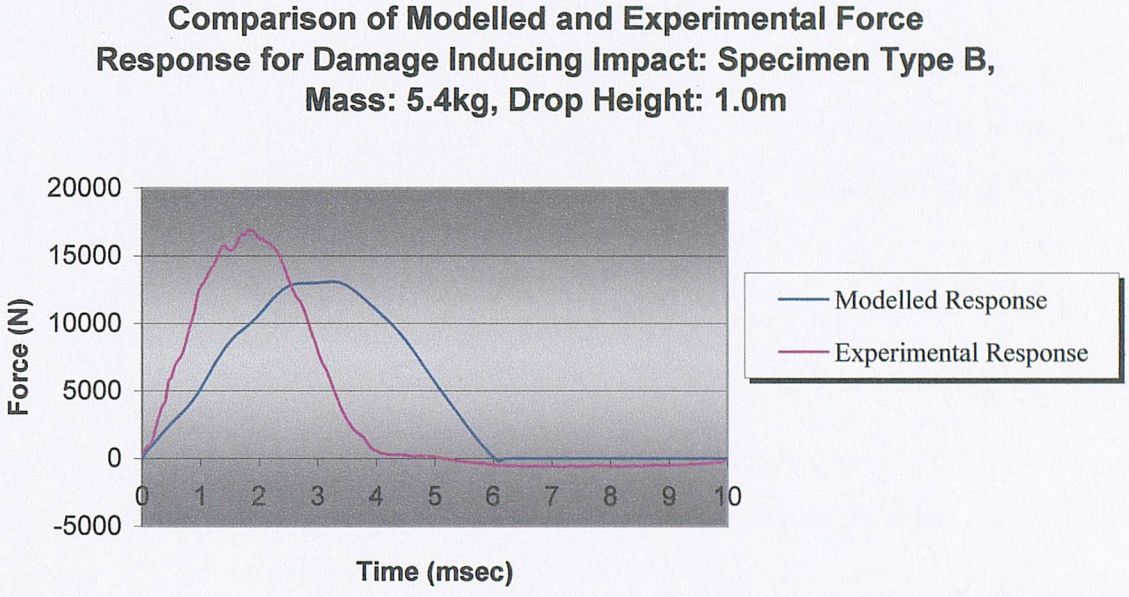


Figure 7.18: Comparison of Modelled and Experimental Force-Time Response for Specimen Type B (80mm x 150mm x 10mm) being impacted by a mass of 5.4kg from a drop height of 1.0m.

Figure 7.18 shows the comparison between the modelled response with the experimental response for the damage inducing impact of Specimen B. Firstly, the predicted period of the force response is greater than that observed. The modelled data gives a peak force prediction that is almost 5kN below what is observed in experiments. When damage is introduced it can be seen that the Force values are all lowered. Therefore, it can be seen that the damage inflicted in these panels does not greatly affect the actual impact response and this can be confirmed by the C-Scan

results from the previous chapter showing only a small area of damage, which is not extensive enough to cause any considerable affects on the impact response. There are also predicted oscillations in the force response that are not observed in the experimental data and as a result causes the predicted force response to occur over a longer period.

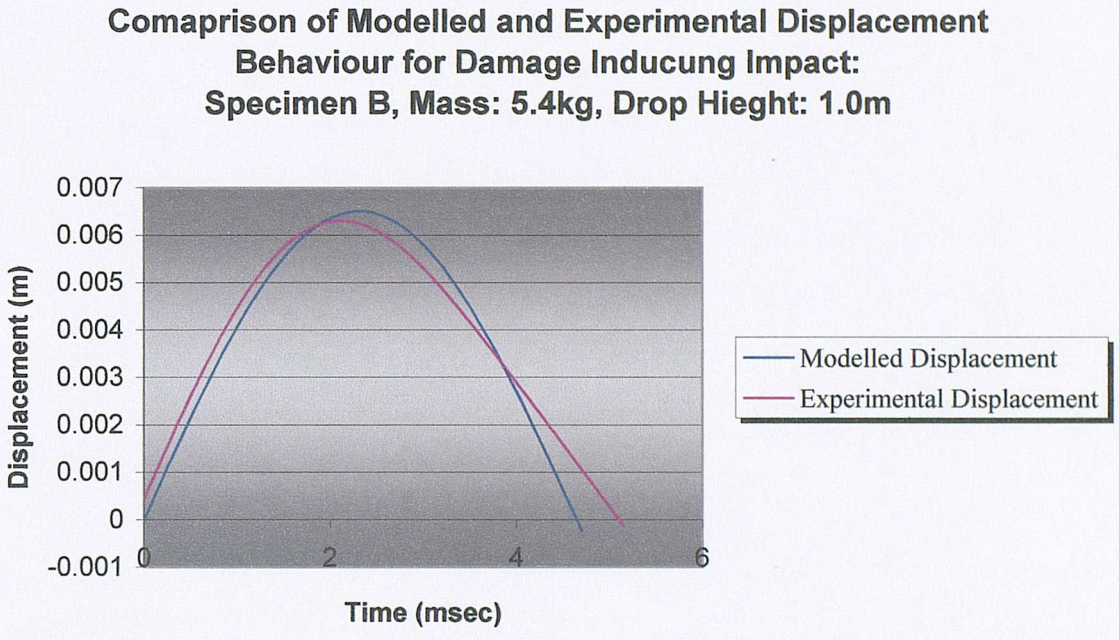


Figure 7.19: Comparison of Modelled and Experimental Impactor Displacement Behaviour for Specimen Type B (80mm x 150mm x 10mm) being impacted by a mass of 5.4kg from a drop height of 1.0m.

Figure 7.19 shows the comparison for the displacement behaviour for these impact conditions. The model shows the displacement behaviour agrees well with the observed experimental behaviour, with very similar values for peak displacement and period of displacement activity. The rate of increase in displacement is predicted to be very similar to that obtained from experimental behaviour, whilst again the rate of decrease is predicted to be slightly greater than that observed and hence predicts a slightly shorter period of displacement behaviour.

7.5 Discussion

The results from this modelling chapter show that the modelling used can give good predictions for the impact responses that occur in the composite laminate impacts that were modelled. Modelling impacts that occur in the thinner (4mm) Type A specimens have been successful in both the non-damage inducing impacts and the damage inducing impacts.

However, the increase in thickness of the specimen from 4mm (Specimen Type A) to 10mm (Specimen Type B) seems to cause the model to under predict the force response and simplifies all the oscillations that occur. In this case the model may have over simplified the impact event and hence the mismatch in predicted and experimental behaviour. The model can be modified further by introducing membrane effects, which would make this work more a reflection of the modelling performed by Olsson in this area of work.

The modelling study has been very helpful in understanding better the complexity of impact damage to composite materials. However, only the contact spring stiffness of the model was changed to simulate damage effects. There is scope, therefore, to make other adjustments to the model that can take into account changes, in for example, the bending stiffness of the laminate.

In addition the effect of damage can be more complex than this. It can depend upon the lay-up and fibre arrangement of the composite and their dimensions. The geometric size of the damage and the thickness levels at which these occur relative to the size of the specimen is another factor. Clearly, for a much larger specimen, the same damage will have less effect on the stiffness. There is, however, a value limit to the detail and extent of modifications to the model to achieve results closer to experimental data. In this study, the interest was in studying the main effects and achieving an explainable description of the effects of onset and development of damage in a specimen.

8. Discussion

The following chapter will discuss the findings that have been gathered throughout the research studies performed and presented in this thesis. There have been three studies into factors which effect the impact damage and damage tolerance of composite materials and a study looking at the possibilities of predicting the impact response as well as predicting the effects that induced damage has on the impact response.

The first study researched how a curved structure reacts to an impact event. Samples with a curvature in the longitudinal (along the length of the specimen) direction and transverse (across the width of the specimen) direction, were impacted on both the convex and concave faces. Impacts were performed using a gas gun, from which 1g steel ball bearing was fired at the samples at pressures of 5 Bar (giving an impact velocity ≈150m/s) and 8 Bar (giving an impact velocity ≈185m/s). The interest in impacting these curved composite structures at these velocities is that often these shapes are used by the aerospace and other industries where there is a strong likelihood of the structure being impacted by low mass/high velocity particles. For this study of the damage levels, high-speed photography was used for observing the dynamic behaviour of curved specimens during the impact event. For post-impact specimen examination, X-Radiography and Scanning Electron Microscopy were used to assess the extent and type of damage that was inflicted on the specimens.

The findings in these investigations indicated that the orientation of the curvature greatly affects the degree of damage that was inflicted. The high-speed sequences and the X-Radiographs gave a good picture of how the level of damage incurred was related to the orientation of curvature and impact conditions. To be expected, an increase of impact velocity from 150 m/s to 185 m/s generally increases the amount of damage inflicted on specimens. However, findings show that the direction in which the curvature runs provides a preferential path for the damage to grow.
The impact damage that occurs in a curved sample under impact relates to the inherent ability of the sample to flex in the orientation and support arrangement that

was provided. The evidence for this is shown when comparing the level of damages and the amount of flexure that is captured in the high-speed photography research. The longitudinally curved specimen with their convex impact face have the least ability to flex due to the constraints of the support arrangement and have the highest intensity of damage, whilst the least damaged specimen have a longitudinal curvature with a concave front-face. These two arrangements are the least and most flexible respectively. This indicates that the flexibility of the specimen is effective in dissipating impact energy. Hence, the stiffest and least flexible sample develops the highest levels of damage from a given impact, whilst the least stiff and most flexible develop the least level of damage of all the orientations. This agrees well with the work performed by Wardle and Lagace (1997) who identified the importance of instability in the damage resistance of composite shells.

The specimens studied showed the different ability to deform in flexure and therefore the onset of damage. The first initial matrix crack is expected to form on the rear face and grow in a reverse pine tree formation as shown in Chapter 2. High-speed photography shows the first signs of delamination towards the centre of the specimen. Further delaminations do not occur progressively towards the front face of the specimen, but progress towards the back-face of the specimen. X-Radiography shows the intensity of the damage in the damage area and was not capable of showing how the damage progressed through the thickness. Therefore, a more comprehensive study into the damage development in the form of sectioning and electron microscopy was employed.

The most intense area of damage was immediately under the impact point. The first sign of damage is below the impact zone, which increases in depth and width (by almost 100%) when the velocity of the impact is increased. The plies in the impact zone can also be seen to have 'caved in' under the impact site. The plies were broken and deformed with the embedding projectile and produced the visible indentation. Beneath this impact zone, the matrix-cracking patterns indicate that the initiation of damage here is caused by compression failure in this zone. However matrix cracking is also observed at the rear face, which is an indication of damage being initiated from a tension failure. With this in mind in, it can be deduced that both types of failure

occur under these impact conditions. This is related to the level of flexure and the amount of indentation that occur. The impact zone contains a large amount of crushed composite from which many of the delaminations initiate, grow and lead to further damage initiation away from the impact site. The longest delaminations occur towards the centre of the thickness and are initiated around the impact site. Looking at these delaminations and comparing the behaviour at the two impact velocities shows that although they appear at different levels of the impact zone, they still are in the centre line of the thickness. This agrees with the theory of the simultaneous initiation paths for damage where the two damage formations merge at the centre line causing the largest delamination. Combining this with what is shown in the high-speed photography sequences, where no signs of delamination stretch across the width of the impact face of the specimen, it can be speculated that when the two damage formations merge the pine tree formation initiated by compression becomes dominant in the damage progression sequence.

There are many possible causes for this behaviour, which include the change in shape of the specimen and the increasing flexure of the specimen, during the impact event. A complexity is that the damage seems to follow the curvature of the specimen and this in turn can be affected by flexing caused by the impact event. Therefore, there is the possibility that the change in shape due to the flexing and relaxing of the sample arrests the tension initiated damage progression travelling from the back face. This damage progressing from the back face encounters an easier progression path when the specimen is in flexure, when the curvature promotes damage progression travelling in this direction. However, when the specimen relaxes the specimen returns to a shape that encourages damage to progress from the front face and hence damage from the front face carries on towards the back face, and the damage in the other direction arrests.

The indications are that there is not a simple relationship between the energy absorbed in flexing the target specimen and the energy consumed by the damage processes. Much depends upon the structure of the composite, its dimensions and the toughness of its fibre components, the host material and the bonding of all these together. Not to

be overlooked is that as damage occurs and where so the flexure and dynamic response of the material appropriately changes.

This leads to the next investigation into how the level of flexibility affects the amount of damage that occurs within an impact sample, and what material and geometrical factors affect the level of flexibility and hence the damage that occurs. This study was based around the impact of thinner, almost skin like, laminates, which were inherently capable of flexing due to their low thickness. Two types of panel were used, using a tough PPS matrix, one with woven carbon fibres and the other woven glass fibres. The fibres were changed rather than the matrix, as it is the fibres, which govern the level of flexibility available. Sample were made of two different lengths, the shorter inherently being stiffer under bending conditions and the longer being more flexible. The study utilised a drop weight impact facility, which allowed for Force-Time data to be collected, in-situ high speed photography to capture the behaviour during impact and C-Scan ultrasonics was used post impact to investigate the levels of damage that occurred in the samples. Drops were made at progressively increasing heights to show how damage area increases with increasing impact energy and how the different materials compare. Low heights were used due to the instability of the thin samples.

During this study it was found that, as was shown by the work performed on the curved samples, the more flexible and less stiff the panel the less damage occurred. Firstly, when the high-speed photography sequences are examined they show that the highest specimen displacements occur in the longer specimens and particularly so for glass fibre specimens. When the C-Scan Damage areas were compared between the different sized specimens and the longer more flexible specimens showed damage initiation at higher drop heights and smaller areas of damage when same sized damaged specimens were compared. It was also shown that the constituent composite materials also had a great effect on the levels of damage that occurred. It was shown that the less stiff glass fibre composite performed better, in terms of damage tolerance, than the carbon fibre composite. This is evident when the damage within the same sized specimens of the two different materials is compared. However, when the damage is studied in all the progressive drops for all the specimens it was shown

that the short, stiff glass fibre specimens had better damage tolerance than the long flexible carbon fibre specimens. This was shown by the first signs of damage occurring at a higher drop height (higher impact energy) and the damage that did occur was much smaller in area. This showed that composites with less stiff fibres are much more damage tolerant than those with stiffer fibres to the extent that a less flexible arrangement of a composite with less stiff fibres being more damage tolerant than a flexible arrangement of a composite containing stiff fibres.

The Force-Time Data collected in this investigation allowed the force response, and with the help of integration, the displacement behaviour of the impactor (an indication of the displacement behaviour of the specimen) for the impact events to be studied. When comparing the behaviour of the peak contact force variations with drop height indications that a plateau peak force is reached in all specimens, which shows that there is a contact force which causes a level of damage that does not allow the specimen to withstand a higher contact force. However this can only be confirmed if further drops are performed at greater heights to ensure that no further increases in contact force occur. Higher peak force values are shown for the carbon specimens and the shorter specimens, showing that the carbon specimens and the shorter specimens are stiffer in this arrangement.

The Displacement-Time data allows for the peak displacement of the impactor, which gives a good indication of the peak displacement of the specimen, confirms the levels of flexibility shown in high-speed photography. However, it was shown that the displacement in the carbon specimens reaches levels that are greater than that in the glass fibre specimens at the highest drop height. The high-speed photography sequences show that, at these heights, the damage that occurs in the carbon specimens are so extensive that specimen fracture occurs, allowing the impactor displacement to reach the same type of levels as that for the glass fibre specimen. This fracture occurrence is confirmed by the C-Scan images of damage were the damage is no longer located in a round area in the centre of the specimen, but shaped in a line across the specimen.

Therefore, from these results it can be seen that the drop height (impact energy level) is, as would be expected, linked with the level of damage that occurs. At the same time the level of damage within an impacted sample may have a significant effect on the level of displacement that occurs due to the loss of integrity of the specimen. This is shown in the high drops for the carbon specimens where the damage that occurs reaches the back face in the form of a split, the integrity of the specimen drops and hence the impactor can travel further than when impacting from the same drop height on the equivalent sized R-Glass specimens which remain relatively intact and still are able to flex and resist deformation, whilst absorbing energy.

The next area of research looked into how changing the dimensions of a test piece would affect the damage induced by impact and also how these changes affected the impact response, in terms of Force, Velocity and Displacement changes throughout the impact event. Laminates where prepared of different lengths and widths and impacted using a drop weight facility. The effects on the responses were investigated using drop conditions that would not produce damage in the specimen, and then they were impacted at conditions that would cause damage and the affects of the changes in dimension on the levels of damage were looked at as well as the way damage affected the response of the specimen to the impact event. Parts of this investigation were then used for developing an analytical model for impact response on composites with the incorporation of damage effects.

The main findings in these sets of test data are that they confirm the specimen dimensions significantly influence the impact behaviour of the specimens. Firstly, a change in the thickness of the sample causes the stiffness to increase and this leads to a higher peak contact force which is reached at a greater rate of increase, which also leads to a lower level of displacement occurring, this is confirmed when the effects of a change in thickness of a laminate were looked at. However, more interesting points were discovered when looking at the effects of changing the width and the length of the specimen. It was discovered that there is a possibility that there is a threshold length at which the behaviour of the specimen changes and hence affects the impact response and energy absorbing properties of the laminate. When the rebound velocity is taken as an indication of the level of energy that is absorbed by the specimen a

change in behaviour was shown when the length of the specimen was changed. The 150mm long specimens all absorbed the same level of energy resulting in their rebound velocities being almost the same, however the 120mm long specimens showed varying rebound velocities with a varying width of specimen. However, the two sets of Force-Time data show no differences in behaviour that would indicate any types of damage being inflicted into the specimen. This indicates that there are optimum conditions for absorbing maximum levels of energy. Many factors could cause the contact conditions to vary. These may include the dynamic response of the laminate to the impact; subsequent contact interference between impactor and specimen; frictional losses at the grip points; vibrational and other flexural energy retained in the specimen after the impactor has separated from the specimen.

If the level of rebound velocity is used as an indication of the amount of energy absorbed, then for the lower rebound velocity, more energy is absorbed. The main mechanism for energy absorption in cases where no damage occurs must be related to the level of displacement that occurs. This relates to the theory of flexure being an energy absorption mechanism as discussed in the previous chapters. However in this investigation, there is evidence that higher displacements can result in higher rebound velocities. This may indicate that energy absorption via the flexure may only occur when damage is actually initiated.

Changing the dimensions of a laminate also affected high energy impacts that introduced damage into the laminates, both in terms of their response and the level of damage that occurs. As would be expected when the thickness is reduced a larger amount of damage would occur, due to the inherent difference in the laminate thickness. Length reduction was also found to increase the level of damage that occurs. However the most interesting effect was changing the width. Evidence is found within this section of the investigation that there is a threshold width at which the level of damage increases. 80mm and 60mm wide samples showed the same levels of damage in the form of an almost circular area surrounding the impact point, whilst when the width was reduced to 40mm the damage became more extensive and stretched across the width of the specimen. Analysis of the Force-Time data showed that there may be cases where the damage does exist and does not show on these C-

Scan, and therefore would surmise that damage mechanisms such as higher density of through the thickness matrix cracking may be present. A comparison of Force-Time data also showed that less energy is required to cause damage in narrow and short samples.

An attempt at modelling the impact response and the effects of damage on the impact response was attempted. A very simple model based on long-standing two degree of freedom spring mass model was used. Initial modelling showed that the impact response could be adequately modelled, in terms of the Force-Time and Displacement-Time behaviour for the thin (4mm) laminate. However, when the model was used on the thick (10mm) samples the Force-Time behaviour was poorly predicted. This could have been due to an error in the measurement of the contact stiffness or some un-foreseen effect of the thickness of the laminate as this model has only previously been used for the impact of thin laminates. This mismatch may also have been caused by the oversimplification of the existing model and the omission of the spring representing membrane effects in the impact event.

It has been shown that this model may be modified for the responses of certain impact situations (Olsson 2001, 2003) and damage can be introduced by added an extra element (Olsson 2001). However, in this case the model was modified to incorporate the effects of the damage that occurs during the impact event. The method for this incorporation was simple and involved the inherent principle that stiffness reduces when damage occurs. Therefore, Stiffness Reduction Factors were introduced at certain levels of indentation of the impactor into the specimen. We introduced three such contact stiffness reduction factors with the reduction factors and levels of indentation adjusted until a satisfactory prediction was obtained. It was found from these modifications that it is possible to show the effects of damage on the impact response in the thin (4mm) laminate, with both the Force-Time Response and the Displacement-Time behaviour being predicted well. The modelling of damage in the thicker laminates showed that the damage that was observed in this laminate does not have a huge effect of the Force-Time Response, however when the Displacement-Time Behaviour is looked at then the damage, only very slight with reduction factors of 0.9, resulted in a much better prediction of the displacement behaviour than the

model without damage does. These finding show promising signs for the incorporation of damage into this established model, and that a even more accurate prediction may be obtained by introducing further stiffness reduction factors at more accurate indentation values that actually correspond to failure event within the impact duration.

Throughout this thesis, several factors have been studied that affect the level of damage that is caused by an impact event. Evidence has been given that shape, size and level of flexibility can be changed in order to improve the level of impact resistance and damage tolerance. It was also shown that it was possible to modify an existing analytical model to incorporate the affects of the introduction of damage during the impact event, and the results shows the possibility of further development that would provide a more accurate introduction of damage and hence a superior impact response prediction.

9. Conclusions

From all the work performed and reported within this thesis, many conclusions have been made regarding the factors that affect the level of impact resistance and damage tolerance in composites. This chapter will list the conclusions for each chapter separately although they can all be related to each other as all the separate investigations were based around the same theories.

9.1 Impact of Curved Composite Laminates

This was the first investigation performed and the findings here were the basis for the rest of the thesis. Several factors were found to affect the level of damage that occurred in the curved samples.

Results showed that the curvature provides a preferential direction for damage to grow in. Damage increases more along the curvature direction than across the curvature when impact energy is increased.

The first indications that flexibility plays a major role in the level of damage that occurs due to impact are also shown in this investigation. Flexibility is shown to be an energy dissipation mechanism resulting in a damage limitation route. The results showed that the more flexible the arrangement the less damage that occurs, whilst the more stiff the arrangement the more damage occurs.

Through thickness damage shows that damage may be initiated simultaneously by compression failure under the impact point and tension failure of the back face due to the flexure of the panel. Also indications show that the change of shape of the curved sample both promotes and arrests progressive damage growth.

9.2 Impact of Thin Laminates

This investigation was a continuation of the theory that flexibility provides a good energy absorption mechanism and within limits the more flexible a panel the more damage tolerant it is.

Results showed that changing the shape and material constituents can prove to be an effective way of increasing flexibility and damage tolerance. A less stiff fibre and longer specimen span gives better flexibility and better damage tolerance. Composites based on glass fibre are much more damage tolerable, such that a stiffer specimen size (short specimen span), which is the less damage tolerant of the glass specimens, is more damage resistant than a more flexible specimen size (longer specimen span), which is the more damage tolerant of the carbon fibre based specimens.

Results indicate that there is a threshold peak contact force that is reached as the drop height (impact energy) increases, indicating that there must be a level of damage or displacement that is reached that does not allow higher contact forces than the threshold value.

Both the Displacement-Time and High Speed Photography Sequences show that Glass Fibre specimens can deform more than the carbon fibre specimens and that at high enough drop heights the damage in the carbon fibre specimens becomes permanent to the extent that the sample is fractured and level of displacement can reach that of the glass fibre specimens.

9.3 The Effects of Dimension Changes

This investigation showed how dimension changes effect the both the impact response and the damage tolerance.

The thicker the specimen the higher the contact forces that occur and the lower the displacement levels in the impactor and the specimen. A decrease in width reduces the peak contact force, and a decrease in length increases the peak contact force level. Using the rebound velocity as an indication of the level of energy that is absorbed, a decrease in length changes the effects on the energy absorbed of a change in width of the specimen. The long specimens all absorb the same level of energy, whilst a decrease in width of the specimen in the short specimen decreases the level of energy absorbed.

A decrease in thickness increases the level of damage that occurs. A decrease in length increases the level of damage. There is a threshold width at which the level of damage increases.

The same trends in Force and Displacement behaviour are observed in the damage inducing impacts are observed in the non-damage inducing impacts.

9.4 Analytical Modelling

An established two-degree of freedom spring mass model was used to model the impact response of two of the seven specimen types used in the dimension changes study. Modifications were also made in order to try and incorporate the effects of damage on the impact response.

The model predicts well the impact response of the 4mm thick samples. However for thicker laminates the model used under predicts the peak force and over predicts the impact duration. The introduction of damage into the model in the form of 3 stiffness reduction factors at critical indentation factors also produced good predictions.

The model results show that the levels of damage in the thick laminates do not affect the Force-Time response but does affect the displacement behaviour, in providing better predictions.

10. Recommendations for Future Work

The thesis has shown the start of research that could be further developed to better understand the findings that have been recorded.

10.1 Experimental Work

- The effects of curvature need to be understood in much greater detail before outright conclusions can be made. Further study can look at how different sized curvatures and different sized curved specimens change the level of damage that occurs. Also more impact conditions could be looked into, high mass, low velocity and intermediate velocities and masses can be used.
- Flexibility of thin laminates can also be looked at in further detail. More degrees of flexibility need to be looked at as well as a wider variety of sample shapes and sizes. A wider variety of impact regimes may also be used.
- A larger variation in drop heights in the thin laminates can be used to verify whether a threshold drop height (impact energy) exists and results in constant peak force, and if this force does exist to determine the actual value of impact energy at which this threshold value occurs for a variety of flexibilities and specimen sizes.
- A larger variety of thickness, length and widths can be used to show in greater detail of how these factors affect both the impact response and the damage that occurs.
- A greater variety of widths can be used to determine the actual threshold width at which damage levels increase and begin to stretch across the specimen as shown in the results in Chapter 6.

All the above research would be of great use as criteria would be established that would be of significant value when designing structures and components from composite materials for application in areas where they would be prone to a variety of impact events.

10.2 Analytical Modelling

Chapter 7 showed that the spring mass model used could be developed using the introduction of three contact stiffness reduction factors at certain levels of critical indentation to predict the changes in the impact response. The model can therefore be further developed and refined to include further stiffness reduction factors at more accurate levels of indentation to provide a more accurate prediction of damage effects.

The stiffness reduction factors and critical indentation levels can be measured using experimental work in the form of progressive static indentation test followed by stiffness measurements of partially damaged sample, therefore providing more accurate data for stiffness reduction and indentation levels at which these occur. This data can then be used to provide better predictions within the model used within this thesis.

Investigations into the possibility of modelling the responses of thin and curved laminates can also be made.

References

Abrate, S. Impact on Laminated Composite Structures. *Applied Mechanics Review*, Vol. 44, No. 4, 155-190. April 1991

Abrate, S.. Impact on Laminated Composites: Recent Advances. *Applied Mechanics Review*, Vol. 41, No. 11, 517-544. November, 1994

Abrate, S. Impact on Composite Structures. ISBN 0-521-47389-6, Cambridge University Press, New York, USA, 1998

Ashby, M. F., Jones, D. R. H.. Engineering Materials 1: An Introduction to their Properties and Applications. ISBN 0-08-026138-8, Pergamon Press Ltd, Oxford, England, 1981

Aymerich, F., Meili, S. Ultrasonic Evaluation of Matrix Damage in Impacted Composite Laminates. Composites Part B: Engineering, Vol. 31. No. 1, 1-6. January 2000.

Baker, A.A., Jones, R., Callinan, R.J.. Damage Tolerance of Graphite/Epoxy Composites. *Composite Structures*, Vol. 4, 15-44. !985

Beks, F.A.. Examination of Impact Response and Damage of Composite Laminates. Ing. Thesis, FFA, The Aeronautical Research Institute of Sweden, Bromma Sweden, 1996

Bland, P.W.. Impact Response and Performance of Carbon Fibre Reinforced Polymer. PhD. Thesis, Imperial College of Science Technology and Medicine, London, England, 2000

Cairns, D.S., Lagace, P.A.. A Consistent Engineering Methodology for the Treatment of Impact in Composite Materials. *J. of Reinforced Plastics and Composites*, Vol 11, 396-412, April 1992

Cantwell, W.J. The Influence of Target Geometry on the High Velocity Impact response of CFRP. *Composite Structures*, Vol. 10, 247-265. 1988

Cantwell, W.J., Curtis, P.T., Morton, J.. An Assessment of the Impact Performance of CFRP Reinforced with High Strain Carbon Fibres. *Composite Science and Technology*, Vol. 25, 133-148. 1986

Cantwell, W.J., Morton, J.. Detection of Impact Damage in CFRP Laminates. *Composite Structures*, Vol. 3, 241-257. 1985

Cantwell, W.J., Morton, J.. Geometrical Effects in the Low Velocity Impact response of CFRP. *Composite Structures*, Vol. 12, 39-59. 1989(a)

Cantwell, W.J., Morton, J.. The Influence of Varying Projectile Mass on the Impact Response of CFRP. *Composite Structures*, Vol. 13, 101-114. 1989(b)

Cantwell, W.J., Morton, J.. The Impact Resistance of Composite Materials – A Review. *Composites*, Vol. 22, No. 5, 347-362. September 1991

Cantwell, W.J., Morton, J.. The Significance of Damage and Defects and their Detection in Comppsite Materials: A Review. *J. of Strain Analysis*, Vol. 27, No. 1, 29-42, 1992

Caprino, G., Crivelli Visconti, I., Di Ilio, A.. Elastic Behaviour of Composite Structures Under Low Velocity Impact. *Composites*, Vol. 15, No. 3, 231-234. July, 1984

Chang, F.K., Choi, H.Y., Jeng, S.T.. Study on Impact Damage in Laminated Composites, *Mechanical Materials*, Vol 10, 83-95. 1990

Chen, J.K., Allahdadi, F.A., Carney, T.C.. High Velocity Impact of Graphite/Epoxy Composite Laminates. *Composites: Science and Technology*, Vol. 57, 1369-1379, 1997

Choi, H.T., Chang, F.K.. A Model for Predicting Damage in Graphite/Epoxy Laminated Composites Resulting from Low Velocity Point Impact. *J. of Composite Materials*. Vol. 26, No. 14, 2134-2169. 1992

Choi, H.Y., Downs, R.J., Chang, F.K.. A New Approach toward understanding Damage Mechanisms and Mechanics of Laminated Composites due to Low Velocity Impact: Part I – Experiments. *J. of Composite Materials*, Vol. 25, 992-1011. 1991

Choi, H.Y., Downs, R.J., Chang, F.K.. A New Approach toward understanding Damage Mechanisms and Mechanics of Laminated Composites due to Low Velocity Impact: Part II – Analysis. *J. of Composites Materials*, Vol. 25, 1012-1038. 1991

Christoforou, A.P.. On the Contact of a Spherical Indentor and a Thin Composite Laminate. *Composite Structures*, Vol. 26, 77-82. 1993

Christoforou, A.P., Swanson, S.R., Beckwith, S.W.. Lateral Impact of Composite Cylinders. *ASTM STP*, Vol 1012, 373-386. 1989

Christoforou, A.P., Yigit, A.S.. Normalised Impact Response and Damage in Thin Composite Laminate Supprted by a Rigid Structure. *J. Composite Materials*, Vol. 28, No. 16, 1553-1573, 1994

Christoforou, A.P., Yigit, A.S.. Characterisation of Impact in Composite Plates. *Composite Structures*, Vol. 43, 15-24, 1998

Chritescu, N., Malvern, L.E., Sierakowski, R.L.. Failure Mechanisms in Composite Plates Impacted by Blunt Ended Impactors. *ASTM STP*, Vol. 568, 158-172. 1975

Clark, G.. Modelling of Impact Damage in Composite Laminates. *Composites*, Vol. 20, No. 3, 209-214, 1989

Collombet, F., Lalbin, X., Bonini, J., Martin, V., Lataillade, J.L.. Damage Criteria for the Study of Impacted Composite Laminates. *Composites: Science and Technology*, Vol. 58, 679-686, 1998

Crook, A.W. A Study of Some Impacts between Metal Bodies by a Piezoelectric Method. *Proceedings of the Royal Society*, London, Series A, Vol. 212, 377-390. 1952

Davies, G.O.A., Hitchings, D., Wang, J.. Prediction of Threshold Impact Energy for the onset of Delamination in Quasi-Isotropic Carbon/Epoxy Composite Laminates under Low Velocity Impact. *Composites Science and Technology*, Vol. 60, 1-7, 2000

Davies, G.O.A., Zhang, X.. Impact Damage Prediction in Carbon Composite Structures. *Int. J. of Impact Engineering*, Vol. 16, No. 1, 149-170, 1995

De Freitas, M., Silva, A., Reis, L.. Numerical Evaluation of Failure Mechanisms on Composite Specimens Subjected to Impact Loading. *Composites Part B: Engineering*, Vol. 31, 199-207, 2000

DeLuca, E., Prifti, J., Betheney, W., Chou, S.C.. Ballistic Impact Damage of 2-Glass-Reinforced Plastic Structural Armour. *Composites: Science and Technology*, Vol. 58, 1453-1461, 1998

De Moura, M.F.S.F., Marques, A.T.. Prediction of Low Velocity Impact Damage in Carbon-Epoxy Laminates. *Composites Part A: Applied Science and Manufacturing*, Vol. 33, 361-368, 2002

Dorey, G., Bishop, S., Curtis, P.. On the impact Performance of Carbon Fibre Laminates with Epoxy and PEEK Matrices. *Composites Science and Technology*, Vol. 23, No. 3, 221-237. 1985

Duan, S.H., Ya, T.Q.. Three Dimensional Frictional Dynamic Contact Analysis for Predicting Low Velocity Impact Damage in Composite Lamiantes. *Advanced Engineering Software*, Vol. 33, 9-15, 2002

Found, M.S., Howard, I.C., Paran, A.P.. Size Effects in Thin CFRP Panels Subjected to Impact. *Composite Structures*, Vol. 38, No. 1-4, 599-607. 1997

Fuoss, E., Straznicky, P.V., Poon, C.. Effects of Stacking Sequence on the Impact Resistance in Composite Laminates – Part: Parametric Study. *Composite Structures*, Vol. 41, 67-77. 1998

Fuoss, E., Straznicky, P.V., Poon, C.. Effects of Stacking Sequence on the Impact Resistance in Composite Laminates – Part 2: Prediction Method. *Composite Structures*, Vol. 41, 177-186. 1998

Garg, A.C.. Delamination – A Damage Mode in Composite Structures. *Engineering Fracture Mechanics*, Vol. 29, No. 5, 557-584. 1998

Gary, G., Zhoa, H.. Dynamic Testing of Fibre Polymer Matrix Composite Plates Under Transverse In-Plane Compression. Composites Part A: Applied Science and Manufacturing, Vol. 31, No. 8, 835-840. August 2000

Gibson, R.F.. Dynamic Mechanical Properties of Advanced Composite Materials and Structures: A Review of Recent Research. *The Shock and Vibration Digest*, Vol. 22, No. 8, 3-12. 1990

Goldsmith, W. Impact:the theory and physical behaviour of colliding solids. Edward Arnold (Publishers) Ltd, London, 1960

Gu, Z.L., Sun, C.T.. Prediction of Impact Damage Regiond in SMC Composites. *Composite Structures*, Vol. 26, No. 3, 179-190. 1987

Johnson, K.L. Contact Mechanics. ISBN 0-521-34796-3, Cambridge University Press, Cambridge, 1985

Jones, R., Paul, J., Tay, T.E., Williams, J.F.. Assessment of the Effect of Impact Damage in Composites: Some Questions and Answers. *Theoretical and Applied Fracture Mechanics*. Vol. 9, 83-95, 1988

Joshi, S.P., Sun, C.T.. Impact Induced Fracture in a Laminated Composite. *J. of Composite Materials*, Vol. 19, 51-66. January, 1985

Kin, J.K., Goo, N.S., Kim, T.K.. The Effect of Curvature on the Dynamic Response and Impact-Induced Damage in Composite Laminates. *Composite: Science and Technology*, Vol. 57, 763-773, 1997

Kim, S.J., Goo, N.S.. Dynamic Contact Responses of Laminated Composite Plates According to Impactor's Shape. *Computers and Structures*, Vol. 65, No. 1, 83-90, 1997

Kostopoulos, V., Markopoulos, Y.P., Giannopoulos, G., Vlachos, D.E.. Finite Element Analysis of Impact Damage Response of Composite Motorctcle Safety Helmets. *Composite Part B: Engineering*, Vol. 33, Issue 2, 99-107, March 2002

Lagace, P.A., Wolf, E.. Impact Damage Resistance of Several Laminated Material Systems. *AIAA Journal*, Vol. 33, No. 6, 1106-1113, June 1995

Lal, K.M.. Residual Strength Assessment of Low Velocity Impact Damage of Graphite-Epoxy Laminates. *J. of Reinforced Plastic Composites*, Vol. 2, 226-238. 1983(a)

Lal, K.M.. Low Velocity Transverse Impact behaviour of 8-Ply, Graphite-Epoxy Laminates. *J. Reinforced Plastic Composites*, Vol. 2, 216-225. 1983(b)

Lal, K.M.. Relationship between Phase Difference and Coefficient of Restitution during Low Velocity Foreign Object Transverse Damage of Composite Plates. *Composites Technology Review*, Vol. 6, No.3, 109-111. 1984

Lee, S.M., Zahuta, P.. Instrumented Impact and Static Indentation of Composites. *J. of Composite Materials*, Vol. 25, 204-222. February, 1991

Lui, D.. Impact Induced Delamination – A View of Bending Stiffness Mismatching. *J. of Composite Materials*, Vol. 22, 674-692. 1988

Lui, D., Malvern, L.E.. Matrix Cracking in Impacted Glass/Epoxy Plates. *J of Composite Materials*, Vol. 21, 594-609. July 1987

Lui, D., Raju, B.B., Dang, X.L.. Size Effects on Impact Response of Composite Laminates. *Int. J. of Impact Engineering*, Vol.21, No. 10, 837-854. 1998

Lui, S. Quasi-Impact Damage Initiationand Growth of Thick-Section and Toughened Composite Materials. *Int. J. Solids and Structures*, Vol. 31, No. 22, 3079-3098, 1994

Lui, S., Kutlu, Z., Chang, F.K.. Matrix Cracking and Delaminations in Laminated Composite Beams Subjected to a Transverse Concentrated Line Load. *J. of Composite Materials*, Vol. 27, No. 5, 436-470. 1993

Matthews, F. L., Rawlings, R.D. Composite Materials: Engineering and Science. ISBN 0-412-55960-9 Chapman and Hall, Oxford, 1994

Mines, R.A.W., Roach, A.M., Jones, N.. High Velocity Perforation Behaviour of Polymer Composite Laminates. *Int. J. of Impact Engineering*, Vol. 22, 561-588, 1999

Moon, F.C.. Waves Surfaces Due to Impact on Anisotropic Plates. *J. of Composite Materials*. Vol. 6, 62-79. 1972

Morita, H., Adachi, T., Tateishi, Y., Matsumoto, H.. Characterisation of Impact damage Resistance of CF/PEEK and CF/Toughened Epoxy Laminates Under Low and High Velocity Impact Tests. *J. Of Reinforced Plastics and Composites*, Vol. 16, No. 2, 131-143, 1997

Morton, J., Godwin, E.W.. Impact Response of Tough Carbon Fibre Composites. *Composite Structures*, Vol. 13, 1-19, 1989

Olsson, R.. Impact Response of Composite Laminates – A Guide to Closed Form Solutions. *FFA Report*, FFA TN 1992-33, 1992(a)

Olsson, R.. Impact Response of Orthotropic Composite Plates Predicted from a One-Parameter Differential Equation. *AIAA Journal*, Vol. 30. No. 6, 1587-1596, 1992(b)

Olsson, R.. Impact Response and Delamination of Composite Plates. PhD Thesis, Department of Aeronautics, Kungliga Tekniska Hogskolan (Royal Institute of Technology, Stockhom, Sweden, 1998

Olsson, R.. Impact and Damage Tolerance of Composites – Status and Future Work at FFA. *FFA Report*, FFA TN 1999-77, 1999

Olsson, R.. Analytical Prediction of Large Mass Impact Damage in Composite Laminates. *Composites Part A: Applied Science and Manucturing*, Vol. 32, No. 9, 1207-1215, 2001

Olsson, R.. Engineering Method for the Prediction of Impact response and Damage in Sandwich Panels. *J. of Sandwich Structures and Materials*, Vol. 4, 3-29, 2002

Olsson, R.. Closed Form Prediction of Peak Load and Delamination Onset under Small Mass Impact. *Composite Structures*, Vol. 59, 341-349, 2003

Olsson, R.. Mass Criterion for Wave Controlled Impact Response of Composite Plates. *Composites Part A: Applied Science and Manufacturing*, Vol. 31, 879-887, 2000

Olsson, R., Asp, L.E., Nilsson, S., Sjogren, A.. A Review of Some Key Devvelopments in the Analysis of Effects of Impact Upon Composite Structures. *Composite Structures: Theory and Practice, ASTM STP 1383*, P.Grant, C.Q. Rousseau, Eds, Ammerican Society for Testing and Materials, West Conchohocken, PA, 12-28, 2000

Olsson, R., McManus, H.L.. Improved Theory for Contact Indentation of Sandwich Panels. *AIAA Journal*, Vol 34, No. 6, 1239-1244, 1996

Olsson, R., Thesken, J.C., Brandt, F., Jonsson, N., Nilsson, S.. Investigations of Delamination Criticaility and Transferability of Growth Criteria. *Composite Structures*, Vol. 36, 221-247, 1996

Pavier, M.J., Clarke, M.P.. Experimental Techniques for the Investigation of the Effects of Impact Damage on Carbon Fibre Compostes. *Composites: Science and Technology*. Vol. 55, 157-169. 1995

Peiffer, D.G.. Impact Strength of Thick Interlayer Composites. *J. of Applied Polymer Science*, Vol. 24, 1451-1455. 1979

Pierson, M.O., Vaziri, R.. Analytical Solution for Low Velocity Impact Response of Composite Plates. *AIAA Journal*, Vol. 34, No. 8, 1633-1640, August 1996

Shivakumar, K.N., Elber, W., Illg, W.. Prediction of Impact Force and Duration Due to Low Velocity Impact on Circular Composite Laminates. *J. of Applied Mechanics*, Vol. 52, 674-680. September, 1985

Razi, H., Kobayashi, A.S.. Delamination in Cross-Ply Laminated Composite Subjected to Low Velocity Impact. *AIAA Journal*, Vol. 31, No. 8, 1498-1502. 1993

Richardson, M.O.W., Wisheart, M.J.. Review of Low Velocity Impact Properties of Composite Materials. *Composites Part A*, Vol 27A, 1123-1131. 1996

Robinson, P., Davies, G.A.O.. Impactor Mass and Specimen Geometry Effects in Low Velocity Impact of Laminated Composites. *Int. J. of Impact Engineering*. Vol. 12, No. 2, 189-207. 1992

Ross, C.A., Sierakowski, R.L.. Studies on the Impact Resistance of Composite Plates. *Composites*, Vol. 4, 157-161. 1973

Ross, C.A., Sierakowski, R.L.. Elastic Waves in Fibre Reinforced Composites. *The Shock and Vibration Digest*, Vol. 7, No. 1, 96-107. 1975

Schoeppner, G.A., Abrate, S.. Delamination Threshold loads fro Low Velocity Impact on Composite Laminates. *Composites Part A: Applied Science and Manufacturing*, Vol. 31, No. 9, 903-915, September 2000

Schonberg, W.P.. Protecting Spacecraft against Orbital Debris Impact Damage usng Composite Materials. *Composites Part A: Applied Science and Manufacturing*, Vol. 31, 869-878, 2000

Sierakowski, R.L., Chaturvedi, S.K.. Dynamic Loading and Characterisation of Fibre Reinforced Composites. John Wiley and Sons. New York, USA. 1997

Sierakowski, R.L., Malvern, L.E., Ross, C.A.. Dynamic Failure Modes in Impacted Composite Plates. in *Failure Modes in Composites III*, Chiao, T.T. (ed), AIME, New York, USA, 73-88. 1976

Sjoblem, P.O., Hartness, J.T., Cordell, T.M.. On Low Velocity Impact Testing of Composite Materials. *J. of Composite Materials*. Vol. 22, 30-52. January, 1988

Stout, M.G., Koss, D.A., Lui, C., Idasetima, J.. Damage Development in Carbon/Epoxy Laminates under Quasi-Static and Dynamic Loading. *Composites: Science and Technology*, Vol. 55, No. 16, 2339-2350, December 1999

Swanson, S.R., Razaee, H.G.. Strength Loss in Composites from Lateral Contact Loads. *Composites: Science and Technology*, Vol. 38, 43-54, 1990

Takeda, N., Sierakowski, R.L., Malvern, L.E.. Wave Propagation Experiments on Ballistically Impacted Composite Laminates. *J. Composite Materials*, Vol. 15, 157-174. March, 1981

Takeda, N., Sierakowski, R.L., Malvern, L.E.. Microscopic Observations of Cross Sections of Impacted Composite Laminates. *Composites Technology Review*. Vol. 4, 40-44. 1982(a)

Takeda, N., Sierakowski, R.L., Ross, C.A., Malvern, L.E.. Delamination-crack Propagation in Ballistically Impacted Glass/Epoxy Composite Laminates. *Experimental Mechanics*, Vol. 22, No. 1, 19-25, January 1982(b)

Tan, T.M., Sun, C.T.. Use of Static Indentation Laws in Impact Analysis of Laminated Composite Plates. *J. Applied Mechanics,* Vol 52, 6-12. 1985

Ting, T.C.T.. Dynamic Response of Composites. *Applied Mechanics Review*, Vol. 33, No. 12, 1692-1635. December ,1980

Tracy, J.T., Pardoen, G.C.. Effect of Delamination on the Flexural Stiffness of Composite Laminates. *Thin Walled Structures*, Vol. 6, 371-383, 1988

Wang, J., Karihaloo, B.L.. Matrix Crack – Delamination in Composite Laminates under Transverse Loading. *Composite Structures*, Vol. 38, N0. 1-4, 661-666. 1997

Wardle, B.L., Lagace, P.A.. Importance of Instability in Impact Response and Damage Resistance of Composite Shells. *AIAA Journal*, Vol. 35, No. 2, 389-396, 1997

Wiggenraad, J.F.M., Zhang, X., Davies, G.A.O.. Impact Damage Prediction and Failure Analysis of Heavily Loaded, Blade Stiffened Composite Wing Panels. *Composite Structures*, Vol. 45, 81-103, 1999

Wu, E., Shyu, K.. Response of Composite Laminates to Contact Loads and Relationship to Low Velocity Impact. *J. Composite Materials*, Vol. 27, No. 15, 1443-1464, 1993

Wu, H.Y.T., Springer, G.S.. Measurements of Matrix Cracking and Delamination caused by Impact on Composite Plates. *J. of Composite Materials*, Vol. 22, 518-532. 1988

Wu, E., Yen, C.S.. The Contact Behaviour between Laminated Composite Plates and Rigid Spheres. *J. Applied Mechanics,* Vol. 61, No. 1, 60-66. 1994

Yang, S.H., Sun, C.T. Indentation Law for Composite Laminates. *ASTM STP*, Vol 787, 425-367. 1982

Yigit, A.S., Christoforou, A.P.. Impact Dynamics of Composite Beams. *Composite Structures*, Vol. 32, 187-195, 1995

Zhang, Y., Wang, S., Petersson, B.. Large Deflection Analysis of Composite Laminates. *J. of Materials Processing Technology*, Vol. 138, 34-40, 2003

Zhou, G.. Damage Mechanisms in Composite Laminates Impacted by a Flat Ended Impactor. *Composites Science and Technology*, Vol. 54, 267-273. 1995

Zhou, G. Static Behaviour and Damage of Thick Composite Laminates. *Composite Structures*. Vol. 36, 13-22, 1996

Appendices

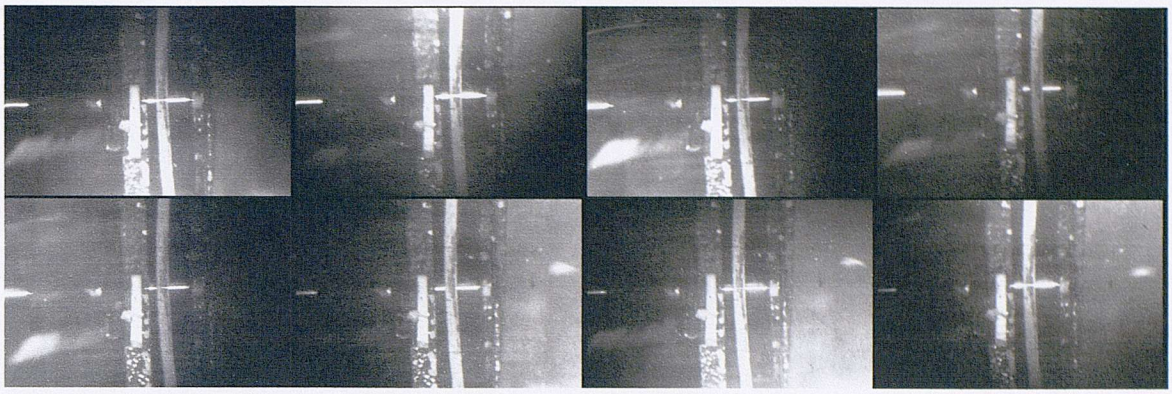
Appendix 1.

High Speed Photography Sequences for Curved Composite Laminates

Part 1:

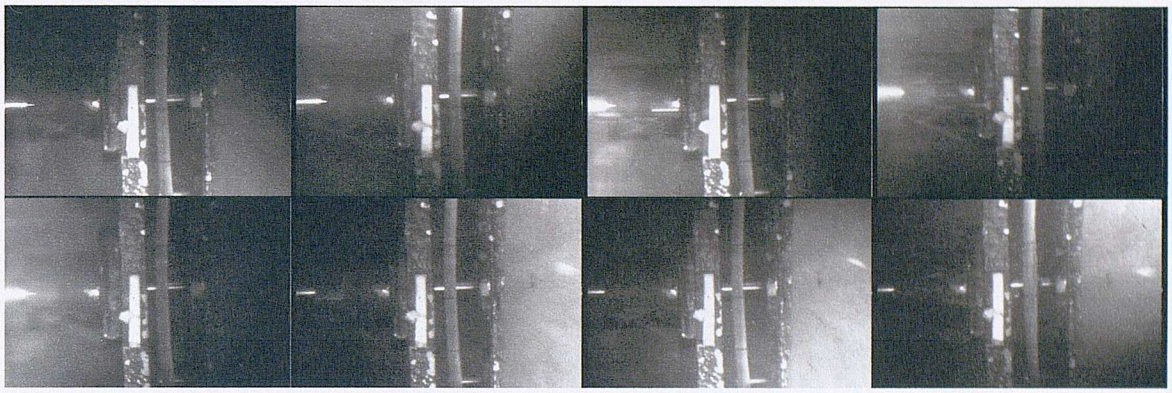
Specimens with a Longitudinal Curvature

Sample LC1



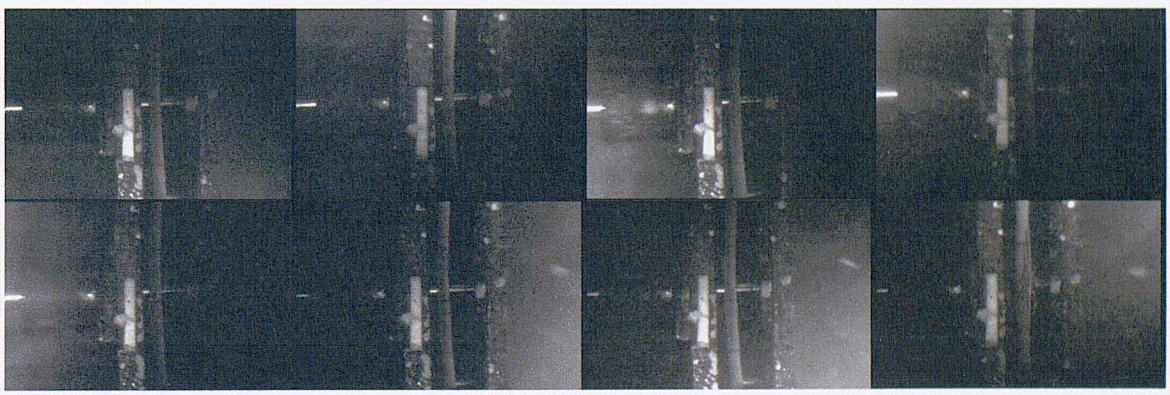
Frame	1	2	3	4	5	6	7	8
Setting (ms)	1.0	1.2	1.4	1.6	1.8	2.0	2.2	2.4
Exposure (μs)	60	60	60	60	60	60	60	60

Sample LC2



Frame	1	2	3	4	5	6	7	8
Setting (ms)	0.5	0.6	0.7	0.8	0.9	1.0	1.1	1.2
Exposure (μs)	60	60	60	60	60	60	60	60

Sample LC3



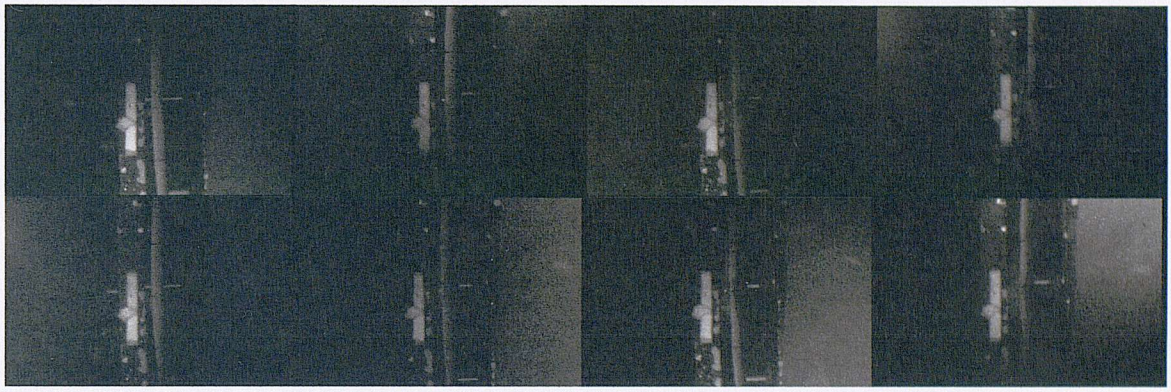
Frame	1	2	3	4	5	6	7	8
Setting (ms)	0.5	0.6	0.7	0.8	0.9	1.0	1.1	1.2
Exposure (μs)	60	60	60	60	60	60	60	60

Sample LC4



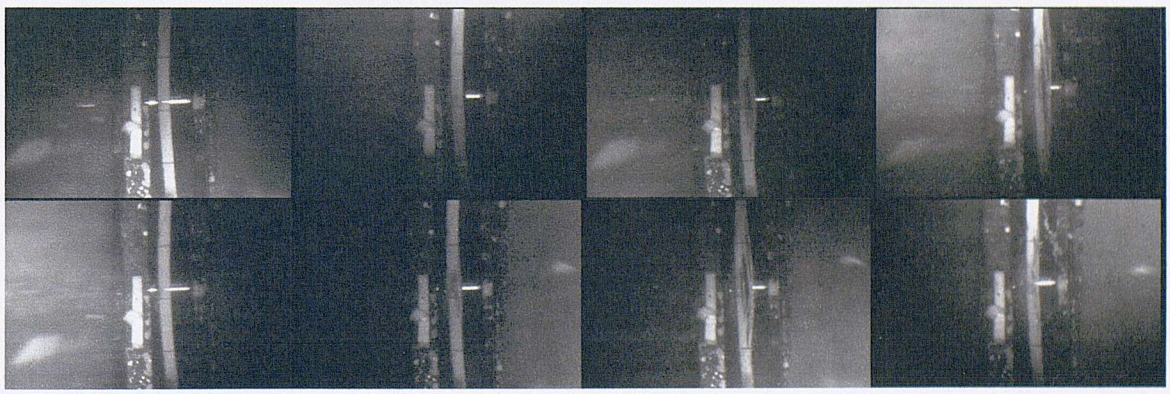
Frame	1	2	3	4	5	6	7	8
Setting (ms)	0.9	0.95	1.0	1.05	1.1	1.15	1.2	1.3
Exposure (μs)	25	25	25	25	25	25	25	25

Sample LC5



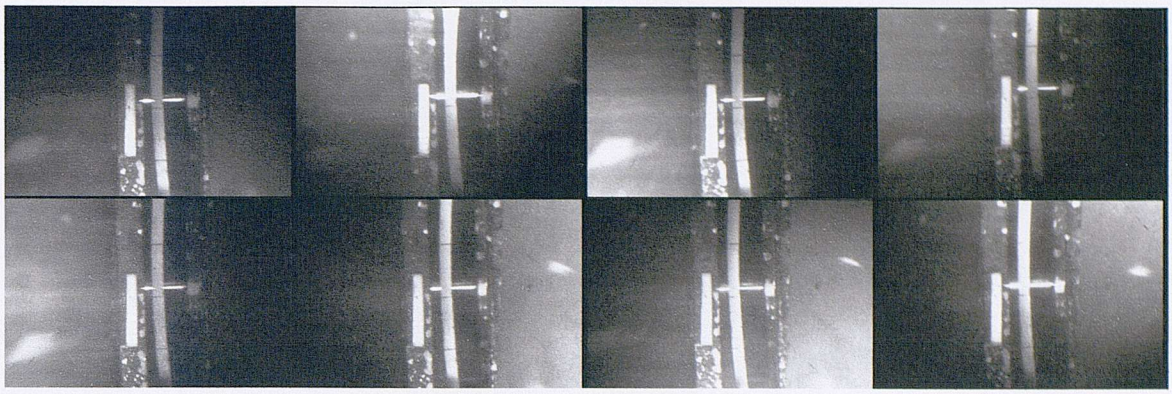
Frame	1	2	3	4	5	6	7	8
Setting (ms)	0.9	1.0	1.1	1.125	1.150	1.175	1.2	1.3
Exposure (μs)	25	25	15	15	15	15	25	25

Sample LC6



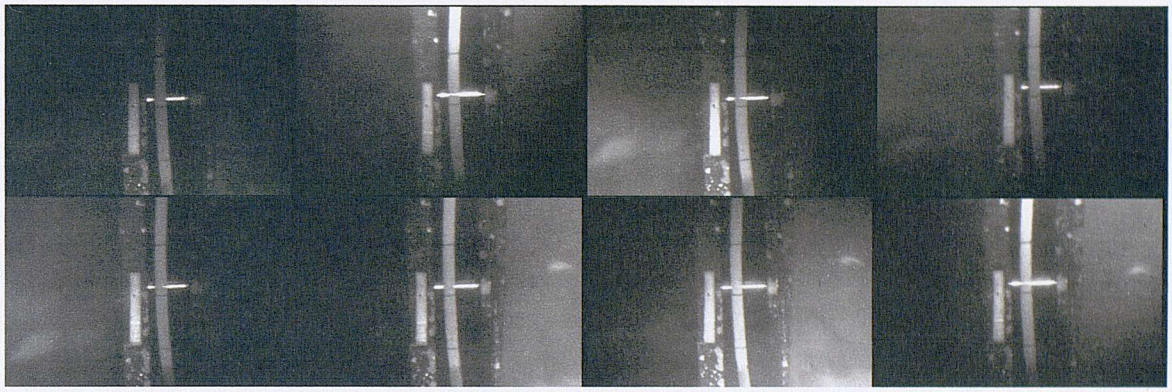
Frame	1	2	3	4	5	6	7	8
Setting (ms)	0.9	1.0	1.1	1.125	1.15	1.175	1.2	1.3
Exposure (μs)	25	25	15	15	15	15	25	25

Sample LC7



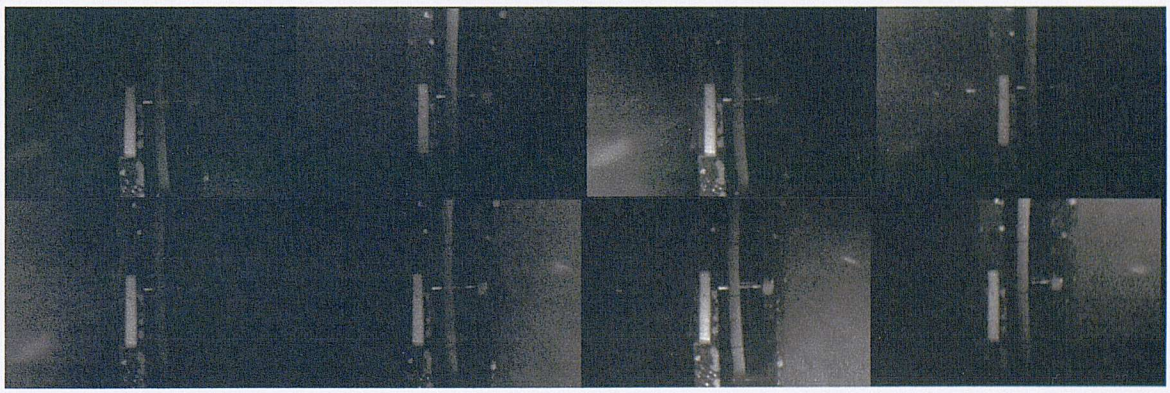
Frame	1	2	3	4	5	6	7	8
Setting (ms)	0.4	0.5	0.6	0.7	0.8	0.9	1.0	1.1
Exposure (μs)	50	50	50	50	50	50	50	50

Sample LC8



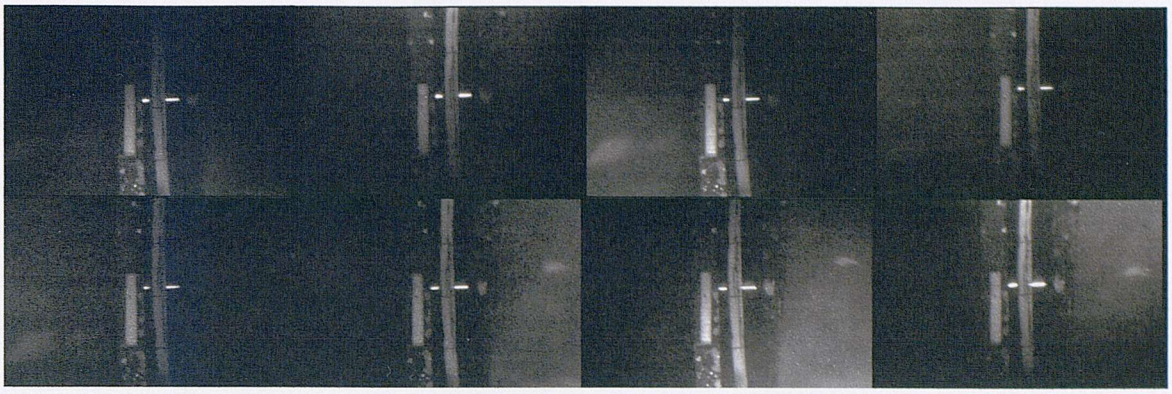
Frame	1	2	3	4	5	6	7	8
Setting (ms)	0.4	0.5	0.6	0.7	0.8	0.9	1.0	1.1
Exposure (μs)	25	25	25	25	25	25	25	25

Sample LC9



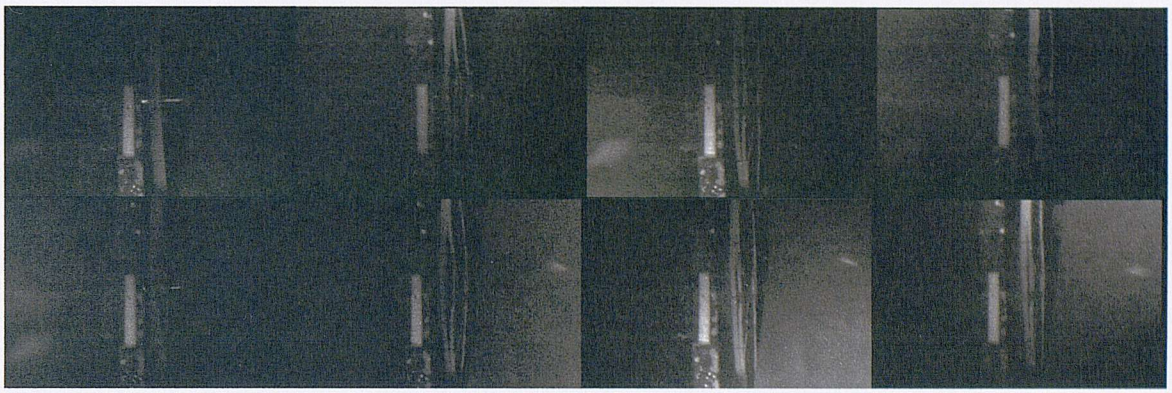
Frame	1	2	3	4	5	6	7	8
Setting (ms)	0.4	0.5	0.6	0.7	0.8	0.9	1.0	1.1
Exposure (μs)	10	10	10	11	12	13	14	15

Sample LC10



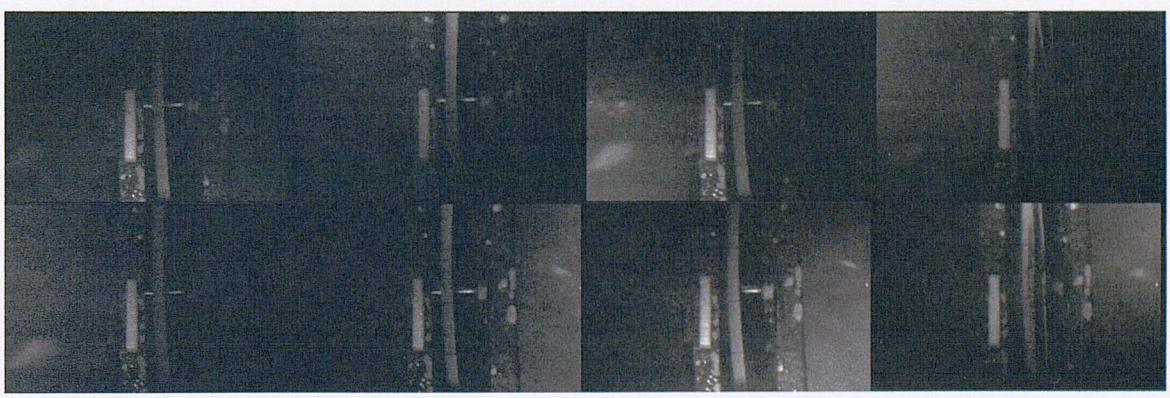
Frame	1	2	3	4	5	6	7	8
Setting (ms)	0.9	1.0	1.05	1.1	1.15	1.2	1.25	1.3
Exposure (μs)	10	10	10	11	12	13	14	15

Sample LC11



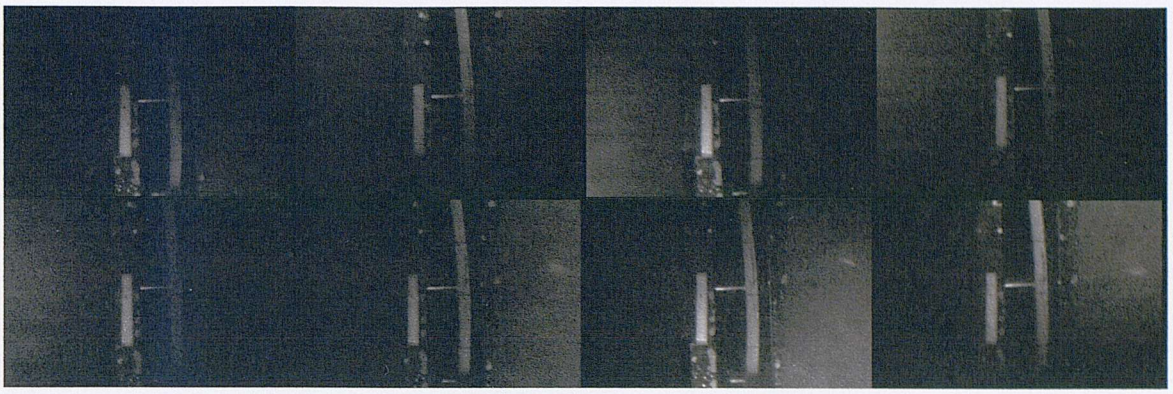
Frame	1	2	3	4	5	6	7	8
Setting (ms)	0.6	0.7	0.75	0.8	0.85	0.9	1.0	1.1
Exposure (μs)	10	10	10	11	12	13	14	15

Sample LC12



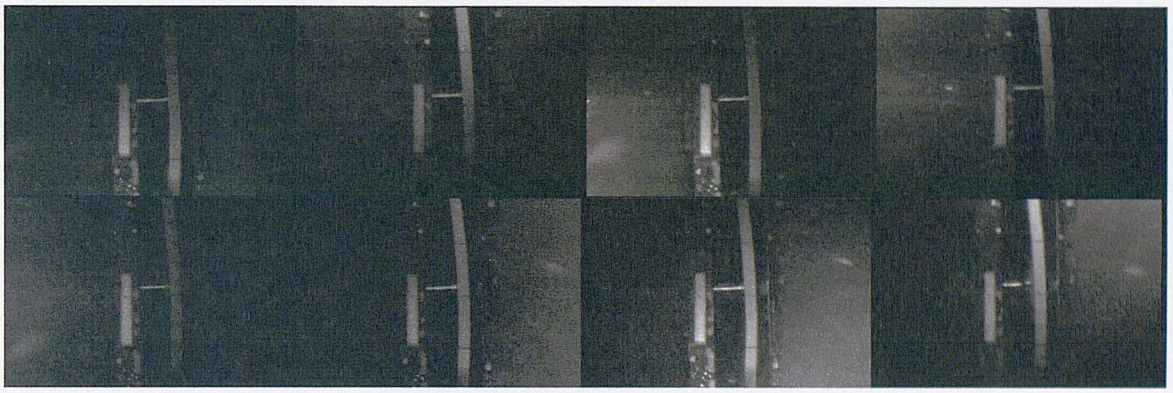
Frame	1	2	3	4	5	6	7	8
Setting (ms)	0.5	0.55	0.6	0.65	0.7	0.9	1.1	1.3
Exposure (μs)	10	10	10	11	12	13	14	15

Sample LC13



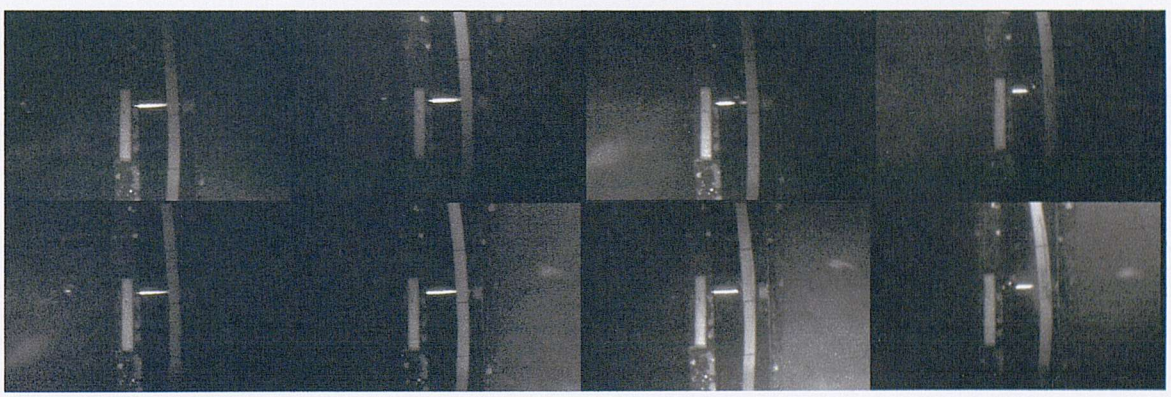
Frame	1	2	3	4	5	6	7	8
Setting (ms)	0.90	1.0	1.1	1.125	1.15	1.175	1.2	1.3
Exposure (μs)	10	10	10	11	12	13	14	15

Sample LC14



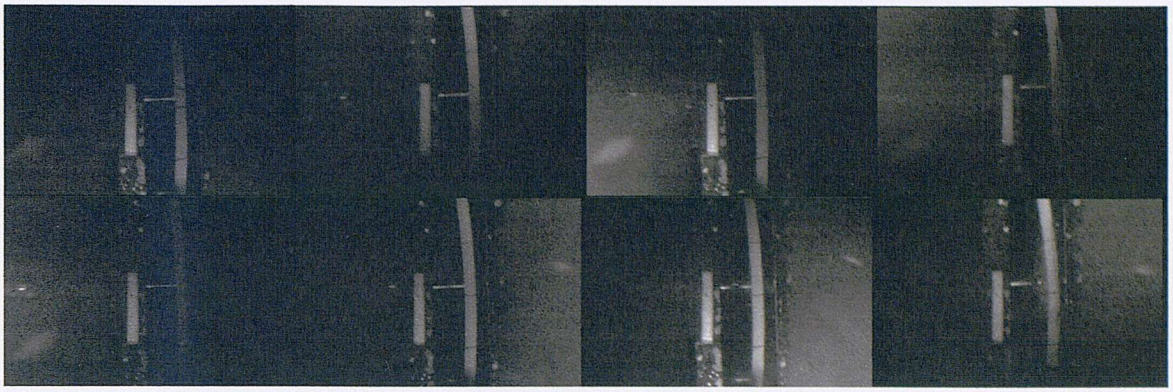
Frame	1	2	3	4	5	6	7	8
Setting (ms)	0.5	0.6	0.65	0.7	0.75	0.8	0.9	1.1
Exposure (μs)	10	10	10	11	12	13	14	15

Sample LC15



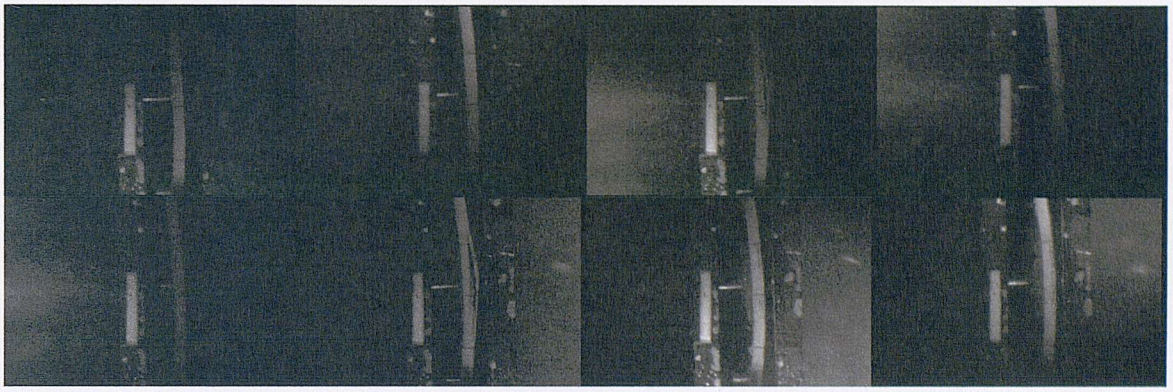
Frame	1	2	3	4	5	6	7	8
Setting (ms)	0.8	0.9	0.95	1.0	1.1	1.15	1.25	1.5
Exposure (μs)	10	10	10	11	12	13	14	15

Sample LC16



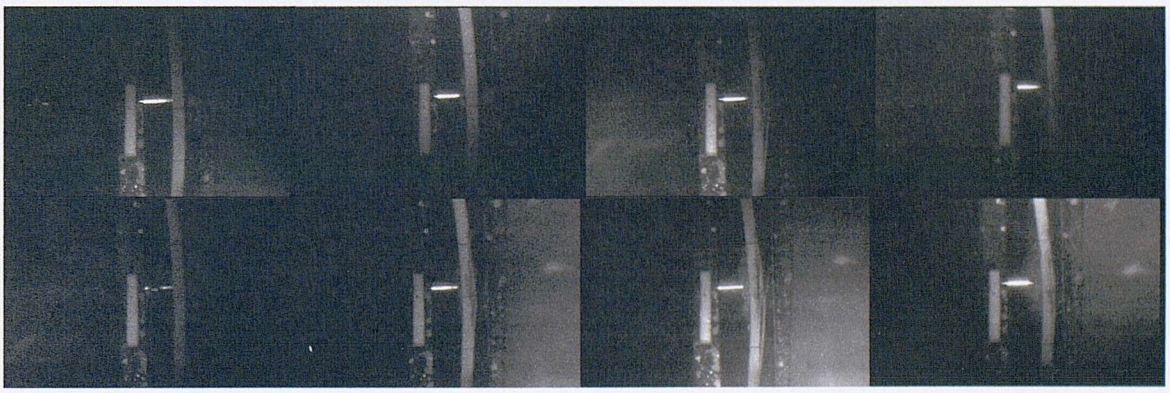
Frame	1	2	3	4	5	6	7	8
Setting (ms)	0.6	0.65	0.7	0.8	0.85	0.9	1.0	1.2
Exposure (μs)	10	10	10	11	12	13	14	15

Sample LC17



Frame	1	2	3	4	5	6	7	8
Setting (ms)	0.7	0.9	0.95	1.0	1.05	1.1	1.15	1.2
Exposure (μs)	10	10	10	11	12	13	14	15

Sample LC18

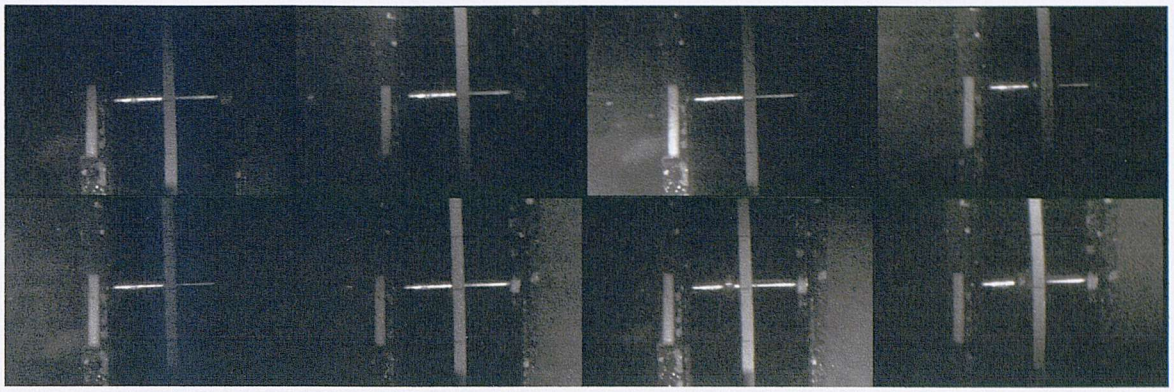


Frame	1	2	3	4	5	6	7	8
Setting (ms)	0.7	0.9	0.95	0.975	1.0	1.025	1.05	1.15
Exposure (μs)	10	10	10	11	12	13	14	15

Part 2:

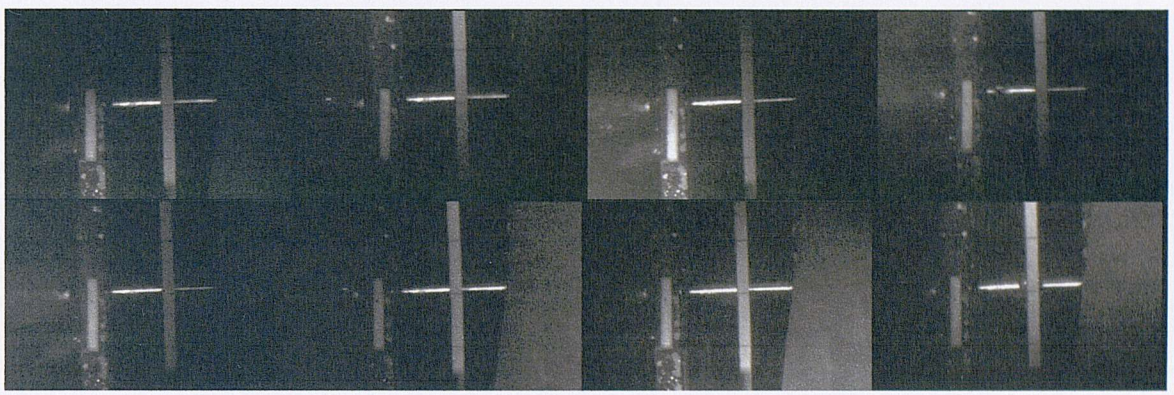
Specimens with a Transverse Curvature

Sample TC3



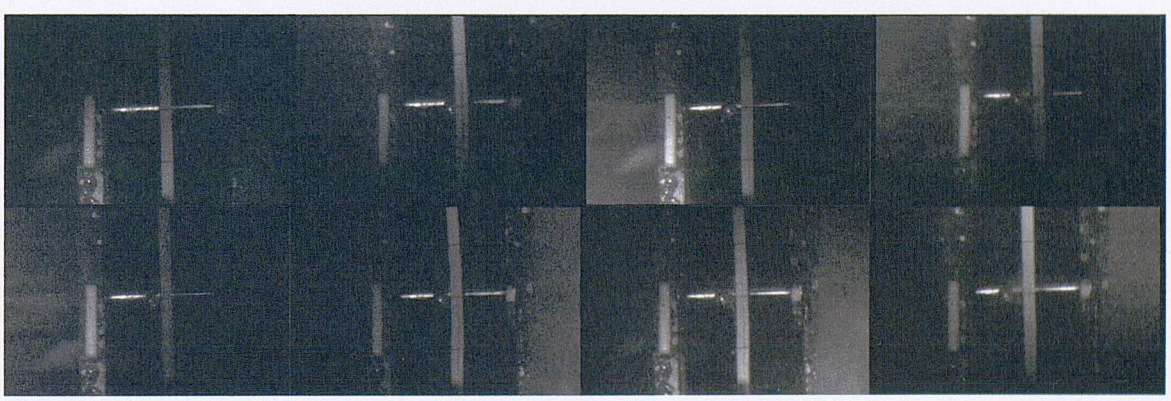
Frame	1	2	3	4	5	6	7	8
Setting (ms)	0.5	0.6	0.7	0.8	0.9	1.0	1.1	1.2
Exposure (μs)	10	10	10	11	12	13	14	15

Sample TC5



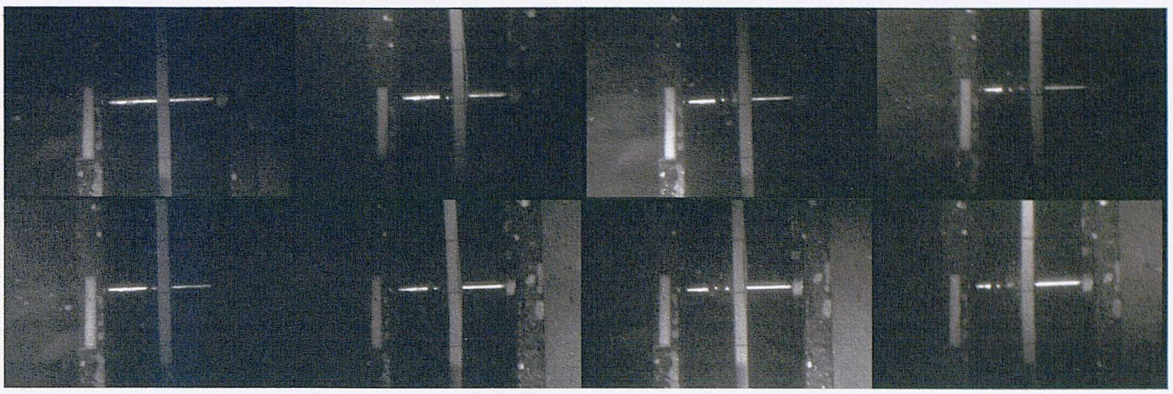
Frame	1	2	3	4	5	6	7	8
Setting (ms)	0.7	0.9	1.0	1.05	1.1	1.15	1.2	1.3
Exposure (μs)	10	10	10	11	12	13	14	15

Sample TC6



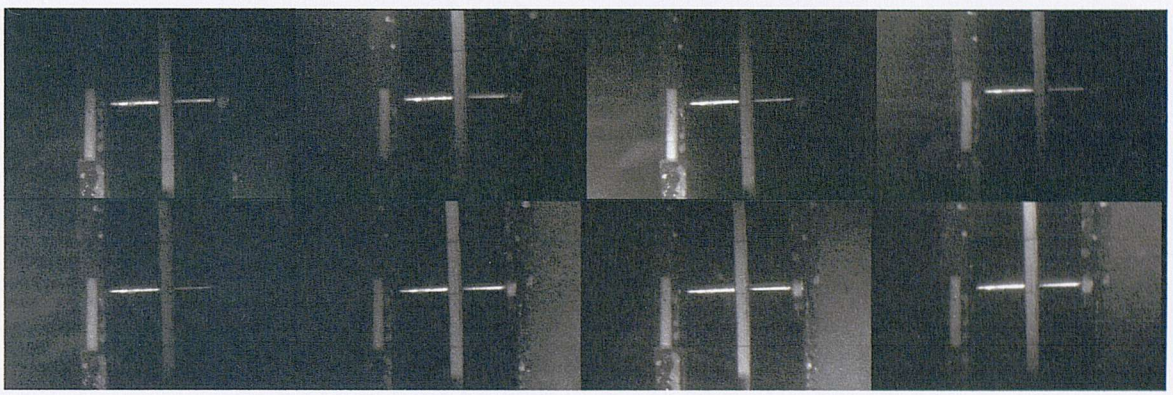
Frame	1	2	3	4	5	6	7	8
Setting (ms)	0.9	1.0	1.1	1.2	1.25	1.3	1.35	1.4
Exposure (μs)	10	10	10	11	12	13	14	15

Sample TC8



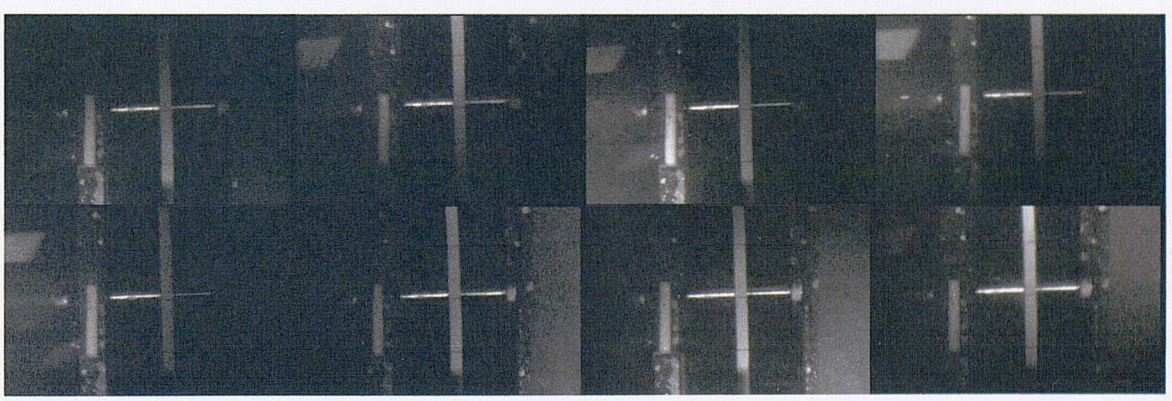
Frame	1	2	3	4	5	6	7	8
Setting (ms)	0.8	1.0	1.1	1.2	1.25	1.3	1.35	1.4
Exposure (μs)	10	10	10	11	12	13	14	15

Sample TC9



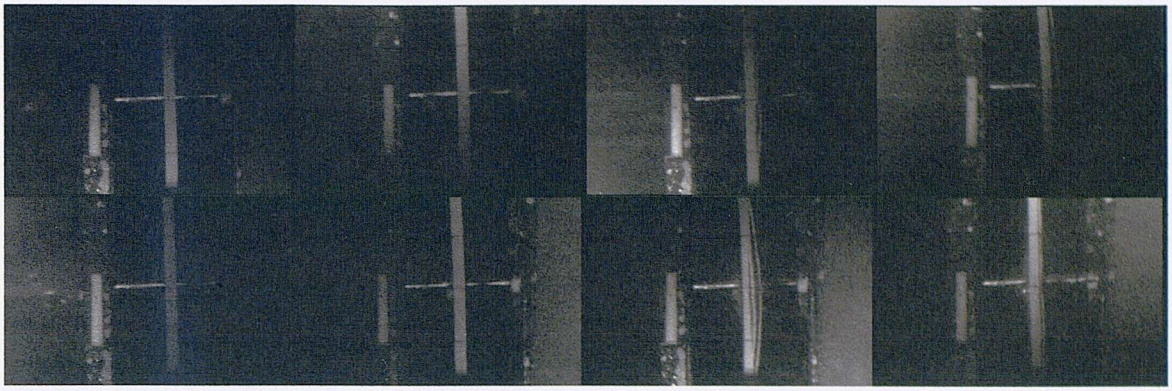
Frame	1	2	3	4	5	6	7	8
Setting (ms)	0.5	0.6	0.7	0.8	0.9	1.0	1.1	1.2
Exposure (μs)	10	10	10	11	12	13	14	15

Sample TC10



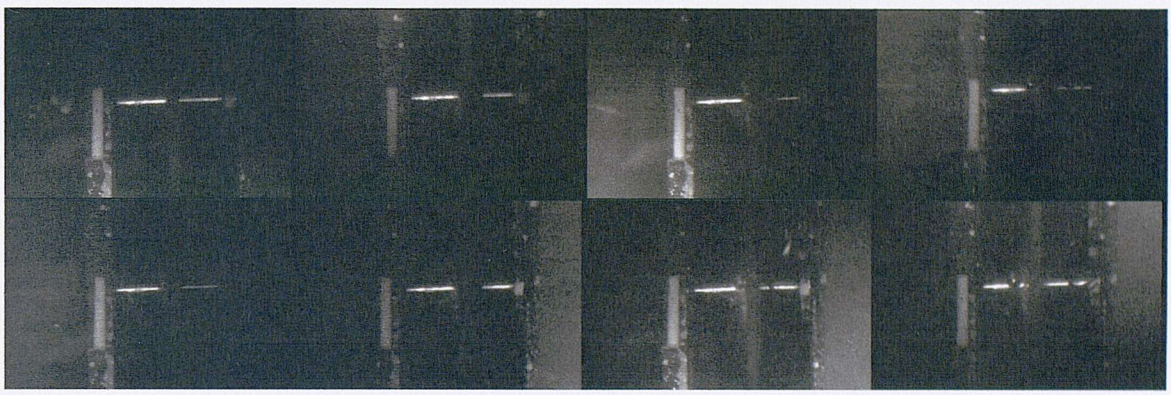
Frame	1	2	3	4	5	6	7	8
Setting (ms)	0.2	0.3	0.35	0.4	0.45	0.5	0.6	0.7
Exposure (μs)	10	10	10	11	12	13	14	15

Sample TC11



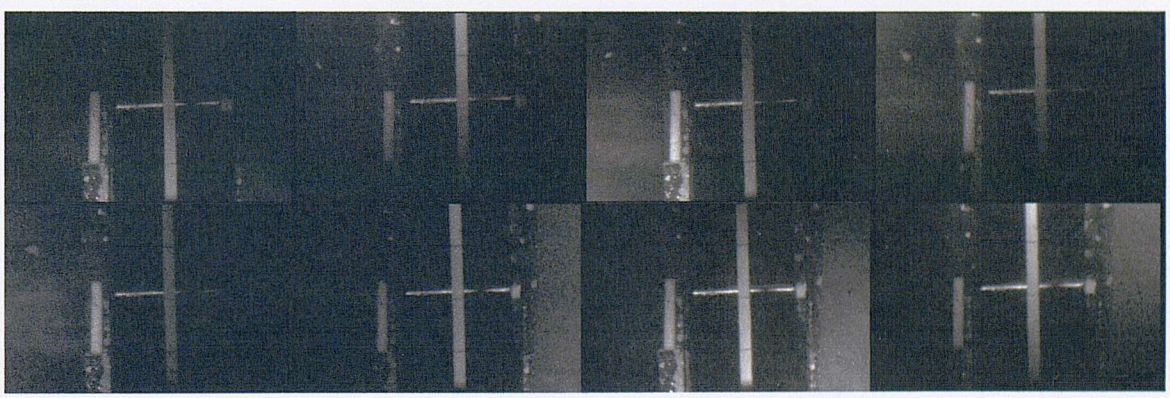
Frame	1	2	3	4	5	6	7	8
Setting (ms)	0.6	0.7	0.8	0.85	0.9	0.95	1.0	1.2
Exposure (μs)	10	10	10	11	12	13	14	15

Sample TC12



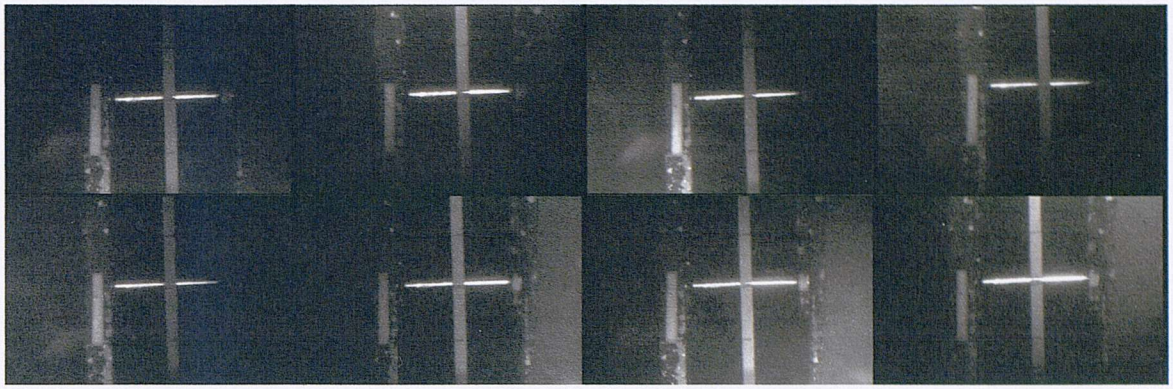
Frame	1	2	3	4	5	6	7	8
Setting (ms)	0.6	0.8	0.85	0.9	0.95	1.0	1.15	1.30
Exposure (μs)	10	10	10	11	12	13	14	15

Sample TC14



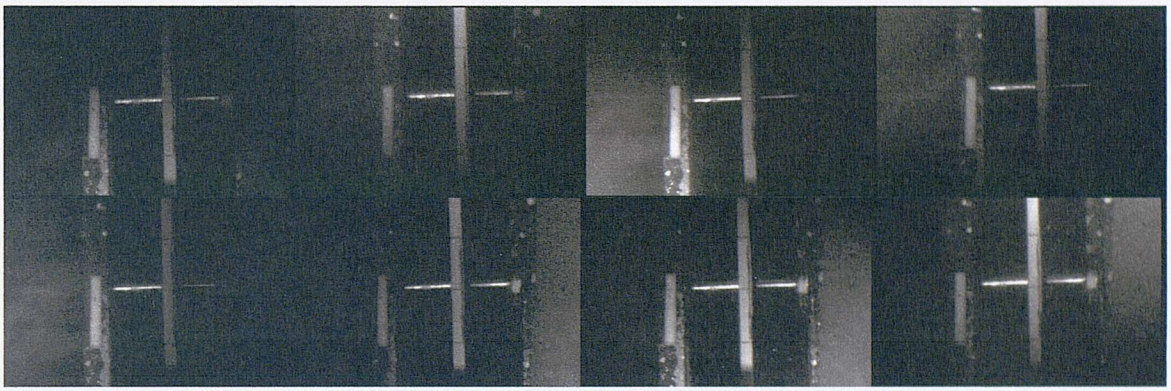
Frame	1	2	3	4	5	6	7	8
Setting (ms)	0.6	0.8	0.85	0.9	0.95	1.0	1.15	1.30
Exposure (μs)	10	10	10	11	12	13	14	15

Sample TC15



Frame	1	2	3	4	5	6	7	8
Setting (ms)	0.7	0.8	0.85	0.9	0.95	1.0	1.15	1.30
Exposure (μs)	10	10	10	11	12	13	14	15

Sample TC16



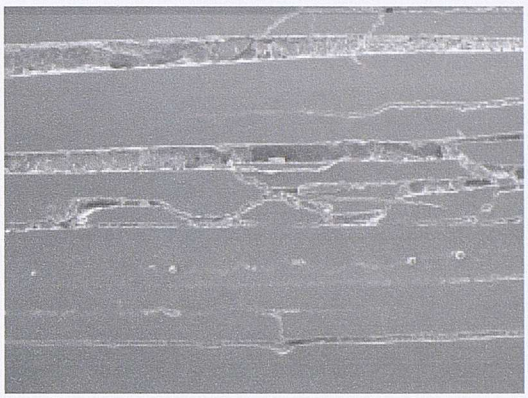
Frame	1	2	3	4	5	6	7	8
Setting (ms)	0.7	0.8	0.85	0.9	0.95	1.0	1.15	1.30
Exposure (μs)	10	10	10	11	12	13	14	15

Note that due to equipment not being set-up properly before gas-gun shots were taken, no images are present for specimens TC1, TC2, TC4, TC7 and TC13. Also specimen TC12 was mounted with the wrong side facing the camera therefore it is quite hard to view this particular specimen in the images.

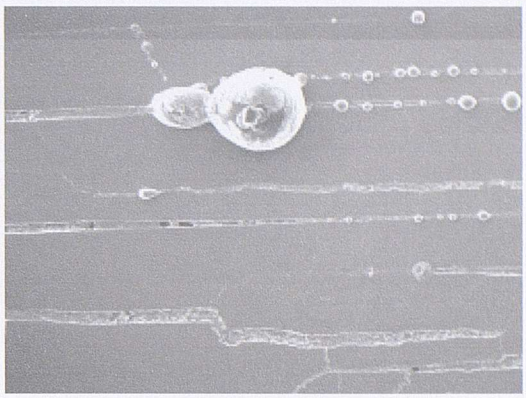
Appendix 2.

SEM Micrographs Showing Through Thickness Damage in Curved Carbon Fibre Laminates

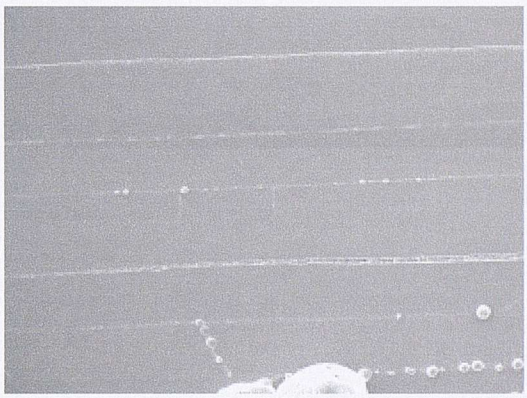
Micrographs For Specimen LC6
Magnification x50



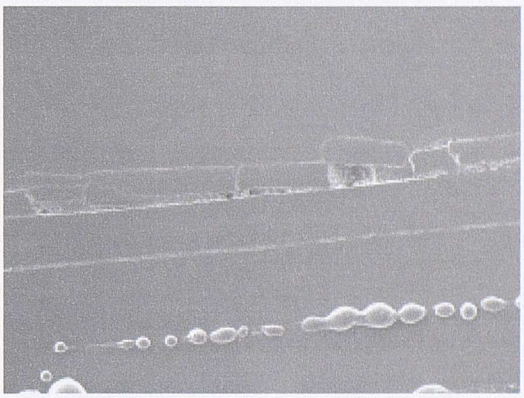
Impact Site



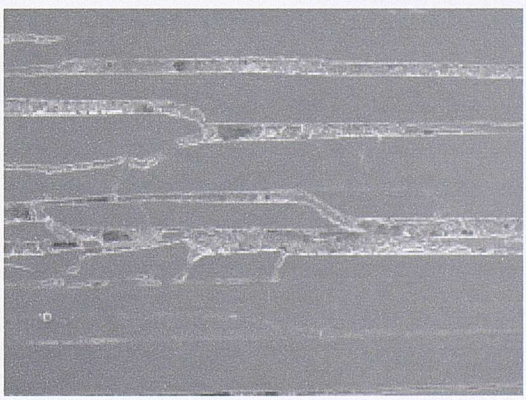
Damage Progression 1



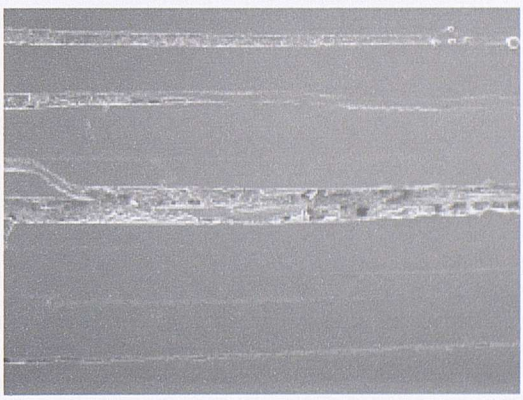
Damage Progression 2



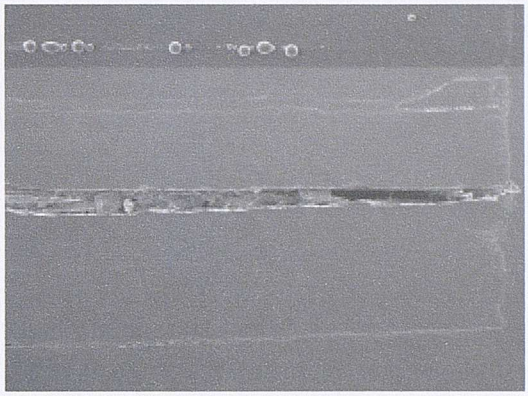
Back Face Spalling



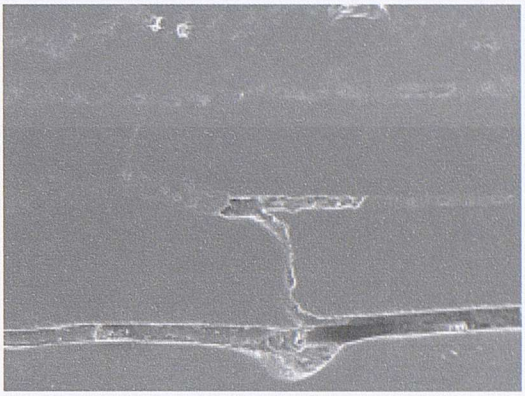
Delamination Growth 1



Delamination Growth 2



Delamination Growth 3

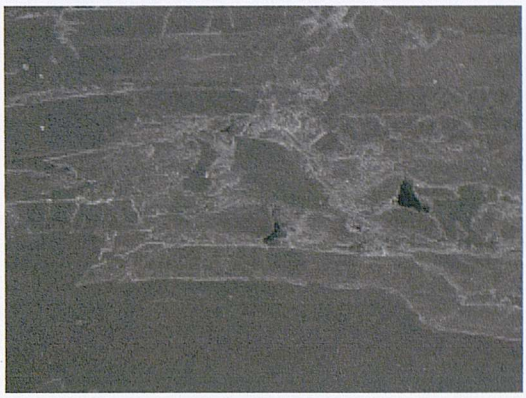


Damage initiation (mag x750)

Micrographs for Specimen LC11
Magnification x50



Impact Point 1



Impact Point 2



Impact Point3



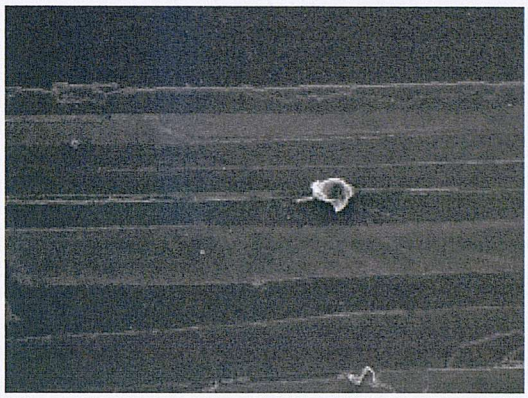
Damage Progression1



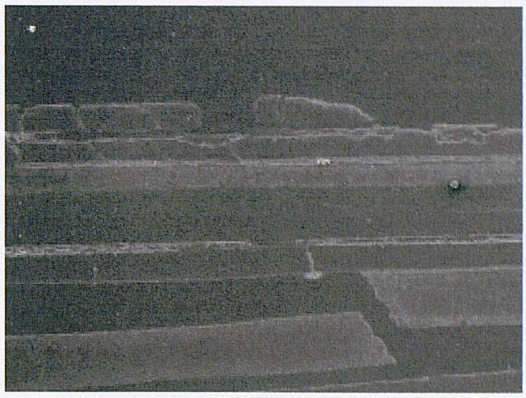
Damage Progression 2



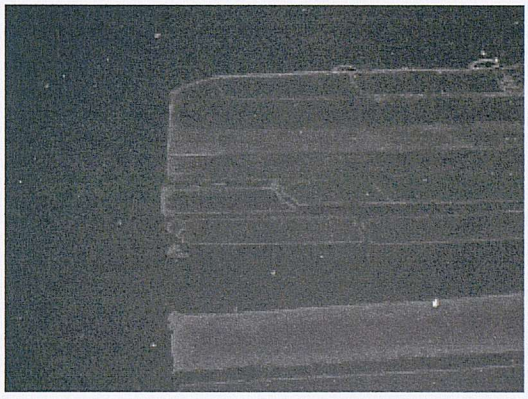
Back Face 1



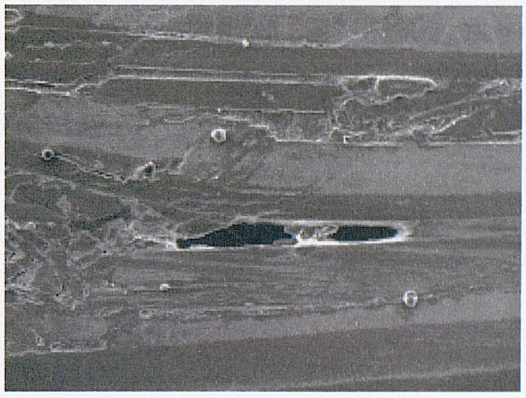
Back Face 2



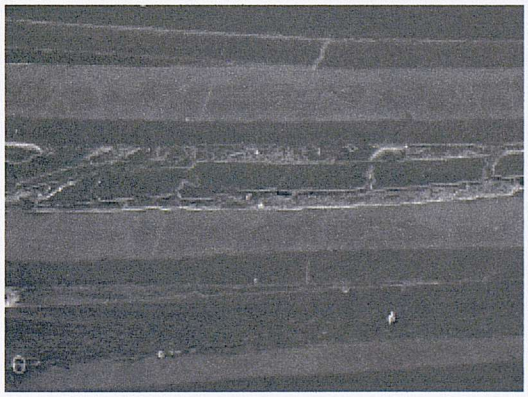
Back Face 3



Back Face 4



Delamination Progression 1



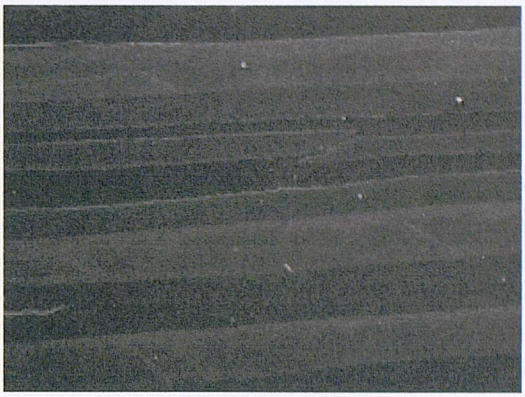
Delamination Progression 2



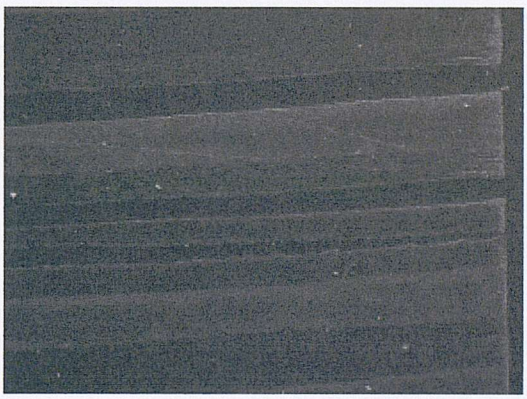
Delamination Progression 3



Delamination Progression 4



Delamination Progression 5



Delamination Progression 6

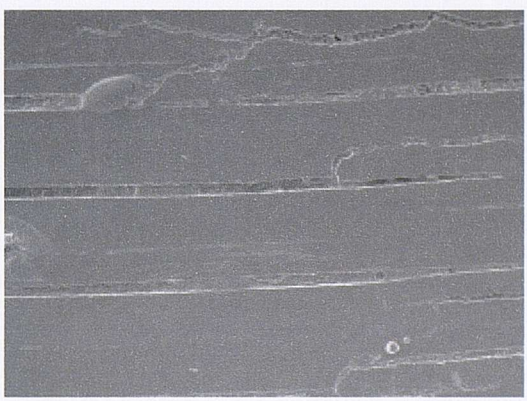
Micrographs For Specimen LC15
Magnification x50



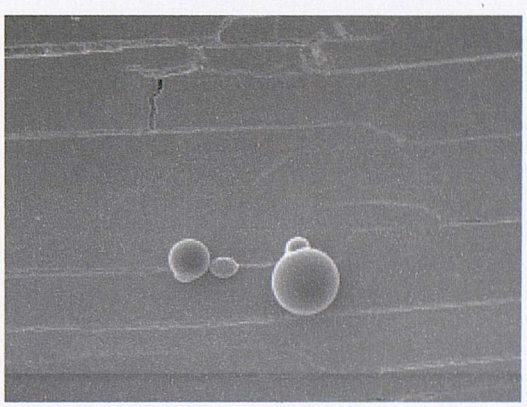
Impact Point 1



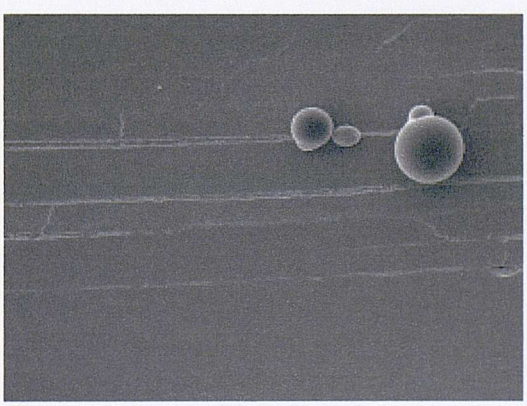
Impact Point 2



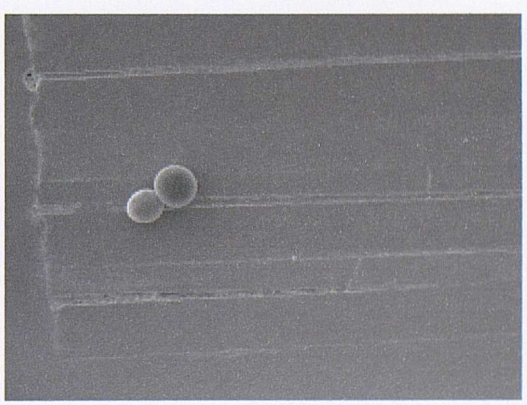
Damage Progression



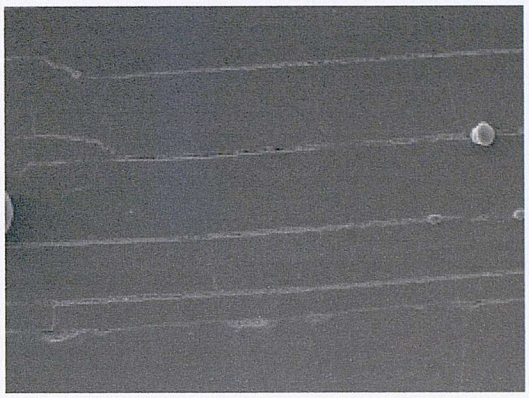
Damage Progression 2



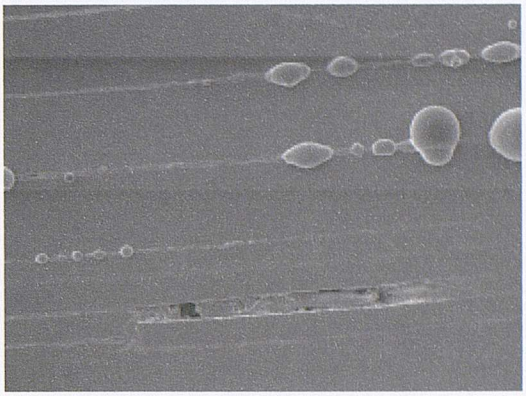
Back Face 1



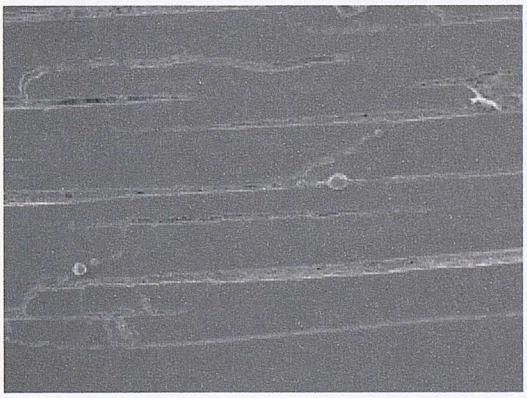
Back Face 2



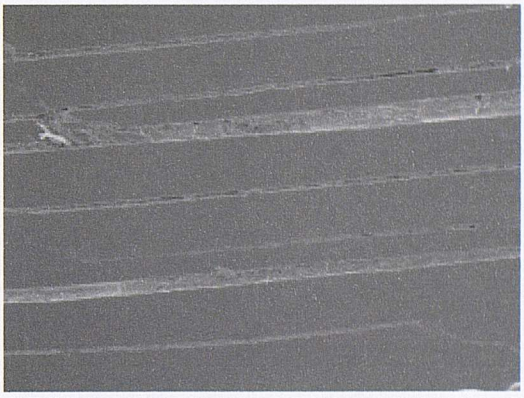
Back Face 3



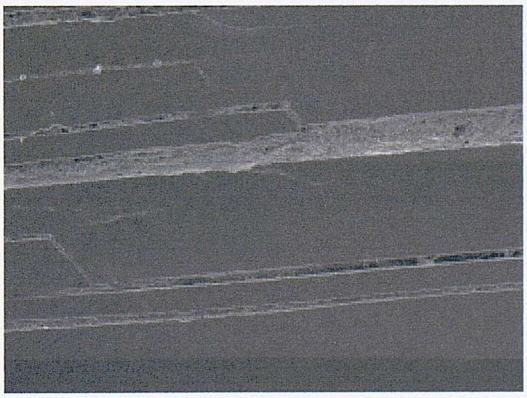
Back Face 4



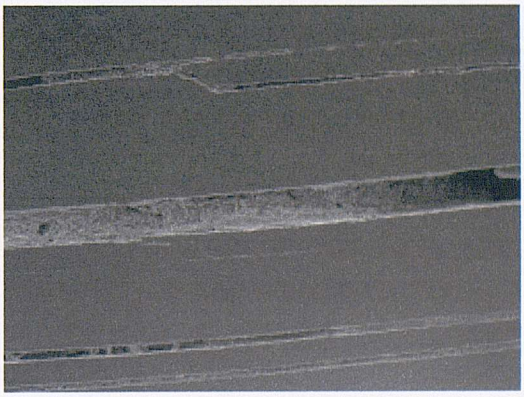
Delamination Progression 1



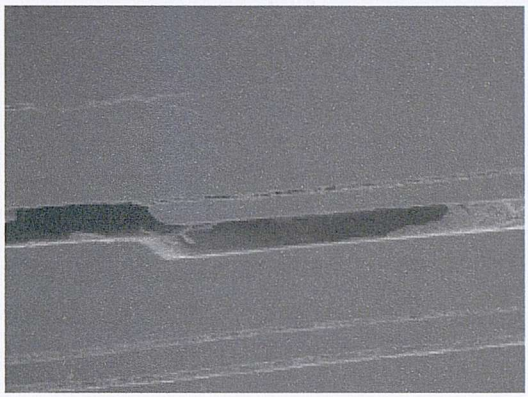
Delamination Progression 2



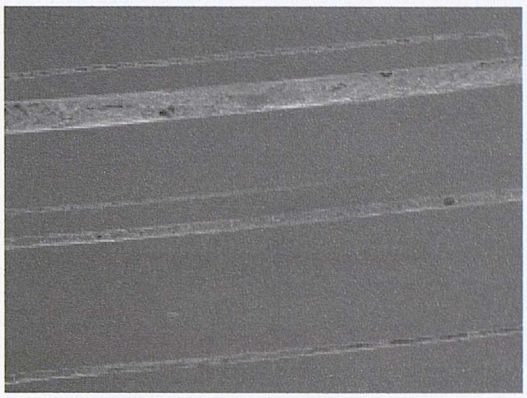
Delamination Progression 3



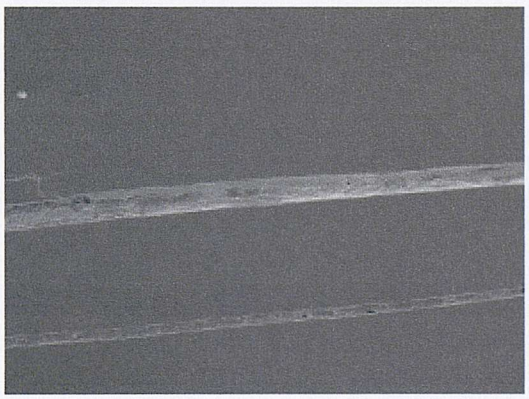
Delamination Progression 4



Delamination Progression 5



Delamination Progression 6



Delamination Progression 7

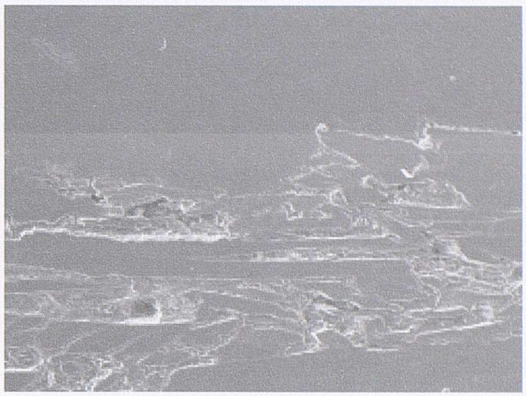


Delamination Progression 8

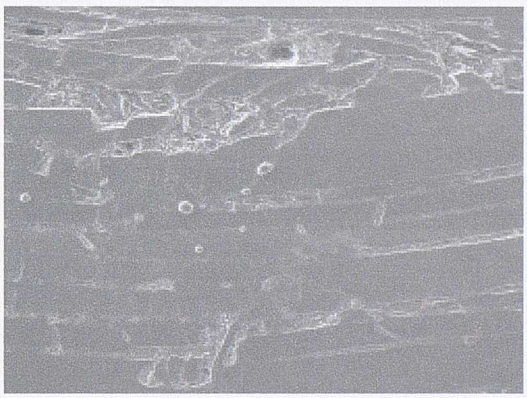
Micrographs For Specimen LC18
Magnification x50



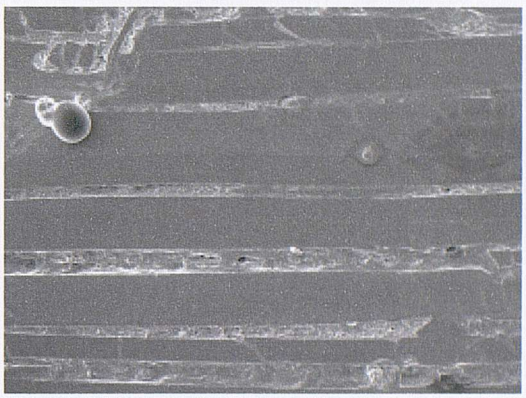
Impact Point 1



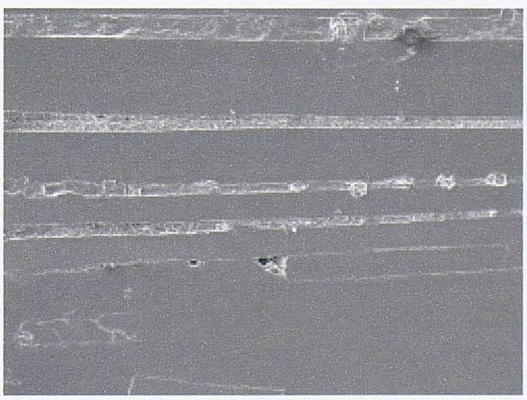
Impact Point 2



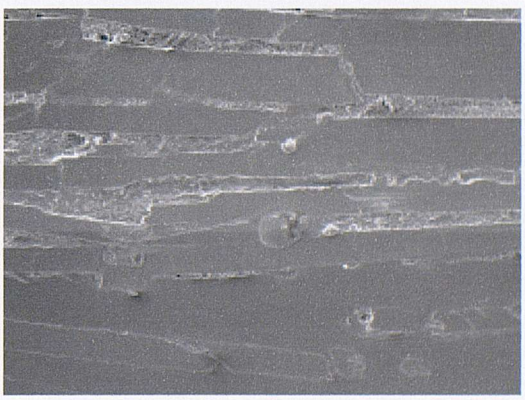
Damage Progression 1



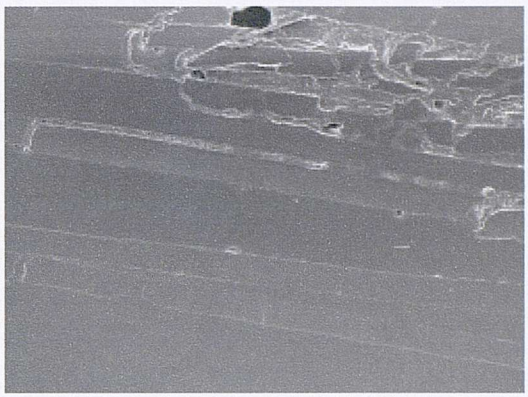
Damage Progression 2



Damage Progression 3



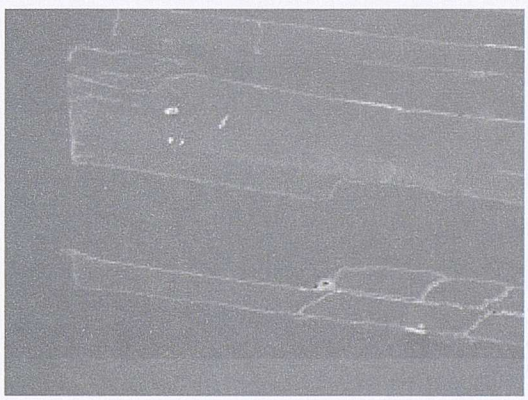
Back Face 1



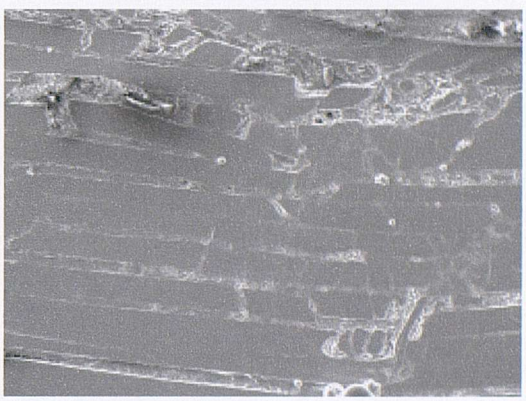
Back Face 2



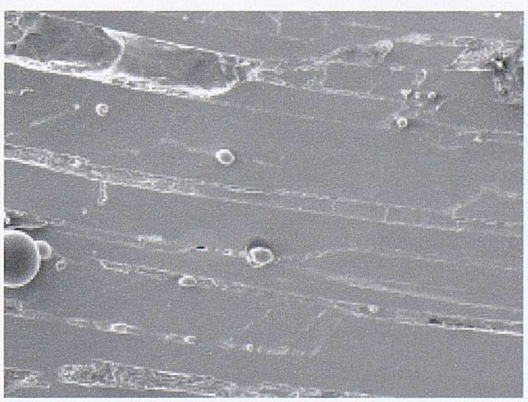
Back Face 3



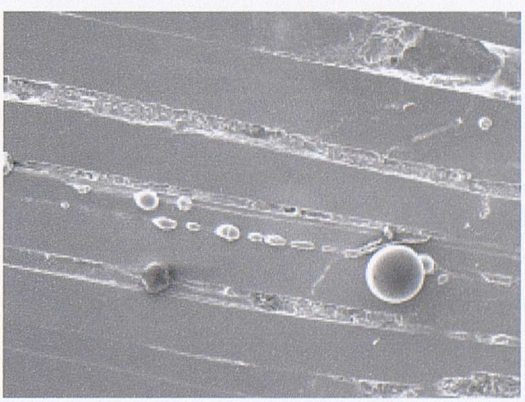
Back Face 4



Delaminaton Progression 1



Delamination Progression 2

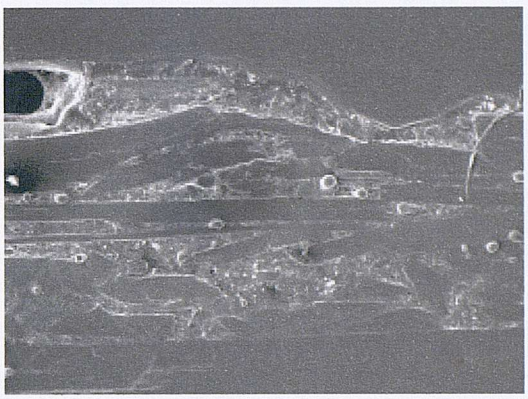


Delamination Progression 3

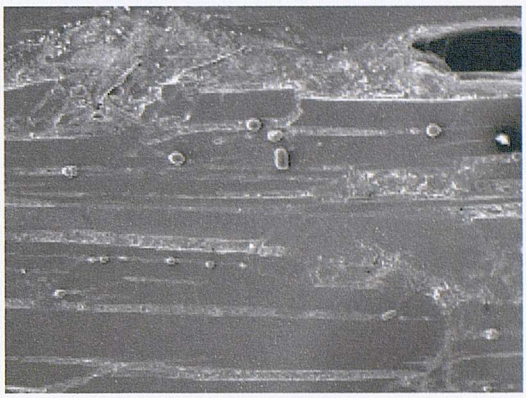


Delamination Progression 4

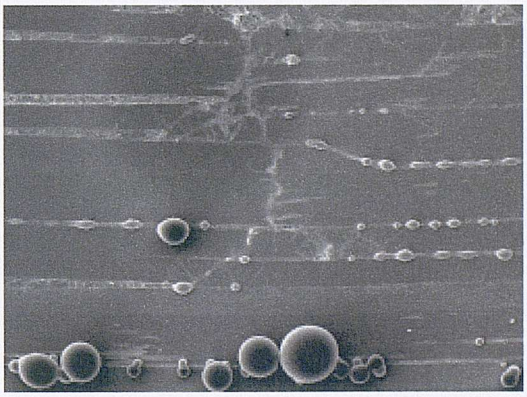
Micrographs for Specimen TC6
Magnification x50



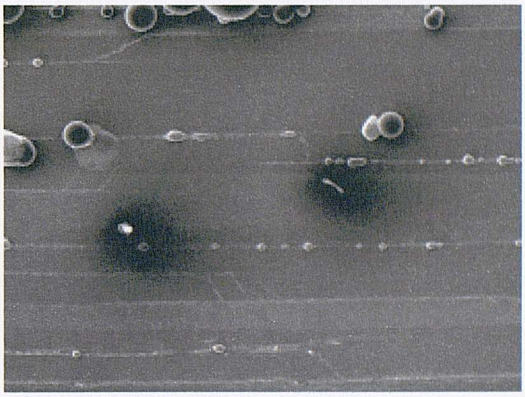
Impact Point 1



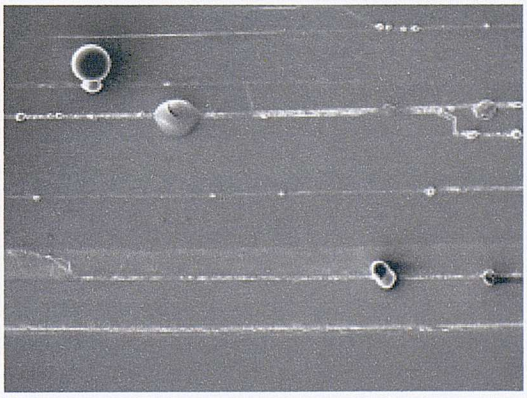
Impact Point 2



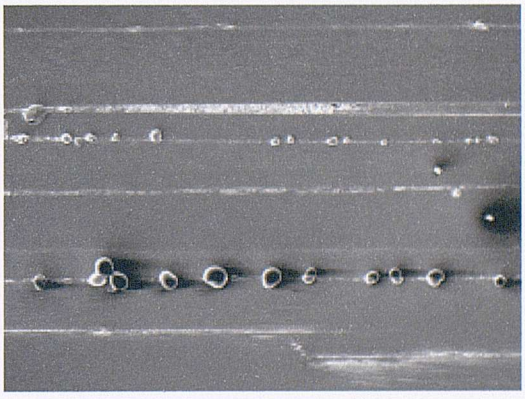
Damage Progression 1



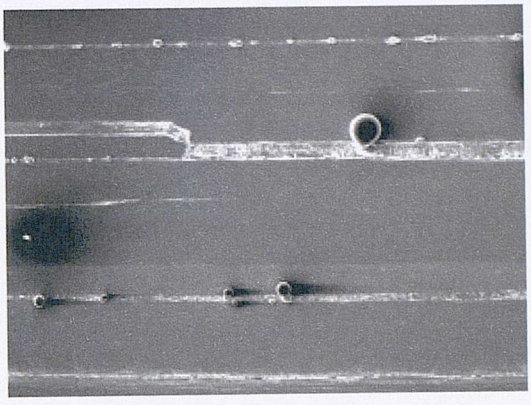
Damage Progression 2



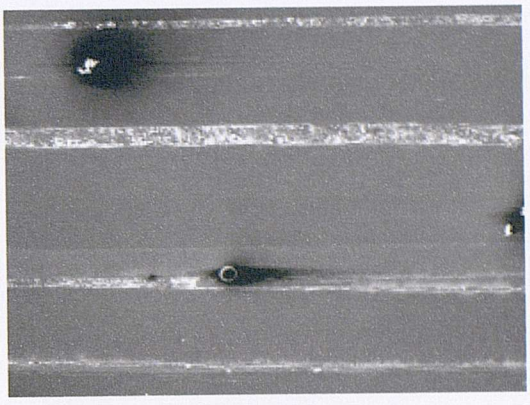
Back Face 1



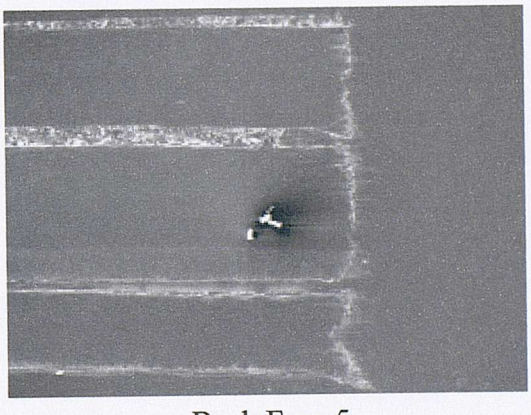
Back Face 2



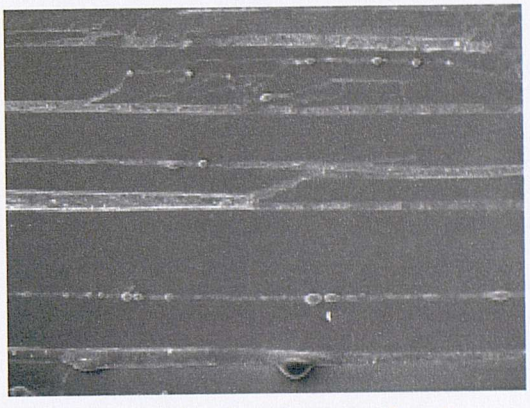
Back Face 3



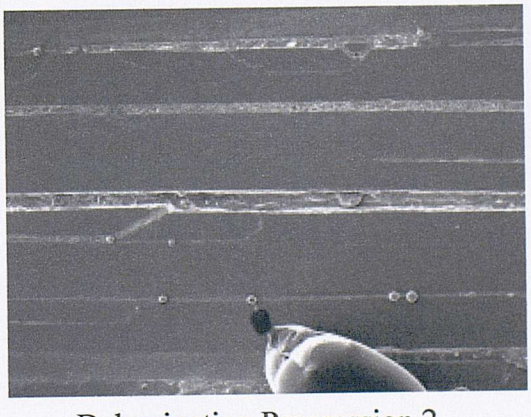
Back face 4



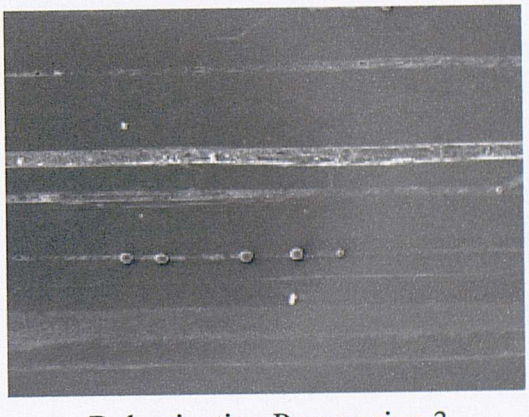
Back Face 5



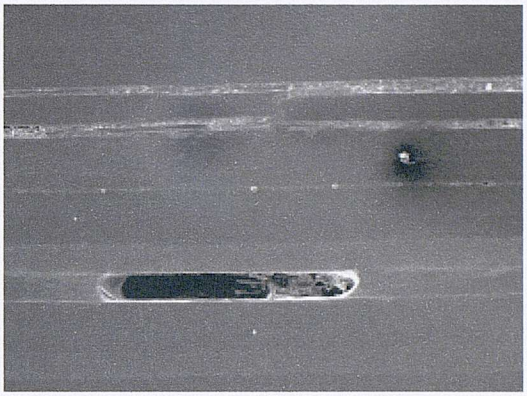
Delamination Progression 1



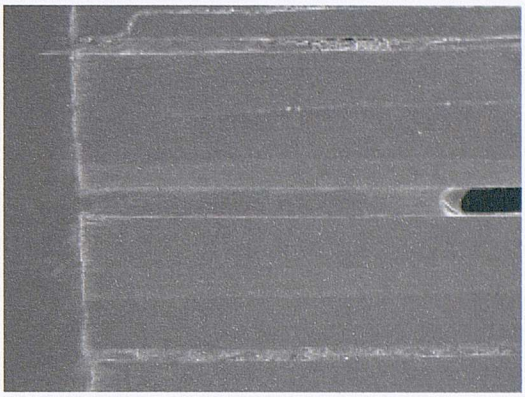
Delamination Progression 2



Delamination Progression 3

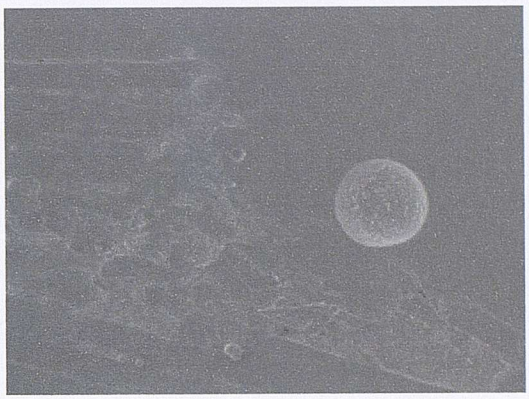


Delamination Progression 4

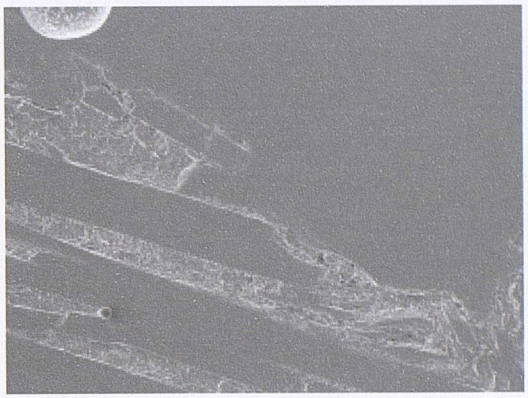


Delamination Progression 5

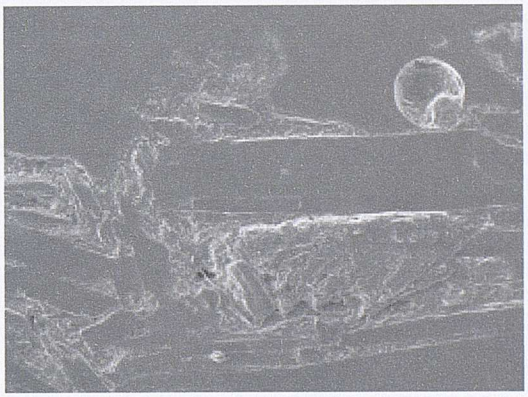
Micrographs for Specimen TC11
Magnification x50



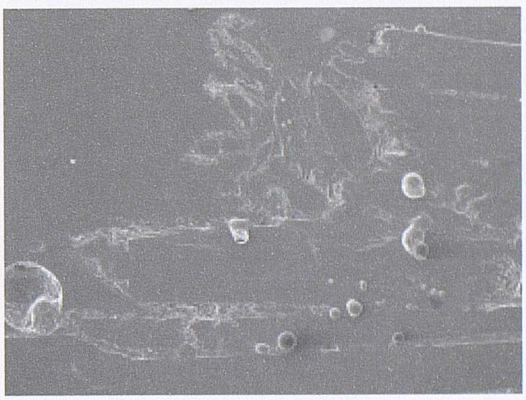
Impact Point 1



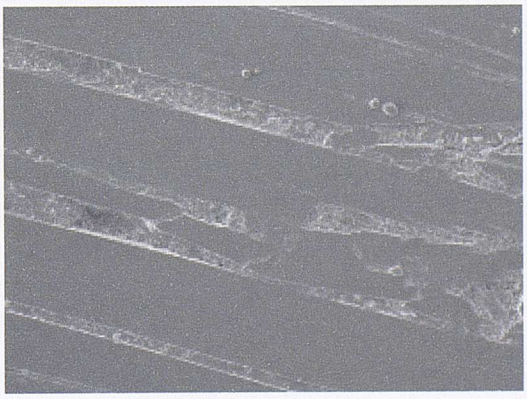
Impact Point 2



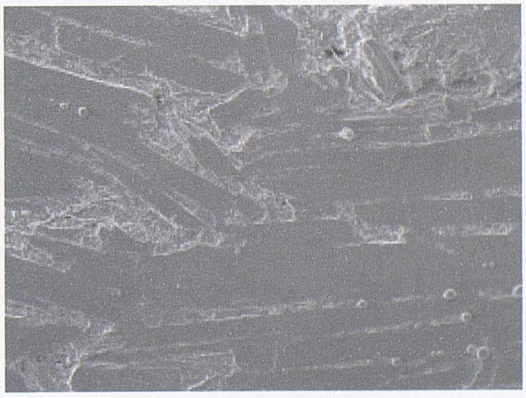
Impact Point 3



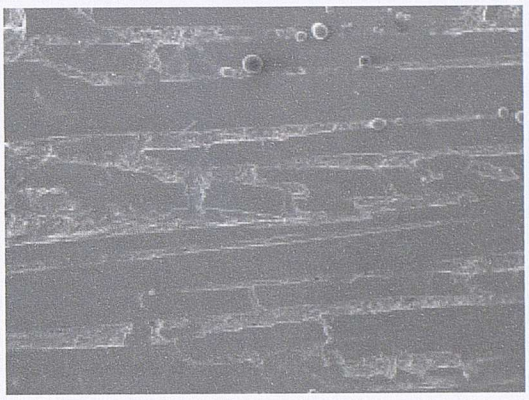
Impact Point 4



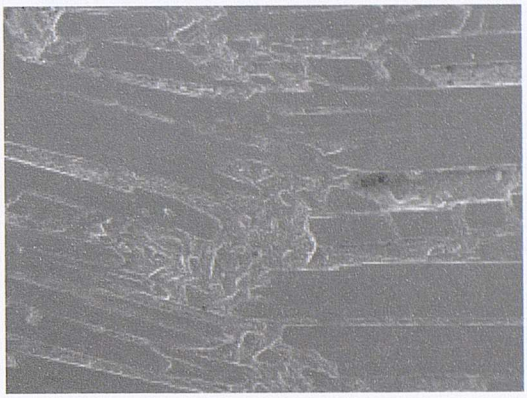
Damage Progression 1



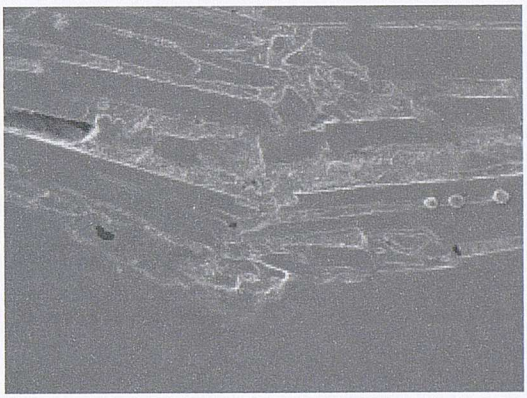
Damage Progression 2



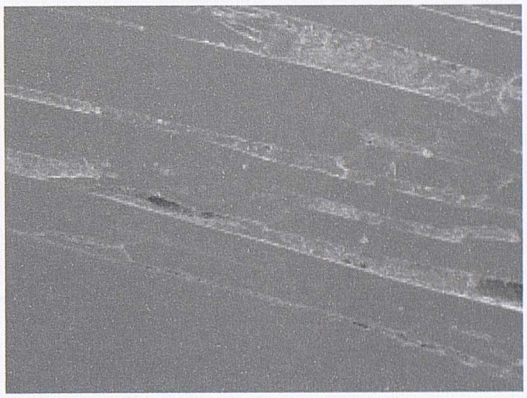
Damage Progression 3



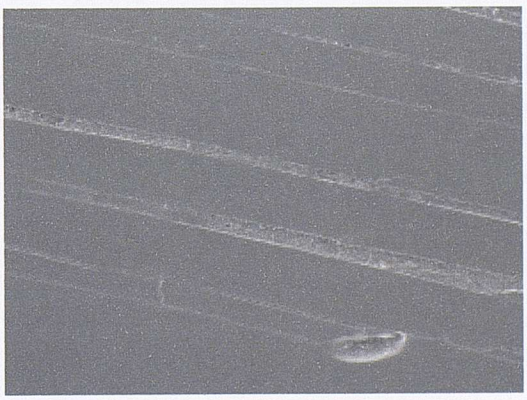
Damage Progression 4



Back Face 1



Back Face 2



Back Face 3



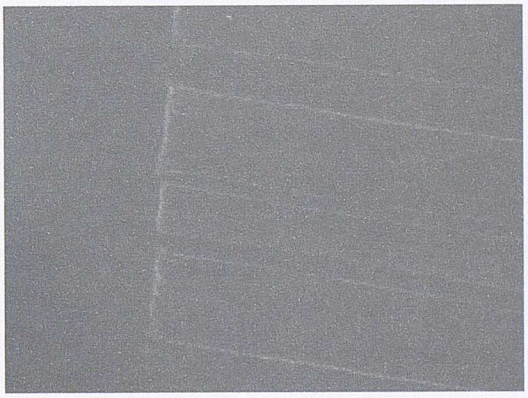
Back Face 4



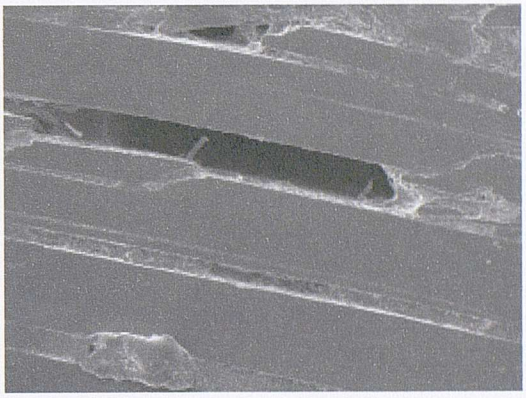
Back Face 5



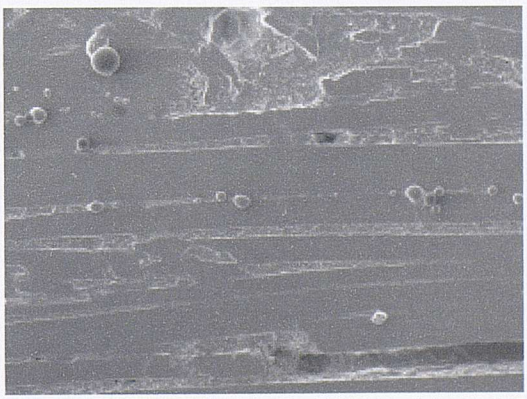
Back Face 6



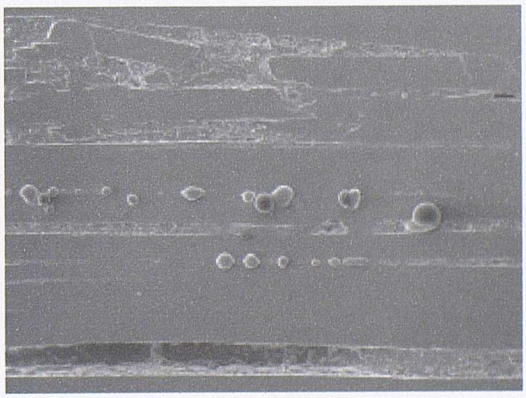
Back Face 7



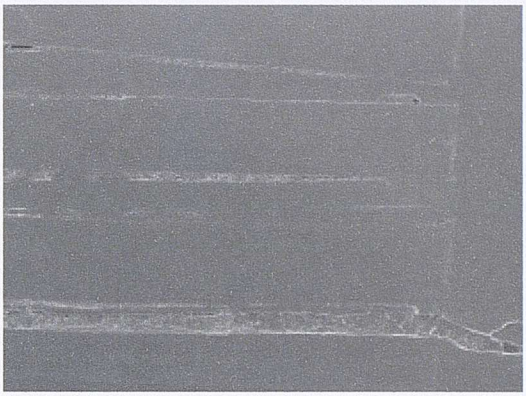
Damage Away from Impact Site



Delamination Progression 1

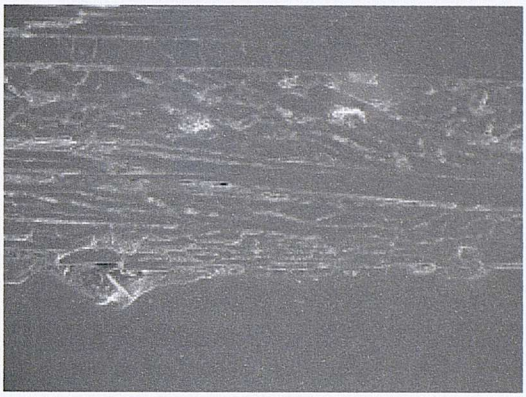


Delamination Progression 2

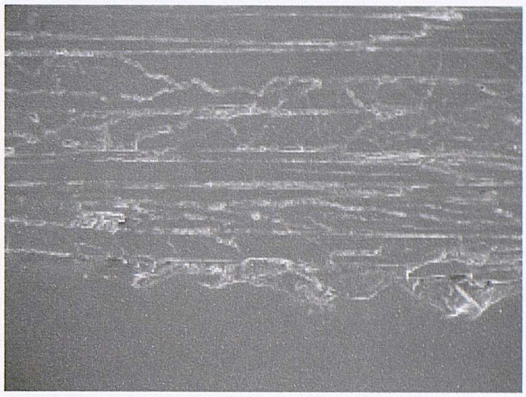


Delamiantion Progression 3

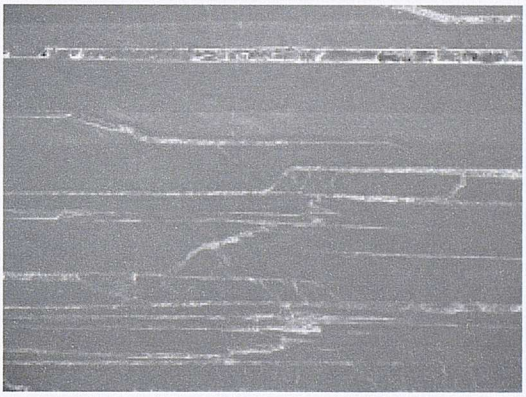
Micrographs for Specimen TC7
Magnification x50



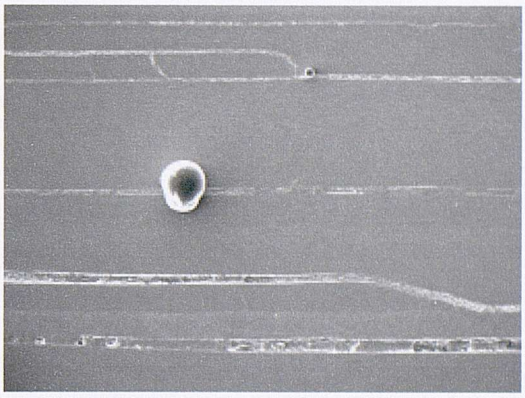
Impact Point 1



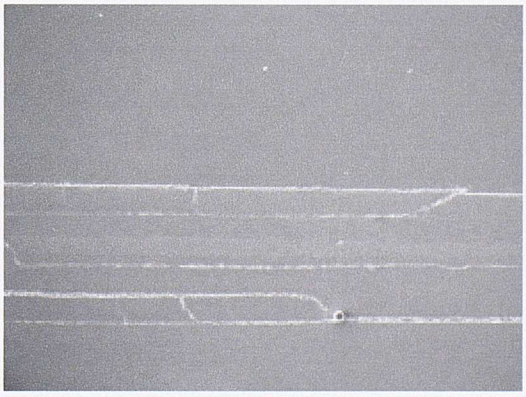
Impact Point 2



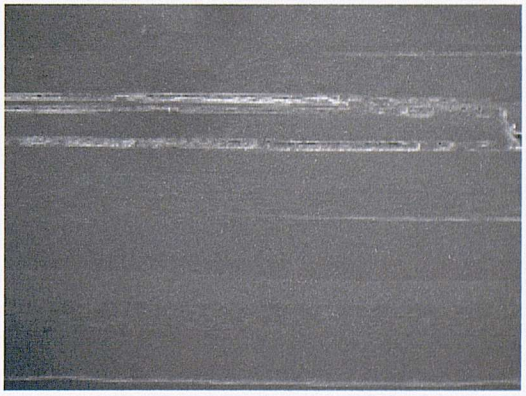
Damage Progression 1



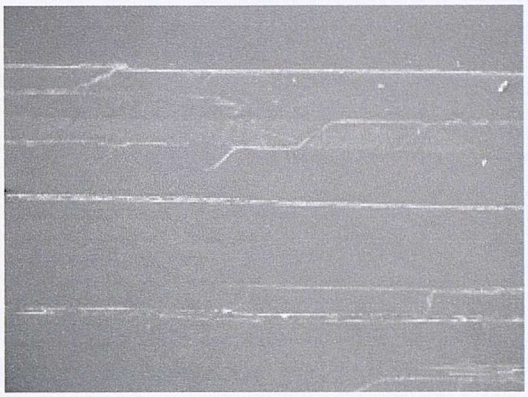
Damage Progression 2



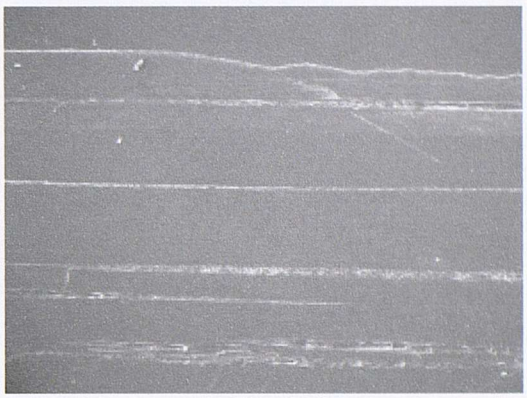
Damage Progression 3



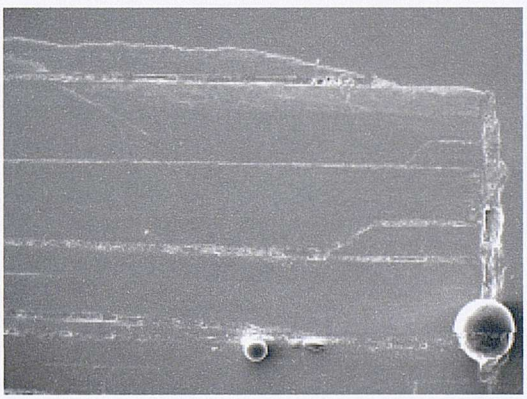
Damage Progression 4



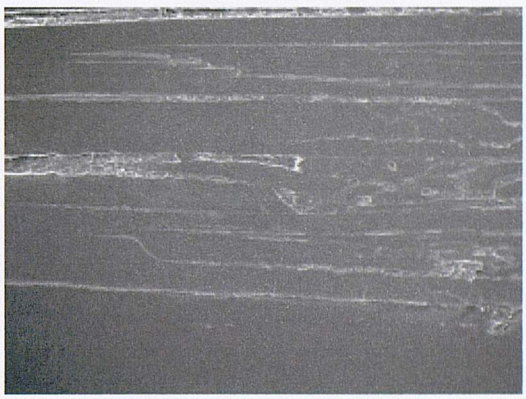
Back Face 1



Back Face 2



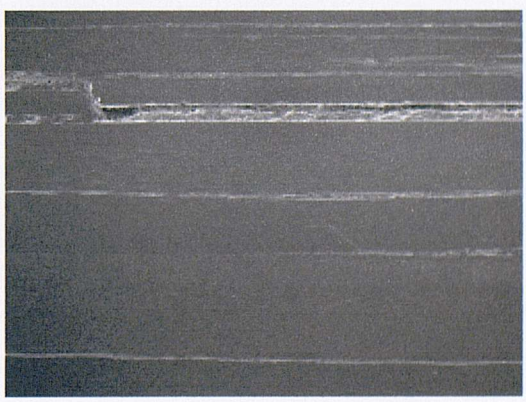
Back Face 3



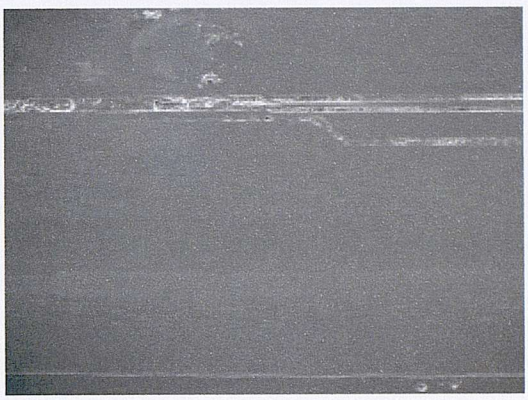
Delamination Progression 1



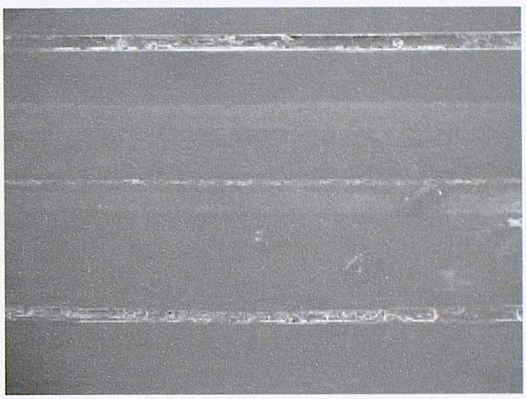
Delamination Progression 2



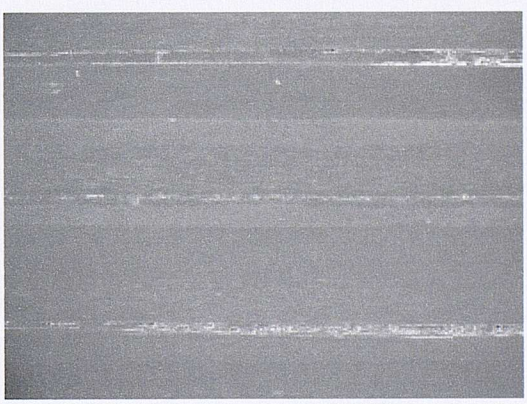
Delamination Progression 3



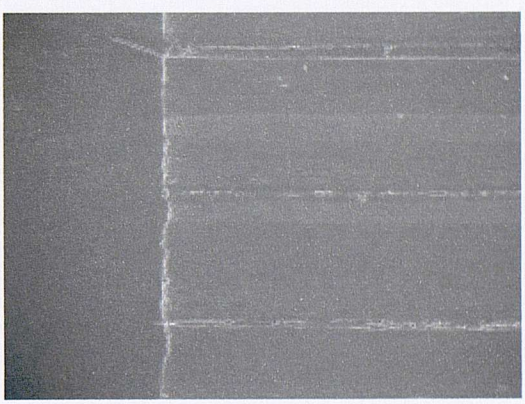
Delamination Progression 4



Delamination Progression 5



Delamination Progression 6

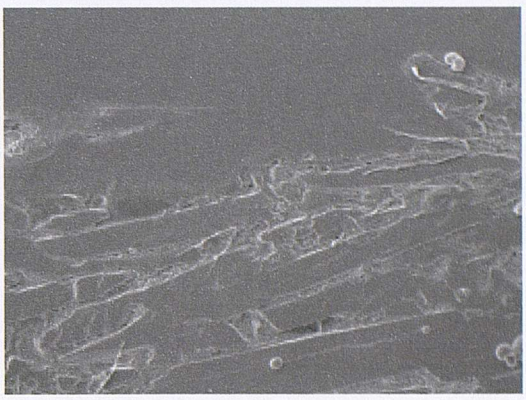


Delamination Progression 7

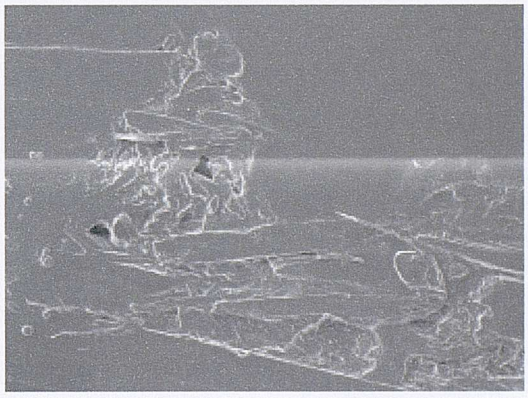
Micrographs For Specimen TC16
Magnification x50



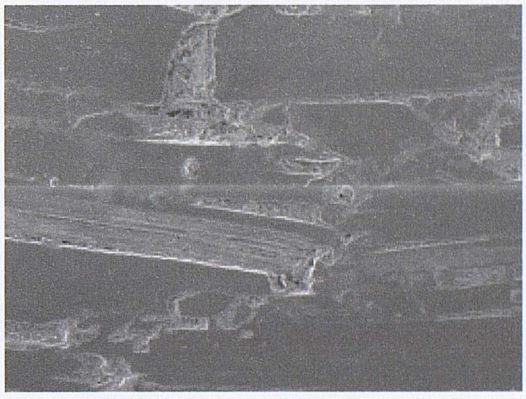
Impact Point 1



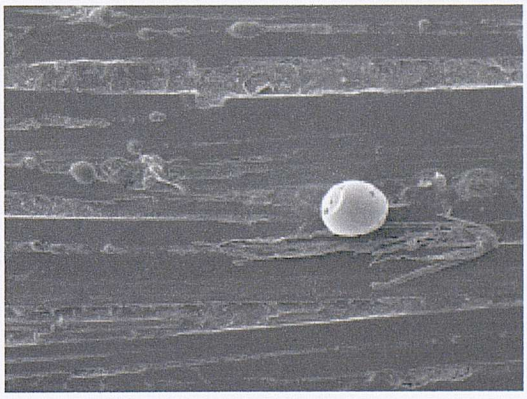
Impact Point 2



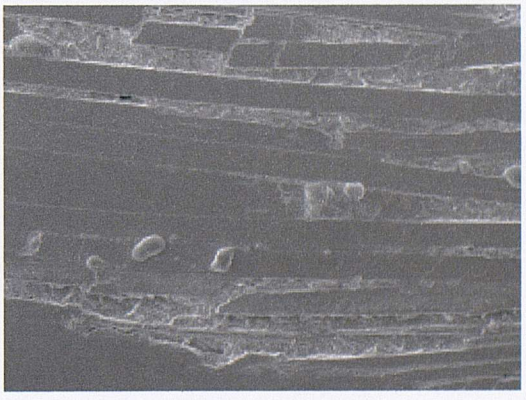
Impact Point 3



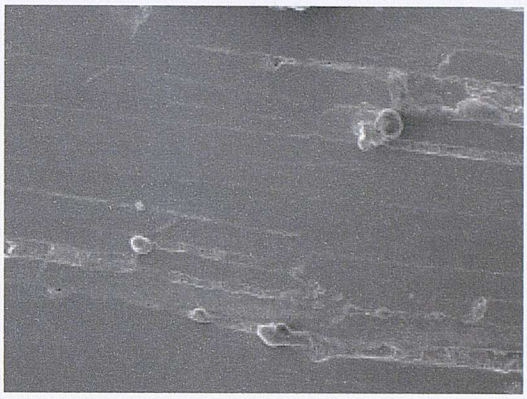
Damage Progression



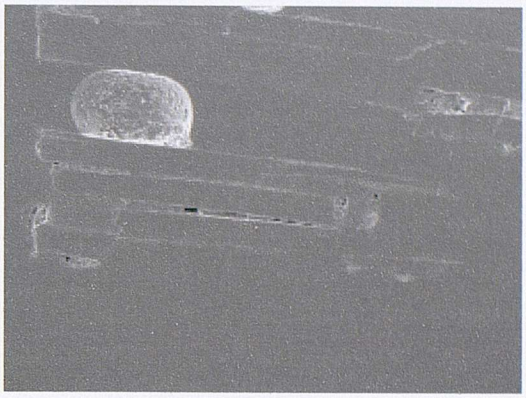
Back Face 1



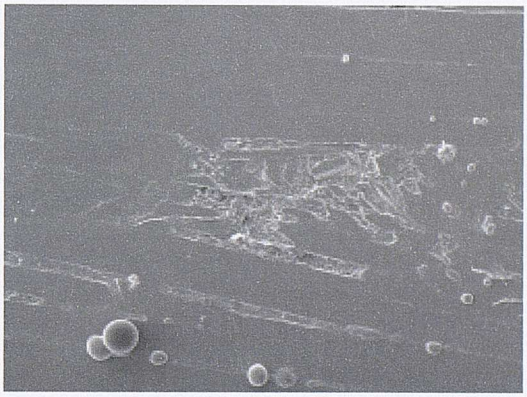
Back Face 2



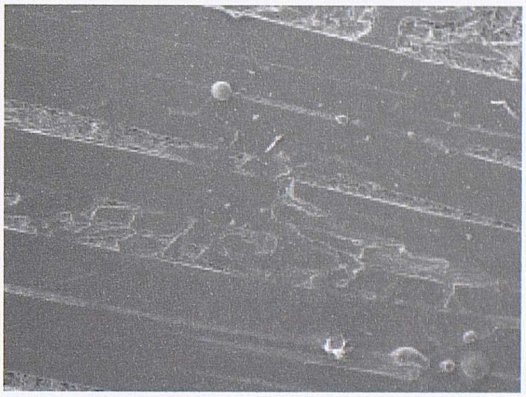
Back face 3



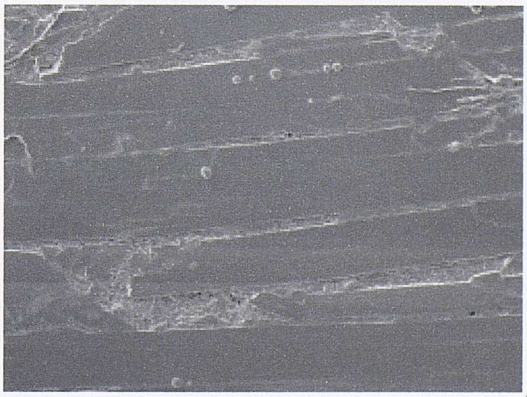
Back face 4



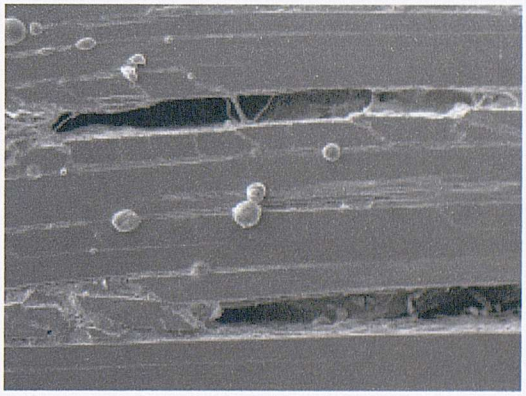
Damage Beyond Impact Site 1



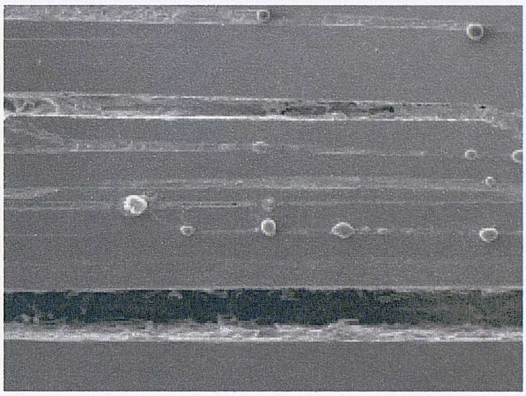
Damage Beyond Impact Site 2



Delamination Progression 1



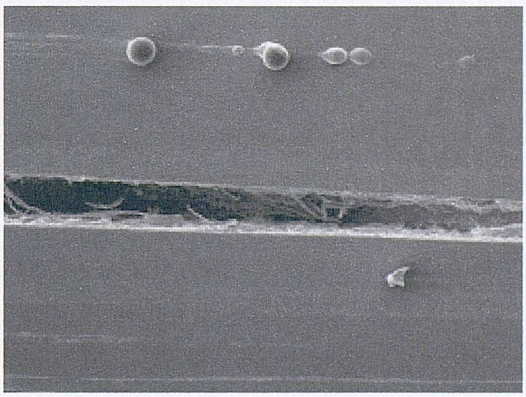
Delamination Progression 2



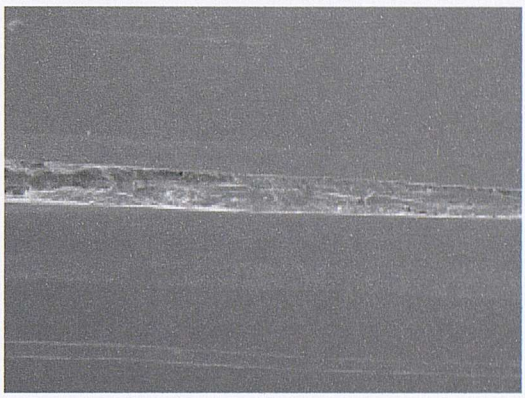
Delamination Progression 3



Delamination Progression 4



Delamination Progression 5



Delamination Progression 6

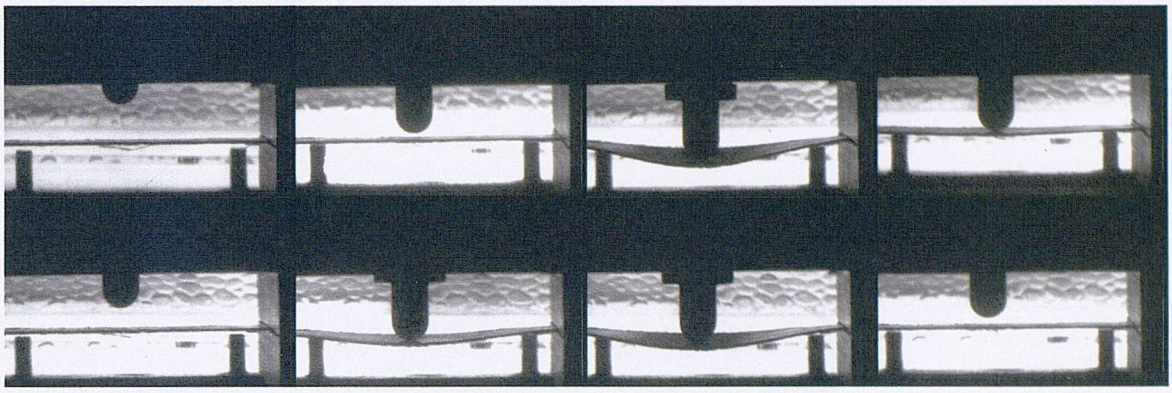
Appendix 3.

High Speed Photography Sequences for Thin Flexible Composite Laminates

Part 1:

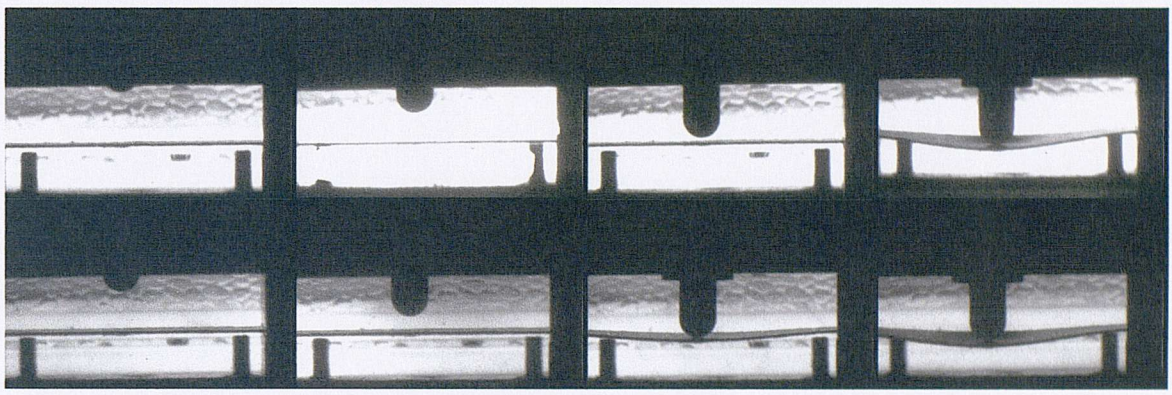
10cm Drop Height

Sample CPPS1



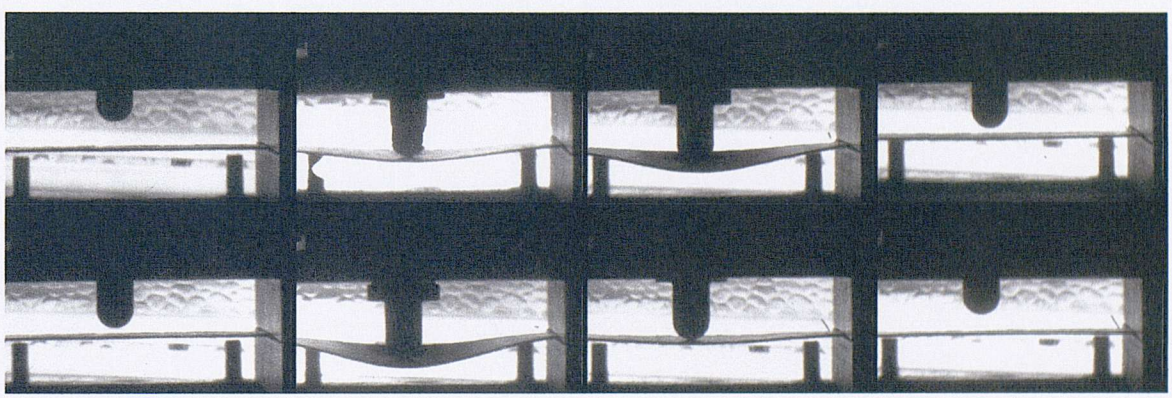
Frame	1	2	3	4	5	6	7	8
Setting (ms)	40	45	50	55	60	65	70	75
Exposure (μs)	150	150	150	150	150	150	150	150

Sample CPPS2



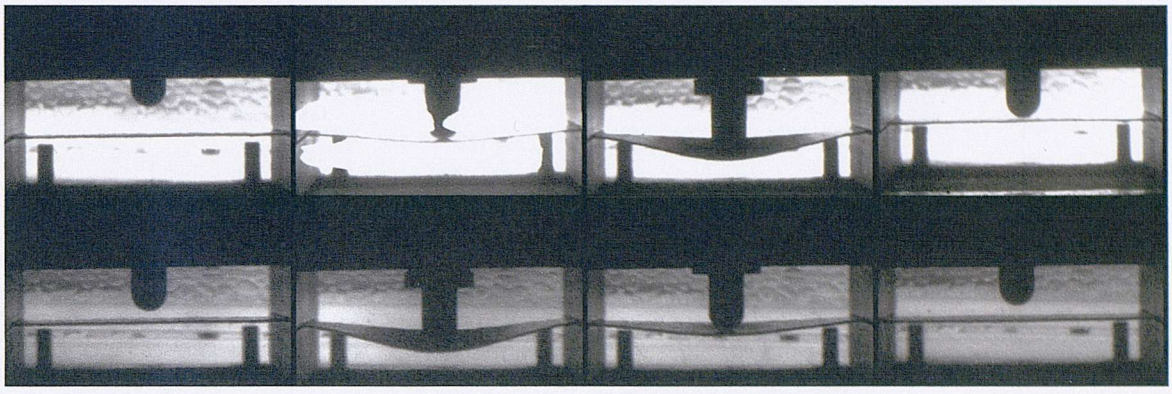
Frame	1	2	3	4	5	6	7	8
Setting (ms)	40	45	50	55	60	65	70	75
Exposure (μs)	150	150	150	150	150	150	150	150

Sample CPPS3



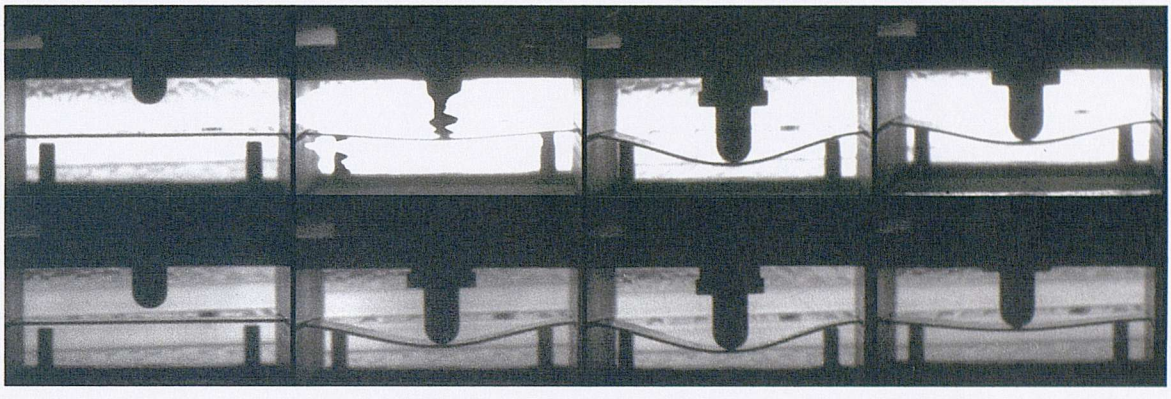
Frame	1	2	3	4	5	6	7	8
Setting (ms)	40	45	50	55	60	65	70	75
Exposure (μs)	150	150	150	150	150	150	150	150

Sample CPPS4



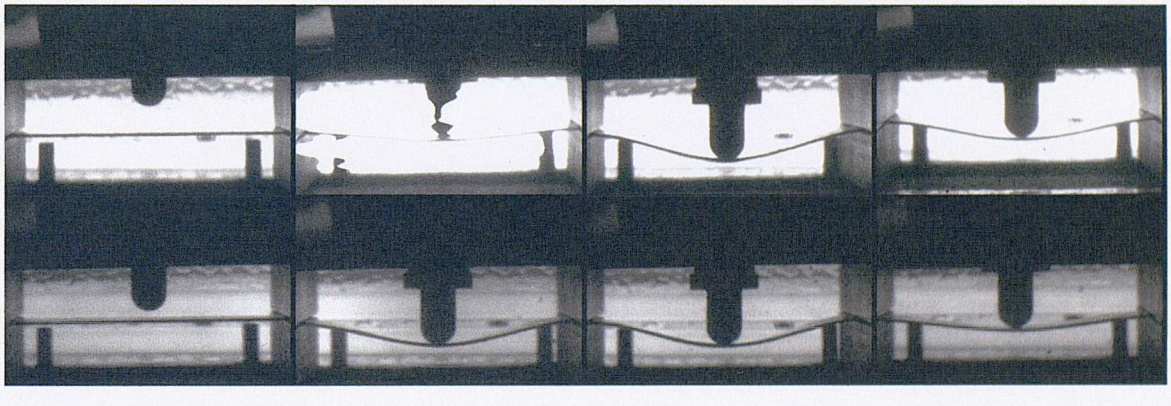
Frame	1	2	3	4	5	6	7	8
Setting (ms)	40	45	50	55	60	65	70	75
Exposure (μs)	150	150	150	150	150	150	150	150

Sample GPPS1



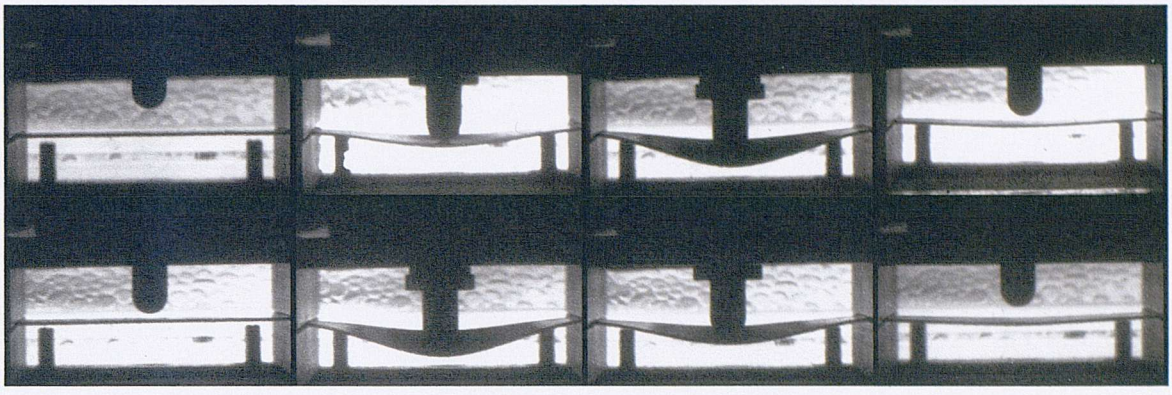
Frame	1	2	3	4	5	6	7	8
Setting (ms)	40	45	50	55	60	65	70	75
Exposure (μs)	150	150	150	150	150	150	150	150

Sample GPPS2



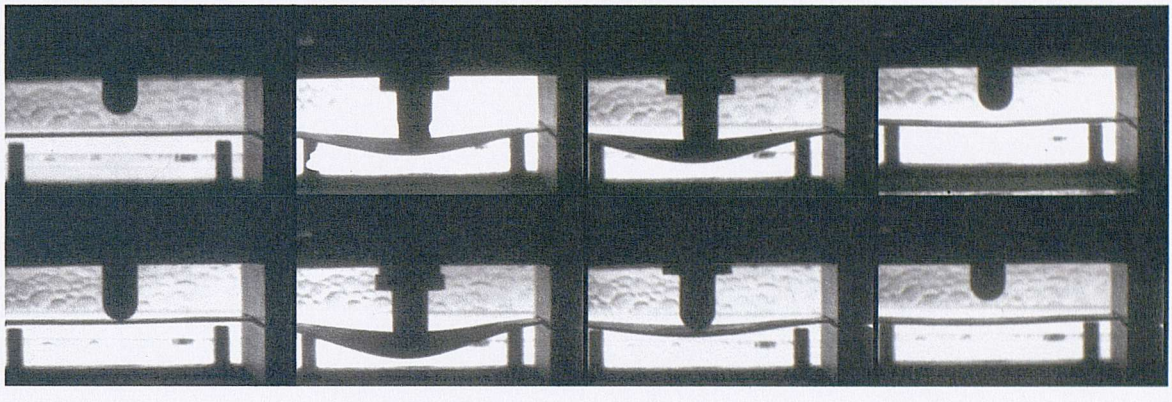
Frame	1	2	3	4	5	6	7	8
Setting (ms)	40	45	50	55	60	65	70	75
Exposure (μs)	150	150	150	150	150	150	150	150

Sample GPPS3



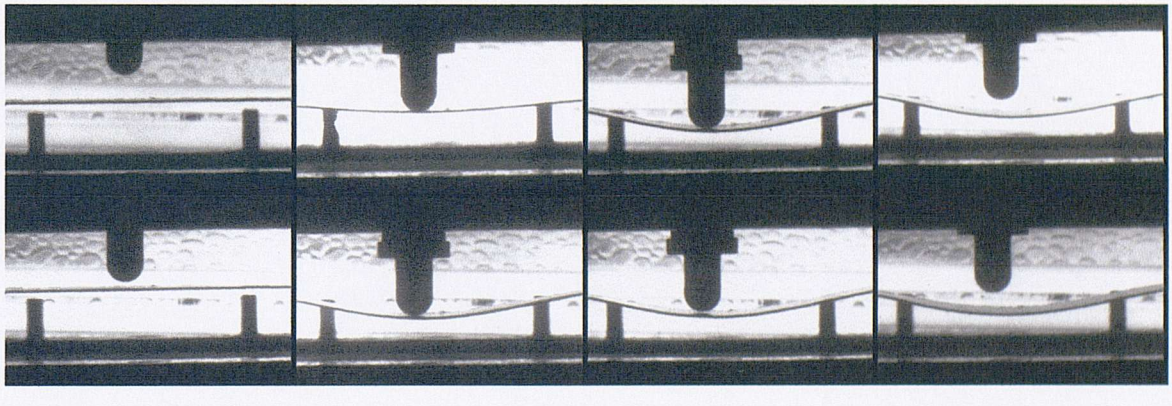
Frame	1	2	3	4	5	6	7	8
Setting (ms)	40	45	50	55	60	65	75	80
Exposure (μs)	150	150	150	150	150	150	150	150

Sample GPPS4



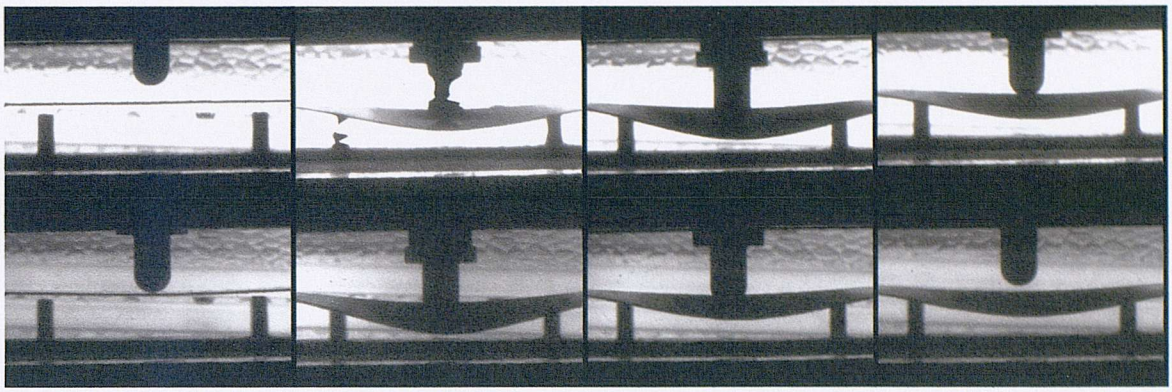
Frame	1	2	3	4	5	6	7	8
Setting (ms)	40	45	50	55	60	65	75	80
Exposure (μs)	150	150	150	150	150	150	150	150

Sample 1CPPS1



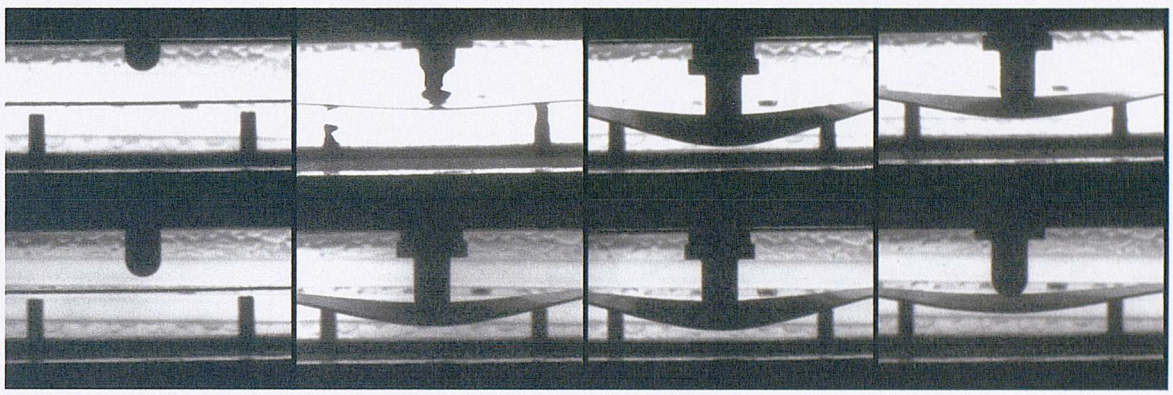
Frame	1	2	3	4	5	6	7	8
Setting (ms)	40	45	50	55	60	65	75	80
Exposure (μs)	150	150	150	150	150	150	150	150

Sample 1CPPS2



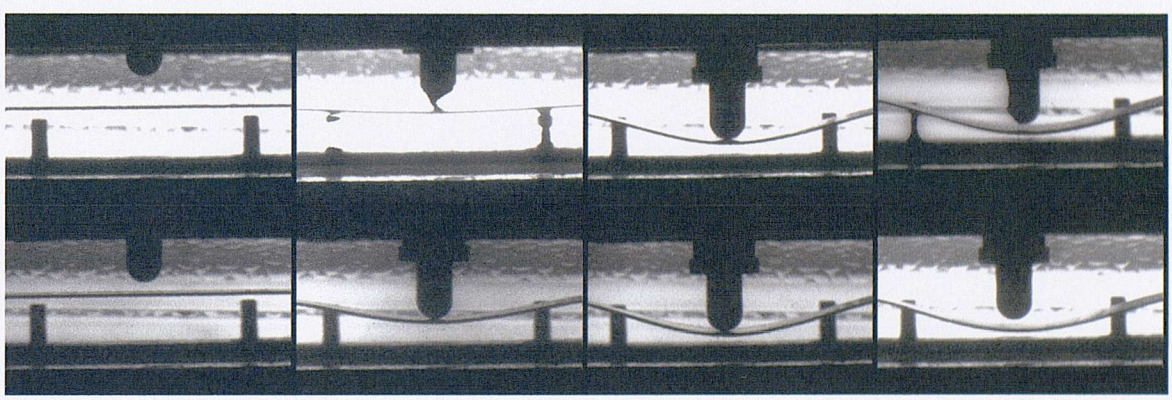
Frame	1	2	3	4	5	6	7	8
Setting (ms)	40	45	50	55	60	65	70	75
Exposure (μs)	150	150	150	150	150	150	150	150

Sample 1GPPS1



Frame	1	2	3	4	5	6	7	8
Setting (ms)	40	45	50	55	60	65	70	75
Exposure (μs)	150	150	150	150	150	150	150	150

Sample 1GPPS3

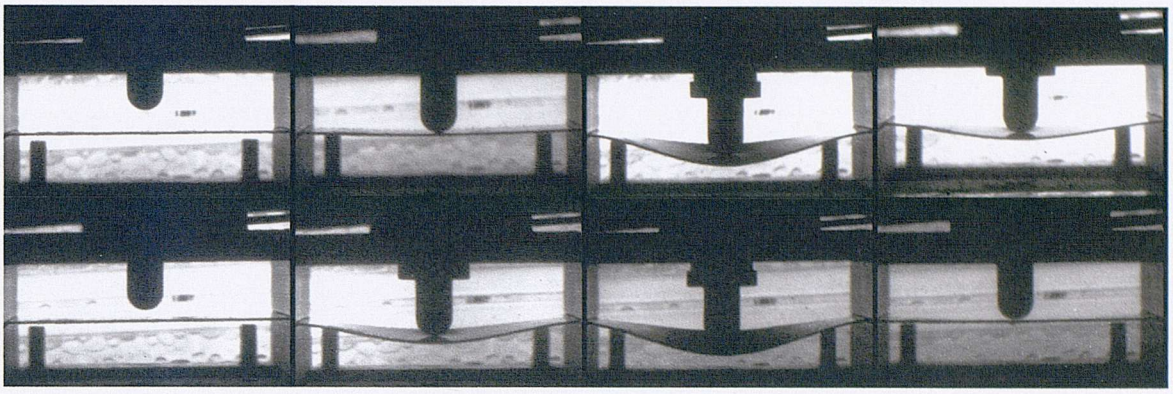


Frame	1	2	3	4	5	6	7	8
Setting (ms)	40	45	50	55	60	65	75	80
Exposure (μs)	150	150	150	150	150	150	150	150

Part 2:

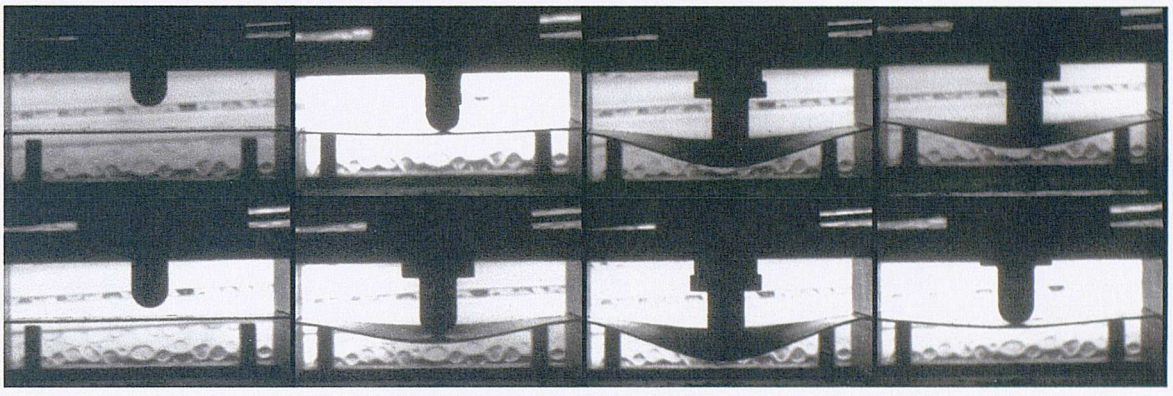
20cm Drop Height

Sample CPPS5



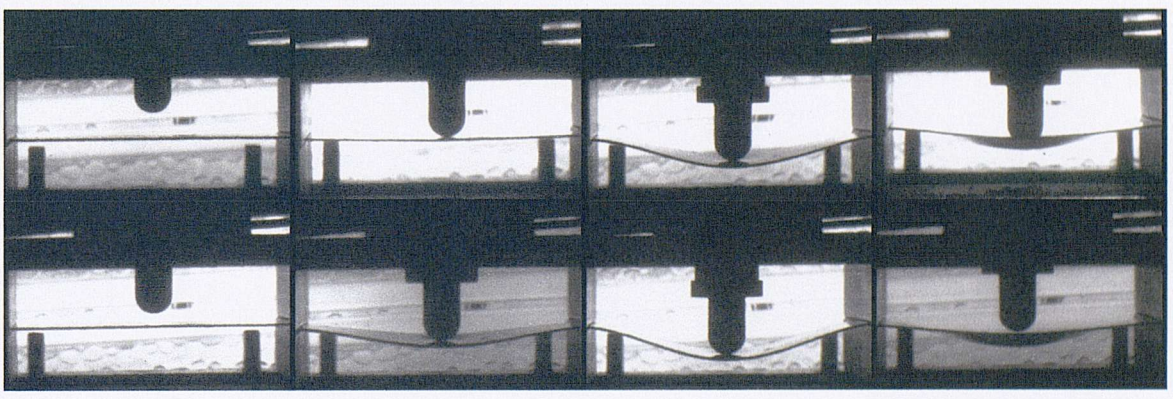
Frame	1	2	3	4	5	6	7	8
Setting (ms)	25	27.5	30	32.5	35	40	45	50
Exposure (μs)	150	150	150	150	150	150	150	150

Sample CPPS6



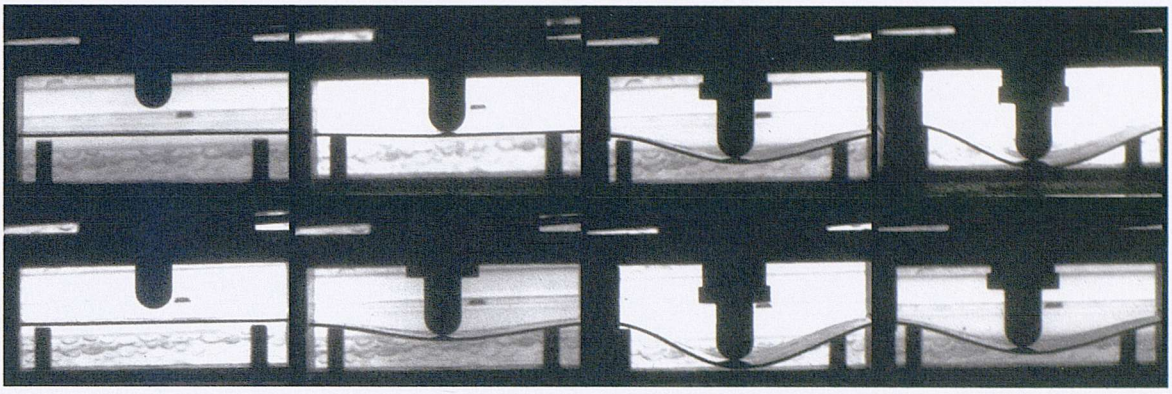
Frame	1	2	3	4	5	6	7	8
Setting (ms)	25	27.5	30	32.5	35	40	45	50
Exposure (μs)	150	150	150	150	150	150	150	150

Sample CPPS7



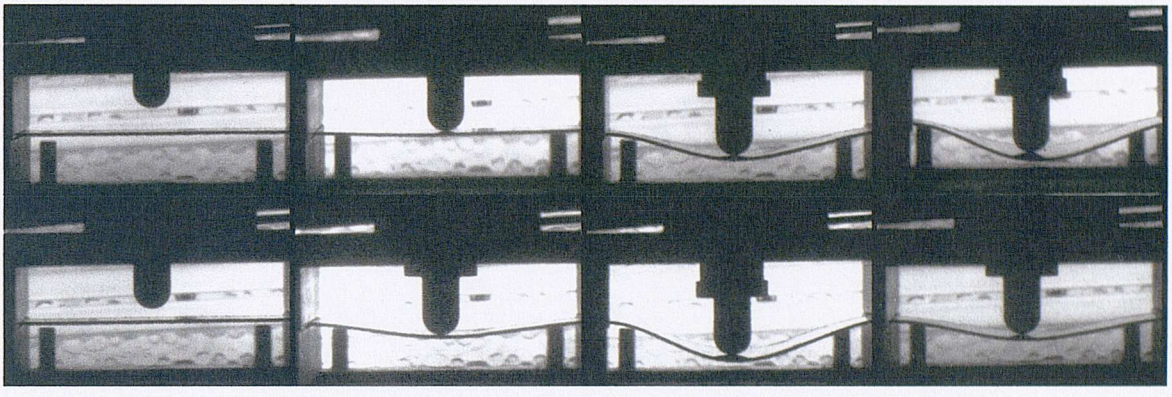
Frame	1	2	3	4	5	6	7	8
Setting (ms)	25	27.5	30	32.5	35	40	47.5	52.5
Exposure (μs)	150	150	150	150	150	150	150	150

Sample GPPS5



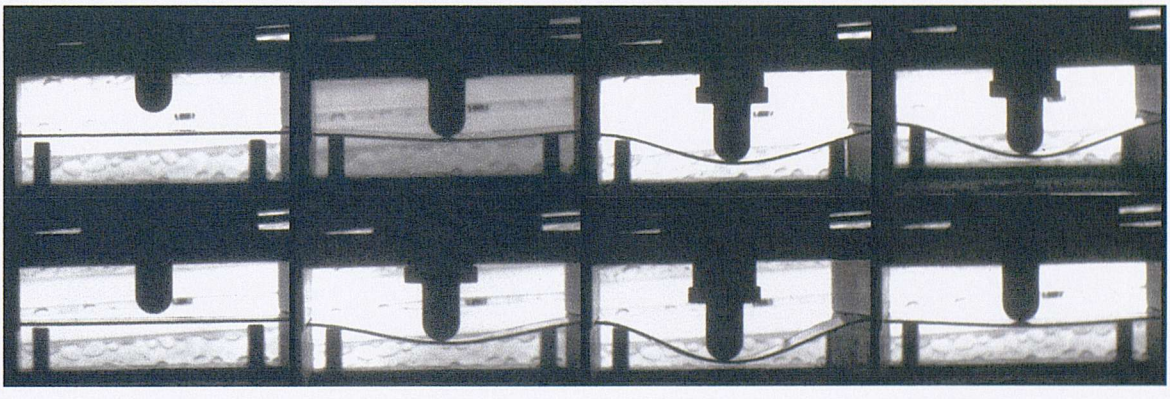
Frame	1	2	3	4	5	6	7	8
Setting (ms)	25	27.5	30	32.5	35	40	47.5	52.5
Exposure (μs)	150	150	150	150	150	150	150	150

Sample GPPS6



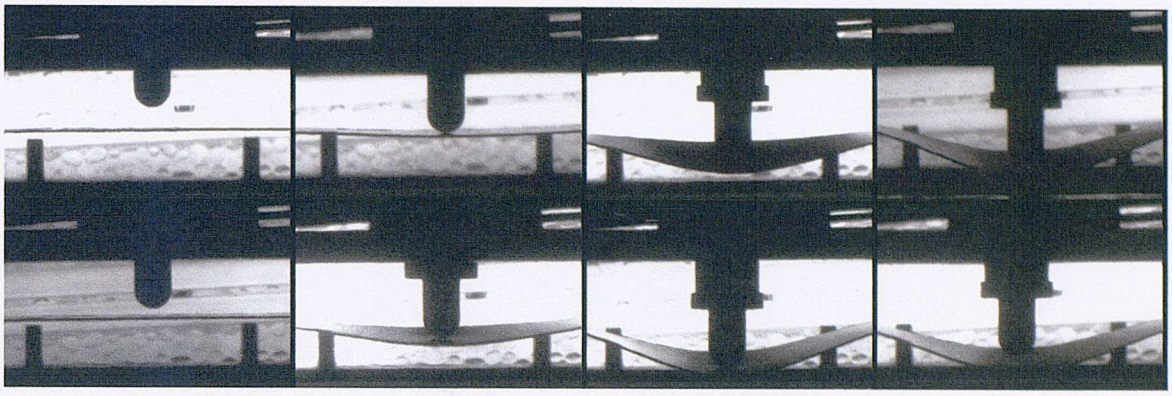
Frame	1	2	3	4	5	6	7	8
Setting (ms)	25	27.5	30	32.5	35	40	45	55
Exposure (μs)	150	150	150	150	150	150	150	150

Sample CPPS7



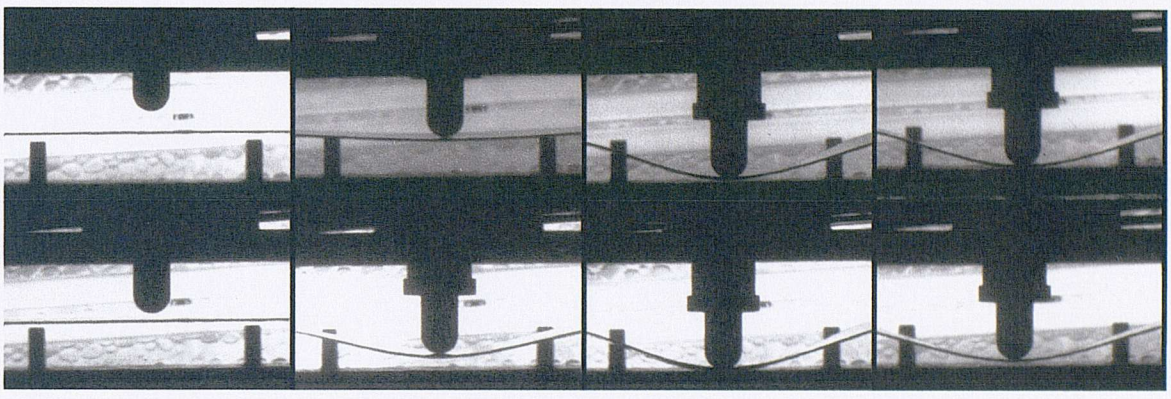
Frame	1	2	3	4	5	6	7	8
Setting (ms)	25	27.5	30	32.5	35	42.5	47.5	55
Exposure (μs)	150	150	150	150	150	150	150	150

Sample 1CPPS3



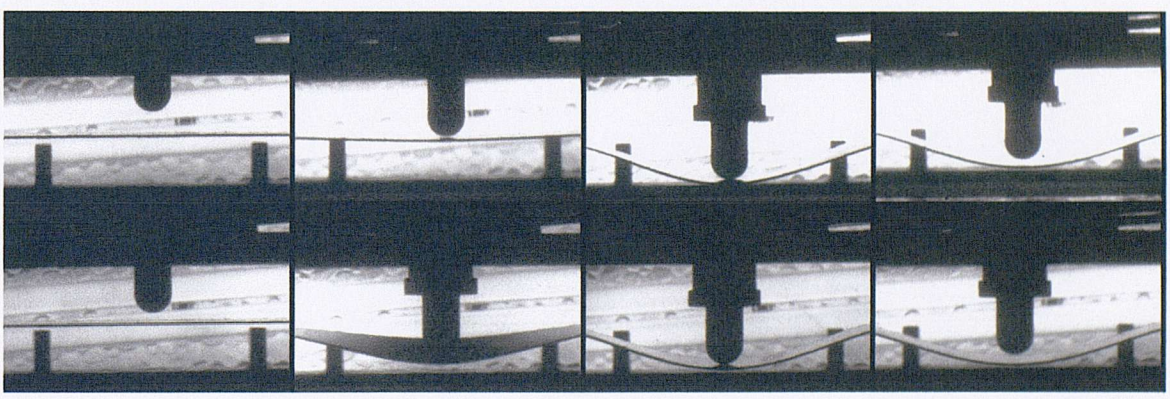
Frame	1	2	3	4	5	6	7	8
Setting (ms)	25	27.5	30	32.5	35	42.5	47.5	55
Exposure (μs)	150	150	150	150	150	150	150	150

Sample 1CPPS4



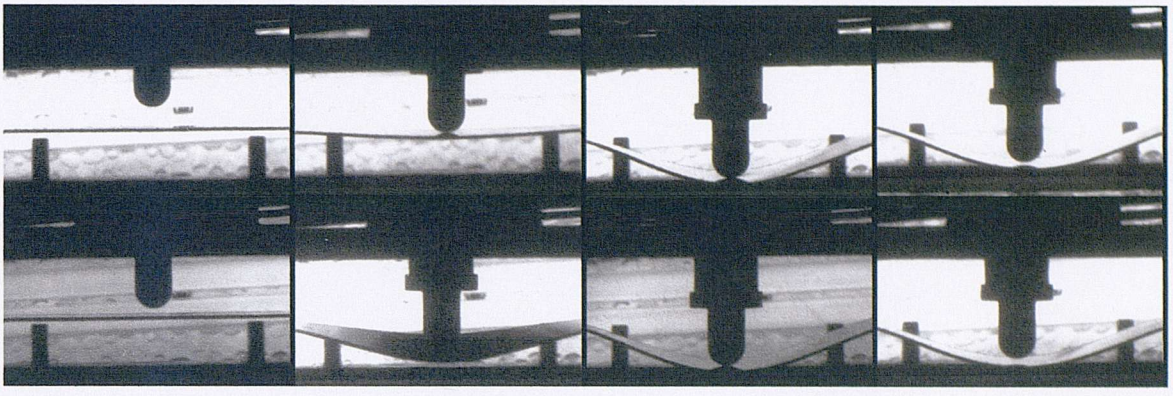
Frame	1	2	3	4	5	6	7	8
Setting (ms)	25	27.5	30	35	40	45	50	52.5
Exposure (μs)	150	150	150	150	150	150	150	150

Sample 1CPPS5



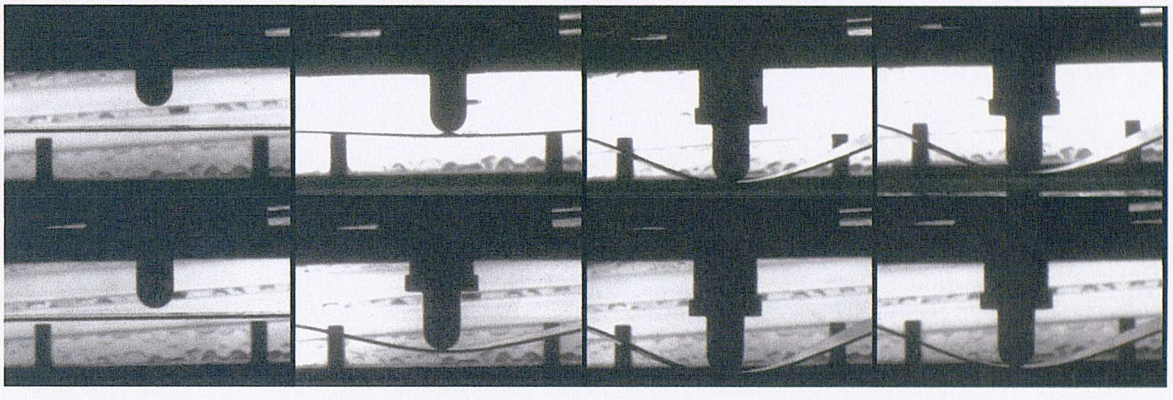
Frame	1	2	3	4	5	6	7	8
Setting (ms)	25	27.5	30	35	42.5	47.5	52.5	55
Exposure (μs)	150	150	150	150	150	150	150	150

Sample 1GPPS4



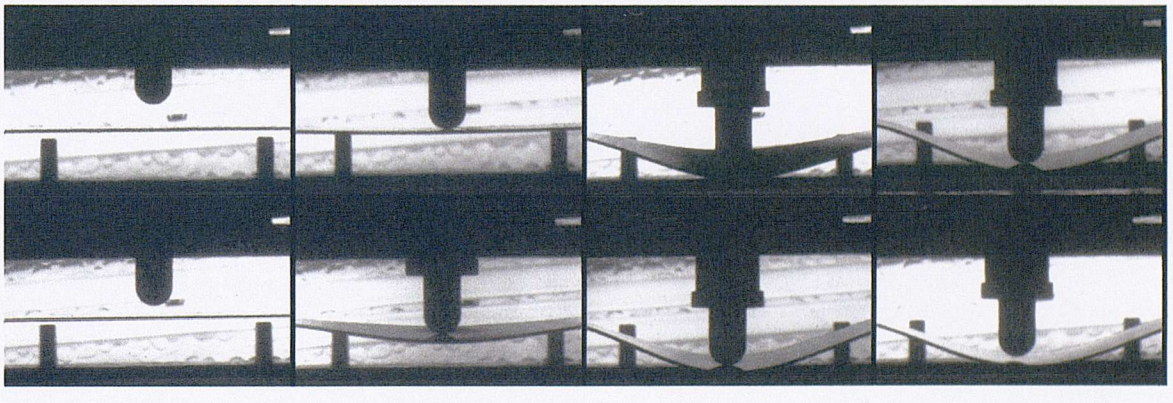
Frame	1	2	3	4	5	6	7	8
Setting (ms)	25	27.5	30	35	32.5	47.5	52.5	55
Exposure (μs)	150	150	150	150	150	150	150	150

Sample 1GPPS5



Frame	1	2	3	4	5	6	7	8
Setting (ms)	25	27.5	30	35	42.5	47.5	50	55
Exposure (μs)	150	150	150	150	150	150	150	150

Sample 1GPPS6

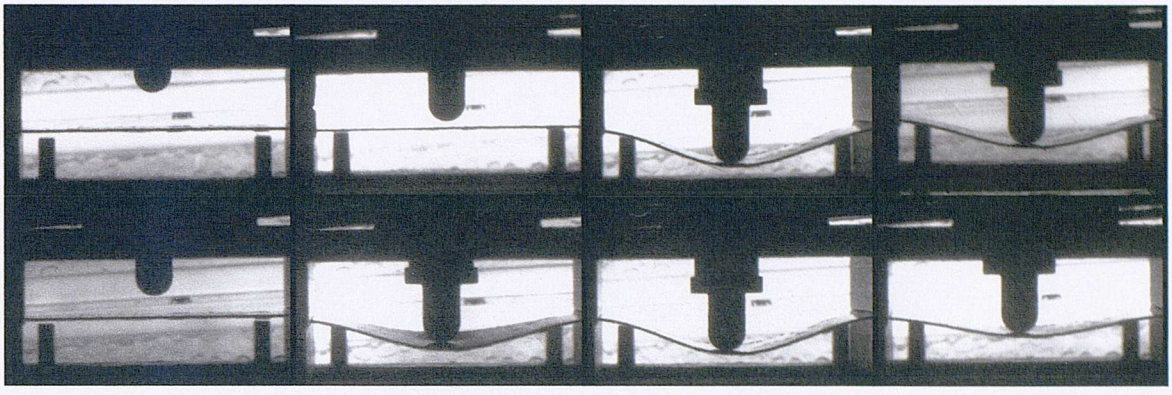


Frame	1	2	3	4	5	6	7	8
Setting (ms)	25	27.5	30	32.5	37.5	42.5	50	55
Exposure (μs)	150	150	150	150	150	150	150	150

Part 3:

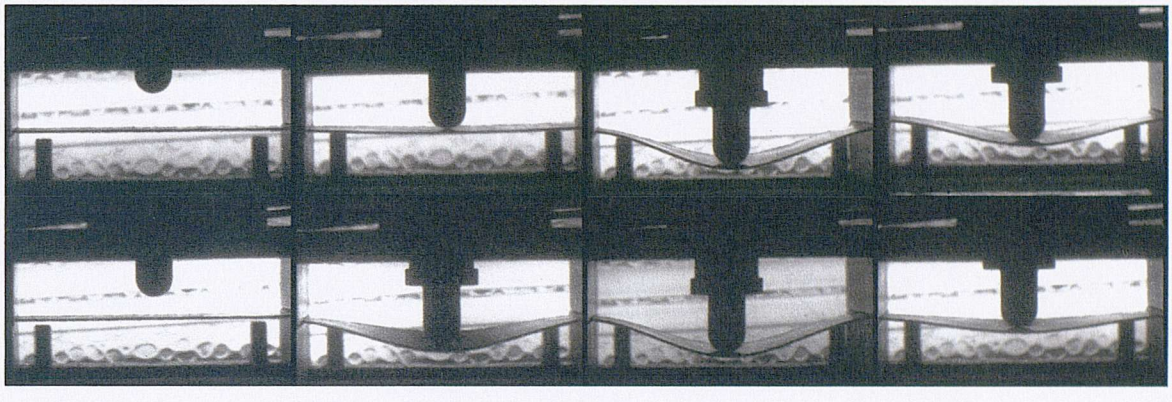
30cm Drop Height

Sample CPPS8



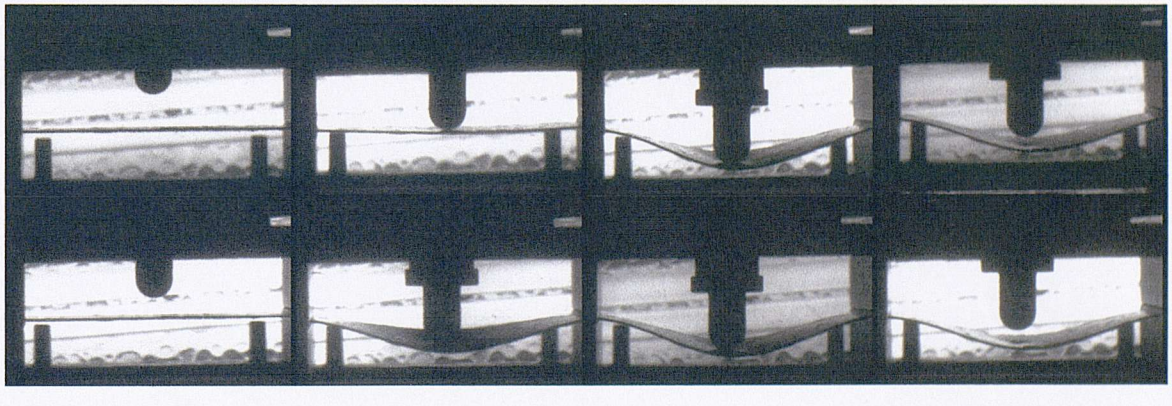
Frame	1	2	3	4	5	6	7	8
Setting (ms)	20	22.5	25	30	35	37.5	42.5	47.5
Exposure (μs)	150	150	150	150	150	150	150	150

Sample CPPS9



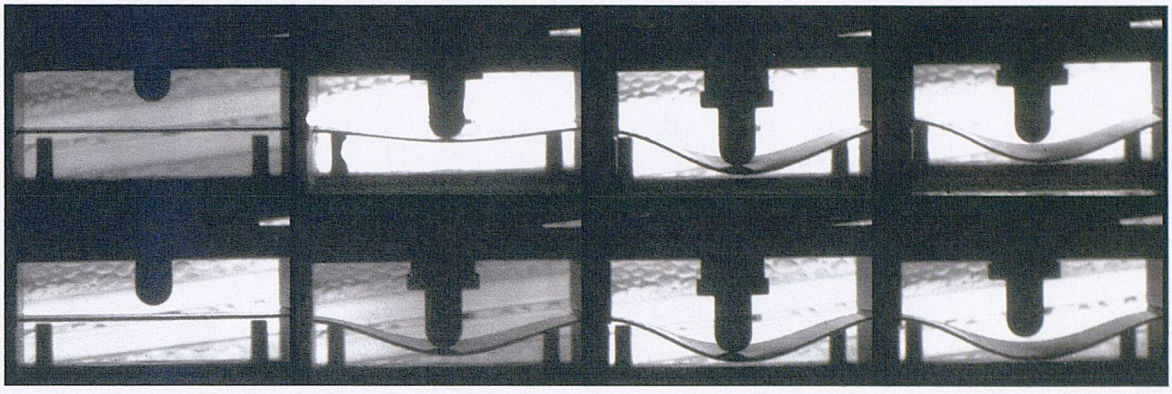
Frame	1	2	3	4	5	6	7	8
Setting (ms)	20	22.5	26	30	35	37.5	45	50
Exposure (μs)	150	150	150	150	150	150	150	150

Sample CPPS10



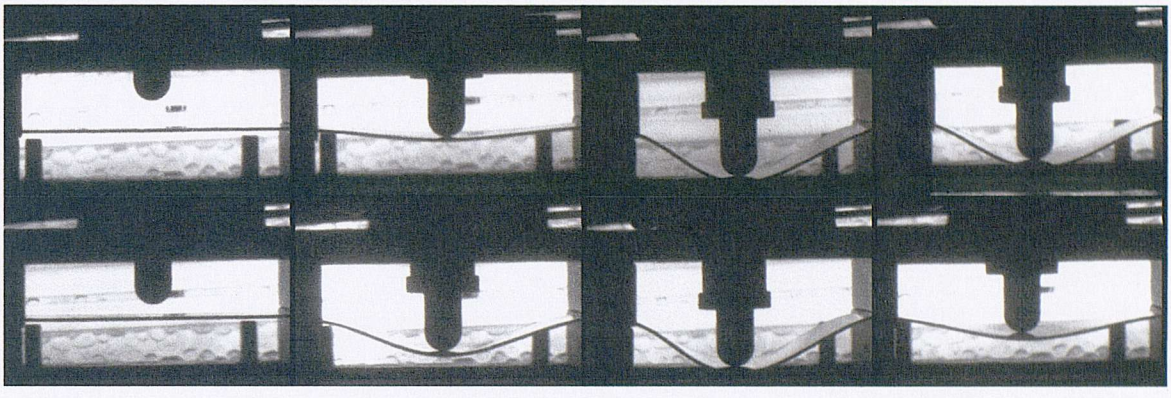
Frame	1	2	3	4	5	6	7	8
Setting (ms)	20	22.5	26	30	35	37.5	47.5	52.5
Exposure (μs)	150	150	150	150	150	150	150	150

Sample GPPS8



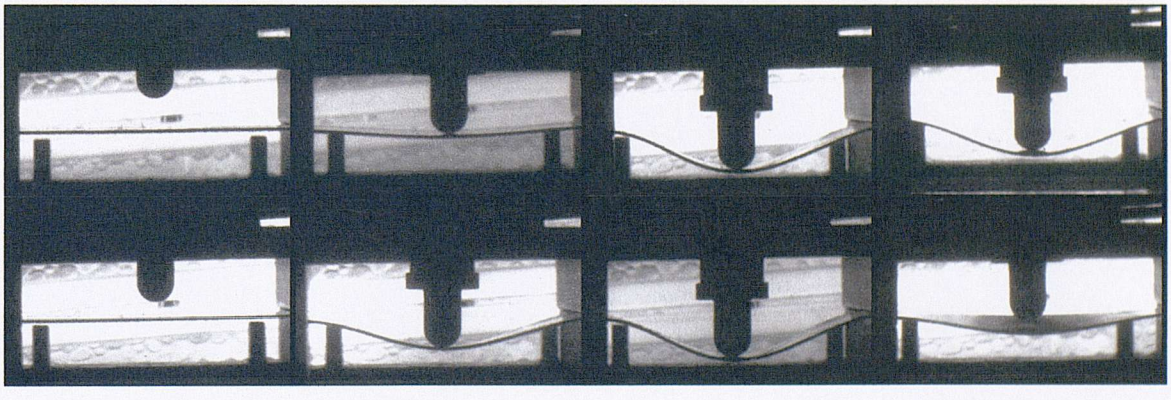
Frame	1	2	3	4	5	6	7	8
Setting (ms)	20	22.5	26	30	35	37.5	47.5	52.5
Exposure (μs)	150	150	150	150	150	150	150	150

Sample GPPS9



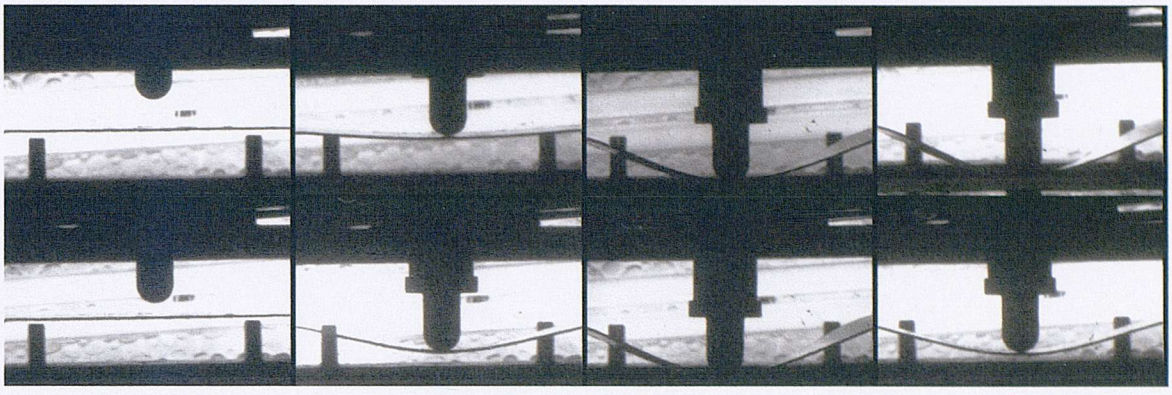
Frame	1	2	3	4	5	6	7	8
Setting (ms)	20	22.5	26	30	35	37.5	42.5	50
Exposure (μs)	150	150	150	150	150	150	150	150

Sample GPPS11



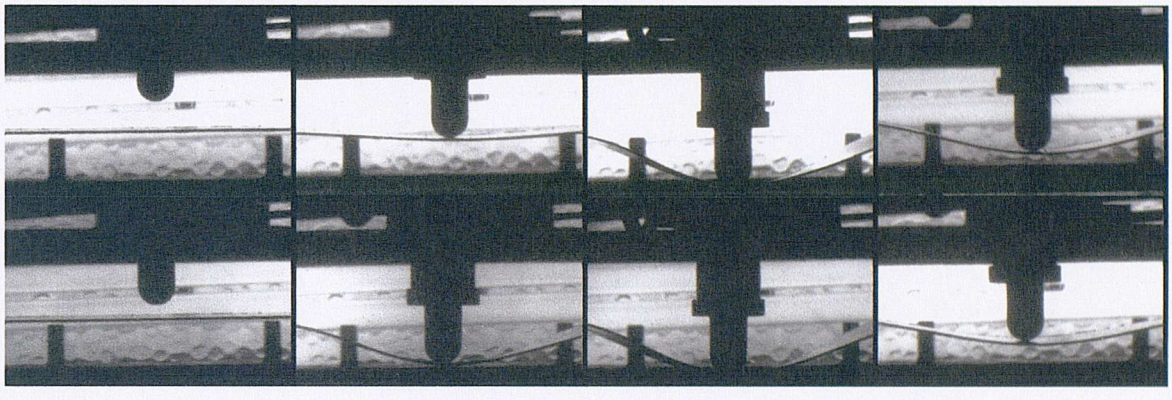
Frame	1	2	3	4	5	6	7	8
Setting (ms)	20	22.5	26	30	35	37.5	42.5	52.5
Exposure (μs)	150	150	150	150	150	150	150	150

Sample 1CPPS6



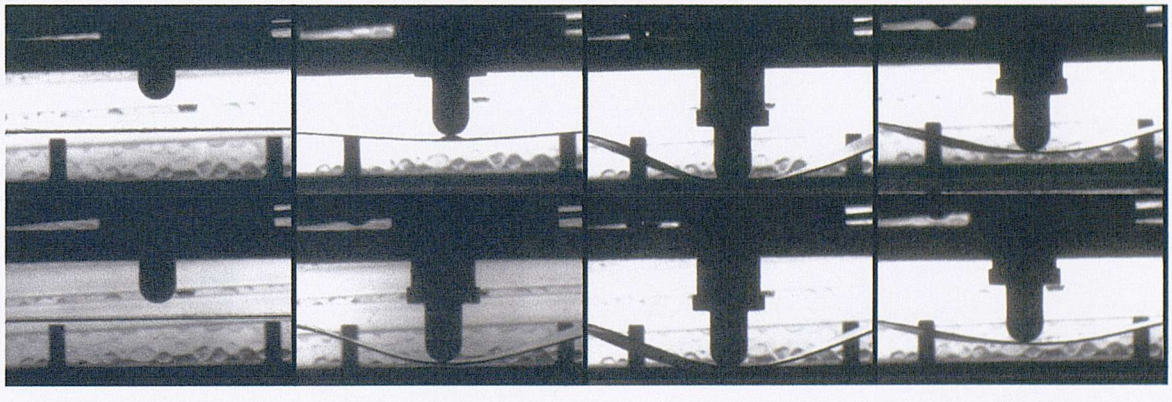
Frame	1	2	3	4	5	6	7	8
Setting (ms)	20	22.5	26	30	35	37.5	42.5	52.5
Exposure (μs)	150	150	150	150	150	150	150	150

Sample 1CPPS7



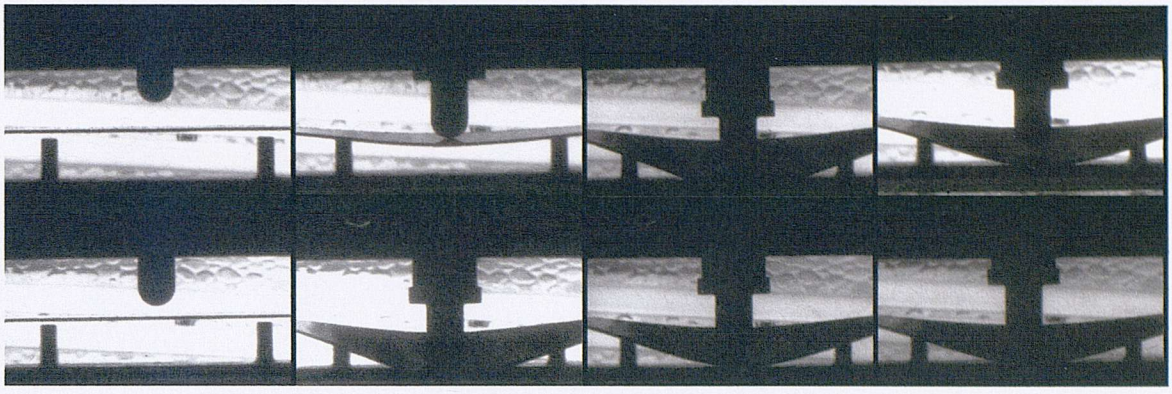
Frame	1	2	3	4	5	6	7	8
Setting (ms)	20	22.5	26	32.5	37.5	42.5	52.5	55
Exposure (μs)	150	150	150	150	150	150	150	150

Sample 1CPPS8



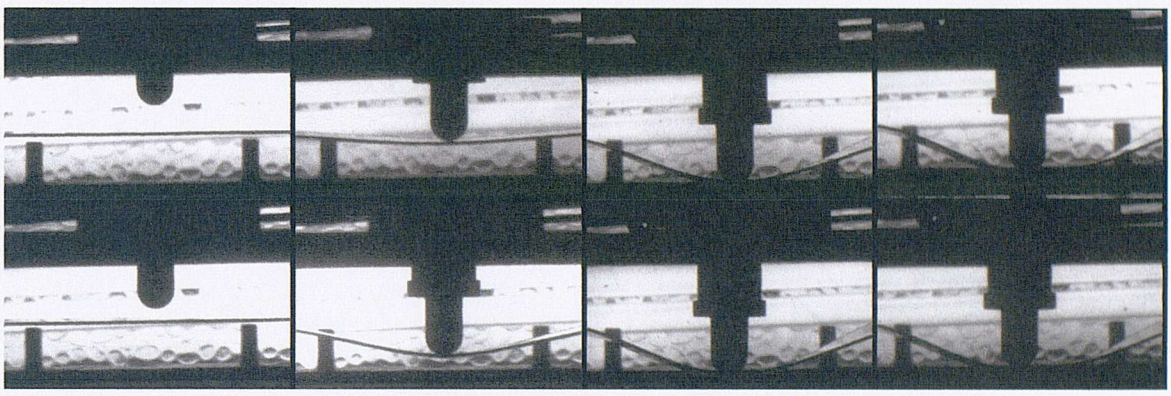
Frame	1	2	3	4	5	6	7	8
Setting (ms)	20	22.5	26	32.5	37.5	47.5	55	57.5
Exposure (μs)	150	150	150	150	150	150	150	150

Sample 1GPPS7



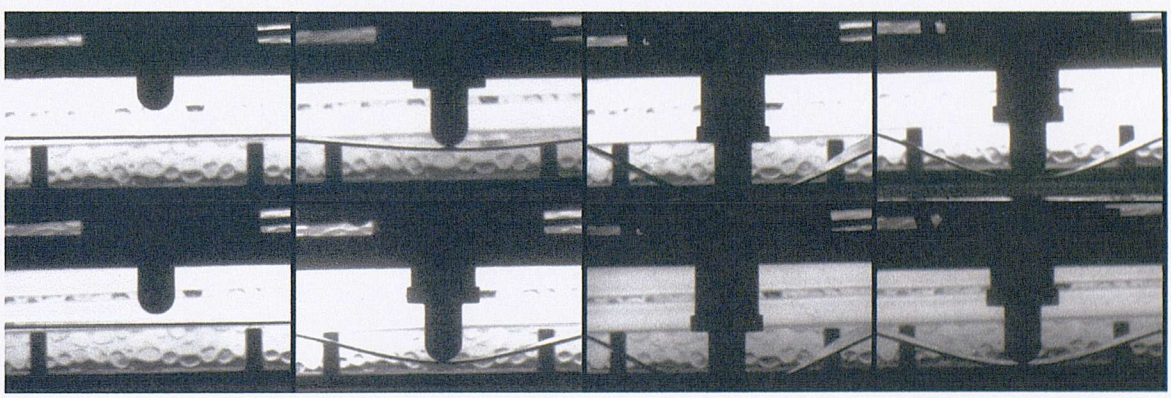
Frame	1	2	3	4	5	6	7	8
Setting (ms)	20	22.5	26	32.5	37.5	47.5	52.5	55
Exposure (μs)	150	150	150	150	150	150	150	150

Sample 1GPPS8



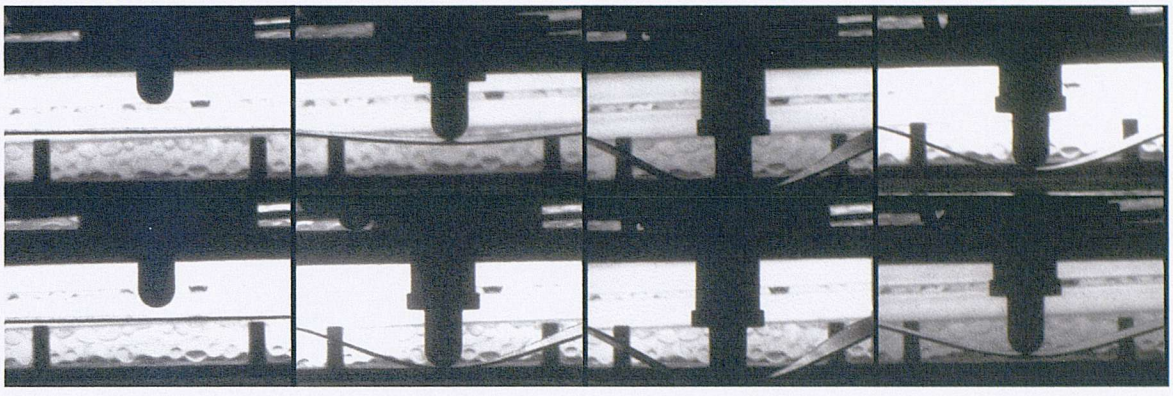
Frame	1	2	3	4	5	6	7	8
Setting (ms)	20	22.5	26	30	35	37.5	47.5	55
Exposure (μs)	150	150	150	150	150	150	150	150

Sample 1GPPS9



Frame	1	2	3	4	5	6	7	8
Setting (ms)	20	22.5	26	30	37.5	45	50	55
Exposure (μs)	150	150	150	150	150	150	150	150

Sample 1GPPS10

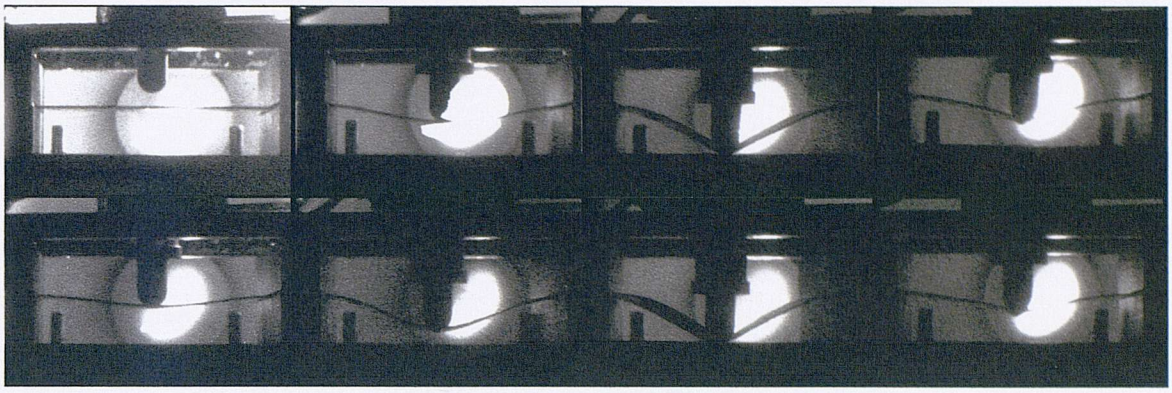


Frame	1	2	3	4	5	6	7	8
Setting (ms)	20	22.5	26	32.5	37.5	45	52.5	57.5
Exposure (μs)	150	150	150	150	150	150	150	150

Part 4:

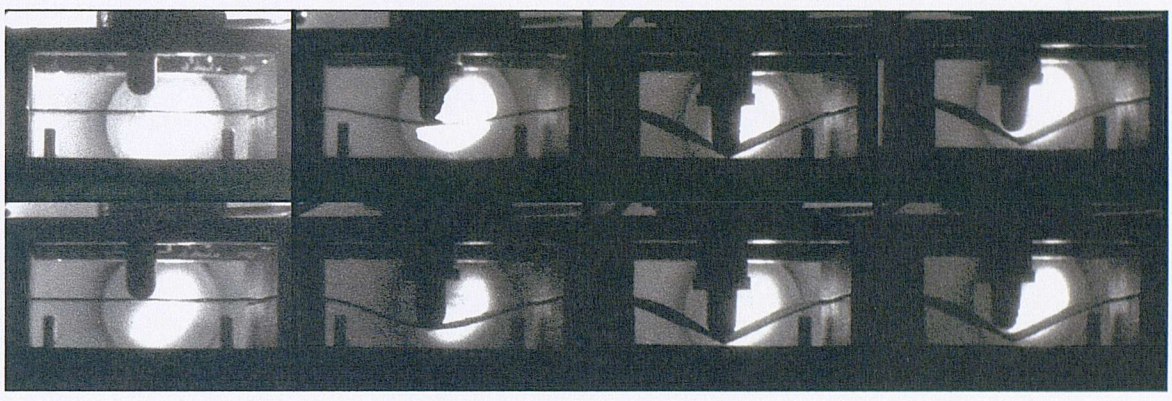
40cm Drop Height

Sample CPPS11



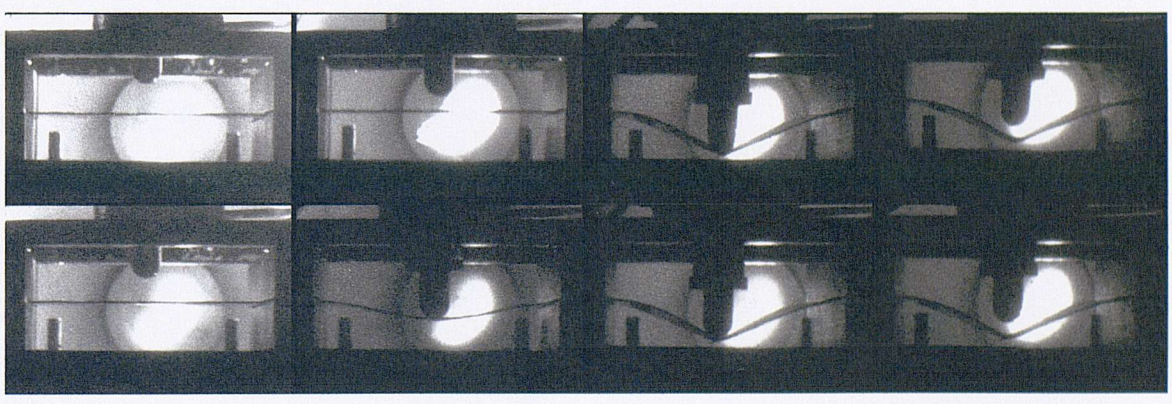
Frame	1	2	3	4	5	6	7	8
Setting (ms)	12.5	16.5	17.5	21	25	30	47.5	50
Exposure (μs)	5	5	5	5	5	5	5	5

Sample CPPS12



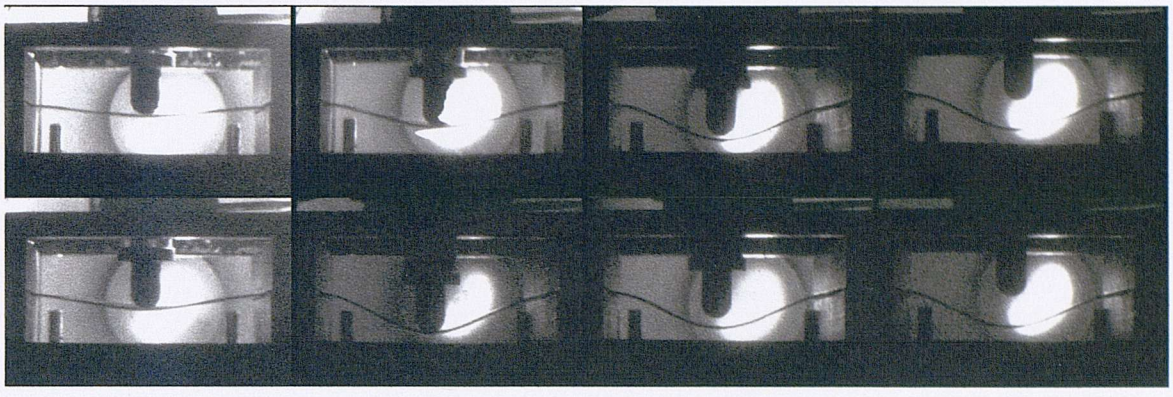
Frame	1	2	3	4	5	6	7	8
Setting (ms)	10	12.5	15	17.5	25	32.5	52.5	55
Exposure (μs)	6	6	6	6	6	6	6	6

Sample CPPS13



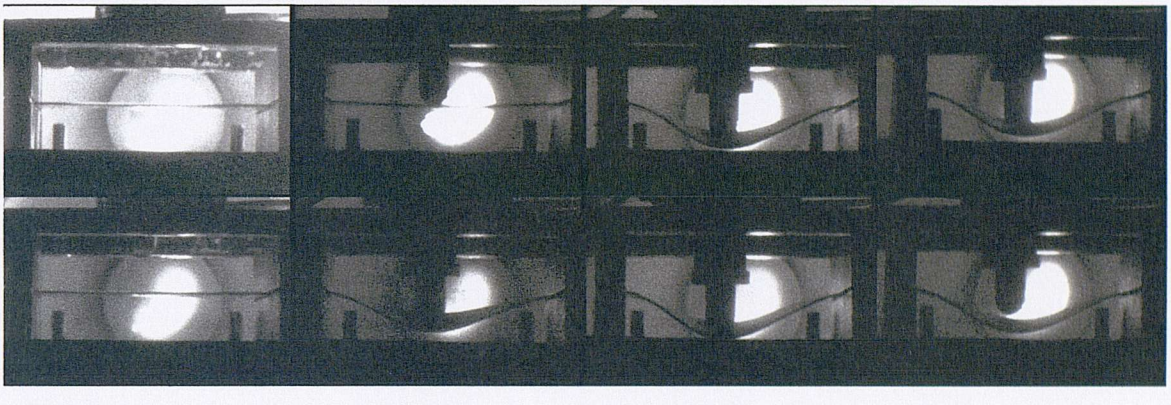
Frame	1	2	3	4	5	6	7	8
Setting (ms)	10	11	12.5	17.5	25	30	52.5	55
Exposure (μs)	6	6	6	6	6	6	6	6

Sample GPPS12



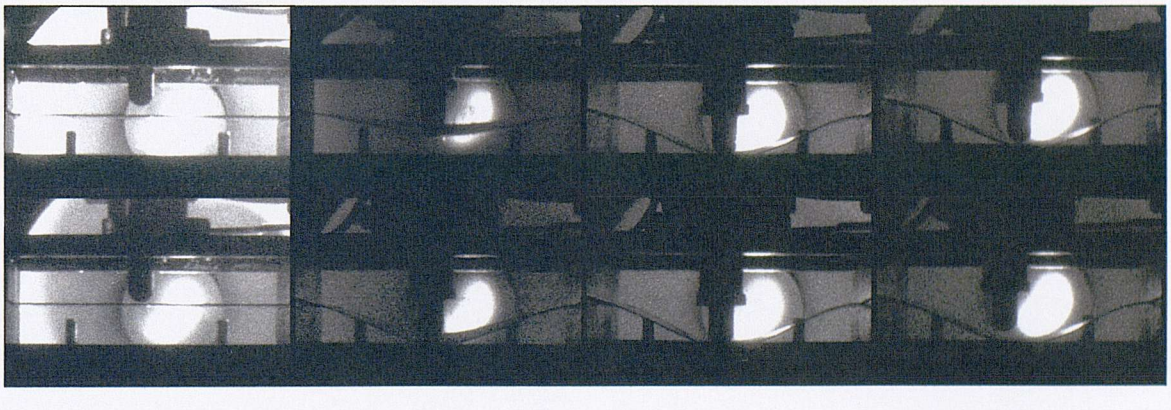
Frame	1	2	3	4	5	6	7	8
Setting (ms)	10	11	12.5	17.5	25	30	52.5	55
Exposure (μs)	6	6	6	6	6	6	6	6

Sample GPPS14



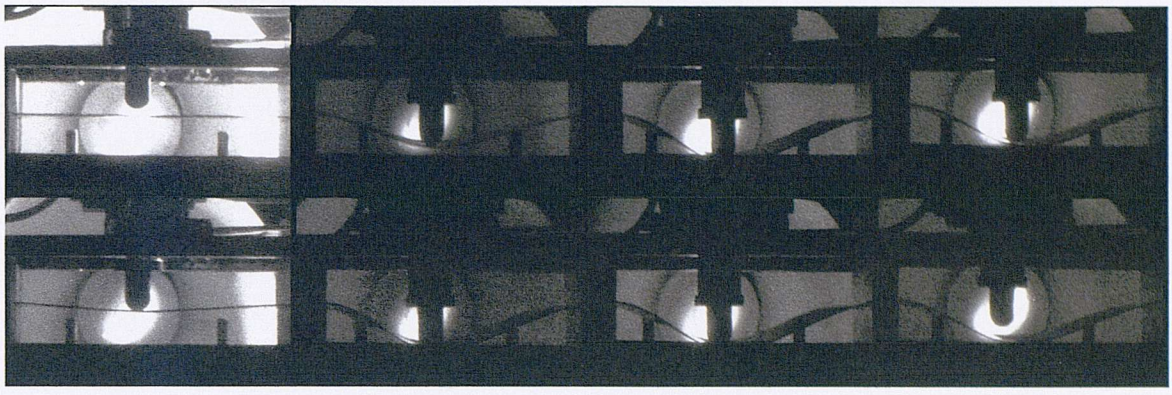
Frame	1	2	3	4	5	6	7	8
Setting (ms)	6	9	15	20	22.5	25	30	40
Exposure (μs)	6	6	6	6	6	6	6	6

Sample 1CPPS9



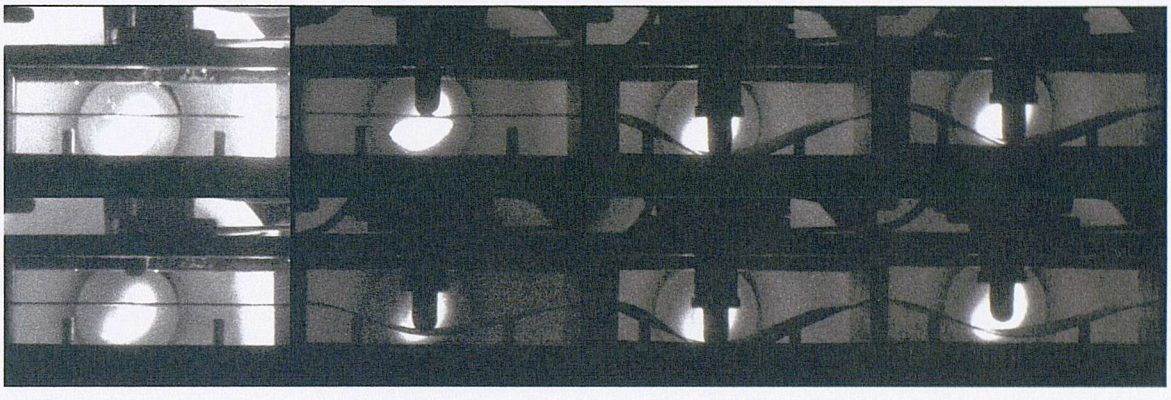
Frame	1	2	3	4	5	6	7	8
Setting (ms)	7.5	9	12.5	17.5	20	25	30	50
Exposure (μs)	6	6	6	6	6	6	6	6

Sample 1CPPS10



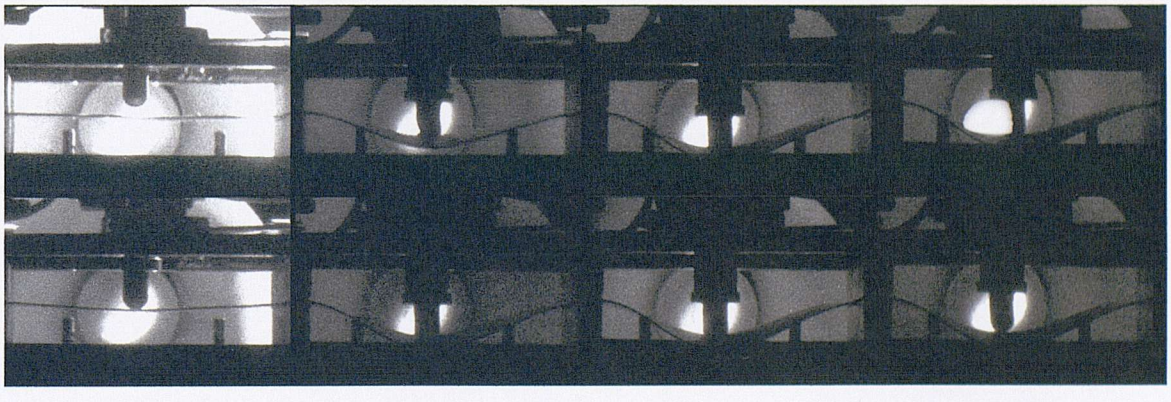
Frame	1	2	3	4	5	6	7	8
Setting (ms)	7.5	10	15	20	25	27.5	35	52.5
Exposure (μs)	6	6	6	6	6	6	6	6

Sample 1CPPS11



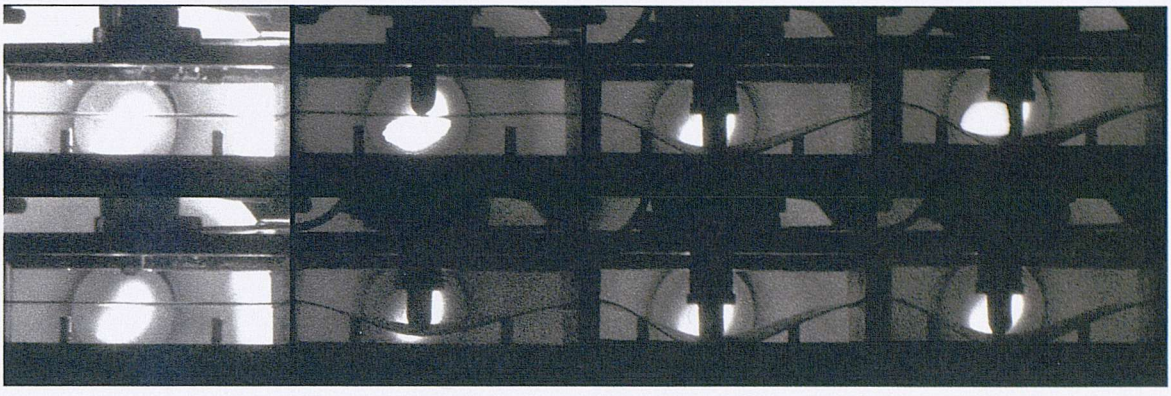
Frame	1	2	3	4	5	6	7	8
Setting (ms)	7.5	9.5	15	20	25	27.5	37.5	52.5
Exposure (μs)	6	6	6	6	6	6	6	6

Sample 1GPPS10



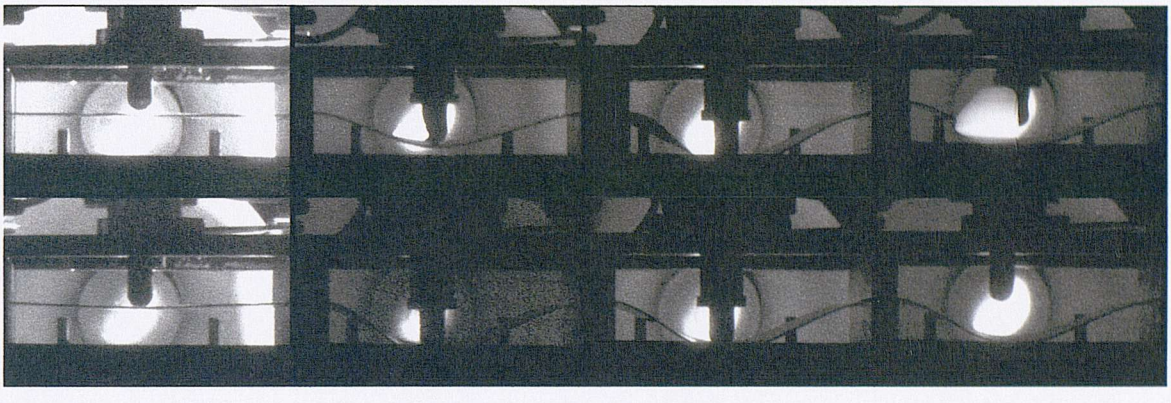
Frame	1	2	3	4	5	6	7	8
Setting (ms)	7.5	10	15	20	25	27.5	35	52.5
Exposure (μs)	6	6	6	6	6	6	6	6

Sample 1GPPS11



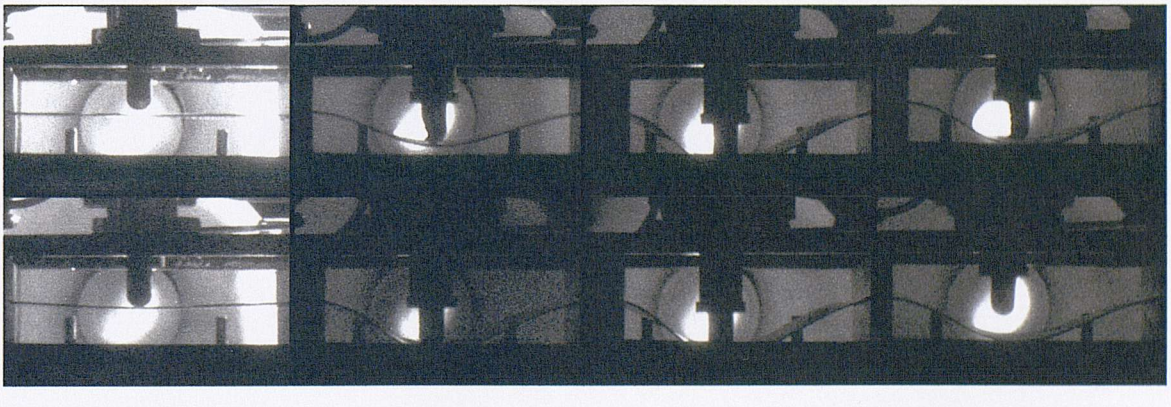
Frame	1	2	3	4	5	6	7	8
Setting (ms)	7.5	9.5	15	20	25	27.5	37.5	55
Exposure (μs)	6	6	6	6	6	6	6	6

Sample 1GPPS12



Frame	1	2	3	4	5	6	7	8
Setting (ms)	8	9.5	15	20	25	27.5	40	57.5
Exposure (μs)	6	6	6	6	6	6	6	6

Sample 1GPPS13

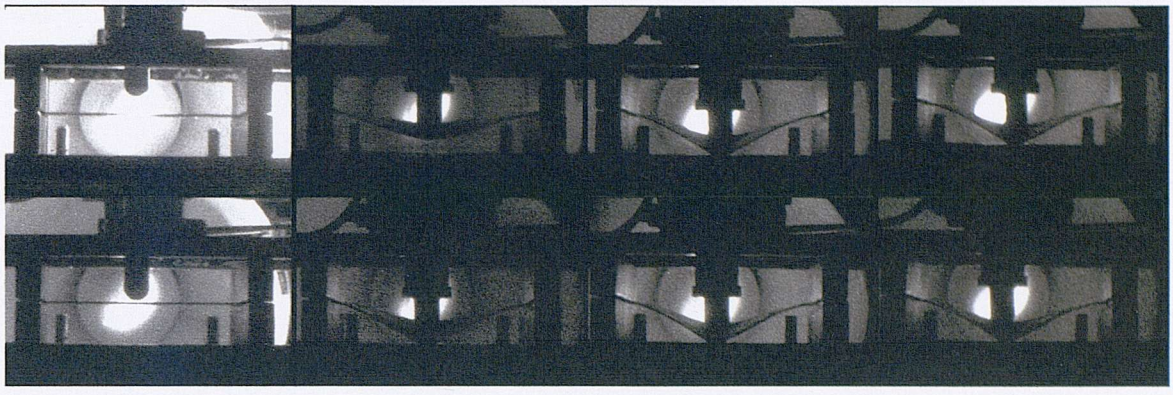


Frame	1	2	3	4	5	6	7	8
Setting (ms)	8	9.5	15	20	25	27.5	40	57.5
Exposure (μs)	6	6	6	6	6	6	6	6

Part 5:

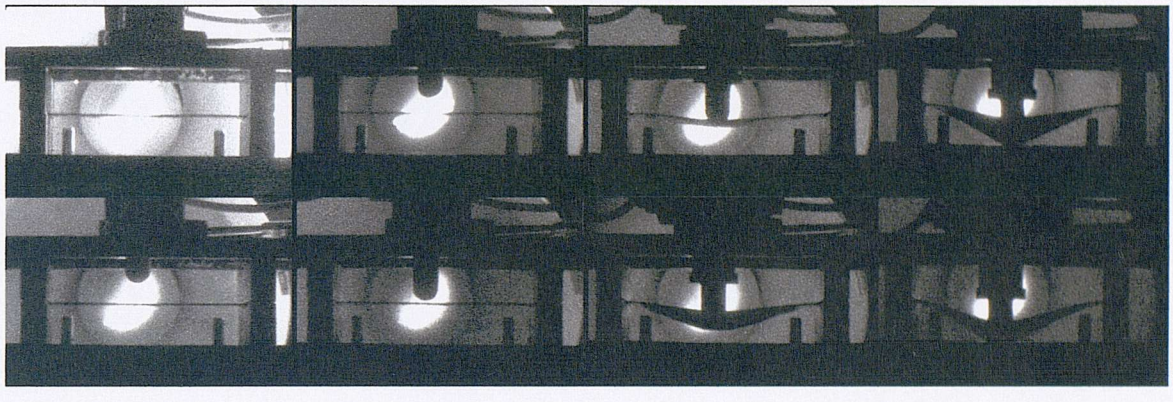
50cm Drop Height

Sample CPPS14



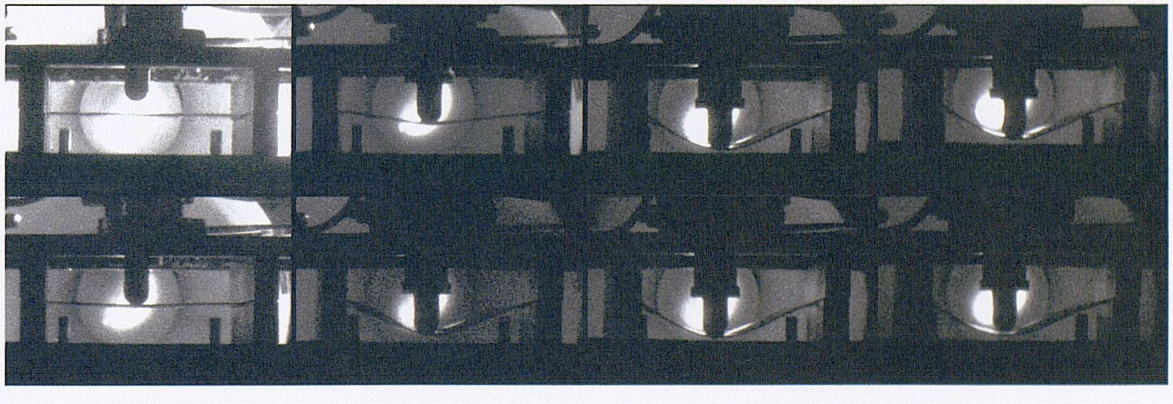
Frame	1	2	3	4	5	6	7	8
Setting (ms)	6.0	8.5	12.5	17.5	22.5	25	35	52.5
Exposure (μs)	6	6	6	6	6	6	6	6

Sample CPPS15



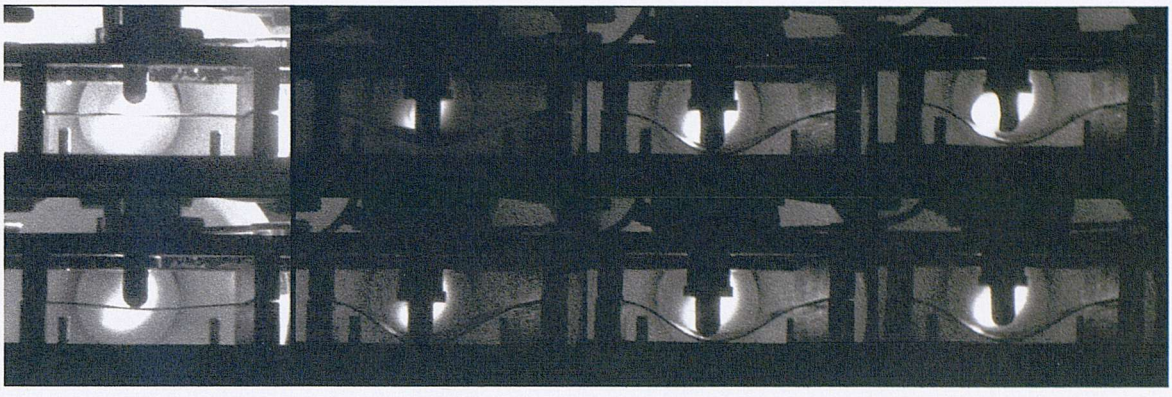
Frame	1	2	3	4	5	6	7	8
Setting (ms)	6	9	10	12	14	16	20	25
Exposure (μs)	6	6	6	6	6	6	6	6

Sample CPPS16



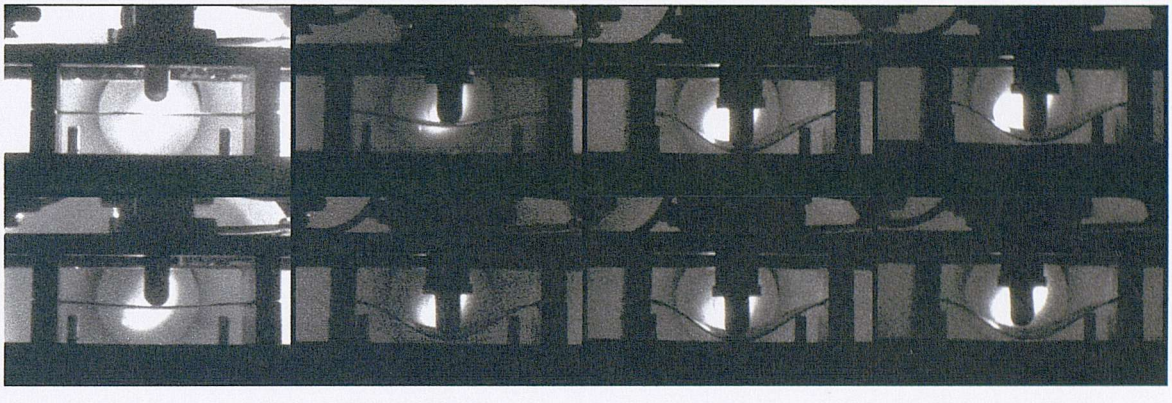
Frame	1	2	3	4	5	6	7	8
Setting (ms)	6	8.5	10	15	18	19	20	27.5
Exposure (μs)	6	6	6	6	6	6	6	6

Sample GPPS14



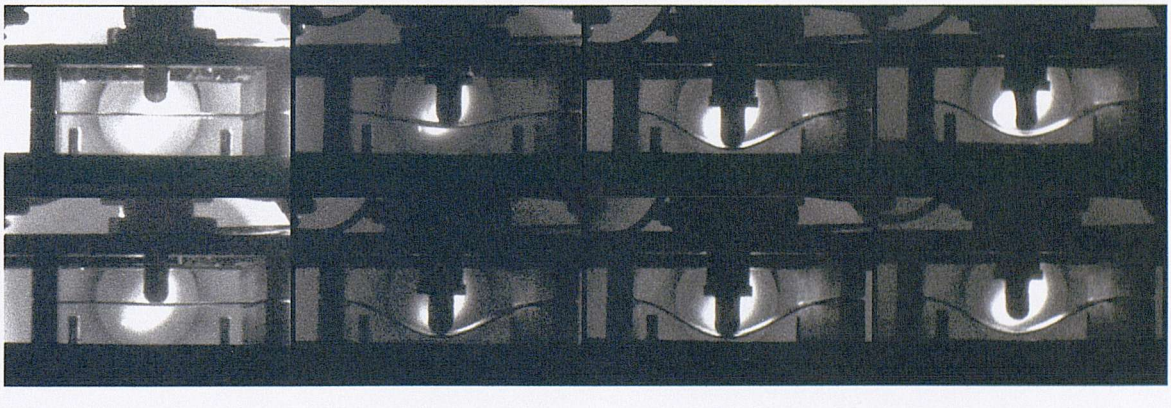
Frame	1	2	3	4	5	6	7	8
Setting (ms)	6	8.5	12.5	17.5	22.5	25	35	52.5
Exposure (μs)	6	6	6	6	6	6	6	6

Sample GPPS15



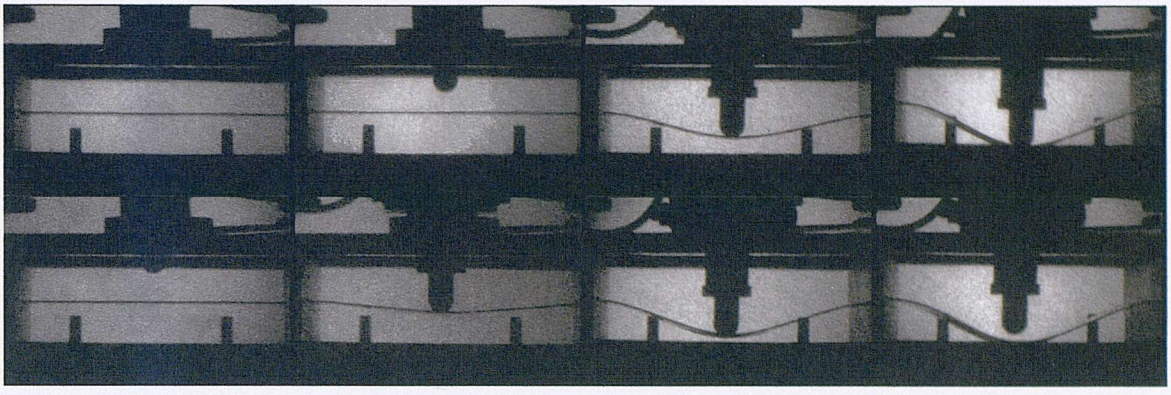
Frame	1	2	3	4	5	6	7	8
Setting (ms)	6	8.5	10	15	17.5	20	27.5	45
Exposure (μs)	6	6	6	6	6	6	6	6

Sample GPPS16



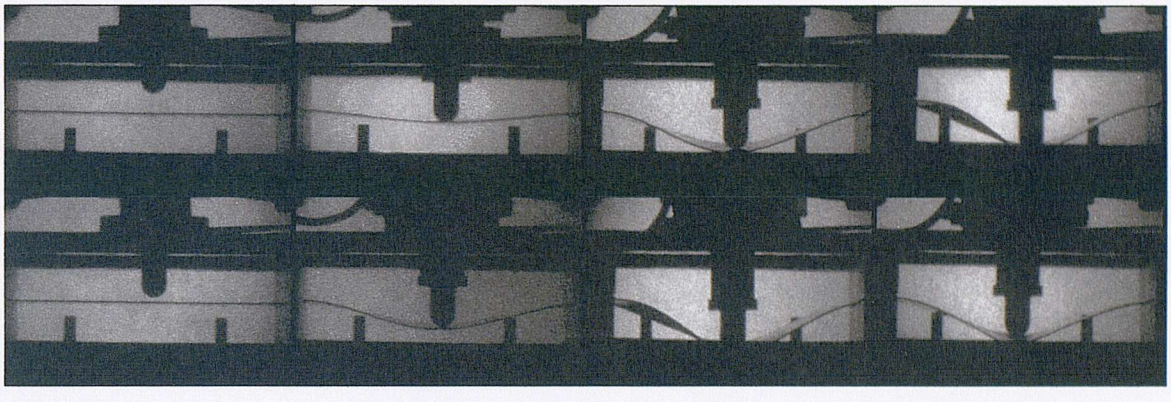
Frame	1	2	3	4	5	6	7	8
Setting (ms)	6	8	10	15	16	18	25	35
Exposure (μs)	6	6	6	6	6	6	6	6

Sample 1CPPS12



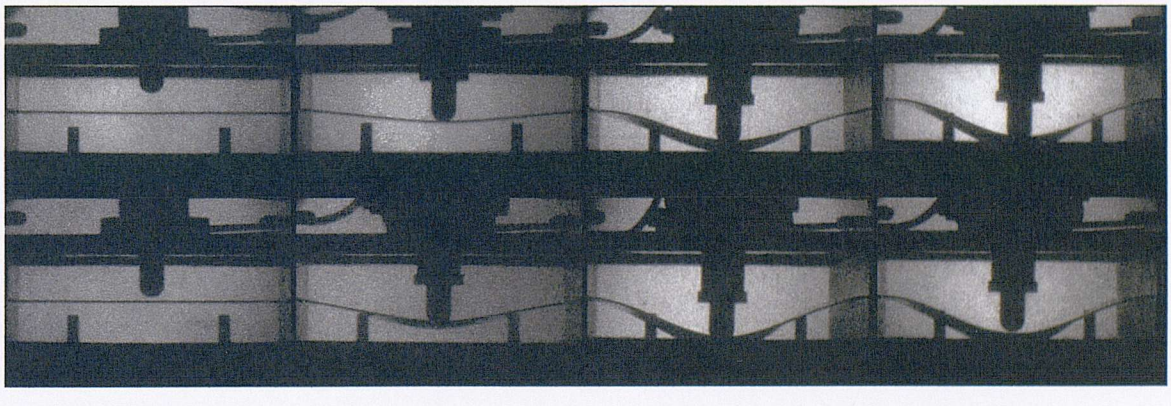
Frame	1	2	3	4	5	6	7	8
Setting (ms)	6	8	12.5	17.5	22.5	25	35	52.5
Exposure (μs)	3	7	7	20	20	20	20	20

Sample 1CPPS13



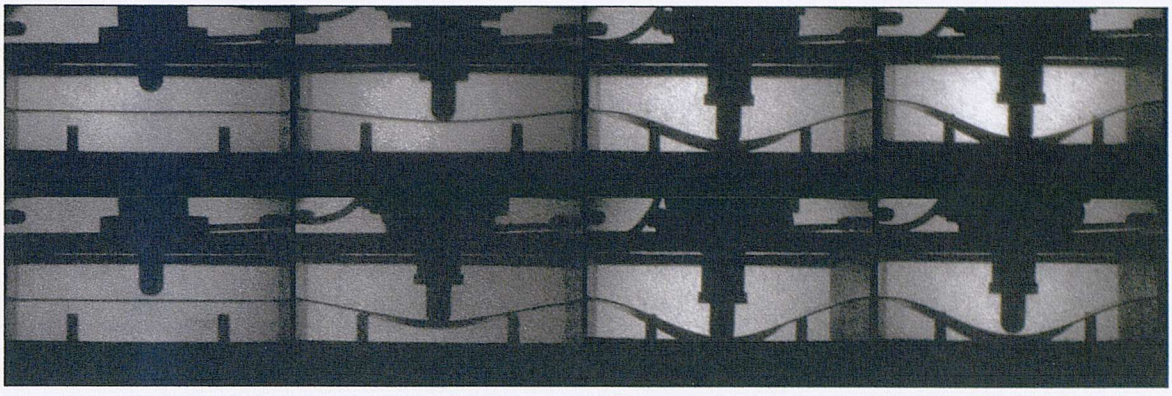
Frame	1	2	3	4	5	6	7	8
Setting (ms)	6	8.5	10	15	17.5	20	27.5	45
Exposure (μs)	3	7	7	30	30	30	30	30

Sample 1CPPS14



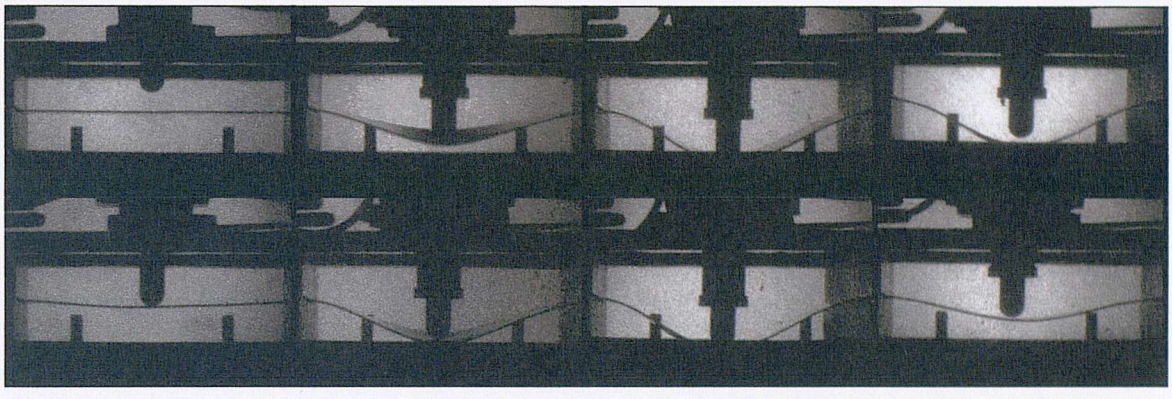
Frame	1	2	3	4	5	6	7	8
Setting (ms)	10	12.5	15	17.5	20	25	30	45
Exposure (μs)	40	40	40	40	40	40	40	40

Sample 1GPPS14



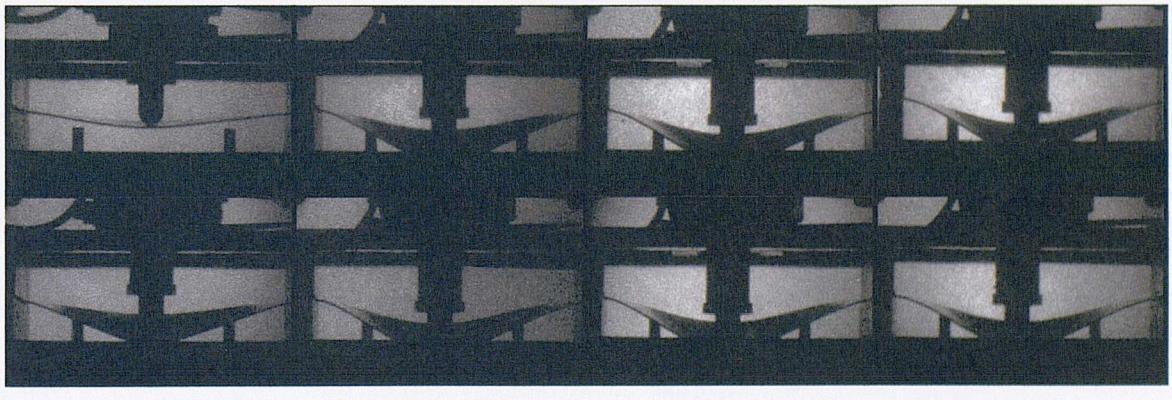
Frame	1	2	3	4	5	6	7	8
Setting (ms)	10	12.5	15	17.5	20	25	30	45
Exposure (μs)	40	40	40	40	40	40	40	40

Sample 1GPPS15



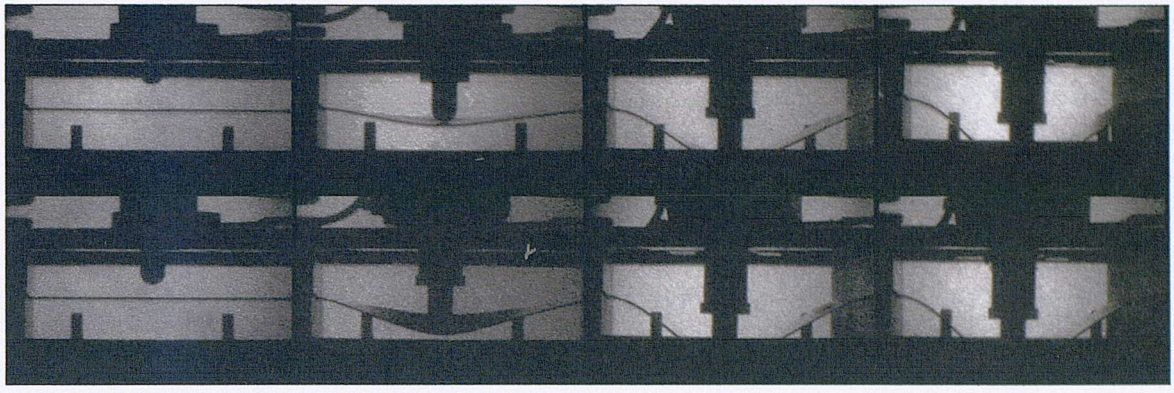
Frame	1	2	3	4	5	6	7	8
Setting (ms)	10	14	18	20	22.5	25	30	45
Exposure (μs)	40	40	40	40	40	40	40	40

Sample 1GPPS16



Frame	1	2	3	4	5	6	7	8
Setting (ms)	10	14	18	20	22.5	25	30	45
Exposure (μs)	40	40	40	40	40	40	40	40

Sample 1GPPS17

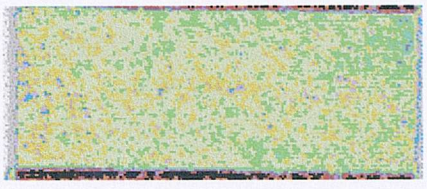


Frame	1	2	3	4	5	6	7	8
Setting (ms)	6	8	12.5	15	20	22.5	27.5	35
Exposure (μs)	40	40	40	40	40	40	40	40

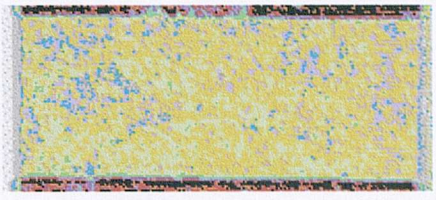
Appendix 4.

C-Scan Images for Damage Analysis of Thin Flexible Composite Laminates

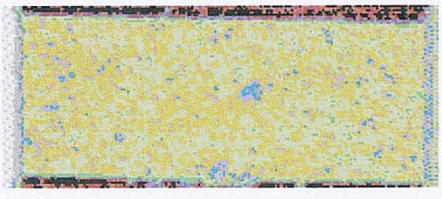
Short Carbon Fibre Specimens



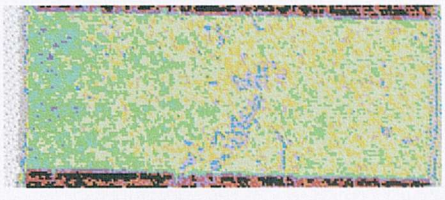
CPPS1
(10cm)



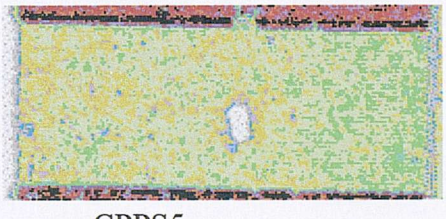
CPPS2
(10cm)



CPPS3
(10cm)



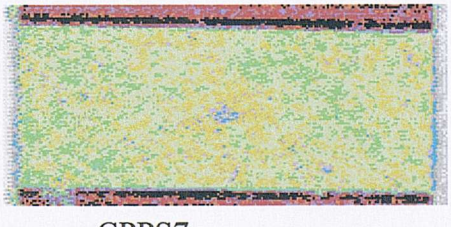
CPPS4
(10cm)



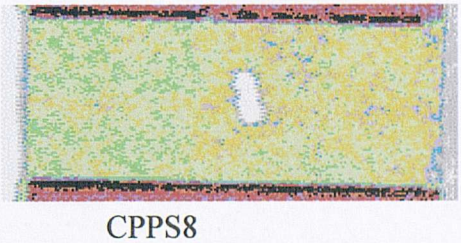
CPPS5
(20cm)



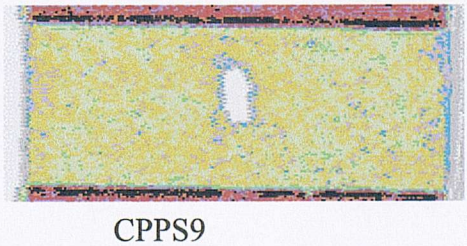
CPPS6
(20cm)



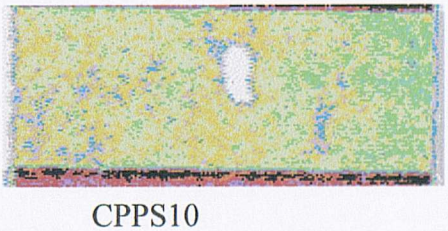
CPPS7
(20cm)



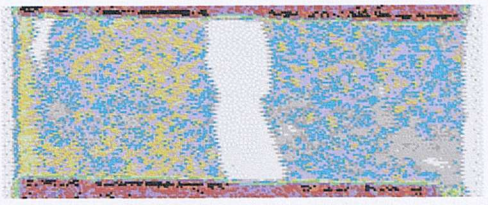
CPPS8
(30cm)



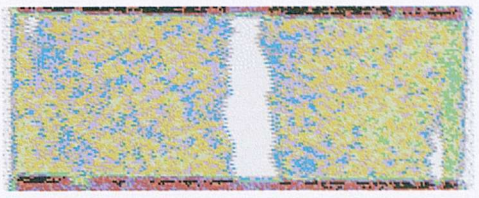
CPPS9
(30cm)



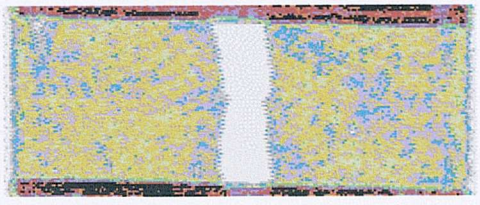
CPPS10
(30cm)



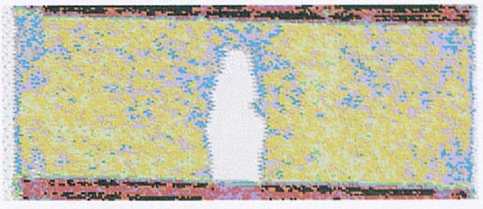
CPPS11
(40cm)



CPPS12
(40cm)



CPPS13
(40cm)



CPPS14
(50cm)

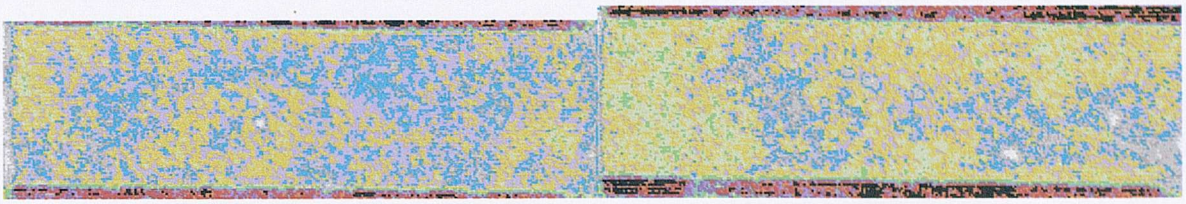


CPPS15
(50cm)



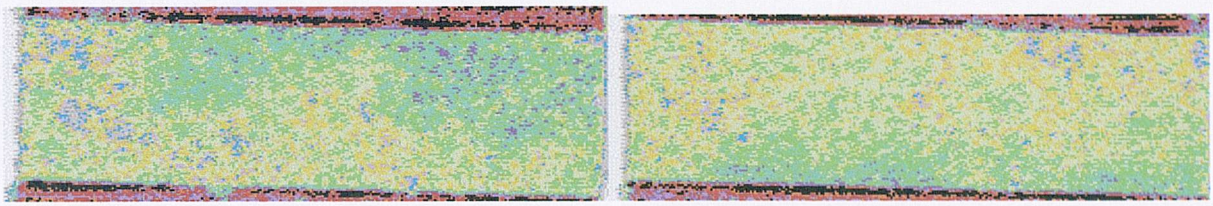
CPPS16
(50cm)

Long Carbon Fibre Specimens



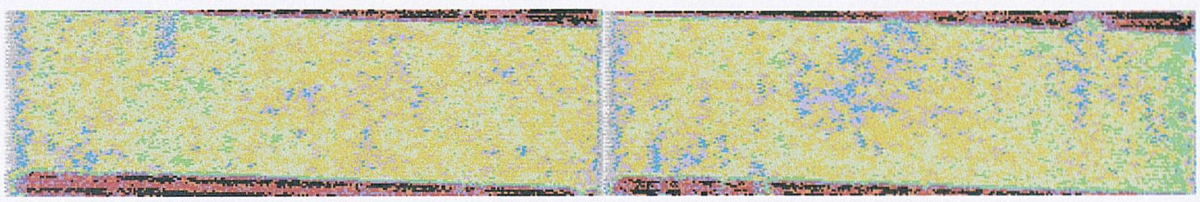
1CPPS1
(10cm)

1CPPS2
(10cm)



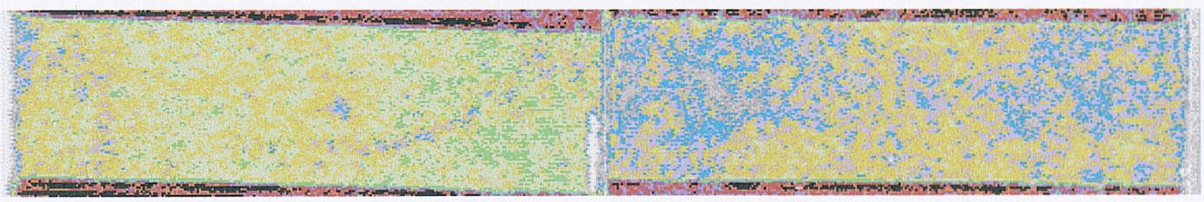
1CPPS3
(20cm)

1CPPS4
(20cm)



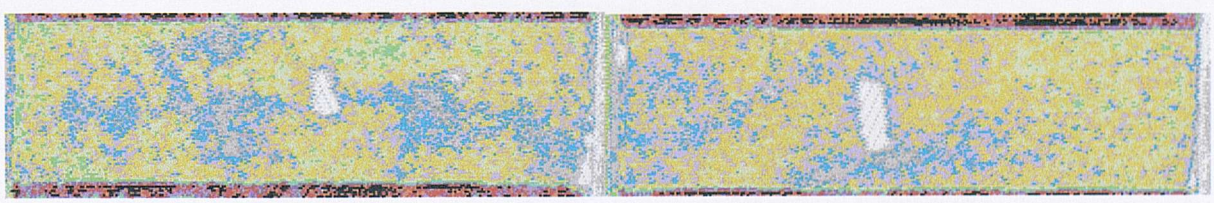
1CPPS5
(20cm)

1CPPS6
(30cm)



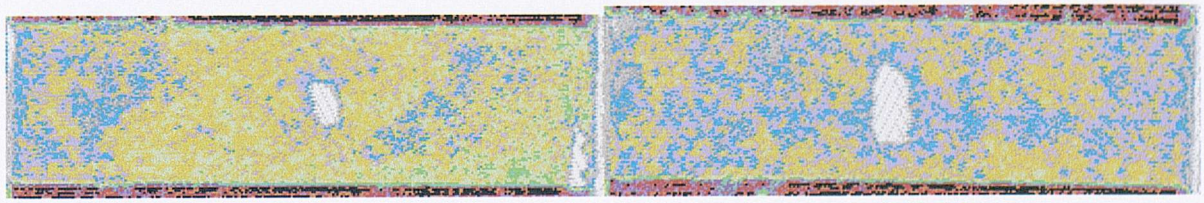
1CPPS7
(30cm)

1CPPS8
(30cm)



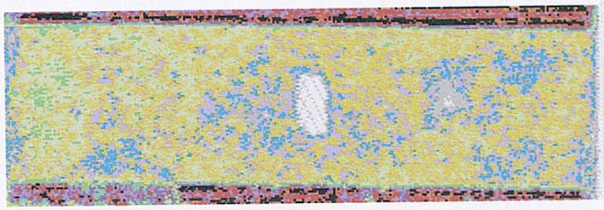
1CPPS9
(40cm)

1CPPS10
(40cm)

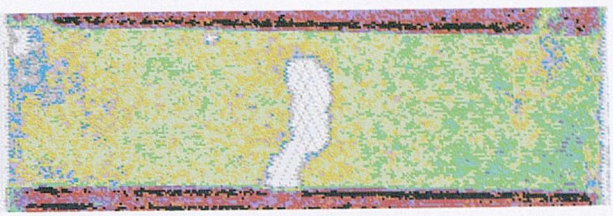


1CPPS11
(40cm)

1CPPS12
(50cm)

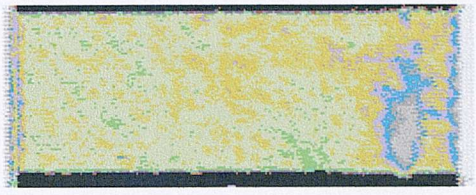


1CPPS13
(50cm)

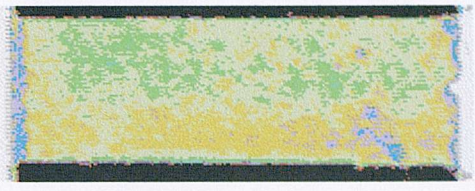


1CPPS14
(50cm)

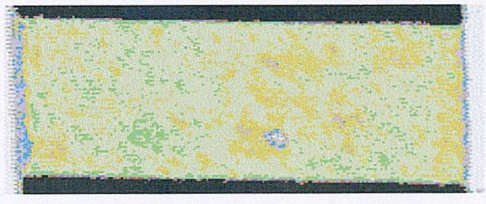
Small R-Glass Fibre Specimens



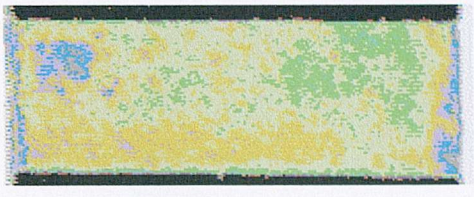
GPPS1
(10cm)



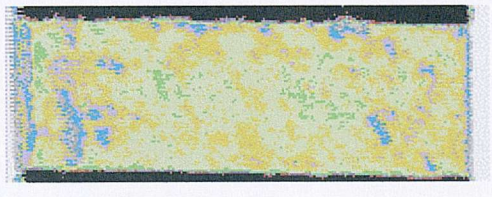
GPPS2
(10cm)



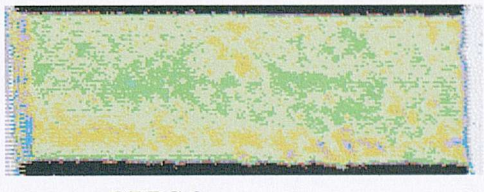
GPPS3
(10cm)



GPPS4
(10cm)



GPPS5
(20cm)



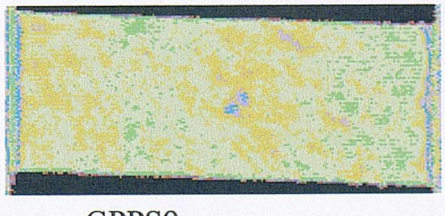
GPPS6
(20cm)



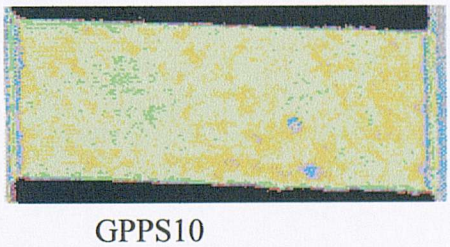
GPPS7
(20cm)



GPPS8
(30cm)



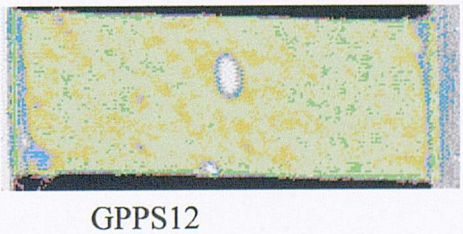
GPPS9
(30cm)



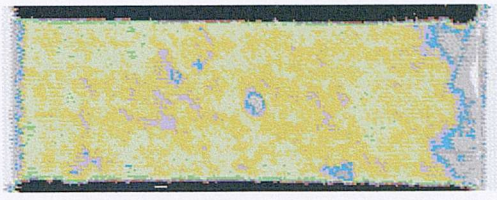
GPPS10
(30cm)



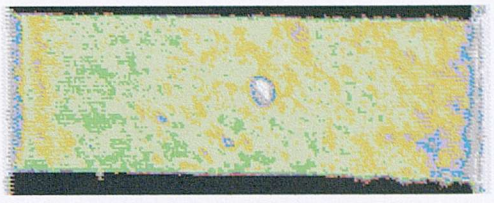
GPPS11
(30cm)



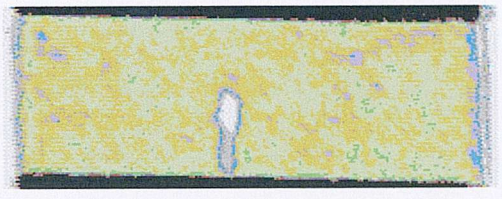
GPPS12
(40cm)



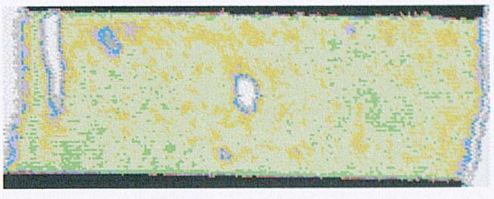
GPPS13
(40cm)



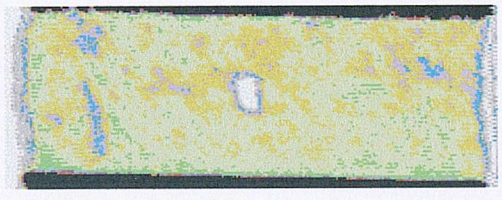
GPPS14
(50cm)



GPPS15
(50cm)

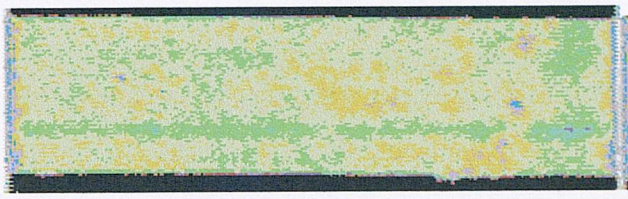


GPPS15
(50cm)



GPPS16
(50cm)

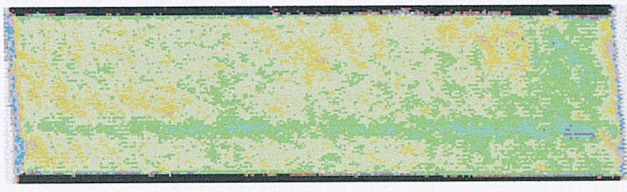
Long R-Glass Fibre Specimens



1GPPS1
(10cm)



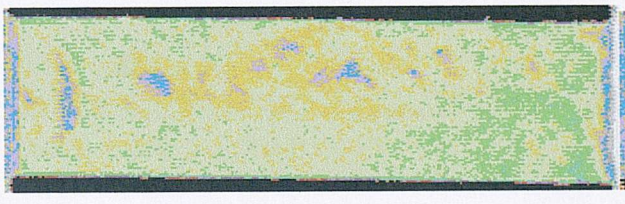
1GPPS2
(10cm)



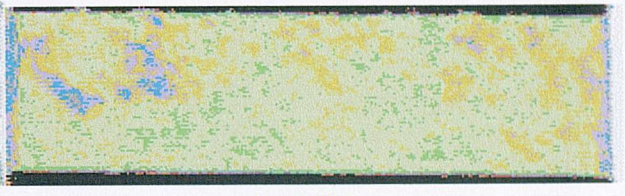
1GPPS3
(10cm)



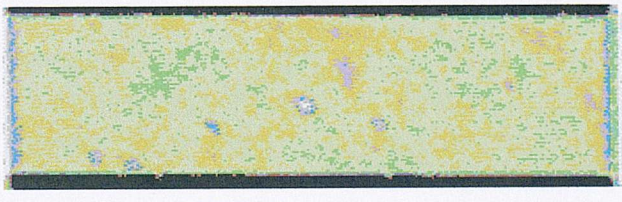
1GPPS4
(20cm)



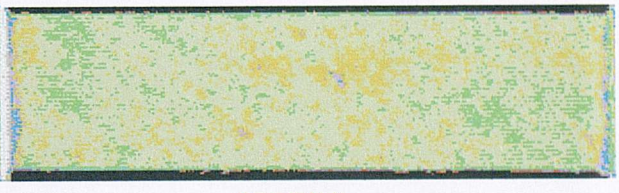
1GPPS5
(20cm)



1GPPS6
(20cm)



1GPPS7
(30cm)



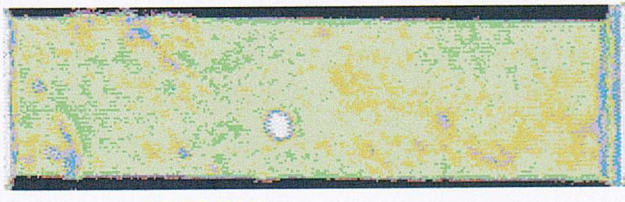
1GPPS8
(30cm)



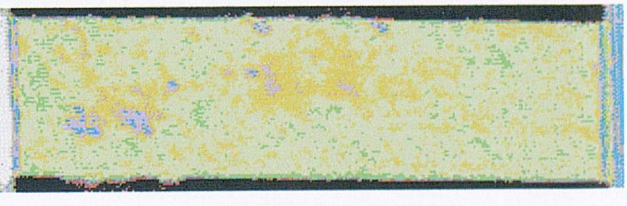
1GPPS9
(30cm)



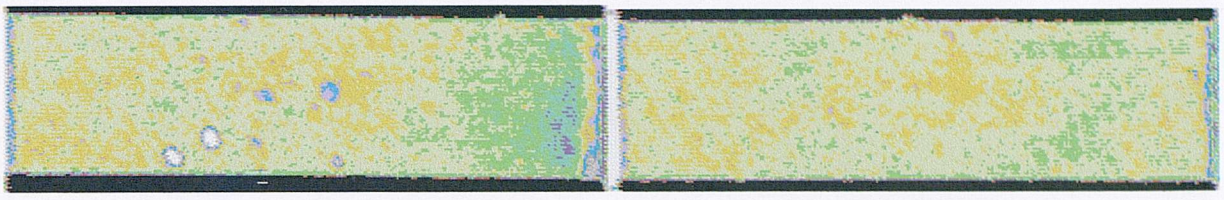
1GPPS10
(30cm)



1GPPS10
(40cm)

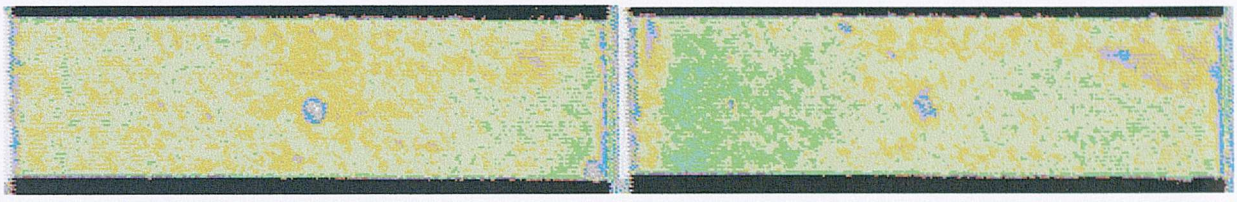


1GPPS11
(40cm)



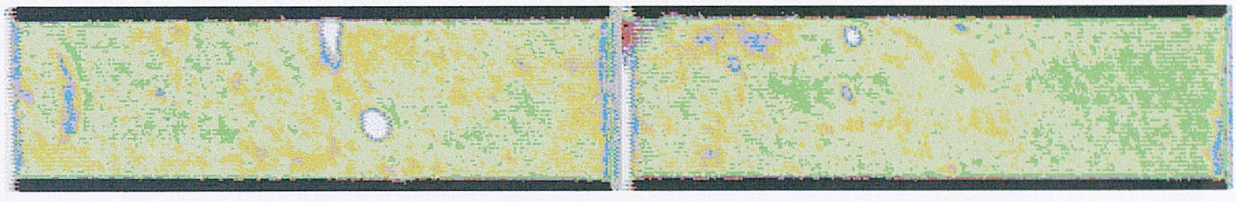
1GPPS12
(40cm)

1GPPS13
(40cm)



1GPPS14
(50cm)

1GPPS15
(50cm)



1GPPS16
(50cm)

1GPPS17
(50cm)